KENS REPORT-Ⅸ

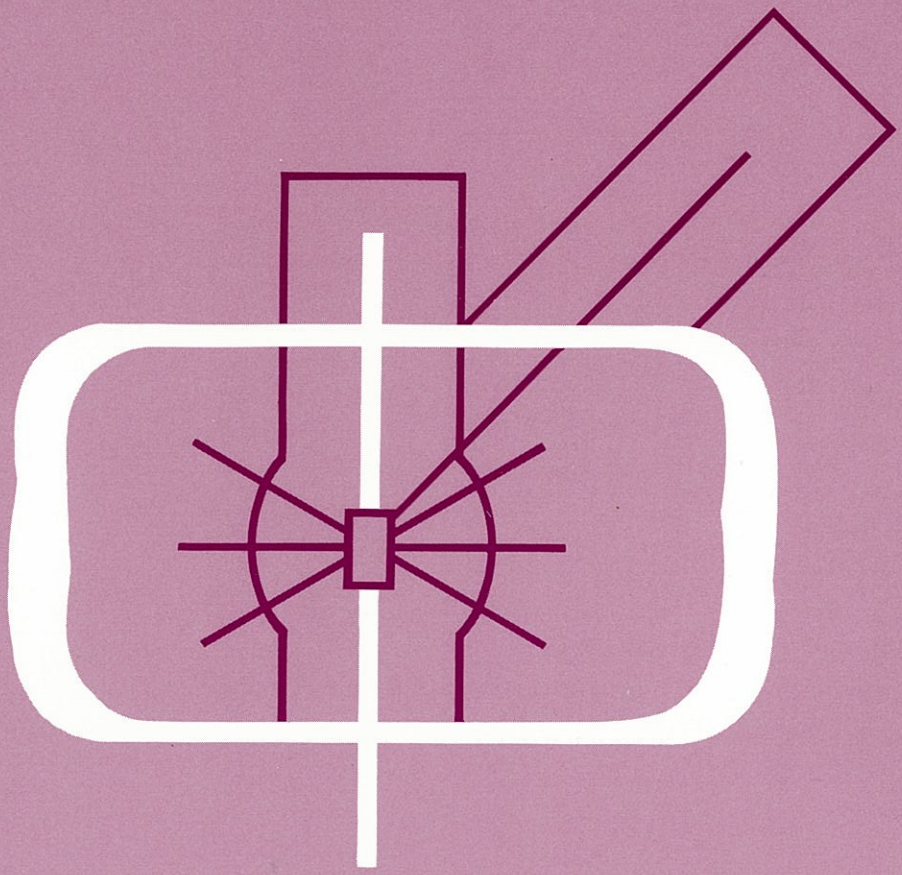

1991/92

NATIONAL LABORATORY FOR HIGH ENERGY PHYSICS, KEK

KENS REPORT - IX

1991/92

Edited by
M. Misawa
Y. Masuda
S. Ikeda

KEK Progress Report 92-2 M

KEK Reports are available from:

Technical Information & Library
National Laboratory for High Energy Physics
1-1 Oho, Tsukuba-shi
Ibaraki-ken, 305
JAPAN

Phone: 0298-64-1171
Telex: 3652-534 (Domestic)
(0)3652-534 (International)
Fax: 0298-64-4604
Cable: KEKOHO

KENS NEUTRON SCATTERING FACILITY

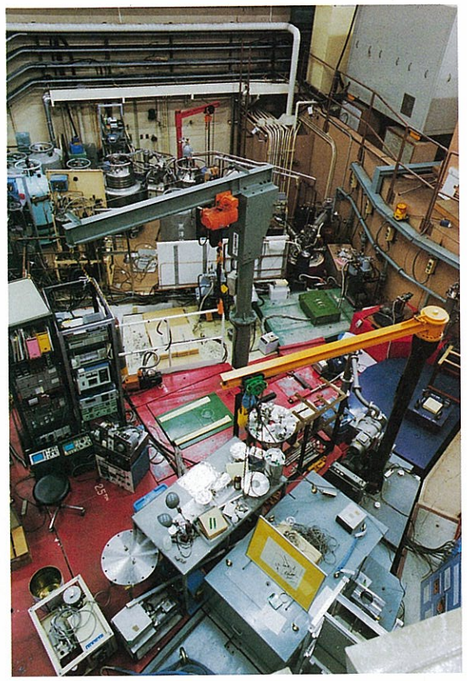

LAM-40, WINK, INC,
RAC, PEN, LAM-D

MAX	Coherent Inelastic Scattering Spectrometer
MRP	Medium Resolution Diffractometer under Extreme Conditions
HIT	Liquid and Amorphous Diffractometer
WIT	Thermal Neutron Small Angle Scattering Instrument
FOX	Single Crystal Diffractometer
LAM-D	Molecular Spectrometer
PEN	Polarized Epithermal Neutron Spectrometer
CAT	Sub-eV Spectrometer
RAT	eV Spectrometer
INC	Chopper Spectrometer
LAM-40	Quasi-elastic Spectrometer
WINK	Small and Medium Angle Scattering Instrument
HRP	High Resolution Powder Diffractometer
TOP	Polarized Cold Neutron Spectrometer
LAM-80ET	High Resolution Quasi-elastic Spectrometer
UCN	Ultra Cold Neutron Machine
SAN	Small Angle Scattering Instrument

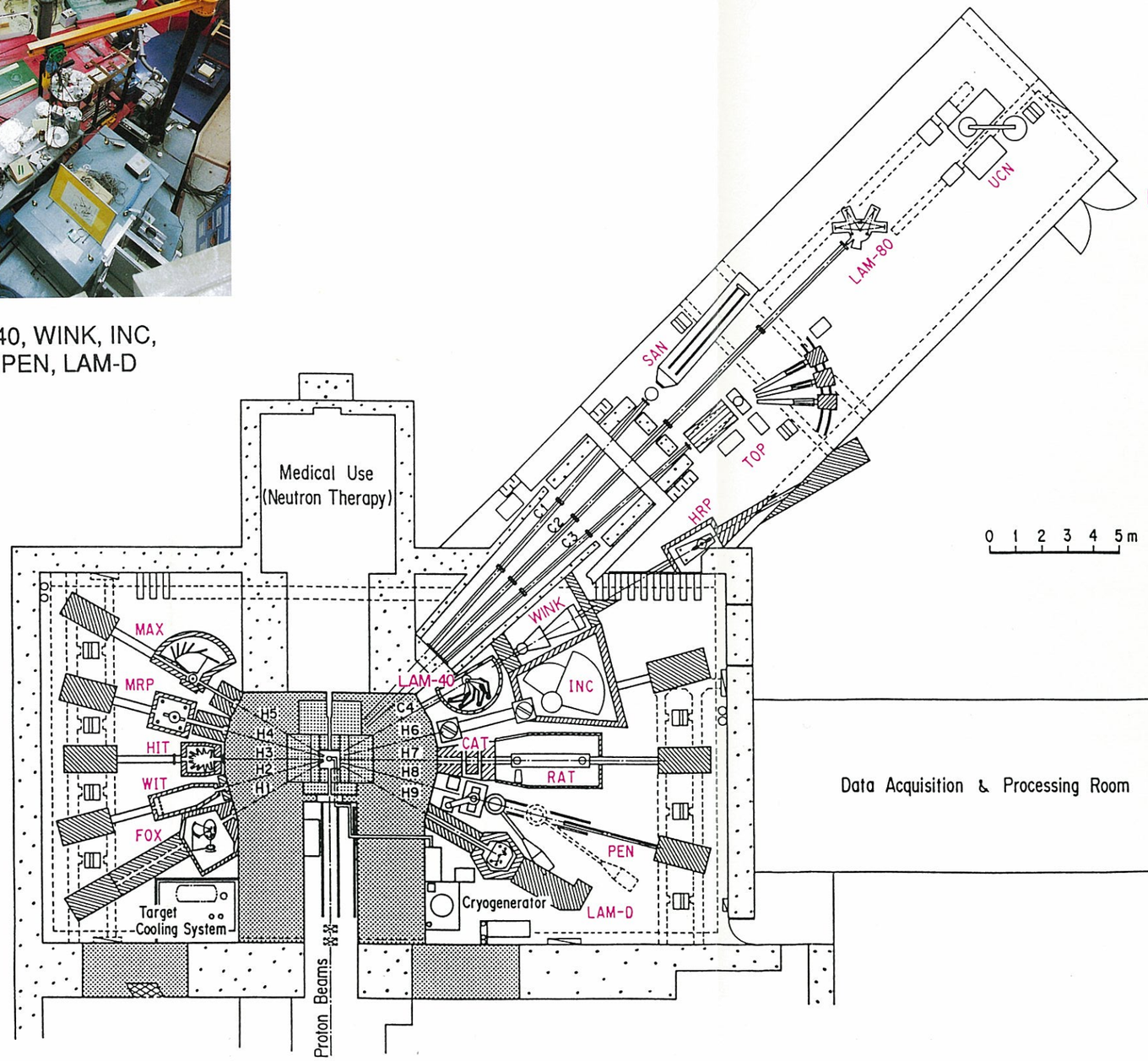

SAN, TOP, LAM-80ET

PREFACE

The present issue follows a previous issue, KENS Report-VIII published in December 1990 and summarizes research progress at the KENS facility during the period between October 1990 and September 1992.

During this period a great deal of efforts was devoted to improve the performance of the existing instruments. The construction of a small and medium-Q instrument, WINK, is almost completed and the instrument has successfully been utilized for the measurement of the micro void structure in SiC fiber, a new material. A glass and liquid spectrometer, HIT, which was very productive over past twelve years, retired recently and a new instrument, HIT-II, has just been installed at the position. A high-resolution powder diffractometer, HRP, is also one of the most productive instrument although this is a prototype one for instrumental development. A new instrument, HRP-II, is under construction, which will be installed at the experimental hall by September 1993. Developing research for new techniques also progressed. One highlight was the development of a ^{3}He polarizer. A polarization of about 50% has already been attained. By increasing the laser power a higher polarization, hopefully more than 80%, will be achieved in near future.

In this period, there was a considerable scientific progress in neutron scattering research. One highlight was a successful measurement of neutron diffraction from monolayer oxygen molecules on graphite. Many workshops and meetings on neutron scattering research in various fields were held at KENS to promote better sciences.

Recently the number of papers from the KENS facility is increasing considerably and seems to be approaching the maximum. Unfortunately the prospect of KENS-II, a next generation source, is still unclear due to the financial reason of the Japanese government. We are very much serious how to keep the scientific activities in near future without the realization of KENS-II. We must find some way out of the difficulty.

Oct. 8, 1992

Noboru Watanabe
Head of Booster Synchrotron
Utilization Facility

Contents

Liquids and Glasses

Polymers

Biologies

Magnetism

Surface

Outline

Prof. Watanabe (left) and Dr. Robinson (right) are discussing a crystal-field excitation.

Overview of the Progress at KENS

Hironobu Ikeda and Noboru Watanabe

Booster Synchrotron Utilization Facility, National Laboratory for High Energy Physics

I. Outline of the KENS Facility

The pulsed spallation neutron facility (KENS) at National Laboratory for High Energy Physics (KEK) began operation in June 1980. It is open to all scientists from the universities and national laboratories in Japan.

The present KENS Facility (KENS-I') has been successfully operated during the period since April 1990. The operation time of the 500 MeV booster synchrotron in the past year was about 3600 hours, and the beam time allocated for neutron experiments was about 1600 hours. The average proton-beam intensity was 1.5×10^{12} protons per pulse (ppp) or less, which was lower than the maximum value of 2×10^{12} ppp already achieved in 1988.

The depleted uranium target has been operated trouble-free since the beginning of its operation in 1985. We experienced no serious problems with the cryogenic moderator (solid methane at 20 K) in this period, because solid methane was renewed every two days before a "burp" can occur.

During the last financial year, 92 experiments including 13 large proposals by groups responsible for the instruments were carried out. Scientists who visited the KENS facility spent about 4000 man-days.

II. Instrumental Developments

There are currently 16 instruments at the KENS facility as shown in Table 1. There was appreciable progress in the instrumentation.

The construction of a new small/medium angle scattering instrument, WINK, started in 1989 and the instrument is now available for users. The instrument was designed to realize a wider coverage in momentum transfer from 0.015 to 20 A^{-1} with a much higher data rate, hopefully more than 10 times as high as that of the existing small angle instrument, SAN. WINK will be equipped with more than 250 conventional He-3 proportional counters at a wider range of the scattering angle from forward to backward within a few years.

In 1990, the highest resolution of about 1 μeV was achieved at KENS on a high-resolution spectrometer (LAM-80ET) by using the 002 reflection of mica as an analyzer crystal (Fig. 1). Note that the energy window simultaneously covered is very wide, -20 ~ +80 μeV.

The development of polarized ^{3}He as a broad-band polarizing filter for thermal and epithermal neutrons is in progress. ^{3}He gas, including a small amount of N_2 and Rb, filled to 3 atm. in an alminosilicate glass cell

Table 1. KENS neutron scattering instruments

Instrument Name		Range of Q & E					Resolution
Liquid and Amorphous Diffractometer	HIT	0.2	≤	Q	≤	$100A^{-1}$	$\Delta Q/Q = 0.006 - 0.05$
Small-Angle Scattering Instrument	SAN	0.003	≤	Q	≤	$4A^{-1}$	$\Delta Q/Q \approx 0.1$
Thermal-Neutron Small-Angle Scattering Instrument	WIT	0.03	≤	Q	≤	$0.7A^{-1}$	$\Delta Q/Q \approx 0.1$
Small/Medium-Angle Diffractometer	WINK	0.015	≤	Q	≤	$20A^{-1}$	$\Delta Q/Q \approx 0.1$
Multi-Purpose Diffractometer	MRP	1	≤	d	≤	5A	$\Delta Q/Q = 0.015 - 0.03$
High Resolution Powder Diffractometer	HRP	0.5	≤	d	≤	5A	$\Delta Q/Q = 0.003$
Single Crystal Diffractometer	FOX	0.2	≤	Q	≤	$40A^{-1}$	
Polarized Cold Neutron Spectrometer	TOP	0.02	≤	Q	≤	$0.6A^{-1}$	
Polarized Epithermal Neutron Spectrometer	PEN	0.02	≤	E	≤	100eV	
Ultra-Cold Neutron Machine	UCN						
High Resolution Quasi-Elastic Spectrometer	LAM-80ET			E	≤	0.3meV	$\Delta E = 1 - 5\mu eV$
Quasi-Elastic Spectrometer	LAM-40			E	≤	10meV	$\Delta E = 100\mu eV$
Molecular Spectrometer	LAM-D			E	≤	200meV	$\Delta E = 300\mu eV$
Sub-eV Spectrometer	CAT	3	≤	E	≤	1000meV	$\Delta E/E = 2\%$
Coherent Inelastic Scattering Spectrometer	MAX	0	≤	E	≤	100meV	$\Delta E = 2.5 - 10meV$
eV Spectrometer	RAT			E	≤	100eV	$\Delta E = 50meV$
Chopper Spectrometer	INC	2	≤	E	≤	1000meV	$\Delta E/E = 2 - 4\%$

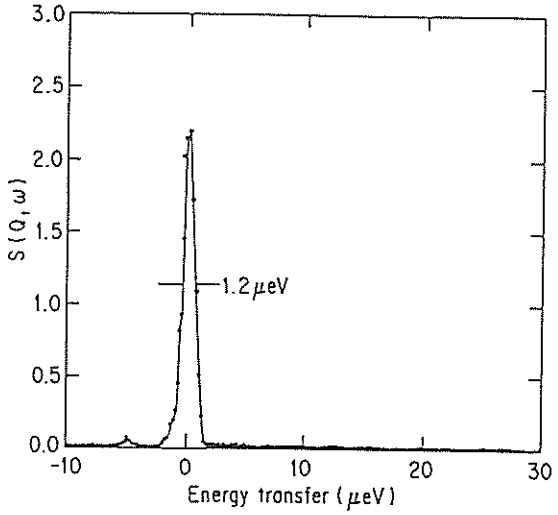

Fig. 1 Energy spectrum around the elastic peak of the N-Oxy γ picoline measured at 5 K on LAM-80ET. The energy resolution is about 1.2 μeV with a wide-energy window, -20~+80 μeV.

(4 cm long and 2.5 cm in diameter) was irradiated by photons (4W) of 795 nm from a titanium sapphire laser. A polarization of about 50% has recently been achieved.

The development of pulsed high magnetic field equipment for scattering experiments is now in progress. The highest field (up to 20 T) in the horizontal direction has already been achieved, and the construction of a new magnet with the field in the vertical direction (15 T) was completed in 1991.

A compact amplifier system for 8 detectors (K-AMP2, $16 \times 33 \times 7$ cm^3 in size) was newly developed. The system involves a pre-amplifier, a main-amplifier, a discriminator and a high-voltage supply for each detector. This system is used at the WINK, HRP-II etc. which are equipped with a huge number of detectors.

An upgrading of HIT, the total scattering spectrometer for S(Q) measurements of liquids and glasses has started. The new machine is called HIT-II, and was designed to realize a better momentum resolution at smaller scattering angles with a higher data-rate. HIT-II will be completed in 1992.

The construction of a new high-resolution powder difractometer, (HRP-II), has started. Although the present HRP is a prototype instrument equipped with only 12 normal He-3 counters, it has been very productive and busy. HRP-II was designed to have large counter banks, comprising of many 1D-PSD's at the backward, 90°, and lower angles in order to improve the data-rates (about 5 times higher than the present HRP), resolution ($\Delta d/d \sim 0.002$) and range of the d-spacing covered. The new instrument will be completed in 1993.

The detailed description for HIT-II and HRP-II is given later.

III. Neutron Scattering Experiments

The determination of the crystal structure of high-Tc superconductors still represents an important research field. Among many substances resolved on HRP, one example which concerns the incommensurate lattice modulation is refered to in Fig. 2.

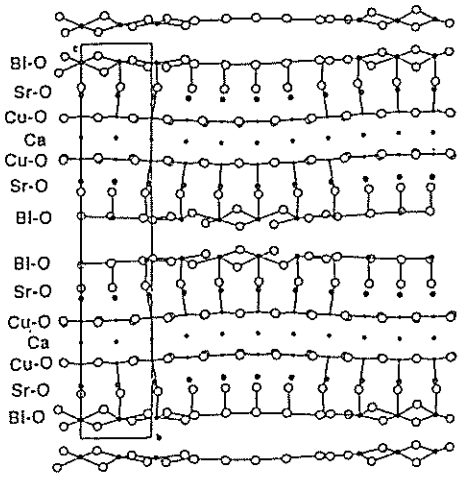

Fig. 2 Modulated structure of $Bi_2(Sr, Ca)_3Cu_2O_{8+x}$ projected on the b-c plane determined from diffraction data obtained on HRP.

The first experiment on the newly developed reflectometer was performed with polarized neutrons. Experiments on an artificial metallic multilayer system, Ni/Ti in which each Ni and Ti layer has a thickness of 50 Å, were successful. Figure 3 shows the reflectivity as a function of the neutron wavelength, where the direction of the incoming neutron polarization is either up or down. It was found from these that the magnetic moment of a few layers of the Ni metals near the interface is absent.

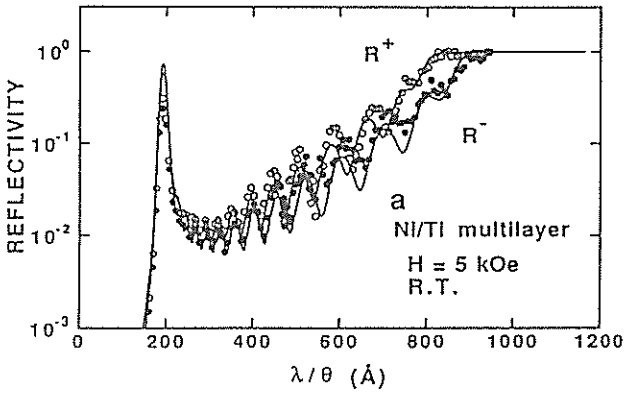

Fig. 3 Polarized neutron reflectivity from a multilayer Ni/Ti.

One interesting recent scattering experiment was the observation of magnetic scattering from oxygen monolayer films adsorbed on grafoil. The experiment was performed on the MRP diffractometer, revealing that the magnetic moments of the oxygen molecules are ordered antiferromagnetically below the phase transition temperature (12 K).

High-resolution spectroscopy experiments involving a methane monolayer adsorbed on graphite were performed on LAM-80ET. The rotational tunneling energy in methane molecules depends on the local symmetry and the electric field surrounding the molecules; high resolution measurements are therefore indispensable to obtain detailed information concerning the molecular structure. Figure 4 shows the energy spectrum in methane molecules measured at T = 5 K.

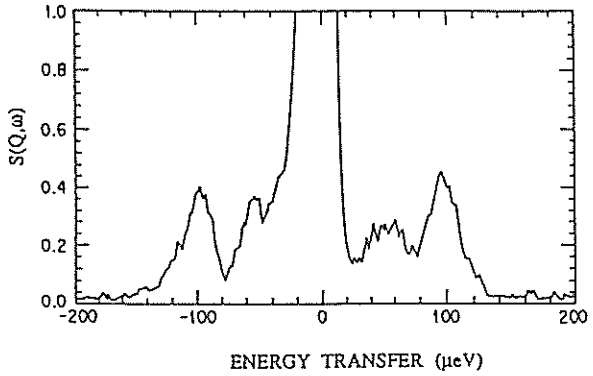

Fig. 4 Inelastic neutron scattering from methane monolayer films adsorbed on graphite (T = 5 K).

Polarized neutron diffraction measurements on multilayered films were carried out using the TOP spectrometer. In Fe/Nd multilayered films on a glass substrate the spin reorientation was observed both in the Fe and Nd layers in the presence of a magnetic field. This fact indicates that the perpendicular anisotropy of the Nd layer is a major origin of the spin reorientation.

At the FOX diffractometer, atomic and magnetic diffuse scattering was observed in a spin-glass system of Ag-20.8 at. % Mn single crystal. By analyzing each diffuse intensity centered at a different reciprocal lattice position, it was found that the correlation length of Mn atoms is different from that of Mn spins. This experiment provides new information concerning a Fermi surface effect on the magnetic interactions in metallic spin glasses.

The scattering functions for Si-C fibers, new structural material working at a higher temperature, was extensively studied over a wide range of momentum transfer covering small-angle scattering and Bragg reflection regions using WINK. Figure 5 shows the S(Q) at small and intermediate Q-range; scattering from the micro-voids was for the first time clearly observed over the range Q = 0.1 ~ 1 $Å^{-1}$. These results are very important for understanding the heat treatment-temperature dependence of the mechanical properties of this material.

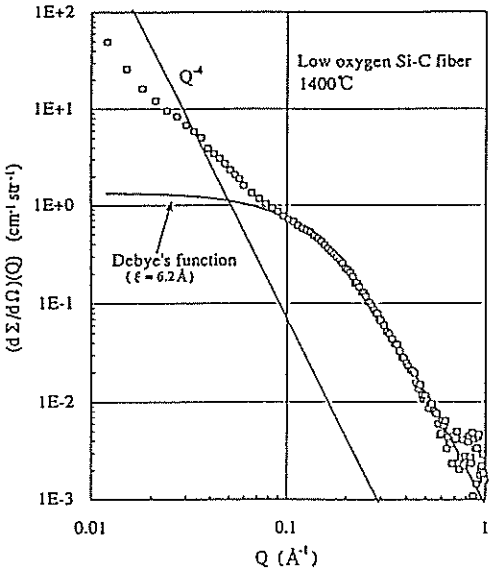

Fig. 5 Scattering function for low-oxygen Si-C fiber after a heat-treatment at 1400°C in small and intermediate Q-ranges.

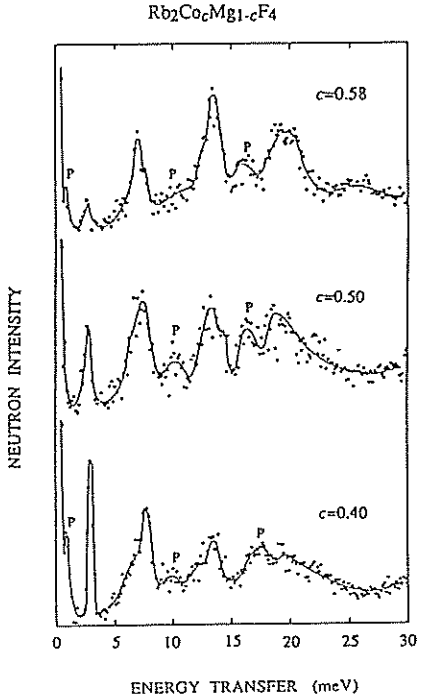

Fig.6 Inelastic neutron scatteing at 25 K from $Rb_2Co_cMg_{1-c}F_4$. The experiments were performed with a fixed outgoing neutron energy of 4.62 meV. The solid lines are guides to the eye. P denotes the phonon peaks identified from the room-temperature measurements.

To elucidate magnetic excitations in a diluted Ising magnet over the entire magnetic concentration, neutron inelastic scattering experiments were performed on two-dimensional Ising magnets ($Rb_2Co_cMg_{1-c}F_4$ (c = 0.1, 0.2, 0.3, 0.4, 0.5, 0.58)) at the LAM-D spectrometer. It was found for the first time that Ising-cluster excitations and intra-cluster excitations coexist over the entire concentration region (Fig. 6).

IV. Future Program

The fundamental concept of the target station for KENS-II, a next-generation Japanese pulsed spallation neutron source in the Japanese Hadron Project, is almost completed; the main part has already been reported in previous KENS Reports. We recently performed further optimization studies on a so-called flux-trap-type target-moderator-reflector configuration by computer simulation, since this configuration has various possibilities for increasing the slow-neutron beam intensity. The detailed discription for the results is given in this volume.

V. Japan-UK Collaboration

KEK arranged for a high-resolution chopper spectrometer, called MARI to be installed it at ISIS. The construction of MARI was completed in 1989; commissioning was carried out in 1990. The instrument has been available to users since 1991. In FY 1991, 14 experiments (7 on MARI, 7 on other instruments) were carried out under the Japan-UK Collaboration Program and new important informations in various scientific fields are now coming up. Some examples are listed below.

Using MARI, spin dynamics in low-dimensional Heisenberg antiferromagnets (La_2NiO_4, $KFeS_2$, $CsVCl_3$, etc.) were successfully studied using single crystals. The hydrogen potential and wave function in a hydrogen-bonded compound KDP was studied, providing an important result in connection with phase transitions. The chemical structure of metal-metalloid amorphous alloy ($Pd_{80}Si_{20}$) was determined from measured dynamical factors $S(Q, \omega)$'s. The phonon density of state (PDOS) of super-and non-superconducting $La_{1.85}Sr_{0.15}Cu_{1-x}Zn_xO_4$ (x = 0, 0.02) were measured; it turns out that there exists a finite difference between both PDOS's which may play an important role in the superconducting mechanism. And so on.

Beam-line Operation and Development

Y. Irie, Y. Yano, H. Fujimori, N, Kaneko, T. Tahara, Y. Kobayashi, S. Muto and T. Adachi*

BSF, National Laboratory for High Energy Physics, 1-1 Oho, Tsukuba-shi, Ibaraki 305
*Accelerator Division, National Laboratory for High Energy Physics, 1-1 Oho, Tsukuba-shi, Ibaraki 305

I. Summary of BSF Operatiron

Table 1 shows a summary of BSF operation from October, 1990 through July, 1992. Total operation time is 7,161 hours and the number of protons delivered to BSF experiments and proton therapy is 4.7×10^{20}. The PS cycle time was changed in October, 1990 from 2.6 sec to 4.1 sec, which increased the duty factor by 8.6% for BSF operation. Also in this October, a three-week run was cancelled due to an ultra-slow muon facility of University of Tokyo which was being under construction, while 12 GeV PS ring was operating. (Just one year later in 1991, the first proton beam was successfully led to the beam dump of the ultra-slow muon facility after fifty minutes beam-line tuning.) A coil-shorting of beam-line magnet VB4, which diverts a beam upward by 7.2 degrees into BSF beam-line, occurred at the end of October in 1990. A new pulsed switching magnet PVB4 was installed as a replacement and it took a week to fix. The new PVB4 facilitates beam sharing between a dump experiment and the existing BSF experiments. Thus nuclear spallation experiments in the dump room have been carried out five times to date by Japan Atomic Energy Research Institute.

In Table 2 are shown, the average beam intensity supplied to BSF in units of 10^{11} protons per pulse (ppp) or an average current and the beam transmission. As can be seen, the beam intensity regained its high

Table 1. Summary of BSF operation from October, 1990 through July, 1992.

	Neutron Experiment	Meson Experiment	Proton Therapy	Spallation Experiment	Beam-line study, etc	Total	Ratio (%)
Beam On	2970.6	2732.4	1108.5			6811.5	95.1
Reject	12.7	83.9	0.8			97.4	1.4
Beam-line fault	12.6	11.2	4.5			28.3	0.4
Accelerator stop	61.0	78.4	12.9			152.3	2.1
Miscellany	5.6	3.1	10.2			18.9	0.3
Utility				27.7	24.9	52.6	0.7
Supplied no. of protons(10^{18})	241.0	218.6	10.1			469.7	

(units are hours unless otherwise specified)

Table 2. Beam intensity and Transmission

experiment / period	NEUTRON Average intensity (10^{11}ppp)	(μA)	TR (1)	(2)	MESON Average intensity (10^{11}ppp)	(μA)	TR (1)	(2)	PROTON THERAPY Average intensity (10^{11}ppp)	(μA)	TR (1)
1990 October - December	9.8	2.8	0.96	0.88	9.2	2.6	0.95	0.87	9.4	2.7	0.98
1991 January - March	9.5	2.7	0.97	0.88	9.1	2.6	0.94	0.87	9.5	2.7	0.98
1991 April - July	8.1	2.3	0.99	0.90	8.9	2.6	0.98	0.89	8.8	2.5	1.01
1991 October - December	7.5	2.2	1.00	0.85	7.2	2.1	0.99	0.87	7.5	2.2	1.02
1992 January - March	14.6	4.2	----	0.96	16.1	4.7	----	0.97	15.4	4.4	----
1992 May - July	16.2	4.7	1.02	0.99	15.1	4.3	1.01	0.98	15.3	4.4	1.00

TR (1) is defined as the ratio of beam intensity at the beam-line exit to that at the entrance.
TR (2) is the ratio of beam intensity at the beam-line entrance to that in the booster synchrotron.

value in the second half of the period, which had been lost since May in 1990 (Fig. 1). The operation at the first crest in March, 1989 revealed a couple of objects which limited the beam intensity from radiation protection point of view. The one was poor shielding around meson-production target and the other was a small vertical aperture of a branching vacuum chamber downstream of a pulsed switching magnet PHB1. These all were cleared by November, 1989. However, the reason of relatively large recession in beam intensity between the last two crests is not clear, but probably due to the fact that the main effort in PS was given to the deuteron acceleration study.

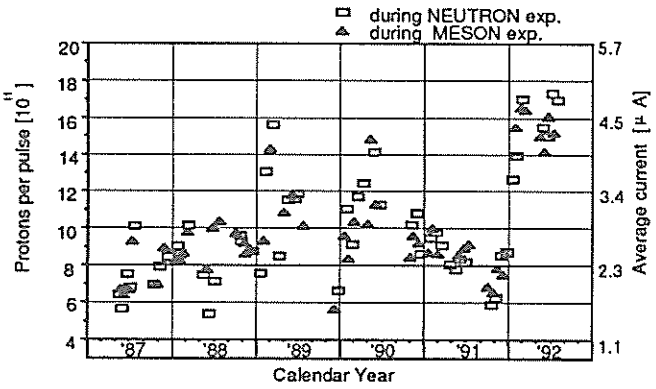

Fig. 1 Average beam intensity and current delivered to neutron and meson experiments during the last five years.

Table 3 shows the dose rate around radiation controlled areas within BSF site, when the beam is supplied to the specific experimental area which is noted in the first line. These data were sampled during February through July, 1992. (The strong influence of 12 GeV ring operation on the data has not been recognized so far.) The highest rate is 80% interlock level at YEL 304 when full pulses, ie 73 pulses per PS cycle time, are delivered to the meson lab No. 2 (ultra-slow muon facility).

Table 3. Exposure dose around BSF area, which is expressed in % per regulation dose and a unit injection current. The regulation dose is 0.2 and 20 mSv/h for YEL and ORG, respectively.

Experimental Area		NEUTRON	MESON No. 1	MESON No.2
Interlock Level		%/μA	%/μA	%/μA
YEL 0.2 μSv/h	301	9.5~10.1	1.6~0.83	(display error)
	302	2.1~3.1	1.9~2.7	~0.6
	304	2.2~3.4	2.5~3.2	12~16
	305	0.7~1.1	0.8~1.2	13~15
ORG 20 μSv/h	303	~0.2	14~16	~0.2
	304	~0.1	9~12	~0.1
	305	7.0~7.5	~0.3	~0.02

II. Instrumentation

Since beam-profile monitors are found to be a major source of high residual radioactivities along the beam-line as well as exposure rate at the area monitors, the profile monitors are only used for initial beam-steering and are then retracted from the line. The beam loss monitor, made of a gas proportional counter, is used instead so as to watch the deviation of the beam orbit afterwards. Twelve sets of counters are now installed along the line, including the primary proton beam-line in meson lab No. 2. Fig. 2 shows the

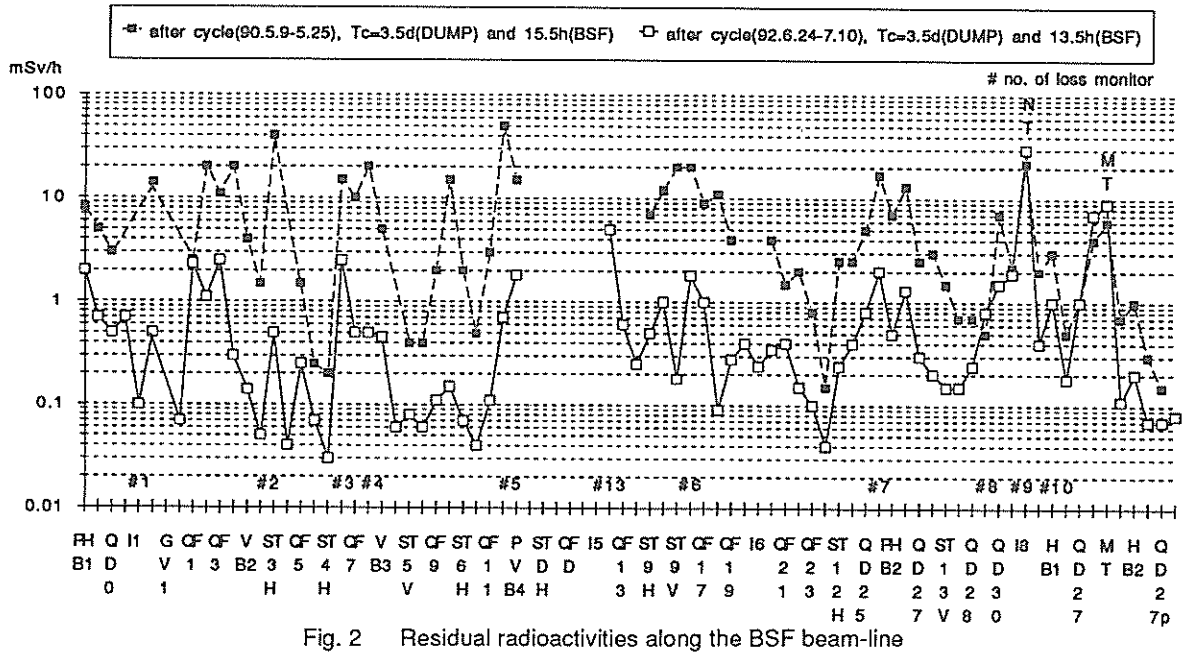

Fig. 2 Residual radioactivities along the BSF beam-line

result of such procedure. Residual radioactivities after the three-week run in July, 1992 were alleviated down to about one-tenth of those in the last crest in May, 1990 when all the profile monitors were set at measuring positions during the whole run.

A pulsed-beam intensity monitor of the induction type was calibrated by feeding a current inside a toroidal core (Fig. 3); the current typically has a 4A peak with a duration of 100 nsec which corresponds to 18×10^{11} ppp. The high-frequency characteristics of the measuring device were corrected for integration of the pulsed current. The accuracy of the calibration is ±0.8% over a variety of pulse conditions. Consequently, the beam transmission from the booster synchrotron through the beam-line entrance in Table 2 was apparently increased by 10%.

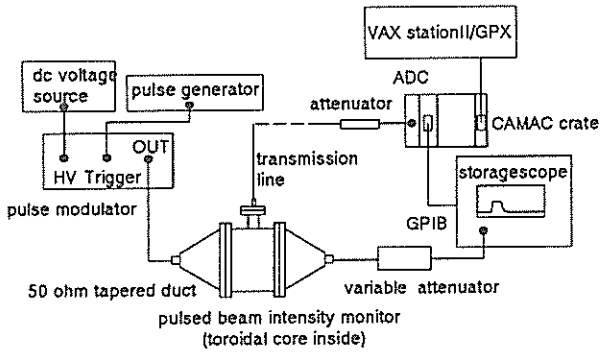

Fig. 3 Schematic diagram of the calibration system

An effort is underway to study new probes such as a nondestructive beam-profile monitor which utilizes scattering of primary protons with residual gas, and a real-time halo monitor which measures the penumbra of the beam by scanning a thin wire across the beam.

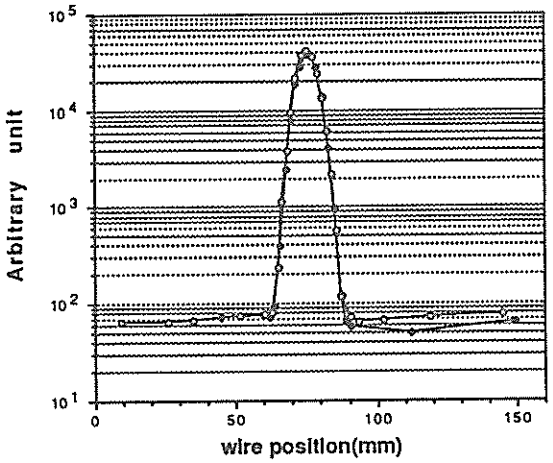

Fig. 4 Horizontal beam-profile measurement with wire scanning.

Fig. 4 shows the result of real-time halo measurements. The scanning wire (1mmϕ) is situated at the T2 focal point on the beam-line. The plastic scintillation counter, located 4 m upwards of the wire, is embedded in the shielding bank. It took about 30 minutes to measure when the beam was delivered to the neutron target.

Meeting

Workshop on Polymer Science by Neutron Scattering

The workshop was mainly devoted to a theoretical as well as experimental aspect of miscells and emulsions, and a related neutron scattering instrumentation. Richard K. Heenann and Alexander Hannon from ISIS in UK were anticipated in the meeting as a part of the Japan-UK collaboration program.

It was organized by H. Hasegawa and M. Furusaka, and held on September 9-10, 1991.

Second Workshop on Phase Separation with Ordering

This is a second workshop on phase separation processes in alloy systems as AlLi alloy which show a complicated behavior due to the coexistence of ordering processes. Three scientists from abroad were invited: D. Laughlin (Carnegie Mellon Univ.), H. Chen (Univ. of Illinois) and C. Windsor (Harwell Lab.).

The workshop was cosponsored by KEK and The Light Metal Educational Foundation, Inc., organized by K. Osamura and M. Furusaka and held on march 16-17, 1992.

Workshop on P- and T-Violation Neutron Experiment

On June 10, 1992, recent status of the P- and T-violation experiment on neutron induced reaction and related topics were discussed at KEK. Polarization of incident neutron, target nucleus, neutron-spin analyzer nucleus were discussed. The method of measure the P-violating neutron-spin rotation, P-violating neutron capture γ-ray angular correlation and the T-violating neutron-spin flip process were also discussed.

Workshop on Neutron scattering from Magnetic Materials

On March 29, 1991, recent scientific problems on magnetic materials were discussed at KEK. Magnetic excitations in triangular antiferromagnets, percolated systems, spin-glasses, heavy fermion systems etc. were discussed. Technical and scientific problems on the future experiments under pulsed high magnetic field and high pressure were also discussed among 80 attendants.

Workshop on Formation of Supermolecular Structures in Composite Fluid

On July 2 and 3, 1992, workshop on formation of supermolecular structures in composite fluid was held at KEK. A special attention was paid to the theoretical approaches to the phase rule and dynamics and the related experiments. Joint discussions between polymer scientists and neutron scientists on the cross-disciplinary sciences were fruitful for the future progress of neutron experiments on low energy excitations and time-resolved small angle neutron scattering.

Workshop on Neutron Scattering for Low Energy Excitations

Workshop on low energy excitations was held on November 13 and 14, 1991 at KEK. Three scientists from abroad, F. Mezei (HMI), a. Magerl (ILL) and R. Zorn (Julich), joined us. New experimental results concerning low energy excitations in glass-transition systems, spin-glasses, disordered systems and surface adsorbed system, and hydrogen tunneling in metals etc. were presented and discussed.

Workshop on Neutron Scattering from High-Tc Superconductors

On December 10 and 11, 1991, workshop on the mechanism of high Tc superconductors was held at KEK. Experimental and theoretical studies to resolve the key mechanism in high Tc superconductivity were reviewed and discussed.

Workshop on hydrogen-bonded Materials

Workshop on hydrogen-bonded materials was held on January 21-22, 1992, and dynamical motion and spatial distribution of hydrogen in ferroelectric compounds and the other chemical materials were discussed. One of interesting topics in this meeting was a role of the hydrogen in the ferroelectric compound KDP. The possibilities of the tunneling model or the order-disorder model were extensively discussed with many theoretical and experimental studies.

Workshop on hydrogen Science

Workshop on hydrogen science was held on September 29-30, 1992. Many experimental studies on ferroelectric, chemical and biological materials obtained by X-ray diffraction, light scattering, NMR and neutron scattering were reported, and the hydrogen position and its motion were discussed in relation to functions of these materials.

International Workshop on Neutrons in Biology

An International Workshop on Neutrons in Biology was held at the Sunpia Hotel closed at JAERI (Japan Atomic Energy Research institute) from September 4-5, 1992. The workshop was one of the satellite meetings of BSR 92 (the 4th International Conference on Biophysics and Synchrotron Radiation). 41 scientists in 7 countries attended. The purpose of the workshop was to introduce the facilities, to exchange the recent results obtained in the different laboratories each other and to discuss plans for neutron crystallography in biology. In spite of the lack of the time, all the discussions were fruitful. The proceedings of the workshop were published.

Workshop on KENS Future Program

Workshop on KENS Future Program was held on 25 March 1992. This workshop was aimed at discussing the upgrade of the present neutron source of KENS. The workshop was organized mainly in three sessions, i.e. 1) upgrading Booster synchrotron accelerator, 2) possibility of increase of neutron yield by reducing the moderator-decoupling energy, 3) modification of moderator system so as to have good pulse shape and good energy resolution.

New Instruments

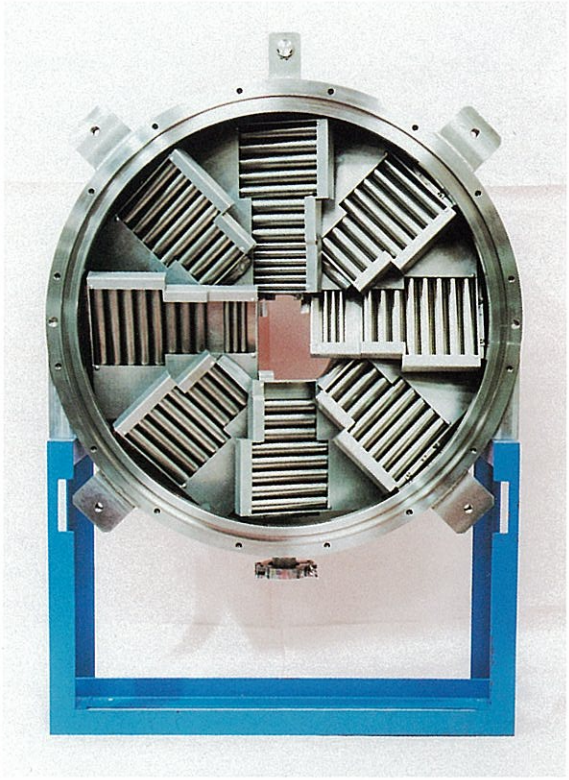

Small angle detector bank of WINK

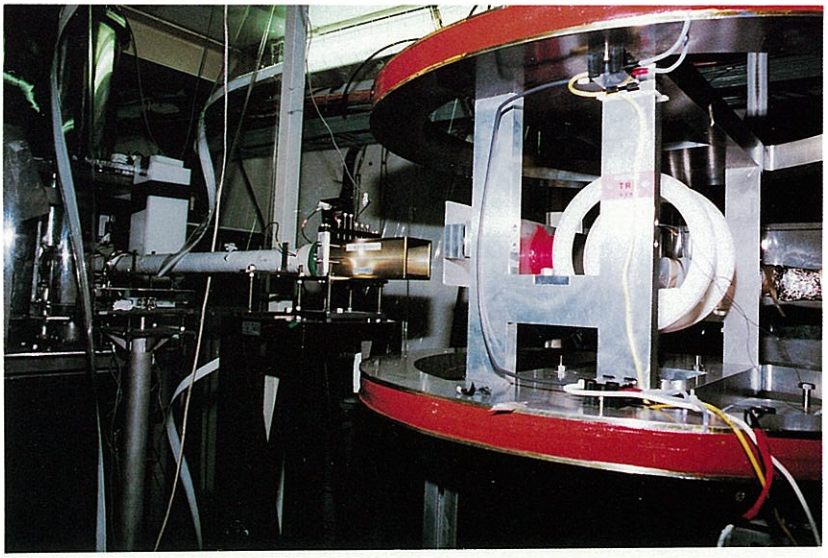

Polarized ^{3}He filter

HRP-II

T. KAMIYAMA[1], H. ASANO[1], N. WATANABE[2], M. FURUSAKA[2], S. SATOH[2], I. FUJIKAWA[2], H. IKEDA[2] and F. IZUMI[3]

[1] Institute of Materials Science, University of Tsukuba, Tsukuba-shi, Ibaraki 305, Japan
[2] National Laboratory for High Energy Physics, Tsukuba-shi, Ibaraki 305, Japan
[3] National Institute for Research in Inorganic Materials, Tsukuba-shi, Ibaraki 305, Japan

HRP-II (Fig. 1) is a high-resolution diffractometer with large back-scattering bank as well as 90° and low angle bank. HRP-II will replace the present high-resolution powder diffractometer (HRP) in the summer of 1993.

HRP has been successfully operated since 1983. After the high-T_c superconductors have been discovered, HRP has been one of the active instruments in the world to determine their crystal structures precisely. However, the measuring time is usually more than ten hours for one data. In many cases, therefore, the measurements have been performed only at room temperature or at several temperatures. There is very high and increasing demand for powder diffraction at many different temperatures for one experiment, especially for studies of the samples with phase transitions. In addition, some of the samples are practically difficult to obtain in a large amount, as in fabricating them under high pressure.

By increasing a detector solid angle at the back-scattering bank, HRP-II will achieve a tenfold increase of neutrons at detectors, and will allow 1/10 of measuring time with a standard sample size, or very small sample volume (300 mm^3) to be studied in ten hours with better resolution($\Delta d/d$=2x10^{-3}).

Another large-area detector bank will be installed at 90°. This bank is designed principally for studies of powder samples under special environment such as high pressure with resolution of $\Delta d/d$=5x10^{-3}. The scattering geometry has significant advantages for experiments of this kind, because suitable collimation of incident and outgoing beams can eliminate scattering from the surrounding of the sample like pressure medium. Studies of textures and materials strength under special environment would also be possible with the 90° bank.

The third large-area detector bank will also be installed at 30°. This bank covers a d-spacing range up to 20 A with resolution better than 2x10^{-2}. The obtained data from this bank will be used to analyze magnetic structures and crystal structures with large unit cells.

One of the remarkable features of HRP-II is to utilize half-inch ^{3}He position sensitive detectors (PSD's) instead of normal ^{3}He detectors. In the back-scattering bank, PSD's can cover the large back-scattering area without sacrificing resolution. We can also check and correct the effect of preferred orientation of the powder sample. Adopting PSD has many other advantages. High resolution single crystal diffraction is one of the promising applications of PSD on HRP-II. PSD and the TOF method enable large area of reciprocal space to be explored simultaneously. The fine structure of the Bragg reflection due to crystalline imperfection and diffuse scattering and their changes with temperature could be overlooked with very good resolution. The 30° bank equipped with PSD would be particularly advantageous for investigations of magnetic scattering from single crystals. The TOF method enables large area of low Q reciprocal space to be explored simultaneously, which would be powerful for searching new magnetic structures.

The design of the instrument is now on the final stage and much of the installation will be completed during the summer of 1993, with first commissioning operation scheduled for following autumn. Until 1992, a hundred detectors have been purchased for back-scattering bank, and the scattering vacuum tank with the detector mounting frames was constructed. The design of detector electronics has been completed and submitted to manufacture. Construction of the 90° bank system has been started in collaboration with National Institute for Research in Inorganic Materials. The majority of the remaining items except the 30° bank will be installed in early 1994. It is anticipated that the 30° bank system (detectors and electronics) will also be installed in the following year.

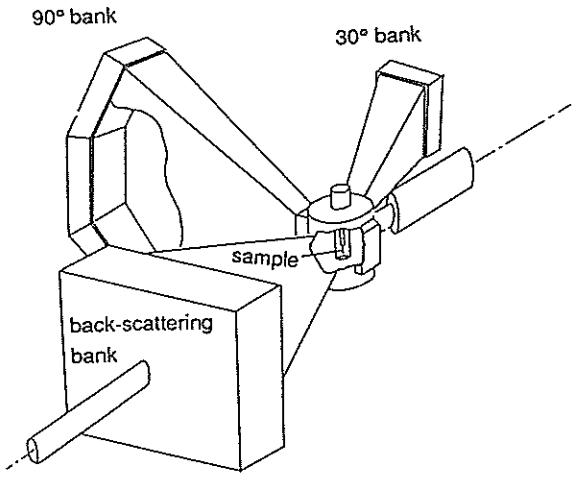

Fig. 1. Layout of HRP-II. The detector banks of back-scattering, 90° and 30° are located approximately at 1m, 2m and 2m position from the sample, respectively. All the detector banks will be filled with dried air to reduce the detector noise.

New High Intensity Total scattering spectrometer (HIT-II)

T. Fukunaga, M. Misawa*, Fujikawa* and S. Satoh*

Department of Crystalline Materials Science, Nagoya University, Furo-cho, Chikusa-ku, Nagoya 464
*National Laboratory for High Energy Physics, 1-1 Oho, Tsukuba-shi, Ibaraki 305

This paper reports the new HIT-II spectrometer that has been designed to investigate the atomic structure of liquids, glasses and amorphous materials. The old HIT-I spectrometer[1] was constructed in 1980 and has been worked for 12 years. During the period a number of measurements on various samples have been carried out. The HIT-I spectrometer was designed to see the high Q region of the structure factor S(Q). The detector array located at lower scattering angle was not enough to accumulate the good data statistically in the low Q region of S(Q). However, recently liquids with light elements have been investigated by using only the low-angle counters, because the analysis of the low angle scattering data allows us to get a precise S(Q) with particularly small correction of recoil or Placzek effects. Therefore, the HIT-II spectrometer has been designed to improve the count rate of the scattered neutrons in the forward scattering direction.

The design of the HIT-II spectrometer was carried out through the following criteria;

1. S(Q) should be measured in the wide Q range.
2. Many neutron detectors were located at the forward scattering angle to get reasonable count rate in comparison with that at the high scattering angle.
3. Resolution should be adequate, no greater than necessary, to keep a reasonable count rate.
4. The sample environment equipments as used in HIT-I, such as the sample changer, high temperature furnace, low temperature refrigerator and magnet, should be used.

Figure 1 shows a schematic diagram of the final form of the HIT-II spectrometer with 208 He-3 detectors located around the vacuum chamber. The detectors are arranged from $2\theta=10^\circ$ to $2\theta=160^\circ$ to get the scattered data of the wide Q range. The forward detectors are separated into 6 banks each of 26 detectors, which are 14 detectors of 12" in height and 1/2" in diameter, 6 detectors of 8" in height and 1/2" in diameter and 6 detectors of 4" in height and 1/2" in diameter. The 156 detectors located in the forward scattering angle may be enough to get reasonable scattering data within an appropriate time. However, only 52 detectors has been installed now due to the financial difficulties. The 150°, 90° and 50° angle detector banks are constructed by 16 detectors of 12" in height and 1" in diameter, 20 detectors of 12" in height and 1" in diameter and 16 detectors of 12" in height and 1/2" in diameter, respectively.

The detailed detector arrangement is shown in Fig. 2. The detectors of 150° angle banks were arranged by geometrical time focusing and electrical hardware focusing method. The 90°, 50° and forward(30°-10°) angle detectors were also set at the electrical hardware focusing positions. The scattered flight path length has been determined to give both high count rates and modest geometrical Q resolution.

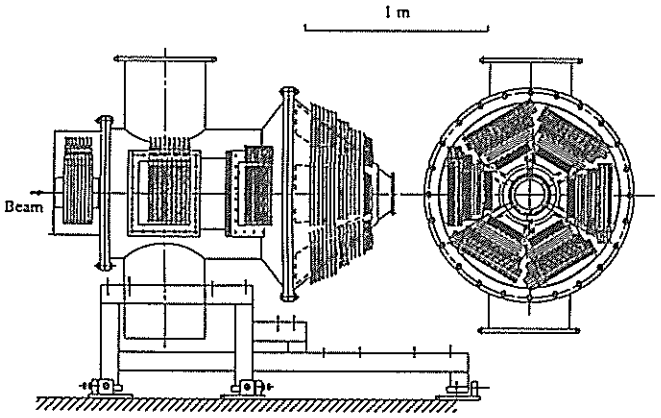

Fig. 1 The schematic diagram of the new HIT-II spectrometer

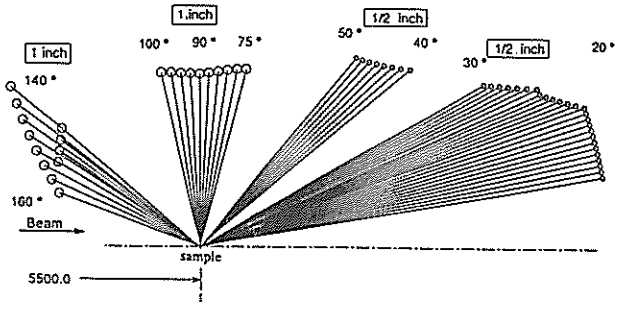

Fig. 2 The detailed detector arrangement, which is shows 1/2 of 150, 90 and 50° banks' detectors and 1/6 of the forward angle detectors.

The electrical hardware time focusing system has been reported[2]. In this system each detector has own time analyzer, the time width $\Delta\tau$ of which chosen easily by a software to satisfy the following time focusing condition.

$$\Delta\tau = \frac{L \sin\theta}{L_r \sin\theta_r} \Delta\tau_r \ ,$$

where L and 2θ are the total flight path length and scattering angle, respectively. Subscript r denotes a reference detector. Improved electronics, such as 8-Input Amplifier Module(K-Amp2)[4] and Time Analyzer Module(TA16) are installed.

The flight path length between the moderator and the sample is 5500 mm. The collimator made of the sintered B_4C was set in the flight path tube before the sample to reduce the background intensity. The neutron beam is collimated to be 50mm in height and 20mm in width at the sample position.

In the design of the HIT-II spectrometer, the geometrical resolution in Q space was calculated by a Monte Carlo technique. The geometrical sizes of moderator (100x100 mm^2), sample (8 mm in diameter and 40mm in height as a typical case) detector (1" or 1/2" in diameter and 4-12" in length) were taken into account for the calculation. The time structure of the incident neutron pulse was included in an approximate manner as well. The resolution ΔQ was defined as a root mean square deviation of the Q value from the mean value Q, i.e. $\Delta Q = \langle (Q-Q)^2 \rangle^{1/2}$. The calculated geometrical resolutions of 150°, 90°, 50° and forward angle counter banks are summarized in fig.3. The resolution of the HIT-II spectrometer improves by a factor of about 1/2 compared with that of the HIT-I spectrometer[3]. Figures 4 and 5 demonstrate the effect of the geometrical resolution on S(Q) calculated for the 25° and 160° detectors, respectively. The solid line shows an exact S(Q) derived from a hard sphere model and the symbol (+) curve is the S(Q) calculated with the geometrical resolution.

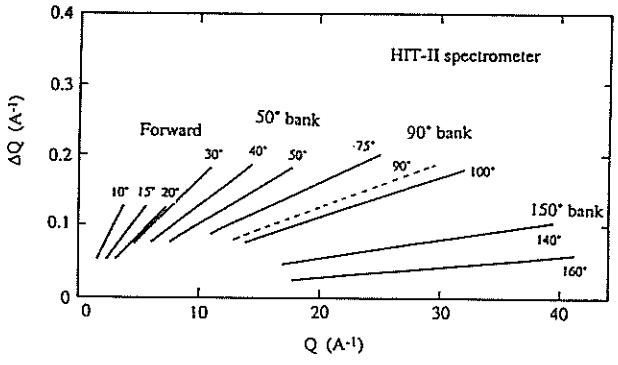

Fig. 3 Geometrical resolution of momentum transfer Q calculated between λ=0.3 and 0.7 Å for various detector banks.

The HIT-II spectrometer was installed during the summer shutdown in 1992 and is now tested on beam. The preliminary experiment revealed that the count rate of neutrons improved by a factor of 3 or 4 in comparison with that for the HIT-I spectrometer. It is felt that the present design of the HIT-II spectrometer is probably optimal given the conflicting demands of the count rate, resolution and space constraints. The experiment using the HIT-II spectrometer will be started on January in 1993.

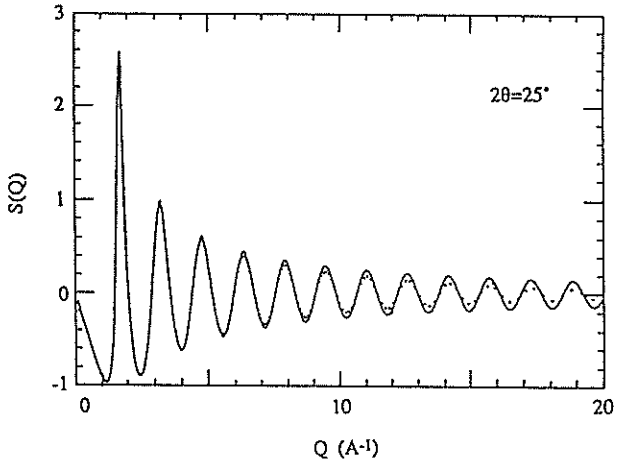

Fig. 4 Effect of the Q resolution on S(Q) observed by the 25 degree angle detector. The solid curve is an exact S(Q) and the symbol (+) curve is the calculated one.

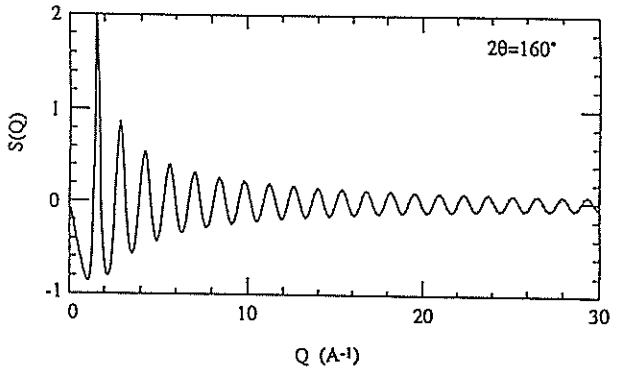

Fig. 5 Effect of the Q resolution on S(Q) observed by the 160 degree angle detector. The solid curve is an exact S(Q) and the symbol (+) curve is the calculated one.

References

1) N. Watanabe, T. Fukunaga, T. Shinohe, K. Yamada and T. Mizoguchi, Proc. of ICANS-IV, KENS Report II 539 (1981)
2) S. Satoh, KEK Internal 85-8 (1985) (in Japanese).
3) M. Misawa, T. Fukunaga, T. Yamaguchi and N. Watanabe, Proc. of ICANS-IX 539 (1986)
4) S. Satoh and M. Furusaka, KEK Internal 92-4 (1992) (in Japanese)

^{3}He nuclear polarization for neutron experiment

Yasuhiro Masuda

National Laboratory for High Energy Physics, 1-1 Oho, Tsukuba-shi, Ibaraki 305

I. Introduction

Neutron polarization is expected to be one of the most important tool to develop a new field in physics concerning neutron spin dependent phenomena. For example, the parity (P) violation and time reversal (T) symmetry violation neutron experiments where P-odd and T-odd correlation terms concerning the neutron spin are measured in eV neutron energy region. The neutron spin will also play an important role in the magnetism of condensed matter, since the information from the neutron magnetic scattering in the wide energy region is very useful. In these studies, the neutron spin polarization and analysis is indispensable. The ^{3}He nuclear polarization is a new tool for this purpose. The principle is the followings. The ^{3}He nucleus has a large capture cross section for the neutron, for example, the value of the cross section is more than ~1000 b below the neutron energy, E_n = 1 eV. The capture process is induced by the resonance reaction of n(^{3}He,p)t. The resonance energy and the width are E_0 = -518 keV and Γ = 1153 keV, respectively.[1] The spin of the resonance state is zero. The neutron spin and the ^{3}He nuclear spin are both 1/2, therefore, neutrons whose spin couple with the ^{3}He nuclear spin in antiparallel are absorbed by ^{3}He nuclei. The scattering cross section of the ^{3}He nucleus is negligible compared with the absorption cross section. We can use this property as a neutron spin filter. If the ^{3}He polarization is 100% and the filter thickness is much larger than the neutron mean free path, neutrons whose spin are parallel to the ^{3}He polarization transmit through the filter without attenuation, on the other hand neurons whose spin is antiparallel are absorbed completely. In principle, the transmittance of the polarized ^{3}He filter becomes 50% and the polarization of the transmitted neutrons achieves 100%. This is a prominent feature of the polarized ^{3}He filter. In previously, the polarized proton filter was unique method to obtain polarized neutrons in the epithermal region.[2] However, the proton has large scattering cross section for the neutron. Because of this reason, the transmittance of the polarized proton filter is rather small than the polarized ^{3}He filter and scattered neutrons may induce background in the neutron experiment. The ^{3}He filter can be also applied to the neutron spin analyzer. Namely, the neutron spin is analyzed by the neutron count after transmission through the filter. A polarized ^{3}He neutron counter is more ambitious application. Since the neutron of antiparallel spin induces the nuclear reaction ^{3}He(n,p)t which produces an electric signal in a proportional chamber, the polarized ^{3}He counter senses only neutrons of antiparallel spin. It means a great gain of the analyzing power for the neutron spin.[3]

Although the ^{3}He nucleus has the prominent property in the application to the neutron spin polarizer and analyzer as mentioned above, the polarized ^{3}He filter has not been realized for neutron experiment. Here, we discuss development of the ^{3}He nuclear polarization for the polarized ^{3}He filter at KEK. We also discuss its application to the polarized neutron experiments.

II. ^{3}He nuclear polarization

For ^{3}He nuclear polarization, a hyperfine interaction between the polarized atomic spin and the ^{3}He nuclear spin is used.[4,5] The rubidium atomic spin is polarized by an optical pumping. Namely, the rubidium atom is polarized upon absorption of circularly polarized D1 resonant light as it is shown in Fig. 1. The 5S1/2 state excites to 5P1/2 state upon absorption of the D1 light, where the magnetic quantum state of m = -1/2 transits to 1/2. The 5P1/2 state deexcites to 5S1/2 state emitting unpolarized D1 light. If another polarized rubidium atom absorbs unpolarized resonant light and the atom depolarizes. A small amount of nitrogen gas is added to quench the unpolarized D1 light. The deexcitation of the 5P1/2 state is induced by a collision with nitrogen molecule without emitting the resonant light. During the atomic collision with nitrogen molecule, the magnetic substates of the 5P1/2 state mixed with each other,

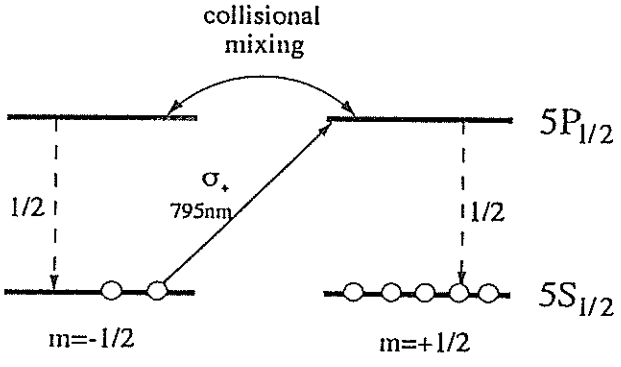

Fig. 1 Optical pumping of rubidium atom

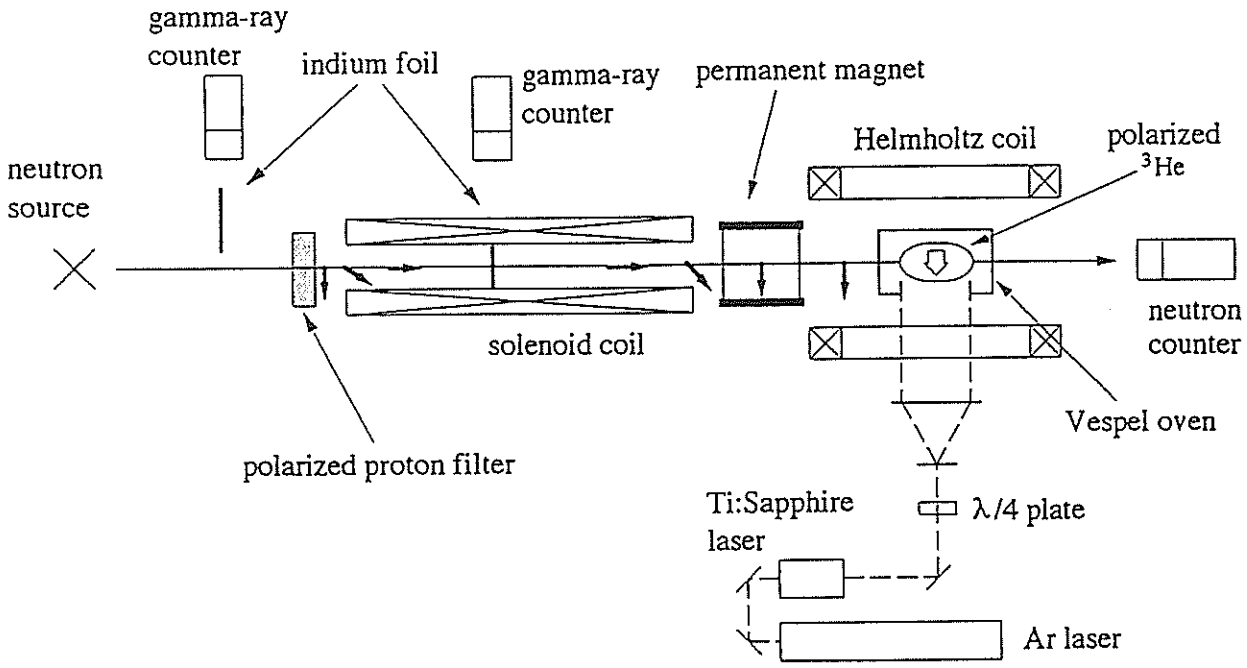

Fig. 2 Experimental set-up of ^{3}He nuclear polarization

therefore, the population of the magnetic substate is equalized. Each magnetic substate of 5P1/2 decays into the magnetic substate of the 5S1/2 without change in magnetic quantum number. As a result, 1/2 of the photon spin is transferred to the 5S1/2 state. The spin transfer rate from the photon to the rubidium is determined by the photon absorption cross section and incident laser intensity. The polarization of rubidium atom, P_{Rb} is limited by the spin destruction during the Rb-Rb and Rb-^{3}He-^{3}He atomic collisions. The incident laser power is applied to overcome the spin destruction rate. As a result, the order of the optical pumping rate of rubidium is the spin destruction rate, whose value is ~1 ms. Rubidium atomic polarization is transferred to the ^{3}He nuclear spin by a hyperfine interaction during the Rb-^{3}He atomic collision. The spin exchange rate from the rubidium atom to the ^{3}He nuclear spin is Γ_{se} ~ 10 h for the rubidium atomic number density of 4×10^{14}/cc. The polarization of ^{3}He nuclei, P_{He} is predicted by a rate equation. As a result, the evolution of ^{3}He polarization is described by

$$P_{He} = [\ \Gamma_{se} P_{Rb}/(\Gamma_{se} + \Gamma)\ ]\ [\ 1 - \exp(-(\Gamma_{se} + \Gamma)t)\ ]. \quad (1)$$

Here, Γ is the relaxation rate of ^{3}He nuclear polarization. The value of P_{He} is directly proportional to the value of P_{Rb}, since the optical pumping rate of rubidium is very fast compared with the spin exchange rate Γ_{se}.

III. Measurement of the ^{3}He polarization

The experimental set-up of the polarized ^{3}He filter is shown in Fig. 2.[6] An alminosilicate glass cell is filled with 3 atm ^{3}He gas, 100 torr N_2 gas and a small amount of rubidium droplet. The glass cell size is 4 cm in length and 2.5 cm in diameter. The cell is placed in the center of a Helmholtz coil of 40 G. The homogeneity of the magnetic field around the cell is 10^{-3}. The temperature of the cell is controlled at 180°C, where the number density of the rubidium atom is 4×10^{14}/cc which satisfies the spin exchange rate of Γ_{se} ~ 10 h. The laser beam from 4-W Ti-Sapphire laser system transmits through a 1/4 λ plate. After the transmission linear polarization of the laser beam is transformed into the circular polarization. The cell was irradiated with a circularly polarized laser beam. The wave length is 795 nm, which corresponds to the D1 light wave length foe the optical pumping. The evolution of the ^{3}He polarization was observed by a polarized neutron transmission measurement. The ^{3}He glass cell is placed in a polarized neutron beamline. Neutrons from the spallation source is polarized upon transmission through a polarized proton filter. The neutron polarization is determined by the transmission enhancement for the polarized proton filter.[2] The neutron polarization is guided to the ^{3}He filter by using an adiabatic passage. Before transmission through the ^{3}He filter, incident neutron beam intensity is monitored by an annular indium capture γ counter. Transmitted neutrons are detected by a ^{10}B-loaded

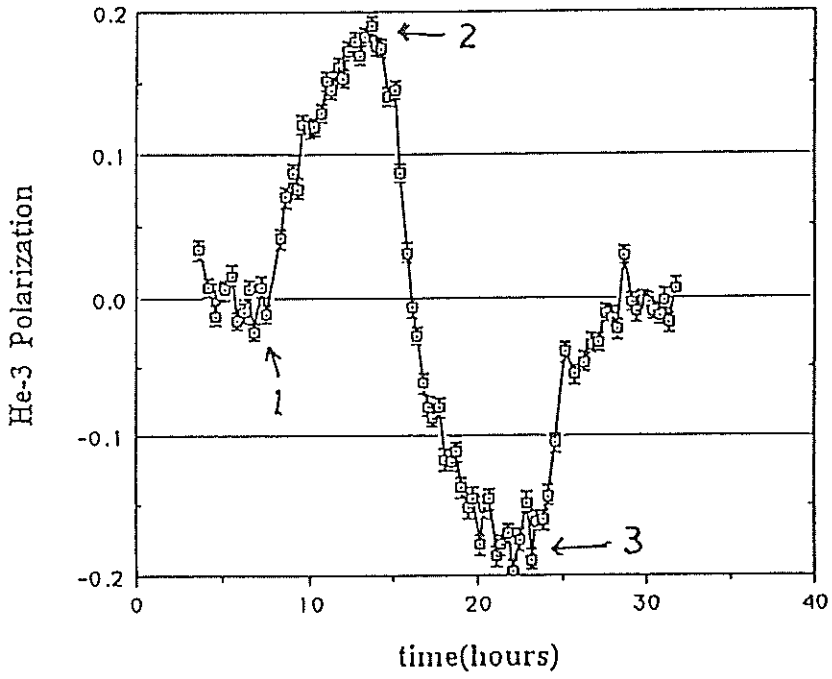

Fig. 3 ^{3}He nuclear polarization

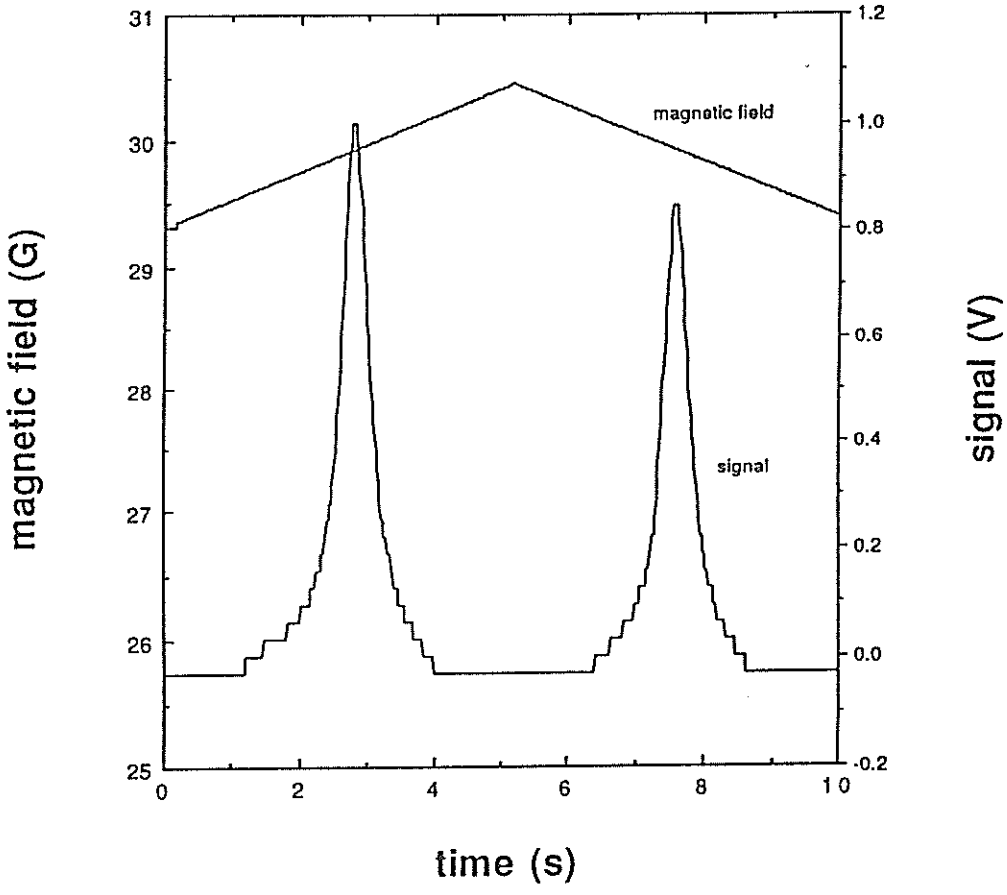

Fig. 4 NMR of ^{3}He nuclear spin

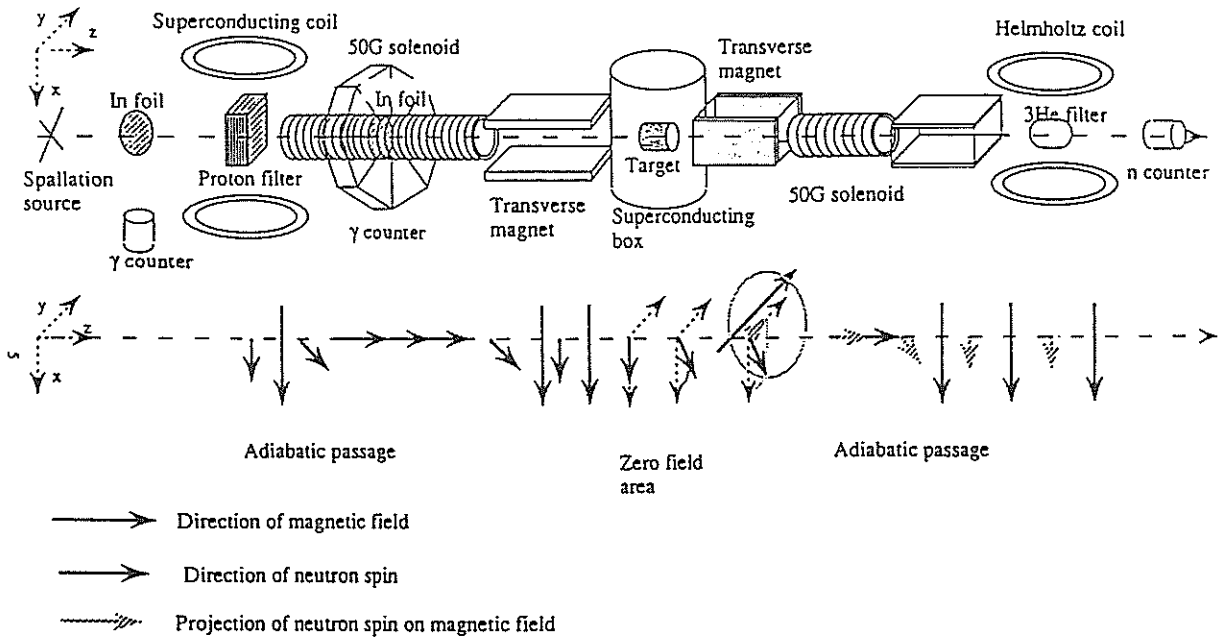

Fig. 5 Experimental set-up for neutron spin rotation

liquid scintillator placed downstream. A typical result of the ^{3}He polarization measurement is shown in Fig. 3. In the figure, the laser beam is switched on at point 1 and the polarization of ^{3}He starts. Since the ^{3}He nuclear spin is polarized in parallel direction to the incident neutron polarization, the neutron transmittance of the filter increases. At point 2, the circular polarization of the laser beam is reversed and ^{3}He nuclei are polarized in antiparallel. Therefore, the neutron transmittance decreases. The value of the ^{3}He polarization is determined by the transmission enhancement ε, which is described as

$$\varepsilon=(1+P_n)\exp(N\sigma t P_{He})/2+(1-P_n)\exp(N\sigma t P_{He})/2. \quad (2)$$

Here, P_n is the neutron polarization, N the nuclear number density of the ^{3}He nucleus, σ the ^{3}He cross section and t the length of the filter. At present, the maximum ^{3}He polarization is more than 40%. At point 3, the laser beam is switched off and ^{3}He polarization relaxation is observed. The time constant of the relaxation is represent by Γ. A spin exchange during collision with some paramagnetic impurities on the glass wall is dominant in the relaxation phenomena. The relaxation rate is estimated by the polarization evolution and relaxation. By using the value of Γ_{se} is 9.4×10^{-2} h^{-1}[5], the value of the relaxation rate was obtained as $\Gamma = 7.4 \times 10^{-2}$ h^{-1} and the value of the rubidium polarization was obtained as $P_{Rb} = 0.66$. For further improvement in the ^{3}He polarization, we should decrease the value of Γ and increase the value of P_{Rb}. We are developing surface treatment of the glass wall by HF to remove the paramagnetic impurity from the glass wall. To improve the rubidium polarization, we need more laser intensity in the glass cell. For this improvement, we developed a NMR method to obtained the value of the ^{3}He polarization without the neutron beam. In the Helmholtz coil, we mounted a drive coil, which apply the RF field ($H_1 \sin\omega t$) to the ^{3}He glass cell. The effective field in the rotating frame whose frequency is same as the RF field (ω) is represent as

$$\mathbf{H}_{eff} = (\mathbf{H}_0 - \omega/\gamma) + \mathbf{H}_1 \quad (3)$$

Here, $\mathbf{H}_0$ is the magnetic field of the Helmholtz coil. When the H_0 is swept across the resonant point, the effective field rotates from up to down or from down to up following the magnetic field sweep. If the sweep velocity satisfies the adiabatic condition, the ^{3}He spin follows the magnetic field rotation. The change of the ^{3}He spin direction is sensed by a pick-up coil. The magnetic induction signal at the pick-up coil is analyzed by a lock-in amplifier system. A typical result is shown in Fig. 4. The NMR signal amplitude was calibrated by the neutron transmission measurement.

IV. Application of ^{3}He polarization

We have constructed an apparatus to measure the neutron spin rotation by the weak interaction in the nucleus by using the polarized ^{3}He filter as a neutron spin analyzer.[7] The experimental apparatus is shown

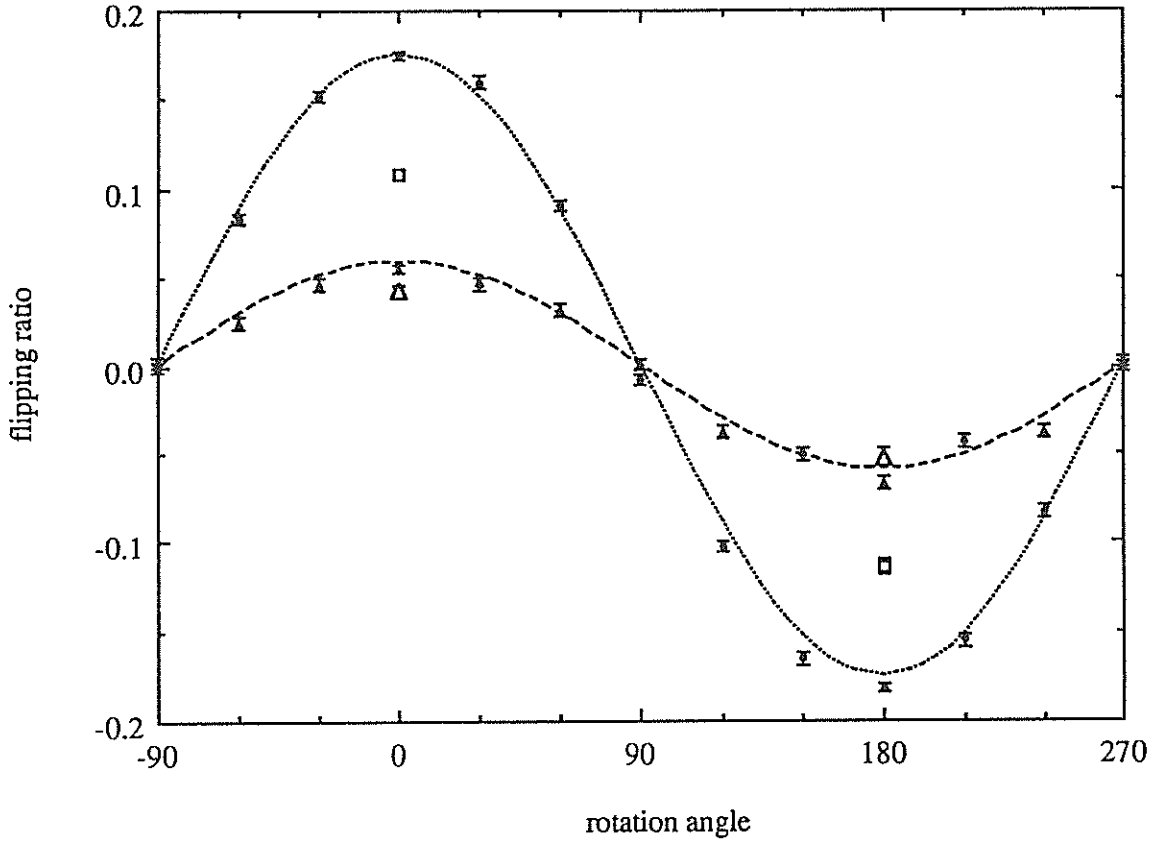

Fig. 6 Result of neutron spin rotation

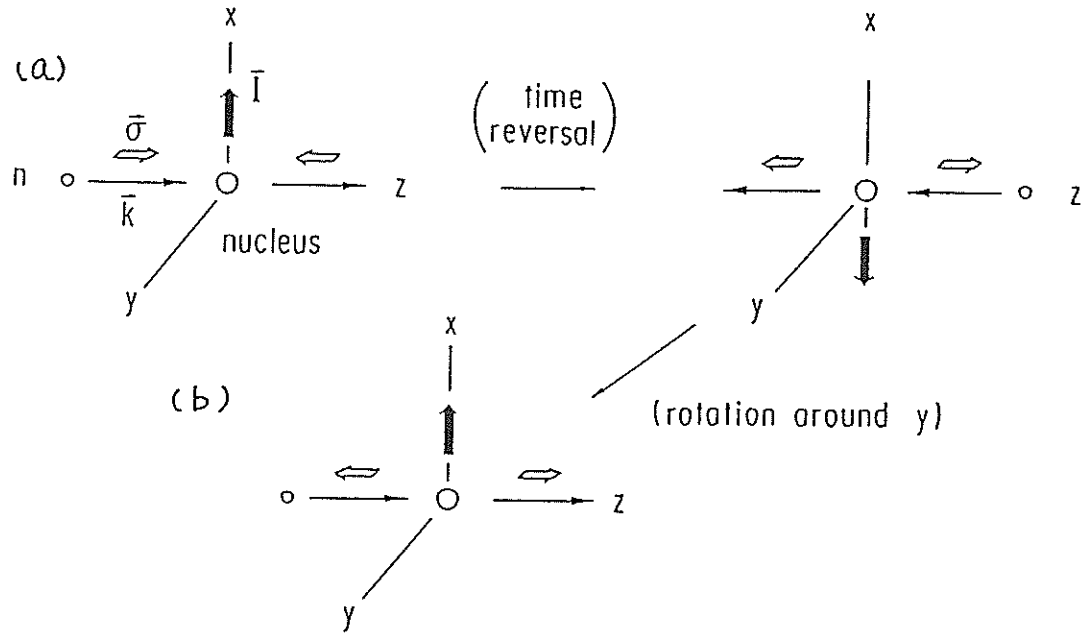

Fig. 7 Principle of spin detailed balance

in Fig. 5. The principle is the following. At the ^{3}He filter, the projection component of the neutron spin on the magnetic field is analyzed. We need to magnetically separate the ^{3}He filter area from the nuclear target area, otherwise the neutron spin follows the magnetic field along the beamline and therefore it is almost impossible to detect the rotation effect in the nuclear target by the ^{3}He filter. We used the Meissner effect of a superconductor for the magnetic field separation. A superconducting box in which the target will be mounted is placed before the ^{3}He filter. The neutron polarization after transmission through the polarized proton filter is held by a solenoid magnetic field in the beamline. Before entering into the superconducting box, a dipole magnet is placed so that the neutron spin rotates from the longitudinal direction (z) to the transverse direction (x) following an adiabatic passage. Since the magnetic field is zero in the superconducting sheet because of the Meissner effect, the neutron experience a suddenly changed in the magnetic field at entering and going out of the superconducting sheet. Therefore the neutron spin enters the box non-adiabatically, namely the neutron spin direction does not change at entering the box. If there is no magnetic field inside the box, the neutron spin travels through the free space keeping it original direction. After travel through the box, the neutron spin enters a transverse dipole field again non-adiabatically. If the direction of the downstream magnetic field is rotated from the upstream magnetic field by θ, $\cos\theta$ component of the neutron polarization is held by the downstream magnetic field. The projection component of the neutron spin on the magnetic filed is guided to the ^{3}He filter by an adiabatic passage and analyzed by the transmission measurement. The transmittance of the ^{3}He filter was measured as a function of θ by using an annular indium counter before the filter and a ^{10}B-loaded liquid scintillator placed downstream. During the experiment, the incident neutron spin was flipped by reversing the upstream dipole magnetic field every 4 sec. The flipping ratio which is defined as

$$R = (T_+ - T_-)/(T_+ + T_-) \quad (4)$$

was obtained. Here, T_+ and T_- are transmittances for flipper off and on states, respectively. The result is shown in Fig. 6. A clear $\cos\theta$ distribution is found in the flipping ratio. The solid and broken lines are results of calculation for the incident neutron energy of 0.1 and 0.75 eV, respectively by using the incident neutron polarization and the ^{3}He polarization. The experimental result are well explained by the calculated results. As a result, the magnetic separation by the superconductor works very well and then the direction of neutron spin can be detected precisely by the present method. In the P-violating neutron spin rotation experiment, a target is mounted in the super conducting box and the rotation angle after transmission through the target will be detected by a change in the ^{3}He transmittance. Now the experiment is going on.

More important application of the present method is for a T-violation neutron experiment.[8] In the T-violation experiment, a T-odd triple correlation term between the neutron spin, neutron momentum and target nucleus spin is measured. The experimental principle is shown in Fig. 7. In the figure, spin flip processes which are the time reversed processes for each other. The T-odd term induces a difference in spin flip probabilities for the two processes. The role

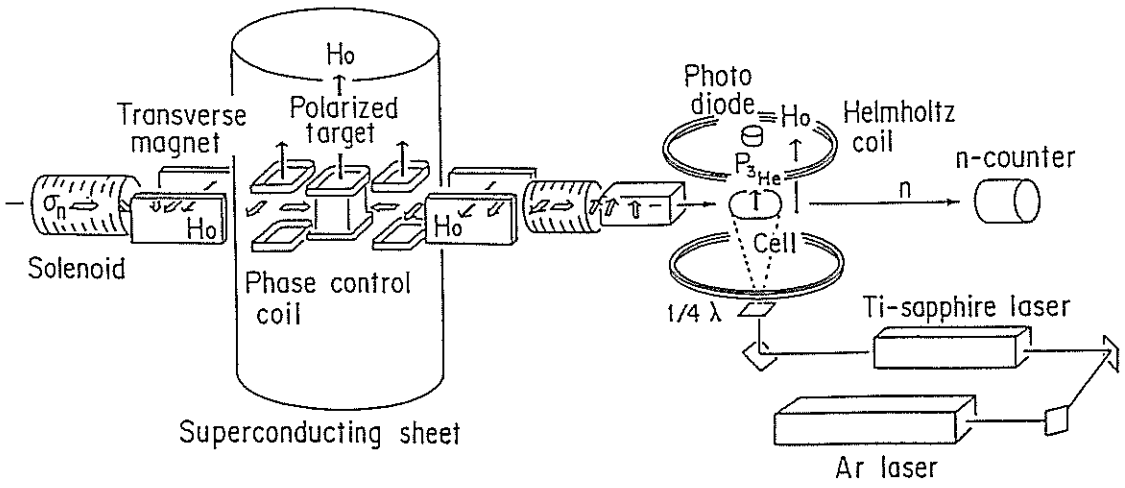

Fig. 8 Experimental scheme for spin detailed balance

of the polarized ^{3}He filter is shown in Fig. 8. A polarized target will be mounted in a superconducting box. Neutrons polarized in x direction enter the target region non-adiabatically. Then the neutron spin rotates from x direction to z direction in the vertical (y) magnetic field. Therefore, the neutron spin is in z direction upon transmission through the polarized target. The neutron spin rotation in the target is controlled so that Larmor and pseudomagnetic precessions are canceled out. Flipped neutron spin after transmission through the target is guided to the ^{3}He filter by the similar magnetic field configuration as the upstream one. Thus the neutron spin flip process is detected by the ^{3}He filter. The difference in the spin flip probabilities for the time reversed processes is searched for the T-violation evidence. The technique of the neutron spin rotation is quite important in the T-violation experiment. The present method to detect neutron spin direction is quite useful for this technique.

References

1) S.F. Mughabghab et al., "Neutron Cross Section" Academic Press (1984).
2) Y. Masuda et al., Nucl. Inst. Meth. A264(1988)169.
3) W.G. Williams, Nucleonika 25(1980)769.
4) K.P. Coulter et al., Nucl. Inst. Meth. A270(1988)90.
5) B. Larson et al., Phys. Rev. A44(1991)3108.
6) H. Sato et al., to be published in Hyperfine Interaction.
7) K. Sakai et al., to be published in Hyperfine Interaction.
8) Y. Masuda et al., to be published in Hyperfine Interaction.

WINK (Small/Medium-Angle Diffractometer)

M. Furusaka, K. Suzuya, N. Watanabe, *M. Osawa, I. Fujikawa and S. Satoh
National Laboratory for High Energy Physics, Tsukuba 305
*Institute of Materials Science, University of Tsukuba, Tsukuba 305

Status

WINK is a special instrument which covers very wide momentum transfer range ($0.01 \leq Q \leq 20$ A^{-1}) by combining a small-angle instrument, a medium-resolution powder diffractometer and/or a total-scattering instrument. Side view of WINK is shown in Fig. 1. WINK is especially useful for research in materials science, polymer, biology, and condensed matter science when these materials reveal not only long-range fluctuations but also changes in crystal structures or local atomic arrangements and so on. A typical result on the study of a SiC-fiber will be described later. Although one can measure both low-Q and high-Q scattering with different instruments the simultaneous measurements over the wide Q-range are frequently desired. It is also better to measure both regions under the same physical configuration.

Incident neutrons with wide wavelength range are also indispensable for the measurement, for example, very small defects or voids in the specimens. In these experiments, elimination of spurious scattering from the multiple-Bragg reflections is indispensable. This can be done by using long wavelength neutrons that is longer than Bragg-cutoff and by measuring scattering function S(Q) up to around $Q \sim 1 A^{-1}$ by using high-angle detectors.

Because the detector system with wide coverage of solid angle and relatively relaxed resolution for the collimation system, counting efficiency of this instrument is very high, particularly in the medium and high-Q range.

WINK sits in between two existing instruments: a low-energy inelastic spectrometer (LAM-40) and a high-resolution powder Diffractometer (HRP). These three instruments share the same neutron beam (C4) viewing directly the solid methane moderator at 20K.

The in-pile collimation system is similar to that of INC (High-Energy Chopper Spectrometer); combination of picture frames

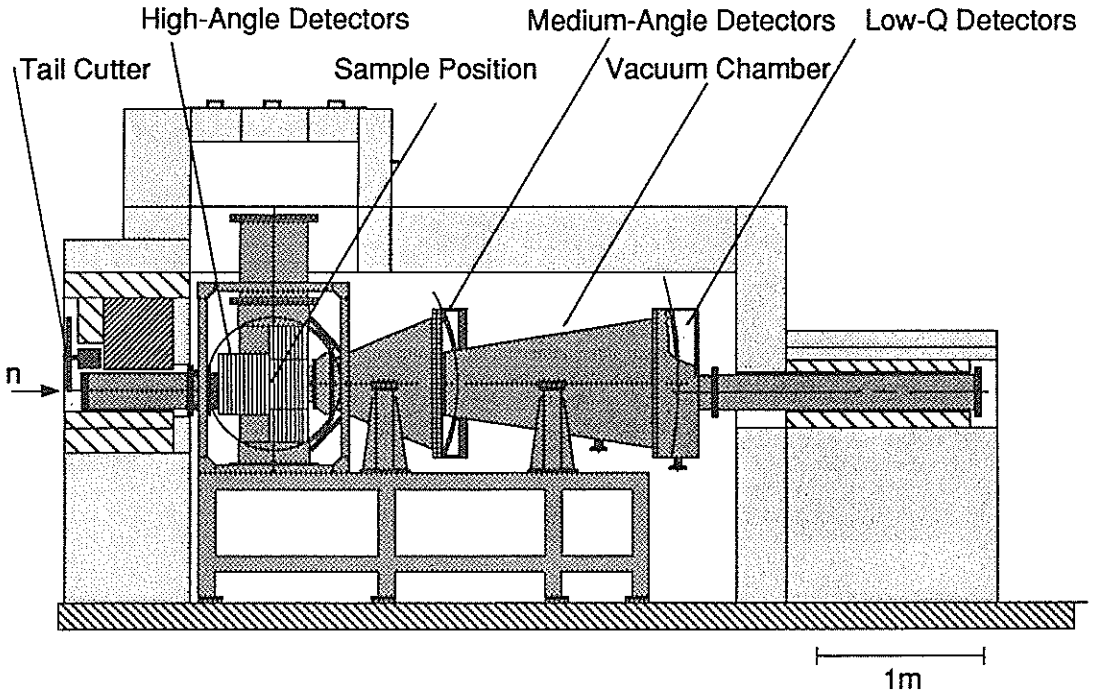

Fig. 1. Side view of WINK.

made of iron and B_4C/resin-mixture, and "Teethes" of sintered B_4C's are implanted inside the frames. Though no filter or t_0-chopper is installed to eliminate high energy neutrons at the beginning of neutron bursts, high energy background is suppressed enough.

A tail-cutter is located far from the moderator, therefore frame overlap is not negligible. By comparing the scattering with identical Q from detectors at different angles with different wavelengths, we can distinguish frame overlapped scattering from non-overlapping ones; this is one of the advantages to use wide-wavelength incident neutrons band.

A sample position is apart from the moderator by 9 m, and the optimum sample size was designed to be 20 mm by 20 mm.

Scattered path-length for the low-Q detector bank is 2.35m ($\varphi = 1.5° \sim 8.4°$), which is much shorter than the desired length of about 4 to 5m. Detectors at the low-Q detector bank are installed inside the vacuum chamber. A similar detector arrangement is used at the medium-angle position ($L_2 = 1.1$m, $\varphi = 12° \sim 19°$), but detectors are outside the chamber. We are now planning to install a high-angle detector-bank ($L_2 = 0.45$m, $\varphi = 25° \sim 145°$).

Typical Scientific Results

We show the recent results on SiC-fiber which clearly reveal the capabilities of WINK. SiC-fiber is a material similar to carbon or boron fiber but with much higher acid- and heat-resisting capability. It is becoming important as the base material to make FRM or FRC. Since this material has very complex structure, relation between its structural changes and the mechanical strength has not been well understood so far. In order to obtain a full understanding of the structure of this kind of materials, neutron scattering measurement over the wide-momentum transfer region, i. e. the combination of all the data from powder diffraction, total-scattering and low-Q scattering, is indispensable. Wide Q-range measurements have been recently performed using WINK. The results were compared with X-ray SANS results which give the different information due to the different scattering cross section from neutrons.

A typical result obtained by WINK is shown in Figs. 2 and 3. As shown in the figures, we could obtain information in the very wide Q-range ($0.01 \leq Q \leq 20$ A^{-1}) at the same time. The result in the low-Q region is depicted in Fig. 2, in which neutron result is shown in (a) and X-ray in (b). They may look very different for the first glance, but this is due to the different scattering cross sections. From these observations, hydrogen contents were obtained from the incoherent scattering intensities around $Q = 1$ A^{-1}, where the coherent cross section is known to be very small. This results is consistent with the chemical analysis. The main contribution to the scattering is from β-SiC particles with the size of 40-50A and there is an additional component due to micro voids with

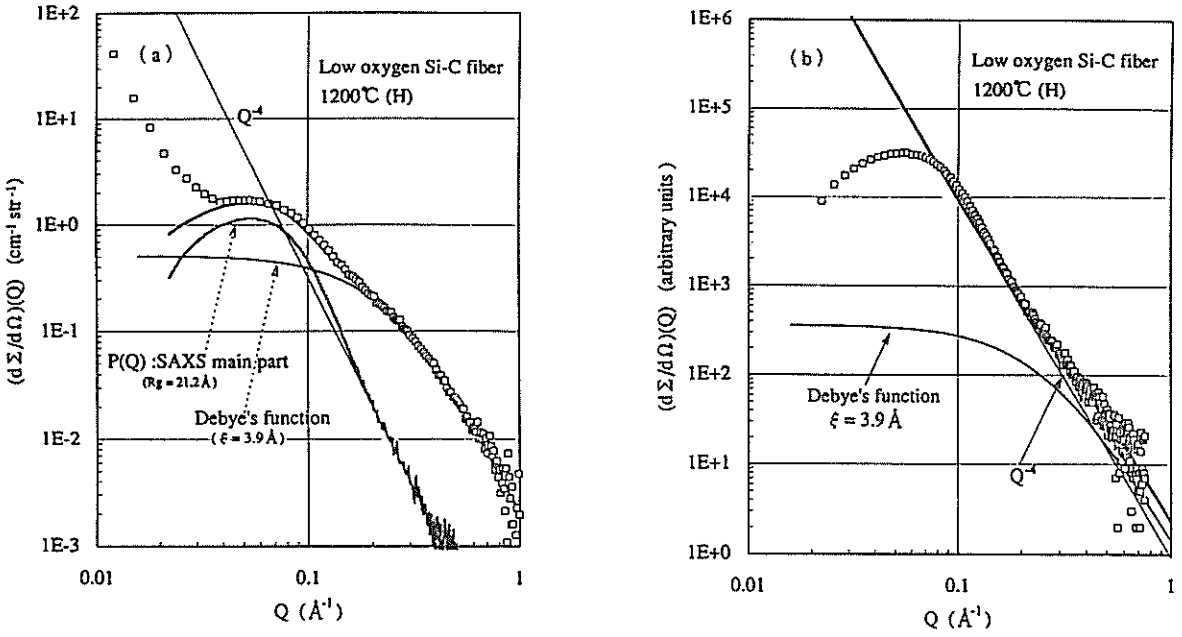

Fig. 2. Small-angle (a) neutron and (b) X-ray scattering from SiC-fiber prepared at 1473K.

much smaller size (diameter = 4 - 10A). It should be noted that it is very difficult to observe such small voids with TEM or X-ray scattering techniques.

From the high angle scattering data in Fig. 3, we can see a powder pattern of β-SiC crystallites. The line-broadening corresponding to the finite size of the crystallites, but the estimated size is remarkably smaller than that obtained from the SANS measurements. This suggests that many smaller β-SiC crystallites with different orientation form a larger β-SiC particle. The former contributes to powder diffraction and the latter to SANS. Several other smaller peaks were observed, and these were compared with the result of the powder diffraction measurements from bulk vitreous silica and carbon. From the measurements, the origins of these small peaks were resolved as is shown in Fig. 3.

In conclusion, WINK is a very powerful machine to resolve very complex materials for real applications like the characteristic structure of SiC fibers. This is our first result, and we are now investigating unresolved problems concerning complex and interesting structures in polymer, biology and materials science.

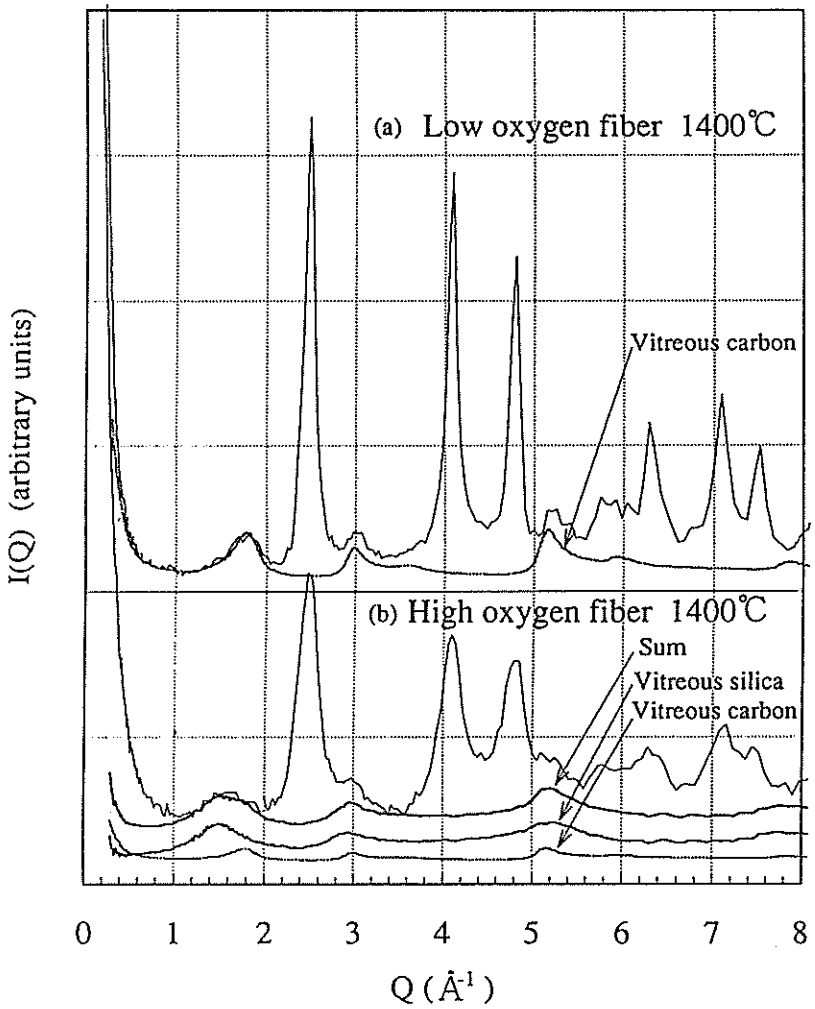

Fig. 3. High-angle neutron diffraction from SiC-fiber prepared at 1473K.

Scientific Reports

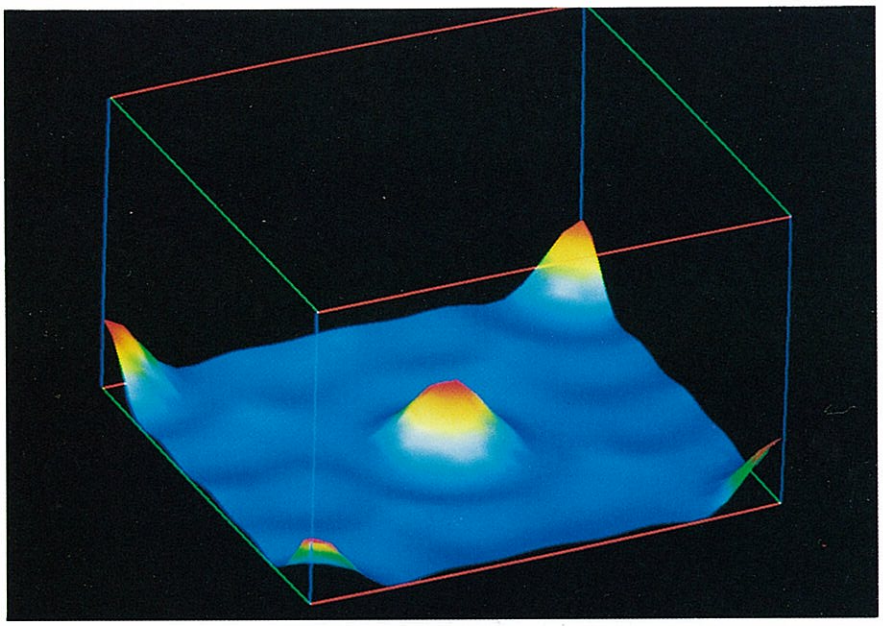

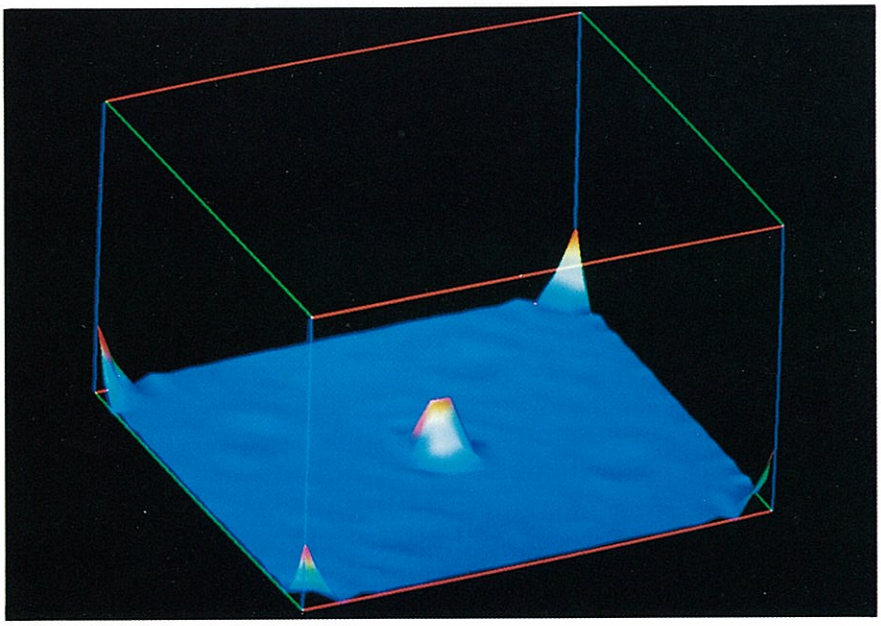

Fourier maps of $SrCeO_3$ obtained by X-ray diffraction (upper) and neutron diffraction (lower).

Neutron Powder Diffraction Study of $RNbO_4$ (R=La, Nd, Ho and Yb)——Distortion of NbO_4 Tetrahedra

S. TSUNEKAWA, T. KAMIYAMA* and H. ASANO*

Institute for Materials Research, Tohoku University, Sendai 980
*Institute of Materials Science, University of Tsukuba, Tsukuba 305

Room temperature phases of rare-earth orthoniobate ($RNbO_4$) crystals have a shear-deformed Scheelite ($CaWO_4$) structure, and their space group is $I2/a$[1-3]. The coordination number of Nb^{5+} is four which is very rare. Regular tetrahedra of NbO_4 in high temperature phase change into distorted tetrahedra with monoclinic symmetry in room temperature phase. In this study, the relation between the distortion of NbO_4 and rare-earth ions was clarified.

$RNbO_4$ (R=La, Nd, Ho and Yb) crystals were grown by floating zone method at 1700 ~ 1850 °C. Neutron powder diffraction for these crystals is more advantageous than single crystal diffraction, because they are ferroelastic and have usually many twins at room temperature. All Rietveld refinement patterns of the HRP data showed a good fit. An example is shown in Fig. 1. Final R-factors with a weight, R_{wp}, are 4.45%, 3.18%, 3.06% and 4.04% for $LaNbO_4$, $NdNbO_4$, $HoNbO_4$ and $YbNbO_4$, respectively. Their lattice and structure parameters are shown in Table 1. Lattice parameters in the parentheses were obtained by X-ray powder diffraction method[4].

Displacement of four oxygen atoms around Nb^{5+} ion has the degree of freedom of 12. The displacement is decomposed into the following modes: a cubic symmetry, Q_1, an orthorhombic symmetry, Q_2, a tetragonal symmetry, Q_3, three monoclinic symmetry, Q_4, Q_5 and Q_6, three translational, Q_7, Q_8 and Q_9, and three rotational modes, Q_{10}, Q_{11} and Q_{12}[5]. These values were estimated by the normal coordinate method (Table 2.).

The following formula shows a rate of the displacement (=a kind of strain):

$$\epsilon_n = Q_n / V^{1/3} \qquad (1)$$

where $V = abc\sin\beta$ is the unit-cell volume of $RNbO_4$. Substituting each value of displacement Q_n into Eq. (1), we get the result as shown in Fig. 2. It is found that the strains ϵ_6, ϵ_9 and ϵ_{12} are almost independent of an ionic radius of rare-earth element and ϵ_1 increases with decreasing the ionic radius. The latter result is inconsistent with the simple model that Nb^{5+} ions fill up the gaps in RO_8 frame work, because ϵ_1 should be almost independent of the ionic radius when the model is valid.

The displacement of Q_1 produces a regular tetrahedron of NbO_4. Four sets of orthogonal coordinates, q^o_{ix}, q^o_{iy} and q^o_{iz} (i=1, 2, 3 and 4) brought about by Q_1 are estimated using an inverse transformation matrix:

$$q^o_{1x}=Q_1/\sqrt{12},\ q^o_{1y}=-Q_1/\sqrt{12} \text{ and } q^o_{1z}=Q_1/\sqrt{12}$$

$$q^o_{2x}=-Q_1/\sqrt{12},\ q^o_{2y}=Q_1/\sqrt{12} \text{ and } q^o_{2z}=Q_1/\sqrt{12}$$

$$q^o_{3x}=Q_1/\sqrt{12},\ q^o_{3y}=Q_1/\sqrt{12} \text{ and } q^o_{3z}=-Q_1/\sqrt{12}$$

and

$$q^o_{4x}=-Q_1/\sqrt{12},\ q^o_{4y}=-Q_1/\sqrt{12} \text{ and } q^o_{4z}=-Q_1/\sqrt{12}$$

These four sets correspond to the position of four oxygen atoms in the regular tetrahedron. Thus the virtual bond length of Nb-O, ℓ_0, is calculated using one of four sets.

$$\ell_0=\{(Q_1/\sqrt{12})^2 + (-Q_1/\sqrt{12})^2 + (Q_1/\sqrt{12})^2\}^{1/2} = Q_1 / 2$$

A mean value of Q_1 becomes 3.668 Å using the values given in Table 2, and then an average value of ℓ_0 is 1.834 Å. This value is nearly equal to the mean bond length $\bar{R}$= 1.828 Å for s (= valence of Nb / coordination number of Nb)= 5/4, where $\bar{R}=R_0 s^{-0.200}$, R_0= 1.911 Å[6] and s is called electrostatic bond strength by Pauling[7] and bond valence by Brown[8]. Ionic radius of Nb^{5+} with coordination number of four, $r_{Nb^{5+}}$, becomes 0.47 Å, subtracting $r_{O^{2-}}$ = 1.36 Å[9] from the mean bond length. This value is nearly equal to the empirical value obtained by Shannon[9].

References

1) L. H. Brixner, J. F. Whitney, F. C. Zumsteg and G. A. Jones, Mat. Res. Bull. 12, 17-24 (1977).
2) S. Tsunekawa and H. Takei, Phys. Stat. Sol. A 50, 695-702 (1978).
3) M. Tanaka, R. Saito and D. Watanabe, Acta Cryst. A 36, 350-352 (1980).
4) A. T. Aldred, Acta Cryst. B 40, 569-574 (1984).
5) M. Kataoka, private communication.
6) I. D. Brown and D. Altermatt, Acta

Cryst. B 41, 244-247 (1985).
7) L. Pauling, J. Amer. Chem. Soc. 51, 1010 -1026 (1929).
8) I. D. Brown, Chem. Soc. Rev. 7, 359-376 (1978).
9) R. D. Shannon, Acta Cryst. A 32, 751-767 (1976).

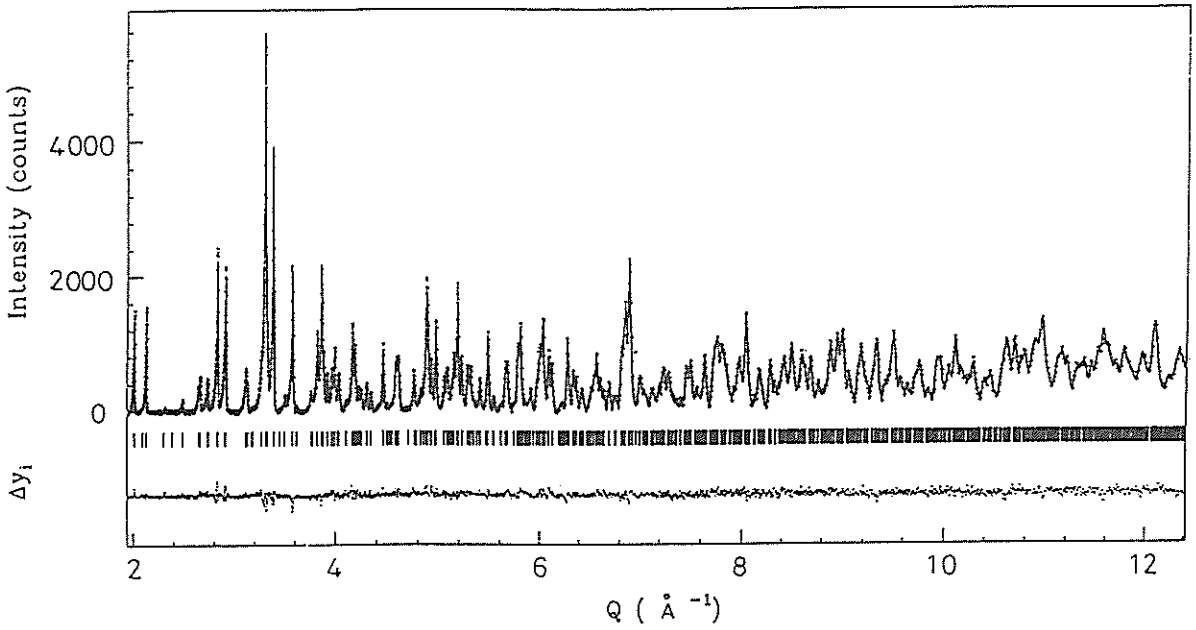

Fig. 1. Rietveld refinement pattern of the HRP data for $HoNbO_4$. $Q = 2\pi/d$, where d is the interplanar spacing , and $\Delta y_i = y_i(o) - y_i(c)$, where $y_i(o)$ is the observed intensity and $y_i(c)$ is the calculated intensity, respectively, at a particular channel, i.

Table 1. Lattice and structure parameters obtained by the Rietveld refinement.

	Lattice parameter				Structure parameter				
	a (Å)	b (Å)	c (Å)	β (o)	Atom	Site	x	y	z
$LaNbO_4$	5.5647(1)	11.5194(2)	5.2015(1)	94.100(1)	La	4e	0	0.6292(1)	1/4
	(5.5667(2))	(11.5245(4))	(5.2020(3))	(94.084(2))	Nb	4e	0	0.1036(1)	1/4
					O(1)	8f	0.2376(2)	0.0337(1)	0.0546(2)
					O(2)	8f	0.1460(2)	0.2042(1)	0.4888(2)
$NdNbO_4$	5.4669(1)	11.2789(2)	5.1463(1)	94.503(1)	Nd	4e	0	0.6296(1)	1/4
	(5.4687(3))	(11.2811(5))	(5.1466(3))	(94.528(4))	Nb	4e	0	0.1040(1)	1/4
					O(1)	8f	0.2399(2)	0.0327(1)	0.0467(2)
					O(2)	8f	0.1508(2)	0.2065(1)	0.4907(2)
$HoNbO_4$	5.2985(1)	10.9465(2)	5.0719(1)	94.531(1)	Ho	4e	0	0.6288(1)	1/4
	(5.3030(2))	(10.9555(3))	(5.0742(2))	(94.548(3))	Nb	4e	0	0.1061(1)	1/4
					O(1)	8f	0.2458(2)	0.0324(1)	0.0415(2)
					O(2)	8f	0.1566(2)	0.2100(1)	0.4971(2)
$YbNbO_4$	5.2394(1)	10.8344(2)	5.0436(1)	94.467(1)	Yb	4e	0	0.6286(1)	1/4
	(5.2429(3))	(10.843(1))	(5.0456(3))	(94.496(7))	Nb	4e	0	0.1067(2)	1/4
					O(1)	8f	0.2473(4)	0.0321(2)	0.0401(3)
					O(2)	8f	0.1583(3)	0.2106(2)	0.4997(3)

Table 2. Displacement of oxygen atoms in NbO_4 of $RNbO_4$ (R= La, Nd, Ho and Yb) crystals for six modes.

	$LaNbO_4$	$NdNbO_4$	$HoNbO_4$	$YbNbO_4$
cubic symmetry				
Q_1	3.658 Å	3.671 Å	3.674 Å	3.669 Å
orthorhombic symmetry				
Q_2	-0.0950 Å	-0.1111 Å	-0.1322 Å	-0.1429 Å
tetragonal symmetry				
Q_3	-0.2215 Å	-0.2391 Å	-0.2658 Å	-0.2767 Å
monoclinic symmetry				
Q_4	0	0	0	0
Q_5	0	0	0	0
Q_6	-0.3155 Å	-0.3356 Å	-0.3254 Å	-0.3163 Å
translational				
Q_7	0	0	0	0
Q_8	0	0	0	0
Q_9	-0.3524 Å	-0.3519 Å	-0.3316 Å	-0.3175 Å
rotational				
Q_{10}	0	0	0	0
Q_{11}	0	0	0	0
Q_{12}	0.6336 Å	0.6070 Å	0.6016 Å	0.5986 Å

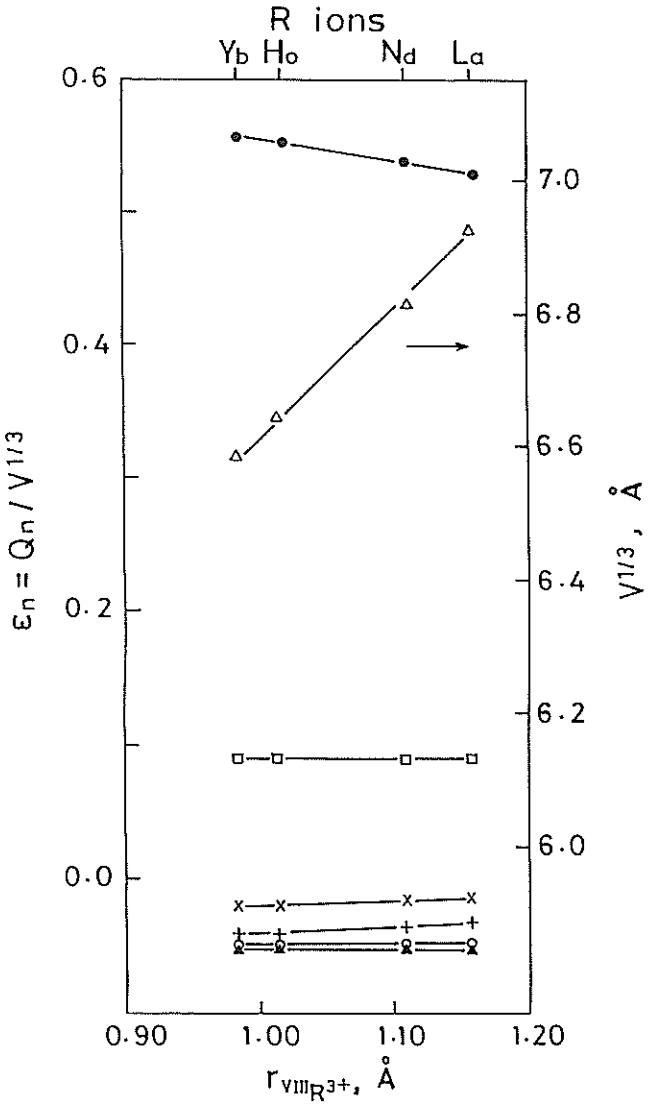

Fig. 2. Plot of ionic radius of rare-earth element vs. a rate of displacement of each mode, Q_n, and $V^{1/3}$, where n=1 (●), n=2 (X), n=3 (+), n=6 (○), n=9 (▲), n=12 (□) and V is the unit-cell volume (△).

STRUCTURAL ANALYSIS OF ORTHORHOMBIC HfO_2 BY NEUTRON POWDER DIFFRACTION

O.OHTAKA, T.YAMANAKA, N.HARA*, H.ASANO* and F.IZUMI**

College of General Education, Osaka University, Toyonaka, Osaka 560
* Institute of Materials Science, University of Tsukuba, Tsukuba, Ibaraki 305
**National Institute for Research in Inorganic Materials, Tsukuba, Ibaraki 305

HfO_2, which has monoclinic symmetry at room temperature under atmospheric pressure, transforms to a high pressure phase with orthorhombic symmetry by compression above about 3 GPa[1]. Present authors performed a time-of-flight neutron diffraction experiment on a powder sample of orthorhombic HfO_2

The starting material was fine-powderes of HfO_2 (grain size was 100 nm) provided by Nacalai Tesque, Inc. The powderes had a purity of 98 % and contained about 2 % of ZrO_2. The orthorhombic HfO_2 powder specimen of about 1 g was prepared using a cubic anvil type device operated at 600℃ and 6 GPa for 30 min[2]. The product consisted of almost all the orthorhombic phase, except for a trace of the monoclinic phase.

The neutron diffraction experiment was performed on a high resolution time-of-flight (TOF) neutron powder diffractometer, HRP[3]. Intensity data were collected at room temperature with gate widths of 4-13 μ s depending on TOF. The least-squares structural refinements were executed with the RIETAN program for the Rietveld analysis of TOF neutron data[4]. The values of scattering length, b, used in the refinement were 7.770 fm for Hf and 5.803 fm for O[5]. Intensity data covering interplanar spacings, d, between 0.05 and 0.328 nm were used for the refinement. No correction for preferred orientation was made because the high pressure sample consisted of very fine and spherical grains. As a small amount of the monoclinic phase coexisted in the sample, the recorded pattern was analyzed assuming a mixture of the monoclinic and orthorhombic phases. In the two-phase refinement, a full matrix refinement of the orthorhombic structure was undertaken with the variables of scale factor, lattice parameters, fractional coordinates and individual isotropic thermal parameters along with refinements of the scale factor and lattice parameters of the monoclinic phase, while other structural parameters of the latter phase were fixed.

The resulting structural parameters and their standard deviations are listed in Table. The lattice constants were refined to be. a=1.00861(4), b=0.52615(2) and c=0.50910(2) nm. The structure is derived from a distorted fluorite (CaF_2) structure by the b-glide parallel to the a axis. The Hf atom is in seven-fold coordination. The oxygen-1 (O1) atom is coordinated by three Hf atoms in an approximately coplanar configuration, while the oxygen-2 (O2) atom has a nearly tetrahedral coordination.

The relation of the orthorhombic structure with the monoclinic structure is of particular interest. The two structures can be compared by setting the a and c axes of the orthorhombic parallel to the a and c axes of the monoclinic structure. Hf and O2 atoms in the monoclinic structure are directly related to those in the orthorhombic structure with slight displacement of these atoms. On the other hand, further substantial displacement of O1 atoms are required for this transformation. Considering a (100) twin of the monoclinic structure, the two structures are related. One unit cell of the orthorhombic is produced by a set of two types of the monoclinic unit cell which are in (100) twin relation.

Table Orthorhombic HfO_2 Space group: Pbca

Atom	g[a]	x	y	z	B(nm^2)[b]
Hf	8e 1.0	0.3845(1)[c]	0.0338(2)	0.2439(4)	2.0(2)*10-3
O1	8e 1.0	0.2902(2)	0.3716(4)	0.3720(4)	5.4(3)*10-3
O2	8e 1.0	0.0227(1)	0.2431(6)	0.0004(5)	3.5(2)*10-3

Rwp=4.77 Rp=3.57 R_E=4.24 R_I=3.44 R_F=1.68

a Site occupancies
b Isotropic thermal parameters
c The figures in parentheses indicate estimated standard deviations of the last significant digit.

References

1)G.Bocquillon, C.Sussee and B.Bodar, Rev. Int. Hautes Temper. et Refract, 5 247-51, (1968)
2)O.Ohtaka, T.Yamanaka and S.Kume, J. Ceram. Soc. Jpn. 99 826-827.(1991)
3)N.Watanabe, H.Asano, H.Iwasa, S.Satoh, H.Murata, K.Karahashi, S.Tomiyoshi, F.Izumi and K.Inoue, Jpn. J. Appl. Phys. 26, 1164-1169, 1987.
4)F.Izumi, Advances in the Rietveld Method, ed. R.A.Young, Oxford University Press, Oxford, UK, in press
5)V.F.Sears, AERE-8490, Chalk River Nuclear Laboratories, Ontario, 1987.

Determination of the proton site in the perovskite-type protonic conductor $SrTiO_3$

N. SATA, S. SHIN, S. HOSOYA*, N. NIIMURA** and M. ISHIGAME***

ISSP, University of Tokyo, Tokyo 188, *Faculty of Science, Tohoku University, Sendai 980
**Laboratory of Nuclear Science, Tohoku University, Sendai 982
***Research Institute for Scientific Measurements, Tohoku University, Sendai 980

It is known that perovskite-type oxides like $SrCeO_3$ have protonic conductivity at high temperature when they are doped with accepter ions[1]. Protonic conductors of this type oxides are expected for applications to fuel cells, hydrogen sensor and so on.

It is clear that protons are bound by oxygen ions in crystal because O-H stretching vibrations are observed in the infrared absorption spectrum[2]. Temperature dependence of the electrical conductivity suggests that protons migrate by hopping from site to site. However, the mechanism of protonic conduction is not clear because the site has not been determined.

The purpose of this study is to determine the proton site in protonic-conductor $SrTi_{1-x}Sc_xO_3$ (x=0.02, 0.03) by the neutron diffraction. Then, we measured Bragg intensity by TOF method at FOX with 128 position sensitive detectors installed at KENS. Single crystals are used because the high S/N ratio is necessary to observe slight changes due to exchanging from proton to deuteron. Two samples were prepared; one was grown by floating zone method using Xe arc imaging furnace and the other by Verneuil method.

Two models of proton site have been proposed (Fig. 1). One is in double minimum potential between O-O which compose hydrogen bonding like formation, and the other is in the site between O-Sr on cube face.

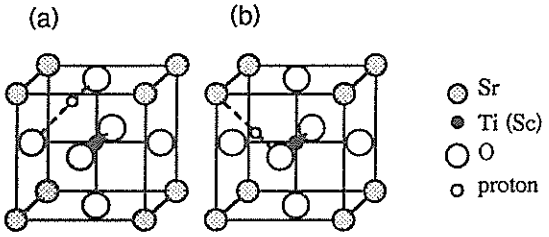

Fig. 1 Two models of the proton site in $SrTiO_3$; (a) oxygen octahedral site (O-O). (b) cube face site (O-Sr).

The Bragg intensity is

$$I(h,k,l) = k \cdot i(\lambda) \cdot |F(h,k,l)|^2 \cdot L(\lambda,\theta) \cdot A(\lambda,\theta) \cdot E(\lambda),$$

where i, F, L, A and E represent incidental neutron intensity, structure factor, Lorentz factor, attenuation correction factor and efficiency of detector, respectively. It is difficult to estimate these factors accurately. Then, we measured the Bragg intensity of proton-doped and deuteron-doped crystals. The Bragg intensity was measured on the same condition that these factors are equivalent. Thus, we may lead an equation to be

$$\frac{I_{host+d}}{I_{host+p}} = \frac{|F_{host}+F_d|^2}{|F_{host}+F_p|^2} = \left|1+\frac{F_d-F_p}{F_{host}+F_p}\right|^2,$$

where F_{host}, F_d and F_p represent structure factors of host, deuteron and proton, respectively. This equation does not include correction factors. Using this equation, we calculated the ratios of structure factors from the Bragg intensity. The ratios were also calculated for several models with various O-H distances, proton concentrations and other parameters to compare with experimental values.

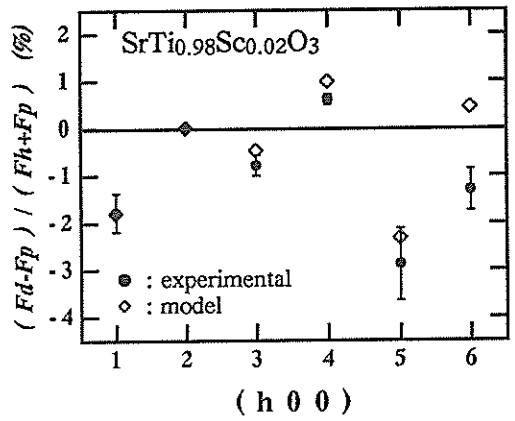

Fig. 2 The ratios of structure factors; experimental results and results of the model site ((a) O-O).

Then, these results lead to the conclusion that proton is in the site between O-O (Fig. 1 (a)) and the concentration of proton is about 2 mol% per unit cell. Furthermore, proton is found to be slightly inside to Ti(Sc) ion with the angle of about 5° between O-O and O-H, and the distance between O and H is about 1.2Å which is rather large as expected from the O-H stretching vibration.

References

1) H. Iwahara et al., Solid State Ionics, 3/4, 359 (1981).
2) S. Shin, H. H. Huang, M. Ishigame and H. Iwahara, Solid State Ionics, 40/41, 910 (1989).

Correlations between Mn atoms and spins in Ag-Mn spin-glass alloys

K. KOGA, K. OHSHIMA, N. NIIMURA* and F. OKAMURA**

Institute of Applied Physics, University of Tskuba, Tsukuba 305
*Laboratory of Nuclear Science, Tohoku University, Sendai 982
**National Institute for Research in Inorganic Materials, Tsukuba 305

Ag-Mn alloy has been regarded a prototype of spin-glasss the same way as Cu-Mn has been. However, to the former less attention has been paid than to the latter from the structural point of view. Ishibashi et al.[1] found the magnetic diffuse maxima in the Ag-Mn alloys.

We have carried out X-ray and neutron diffuse scattering experiments on three Ag-Mn single crystals. In this report, neutron scattering results of Ag-20.8 at.% Mn alloy are presented, which were obtained between room temperature and 11 K using a four-circle goniometer with a refrigerator placed in the instrument FOX installed at a pulsed neutron source KENS. We have found that the diffuse intensity does not change between room temperature and 200 K and it increases gradually below around 200 K. This signifies that the spin state above 200 K was fully paramagnetic and that magnetic short-range order (MSRO) developed below 200 K. The magnetic diffuse intenities in the spin-glass state at 11 K were obtained by the intensity differences between the room temperature value and that at 11 K. The background intensity was measured without the sample and substracted from the observed one. The observed intensity was normalized by the use of an incident neutron spectrum from a vanadium sample and converted to units of the paramagnetic scattering intensity from a Mn^{2+} ion with both an amount of the Ag-Mn sample and that of the vanadium one. The resolution correction was achieved by a deconvolution procedure using the profiles of 200 nuclear reflection. With the above correction, we have taken the exact intensity distribution of the magnetic diffuse scattering as shown in Fig. 1 on the (hk0) reciprocal-lattice plane. Sharp maxima at 1, 0.28,0 and 1, 0.72, 0 appeared elongated along the [1, 0, 0] and [0, 1, 0] directions, respectively. This three-dimensional shape of the diffuse scattering was ellipsoidal. After Fourier inversion of diffuse intensity, MSRO parameters were determined. The first-nearest MSRO parameter (for 110) is -0.821. It means the presence of strong antiferromagnetic coupling between the first nearest spin pairs. The parameters for 200, 400, 600 and 800 are all positive. It means the existence of a ferromagnetic linking along the <100> directions. It may become a key point to understand the spin-glass freezing mechanism.

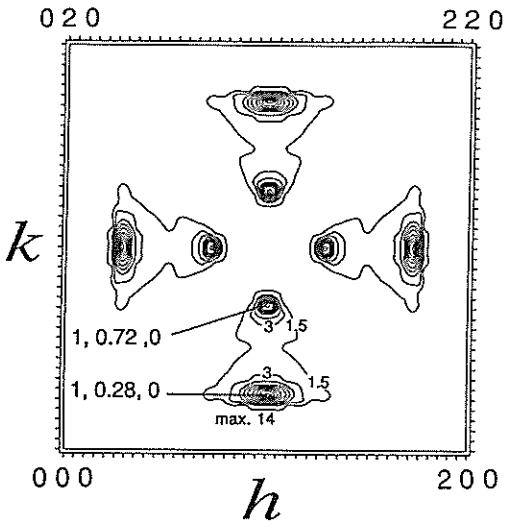

Fig. 1 Magnetic neutron diffuse scattering of Ag-20.8 at.% Mn alloy on (hk0) plane.

References

1) K. Ishibashi, Y. Tsunoda, N. Kunitomi and J. W. Cable, Solid State Commu. 56, 585 (1985).

Crystal Structure of the Ferromagnetic Copper Oxide $La_{1.8}Ba_{1.2}CuO_5$

T. MOCHIKU, H. ASANO[a], F. IZUMI[b],
F. MIZUNO[c], H. MASUDA[c], I. HIRABAYASHI[c] and S. TANAKA[c]

National Research Institute for Metals, Tsukuba, Ibaraki 305
[a]Institute of Materials Science, University of Tsukuba, Tsukuba, Ibaraki 305
[b]National Institute for Research in Inorganic Materials, Tsukuba, Ibaraki 305
[c]Superconductivity Research Laboratory, ISTEC, Nagoya 456

$La_{2-x}Ba_{1+x}CuO_5$ has recently been found to be an insulator which exhibits ferromagnetic transition at about 5 K.[1] This system was first identified by Michel *et al.*[2] using X-ray powder diffraction. The structure parameters of oxygen and the distribution ratio of La and Ba atoms between the two metal sites could not accurately been determined by X-ray powder diffraction. A more detailed knowledge of the crystal structure is desired to explore the mechanism of its ferromagnetism. This study was undertaken to refine the crystal structure of $La_{2-x}Ba_{1+x}CuO_5$ (x=0.2) by Rietveld analysis of neutron powder diffraction data.[3]

Neutron powder diffraction data were taken on a time-of-flight neutron powder diffractometer, HRP, at KENS. The structure of $La_{1.8}Ba_{1.2}CuO_5$ was refined using a Rietveld refinement program RIETAN on the basis of the structure model given by Michel *et al.*[2] (see Fig. 1). Table I lists final R factors, lattice and structure parameters and their standard deviations.

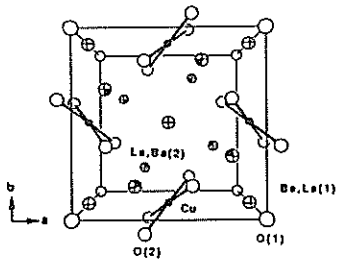

Fig. 1. Crystal structure of $La_{1.8}Ba_{1.2}CuO_5$ viewed along the [001] direction. Oxygen atoms at (1/2,1/2,0) and (1/2,1/2,1) are not drawn for clarity.

The g values of the Cu, O(1) and O(2) sites obtained in a preliminary refinement were 0.994(5), 1.008(6) and 0.992(4), respectively. These g values give a chemical formula of $La_{1.8}Ba_{1.2}Cu_{0.994}O_{4.968}$ if we assume that g(O(1)) = 1. This formula is widely different from that reported by Michel *et al.* : $La_{1.8}Ba_{1.2}Cu_{0.9}O_{4.8}$.[2] The above g values of the three sites can be regarded as unity in view of the underestimation of standard deviations in Rietveld analysis. In addition, the B_{eq} values obtained by assuming g(Cu) = g(O(1)) = g(O(2)) = 1 are quite normal, as shown in Table I. Thus, we can safely conclude that no deficiencies exist, at least, in our sample.

An effective Cu valence, $2+p$, or a concentration, p, of doped holes per (Cu-O) unit can be determined from the chemical formula $La_{1.8}Ba_{1.2}CuO_5$ under the condition of electrical neutrality in this compound. The value of p calculated in this way is 0.2, which indicates that an excess amount of Ba generates holes on the CuO_4 plane. Masuda *et al.*[4] observed spin dilution accompanying Ba substitution for La in $La_{2-x}Ba_{1+x}CuO_5$. The effective Bohr magneton obtained from Curie-Weiss plots decreases linearly with increasing x. The ferromagnetic-transition temperature also decreases with increasing x. These results indicate that the spin of Cu^{2+} is diluted by non-magnetic Cu^{3+}, and are consistent with the hole doping on the CuO_4 plane concluded in this structural study.

Table 1. Final result of the Rietvelt refinement for $La_{1.8}Ba_{1.2}CuO_5$ (tetragonal , P4/mbm, Z=2). a = 0.68652(1) nm and c = 0.58698(1) nm. R_{wp} = 2.88%, R_p = 2.28%, R_I = 2.61%, R_F = 1.60% and R_e = 2.78%. B_{eq} values are equivalent isotropic thermal parameters in nm^2.

Atom	Site	x	y	z	g	B_{eq}
La(1)	2b	0	0	1/2	0.025(8)	0.0073
Ba(1)	2b	0	0	1/2	0.975(8)	0.0073
La(2)	4g	0.17409(8)	=1/2+x	0	0.888(8)	0.0027
Ba(2)	4g	0.17409(8)	=1/2+x	0	0.112(8)	0.0027
Cu	2c	0	1/2	1/2	1	0.0035
O(1)	2a	0	0	0	1	0.0075
O(2)	8k	0.36187(8)	=1/2+x	0.2656(1)	1	0.0080

References

1) F. Mizuno *et al.*, Nature (London) **345** (1990) 788.
2) C. Michel *et al.*, J. Solid State Chem. **39** (1981) 161.
3) T. Mochiku *et al.*, J. Phys. Soc. Jpn. **60** (1991) 1959.
4) H. Masuda *et al.*, Proc. 3rd Int. Symp. Superconductivity, Sendai, 1990 (Springer-Verlag, Tokyo, 1991) p.241.

Crystal Structure of Cu_6O_8InCl and $Cu_6O_8Cu_2Cl$

H. HAYAKAWA, E. AKIBA, S. ONO, H. IHARA*, F. IZUMI† and H. ASANO§

National Chemical Laboratory for Industry, 1-1 Higashi, Tsukuba, Ibaraki 305
*Electrotechinical Laboratory, 1-1-4 Umezono, Tsukuba, Ibaraki 305
†National Institute for Research in Inorganic Materials, 1-1 Namiki, Tsukuba, Ibaraki 305
§Institute for Materials Science, University of Tsukuba, Tenoudai, Tsukuba, Ibaraki 305

Cu_6O_8InCl has a three-dimensional network composed by Cu-O bondings and shows metallic conductivity[1]. In atom can be replaced by Cu and $Cu_6O_8Cu_2Cl$ was obtained[2]. However, $Cu_6O_8Cu_2Cl$ is found to be a semiconductor. These two compounds that have different structures[1,2] have been synthesized as pure phases by heating mixtures of hydrates of copper(II) nitrate and copper(II) chlorine, or indium nitrate. These crystal structures have been refined by the Rietveld method using neutron and X-ray powder diffraction data. Cu_6O_8InCl is a stoichiometric compound and has a murdochite-like structure[3]. The obtained crystallographic data are space group, *Fm3m*, a unit cell parameter a =9.1555(2)Å, d_0=5.69g/cm^3, Z=4. R_{WP} was 4.74%. The crystallographic parameters are shown in Table 1. [Cu_6O_8] blocks, a 3-dimensional network of 26 polyhedra, are composed of [CuO_4] planes sharing oxygen atoms (Cu-O : 1.908Å). Another block is a network of [InO_8] cubes sharing oxygens with the 26 polyhedra at the corners (In-O : 2.257Å). The centers of each block are occupied by Cl and In, respectively. The oxygen and chlorine sites (32f and 4b) were found to be fully occupied. It is concluded that this compound has the ordered structure of Cu_6O_8InCl.

As for $Cu_6O_8Cu_2Cl$, the Cl sites were found to be partly substituted by NO_3. The crystallographic data are space group: *Fm3m*, a =9.381(1)Å, d_0=4.95 g/cm^3, Z=4. R_{WP} was 4.09 %. Table 2 lists the crystallographic parameters of this sample. The crystal structure of $Cu_6O_8Cu_2Cl$ is essentially the same as that of Cu_6O_8InCl except the Cu sites(Cu(2)) corresponding to the In sites. The Cu(2) atoms are not located at the center of the cube, but distributed among the 6 equivalent sites (24e) around the center of the oxygen cube with the occupation factor of about 29 %. A Cu(2) atom of the cubes is coordinated with 4 oxygens forming distorted [CuO_4] planes and the cube made by Cu(2) forms a 3-dimensional network with the 26 polyhedra sharing the [CuO_4] plane. Therefore, this type of compounds can be expressed as $Cu_{6-m}O_8{\cdot}Cu_{2-n}Cl_{0.7}(NO_3)_{0.3}$ where m+n are 0.4. For the sample used in this work, m was 0.1. $Cu_6O_8Cu_2Cl$ has the larger unit cell than Cu_6O_8InCl. It is explained by that the former contains large NO_3 anions instead of Cl atoms.

Table 1. Crystallographic data of Cu_6O_8InCl

Atom	Site	Occup.	x	y	z	B_{iso}(Å^2)
In	4a	0.98(1)	0.00	0.00	0.00	0.54(6)
Cu(1)	24d	1.00(1)	0.00	0.25	0.25	0.48(1)
Cl	4b	1.00(1)	0.50	0.50	0.50	2.72(8)
O(1)	32f	1.00(1)	0.14232(5)	x	x	0.49(1)

R_{WP}=4.74%; R_P=3.46%; R_E=4.57%; R_I=2.45%
R_F=2.18%, R_{Index}= R_{WP}/R_E= 1.04

Table 2. Crystallographic data of $Cu_6O_8Cu_2Cl$

Atom	Site	Occup.	x	y	z	B_{iso}(Å^2)
Cu(1)	24d	0.98(1)	0.00	0.25	0.25	1.01(5)
Cu(2)	24e	0.29(1)	0.1305(10)	0.00	0.00	0.2(1)
O(1)	32f	1.00(1)	0.1441(2)	x	x	0.92(5)
Cl	4b	0.71(5)	0.50	0.50	0.50	3.1(2)
O(2)#	24e	0.0481	0.39(2)	0.00	0.00	3.1(2)
O(3)#	96j	0.0241	0.44(1)	0.12(1)	0.00	3.1(2)

R_{WP}=4.09%; R_P=3.19%; R_E=3.57%; R_I=5.17%
R_F=3.17%; R_{Index}= R_{WP}/R_E= 1.15
#)taken from ref. 4

References

1) H. Hayakawa, E. Akiba, I. Yazawa, H. Ihara and S. Ono, *Jpn. J. Appl. Phys.*, **29**, L1796-8 (1990).
2) H. Hayakawa, E. Akiba, H. Ihara and S. Ono, *Jpn. J. Appl. Phys.*, **30** L1303-6 (1991).
3) E. Dubler, A. Vedani and H. R. Oswald, *Acta Crystallogr.*, **C39**, 1143-6 (1983).
4) C. H. Wong, T. H. Lu, C. N. Chen and T. J. Lee, *J. Inorg. Nucl. Chem.*, **34**, 3253-7 (1972)

Structure Refinements of $La_{1.82}Ca_{1.18}Cu_2O_{6\pm\delta}$ from Neutron Diffraction Data

K. KINOSHITA, F. IZUMI*, T. YAMADA and H. ASANO**

NTT Basic Research Laboratories, Midori-cho, Musashino-shi, Tokyo 180
*National Institute for Research in Inorganic Materials, Tsukuba-shi, Ibaraki 305
**Institute of Materials Science, University of Tsukuba, Tsukuba-shi, Ibaraki 305

Bulk superconductivity has recently been achieved in "2:1:2:6-type" copper oxides synthesized under high O_2 pressure – in compounds not doped with Sr and in Sr-doped ones [$La_{2-x}Ca_{1+x}Cu_2O_{6-x/2+\delta}$, $La_{2-x}Sr_xCa Cu_2O_6$ and $La_{2-x}(Ca_{1-y}Sr_y)_{1+x}Cu_2O_{6-x/2+\delta}$][1-7]. The relations between crystal structure and superconductivity in superconducting $La_{1.6}Sr_{0.4}CaCu_2O_{5.94}$ and $La_{1.8}Sr_{0.2}CaCu_2O_6$ and in weakly superconducting $La_2CaCu_2O_{6.04}$ have been investigated by use of neutron powder diffraction[8-10], because the 2126 compounds are not superconducting if they are conventionally synthesized in air or in 1-atm O_2, and special attention has been given to oxygen stoichiometry. However, no consistent results have been obtained. Furthermore, no detailed comparison of crystal structures between superconducting and nonsuperconducting compounds has yet been reported. This paper reports results of precise structure refinements for superconducting and nonsuperconducting $La_{1.82}Ca_{1.18}Cu_2O_{6\pm\delta}$ with neutron powder diffraction data.

Samples were synthesized from La_2O_3, $CaCO_3$, and CuO powders with purities higher than 99.9%. Nonsuperconducting $La_{1.82}Ca_{1.18}Cu_2O_{6-\delta}$ was prepared by firing the mixture at 1060°C for 50 h under 2 atm of fowing O_2. Superconducting $La_{1.82}Ca_{1.18} Cu_2O_{6+\delta}$ was obtained by sintering the nonsuperconducting compound again at 1080°C for 100 h in 20% O_2 + 80% Ar at a total pressure of 2000 atm (P_{O_2} of 400 atm) using a furnace for hot isostatic pressing (HIP).

Neutron-diffraction data were collected at room temperature on a time-of-flight (TOF) neutron powder diffractometer, HRP, at the pulsed-spallation neutron source[11]. The gate width was appropriately set at 4–16 μs, depending on the TOF.

Structure parameters were refined by using RIETAN[12] for the Rietveld analysis of TOF neutron-diffraction data on the basis of $I4/mmm$ space group[13,14]. The crystal structure of the 2126 compound is shown in Fig. 1. Wycoff positions are 2a (0,0,0) for La(1) and Ca(1), 4e (0,0,z) for La(2), Ca(2), Cu, and O(2), 8g (0,1/2,z) for O(1), and 2b (0,0,1/2) for O(3). Anisotropic thermal parameters were assigned to all sites except for an interstitial 2b site of O(3) whose isotropic thermal parameter B was arbitrarily fixed at 1 Å^2 because of its very low occupancy. Refinement of the occupancy for the O(3) site in the nonsuperconducting compound gave a very small negative value, so it was fixed at zero in the final refinement. The site occupancies g's were refined under the following linear constraints: $g(\mathrm{Ca(1)}) = 1 - g(\mathrm{La(1)})$, $2g(\mathrm{La(2)}) = 1.82 - g(\mathrm{La(1)})$, and $2g(\mathrm{Ca(2)}) = 1.18 - g(\mathrm{Ca(1)})$. The coherent scattering lengths used for the Rietveld analysis were 8.24 (La), 4.90 (Ca), 7.718 (Cu), and 5.803 fm (O).

Figure 2 compares temperature dependence of electrical resistivity for the superconducting and nonsuperconducting compounds. Note that both of the compounds show almost the same electrical resistivity at temperatures higher than 100 K but their electrical resistivities differ significantly at lower temperatures. The superconducting compound showed T_c(onset) ≈ 60 K and T_c(zero) ≈ 49 K. Its Meissner volume fraction was more than 15%.

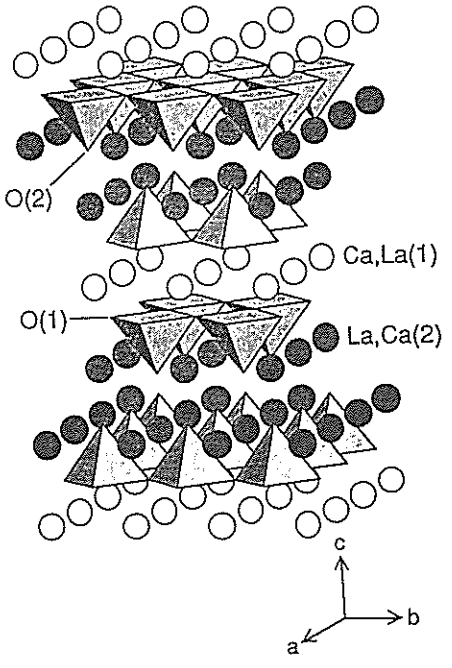

Fig. 1 Crystal structure of $La_{2-x}Ca_{1+x}Cu_2O_6$.

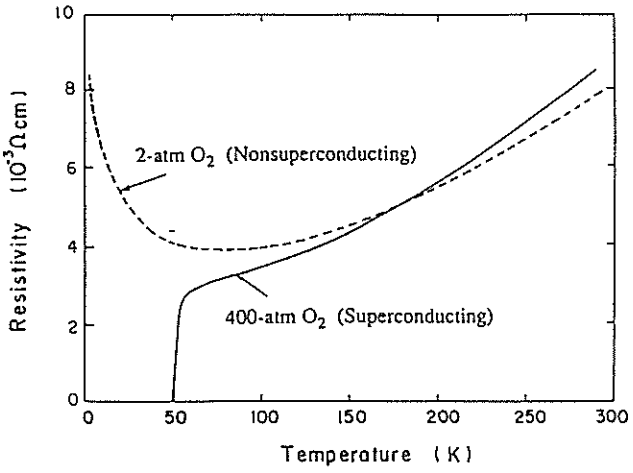

Fig. 2 Dependence of electrical resistivity on temperature for superconducting and nonsuperconducting $La_{1.82}Ca_{1.18}Cu_2O_{6\pm\delta}$.

Final refinable structure parameters and selected interatomic distances are summarized in Table 1, and the observed, calculated, and difference patterns for superconducting $La_{1.82}Ca_{1.18}Cu_2O_{6+\delta}$ are shown in Fig. 3. No signs of impurities were detected in the neutron diffraction patterns of the two samples, and very small R factors show ecellent agreements between calculated and observed intensities.

Table 1. Lattice parameters *a*, *c* (Å), occupation factors *g*, *z* coordinates, interatomic distances (Å), and *R* factors in superconducting and nonsuperconducting $La_{1.82}Ca_{1.18}Cu_2O_{6\pm\delta}$. Estimated standard deviations shown in parentheses refer to the least significant digit(s).

	Superconducting	Nonsuperconducting
a	3.81604(6)	3.82199(7)
c	19.4214(3)	19.4164(4)
La(1): *g*	0.043	0.062
Ca(1): *g*	0.957(15)	0.94(2)
La(2): *g*	0.889	0.88
Ca(2): *g*	0.111	0.12
O(2): *g*	1	0.995(12)
O(3): *g*	0.014(7)	0
Cu: *z*	0.41509(9)	0.41504(13)
O(1): *z*	0.08186(7)	0.08215(11)
O(2): *z*	0.29604(13)	0.2958(2)
Ca,La(1)–O(1) (×8)	2.4836(9)	2.4892(14)
La,Ca(2)–O(1) (×4)	2.6424(14)	2.639(2)
La,Ca(2)–O(2) (×4)	2.7525(5)	2.7579(7)
La,Ca(2)–O(2) (×1)	2.332(2)	2.329(4)
Cu–O(1) (×4)	1.9089(1)	1.9118(1)
Cu–O(2) (×1)	2.312(3)	2.315(5)
R_{wp} (%)	4.57	4.99
R_p (%)	3.40	3.62
R_I (%)	2.30	2.84
R_F (%)	1.81	1.74
R_e (%)	4.08	3.83

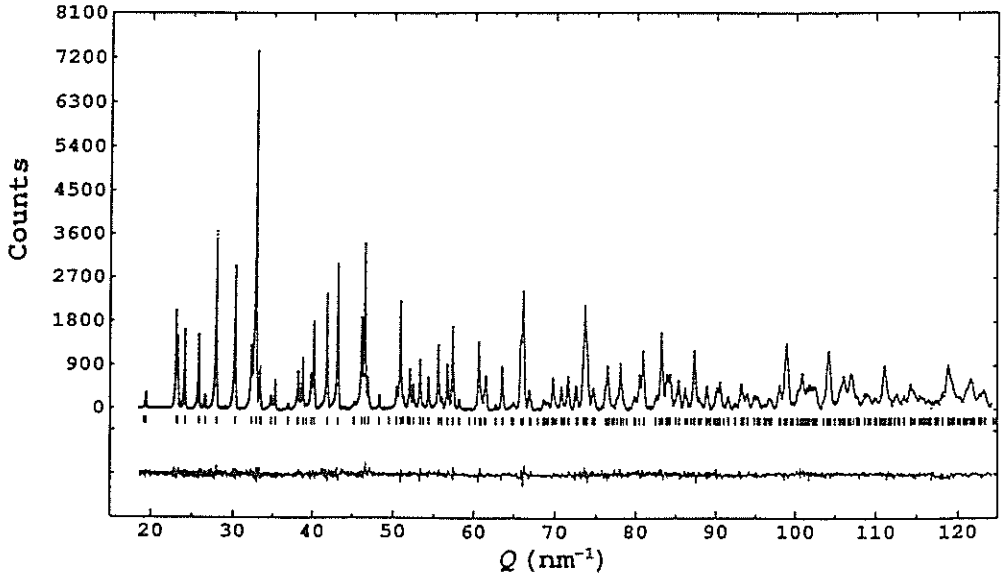

Fig. 3 Rietveld refinement patterns for superconducting $La_{1.82}Ca_{1.18}Cu_2O_{6+\delta}$ plotted against Q (= $2\pi/d$). The background is subtracted. Plus marks show observed neutron-diffraction intensities.

Cation ordering at the 2a and 4e sites is important for determining the location of doped holes. When La is at 4e site and Ca is at 2a site, the Madelung potential of the apical O(2) atom relative to that in the CuO_2 plane is positive and holes are thus doped on the plane[15]. When the La and Ca atoms are disordered, this Madelung potential is negative and the doped holes enter the apical O(2) site. Superconductivity appears when the doped holes enter the CuO_2 plane[15,16]. The superconducting compound has slightly larger occupation of La(2) at the 4e site and Ca(1) at the 2a site than the nonsuperconducting one. Similar results were obtained from the Rietveld analysis of X-ray powder diffraction data[2,6]. However, the difference in g(Ca(1)) between the two samples is so little that their g(Ca(1)) values agree with each other within estimated standard deviations. The effective ionic radii for La^{3+} and Ca^{2+} ions in eight coordination are 1.16 Å and 1.12Å, respectively, which suggest that the Ca,La(1)–O(1) bond length decreases with increasing g(Ca(1)). In fact, the Ca,La(1)–O(1) bond length decreases to the largest extent by the HIP treatment as shown in Table 1. This finding gives indirect evidence in favor of the higher ordering of La^{3+} and Ca^{2+} ions in the superconductor.

The O(1) site was fully occupied in both superconducting and nonsuperconducting compounds. The apical O(2) site of the superconductor was also fully occupied. The occupancy of O(2) for nonsuperconductor was refined to be slightly less than 1 in the present analysis: 0.995(12). Within the estimated standard deviation, however, the O(2) site in the nonsuperconductor can also be regarded as fully occupied.

A slight amount of oxygen [g = 0.014(7)] is intercalated at the O(3) site between two CuO_2 planes of the superconductor but not of the nonsuperconductor. Slight amounts of excess oxygen between two CuO_2 planes are also observed in superconducting $La_{1.8}Sr_{0.2}CaCu_2O_6$ (ref. 9) and in weakly superconducting $La_2CaCu_2O_{6.04}$ (ref. 10). Therefore, the presence of interstitial oxygen may be essential for the superconductivity of the 2126 compounds.

Antiferromagnetic Néel temperature for Ar-annealed $La_{1.82}Ca_{1.18}Cu_2O_{6-\delta}$ and hydrogenated $La_{1.9}Ca_{1.1}Cu_2O_6H_x$ are higher than 300 K and those for $La_{1.82}Ca_{1.18}Cu_2O_{6-\delta}$ synthesized in 0.2 - 2 atm O_2 are around 20 K[17,18]; antiferromagnetic order disappears in superconductors[3]. In layered compounds, the Néel temperature is generally evaluated by the product of the effective coupling between planes and the magnetic correlation length within a layer. The small amount of interstitial oxygen may frustrate interplane coupling and destroy three-dimensional long-range antiferromagnetic order by bridging the CuO_2 planes, or they may frustrate two-dimensional antiferromagnetic Cu^{2+}-Cu^{2+} spin correlations within CuO_2 planes by increasing holes in them[3]. Superconductivity in this system may appear as a result of such frustrations for antiferromagnetic order.

However, a large amount of excess oxygen destroys superconductivity of the 2126-type compounds[19] by disturbing the regularity and two-dimensionality of the CuO_2 planar network. In reality, $La_{1.82}Sr_{1.18}Cu_2O_{6.24}$, which has a considerable amount of excess oxygen between two CuO_2 planes, is not superconducting even if synthesized under a high-O_2 pressure[2].

The oxygen contents $6 \pm \delta$ calculated from the occupancies of the O(1). O(2), and O(3) sites were 6.014 ± 0.007 for the superconducting compound and 5.99 ± 0.02 for the nonsuperconducting compound. The difference in oxygen content corresponds to an increase in Cu valence as much as 0.024 in the superconductor. This increment is fairly close to the difference in bond valence sum between the two samples: 0.019. These results clearly show that the hole concentration on the CuO_2 plane is increased by the HIP treatment.

References

1) K. Kinoshita, H. Shibata and T. Yamada, Physica C 171, 523 (1990)
2) K. Kinoshita, H. Shibata and T. Yamada, Physica C 176, 433 (1991)
3) K. Kinoshita and T. Yamada, Phys. Rev. B 46 (in the press)
4) R. J. Cava et al., Nature 345, 602 (1990)
5) K. Kinoshita, H. Shibata and T. Yamada, Jpn. J. Appl. Phys. 29, L1632 (1990)
6) K. Kinoshita, H. Shibata and T. Yamada, Phase Transitions 37, 121 (1992)
7) T. Sakurai et al., J. Appl. Phys. 69, 3190 (1991)
8) R. J. Cava et al., Physica C 172, 138 (1990)
9) T. Sakurai et al., Physica C 174, 187 (1991)
10) A. Fueertes et al., Physica C 170, 153 (1990)
11) N. Watanabe et al., Jpn. J. Appl. Phys. 26, 1164 (1987)
12) F. Izumi et al., J. Appl. Crystallogr. 20, 411 (1987)
13) N. Nguyen et al., Mater. Res. Bull. 15, 891 (1980)
14) F. Izumi et al., Physica C 157, 89 (1989)
15) J. Kondo et al., J. Phys. Soc. Jpn. 57, 4334 (1988)
16) Y. Ohta et al., Physica C 166, 385 (1990)
17) W. Ye, T. Takabatake, T. Ekino and H. Fujii, Supercond. Sci. Technol. 4, S208 (1991)
18) T. Furubayashi K. Kinoshita, T. Yamada and T. Matsumoto, Physica C 185-189, 1231 (1991)
19) P. Lightfoot et al., Physica C 169, 464 (1990)

Mechanism of Hole Doping in the Superconducting Copper Oxide Carbonate $(Ba_{1-x}Sr_x)_2Cu_{1+y}O_{2+2y+z}(CO_3)_{1-y}$

F. IZUMI, K. KINOSHITA* and Y. MATSUI

National Institute for Research in Inorganic Materials, 1-1 Namiki, Tsukuba, Ibaraki 305
*NTT Basic Research Laboratories, 3-9-11 Midori-cho, Musashino, Tokyo 180

A tetragonal compound in the Ba-Sr-Cu-C-O system discovered by Kinoshita and Yamada[1] is the first superconducting copper oxide containing carbon as a principal constituent. In a previous study[2], we determined its structure by adopting space group $P42_12$ or $P\bar{4}2_1m$. The true space group later proved to be P4bm, $P\bar{4}b2$, or P4/mbm from the condition limiting possible reflections: $k = 2n$ for $0kl$. Fortunately, the crystal structure reported by us differs only slightly from those analyzed on the basis of the possible space groups.

The lattice parameters of the superconductor are $a \approx 0.556$ nm $\approx \sqrt{2}a_p$ and $c \approx 0.786$ nm $\approx 2a_p$ (a_p: unit-cell dimension of the perovskite-type compound, ABO_3). High-resolution transmission electron microscopy suggests that its structure consists of two perovskite-like units, where A sites are occupied by Ba^{2+} and Sr^{2+} ions, and B sites by Cu and C atoms alternately along the [001] direction (Fig. 1). Rietveld analysis of TOF neutron diffraction data revealed that the compound is a member of a solid solution with the general formula $(Ba_{1-x}Sr_x)_2Cu_{1+y}O_{2+2y+z}(CO_3)_{1-y}$ ($x = 4/9$, $y = 1/9$, and $z = 0.10$).

The superconductor is closely related in structure to $Sr_2CuO_2CO_3$ (ref. 3), which is an end member of the solid solution: $x = 1$, $y = 0$, and $z = 0$. CuO_2 conduction sheets ($z = 1/2$ plane in Fig. 1) and carbonate slabs, $(Ba_{1-x}Sr_x)_2Cu_yO_{2y+z}(CO_3)_{1-y}$, acting as charge reservoirs are stacked alternately along the c axis. As the formula of the slab shows, about 11% of C atoms are substituted by excess Cu(2) atoms coordinated to O(5) and O(6) atoms, which respectively amount to $2y$ and z in the formula unit. O(5) and O(6) occupy positions that correspond to an apical O site and a partially occupied O site on a $z = 0$ plane in tetragonal $Ba_2YCu_3O_{7-z}$, respectively. These substitutional and interstitial defects enable hole carriers to move from the carbonate slab to the CuO_2 sheet, making the oxide carbonate superconducting. This is a much more complex method of hole doping than the isomorphous replacement of cations and the incorporation of interstitial O atoms which have been observed in hitherto known superconducting oxides.

Two O atoms in the CO_3 group are situated at apical positions of Cu(1), and the other one is coordinated to alkaline earth cations. The distances between Cu(1) and the two apical O atoms (0.263 and 0.317 nm) are much longer than C–O distances (*ca.* 0.13 nm); one of the apical O atoms should be regarded as residing outside the first-coordination sphere of the Cu(1) ion. These facts show that the apical O atoms are bonded to Cu(1) through relatively weak electrostatic forces of attraction.

References

1) K. Kinoshita and T. Yamada, *Nature* **357**, 313 (1992).
2) F. Izumi, K. Kinoshita, Y. Matsui, K. Yanagisawa, T. Ishigaki, T. Kamiyama, T. Yamada and H. Asano, *Physica C* **196**, 227 (1992).
3) Y. Miyazaki, H. Yamane, T. Kajitani, T. Oku, K. Hiraga, Y. Morii, K. Fuchizaki, S. Funahashi and T. Hirai, *Physica C* **191**, 434 (1992).

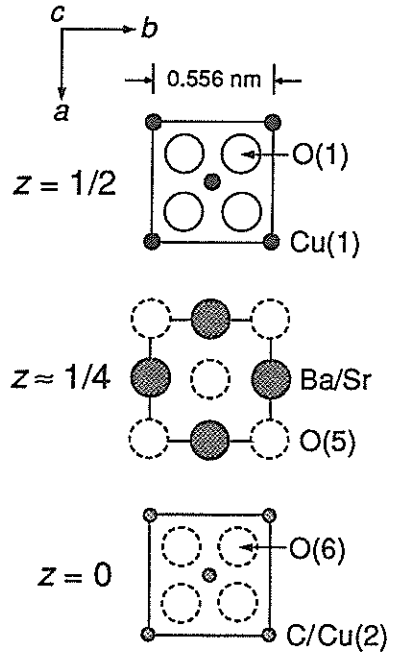

Fig. 1. Cross sections of the unit cell for the Ba-Sr-Cu-C-O superconductor. Dashed circles represent the partially occupied sites of O bonded to Cu(2).

Crystal Structure of $SrT_xV_{6-x}O_{11}$ (T = Ti, Cr, Fe)

Y. Kanke, F. Izumi, E. Takayama-Muromachi, K. Kato, T. Kamiyama* and H. Asano*

National Institute for Research in Inorganic Materials, 1–1 Namiki, Tsukuba, Ibaraki 305
*Institute of Material Science, University of Tsukuba, Tennodai, Tsukuba, Ibaraki 305

NaV_6O_{11}[1–3] and SrV_6O_{11}[3, 4] (AV_6O_{11} phase: hexagonal, $P6_3/mmc$) are structurally related to $BaFe_{12}O_{19}$ (hexagonal, $P6_3/mmc$), a well known magnetoplumbite-type ferrite. NaV_6O_{11} behaves as metallic both above 240 K and below 64.2 K[2, 5], and shows spontaneous magnetization (T_c=64.2 K)[5]. $BaFe_{12}O_{19}$ is formed by alternate stacking of spinel- and R-blocks. The AV_6O_{11} phases consist exclusively of the R-block. The unit formula of AV_6O_{11} contains three octahedral V(1) sites, two octahedral V(2) sites and one trigonal-bipyramidal V(3) site. The V(1) octahedra form edge-shared networks perpendicular to [001]. Two V(2) octahedra adjoin each other across a mirror plane perpendicular to the c-axis and form a face-shared dimer. The V(3) site is placed in the mirror plane. In $BaFe_{12}O_{19}$, all Fe atoms are trivalent. In the AV_6O_{11} phases, on the other hand, both trivalent and tetravalent V atoms are contained, and their ratio depends on the valence of the A atom. Cation distributions in AV_6O_{11} phases are of great interest in connection with their electric and magnetic properties.

In the present study, we found new compounds $SrT_xV_{6-x}O_{11}$ (T=Ti: $0<x\leq1.5$, Cr: $0<x\leq1.0$ and Fe: $0<x\leq1.4$), and determined the structures of $SrTiV_5O_{11}$, $SrTi_{1.5}V_{4.5}O_{11}$, $SrCrV_5O_{11}$ and $SrFeV_5O_{11}$ by Rietveld analyses of their neutron powder diffraction data taken on the TOF neutron powder diffractometer, HRP, at the KENS. Detailed procedures of syntheses and analyses are described elsewhere[4]. Final R factors (%) were R_{wp}=5.30, R_e=5.44, R_p=4.22 and R_I=3.16 ($SrTiV_5O_{11}$), R_{wp}=5.55, R_e=4.65, R_p=4.14 and R_I=3.50 ($SrTi_{1.5}V_{4.5}O_{11}$), R_{wp}=5.07, R_e=5.19, R_p=3.82 and R_I=2.64 ($SrCrV_5O_{11}$: see Fig. 1) and R_{wp}=4.41, R_e=4.36, R_p=3.48 and R_I=2.81 ($SrFeV_5O_{11}$). Ti, Cr and Fe were easily distinguished from V because the absolute value of the coherent scattering length for V is much smaller than those of the other three metals.

Madelung energy calculations for $SrT_xV_{6-x}O_{11}$ phases indicated that the V(1) and V(3) sites prefer trivalent cations, while the V(2) site tetravalent cations. Fe^{3+} prefers not only octahedral sites but also trigonal-bipyramidal ones. Both Ti^{4+} and V^{4+} are known to occupy five-coordinated sites. V^{3+} is hardly located in five-coordinated sites. Cr^{3+} occupies octahedral sites, exclusively. Therefore, if we assume that metal atoms in $SrT_xV_{6-x}O_{11}$ are ionic and d-electrons in them are localized, Ti is expected to occupy the V(2) site, Cr the V(1) site and Fe the V(3) site. However, none of the three T atoms are concentrated at expected sites (Table 1). Though Fe atoms are not located in the V(1) site and Cr atoms hardly occupy the V(3) site, cation distribution in $SrT_xV_{6-x}O_{11}$ seems to be disordered rather than ordered. Above discussion suggests random distribution of V^{3+} and V^{4+} and the possible existence of itinerant d-electrons in SrV_6O_{11} and $SrT_xV_{6-x}O_{11}$.

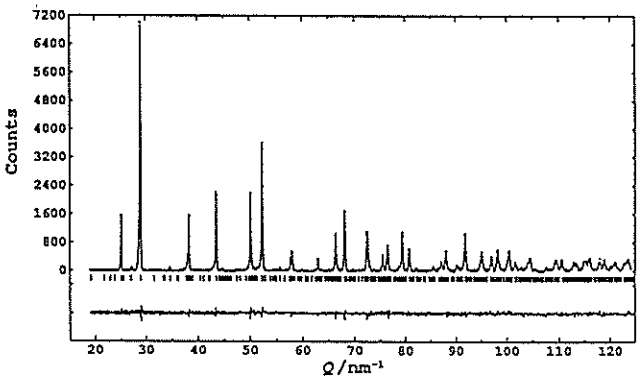

Fig. 1 Observed, calculated and difference neutron powder diffraction patterns of $SrCrV_5O_{11}$.

Table 1 Occupancies of T atoms at V(n) sites in $SrT_xV_{6-x}O_{11}$.

site	$SrTiV_5O_{11}$	$SrTi_{1.5}V_{4.5}O_{11}$	$SrCrV_5O_{11}$	$SrFeV_5O_{11}$
V(1)	0.12(2)	0.13(2)	0.15(1)	0
V(2)	0.24(3)	0.39(3)	0.23(2)	0.238(4)
V(3)	0.16(7)	0.35(9)	0.07(6)	0.564(8)

References

1) M. E. de Roy, J. P. Besse, R. Chevalier and M. Gasperin, J. Solid State Chem. 67, 185 (1987).
2) Y. Kanke, E. Takayama-Muromachi, K. Kato and Y. Matsui, J. Solid State Chem. 89, 130 (1990).
3) Y. Kanke, K. Kato, E. Takayama-Muromachi and M. Isobe, Acta Cryst. C48, 1376 (1992).
4) Y. Kanke, F. Izumi, E. Takayama-Muromachi, K. Kato, T. Kamiyama and H. Asano, J. Solid State Chem. 92, 261 (1991).
5) Y. Uchida, Y. Kanke, E. Takayama-Muromachi and K. Kato, J. Phys. Soc. Jpn. 60, 2530 (1991).

TOF Neutron Diffraction of D_2O under Pressure

Kazuo KAMIGAKI, Yosikazu ISIKAWA,
Takashi SUZUKI* and Shoichi TOMIYOSHI**
Department of Physics, College of Liberal Arts, Toyama University, Toyama 930
*Department of Physics, Tsukuba University, Tsukuba 305
**Institute for Materials Research, Tohoku University, Sendai 980

Abstract

Experimental systems for time-of-flight (TOF) neutron diffraction are developped for the study of materials under high pressure and low temperature. Fuendamental properties required for the apparatus are discussed in detail. The system is applied for the study of polymorphism in heavy ice, and successive transformations are observed with varying the pressure.

1 Introduction

X-ray diffraction has been used effectively for the study of materials under high pressure. The diamond anvil cell is the most effective tool for the X-ray study under pressure. Some specific properties of diamond are the usefull points: hard and high strength, nearly transparent for X-rays, coherent scattering of X-rays is limited in definite spots. Neutron beams have some preferences to X-rays: the absorption is independent of the atomic number, the scattering is high even for light elements. The present authors planned to construct systems for neutron diffraction of D_2O under high pressure and low temperature.

A variety of experimental technics has been realized for the neutron diffraction at ambient pressure, most of the technics can be applied for high pressure experiments. For example, we can grow single crystals of a substance under pressure at controlled temperature. But we can not observe the growth process directly, because the high pressure container is not transparent. The in-situ monitoring using the neutron diffraction technique under pressure will serve a powerfull tool for analyzing the growth mechanism. A wide range of application will be developed by a precise analysis of the technics developed here. Some of practical points are discussed in detail.

2 Necessary condition for high pressure apparatus

There are some specific conditions required for the apparatus of neutron diffraction under high pressure. The conditions depend primarily on the purpose of the experiment: The first is the measurement of compressibility. The shift of lines must be determined precisely in the diffraction pattern. For the detection of an anisotropic deformation of the lattice, precise analysis is required even in the shape of lines or spots.

The second will be the observation of the pressure induced transformation in the materials. Measurements are made on the variation of crystal structure, change in the volume at the transformation, accompanied change in the other physical properties such as electrical conductivity, magnetic properties, and so on. Variations with temperature of the compressibility and of the critical point for the transformation are also important.

There are some specialities in the neutron diffraction under pressure: the most important is the existence of the pressure cell and the pressure transmitting medium, in contrast with the case of the ordinary diffraction where the specimen is kept in vacuum, or contained in a thin capirary tube of amorphous glass.

The materials around the specimen cause some extra-scattering and contamination of extra-lines in the pattern. If the material does not cause the coherent scattering, background level of the pattern is raised and the signal to noise ratio is made worse. All such effects act to reduce the quality of the experiment.

Incoherent alloys such as Ti-Zr alloy do not make coherent scattering, but cause a flat background for thermal neutrons [1, 2]. The absorption of thermal neutrons in Ti-Zr alloy is in a range of ordinary metals, but not so small. To use the intense beam source or to extend the exposure time is necessary to get results of high quality.

Both the angle dispersive method and the energy dispersive or the time-of-flight (TOF) method are used for the diffraction experiment. In the former, both the incident beam and the scattered beam scann a range of angle around the specimen, a large volume of pressure transmitting medium are swept by the neutron beam becomes, and the effects of the extra-scattering become large [1]. The geometry of neutron beams is fixed in the latter, and the design of the apparatus is simple.

In the X-ray diffraction under high pressure using diamond anvil cell, diffracted spots from the single crystalline diamond are superimposed to the pattern of the specimen. The spots are separated easily from the pattern concerned, and the influence to the original pattern

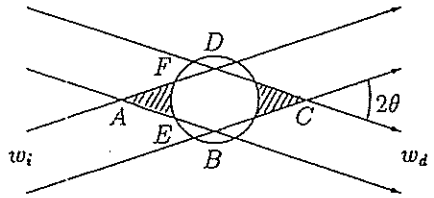

Figure 1: Geometry of diffraction: incident beam; width: w_i, aperture of the detector; width: w_d, specimen; diameter: d, and diffraction angle: 2θ.

is reduced. A simple crystal such as saphire was used for the anvil cell for neutron [3], a good performance was obtained for the monochromatic beam. Aluminum is low absorbing for thermal neutrons, angular arrangement of diffraction lines is simple, and some aluminum alloys will be used as a pressure medium at special conditions in the angle dispersive experiments.

3 Geometrical considertions

3.1 Size of the specimen

Let the neutron beam is applied to a polycrystalline specimen of cylindrical form with diameter d, the scattered intensity will be proportional to the number of reflecting planes contained in the specimen, or to the diameter d. The rate of absoption by the specimen is proportional to $\exp(-\mu d)$, where μ is the linear absorption coefficient. If we wish to maximize the resultant intensity, $d\exp(-\mu d)$ is to be maximized with respect to d. This is realized when $d = 1/\mu$, or it is preferable to make diameter of the specimen equal to the inverse of the linear absorption coefficient.

3.2 Width of slits

The diffracted neutron beam is contaminated frequently with extra- scattering originated from the materials surrounding the specimen. Such contamination is reduced by using slits to adjust the irradiated area outside the specimen, and to limit the visual field of the detector. The geometry of diffraction is shown in Fig. 1, where the widths of incident beam w_i and aperture of the detector w_d are same and w, diameter of the specimen is d, and the diffraction angle is 2θ. Geometrical conditions neccessary for realizing clear and intense pattern are considered on the basis of this Figure. Matrials contained in the width w_i diffract the neutron beam, and the portion of the beam diffracted by materials included in the aperture w_d is caught by the detector. Hence, a part of materials contained in the rhombus $ABCD$ in Fig. 1 contribute to the diffraction. If the rhombus is perfectly included

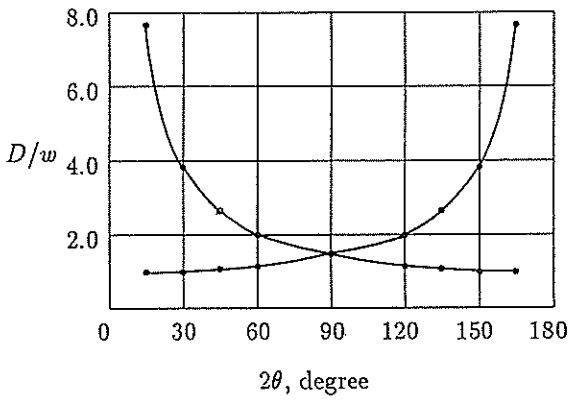

Figure 2: Variation of diagonal length of rhombus with the angle 2θ.

in the specimen, and if the other materials are not contained in that area, no contamination will be observed in the diffraction pattern. Diagonals of the rhombus are $D_{AC} = w/\sin\theta$ and $D_{BD} = w/\cos\theta$, and vary with 2θ as shown in Fig. 2. If the width of slits is taken as $w = d\sin\theta$, $(2\theta \leq^{\circ})$, or $w = d\cos\theta$, $(2\theta \geq 90^{\circ})$, w changes with 2θ as $0.13d$ at 15°, $0.5d$ at 60°, and maximum width $0.7d$ is available at 90°. In these cases, the rhombus is included in the area of the specimen, and no contamination will be expected.

3.3 Rate of the extra-scattering

The ratio of the extra-scattering will be proportional to the partial area of the rhombus penetrating to the outside of the specimen. In the geometry shown in Fig. 1, this part is the shaded area AEF, nearly equal to $\triangle AEF$, or $(D_{AC} - d)^2\tan\theta/8$. The ratio R of the sum of two shaded areas to the part of rhombus included in the specimen is $R = 1/((D/(D-d))^2 - 1)$, where $D \equiv D_{AC}, D_{BD} > d$. If the coherent scattering amplitude of the material at the shaded area is same with that of the specimen, the above expression represents the rate of the extra-scattering. The value of R is expressed in Fig. 3 as a function of D/d.

In the figure, if D is less than $2d$, R is less than 1/3, and the extra-scattering expected is less than one third of the specimen. In comparison with Fig. 2, if $w = d/2$, the condition for 1/3-contamination is $D = 2d = 4w$, or allowed range of 2θ is extended to 30° – 150°. The nature of the extra-scattering contained in the pattern will be characterized by its intensity and the disturbance due to superposition to the original lines of the specimen. If extra-lines do not coincide with principal lines and subtracted by a conventional way, the pattern will be analyzed clearly.

3.4 Incoherent alloy

If elements with opposite sign in the scattering length are mixed to form a solid solution to make a zero length, the

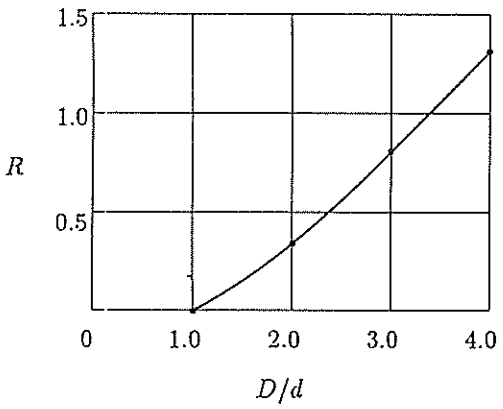

Figure 3: Ratio of area of the rhombus existing at the outside of the specimen.

alloy has no coherent scattering. Ti-Zr alloy system is a perfect slid solution, both elements sit on the lattice points randomly. The scattering length for Ti is -3.438 fm, for Zr is 7.16 fm, and opposite in the sign. In 50 wt-% Ti-Zr alloy the scattering length is nearly cancelled and a good example of such alloy. The Ti-Zr alloy is made by arc-melting in high purity argon atmosphere, the alloy is machinable and formed to a cylinder easily [1, 6]. The mechanical strength is nearly same with brass and to be used to generate pressures as high as 10 kbar.

In a precision measurement, a wavy pattern due to atomic correlation is observed in the disordered Ti-Zr alloy [7], an analysis of the background must be made carafully.

3.5 Aluminum alloy

If the incident neutron beam is weak, the absorption by the cell is an important factor. In some high-strength alloys of aluminum, the mechanical strength is not so low and can be used for the cylinder. Both the coherent scattering length(3.449 fm) and the absorption coefficient of Al are not so large, and allowed range of R can be taken large. Hence, the alloy will be used as cylinders with comparatively wide width of slits. Therefore the alloy is useful for weak source, but the pressures will be limited to low values as $\sim$ 10kbar.

3.6 High-strength steel

Some high-strength alloys are developed recently, popular in the market, and a variety of choice is available. In the ordinary maraging steel, 250kg/mm^2 is attained by a proper heat treatment, and pressures higher than 20 kbar will be reached. The coherent scatterring length is large in Fe(9.45 fm) or Ni(10.3 fm), and the ratio w/d must be made small to meet the requirements mentioned in sections 3.2 and 3.3. And, moreover, the absorption coefficient is not so small. In regard with these factors, if the intense neutron sourse is available, the higher pressure will be achived by such materials.

4 Experimental system

4.1 High pressure cell

The heigh pressure cell is a piston and cylinder type, composed of pistons made of tungsten carbide or hardened steel ,and a cylinder of Ti-Zr alloy or aluminum alloy, reinforced by an outer binding ring made of hadened steel. The incident neutron beam is induced through a slit cut in the outer ring. The scattered beam is taken out through another slits in the ring.

The width and the angular position of slits are designed in consideration with the final intensity and the range of lattice spacing to be covered. If the beam width is narrow and the diameter of the cylinder hole is wide, the contamination is reduced remakably. However, both the resultant beam intensity and the attained pressure are reduced. If the incident beam is strong enough, high-strength alloys such as maraging steel is used for the cylinder and the limit of pressure will be improved.

In the present system, center hole in the cylinder is 0.8 - 1.2 cm in diameter and outer diameter is about 3 - 4 cm, slit width is 0.5 cm, and two-theta angles are in a range 60 - 120 degrees. A cylindrical tube of boron-plastic is placed outside the binding ring, to reduce the extra-scattering. The pressure is loaded by a hydraulic press, maximum output of which is twenty tons.

4.2 Low temperature

Two types of cryostat are designed for keeping the cell at low temperatures: the one is to attach a liquid nitrogen container to the cell [4], and the other is to use a small refrigerator [5]. In the liquid nitrogen system, an automated suplyer of coolant is prepared to keep a run for long duration.

One problem in the design of the apparatus is the compatibility of insulation of heat flow with transmission of the compressing force. Higher pressure is supported by a plastic of larger cross section, but the heat flow becomes larger at the sametime, and the lowest temperature attained is limited to higher. In the present system, reinforced plastics of phenolic resin or epoxy resin is used for the pressure transmitting parts.

4.3 Utilization of boron plastics

Mixtures of epoxy resin with boron-carbide (B_4C) powder are molded to form parts for shielding of neutrons to reduce extra-scattering from the complicated structure of the apparatus. The most effective shielding to improve the background scattering is a concentric cylindrical tube fixed to cover the binding ring, thin slits are cut for the incidence and transmission of neutron beams. No coating with neutron absorbing material is made on the inner surface of slits, but no extra-scattering is observed.

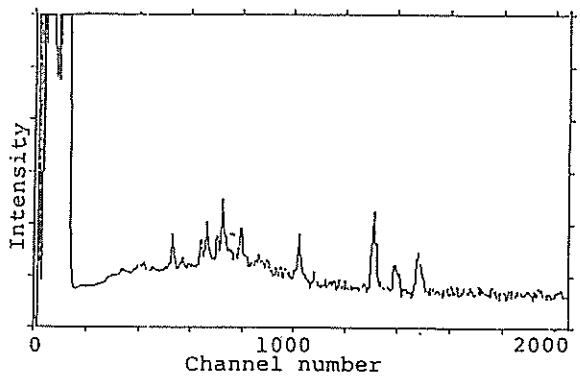

Figure 4: Neutron diffraction of D_2O, at 1 bar and 200 K, $2\theta = 120°$.

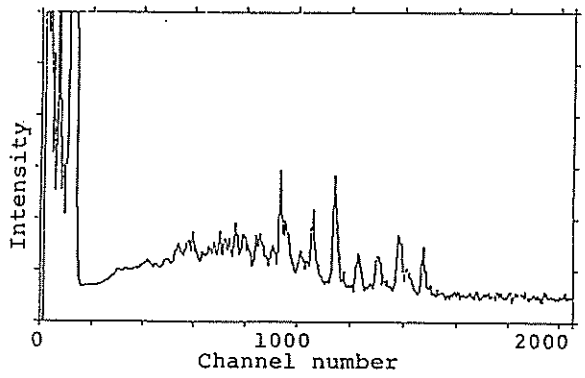

Figure 5: Neutron diffraction of D_2O at 3 kbar and 200 K, $2\theta = 120°$.

5 Neutron diffraction of D_2O under high pressure

Neutron diffraction experiments are performed on D_2O ice under pressure by MRP diffractometer installed at the National Laboratory for High Energy Physics (KEK), Tsukuba. Preliminary works were done by diffractometers at the pulsed neutron source of the Laboratory of Nuclear Science, Tohoku Unibersity, located in Mikamine, Sendai.

The apparatus is a piston and cylinder type, diameter of the cylinder hole is 12 mm, width of slits are 5 mm, and diffraction angles are set at 60, 90 and 120 degrees. Liquid D_2O is filled in a capsule made of teflon, thickness of the wall is about 0.2 mm, and inserted into the cylinder. Hence, the specimen is compressed directly by pistons, without using some pressure transmitting mediums such as CS_2. The experimental procedure is as follows: The specimen is coolded down at first to about 200K without loading pressure, the pattern observed at this stage is shown in Fig. 4. Channel number in the figure corresponds to the time of flight of neutrons, the larger number represents the longer time of flight, or the larger lattice spacing. This pattern corresponds to that of hexagonal ice, no extra-lines originated from materials around the specimen are observed.

The background shows a wide peak from $\sim$ 200 to $\sim$ 1200 channels. The shape of the background reflects the energy distribution (so-called I–λ relation) in the incident neutron beam, and the whole pattern is normalized by the incident beam. The background is obtained by inserting a vanadium rod in the cylinder instead of the specimen. Time duration needed for collecting the data is about six hours in this pattern.

Then, the pressure is increased to 3 kbar, and the pattern obtained here is shown in Fig. 5, other conditions are same as those in Fig.4. This pattern corresponds to the rhombohedral phase of ice.

Diffracted neutrons distribute in a whole range of channels, the pattern grows up simultaneously with time, but a duration is neccessary for collecting counts to build up a pattern with a proper form. The pressure must be kept constant for such duration, and intense source and high counting rate are neccessary to observe an instantaneous change of crystal structure.

A monoclinic structure is observed when the pressure is raised to kbar. The phase of D_2O ice thus observed changes from I to II and then to III with increasing of pressure. In the decreasing cycle of pressure change, the structure changes in a reverse way from III to II, and then to I. The critical pressures for the phase change shift to lower pressure side in reducing the pressure in comparison with increasing cylce.

In this way, structural transformations in the crystalline phase of D_2O-ice are studied successfully [6]. Further application is in progess now to the study of high-density amorphous phase in ice [8].

References

[1] K. Kamigaki, Jpn. J. Appl. Phys., **19**, 2507 (1980)

[2] K. Kamigaki *et al.*, Sci. Rep. RITU, **A39**, 225 (1983)

[3] H. Ahsbahs, R. Dornwarth and W. F. Kuhs, High Press. Res., **5**, 807 (1990)

[4] K. Kamigaki, Res. Rep. Nucl. Sci., **17**, 62 (1984)

[5] K. Kamigaki *et al.*, Res. Rep. Nucl. Sci., **24**, 213 (1991)

[6] K. Kamigaki *et al.*, High Press. Res., **8**, 501 (1991)

[7] K. Gobrecht, private communication.

[8] O. Mishima, L. D. Calvert and E. Whalley, Nature, **310**, 393 (1984)

Structure Refinement of the Orthorhombic $(La_{1-x}Ca_x)_2CuO_4$ (x=0.05)

H. KITO, J. AKIMITSU, F. IZUMI*, T. KAMIYAMA** and H. ASANO**

Department of Physics, Aoyama-Gakuin University, 6-16-1 Chitosedai, Setagaya, Tokyo 157
*National Institute for Research in Inorganic Materials, 1-1 Namiki, Tsukuba, Ibaraki 305
**Institute of Materials Science, University of Tsukuba, Tennodai, Tsukuba, Ibaraki 305

Superconducting copper oxides with the K_2NiF_4–type structure have been studied extensively since the discovery of superconductivity in $(La_{1-x}Ba_x)_2CuO_4$ in 1986[1].

The T_c of $(La_{1-x}A_x)_2CuO_4$ is dependent on both the kind and content of A, where A is Ca,Sr and Ba ions. The maximum superconducting transition temperature is achieved in $(La_{0.925}Sr_{0.075})_2CuO_4$ where the crystal lattice undergoes the phase transition from the high-temperature tetragonal (HTT) to medium-temperature orthorhombic (MTO) phase below room temperature.[2] The maximum T_c (T_c=25K) in $(La_{1-x}Ca_x)_2CuO_4$ (LCCO) is the lowest among the three solid solutions. These differences in superconducting properties seem to be related with differences in effective ionic radii for the three metal ions in 9-coordination: 0.118 nm for Ca^{2+}, 0.131 nm for Sr^{2+} and 0.138 nm for Ba^{2+}.[3] For example, $(La_{0.925}Sr_{0.075})_2CuO_4$ shows a pressure coefficient of T_c, dT_c/dp = 3 K GPa^{-1}; that is, its T_c rises with increasing pressure.[4] This fact suggests that application of "chemical pressure" by replacing larger Sr^{2+} ions with smaller Ca^{2+} ions may lead to a rise in T_c, which is, however, not the case. Why the T_c of LCCO is so lower compared to that of $(La_{1-x}Sr_x)_2CuO_4$? At what temperature does the HTT-MTO transition occur in LCCO? The present study was undertaken to answer these questions. At first, we examined the solubility limit in this solid–solution system and prepared two single phased samples with the highest Ca content. Then, we refined the crystal structure of the samples by Rietveld analysis of the time–of–flight (TOF) powder neutron diffraction data. Since no crystal data on LCCO have been reported in the literature, those described in this paper are believed to be valuable when considering the relationship between structure and superconducting behavior in the $(La_{1-x}A_x)_2CuO_4$ systems.

Samples of LCCO with x=0.05 were prepared by solid–state reaction of La_2O_3, $CaCO_3$ and CuO. Detailed procedures will be published elsewhere. Oh-ishi et al.[5] reported that the solubility limit in LCCO was x ≈0.2. However, we could not obtain a single phase even at x=0.075. Powder X-ray diffraction on the samples with x=0.05 indicated that samples were approximately single phased.

Magnetization measurements showed that T_c of annealed LCCO was 24K and T_c of quenched LCCO was 23K. The Meissner volume fractions of both samples reached 20%.

Neutron powder diffraction data were obtained at room temperature (both samples) or at 18±4 K (annealed LCCO) on a high-resolution TOF neutron powder diffractometer[6], HRP, at the KENS pulsed spallation neutron source. Intensity data was measured using twelve ^3He counters installed at an average 2θ of 170°. The samples were put into a cylindrical vanadium cell (10 mm in diameter, and 42 mm length), which was then placed in an aluminum vacuum chamber. A CRYOMINI refrigerator was used for the low-temperature experiment.

The structural parameters of LCCO were refined by the Rietveld method[7] with a RIETAN program for TOF neutron powder diffraction. The refinements included 3504 data points covering a lattice–plane spacing (d) range from 0.0498 to 0.3336 nm. The structure parameters of LCCO were refined on the basis of space group I4/mmm (tetragonal, No.139) and Cmca (orthorhombic, No.64). The occupation factors, g, of La and Ca at the metal site (hereinafter called as M site) were fixed at 0.95 and 0.05, respectively. The g values of the oxygen sites were fixed at 1. In the Rietveld analysis of the room-temperature data, R_{wp}[8] values for the orthorhombic model were significantly lower than those for the tetragonal model in both samples: 6.39%(I4/mmm) and 4.02%(Cmca) in annealed LCCO, and 6.88%(I4/mmm) and 4.34%(Cmca) in quenched LCCO. Then we concluded that both samples display orthorhombic symmetry at room temperature or below, and the low-temperature structure for annealed LCCO was refined by adopting only Cmca space group.

Table I

Structure parameters of annealed $(La_{0.95}Ca_{0.05})_2CuO_4$ (Z=2) at room temperature. The space group was assumed to be Cmca. R factors were R_{wp}=4.02%, R_e=3.37%, R_p=3.05%, R_R=6.86%, R_I=2.31% and R_F=1.77%. a=0.534179(9) nm, b=1.31697(2) nm, and c=0.535951(9) nm. As described in the text, the g values for site M were fixed at 0.95 for La and 0.05 for Ca. B_{eq} is the equivalent isotropic thermal parameter, and U_{ij}'s are anisotropic thermal parameters when the temperature factor is defined as $\exp[-2\pi^2(h^2a^{*2}U_{11}+k^2b^{*2}U_{22}+l^2c^{*2}U_{33}+2hka^*b^*U_{12}+2hla^*c^*U_{13}+2klb^*c^*U_{23})]$.

The numbers in parentheses are statistical uncertainties of the last significant digit.

Atom	Site	x	y	z	B_{eq} (nm^2)
M	8f	0	0.36098(7)	0.0050(5)	0.00363[a)]
Cu	4a	0	0	0	0.00329[b)]
O(1)	8e	1/4	0.0048(3)	1/4	0.00561[c)]
O(2)	8f	0	0.18315(13)	-0.0189(8)	0.01140[d)]

a)for M : U_{11}=4.4(7)x 10^{-3} nm^2,
U_{22}=3.9(4)x 10^{-3} nm^2,
U_{33}=5.5(8)x 10^{-3} nm^2,
$U_{12}=U_{13}=0$, U_{23}=0.06(11)x 10^{-2} nm^2

b)for Cu : U_{11}=3.6(9)x 10^{-3} nm^2,
U_{22}=6.5(7)x 10^{-3} nm^2
U_{33}=0.24(10)x 10^{-2} nm^2,
$U_{12}=U_{13}=0$, U_{23}=-0.22(20)x 10^{-2} nm^2

c)for O(1): $U11$=5.1(9)x 10^{-3} nm^2,
U_{22}=1.07(9)x 10^{-2} nm^2
U_{33}=5.5(9)x 10^{-3} nm^2, $U_{12}=U_{23}=0$,
U_{13}=-1.4(4)x 10^{-3} nm^2

d)for O(2): U_{11}=1.75(10)x 10^{-2} nm^2,
U_{22}=3.6(6)x 10^{-3} nm^2,
U_{33}=2.22(14)x 10^{-2} nm^2, $U_{12}=U_{13}=0$,
U_{23}=-0.06(17)x 10^{-2} nm^2

Table II

Structure parameters of $(La_{0.95}Ca_{0.05})_2CuO_4$ quenched(Z=2) at room temperature. The space group was assumed to be Cmca. R factors were R_{wp}=4.34%, R_e=3.74%, R_p=3.29%, R_R=6.62%, R_I=2.23%, and R_F=1.80%. a=0.534186(9) nm, b=1.31696(2)nm, and c=0.535931(9) nm.

Atom	Site	x	y	z	B_{eq} (nm^2)
M	8f	0	0.36099(6)	0.0054(5)	0.00421[a)]
Cu	4a	0	0	0	0.00374[b)]
O(1)	8e	1/4	0.00482(3)	1/4	0.00599[c)]
O(2)	8f	0	0.18310(13)	-0.0188(7)	0.01214[d)]

a) For site M : U_{11}=4.6(7)x 10^{-3} nm^2,
U_{22}=4.4(4)x 10^{-3} nm^2
U_{33}=7.0(8)x 10^{-3} nm^2
U_{12}=U_{13}=0, U_{23}=0.15(10)x 10^{-2} nm^2

b) For site Cu : U_{11}=3.1(8)x 10^{-3} nm^2,
U_{22}=7.4(7)x 10^{-3} nm^2
U_{33}=3.6(9)x 10^{-3} nm^2
U_{12}=U_{13}=0, U_{23}=-0.26(15)x 10^{-2} nm^2

c) For site O(1): U_{11}=4.7(8)x 10^{-3} nm^2,
U_{22}=1.19(8)x 10^{-2} nm^2
U_{33}=6.2(9)x 10^{-3} nm^2,
$U_{12}=U_{23}=0$, U_{13}=-1.5(4)x x10^{-3} nm^2

d) For site O(2): U_{11}=1.83(10)x 10^{-2} nm^2,
U_{22}=5.0(6)x 10^{-3} nm^2
U_{33}=2.28(13)x 10^{-2} nm^2,
$U_{12}=U_{13}=0$, U_{23}=-0.20(17)x 10^{-2} nm^2

Table III

Structure parameters of annealed $(La_{0.95}Ca_{0.05})_2CuO_4$ (Z=2) at 18K The space group was assumed to be Cmca. R factors were R_{wp}=4.07%, R_e=3.19%,R_p=3.11%, R_R=5.61%, R_I=1.942% and R_F=1.28%. a=0.532023(7) nm, b=1.31238(2) nm and c=0.537404(7) nm.

Atom	Site	x	y	z	B_{eq} (nm^2)
M	8f	0	0.36104(7)	0.0075(3)	0.00050[a)]
Cu	4a	0	0	0	0.00069[b)]
O(1)	8e	1/4	0.00704(16)	1/4	0.00216[c)]
O(2)	8f	0	0.18291(13)	-0.0331(3)	0.00446[d)]

a) For site M : U_{11}=0.2(4)x 10^{-3} nm^2,
U_{22}=0.5(4)x 10^{-3} nm^2
U_{33}=1.2(4)x 10^{-3} nm^2
$U_{12}=U_{13}=0$, U_{23}=0.3(6)x 10^{-3} nm^2

b) For site Cu : U_{11}=0.4(5)x 10^{-3} nm^2,
U_{22}=1.7(6)x 10^{-3} nm^2
U_{33}=0.5(6)x 10^{-3} nm^2
$U_{12}=U_{13}=0$, U_{23}=-0.7(8)x 10^{-3} nm^2

c) For site O(1) : U_{11}=1.4(5)x 10^{-3} nm^2,
U_{22}=4.4(7)x 10^{-3} nm^2
U_{33}=2.4(5)x 10^{-3} nm^2
$U_{12}=U_{23}=0$, U_{13}=-0.5(4)x 10^{-3} nm^2

d) For site O(2) : U_{11}=8.0(5)x 10^{-3} nm^2,
U_{22}=1.8(5)x 10^{-3} nm^2
U_{33}=7.2(7)x 10^{-3} nm^2
$U_{12}=U_{13}=0$,.U_{23}=-0.5(8)x 10^{-3} nm^2

Table IV

Interatomic distances l (nm) between the metal and oxygen atoms in the annealed and quenched LCCO at room temperature and 18K.

	l (nm)			N
	room temperature		18K	
Bonds	annealed LCCO	quenched LCCO	aneealed LCCO	
M[i)] –O(1)	2.346(2)	2.346(2)	2.348(2)	1
M[ii)] –O(1)	2.7344(4)	2.7342(4)	2.7254(4)	2
M[iii)]–O(1)	2.617(5)	2.616(4)	2.535(2)	1
M[iv)]–O(1)	2.867(5)	2.868(4)	2.962(2)	1
M[i)] –O(2)	2.603(4)	2.604(3)	2.5848(18)	2
M[ii)]–O(2)	2.664(4)	2.663(4)	2.6718(19)	2
Average M–O	2.6480	2.6480	2.64544	
Cu[iii)]–O(1)	1.8928(1)	1.8928(1)	1.8928(1)	2
Cu[iv)]–O(2)	2.4141(17)	2.4134(17)	2.4071(16)	4

N is numbers of equivalent bonds.
symmetry codes: i) 0, y, z;
ii) 1/2,1/2-y, -z; iii) 0, y, -1/2+z;
iv) 0, 1/2-y,1/2+z

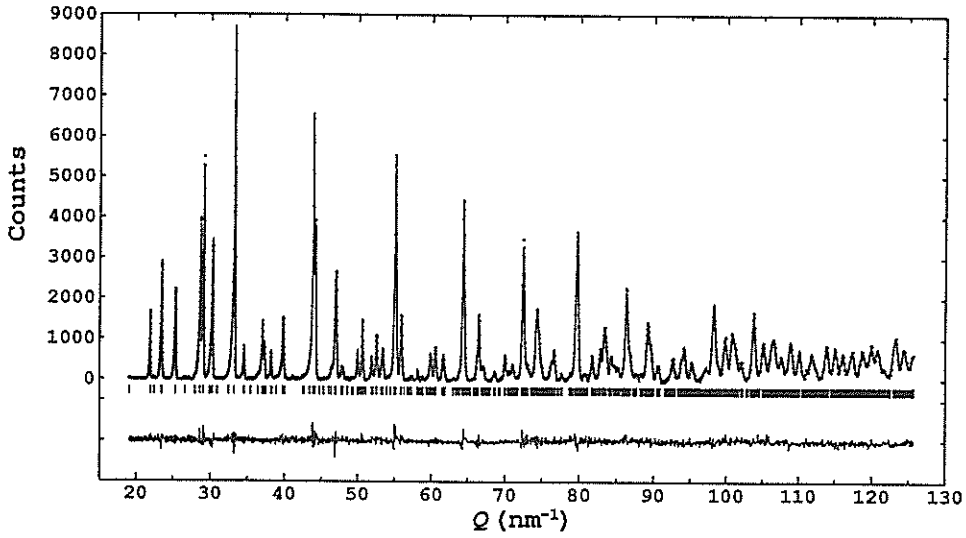

Figure 1. Rietveld refinements patterns of the annealed LCCO (orthorhombic model) at room temperature.

Tables I to III respectively list results for annealed LCCO and quenched LCCO at room temperature and for annealed LCCO at low temperature. Table IV gives the metal-oxygen interatomic distances, *l*, calculated with ORFFE[9]. Figures 1, for example, shows the resultant Rietveld refinement patterns of annealed LCCO at room temperature.

The tetragonal model refinements gave $\chi^2=(R_{wp}/R_p)^2=11.38$ for quenched LCCO and $\chi^2=12.89$ for annealed LCCO, whereas the orthorhombic model gave corresponding values of $\chi^2=1.82$ and $\chi^2=2.03$. From these results, it can be concluded that the room-temperature crystal structure of $(La_{0.95}Ca_{0.05})_2CuO_4$ is in an orthorhombic form. Tables I and II also indicate a tetragonal unit cell consequence of nearly equal to parameters *a* and *c* in the orthorhombic form. Tables I and II also indicate that the structural parameters of quenched and annealed LCCO are nearly the same. Orthorhombic distortion $2(c-a)/(a+c)$ are $3.32(4)\times10^{-3}$ for annealed LCCO and $3.26(3)\times10^{-3}$ for quenched LCCO, which are far smaller than that of $La_2CuO_{4-\delta}$[10]: $8.77(4)\times10^{-3}$.

Orthorhombic distortion for annealed LCCO at low temperature is $1.006(2)\times10^{-2}$. This value should be compared with $5.74(4)\times10^{-3}$ for $(La_{0.925}Sr_{0.075})_2CuO_4$[11] at 10K. Cu-O(1) bond angles are 90.71(1)° and 89.29(1)° and tilt angle of the $[CuO_6]$ octahedra is 2.8(13)° in LCCO at low temperature. These values are also larger than the corresponding value for $(La_{0.925}Sr_{0.075})_2CuO_4$[11] at 10K; 90.42(1)°, 89.58(1)° and 2.3(2)°. From these results, $[CuO_6]$ octahedra of LCCO at low temperature are more strained and more leaned than those of $(La_{0.925}Sr_{0.075})_2CuO_4$ small substitution of Ca for La. Namely, it seems difficult to substitute the small Ca^{2+} ions for La^{3+} ions in La_2CuO_4 maintaining the K_2NiF_4 structure. As the result, the hole concentration in $(Cu\text{-}O)^+$ is lower and hence the maximum value of T_c in LCCO is lower than $(La_{1-x}Sr_x)_2CuO_4$'s.

References

1) J.B.Bednorz and K.A.Müller: Z.Phys.**B64** (1986) 189.

2) R. B. van Dover, R.J.Cava, B.Batlogg and E.A.Rietman: Phys.Rev.**B35** (1987) 5337.

3) R.D.Shannon: Acta Crystallogr. **A32** (1976) 751.

4) Shiyou Pei, J.D.Jorgensen, D.G.Hinks, B.Dabrowski, P.Lightfoot and D.R.Richards: Physica **C169** (1990) 179.

5) K.Oh-ishi, M.Kikuchi, Y.Syono, N.Kobayashi, T.Sasaoka, T.Matsuhira, Y.Muto and H.Yamauchi: Jpn.J.Appl.Phys.**27** (1988) L1449.

6) F.Izumi, H.Asano, H.Murata, and N.Watanabe: J.Appl.Crystallogr.**20** (1987) 411.

7) H.M.Rietveld: J.Appl.Crystallogr.**2** (1969) 65.

8)R.A.Young, E.Princes and R.A.Sparks: J.Appl.Crystallogr.**15** (1982) 357.

9) W.R.Busing, K.O.Martin and H.A.Levy, in: Report ORNLTM-306, Oak Ridge National Laboratry, Tennessee (1964).

10) T.Kamiyama, F.Izumi, H.Asano, H.Takagi, S.Uchida, Y.Tokura, E.Takayama-Muromachi, M.Matsuda, K.Yamada, Y.Endoh and Y.Hidaka: Physica **C172** (1990) 120.

11) F.Izumi, E.Takayama-Muromachi, A.Fujimori, T.Kamiyama, H.Asano, J.Akimitsu and H.Sawa: Physica **C158** (1989) 440.

12) R.J.Cava, A.Santoro, D.W.Johnson,Jr and W.W.Rhodes: Phys Rev **B35** (1987) 6716.

Sr-INDUCED OXYGEN DEFECTS IN $La_{2-x}Sr_xCuO_{4-\delta}$

T. KAMIYAMA[1], F. IZUMI[2], H. ASANO[1], H. TAKAGI[3], S. UCHIDA[3], Y. TOKURA[4], E. TAKAYAMA-MUROMACHI[2], M. MATSUDA[5], K. YAMADA[5], Y. ENDOH[5] and Y. HIDAKA[6]

[1] Institute of Materials Science, University of Tsukuba, Tennodai, Tsukuba-shi, Ibaraki 305, Japan
[2] National Institute for Research in Inorganic Materials, Namiki, Tsukuba-shi, Ibaraki 305, Japan
[3] Engineering Research Institute, University of Tokyo, Yayoi, Bunkyo-ku, Tokyo 113, Japan
[4] Department of Physics, University of Tokyo, Hongo, Bunkyo-ku, Tokyo 113, Japan
[5] Department of Physics, Tohoku University, Aramaki, Aoba-ku, Sendai-shi, Miyagi 980, Japan
[6] NTT Applied Electronics Laboratories, Tokai-mura, Naka-gun, Ibaraki 319-11, Japan

Tan *et al.* [1] have recently reported that a remarkable feature in XANES (X-ray absorption near-edge structure) spectra of $La_{2-x}Sr_xCuO_4$ resulted from the movement of the apical O(2) atom of the CuO_6 octahedron to an interstitial site (shown by the hatched circle in Fig.1) near an Sr atom. They also insisted that the deficient O(2) site could be partially filled by oxygen annealing and that T_c increased slightly with increasing occupancy of this site. They concluded that interstitial oxygen atoms, O(3), trapped near the Sr atoms were intrinsic to Sr doping and caused hole doping into the CuO_2 sheet. However, the results reported by Tan *et al.* [1] contradict with a previous structure model [2,3,4], where the occupancy of the O(3) site is zero and that of the O(2) site is almost unity.

In the present work, we judged the validity of their oxygen-defect structure model by neutron powder diffraction which is the most reliable technique to refine positions and occupancies of oxygen. Rietveld refinements of diffraction patterns gave the occupation factors, g, of O(3) slightly less than 0; the resulting g values were -0.014(2), -0.015(3), -0.018(3), -0.019(4), -0.01(1) and -0.008(7) for x=0, 0.11 (oxidized), 0.11 (reduced), 0.15, 0.30 and 0.60, respectively. These values can be regarded as essentially zero within the actual uncertainty in g in Rietveld refinement, indicating that the interstitial O(3) site is not occupied by oxygen in any of our samples.

Tan *et al.* [1] claimed that the amount of interstitial oxygen atoms is comparable to that of doped Sr atoms. Neutron powder diffraction can easily detect the interstitial oxygen with occupancies as high as 0.15-0.6 (=x). Therefore, we can safely conclude that no oxygen atoms exist at the O(3) site, and that the oxygen-defect structure model proposed by Tan *et al.* is not real. XANES spectra for various samples of $La_{2-x}Sr_xCuO_{4-\delta}$ should be interpreted on the basis of another model consistent with the present results of neutron diffraction.

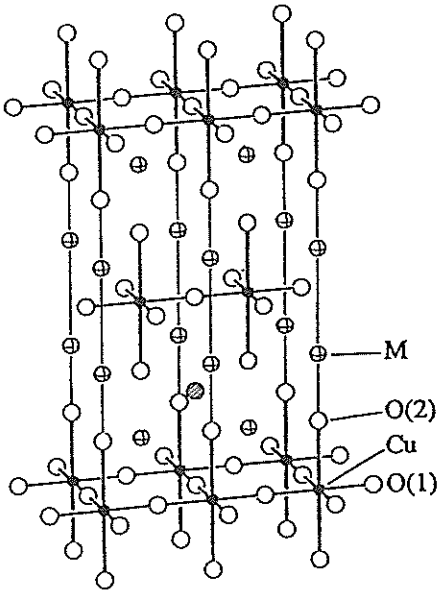

Fig. 1. Crystal structure of tetragonal (I4/mmm) $La_{2-x}Sr_xCuO_{4-\delta}$. Cu-O bonds are shown with thick solid lines. Two unit cells are drawn with thin solid lines. The hatched circle shows the O(3) atom proposed by Tan *et al.* [1].

References

[1] Z. Tan, M. E. Filipkowski, J. I. Budnick, E. K. Heller, D. L. Brewe, B. L. Chamberland, C. E. Bouldin, J. C. Woicik and D. Shi, Phys. Rev. Lett. 64 (1990) 2715.

[2] J. D. Jorgensen, Jpn. J. Appl. Phys. Suppl.3 (1987) 2017.

[3] M. François, K. Yvon, P. Fischer and M. Decroux, Solid State Commun. 63 (1987) 35.

[4] R. J. Cava, A. Santoro, D. W. Johnson, Jr. and W. W. Rhodes, Phys. Rev. B 35 (1987) 6716.

Precipitation Structure of Fe-Cu and Fe-Cu based alloys

H.OKUDA, K.OSAMURA, K.ASANO* and M.FURUSAKA**

Department of Metallurgy, Kyoto Univ. Kyoto 606
*Graduate School, Kyoto Univ. Kyoto 606
**National Laboratory for High Energy Physics, 1-1 Oho, Tsukuba-shi, Ibaraki 305

Precipitation process of low carbon Fe-Cu and Fe-Cu-Ni-X system has been investigated by means of small-angle neutron scattering (SANS) under the magnetic field of about 1 tesla. These alloy systems draw attention as a low-temperature age-hardenable materials. For Fe-Cu binary alloy, Cu precipitates with coherent bcc structure are formed in the early stage of precipitation, and they lose coherency to form fcc pure Cu. Segregation of Ni and Mn is reported for the large precipitates in Fe-Cu-Ni alloys by Busswell et al. using FIM, or in Fe-Cu-Ni-Mn alloy by Korosawa et al. using EM.

The scattering intensity for the magnetic and the nuclear components have been obtained from the scattering profiles parallel and perpendicular to the applied magnetic field.

It has been observed that the ratio of the magnetic scattering to the nuclear scattering, A, increased during early stage of aging in Fe-Cu binary alloy, which corresponds to the structural change in Cu precipitates as mentioned above. Guinier radius increased almost by the power of 1/3 against time after the saturation in A. Guinier radii obtained from the magnetic scattering and the nuclear scattering were almost the same for Fe-Cu alloys.

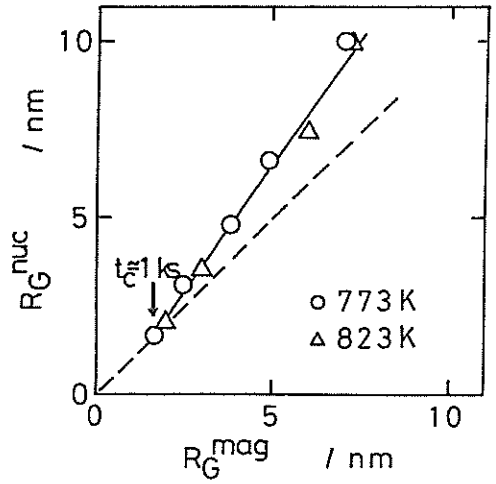

Fig. 1 Guinier radius for the Fe-Cu-Ni alloy. RG for the nuclear scattering is always larger than that for the magnetic scattering for t>1ks.

For Fe-1.6Cu-0.29Ni-0.25Mn alloys, Guinier radius obtained from the magnetic scattering agreed with that from the nuclear scattering in the early stage of aging. The radius from the nuclear scattering is larger than that from the magnetic scattering in the later stage as shown in Fig.1. The critical time, tc in Fig.1 almost agreed the time when the integrated intensity for the magnetic scattering was saturated.

Since the Guinier radius is larger for the nuclear scattering, this discrepancy is not explained by the disordering of magnetic domain at the precipitate interface. Figure 2 shows a model decribing a 'shell structure' of the precipitates, corresponding to the interfacial segregation. Since the scattering length density,ρ_b,for Fe is larger than that for Cu, and Mn is much lower than that for Cu, segregation of Mn and Ni at the precipitate interface can explain the experimental results.

The integrated intensity for the nuclear scattering kept increasing slowly, even after the saturation in the magnetic scattering. It suggests that Mn atoms segragated from the matrix after 1ks, which contributed mainly to the nuclear scatteing. This picture is consistent with the change of Guinier radius.

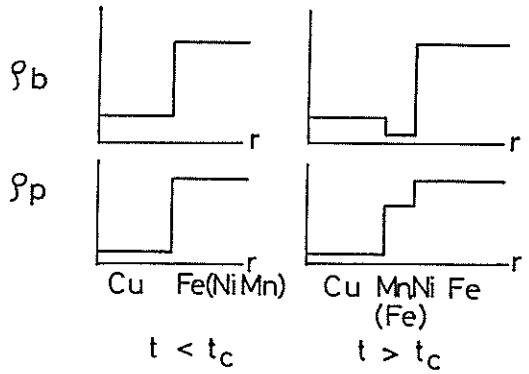

Fig.2 A model structure of precipitates before and after the critical time, tc.

References

1) K.Osamura,H.Okuda,M.Takashima,K.Asano and M.Furusaka: submitted to Mater.Trans.JIM.
2) J.T.Buswell,C.English, M.Hetherington, W. Phythian, G.Smith and G.Worrall : in Effects of Radiation on Materials, pp127.
3) F.Kurosawa: private communication

Vibrational modes of Deuterium in KD_2PO_4

Kohji MIZOGUCHI, Yusuke NAKAI[+], Susumu IKEDA[*],
Akane AGUI[**] and Yasunori TOMINAGA[**]

Department of Applied Physics, Osaka University. 2-1 Yamadaoka, Suita 565
[+]Institute of Materials Science, University of Tsukuba. 1-1-1 Tenodai, Tsukuba, Ibaraki 305
[*]National Laboratory for High Energy Physics. 1-1 Oho, Tsukuba-shi, Ibaraki 305
[**]Department of Physics, Ochanomizu University. 2-1-1 Ohtsuka, Bunkyo-ku 112

The hydrogen-bonded ferroelectric compound KH_2PO_4 (KDP) shows a remarkable isotope effect on the ferroelectric phase transition temperature. There have been a lot of investigations on the mechanism of phase transition of KDP and KD_2PO_4 (DKDP)[1-6]. The main interest of the KDP problem has been confined to two typical models which are the proton tunneling model and the PO_4 order-disorder model. It is important to clarify the dynamics of the hydrogen or deuterium in these compounds. Recently, Shibata et al.[7] have assigned the bending and stretching modes of the H-atom in KDP by inelastic neutron-scattering measurements.

In the present work we have newly found the vibrational modes of deuterium (D-atom) in DKDP by inelastic neutron-scattering measurements. In contrast to the H-atom in KDP, the neutron-scattering cross section of the D-atom in DKDP is as small as that of PO_4 tetrahedrons. Therefore the neutron spectra was compared with Raman spectra, and the modes in DKDP were assigned.

The samples used were KH_2PO_4 and $K(D_xH_{1-x})_2PO_4$ (x=95%, denoted as 95% DKDP) powder samples. The ferroelectric transition temperature (Tc) of KDP was 122K by Differential Scanning Calorimetry measurement. The Tc of 95% DKDP samples was 215K. The crystal structure of the 95% DKDP sample was confirmed to be the tetragonal phase at room temperature by a powder x-ray analysis.

Inelastic neutron scattering measurement on these compounds were performed using a CAT spectrometer[8]. Each powder sample was filled into an aluminum cell (70 mm square, 5 mm thick). The samples were kept at 40K within 3K.

The neutron-scattering spectrum of the DKDP was obtained by subtracting the reduced spectrum of KDP from the spectrum of 95% DKDP. Neutron-scattering spectra of DKDP and KDP are shown in Fig. 1. The neutron-scattering spectrum of DKDP has four large peaks in the energy range $40<\varepsilon<130$ meV. These four peaks correspond to the D-modes as well as the molecular vibration for PO_4 tetrahedrons (PO_4-modes).

In order to investigate H-, D-, and PO_4-modes in neutron-scattering spectra, we have compared the Raman-scattering spectra of KDP and 98% DKDP with their neutron-scattering spectra. Raman-scattering spectra of KDP and DKDP are shown in Fig. 1. As shown in the Raman spectrum of KDP, PO_4-modes appear in the frequency region between 30-150 meV. These modes are denoted as $\nu 2$, $\nu 4$, $\nu 1$, and $\nu 3$ from low frequency side[6]. Therefore, the broad peaks in the energy range $30<\varepsilon<80$ meV in neutron-scattering spectra of KDP can be explained as PO_4-modes ($\nu 2$,$\nu 4$) by comparison with the Raman-scattering spectrum. PO_4-modes ($\nu 1$,$\nu 3$) should be also observed in the energy range $80<\varepsilon<150$ meV. However, these modes are hardly observed in the neutron scattering spectrum of KDP, because those are buried under the H-modes. Then, we considered that the neutron-scattering spectrum of KDP in the energy range $80<\varepsilon<170$ meV is made of the superposition of the H-modes and PO_4-modes. In order to define the peak energy of the H-modes and the PO_4-modes, the neutron-scattering spectrum of KDP was fitted with the superposition of 15 Lorentzian functions in the energy range from 30 meV to 200 meV. The result is shown by a solid curve in Fig. 1. In the above energy range the observed spectrum has been well fitted with the calculated one. The result is that the H-modes were observed at $\varepsilon(H1)=126.4$ and $\varepsilon(H2)=160.6$ meV. These peak values agree with the results reported by Shibata et al.[7]. Nine PO_4 modes in the neutron-scattering spectrum were found by fitting the calculated spectrum to the observed one, and the peak energies almost agreed with those

obtained from the Raman-scattering spectrum. However, the number of PO_4-modes in the neutron-scattering spectrum of KDP is fewer than that in the Raman-scattering spectrum. This may arise from the poor resolution of the CAT spectrometer.

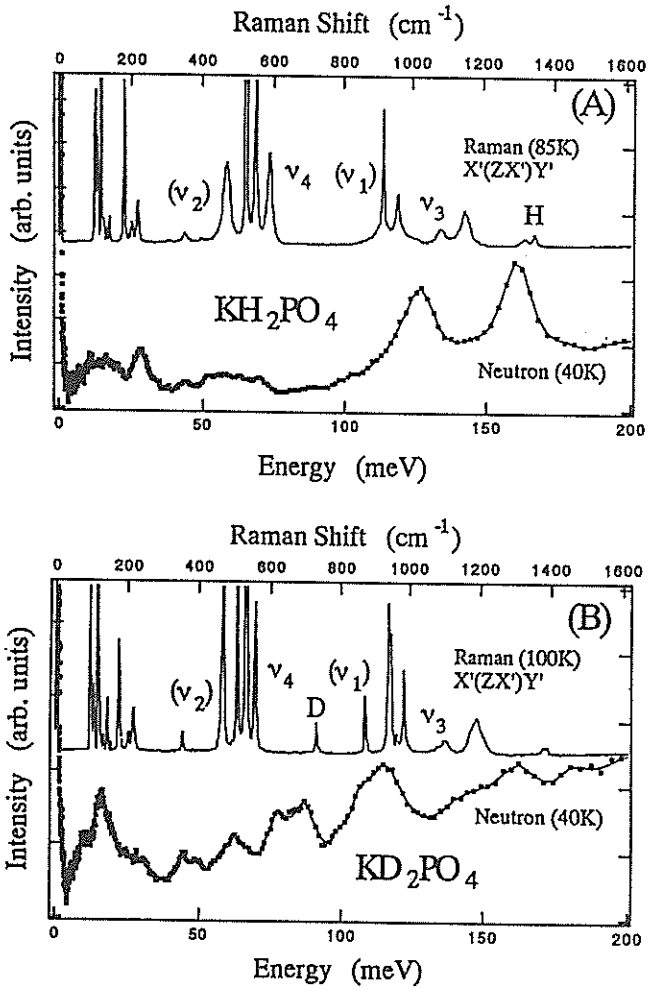

Figure 1. Neutron-scattering spectra obtained from powder samples of (A) KH_2PO_4(KDP), (B) 100% KD_2PO_4(DKDP). The solid curves show the calculated spectra by the superposition of the 15 Lorentzian modes. Raman-scattering spectra obtained from KDP(A) and 98% DKDP(B) are shown by dashed curve.

In the same way, the corrected neutron-scattering spectrum of DKDP was fitted with the spectrum calculated by the superposition of 15 Lorentzian functions in the spectral range from 30 meV to 200 meV. The fitting curves is shown by a solid curve in Fig. 1. The observed values have been well fitted with the calculated spectrum. The peak energies of the PO_4 modes obtained from the neutron-scattering spectrum almost agree with those obtained from the Raman-scattering spectrum. These energies were $\varepsilon(D1)=86.7$ and $\varepsilon(D2)=106.1$ meV (Table 1). In this analysis, we found two D-modes. The ratios of $\varepsilon(H1)/\varepsilon(D1)$ and $\varepsilon(H2)/\varepsilon(D2)$ are 1.5. These ratios are almost the same as the expected values in the simple harmonic oscillator case (1.4). This result may suggest that the hydrogen (deuterium) potential is harmonic, and the hydrogen (deuterium) potential is almost unchanged between KDP and DKDP.

Table 1. The peak energies of the vibrational modes of the H-atom, the D-atom.

Mode	Neutron (meV)	Raman (meV)
H	160.6	161.9
	126.4	125.7
D	106.1	119.5
	86.7	88.3

References

1) J. C. Slater: J.Chem.Phys.,9(1941)16.
2) G. A. Samara: Ferroelectrics 5(1973)25.
3) J. E. Tibballs, R.J.Nelmes and G.J.McIntyre: J. Phys. C (Solid State Phys.), 15(1982)37.
4) R. J. Nelmes, G. M. Meyer and J. E. Tibballs: J. Phys. C (Solid State Phys.), 15(1982)59.
5) R. J. Nelmes: J. Phys. C (Solid State Phys.), 21 (1988) L881.
6) Y. Tominaga, H. Urabe and M. Tokunaga; Solid State Communications, 48(1983)265.
7) K. Shibata and S. Ikeda: J. Phys. Soc. Jpn., 61 (1992) 411.
8) S. Ikeda and N. Watanabe: J. Phys. Soc. Jpn., 56 (1987) 565.

Hydrogen modes in RbH_2PO_4

A. Agui, Y. Nakai*, K. Mizoguchi**, Y. Tominaga, and S. Ikeda***

Department of Physics, Ochanomizu University, Ohtuka 2-1-1, Bunkyouku, Tokyo 112
*Institute of Material Science, University of Tsukuba, Tennodai 1-1-1, Tukuba, Ibaraki 305
**Faculty of Engineering, Osaka University, Yamadaoka Suitashi, Osaka 565
***National Laboratory for High Energy Physics, Oho 1-1, Tsukuba, Ibaraki 305

RbH_2PO_4(RDP) which is a typical hydrogen bonded crystal comes into the ferroelectric phase at T_c=148K. To clarify a role of the hydrogen bonds in this phase transition mechanism, the temperature dependence of the hydrogen modes in RDP have been investigated by using a CAT spectrometer.

Figure 1 shows a neutron scattering spectrum obtained from the powder RDP specimen at 40K. There appear two large peaks. We denote the two modes at ε=124meV and 159meV as A and B, respectively. Since hydrogen has a large cross section incoherent-neutron-scattering cross section, both A and B modes can be assigned to the hydrogen modes. The similar structure has already been obtained in KH_2PO_4(KDP) by Shibata and Ikeda.[1)]

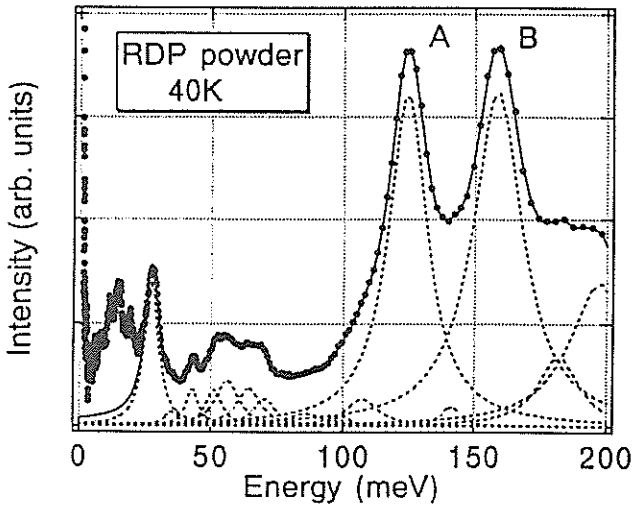

Fig.1 The dots are the measured spectrum of the powder RDP at 40K. The solid curve gives the calculated spectrum using a superposition of 15 Lorentzian functions, which are shown in dashed curves.

We have carried out a spectral fitting to the neutron spectra obtained from the powder RDP with 15 Lorentzian functions. In Fig. 1 a solid curve gives the calculated spectrum. We have also compared the neutron scattering spectra in the energy range of 40 < ε < 80 meV with Raman scattering spectra and found that there peak's energy in this range are almost agreed with the Raman frequencies of the internal modes of PO_4 tetrahedrons.[2)]

Figure 2 shows the temperature dependence of the spectral line widths (Full Width at Half Maximum) of A and B hydrogen modes. The *FWHM* of hydrogen modes drastically changes around T_c

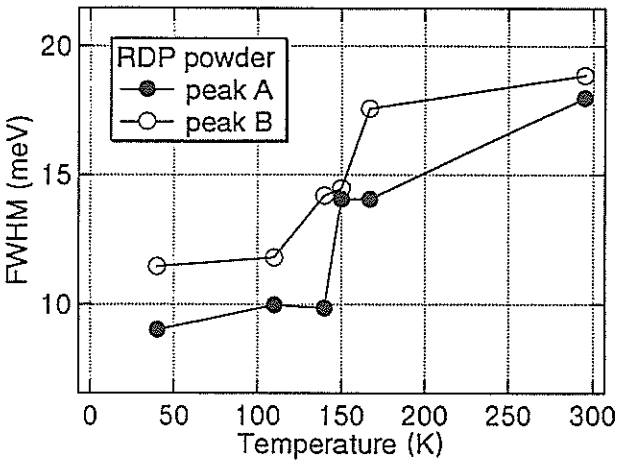

Fig.2 The full widths at half maximum (*FWHM*) are shown, closed circles denote peak A and open circles denote peak B.

This may suggest that the line width of hydrogen mode is strongly affected by the disordemess of PO_4 tetrahedrons.

References

1) K. Sibata and S. Ikeda: J. Phys. Soc. Jpn. 61 (1992) 411.
2) Y. Tominaga, H. Urabe and M. Tokunaga: Solid State Commun. 48 (1983) 265.

Temperature Dependence of the 28meV Mode in KDP

Y Todate, S Ikeda†, Y Nakai†† and A Agui

Department of Physics, Faculty of Science, Ochanomizu University, Bunkyo-ku, Tokyo 112
†National Laboratory for High Energy Physics, Oho, Tsukuba, Ibaraki 305
††Institute of Materials Science, University of Tsukuba, Ten-nodai, Tsukuba, Ibaraki 305

Temperature variation of incoherent inelastic scattering from hydrogen bonded ferroelectric KH_2PO_4 (KDP) has been measured using CAT spectrometer. Here we mainly focus on the unassigned 28meV peak found by Shibata and Ikeda[1]. Since this peak has much lower energy than that of usual proton local modes and seems to disappear above T_c, much attention has been attracted. Measurements were carried out at temperatures 25K, 80K, 115K, 128K and 225K using powdered specimen. The same experiments as on KDP have been done on partially deuterized DKDP in order to see the relation between the transition temperature and the excitation energy of this mode. The resultant temperature dependence of the inelastic spectrum is shown in Figs 1 and 2. The peak position, the energy width and the integrated intensity for KDP are plotted in Fig 3. Since the intensity depends inevitably on the estimation of background, it is difficult to derive the accurate intensity change at T_c. The temperature dependence of the Debye-Waller factor[2] has not been separated from the plotted intensity variation. It is safe, however, to conclude that the peak does not disappear but significantly broadens at T_c when the temperature is raised. The abrupt broadening of the peak at T_c can be observed for both KDP and DKDP(90%D). For DKDP(90%D), however, the meaningful background subtraction is not possible for the spectra above T_c.

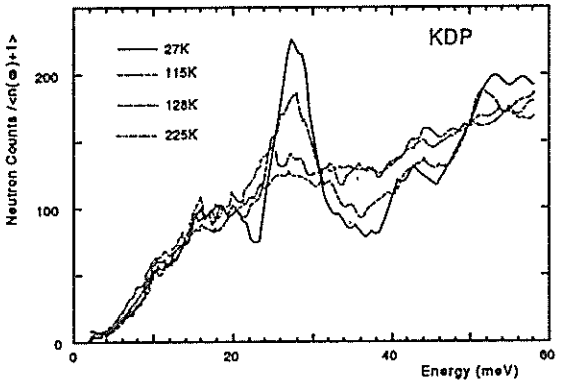

Fig 1 Temperature dependence of the incoherent inelastic scattering from KDP. Displayed energy range is limited in order to see the change of the 28meV peak. The spectra are normalized by the Bose factor.

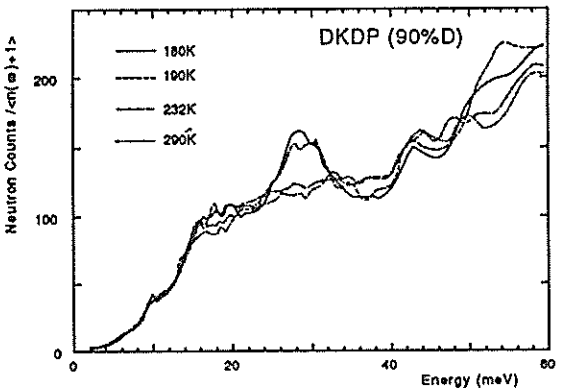

Fig 2 The same plot as Fig 1 obtained for DKDP(90%D). Note that the peak at 29meV seems to be the incoherent scattering from residual 10% proton in the sample.

An energy shift on deuteration has been recognized and +7% shift of the energy on the 90% deuteration suggests that this mode does not correspond to the "collective" proton (deuteron) motion such as the collective tunneling assumed to exist in the proton coupled soft optic-phonon model[3]. Moreover it has been shown that the amplitude of the proton motion involves a substantial z-component[4] which is perpendicular to the direction of the hydrogen bond. It seems more plausible to discuss this mode as an optical mode motion of the atoms rather than a purely local (single-site) proton mode in an asymmetric double-well potential because, in this energy region, the proton motion cannot be independent of the motion of the surrounding atoms. Rather a distinct incoherent peak may correspond to the localized character of the mode reflecting sharp density of states. The peak has the finite energy-width, which, corrected the instrumental resolution, can be estimated to be 2.5meV (FWHM).

Although the observed proton motion in KDP and DKDP obviously relates to the phase transition, the mode has still not been assigned. For assignment it would be helpful to compare the neutron scattering spectrum with that obtained by the Raman scattering experiments. Many Raman scattering experiments suggest order-disorder nature of the phase transition[5,6,7]. Present neutron scattering results also suggest that the mode strongly couples to the fluctuation of the dipole moments and a qualitative explanation seems to be given by introducing an Ising-spin variable based on the order-disorder model. It is therefore interesting to investigate the relation between the 28meV mode motion and the formation or the fluctuation of the dipole moments.

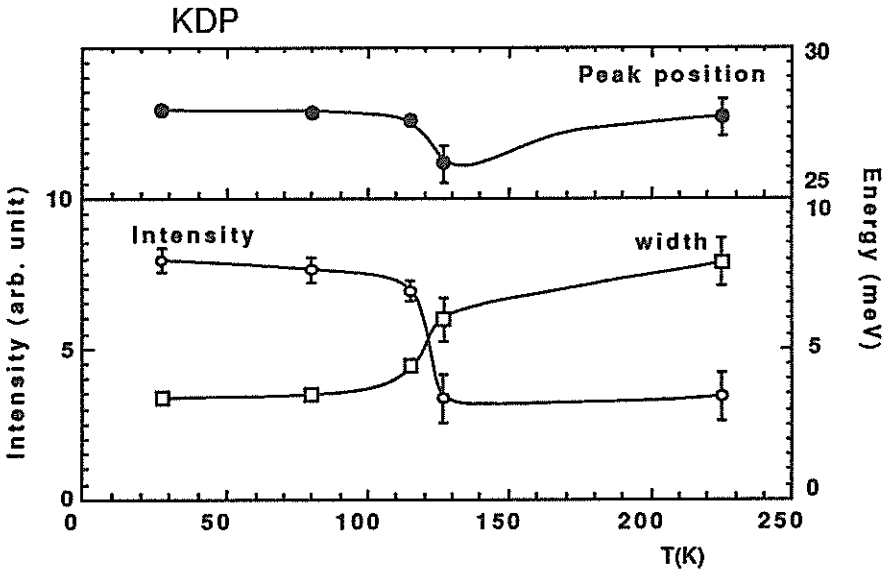

Fig 4 Temperature dependences of the peak position, the energy width and the integrated intensity for the 28meV peak in KDP. The lines are guides to the eye.

References

1) K.Shibata and S.Ikeda, J. Phys. Soc. Japan, **61** (1992) 411.
2) G.B.Bacon and R.S.Pease, Proc. R. Soc. **A230** (1955) 359.
3) K.Kobayashi, J.Phys. Soc. Japan, **24** (1968) 497.
4) Y.Todate and S.Ikeda, KENS REPORT IX (this volume).
5) I.Laulicht, J. Phys. Chem. Solids **39** (1978) 901.
6) Y.Tominaga, H.Urabe, M.Tokunaga, Solid State Commun. **48** (1983) 265.
7) Y.Tominaga, M.Kasahara, H.Urabe and I.Tatsusaki, Solid State Commun. **47** (1983) 835.

Angle Dependence of the Proton Incoherent Scattering from KDP

Y Todate and S Ikeda†

Department of Physics, Faculty of Science, Ochanomizu University, Bunkyo-ku, Tokyo 112
†National Laboratory for High Energy Physics, Oho, Tsukuba, Ibaraki 305

An incoherent inelastic peak at $\hbar\omega$=28meV found in KH_2PO_4 (KDP) by Shibata and Ikeda[1] has much lower energy than that of usual proton local modes ($\hbar\omega$>100meV) and seems to disappear above the ferroelectric transition temperature T_c. It is interesting to investigate the relevant motion of the protons which are forming hydrogen bonds. In this study an angle dependence of the scattering intensity has been measured using MAX crystal analyzer spectrometer with single crystal KDP. If the peak consists of a single normal mode, it is possible to determine the polarization vector of the mode even by the incoherent scattering. Although the angle dependence of the scattered intensity of 28meV peak has already been reported[1], a measurement with better Q (or angular)-resolution is desirable. In the measurement, E_f of each detector was selected so that the magnitude of the scattering vector Q became 5Å^{-1} for the energy transfer of 28meV. Typical Q-resolution $\Delta Q/Q$ is 3% and the energy widths $\Delta\hbar\omega$ are smaller than 3.5meV at $\hbar\omega$=28meV. Rotating the sample crystal in the a-c plane, TOF spectra were collected at 18K. Note that all the hydrogen bonds are within the c-plane. Normalized integrated intensities of the peak are plotted in Fig 1 as a function of the angle between a-axis and Q. Intensity difference due to the anisotropic Debye-Waller factor[2,3] is not large at low temperature and was therefore neglected. Maximum intensity has been obtained when Q //a and minimum when Q //c.

As far as the proton motion is concerned, as a result, the predominant character of the mode is of stretching with respect to the hydrogen bond as already reported[1]. It should be noted, however, that the intensity in the configuration $Q \perp a$ is much larger than that comes from the finite instrumental resolution effect in the case of vanishing inelastic structure factor: i.e. in the case that the mode eigenvector is exactly perpendicular to Q.

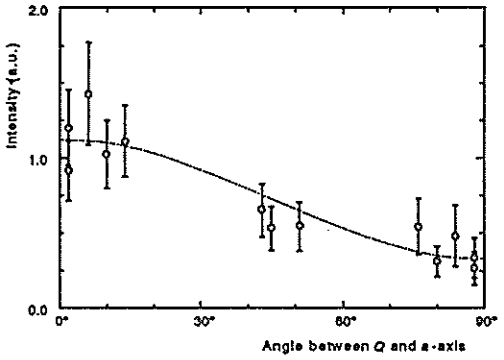

Fig. 1 Plot of the integrated intensity of the 28meV peak as a function of the angle between a-axis and the scattering vector Q. The line indicates the expression $c_{xy}^2\cos^2\theta + c_z^2\sin^2\theta$,where c_{xy} and c_z are the xy- and z-component of the mean amplitude respectively.

This remainder intensity indicates that the mode has a substantial perpendicular (z-) component c_z of the amplitude with respect to the direction of the bond. Mean z- and xy-amplitude of the proton motion have been determined. The ratio of the mean z-amplitude to the xy-component can be estimated from Fig 1 to be as large as 54%, indicating that the proton motion is not a simple two-site excursion between the hydrogen bond. A large z-component for the proton (deuteron) motion has also seen in the ferroelectric fluctuation in DKDP near T_c measured by neutron quasi-elastic scattering[4]. Further investigation on this excitation will also be reported in KENS REPORT separately.

References

1) K.Shibata and S.Ikeda, J. Phys. Soc. Japan, **61** (1992) 411.
2) G.B.Bacon and R.S.Pease, Proc. R. Soc. **A230** (1955) 359.
3) R.L.Nelmes, G.M.Meyer and J.E.Tibballs: J. Phys. C, Solid State Phys. **15** (1982) 59.
4) J.Skalyo, B.C.Frazer and G.Shirane, Phys. Rev. **B1** (1970) 278.

Low-Energy Excitation in CuI

T. Sakuma and K. Shibata*

Department of Physics, Faculty of Science, Ibaraki Univ., Mito 310
*Institute for Materials Research, Tohoku Univ., Sendai 980

Copper iodide (CuI) exhibits high-temperature phase transitions at 369°C and at 407°C. The high temperature β– and α–phases are well known as having a high ionic conductivity. The crystal structures of CuI were reexamined by X-ray diffraction method.[1)]

Inelastic neutron scattering measurements were performed at 25, 200, 280 and 300°C by the use of the TOF spectrometer LAM-40 installed at the pulse spallation neutron facility KENS. A powder specimen of CuI was contained in a cylindrical aluminum tube of 13mm diameter and 80 mm length with thin wall. The range of Q ($4\pi\sin\theta/\lambda$) covered by this spectrometer is 0.2-2.5 $Å^{-1}$ at elastic scattering and the energy resolution was about 200 meV (FWHM). The data collection time for each temperature was about 5 h.

A low-lying dispersionless excitation near 3.4 meV was observed in the inelastic scattering spectra[1] of a powder sample of CuI over the measured range of Q. The observed inelastic scattering spectra $I(Q,\omega)$ of CuI with Q=2.3 $Å^{-1}$ at various temperatures are shown in Fig. 1. As the temperature is lowered the excitation near 3.4 meV becomes clear and the intensity of the inelastic scattering spectra in energy range 1-3 meV decreases.

The analysis of the inelastic scatteirng was performed in the same manner as that of copper-ion conductors recently carried out by the present authors.[2)] The model scattering function for the generalized density of states consitsts of two components: the low-energy excitation mode and the phonon modes mainly due to the transverse acoustic branch.

The value of low-energy excitation (~3.4 meV) is almost independent of temperature. When the temperature increases, the half-width Γ of the low-energy excitation mode increases at temperature above 200°C. The temperature dependence of the half-width of the low-energy excitation mode could be associated with that of the electrical conductivity.

The feature of the observed inelastic neutron scattering spectra in Fig. 1 is similar to that in the silver ion conductor $RbAg_4I_5$ reported by Shapiro et al.[3)]

Recently, an ionic plasma model to describe the low-energy excitation of cation superionic conductors was presented to explain the low-energy excitation in superionic conductors.[4)] At present, the value of the effective charge of each substance has not been reported. Therefore, we could not investigate the validity of the ionic plasma model.

The results are to be published in Solid State Ionics.

References

1) T. Sakuma, J. Phys. Soc. Jpn. 57(1988)565.
2) T. Sakuma, K. Shibata and S. Hoshino, Solid State Ionics 40/41(1990)337.
3) S. M. Shapiro, D. Semmingsen and M. Salamon, Proc. Int. Conf. on Lattice Dynamics, ed. M. Balkanski (Flammarion, Paris, 1978).
4) M. Kobayashi, T. Tomoyose and M. Aniya, J. Phys. Soc. Jpn. 60(1991)3742.

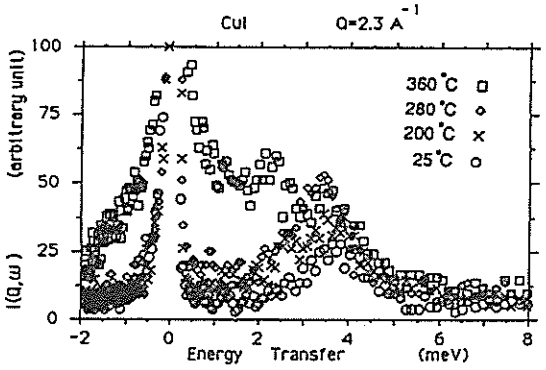

Fig. 1 The observed inelastic neutron scattering spectra of CuI at 25, 200, 280 and 360°C.

Methyl Group Dyanmics of Poly(γ-methyl L-glutamate) by LAM-40

T. HIRAOKI, K. SHIBATA*, Y. IZUMI# and A. TSUTSUMI

Department of Applied Physics, Hokkaido University, Sapporo 060
*Institute for Material Research, Tohoku University, Sendai 980
#Macromolecular Research Laboratory, Department of Engineering,
Yamagata University, Yonezawa 992

Poly(α-amino acid)s take several conformations in the solid state. The side chain has great influence upon the conformation and the property of the polymer. Side chain motions are reflected in various relaxation phenomena. The main chain of poly(γ-methyl L-glutamate)(PMLG) is known to take an α-helical conformation in the solid state. The structure and relaxation phenomena for PMLG in the solid state of rodlike molecules surrounded by side chains were investigated and well characterized.[1] The side chain relaxation of PMLG is caused by micro-Brownian motion around room temeparture. The methyl group in the end of the side chain undergoes rotational motion about the C_3 axis even in 77K.[2] In order to investigate the dynamical behaviors of the methyl group of PMLG, we carried out neutron quasielastic scattering measurements, obtained by LAM-40 at 297K. Experiments were done on both PMLG and deuterio-methyl PMLG(PMLG-d3), to extract the contribution from only the methyl group.

Fig.1 (a) shows the quasielastic scattering spectra of PMLG and PMLG-d3. These are the sum of spectra for the scattering angles of 72°, 88°, and 104°. The clear difference between both samples is observed in the region within ω = ± 2 meV. Difference spectrum is shown in Fig.1 (b). This spectrum would be empirically fitted to a model of a Lorentz function. The half width at half maximum of the spectrum is calculated to be ~2 meV, which corresponds to 2 ps, showing the rate of the methyl rotation. This value is in good agreement with that of ^{2}H-NMR results.[3] And NMR results indicate that the mode of the methyl rotation to be the three-site jump and the presence of the C_3 axis motion of the order of 10 kHz at room temperature. Detailed analysis is in progress.

References

1) A. Tsutsumi, et al., J. Macromol. Sci. -Phys. B8, 413 (1973)
2) A. Tsutsumi, Jpn. J. Appl. Phys. 9, 1125 (1970)
3) T. Hiraoki, A. Kogame, K. Matsuo and A. Tsutsumi, Rept. Prog. Polym. Phys. Jpn. 23, 541(1990)

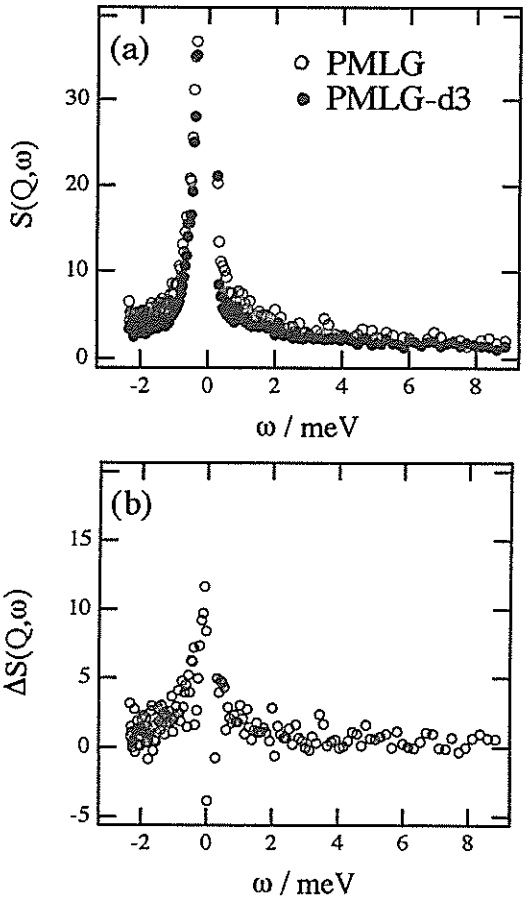

Fig. 1 Neutron quasielastic scattering spectra of PMLG and PMLG-d3 (a), and difference spectra between PMLG and PMLG-d3 (b).

Calorimetric and Neutron Spectroscopic Studies of Pyridinium Iodide Crystal

M.OGUNI, M.HANAYA, S.IKEDA* and K.SHIBATA**

Department of Chemistry, Faculty of Science, Tokyo Institute of Technology, Tokyo 152
*National Laboratory for High Energy Physics, 1-1 Oho, Tsukuba-shi, Ibaraki 305
**Institute for Materials Research, Tohoku Univ. Sendai 980

In pyridinium iodide crystal (PyHI), a pyridinium ring is surrounded by six iodide anions and has orientational degree of freedom characterized by the direction of NH bond of the pyridinium ring within the distorted octahedron of the iodide anions. The NH is considered to be directed toward just in between two anions with the orientational disorder of the pyridinium ring at equivalent six sites in a high-temperature phase, and to be directed straight toward one of the six anions in a low-temperature ordered phase forming a hydrogen bond with the anion.[1)]

This orientational change in the phase transition is very interesting, because this change suggests the possibility that the pyridinium ring is in a rotational tunnel state of two-minimum potential as shown in Fig. 1 at low temperatures. Therefore we examined calorimetric and neutron spectroscopic studies for PyHI in order to elucidate the orientational change of the pyridinium ring in the disordering process. The experiments were carried out in the temperature region of 4 to 320K for the calorimetry and 10 to 200K for the neutron spectroscopy, respectively. Neutron scattering experiment was performed with the time-of-flight (TOF) spectrometer LAM-D installed at KENS.

The obtained molar heat capacities of PyHI are plotted in Fig. 2. As has been reported,[2)] PyHI exhibited heat-capacity anomaly with a sharp peak at about 250K and with wide skirts on both the low- and high-temperature sides of the peak. The phase transition temperature was determined to be 249.65K, and the transition was

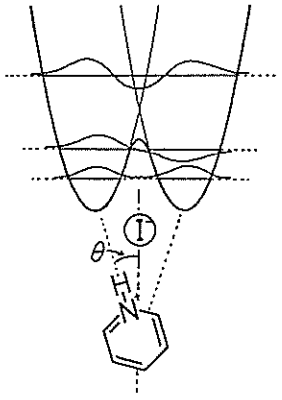

Fig. 1 Schematic potential curve for the orientation of pyridinium ring.

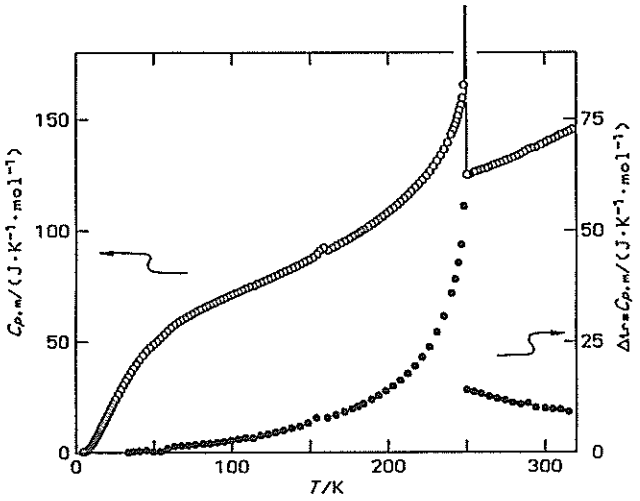

Fig. 2 Molar heat capacity (○) and the anomalous part (●) of PyHI.

decided to be of the first order because of the thermal hysteresis of the heat capacity observed in the transition temperature range.

The anomalous part of the heat capacity due to the order-disorder phase transition was obtained, as also shown in Fig. 2, by extracting the heat-capacity contributions from intra-ionic and rotational vibrations of pyridinium cation, lattice vibrations, and $(C_{p,m}-C_{v,m})$ correction term from the obtained heat capacities. The transition entropy evaluated from the anomalous part was 18.6~25.6 $J\cdot K^{-1}\cdot mol^{-1}$, and the result means that the pyridinium ring has at least 9 and less than 22 distinguishable orientations in the high-temperature phase, when we assume that the pyridinium ring is allowed to take only one orientation at the lowest temperature of measurement.

It has been long believed that there is no hydrogen bonding between NH proton and iodide anion in the high-temperature phase and that the NH is directed toward just the middle between two anions. However, there should be coulomb interaction between anion and cation even in the high-temperature phase and the pyridinium NH existing in between two anions is expected to interact with one anion much stronger than with the other, so that at any one of stable orientations of pyridinium ring the NH is not directed toward right the middle between two anions but is located closer to one anion than

to the other of the two anions. This model brings 12 orientations allowed for the pyridinium ring in the disordered state, as is well consistent with the experimental result.

Figures 3 and 4 show the neutron energy-transfer spectra observed at various temperatures. In the high-energy region, as shown in Fig. 3, clear peaks due to the intra-ionic vibrations of the pyridinium cation were observed below 100K and the peaks were assigned as indicated in the figure by comparing with the result by the IR spectroscopy.[3] In this intra-ionic vibrational region, peak shift was hardly observed with temperature. On the other hand, in the low-energy region shown in Fig. 4 some peaks due to the lattice and rotational vibrations in PyHI were observed and low-energy shifts of the peaks appeared above 53K. Since the heat-capacity anomaly also appeared in the temperature range above 50K (Fig. 2), the peak shift observed here is considered to be relevant to the disordering process, i.e. the peak shift is attributable to the softening of the lattice in PyHI accompanied with the orientational disordering of the pyridinium ring.

In the disordering process, it is expected that the θ indicated in Fig. 1 increases with increasing temperature and the tunnel splitting should decrease toward 0. However, in the neutron energy-transfer spectra, we could not find such a peak as shifts largely with the variation in temperature. This result suggests that in the pyridinium salt with a weak hydrogen bonding such as PyHI the NH of pyridinium ring would not be directed just toward the iodide anion. It means that the θ is too large to form tunneling states, even in the low-temperature ordered state differently from the case of pyridinium chloride (PyHCl) with strong hydrogen bonding. Further substantiation of the picture definitely necessitates detailed experiments both on the crystal structure of PyHI in the ordered state and on the phase behavior of PyHCl as a function of temperature. Calorimetric study of PyHCl is now in progress in our laboratory for that, and the orientational disordering appears to proceed through phase transition of two steps differently from that in the present PyHI case.

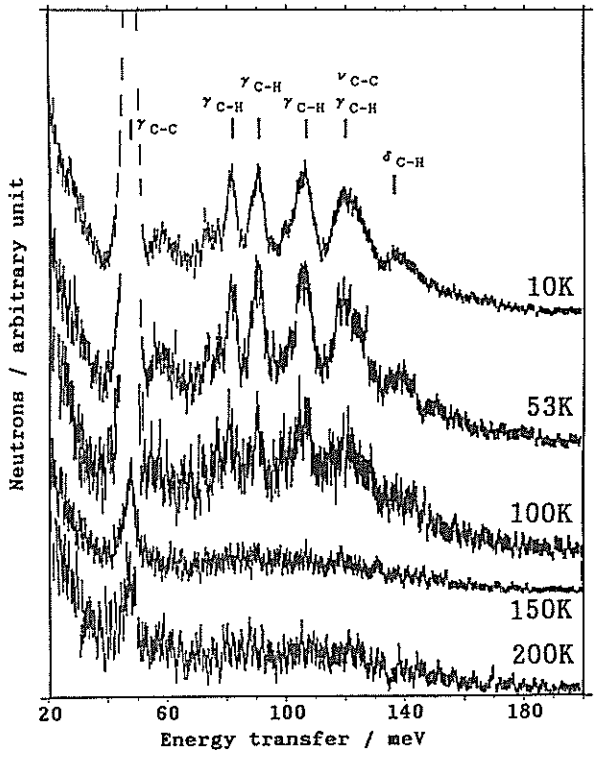

Fig. 3 Neutron energy-transfer spectra of PyHI in high-energy region at various temperatures.

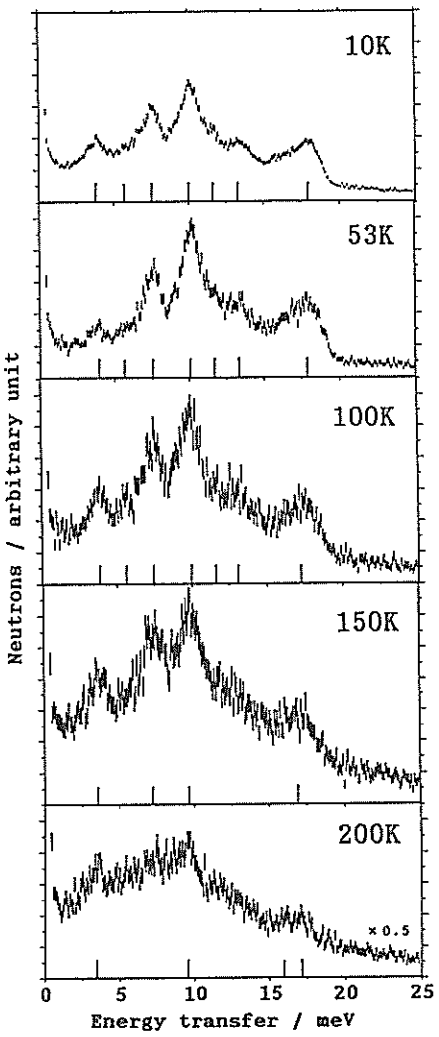

Fig. 4 Neutron energy-transfer spectra of PyHI in low-energy region at various temperatures. The intensities were normalized from the elastic peak intensities.

References

1) J.A.Ripmeester, *Can.J.Chem.* 54, 3453(1976)
2) M.Hanaya et al., *J.Phys.Chem.Solids*, in press
3) D.Cook, *Can.J.Chem.* 39, 2009(1961)

Tunneling of Hydrogen Chloride Molecule in the Hydroquinone Clathrate Compounds

S. Takeda, H. Kataoka and S. Ikeda[¥]

Department of Chemistry, Faculty of Science, Osaka University,
Toyonaka Osaka 560, Japan
[¥]National Laboratory for High Energy Physics, Tsukuba 305, Japan

Hydrogen chloride molecule in its β-hydroquinone clathrate compound is confined in the host cavity which is approximately spherical with a "free diameter" of ca. 4.8 Å. The chlorine atom of HCl molecule lies on the C_3 symmetry axis of the crystal (rhombohedral, space group R3) and the HCl molecule is considered to precess around this axis (Fig.1) from the analysis of the position of H atom by neutron diffraction previously done at room temperature[1]. At low temperature, 12.3 K, a phase transition of this clathrate compound was observed by calorimetric study[2] and we investigated the rotational motion of HCl in $[C_6H_4(OH)_2]_3(HCl)_{0.99}$ and of DCl in $[C_6H_4(OD)_2]_3(DCl)_{0.82}$ by proton and deuteron NMR method respectively in relation to the phase transition.

These experiments revealed that the HCl molecule is an almost free rotor precessing about the C_3 axis in the high temperature phase and that the rotational states of the HCl and DCl molecules do not change appreciably across the phase transition as evidenced by the continuity of the temperature dependence of the spin-lattice relaxation rate T_1^{-1} over this range. From the temperature dependence of T_1^{-1}, we tried to estimate the energy splitting between the tunneling levels of HCl and DCl. The splitting is around a few meV, however, the unique estimation has not been achieved, because the splitting may be distributed due to a possible interaction between hydrogen chloride molecules in neighboring cavities.

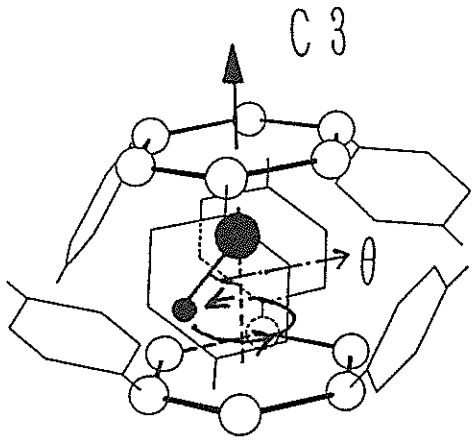

Fig. 1 Host cavity of hydroquinone clathrate and HCl molecule confined in the cavity.

To investigate directly the dynamic behavior and tunneling splitting of HCl in the clathrate compound, the neutron scattering spectra were measured around the phase transition temperature by LAM-40 spectrometer. The spectra of $[C_6D_4(OH)_2]_3(HCl)_{1.0}$ are shown in Fig. 2. A very broad peak at 4.5 meV is the tunneling transition, which did not appear in the spectrum of DCl in the clathrate compound, $[C_6D_4(OD)_2]_3(DCl)_{0.87}$. A half of the half width is 2 meV, which is much larger than the resolution of the spectrometer (0.2 meV), did not change on cooling from 4.2 K to 2.3 K. This result suggests that the width is

not due to the life time broadening but the energy level is intrinsically broad. One of the possible mechanisms to diffuse the energy levels may be a perturbative interaction between HCl molecules in neighboring cavities.

Above the phase transition temperature (12.3K) quasielastic scattering appeared. The Q-dependence of the quasielastic scattering intensity at 22 K showed a maximum at 1.7 $Å^{-1}$ and was fitted well by a model of proton jumping between equivalent three sites. The angle Θ in Fig. 1 was estimated to be 42 degree at 22 K.

At 2.3 K Q-dependence of the intensity of the inelastic peak at 4.5 meV showed a maximum near 2.2 $Å^{-1}$ and was successfully fitted by a model formula in the case of proton tunneling in the three-fold symmetric potential wells. The angle Θ of precession of HCl at this temperature was estimated to be 30 degree. The symmetry of the low temperature phase is known to be lower than the high temperature phase but the deviation from the three-fold symmetry of the hindering potential seems small. The spin-lattice relaxation rate of H-NMR in the low temperature phase was good consistent with the dynamic aspects of HCl molecule described above, if we take into account the width of 2 meV of gaussian distribution of the tunneling splitting.

The tunneling behavior of DCl in the clathrate compound, $[C_6H_4(OD)_2]_3(DCl)_{0.82}$, which was deduced from the spin-lattice relaxation rate of D-NMR, was similar to that of HCl.

The authors would like to express their thanks to LAM group of KEK especially to Dr. K. Shibata of Tohoku University for their stimulated discussions.

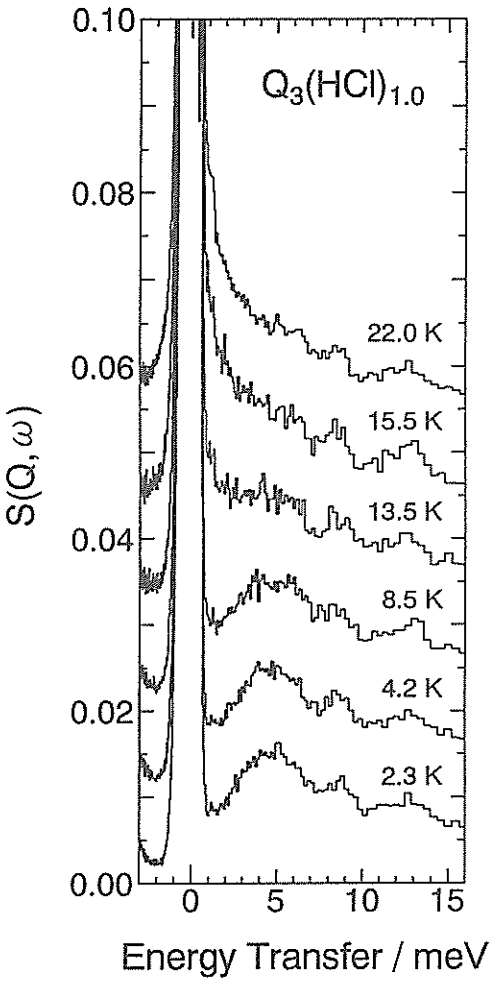

Fig. 2 Inelastic neutron scattering spectra of $[C_6D_4(OH)_2]_3(HCl)_{1.0}$. Each spectrum is shifted along ordinate by 0.01 to prevent overlapping.

References

1) J.C.A. Boeyens and J.A. Pretorius, Acta Cryst. B33 (1977) 2120.

2) H. Ukegawa, T. Matsuo and H. Suga, Solid State Commun., 76 (1990) 221.

Rotational Tunneling Dynamics of Methyl Groups in Coupled Methyl Systems

S. Takeda, H. Kataoka and S. Ikeda*

Department of Chemistry, Faculty of Science, Osaka University,
Toyonaka Osaka 560, Japan
*National Laboratory for High Energy Physics, Tsukuba 305, Japan

Proton NMR field cycling technique revealed two tunneling splittings (7.9 and 9.6 MHz) of methyl groups of hexamethylbenzene (HMB) crystal at 4.2 K. One of the splittings decreased to zero sharply as temperature increased, whereas the other remained almost constant up to 30 K[1,2]. This result is very curious from the theoretical point of view of a tunneling methyl group, because methyl groups in the crystal stay in similar environment and the anomalous temperature dependence seems to come from a coupling effect between the methyl groups in a HMB molecule in which six methyl groups are very closely located and are tied in a ring.

The aim of this study is to investigate more clearly whether the coupled tunneling of six methyl groups is evident or not. To make HMB molecule isolated in crystal, HMB were diluted (5 mol%) in hexabromobenzene (HBB) of which the molecular size is very similar to that of HMB. The measurement of spin-lattice relaxation rate (T_1^{-1}) of proton and powder X-ray diffraction of several diluted specimens (around 5 mol%) indicated that HMB molecules were diluted microscopically in HBB lattice. From the temperature and frequency dependence of T_1^{-1} of proton, different two classes of tunneling splittings were deduced, one of which is about 0.4 μeV near 40 K and the other is about 0.4 meV at liquid helium temperature.

Figure 1 shows the inelastic neutron scattering spectrum of HMB(5 mol%)/ HBB which was observed at 5.7 K by LAM-80ET spectrometer of KENS with mica analyzer ([006] reflection). A broad peak centered at 0.4 meV was found in

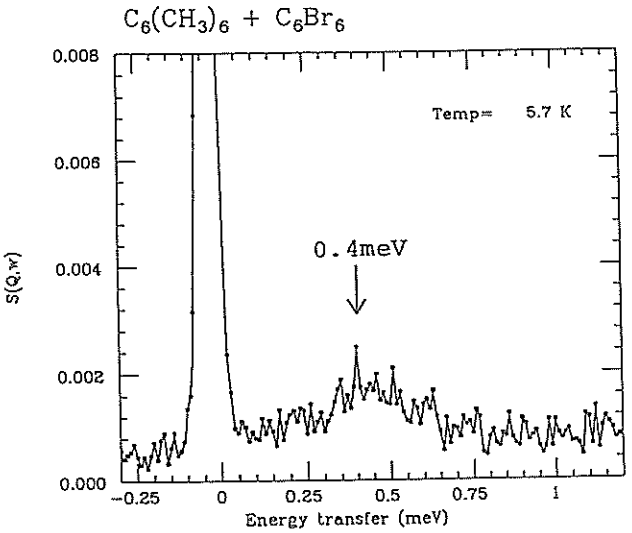

Fig. 1 Inelastic neutron scattering spectrum of HMB(5 mol%)/HBB measured at 5.7 K by LAM-80ET spectrometer of KENS.

the neutron energy loss region, which is good consistent with the slope of T_1^{-1} of proton of the same sample below 10K and the peak did not appear in the spectrum of pure HBB. The large tunneling splitting (0.4 meV) seems to belong to gearing rotational mode of six methyl groups which is one of the normal modes of rotational freedom of six methyl groups in a HMB molecule. The hindering potential of the gearing rotation is much smaller than other rotational normal modes, which was examined by a calculation of the potential barrier by assuming additive pair potential function. The tunneling splittings of other modes are so small as invisible in Fig. 1, which is consistent with NMR result and torsional excitations of these modes were observed to be 11.0, 13.5, 14.5 and 17.0 meV at 12 K by LAM-D spectrometer of KENS (Fig.

2), which are also good consistent with an averaged energy of torsional excitation derived from temperature dependence of T_1^{-1} between 10 and 40 K

In conclusion, the coupled tunneling of methyl groups of HMB seems discernible in diluted system (5 mol% HMB in HBB) and gearing mode of six methyl groups was separetely observed from other modes. A detailed analysis and a similar study on scandium acetate are now underway.

The authors would like to express their thanks to LAM group of KEK especially to Dr. K. Shibata of Tohoku University for their stimulated discussions.

References

1) S. Takeda, G. Soda and H. Chihara, Solid State Commun., **36** (1980) 445.
2) S. Takeda, T. Fujiwara and H. Chihara, J. Phys. Soc. Jpn., **58** (1989) 1793.

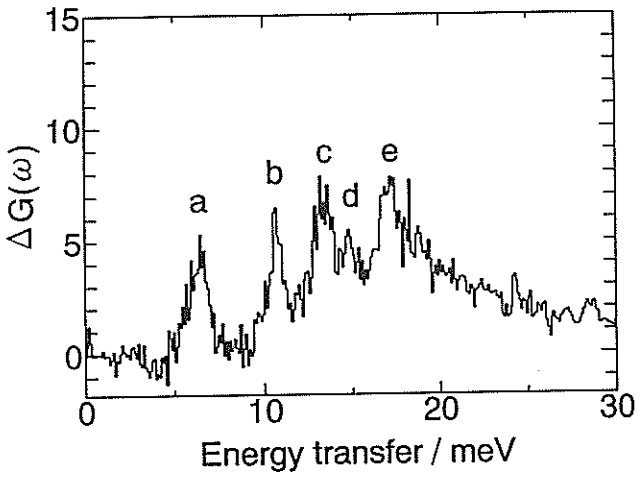

Fig. 2 Difference, $\Delta G(\omega)$, of inelastic neutron scattering spectra at 12 K; the result of subtraction of $G(\omega)$ of hexabromobenzene from $G(\omega)$ of hexamethylbenzene(5 mol%)/hexabromobenzene. The spectra were measured at scattering angle of 85 degree by LAM-D spectrometer of KENS. Peak a is tentatively assigned to the libration of hexamethylbenzene molecule and peaks b through e are torsional normal modes of methyl groups of hexamethylbenzene diluted in hexabromobenzene.

THE STRUCTURAL STUDY OF LIQUID BI-SE ALLOYS

F. Kakinuma, T. Fukunaga*, M. Misawa** and K. Suzuki***

Niigata College of Pharmacy, Kamishin'ei-cho 5-13-2, Niigata 950-21, Japan
*Department of Crystalline Materials Science, Nagoya University, Furo-cho, Chikusa-ku, Nagoya 464
**National Laboratory for High-Energy Physics, Oho 1-1, Tsukuba-shi,Ibaraki 305
***Institute for Material Research, Tohoku University, Katahira 2-1-1, Aoba-ku, Sendai 980

The liquid semiconductors can be classified into two groups according to the temperature variation of the electrical conductivity. One has a low conductivity and shows the linear behaviour in the Arrhenius plot of ln σ vs T^{-1}. The other has a relatively large conductivity which increase gradually with increasing temperature. The Se-rich Bi-Se alloys belong to the later group. The structure of liquid $Bi_{1-x}Se_x$ alloys with x = 0.3, 0.5, 0.6 and 0.65 was investigated to study the change in the chemical short-range order caused by the change of concentration. Neutron scattering experiments were carried out using the High Intensity Total scattering spectrometer (HIT).

Figure 1 shows the total structure factor, S(Q), for Bi-Se alloys at 740 °C together with the data of liquid Bi and Se [1]. Except for Se the height of the first peak decreases, while the height of the second peak increases with Se concenration accompanying the shift of the third peak position to the higher Q side. The characteristic peak at Q = 3.2 A^{-1} in S(Q) has also been observed for liquid Te and Te-based alloys [2,3]. This peak for liquid Te disappears with increasing temperature. Based on the study of the partial structure factor for liquid Cu_2Te [4], Hawker et al. suggested that the second peak in S(Q) for liquid Te is related to the covalent character of Te ions. The second peak in S(Q) for the Se-rich Bi-Se alloys, therefore, seems to be related to the degree of covalency in the bonding nature for these alloys.

The position of the first peak for $Bi_{0.35}Se_{0.65}$, Bi_2Se_3 and $Bi_{0.5}Se_{0.5}$ is independent of concentration and is located at 2.15 A^{-1}. A significant change in S(Q) is observed going from x = 0.3 to 0.5. The peak position of the first peak for $Bi_{0.7}Se_{0.3}$ is 2.10 A^{-1} which is the same as that for liquid Bi. The peak around Q = 3.2 A^{-1} is hardly seen for $Bi_{0.7}Se_{0.3}$. Liquid $Bi_{0.7}Se_{0.3}$ has the electrical conductivity with a negative tenperature coefficient and is almost metallic in character. Then the bonding nature, and hence the liquid structure of $Bi_{0.7}Se_{0.3}$ differs considerably from those for Se-rich alloys.

The hump in S(Q) was observed for the Se-rich Bi-Se alloys and it faded away with increasing Bi concentration. The electronic behaviour of the Se-rich alloys is closely related to the change in the medium-range structure.

references

1) Y. Waseda, The Structure of Noncrestalline Materials (McGraw-Hill,1980)
2) J. E. Enderby and M. Gay,J.Non-Cryst. Solids 35&36 (1980) 1296.
3) Y. Waseda, Y. Tsuchiya and S. Tamaki, Z. Phys. B32 (1979) 253.
4) J.Hawker, R.A.Howe and J.Enderby, Proc.5th Inter.Conf. on Amorphous and Liquid Semiconductors,(Taylor and Francis, London,1973) p.85.

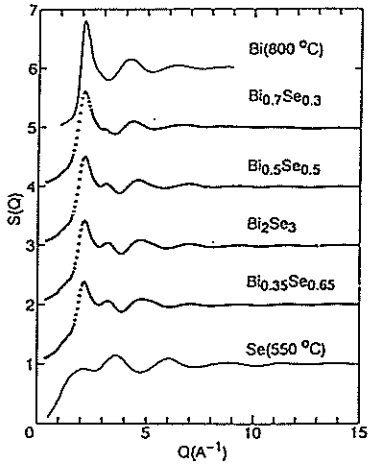

Figure 1. Structure factors for Bi-Se alloys at 740 °C and the data of liquid Bi and Se.

Neutron Diffraction Study of Amorphous As-S-I System

Y.SUGAWARA, Y.KAMEDA and O.UEMURA

Department of Chemistry, Faculty of Science, Yamagata University, Yamagata 990, Japan

Chalcogenide glasses indicate a large intrinsic loss in the mid-infrared, while, halide glasses have a poor chemical durability. In order to improve weak points of both glasses, studies on chalcohalide glasses have extensively been made in recent years[1]. As-S-I glasses are the most studied because of the ease of glass preparation and wide glass-forming composition range.

This report is to describe results of TOF neutron diffraction measurements on amorphous (and partly liquid) As_2S_3-AsI_3 system.

Samples of $(As_2S_3)_{1-x}(AsI_3)_x$ (x=0, 0.238, 0.455, 0.522, 0.588 and 0.652) were prepared by mixing required amounts of the starting materials in the molten state in an evacuated quartz tube and subsequently quenching to room temperature. The time-of-flight neutron diffraction measurements were carried out at 25°C using HIT spectrometer. The scattering neutrons from the samples, sealed in evacuated thin walled quartz cell with 8mm in inner diameter, were detected by ^{3}He counters located at 2θ=8, 14, 25, 32, 44, 91 and 150°. After corrections for the background, absorption, incoherent and multiple scatterings, the observed count rate was converted to the absolute scale by using the scattering data from the vanadium rod.

The observed coherent scattering cross section for respective samples is described in Fig.1. The intensity of the prepeak at 1.2 Å^{-1} for pure As_2S_3

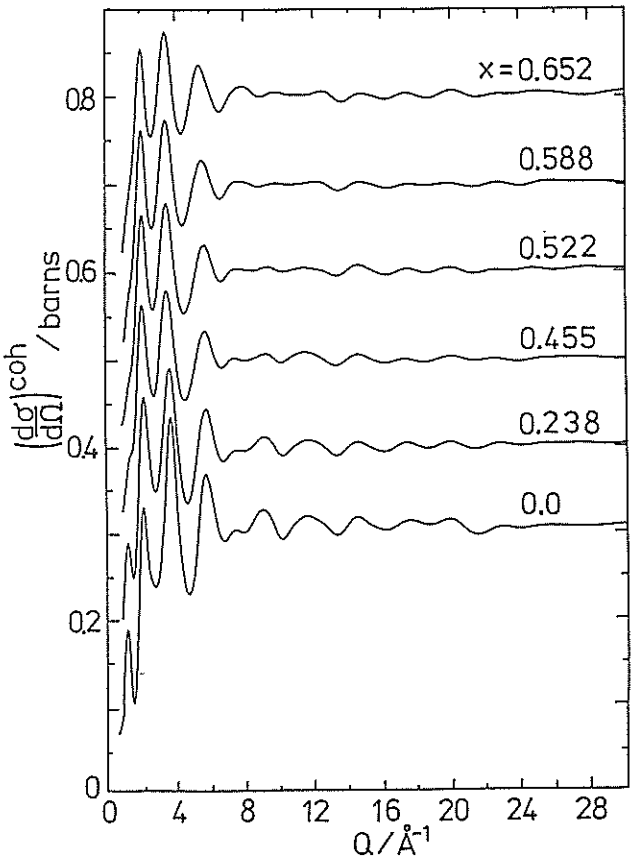

Fig.1 Observed coherent scattering cross sections for the $(As_2S_3)_{1-x}(AsI_3)_x$ system in the amorphous state, and x=0.588 and 0.652 in the liquid state, respectively.

gradually decreases with increasing AsI_3 content. However it remains as a little shoulder even in AsI_3 richer compositions, suggesting that the connection of $AsS_{3/2}$ structural unit is not easily destroyed when iodine atoms are incorporated in the system.

Fig.2 shows the composition dependence of the reduced radial distribution function, G(r), obtained from the Fourier transform of the interference function truncated at Q_{max}=20 $Å^{-1}$. The G(r) for all compositions shows well-resolved peaks at r=2.27 and 3.64 Å, assigned to As-S and S-S correlations in the $AsS_{3/2}$ structural unit. The peak positions remain unchanged for all compositions investigated. The peaks at r=2.62 and 3.98 Å in G(r) growing with increasing AsI_3 content can be assigned to As-I and I-I interactions. The position of the peaks is very close to that of corresponding interactions in the pyramidal AsI_3 molecules in the crystalline (r_{As-I}=2.591 Å, r_{I-I}=3.959 Å)[2] and liquid (r_{As-I}=2.65 Å)[3] AsI_3. The position of these peaks also shows little composition dependence. The area under the peaks at r=2.27 and 3.62 Å proportional respectively to the number of $AsS_{3/2}$ units and AsI_3 molecules changes systematically with sample composition.

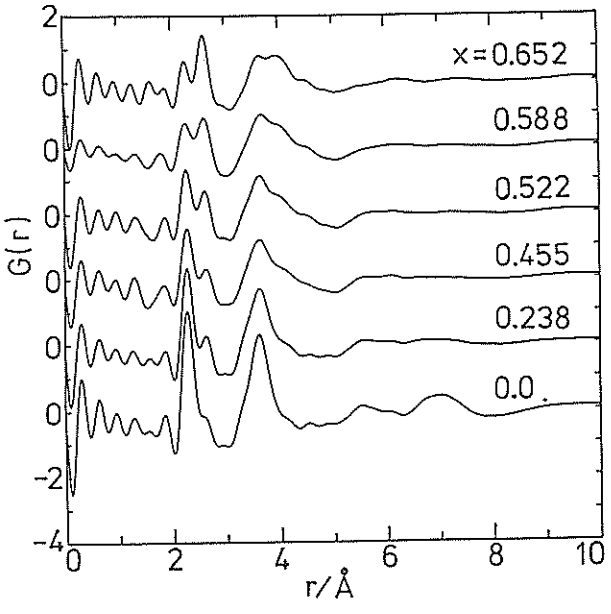

Fig.2 Reduced distribution functions for the $(As_2S_3)_{1-x}(AsI_3)_x$ system.

The previous X-ray diffraction work has proposed the twisted chain model consisting of AsS_2I units interconnected by double sulfur(-S-S-) and/or single sulfur(-S-) bridges[4]. On the other hand, the Raman scattering studies have postulated that discrete AsI_3 molecules are formed rather than $AsS_{3-n}I_n$ units[5]. The results obtained in this work show that AsI_3 molecules rather than $AsS_{3-n}I_n$ units are formed by inserting iodine atoms into the $As_{3/2}$ network structure of amorphous As_2S_3.

We would like to acknowledge the member of HIT group during the course of diffraction measurements.

References

1) J.S.Sanghera, J.Heo and J.D.Mackenzie J.Non-Cryst.Solids 103(1988)155
2) R.Enjalbert and J.Galy, Acta Cryst. B36(1980)914
3) Yu.G.Poltavsev, Usp.Fiz.Nauk. 120(1976)581
4) T.E.Hopkins, R.A.Pasternak, E.S.Gould and J.R.Herndon, J.Phys.Chem. 66(1962)733
5) L.Koudelka and M.Pisarcik J.Non-Cryst.Solids 64(1984)87

The Intramolecular Structure of D_3O^+ in Concentrated Aqueous DCl Solutions

Y.KAMEDA and O.UEMURA

Department of Chemistry, Faculty of Science, Yamagata University, Yamagata 990, Japan

Oxonium ion is one of the most important chemical species in extensive fields of science. However, the intramolecular structure of D_3O^+ in the liquid phase has remained a matter of controversy for several decades. The molecular orbital calculation[1] and ^{17}O NMR[2] works have suggested a planar equilateral triangle geometry for D_3O^+. On the other hand, a trigonal pyramidal structure for the oxonium ion has indicated by the Raman spectroscopic study[3].

In this report, we describe on the experimental results of TOF neutron diffraction on concentrated aqueous DCl solutions, for the purpose of determining the molecular geometry of oxonium ion in the liquid phase.

Pure D_2O (99.8% D), 10mol% and 23mol% DCl solutions in D_2O were sealed into a cylindrical thin walled quartz cell with 8mm in inner diameter and 0.4mm in wall thickness. TOF neutron diffraction measurements were performed at 25°C using a total scattering instrument HIT. Measurements were made in advance for an empty cell, background and a vanadium rod which has the same dimension as the sample.

After corrections for the background, absorption and multiple scattering, the observed count rate was converted to the absolute scale by using the scattering data from the vanadium rod. The observed cross sections at small scattering angles below 44° exhibit almost a similar oscillation amplitude around the static limit. Much greater deviations from the static limit in addition to the obscurity in oscillation amplitude of the interference, which are considered to arise from the inelasticity effect, were observed in 91 and 150° data. The reliability of the

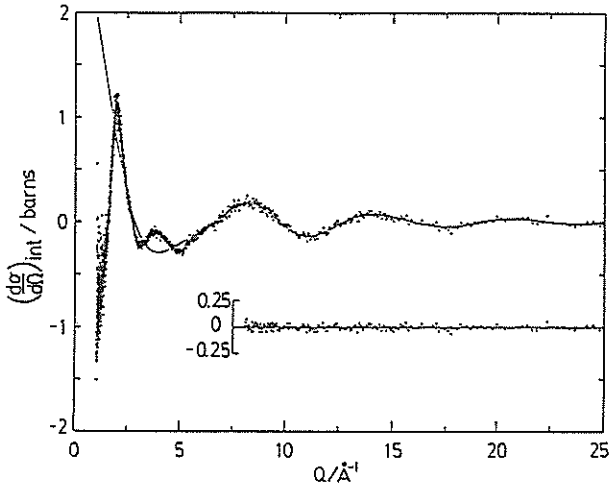

Fig.1 The observed total interference term (dots) and the best fit with the intramolecular term (silid line) for liquid D_2O. The residual function (dots) is shown in below.

functional form for the inelasticity correction seems to be open in the present time except for D_2O molecule. Consequently, taking into consideration of minimizing both the inelasticity effect and the instrumental resolution, we adopted only the data at $2\theta=44^\circ$ for the subsequent structural analysis.

The corrected total interference term for pure liquid D_2O is shown in Fig.1. Two internuclear distances, $r_{OD}=0.983\pm0.005$ Å and $r_{DD}=1.55\pm0.04$ Å, and two root mean square displacements $l_{OD}=0.067\pm0.008$ Å and $l_{DD}=0.12\pm0.04$ Å, were determined through the least square fit in the range of $8<Q<25$ Å^{-1}. These parameters agree well with those from earlier studies in which the inelasticity correction for the intramolecular interference term has been applied. This implies that the inelasticity distortion for the interference term is sufficiently small at $2\theta=44^\circ$.

The molecular parameters for D_3O^+ were determined by the least square fit of the theoretical intramolecular interference term of 23mol% DCl solution as depicted in Fig.2. The inelasticity effect for the intramolecular interference term in the data can be again postulated to be sufficiently small. The structure parameters for D_2O molecule in the solution were assumed to be the same as the values for pure liquid D_2O, which are already determined. The OD and DD distances in D_3O^+ with their root mean square displacements are determined to be $r_{OD}=1.04\pm0.04$ Å, $r_{DD}=1.63\pm0.05$ Å, $l_{OD}=0.07\pm0.02$ Å and $l_{DD}=0.12\pm0.06$ Å, respectively, through the similar fitting procedure. The bond angle, $\angle DOD=103\pm10^\circ$, derived from these parameters obviously exhibits the trigonal pyramidal structure of oxonium ion in the solution. It is noteworthy that these parameters determined in this work were obtained without any assumption on the molecular geometry of D_3O^+. The values of root mean square displacements for D_3O^+ agree well with those for D_2O molecule. This agreement is reasonably supported from the fact that the molecular force constants for D_3O^+ are very similar to those for D_2O in the liquid phase according to the spectroscopic data[3].

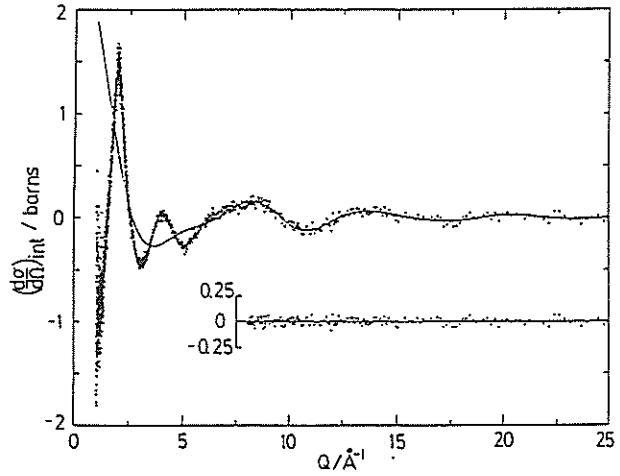

Fig.2 The same notation as Fig.1 except for 23mol% DCl solution.

The authors would like to acknowledge the members of HIT group during the cource of diffraction measurements.

References

1) M.D.Newton and S.Ehrenson, J.Am.Chem.Soc.,93(1971)4971
2) G.D.Mateescu and G.M.Benedikt, J.Am.Chem.Soc.,101(1979)3959
3) R.C.Taylor and G.L.Vidale, J.Am.Chem.Soc.,78(1956)5999

Direct Correlation between Lithium Cation and Carboxyl Anion in Highly Concentrated Aqueous Solution*)

KAZUHIKO ICHIKAWA, SEIICHI KOTANI and TOSHIHARU FUKUNAGA**

Department of Chemistry, Hokkaido Univ., Sapporo 060
**Department of Crystalline Materials Science, Nagoya Univ., Nagoya 464

In the active site of a cavity or groove in protein and DNA, a water molecule is isolated from other water molecules and is kept under the electrostatic field established by the surrounding ions, such as metal cation, halide anions[1] carboxyl anion $-COO^-$, protonated amine or imine $-NH_3^+$ or $=NH_2^+$, and phosphate anion $-OPO_3^{2-}$. That is to say, the anions, as well as some water molecules, coordinate to a central metal cation in the cavity or groove arranged by the preorganization of biomolecules. The first order-difference method of neutron diffraction shows that Li^+ in both completely and incompletely hydrated solutions coordinates directly to Cl^-.[2] It is also interesting to study the configuration between carboxyl anions and metallic cation. Carboxyl anions are very familiar in biological system and play an important role as the binding site of metallic cations.

Theory

The interference term consists of the contributions from the intramolecular and intermolecular parts. The Fourier transform of intermolecular interference function gives the intermolecular distribution function $G(r)$.[3]

we introduce the difference, $\Delta_{Li}(Q)$, between two intermolecular interference terms[2]; they are identical in all respects except that the isotopic composition of Li nucleus is changed. The difference $\Delta_{Li}(Q)$ consists of the eight terms of intermolecular interference function $a_{Li-\alpha}(Q)$.

The Fourier transform of $\Delta_{Li}(Q)$ gives the distribution function $\bar{G}_{Li}(r)$

$$\bar{G}_{Li}(r)= \frac{1}{2\pi^2\rho r}\int \Delta_{Li}(Q)\, Q\sin(Qr)dQ \qquad (1)$$

Experimental

We prepared samples of two different lithium acetates in which the isotopic composition of $Li(^6Li/^7Li)$ was changed.[4] At first, the two isotopically enriched samples CD_3COO^6Li and CD_3COO^7Li, were prepared from $^6Li_2CO_3$(95.0 at% ^6Li-enriched), ^7LiOH(99.9 at% ^7Li-enriched), and acetic acid-d_4 (99.5 at% D-enriched) under vacua at ca. 90°C; the residual water was removed by heating over a day at ca. 60°C under vacuum. The infrared spectra of the reactants showed no complex ions of CO_3^{2-} and OH^- in the Li-enriched solid CD_3COOLi products. The reasons why we chose the two isotopic compositions (i.e., $CD_3COO^{6,7}Li$ and CD_3COO^7Li) prepared by weighting the above two enriched CD_3COOLi products are as follows: for the Li-isotopic mixture at ca. 54 at% ^6Li the value of the neutron-scattering length b_{Li} of Li nucleus is almost equal to zero: b_{Li} = 0.546 x b_6(=2.0fm) + 0.454 x b_7(=-2.22fm) = 0.08fm. Thus, the contribution from the pairs of Li-α (α=Li, C_1, C_2, O_a, D_a, D_w, O_w) are absent in the interference term for the hydrated solution at 19.0 mol% $CD_3COO^{6,7}Li$.

*)J.Molec.Phys., in press.

Analyses, Results and Discussion

When the inverse Fourier transform of the corrected G(r) reproduced the observed intermolecular interference term, it was used to obtain the difference $\Delta_{Li}(Q)$ of (1).

Environmental structure around Li^+: The algebraic difference Δ_{Li}, given by

$$\Delta_{Li}(Q) = (d\sigma/\Omega)_{int}^{inter} \text{ (for } CD_3COO^{6,7}Li) - (d\sigma/\Omega)_{int}^{inter} \text{ (for } CD_3COO^{7}Li) , \quad (2)$$

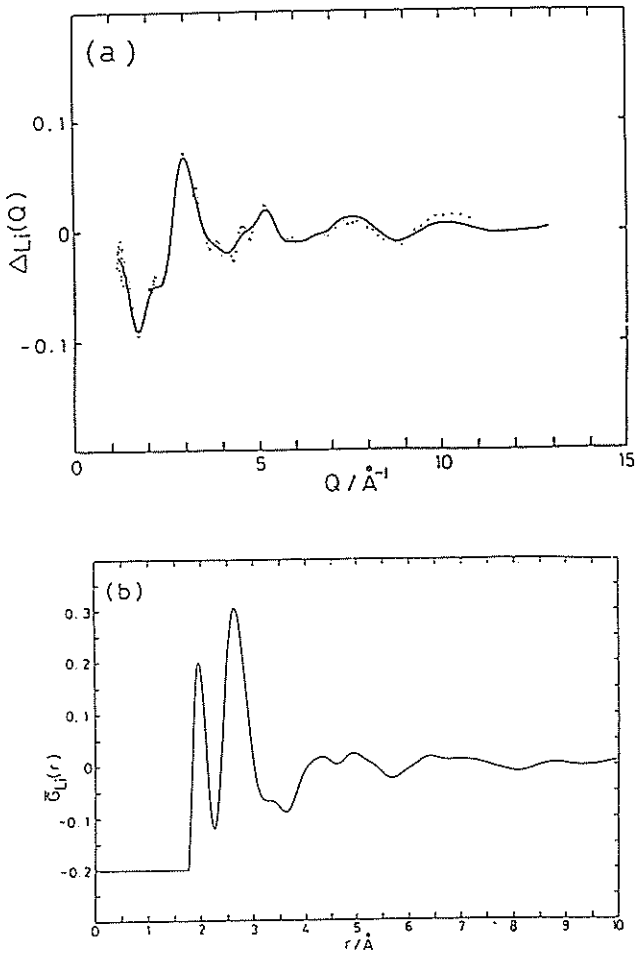

Fig.1(a) The observed difference $\Delta_{Li}(Q)$ (dots). (b) The environmental distribution function around Li^+, $\overline{G}_{Li}(r)$, obtained by the Fourier trnasform of $\Delta_{Li}(Q)$. The solid line in (a) was given by the inverse Fourier transform of $\overline{G}_{Li}(r)$ in (b).

was calculated from the two observed intermolecular interference functions, as shown by dots in fig. 1(a). The Fourier transform of $\Delta_{Li}(Q)$ gives $\overline{G}_{Li}(r)$, as shown in fig. 1(b).

The form of $\overline{G}_{Li}(r)$ shown in fig. 1(b) indicates the following. (i) The first and second peaks located at 1.96±0.03 Å and 2.63±0.03 Å. The former can be identified as the intermolecular correlations between Li-O. (ii) The nearest neighbour coordination number n_{LiO} is equal to 3.0±0.3 obtained by integrating 1.8 Å<r<2.3 Å.

The local configuration around Li^+ indicates the following. (i) The hydration number is 3.0±0.3. (ii) An anion of CD_3COO^- is partially located across and over the first hydration shell which is definitely deficient in water molecules hydrated around Li^+; the two oxygen atoms in a CD_3COO^- are equivalent from Li^+. (iii) Some water molecules coordinated to CD_3COO^- can be located just outside of the first shell around Li^+ because of the sufficient reproducibility of the second peak in the observed radial distribution function around Li^+, $\overline{RDF}_{Li}(r)$. The local structure of the hydrated solution at ca. 20 mol% CD_3COOLi is somewhat different from the structure of crystalline $CH_3COOLi \cdot 2H_2O$. Thus, the space and time averaged local structure around Li^+ in the liquid state may not reflect crystal structure.

References

[1] Ichikawa, K., and Kameda, Y., 1989, J.Phys.Condens.Matter,1,257

[2] Ichikawa, K., Kameda, Y., Matsumoto, T., and Misawa, M., 1984, J. Phys. C: Solid State Phys., 17, L725

[3] Kameda, Y., Kotani, S., and Ichikawa, K., 1992, Molec. Phys., 75, 1

[4] Kameda, Y., and Ichikawa, K., 1987, J.Chem. Soc., Faraday Trans. 1, 2925

The Molecular Structure of Bismuth Subiodide Anions in Liquid State

KAZUHIKO ICHIKAWA, SEIICHI KOTANI AND TOSHIHARU FUKUNAGA*

Department of Chemistry, Hokkaido Univ., Sapporo 060
* Department of Crystalline Materials Science, Nagoya Univ., Nagoya 464

Any solution of a metal in its own liquid halide (i.e., $M+MX_n$, n=1,2 and 3) can be classified into two categories. The first includes liquid alkali metal with its molten halide and invariably separates into the metal and the salt on freezing. The second includes the polyvalent metal halide solutions that form stable subhalides and homopolyatomic ions consisting only of metal in a lower oxidation state. We made investigations of the heat capacity C_p of the $Bi+BiI_3$ system[1] which belongs to the second typical system. The heat capacity is of considerable value as it combines the bonding or electronic properties including the internal motions in bismuth subiodide ions, and polyatomic species.

In this paper we report pulsed-neutron diffraction in molten BiI_3 and $Bi_{0.243}(BiI_3)_{0.757}$ at the salt-rich region. This paper focuses on the molecular structures of bismuth subiodide ions to make clear what the structural units are in liquid state.

Experimental

Materials: the guaranteed reagent bismuth tri-iodide was purified by sublimation or distillation *in vacuo* while the bimuth itself was 99.9999% pure.

Time-of-flight neutron diffraction measurements: We carried out the time-of-flight(TOF) neutron diffraction measurements for $Bi_{xm}(BiI_3)_{1-xm}$ melts at 480±3°C by using a high intensity total scattering spectrometer(HIT).

Theory

The observed total scattering cross section can be divided into a self-term and an interference term, $(d\sigma/d\Omega)_{self}$ and $(d\sigma/d\Omega)_{int}$. The latter, scaled by a molecule formulated as $Bi_xI_{(1-x)}$, can be expressed by

$$(d\sigma/d\Omega)_{int}= \bar{X}^2 b_{Bi}^2(a_{BiBi}(Q)-1) +2\bar{X}(1-\bar{X})b_{Bi}b_I(a_{BiI}(Q)-1) +(1-\bar{X})^2 b_I^2(a_{II}(Q)-1) \quad (1)$$

where $x=1/(4-3x_m)$. b_i stands for the scattering length for nucleus i. The interference term includes all the information about the liquid structure and consists of two contributions, an intra-molecular and an inter-molecular part.

The Fourier transform of eq(1) gives D(r) which is equal to radial distribution function RDF(r) referred to average number density distribution function $4\pi\rho r^2$

$$D(r)= RDF(r) - 4\pi\rho r^2 \quad (2)$$

where ρ is the average number density of molecules and $g_{ij}(r)$ is defined as

$$g_{ij}(r)=1+\frac{1}{2\pi^2\rho r}\int (a_{ij}(Q)-1)Q\sin(Qr)dQ \quad (3)$$

The number of j atoms around i n_{ij} is described as

$$n_{ij}=C_j\int 4\pi\rho r\, g_{ij}^2(r)dr \quad (4)$$

where C_j stands for atom fraction of j atom (x or 1-x).

Results and Discussion

Fig. 1 shows the observed $(d\sigma/d\Omega)_{int}$ of BiI_3(x_m=0) and $Bi_{0.243}(BiI_3)_{0.757}$ melts (denoted by dots). Fig. 2 shows D(r): its inverse Fourier transform reproduced the intermolecular interference terms observed between 2 $Å^{-1}$ and 26 $Å^{-1}$, and

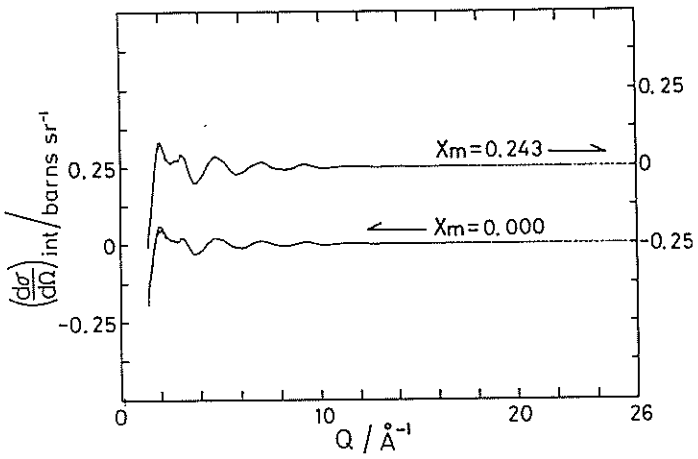

Fig. 1 The observed $(d\sigma/d\Omega)_{int}$ denoted by dots; the solid line was calculated by the inverse Fourier transform D(r) in Fig. 2.

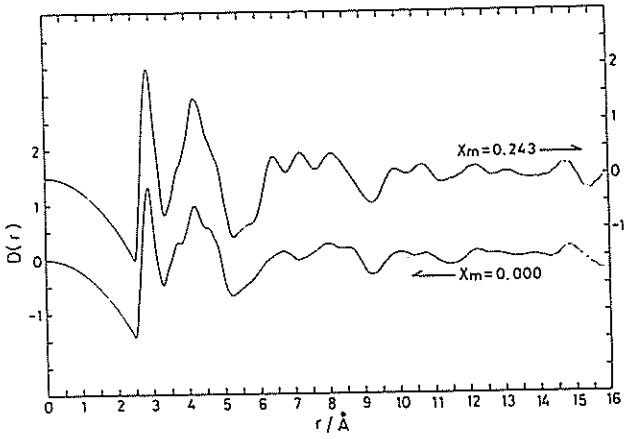

Fig. 2 D(r) for molten BiI_3 and $Bi_{0.243}(BiI_3)_{0.757}$ at 480 °C

the calculated curves were denoted by solid lines as shown in Fig. 1.

The form of D(r) shown in Fig.2 indicates the follwing. (i) The first peak locates at 2.89 Å and can be identified as the intraatomic correlation between Bi-I. (ii) The second peak has a maximum at 4.22 Å and has the two saddle points at ca. 3.7 Å and 4.5 Å. The correlations at 4.22 Å and ca. 4.5 Å can be identified as I-I and the other correlation at 3.7 Å as Bi-I. The first peak at ca. 2.9 Å in RDF(r) defined in eqn(2) was reproduced by the sum of the two Gaussian curves which located at 2.89 Å and 3.22 Å; the numbers n_{BiI} of I around Bi(III) were equal to two and one, respectively. On the other hand, Raman spectra of bismuth-trihalide melts can be understood as originating from a mixture of charged bismuth subhalide complexes, i.e., BiX_2^+ and BiX_4^-, and but from no halide ion (e.g., X_3^- and X^-).[2] Thus, the BiI_3 melt consists of the same number of the BiI_2^+ and BiI_4^- complexes: the former has the two Bi-I correlations at 2.89 Å and the latter has the two Bi-I bonds of 2.89 Å in length and the two Bi-I bonds of 3.22 Å in length. The crystal of BiI_3 is rhombohedral: bismuth is situated at the centre of iodine octahedron. Thus, the space and time averaged local structure around Bi(III) in the liquid state can not reflect crystal structure.

References

[1] Ichikawa, K., 1985, J. Phys. C: Solid State Phys., 18, 4631.

[2] Ichikawa, K., and Fukushi, K., 1986, J. Raman Spect., 17, 139.

STRUCTURE OF STRONGLY SUPERCOOLED TELLURIUM NANO-DROPLET

H.ENDO, M.YAO, T.TSUZUKI, K.KAWAKITA, and M.MISAWA*

Department of Physics, Faculty of Science, Kyoto University, Kyoto 606-01
*National Laboratory for High Energy Physics, 1-1 Ouho,Tsukuba, 305

Introduction

Liquid Te shows metallic behavior, unlike other chalcogens which retain semiconducting properties on melting. There are many studies on the origin of metallic nature of Te, but conclusive results have not been obtained yet. It should be emphasized that there exists a strong correlation between electronic states and atomic arrangements in chalcogens. It is expected that the metallic nature of liquid Te changes in a strongly supercooled state, which accompanies a modification of local atomic configuration. Nano-droplets tend to have a wide ranged supercooled state, because they contain a lower probability of nucleation sites[1]. In this paper, we report the result of neutron diffraction measurement for Te droplets in the supercooled state.

Experimental

Sample was prepared by alternating vacuum evaporation of Te and KI to form isolated Te islands in KI matrix. The size of droplets was determined by electron microscopy. From differential scanning calorimetry measurements, it was found that Te droplets with average diameter of 20nm were supercooled down to 240°C, 210 degrees below the melting point. The neutron diffraction experiment was performed using the HIT spectrometer installed at BSF in the National Laboratory for High Energy Physics. The specimen was made into a pellet form of 8mm diameter and 16mm height, and was held with Ar gas in a cylindrical cell made of Ti-Zr null alloy. More than ten thousand neutrons were accumulated per channel in time analyzers. In order to extract the structure factor S(Q) of Te from S(Q) of sample which is a mixture of Te and KI, the diffraction of KI powder was also measured.

Results and Discussion

Figure 1 shows the structure factor S(Q) of Te droplets at 430°C, 350°C, and 280°C. When the temperature decreases, the height of the first peak decreases and becomes lower than that of the second peak. Figure 2 shows the pair distribution function g(R). The profile of g(R) for the droplet at 430°C is quite similar to that for the bulk liquid Te. At 430°C, the first peak appears at 2.78Å and the width is slightly broad. Since the first peak overlaps largely with a broad second peak, it is diffi-

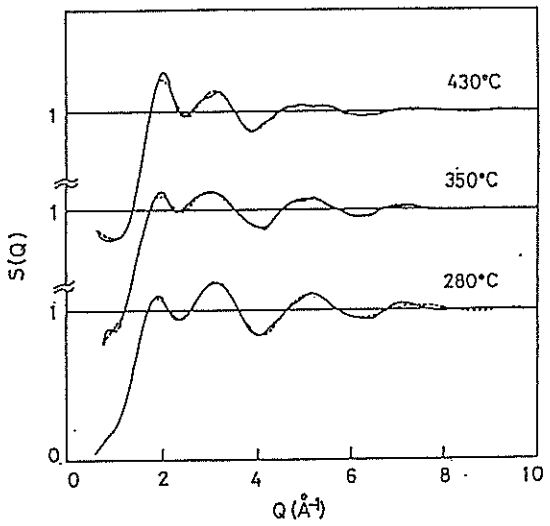

Figure.1 The correlation function S(Q) for Te droplets with 20nm diameter in KI matrix at 430°C, 350°C, and 280°C. Dotted lines denote the fitting result.

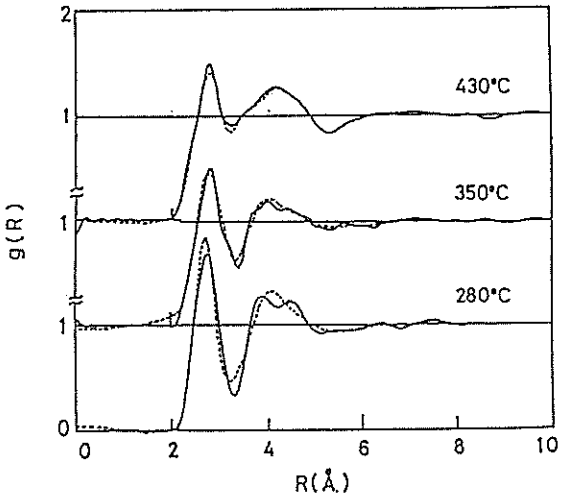

Figure.2 The pair distribution function g(R) for Te droplets with 20nm diameter in KI matrix at 430°C, 350°C, and 280°C. Dotted lines denote the fitting result.

cult to deduce the first coordination number. At 350°C, the position of the first peak is at 2.8Å and there appears a subpeak around 3.1Å. This fact suggests the existence of longer and shorter bonds in Te chains, which is consistent with the EXAFS results of our recent research[2]. At 280°C, the first peak becomes more prominent and first minimum becomes much deeper. The shoulder seen at 350°C disappears. The second peak splits into two humps at 3.8Å and 4.4Å. The coordination number at 280°C is estimated to be 2. The profile of S(Q) is similar to that of liquid Se[3].

Recently Misawa estimated the average chain length of liquid Te from neutron diffraction measurement[4]. The chain length is considerably short compared with that of liquid Se. Based on this short chain model, we have analyzed g(R) with the method developed for molecular liquids by Misawa[5]. In this analysis, Te dimer was regarded as a basic unit and both interchain and intrachain orientational correlation were elucidated. The fitted S(Q) and g(R) are shown by dots in Figure 1 and Figure 2. The agreement with experimental curves is reasonably good. The structural parameters obtained are listed in Table 1. At 430°C and 350°C, the chain of liquid Te consists of shorter and longer bonds. The dihedral angle is close to 180° and the tilting angle is very small, suggesting the planar zigzag chains spacing parallel with each other. Under the pressure of 40kbar, crystalline Te has a metallic phase, which consists of dimerized planar zigzag chains with shorter bonds (2.8Å) and longer bonds (3.1Å) stacking in staggered puckered layers[6]. It is considered that liquid Te has a local structure similar to that of high pressure metallic crystal. At 280°C, the chain is formed mainly by shorter bonds. The bond angle and dihedral angle are nearly 90°, which suggests that helical conformation is dominant at this temperature.

Conclusion

The results indicate that near melting point, liquid Te has a local structure similar to that of high pressure metallic crystal. As temperature decreases, the average chain length increases and the planar zigzag geometry becomes unstable. In the vicinity of 280°C, helix conformation becomes dominant, which may cause metal-semiconductor transition accompanied by volume expansion[7].

Acknowledgement

Authors would like to thank professor T.Fukunaga and Mr. H.Akatsuka for collaborating neutron diffraction measurement.

References

1) J. H. Perepezko, B. A. Muller, J. J. Rechmond and K. P. Cooper, *Rapidly Quenched Metals* S. Steeb and H. Warlimont (eds.) Elsevier Science Publishers B.V., (1985) P43.

2) K. Tamura, M. Inui, M. Yao, H. Endo, S. Hosokawa, H. Hosino, Y. Katayama and K. Maruyama, *J. Phys.: Condens. Matter* **3** (1991) 7495.

3) M. Misawa, S. Suzuki, *Trans. JIM* **18** (1977) 427.

4) M. Misawa, *J. Phys.: Condens. Matter* **4** (1992) in print.

5) M. Misawa, *J. Chem. Phys.* **91** (1989) 2575.

6) K. Aoki, O. Shimomura and S. Minomura, *J. Phys. Soc. Jpn.* **48** (1980) 551.

7) Y. Tsuchiya, *J. Phys.: Condens. Matter* **3** (1991) 3163.

Table.1 The structure parameters of Te droplets with 20nm diameter in KI matrix, obtained from the analysis based on short chain model[4)5)]. l_S and l_L : shorter and longer bond length, respectively. θ_b : bond angle. ϕ_d : dihedral angle. σ : effective diameter of Te dimer. R_c and Θ : polar coordinates for the center of correlated dimer. θ : tilting angle of correlated dimer. n_{inter} : the number of correlated dimers in the equivalent configuration.

T (°C)	l_S (Å)	l_L (Å)	θ_b (deg)	ϕ_d (deg)	σ (Å)	R_C (Å)	Θ (deg)	θ (deg)	n_{inter} (adjacent dimers)
430	2.6	2.9	119	179	4.1	4.1	56	0.0	3.92
350	2.7	2.9	112	178	3.8	3.9	69	1.1	1.92
280	2.7	-	95	75	4.7	4.4	59	-2.1	2.51

Inelastic Neutron Scattering of Porous Glasses

H. YUGAMI, S. MATSUO, M. ISHIGAME and K. SHIBATA*

Research Institute for Scientific Measurements, Tohoku Univ.,
*Institute for Materials Research, Tohoku Univ., Sendai 980

Vibrational states in glasses at low frequency below 100cm^{-1} is very different from those of crystalline solids. Recently, the fractal concept has been applied on the analysis of low-frequency Raman intensity for some kind of glasses[1,2] and polymers[3], etc. For example, the reduced Raman intensity between 10 and 200cm^{-1} in silica gels varied as ω^{ν}, where ν is a constant, and was interpreted by the scattering from fractons[1]. Since, reduced Raman intensity, however, involve both the density of states $g(\omega)$ and a frequency depend coupling factor $C(\omega)$, the $g(\omega)$ can not be readily deduced from the slope of reduced Raman intensity[4]. This is the most serious problem on the analysis for low-frequency Raman intensity of disordered materials.

We have measured generalized density of states in porous glasses using the inelastic neutron scattering spectroscopy, and have compared these with results obtained by Raman scattering spectroscopy. The experiments have been carried out on several powder samples with different pore diameter, by using the LAM40 spectrometer installed at KENS. The energy resolution is about 150 μeV at hν=0meV, and the typical scattering vector Q ranges 0.2 to 2.6 A^{-1}.

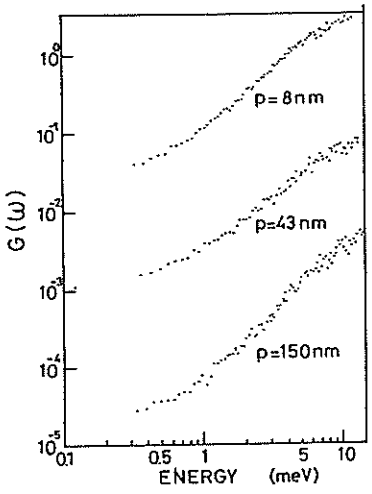

Fig.1 Energy dependence of g(ω)

Figure 1 shows the generalized density of states g(ω) of porous glasses at room temperature.
The energy dependence of g(ω) shows a power law in the range between 0.8 to 8 meV. The Raman intensity of these samples also show a power law dependence in this same energy range. The slopes obtained from neutron and Raman scattering spectra are plotted in Fig.2 for several samples with different pore diameter. The slope obtained by neutron scattering, which represents the slope of g(ω), is almost the same that obtained by Raman spectra. This result indicates that the coupling constant C(ω) is almost energy independent in these samples. Furthermore, the slope of g(ω) is far larger than the theoretically predicted slope of g (ω)((ν=0.3) in fractal lattice[5]. From this fact, it may be concluded that the fracton interpretation of Raman spectra in this energy range is not suitable in this system, while Raman spectra show a clear power law dependence.

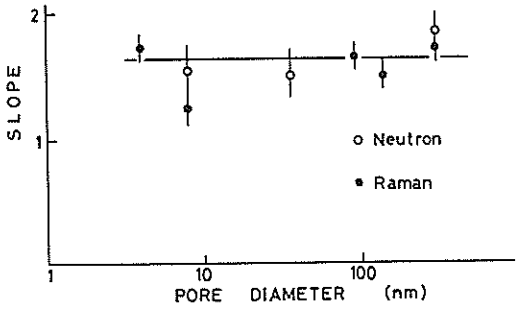

Fig.2 Slope of g(ω) and Raman intensity

References

1) A. Boukenter et. al., Phys. Rev. Lett. 57,2391(1986).
2) Y. Tsujimi et. al., Phys. Rev. Lett., 60,2757(1986).
3) S. Saikan et. al., Chem. Phys. Lett. 166, 358(1990).
4) R. Shuker and R.W. Gammon, Phys. rev. Lett., 25, 222(1970).
5) S. Alexander and R. Orbach, J. de Phys. 43, L625(1982).

Structual Study of Molten Thallium Chloride

Ryo Ishii; Susumu Okazaki; Osamu Odawara; Isao Okada
Masakatsu Misawa*; Toshiharu Fukunaga**

Department of Electronic Chemistry, Tokyo Institute of Technology, 4259, Nagatsuta, Midori-ku, Yokohama 227
*National Labolatory for High Energy Physics, Oho, Tsukuba 305
**Department of Crystalline Materials Science, Nagoya University, Furo-cho, Chikusa-ku. Nagoya 464

The monovalent transition metal cations are similar to the alkali metal ions in their physical properties such as ionic radii. Although the crystalline structure of the former salts are mainly categorized in a NaCl - type or a CsCl - type at room temperature, few structural investigations have been done for the melts. In the present study, a neutron diffraction measurement of molten TlCl has been performed in order to investigate this analogy of the structural properties in the liquid state.

The structure of TlCl crystal at room temperature is the CsCl type structure and no phase transition below the melting point (702K) was observed by a DTA measurement. The ionic radii of the cation and the anion are 1.50 Å and 1.81 Å[1], respectively. For the melt, however, There is no data in literature because that an X - ray diffraction measurement has difficulties such as the high vapor pressure of the sample and the large difference of the X - ray scattering length between the cation and the anion. The present neutron diffraction measurement yields the total structure factor and radial distribution function, g(r). In this study, molecular dynamics (MD) simulation of molten TlCl has also been done, which enables us a further detailed analysis of the liquid structure.

The sample salt was vacuum - dried for 13 hours and sealed in a quartz tube. Neutron diffraction was performed at 800 K using the High Intensity Total Scattering Spectrometer (HIT) at the National Laboratory for High Energy physics(KEK), Tsukuba. The scattered neutrons were detected by ^{3}He detectors at the scattering angles , 2θ, of 8°, 13°, 23°, 32°, 42°, 90° and 150°. We mainly analyzed with the scattering intensity at the scattering angle of 42° for the analysis. Scattering intensities from a vanadium rod and a vacant cell as well as background intensities were also measured for analysis. The observed intensities were corrected for the cell, background, absorption, multiple and incoherent scattering, being normalized by the intensity of the vanadium rod. The total structural factor S(Q) was obtained. The neutron weighted radial distribution function was calculated by Fourier transformation of the structure function Q(S(Q)-1) over the range to 25 Å^{-1}.

The MD simulation has been executed using the pair potentials of the Born - Mayer - Huggins type with the parameters presented by Mayer.[2] The functions were originally presented for the TlCl crystal based on a rigid ion model. A cubic cell with the periodic boundary condition contained 108 cations and 108 anions. The NEV ensemble was constructed according to a Gear's predictor - corrector method with a time step of 4 fs. The aimed temperature for the simulation was 800 K to compare the result obtained from the experimental measurement. The 8000 steps of the trajectories after establishing an optimum configuration (the 3000 of the initial equilibrium run) were analyzed to obtain the radial distribution functions.

The experimental and calculated radial distribution functions are shown in Fig. 1. The peak positions are found at r = 2.96 Å, 4.4 Å, 6.3 Å in the experimental g(r) and r = 2.90 Å, 4.32 Å, 6.42 Å in the calculated one, which shows good agreement between them. The ratio of the r value of the second peak to the first is 1.49 both for the former and the latter. The calculated coordination number was 5.6 . The ratio is $\sqrt{2}$ = 1.41 and $2/\sqrt{3}$ = 1.15 for NaCl and CsCl type crystalline structure, respectively, and the coordination number 6 and 8 for the former and the latter, respectively. Thus it should be noted that TlCl changes in its structure from CsCl - type crystalline to quasi NaCl - type liquid on (or after) melting. A structural change on the liquid state side near the solid - liquid phase transition line has been reported for a more complex organic compound.[3] It is noticeable that the phase change in the liquid was also found in the simple ionic compound as the present one. However, the shape of the function is considerably different from each other. The peaks of the experimental function are much broader than those of the calculated one. In particular, the first and the second peaks are so broad that they are almost unified to form a very broad one, the latter appearing only as a shoulder. The radial distribution functions of a series of molten alkali chlorides obtained by our neutron diffraction measurements[4] are shown in Fig. 2. The literature values of polarizabilities

are also given in Table 1. It is clear from this figure and the table that the peak of radial distribution function becomes broad with increasing polarizability. This suggests that the disagreement in the width of the peaks in Fig. 1 is caused by the neglecting the ionic polarization in the calculation. In fact, Gartrell – Hills and McGreevy[6] showed in their simulation study that the inclusion of polarizability in the ionic potential model leads to the broadening in radial distribution function in molten CsCl. Furthermore, the experimental first peak position was at 2.96 Å, which is considerably shorter than the summation of ionic radii of the cation and anion; i.e. 3.31 Å. This also substantiates the strong polarization of the Tl^+ ion. Thus, the potential function used in the MD calculation should include not only the interaction between induced dipole and charge but also the reduction of electron overlapping between the cation and anion; i.e. the change in the shape of the ions.

In conclusion, the TlCl crystal, which is known to have a CsCl – type structure at room temperature, has not showed any phase transition below the melting point (702K). Meanwhile, it has been found from the neutron diffraction that TlCl has a quasi NaCl – type structure[1] in the molten state (800 K), which has been reproduced by MD simulation based on the rigid model. However, since the MD simulation based on this model yielded much sharper peaks in the radial distribution function than those of the neutron diffraction, it is suggested that the polarization plays an important role for the structure of molten TlCl.

Reference

1) R. D. Shannon, Acta. Cryst., A32, 751(1976)
2) J. E. Mayer, J. Chem. Phys., 1, 327(1933)
3) T. Atake, H. Chihara, Chem. Phys. Lett., Vol 56, Num 2, 330(1978)
4) Y. Miyamoto, S. Okazaki, I. Okada, O. Odawara, T. Fukunaga and M. Misawa, to be published.
5) T. L. Hill, "Lecture on Matter and Equilibrium", W. A. Benjamin Inc., New York, N. Y. (1966) P.40 .
6) P. R. Gartrell-Mills, R. L. McGreeby, Mol. Sim., Vol 2, 209(1989)

Table 1. The polarizabilities of Alakai metal ions,[a] thallium ion and chloride ion.

Ions	polarizability($10^{-24}cm^3$)
Li^+	0.030
Na^+	0.182
K^+	0.844
Rb^+	1.42
Cs^+	2.45
Tl^+	3.50
Cl^-	3.66

a) reference 5.

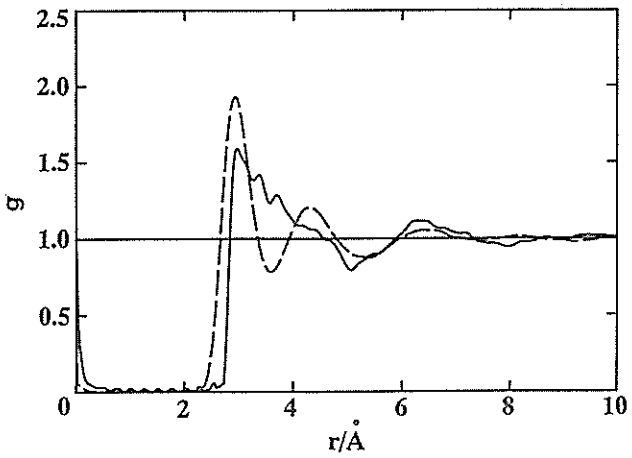

Figure.1 Total radial distribution function g(r) for TlCl at 800K ( ) experimental, ( )calculated

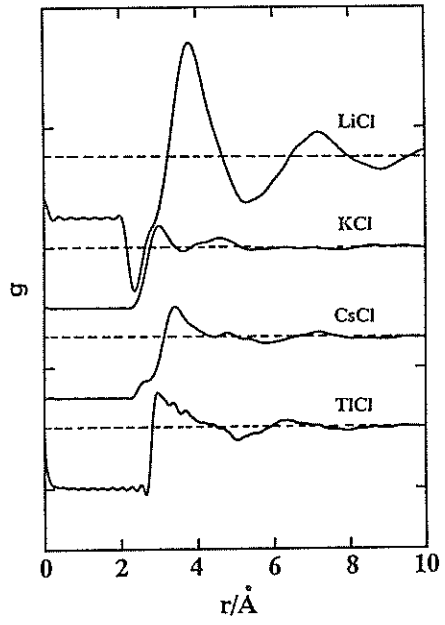

Figure.2 Total radial distribution functions of molten alkali chloride and molten TlCl

The Solvation of Chloride Ion in Water, Methanol and N,N-dimethylformamide by Neutron Diffraction

M. Yamagami, T. Yamaguchi, H. Wakita, and M. Misawa*

Department of Chemistry, Fukuoka University, Nanakuma, Jonan-ku, Fukuoka 814-01

*National Laboratory for High Energy Physics, Oho, Tsukuba 305

The macroscopic properties of electrolyte solutions depend strongly on the nature of the solvent. The structure of electrolyte solutions, in particular, alkali halide solutions, has widely been investigated by means of X-ray[1] and neutron[2] diffraction and computer simulation method,[3] from which the structure and properties of hydrated ions have been revealed.

In the present study, the solvation structures of Cl^- ion in water, methanol(MeOD), and N,N-dimethylformamide(DMF) at room temperature have been determined by the neutron first-order difference method.

Sample solutions were prepared by the following procedure. Lithium carbonate was dissolved in isotopically labeled aqueous hydrochloric acid ($H^{35}Cl$ and $H^{37}Cl$) and then substituting light water with heavy water. The compositions of the sample solutions were adjusted so that the solutions contained the same amount of constituents except for chloride isotopes (Table 1). Neutron diffraction measurements were performed on the HIT spectrometer. The sample solution was contained in a Ti-Zr cell of inner diameter of 8 mm. The data were corrected for absorption and multiple scattering, and then normalized using the data of a vanadium rod.

A difference $\Delta_{Cl}(Q)$ between the structure factors S(Q) of $^7Li^{35}Cl$-D_2O and $^7Li^{37}Cl$-D_2O solutions can be written in the form

$$\Delta_{Cl}(Q) = A[S_{ClO}(Q)-1]+B[S_{ClD}(Q)-1]+C[S_{LiCl}(Q)-1] +D[S_{ClCl}(Q)-1],$$

$A=2c_Oc_{Cl}b_O\Delta b_{Cl}$, $B=2c_Dc_{Cl}b_D\Delta b_{Cl}$

$C=2c_{Li}c_{Cl}b_{Li}\Delta b_{Cl}$, $D=2c_{Cl}^2(b_{35Cl}^2-b_{37Cl}^2)$,

$Q=4\pi\sin\theta/\lambda$, $\Delta b_{Cl}=b_{35Cl}-b_{37Cl}$,

where c_i and b_i are, respectively, the atomic fraction and the coherent scattering length of the i-th particle. The radial distribution function is then given by

$$\Delta G_{Cl}(r)=(2\pi^2\rho r)^{-1}\int Q\Delta_{Cl}(Q)\exp(-0.005Q^2)\sin(Qr)dQ.$$

Here ρ is the number density of the sample solution.

The difference functions, $\Delta_{Cl}(Q)$, and radial distribution functions, $\Delta G_{Cl}(r)$, in water, methanol and N,N-dimethylformamide are given in Figures 1 and 2, respectively. The first peak in $\Delta G_{Cl}(r)$ are ascribed to the Cl^--D interactions within the solvation shell. The area of the first peak for methanol decreases, compared with that for water. Furthermore, in N,N-dimethylformamide the first peak becomes very broad and is not distinguished from the second peak, indicating that solvent molecules are not firmly bonded to a chloride ion in the solution. These variations of the first peak result from different acceptor properties of the solvents. In order to analyze the individual peak quantitatively, we employed a least squares fitting procedure using Gaussian function to represent each peak. The interatomic distances and the solvation number were estimated from the positions and the areas of the individual Gaussian finally obtained. The chloride-deuterium interatomic distances and solvation number of chloride ion changes from 2.29 A and 5.8 in water to 2.21 A and 3.6 in methanol, respectively. The final results obtained in the present study are summarized in Table 2.

References

1) A. H. Narten, F. Vaslow, and H. A. Levy, J. Chem. Phys., 58, 5017(1973).

2) J. R. Newsome, G. W. Neilson, and J. E. Enderby, J. Phys. C: Solid State Phys., 13, L923(1980).

3) K. Heinzinger, Stud. Phys. Teor. Chem., 27, 61(1983).

Table 1 The compositions and important parameters for the sample solutions at 298 K.

	I	II	III	IV	V	VI
Scattering lengths (10^{-12} cm)						
b_{Li}	-0.222	-0.222	-0.222	-0.222	-0.222	-0.222
b_{Cl}	1.163	0.345	1.163	0.345	1.163	0.345
Molality (mol kg^{-1})	9.615	9.417	6.859	7.009	1.710	1.693
$[D_2O]/[LiCl]$	5.195	5.305	4.042	3.956	7.299	7.368
Density (g cm^{-3})	1.271	1.285	1.073	1.088	1.101	1.104
Total absorption cross section for 2200 m/s neutron (10^{-24} cm)	2.52	0.155	1.69	0.110	0.653	0.188

I) $^7Li^{35}Cl+D_2O$ II) $^7Li^{37}Cl+D_2O$ III) $^7Li^{35}Cl$+MeOD IV) $^7Li^{37}Cl$+MeOD V) $^7Li^{35}Cl$+DMF VI) $^7Li^{37}Cl$+DMF

Table 2 Structural parameters for the chloride ion solvation obtained in the present study. r, n, and Δr are the interatomic distance, the solvation number, and the half width at half maximum, respectively.

	$r_{Cl-D(1)}$/A	$n_{D(1)}$	$\Delta r_{Cl-D(1)}$/A
D_2O	2.29(1)	5.8(5)	0.27(3)
MeOD	2.21(3)	3.6(5)	0.20(3)

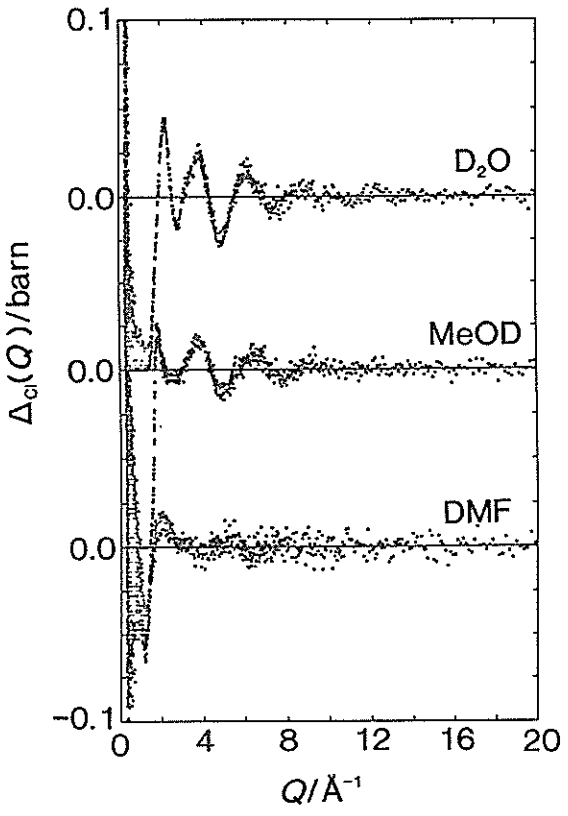

Fig. 1 $\Delta_{Cl}(Q)$ for the LiCl-D_2O solution in water, methanol and N,N-dimethylformamide.

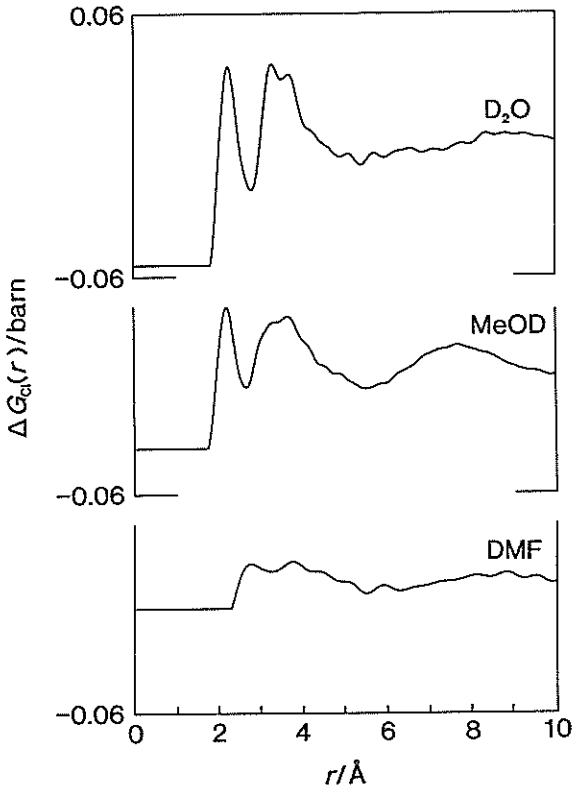

Fig. 2 $\Delta G_{Cl}(r)$ for the LiCl-D_2O solution in water, methanol and N,N-dimethylformamide.

Neutron Diffraction Study on Lithium(I) Hydration in Aqueous Chloride Solution in the Temperature Range 173 - 295 K

M. Yamagami, T. Yamaguchi, H. Wakita, and M. Misawa*

Department of Chemistry, Fukuoka University, Nanakuma, Jonan-ku, Fukuoka 814-01

*National Laboratory for High Energy Physics, Oho, Tsukuba 305

A lithium(I) ion is one of the interesting cations because it has a very small ionic radius. Therefore, a large number of studies have been devoted to structures of lithium salts in aqueous solutions by X-ray[1] and neutron[2] diffraction, molecular dynamics,[3] and Monte Carlo[4] simulation methods. According to the previous structural studies on aqueous lithium salts solutions, the hydration number of lithium(I) ion changes from four to six, depending on the concentration of solutions. Almost all of these investigations have so far been reported at room temperature.

In the present study, the hydration structures of lithium(I) ion in a 9.5 molal aqueous lithium chloride solution at ambient and supercooling temperatures (258, 213 and 173 K) have been determined by a neutron first-order difference method using lithium isotopes. Lithium chloride was chosen because it is highly soluble in water to form supercooled aqueous solution.

Sample solutions were prepared by the following procedure. The isotopically labeled lithium carbonate ($^7Li_2CO_3$ and $^0Li_2CO_3$) were dissolved in aqueous hydrochloric acid and then substituting light water with heavy water. The compositions of the sample solutions were adjusted so that the solutions contained the same amount of constituents except for lithium isotopes (Table 1). Neutron diffraction measurements were made on the HIT spectrometer. The sample solution was contained in a Ti-Zr cell of inner diameter of 8 mm. The data were corrected for absorption and multiple scattering and then normalized using the data of a vanadium rod.

A difference $\Delta_{Li}(Q)$ between the structure factors S(Q) of ^7LiCl-D_2O and ^0LiCl-D_2O solutions can be written in the form

$$\Delta_{Li}(Q) = A[S_{LiO}(Q)-1]+B[S_{LiD}(Q)-1]+C[S_{LiCl}(Q)-1] +D[S_{LiLi}(Q)-1],$$

$A=2c_Oc_{Li}b_O\Delta b_{Li}$, $B=2c_Dc_{Li}b_D\Delta b_{Li}$

$C=2c_{Cl}c_{Li}b_{Cl}\Delta b_{Li}$, $D=2c_{Li}^2(b_{0Li}^2-b_{7Li}^2)$,

$Q=4\pi\sin\theta/\lambda$, $\Delta b_{Li}=b_{0Li}-b_{7Li}$,

where c_i and b_i are, respectively, the atomic fraction and the coherent scattering length of the i-th particle. The radial distribution function is then given by

$$\Delta G_{Li}(r)=(2\pi^2\rho r)^{-1}\int Q\Delta_{Li}(Q)\exp(-0.005Q^2)\sin(Qr)dQ.$$

The difference functions, $\Delta_{Li}(Q)$, and radial distribution functions, $\Delta G_{Li}(r)$, at various temperature are given in Figures 1 and 2, respectively. The first and second peaks in $\Delta G_{Li}(r)$ are ascribed, respectively, to lithium-oxygen and lithium-deuterium interactions within the hydrated lithium(I) ions in the solution. The sharp peak clearly demonstrates that heavy water molecules are firmly bonded to a lithium(I) ion in the solution. In order to analyze the individual peak quantitatively, we employed a least squares fitting procedure using Gaussian function to represent each peak. The interatomic distances and the solvation number were estimated from the positions and the areas of the individual Gaussian finally obtained. The peak areas for the lithium-water interactions at 173 K decrease, compared with that at ambient temperature; a broad peak appears at 3.0 - 5.0 A. The results suggest that the second hydration shell of the lithium(I) ion will change with temperature. The interatomic distances, r_{LiO} and r_{LiD}, do not change within experimental errors in the temperature range 173 - 295 K. On the other hand, the hydration number of lithium(I) ion changes from 4 at ambient and supercooling temperatures (258 and 213 K) to 3 at 173 K. The final results obtained in the present study are summarized in Table 2.

References

1) A. H. Narten, F. Vaslow, and H. A. Levy, J. Chem. Phys., 58, 5017(1973).

2) K. Ichikawa, Y. Kameda, T. Matsumoto, and M. Misawa, J. Phys. C: Solid State Phys., 17, L725(1984).

3) K. Heinzinger, Stud. Phys. Teor. Chem., 27, 61(1983).

4) F. T. Marchese and D. L. Beveridge, J. Am. Chem. Soc., 106, 3713(1984).

Table 1 The compositions and important parameters for the sample solutions.

	I	II
Scattering lengths (10^{-12} cm)		
b_{Li}	0.011	-0.222
b_{Cl}	0.958	0.958
Molality (mol kg^{-1})	9.322	9.419
$[D_2O]/[LiCl]$	5.356	5.301
Density (g cm^{-3})		
R.T.	1.268	1.273
258 K	1.283	1.287
213 K	1.301	1.305
173 K	1.318	1.323
Total absorption cross section for 2200 m/s neutron (10^{-24} cm)	30.7	1.91

I) $^{0}Li\ ^{nat}Cl + D_2O$ II) $^{7}Li\ ^{nat}Cl + D_2O$

Table 2 Structural parameters for the lithium ion hydration obtained in the present work. r, n, and Δr are the interatomic distance, the hydration number, and the half width at half maximum, respectively.

	r_{Li-O}/A	r_{Li-D}/A	n_O	$\Delta r_{Li-O}/A$	$\Delta r_{Li-D}/A$
R.T.	2.02(5)	2.61(5)	3.8(5)	0.18(3)	0.27(3)
258 K	1.95(5)	2.58(5)	4.0(5)	0.22(3)	0.31(3)
213 K	2.03(5)	2.62(5)	3.6(5)	0.20(3)	0.28(3)
173 K	2.04(5)	2.57(5)	2.7(5)	0.17(3)	0.26(3)

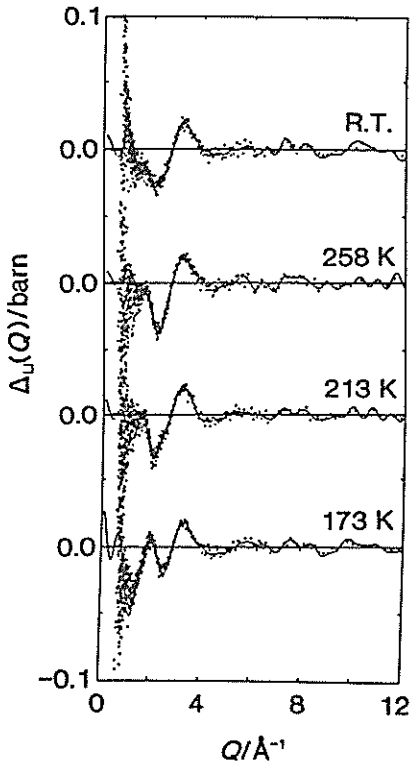

Fig. 1 $\Delta_{Li}(Q)$ for the LiCl-D_2O solution at various temperatures.

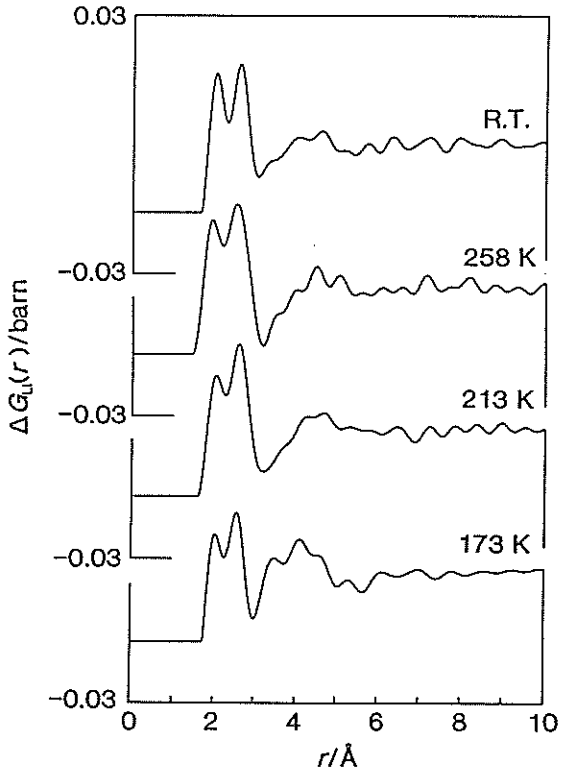

Fig. 2 $\Delta G_{Li}(r)$ for the LiCl-D_2O solution at various temperatures.

Pore Size Effect on Structure and Dynamics of Water Molecules in Porous Silica

T. Takamuku, M. Yamagami, T. Yamaguchi, H. Wakita, M. Misawa,* and Y. Izumi**

Department of Chemistry, Fukuoka University, Nanakuma, Jonan-ku, Fukuoka 814-01

*National Laboratory for High Energy Physics, Oho, Tsukuba 305

**Macromolecular Research Laboratory, Yamagata University, Yonezawa, Yamagata 992

The structure and dynamics of water molecules in micropores are essential to understand chemical reaction in pores on catalysts, and chemical absorption and properties of ion exchange resins. Furthermore, water in pores may be a model of non-freezing water in a biological cell because supercooled water is easily formed in the pores.

In the present study, porous silica of two different pore sizes (30 and 100 Å) were used to investigate the pore size effect on the structure and dynamics of water molecules in the pores. The structures of water in the pores at various undercooled temperatures were examined by neutron diffraction. Moreover, quasi-elastic neutron scattering experiments were made on these silica containing water at various temperatures to examine the dynamics of water molecules in the pores.

Porous silica, Develosils 30-3 and 100-3 (Nomura Chemicals), have a particle diameter of 3 μm and pore diameters of 30 and 100 Å, respectively. These pores were filled up to about 76~97 % of the volume with heavy or light water by a evaporation method. Neutron scattering measurements were made on Develosil 100-3 containing D_2O at various temperatures from 295 to 213 K and on pure D_2O at 213 K using the HIT spectrometer. A similar experiment with D_2O in Develosil 30-3 was carried out and has previously been reported.[1] Dry Develosil was also measured at 295 K. Quasi-elastic neutron scattering experiments with the LAM-40 spectrometer were also performed at 295, 275, 258, and 243 K for both H_2O filled Develosils, and at 213 K only for H_2O filled Develosil 30-3. Dry Develosil and an empty Al container were also measured at 295 K.

The contribution from D_2O in the total scattering intensities was obtained by subtracting the scattered intensities of dry Develosil from those of the D_2O filled sample. The structure factors S(Q) of D_2O in the pores at various temperatures and of pure D_2O ice at 213 K are shown in Fig. 1. As seen in Fig. 1, the Bragg pattern due to crystallization of D_2O appears in the S(Q) for the Develosil sample below 238 K, in contrast with non-freezing liquid D_2O down to 193 K in Develosil 30-3 as found in the previous study.[1] These findings indicate the presence of more bulk D_2O in Develosil 100-3 than in Develosil 30-3. From assignment of the Bragg pattern for D_2O in Develosil 100-3 and bulk D_2O at 213 K, it has been found that ice I_c is formed in the pores, whereas ice I_h crystallizes in the bulk. This result agrees with that from a neutron diffraction study on Spherisorb S20W of pore size 90 Å, by Dore et al.[2] However, the phase transition from I_h to I_c reported for D_2O at 252 K in Spherisorb S20W[2] was not observed in the present study.

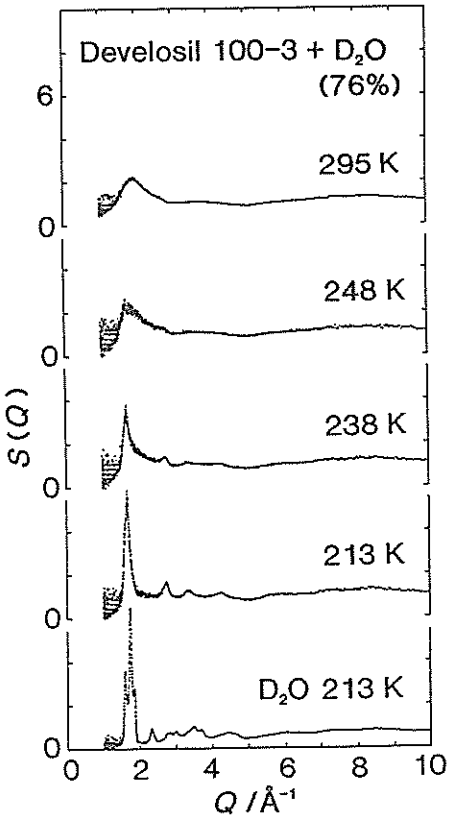

Fig. 1 The neutron scattering patterns of D_2O in Develosil 100-3 at various temperatures and of pure D_2O ice at 213 K.

The observed quasi-elastic neutron scattering spectra for H_2O filled Develosil (Fig. 2) were corrected for background scatterings of dry silica and Al container, the counter efficiency, and the incident neutron spectrum. The corrected spectra were fitted by a least-squares procedure using the sum of two Lorentzians and a δ-function (solid lines in Fig. 2). The peak width for both samples decreases with lowering temperature, indicating that the motion of water molecules in the pores is restricted with temperature. The half-width at half-maximum (HWHM) of the narrow component Γ_n at 295 and 275 K were plotted against Q^2 values in Fig. 3. The results below 258 K are not shown because of the resolution of LAM-40 spectrometer. A comparison of the Q^2 dependence of Γ_n values for the two samples at the same temperature has shown that the Γ_n values for Develosil 30-3 are smaller than those for Develosil 100-3. This result indicates that the motion of water molecules is more hindered in the smaller pores. Quantitative analyses were made on the Q^2-Γ_n data with the proton jump diffusion model:

$$\Gamma_n = D_H Q^2/[1 + D_H Q^2 \tau_0]. \qquad (1)$$

where D_H represents the proton self-diffusion coefficient, and τ_0 is the lifetime of the proton oscillatory motion. The solid lines in Fig. 3 well explain the experimental Q^2-Γ_n values. Furthermore, the mean jump length of proton, L, was evaluated by the relation $D_H = \langle L^2 \rangle / 6\tau_0$. These parameter values are summarized in Table 1. The D_H value for H_2O in Develosil 100-3 at 295 K, 5.37×10^{-10} m^2/s, is comparable with that for Spherisorb S20W at ambient temperature, 6×10^{-10} m^2/s, determined by Clark et al.[3] As seen in Table 1, the D_H value decreases with decreasing temperature and pore size. The mean jump length of proton, however, was shorter than the distance (1.519 Å) between two protons in a water molecule.

We are analyzing the quasi-elastic neutron scattering spectra measured with the LAM-80ET spectrometer of higher resolution to obtain information on the motions of water molecules in the pores at lower temperatures.

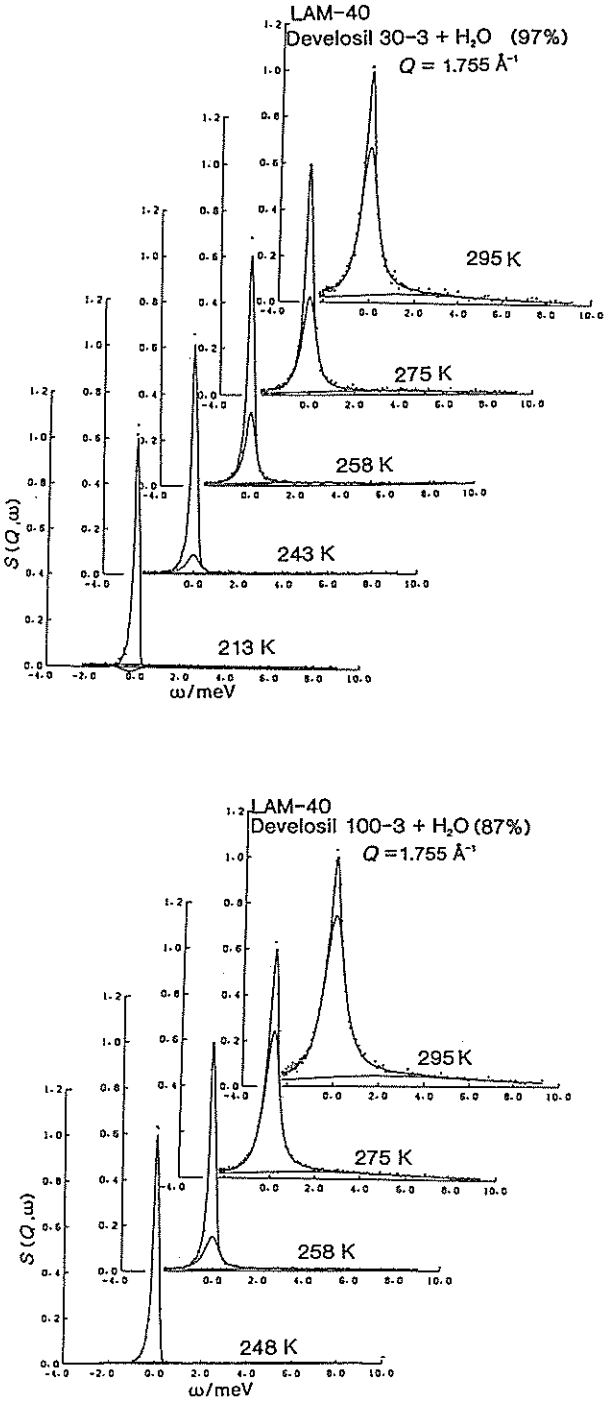

Fig. 2 Quasi-elastic neutron scattering spectra at Q = 1.755 Å^{-1} for H_2O in Develosil 30-3 and 100-3 at various temperatures.

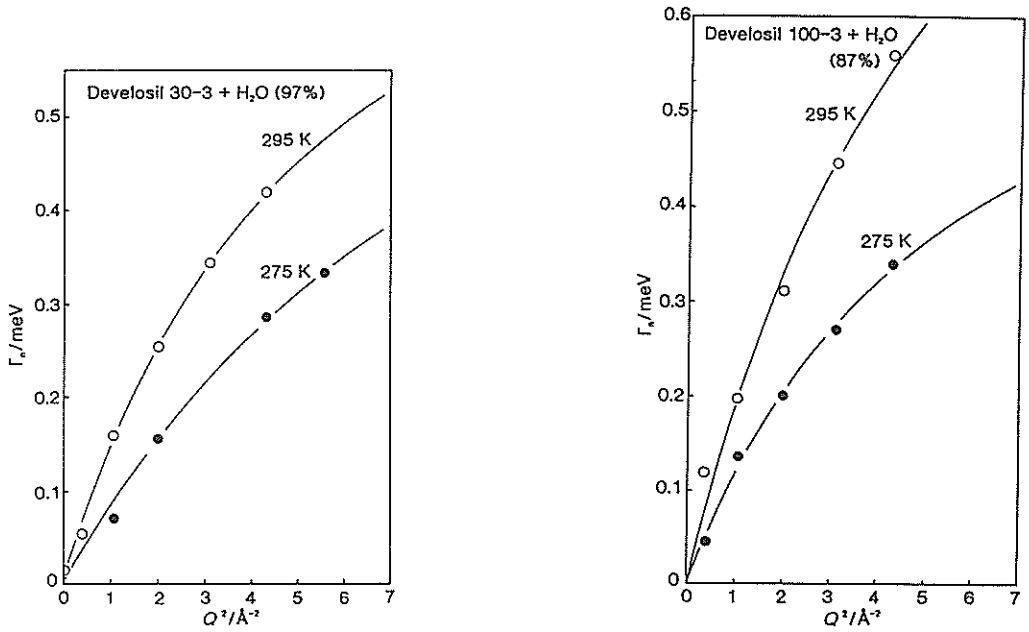

Fig. 3 Q^2 dependence of HWHM on the quasi-elastic narrow component Γ_n for Develosil 30-3 and 100-3.

Table 1. Parameters of the jump diffusion model estimated by LAM-40 experiments.

Sample	T/K	τ_0/ps	L/Å	$10^{10}D_H/m^2s^{-1}$
Develosil 30-3	295	4.49	1.09	4.30
	275	4.4	0.77	2.26
100-3	295	3.20	1.02	5.37
	275	5.5	1.06	3.41

References

1) T. Yamaguchi, Y. Kato, H. Wakita, and M. Misawa, KENS Report, 8, 85 (1990).

2) J. C. Dore, M. Dunn, and P. Chieux, J. Phys. Coll. C1, suppln 3, 48, 457 (1987).

3) J. W. Clark, P. G. Hall, A. J. Pidduck, and C. J. Wright, J. Chem. Soc., Faraday Trans. 1, 81, 2067 (1985).

Dynamics of Water Molecules in Supercooled Aqueous Zinc(II) Bromide Solutions

T. Takamuku, T. Hirano, T. Yamaguchi, H. Wakita, and Y. Izumi*

Department of Chemistry, Fukuoka University, Nanakuma, Jonan-ku, Fukuoka 814-01

*Macromolecular Research Laboratory, Yamagata University, Yonezawa, Yamagata 992

Microscopic structure and dynamics of supercooled and glassy aqueous electrolyte solutions are essential for understanding crystallization of solutions since the supercooled and glassy solutions lie between the liquid and solid states. We have investigated supercooled and glassy aqueous zinc(II) bromide solutions by Raman spectroscopy and X-ray diffraction.[1] These results have shown that the tetrabromozinc(II) and aqua complexes, $[ZnBr_4]^{2-}$ and $[Zn(OH_2)_6]^{2+}$, increase with lowering temperature, while the dibromo- and tribromozinc(II) complexes, $[ZnBr_2(OH_2)_2]$ and $[ZnBr_3(OH_2)]^-$, are formed as main species at ambient temperature. Therefore, the equilibrium shifts (1) and (2) to the right-hand-side with decreasing temperature have been proposed to take place in the supercooled and glassy solutions:

$$3[ZnBr_2(OH_2)_2] + 2H_2O \longrightarrow 2[ZnBr_3(OH_2)]^- + [Zn(OH_2)_6]^{2+}, \quad (1)$$

$$4[ZnBr_3(OH_2)]^- + 2H_2O \longrightarrow 3[ZnBr_4]^{2-} + [Zn(OH_2)_6]^{2+}. \quad (2)$$

Strengthened hydrogen bonding of the water-water and anion-water interactions in the supercooled and glassy solutions will be responsible for the equilibrium shifts (1) and (2). Thus, a study of water dynamics in the solutions is very important to elucidate the mechanism of the equilibrium shifts from a dynamics point of view.

In the present study, quasi-elastic neutron scattering measurements were performed on aqueous zinc(II) bromide solutions at ambient and supercooled temperatures to investigate dynamic properties of water molecules in the solutions. The results in the present study are compared with those obtained by ^{1}H-NMR spin-echo method in a previous study.[2]

Sample solutions were prepared by dissolving zinc(II) bromide (Wako Pure Chemicals, 99.9%) without further purification in distilled water to reach the $[H_2O]/[ZnBr_2]$ molar ratios (R) of 5 and 10. The sample solutions were kept in a doubly walled tantalum container. Quasi-elastic neutron scattering measurements were carried out using the LAM-40 spectrometer at 233 and 295 K for the solution with R = 5, at 233, 263, and 295 K for the solution with R = 10. The spectra of the empty tantalum container and vanadium tube were also measured for correction of background and normalization, respectively.

After corrections for background, counter efficiency, and the incident neutron spectrum, the observed scattering spectra were analyzed by a curve-fitting method using a model function of the sum of two Lorentzians as seen in Fig. 1. The half-width at half-maximum (HWHM) of the narrow component Γ_n was plotted against Q^2 in Fig. 2. The temperature and composition dependences of the Q^2-Γ_n correlations are shown in Fig. 2. The Γ_n values versus Q^2 were analyzed on the basis of a jump diffusion model:

$$\Gamma_n = D_H Q^2/[1 + D_H Q^2 \tau_0]. \quad (3)$$

Here, D_H represents the proton self-diffusion coefficient, and τ_0 is the life time of the proton oscillatory motion. The self-diffusion coefficient, D_H, can be expressed by the mean jump length of proton, L, and τ_0 as:

$$D_H = \langle L^2 \rangle / 6\tau_0. \quad (4)$$

The obtained parameter values are summarized in Table 1. As seen in Fig. 2, the experimental Γ_n values above 263 K for the solutions were well explained by the theoretical curves using the values in Table 1. However, the Γ_n data at 233 K for both solutions are not shown because of the resolution of LAM-40 spectrometer.

As seen in Table 1, the self-diffusion coefficient decreases for both solutions with lowering temperature, indicating that the translational motion of water molecules is restricted with temperature. This is probably because the water-water interaction will be enhanced with decreasing temperature. The self-diffusion coefficients estimated in the present study are less than those

determined by the NMR method. The mean jump length estimated is shorter than the distance (1.519 Å) of intramolecular protons in a water molecule.

Analysis using another model, such as a Sears model[3] is being performed to separate the translational and rotational motions of water molecule in the solutions.

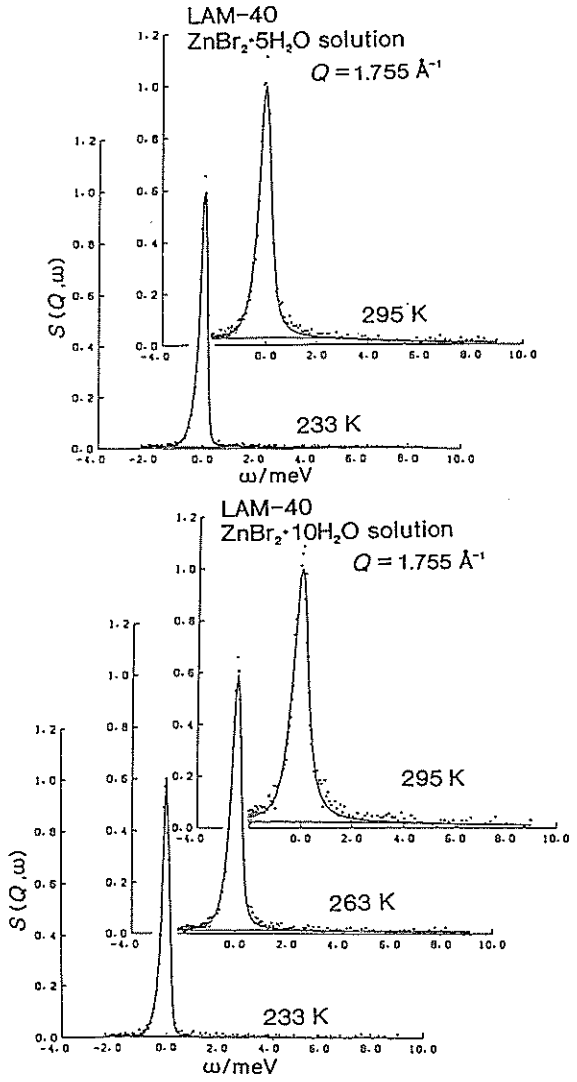

Fig. 1 Quasi-elastic neutron scattering spectra at Q = 1.755 Å^{-1} for the solutions with R = 5 and 10 at various temperatures.

Table 1. Parameters for the jump diffusion model estimated by the LAM-40 experiments and the proton self-diffusion coefficients determined by the NMR spin-echo method.

R	T/K	τ_0/ps	L/Å	$10^{10}D_H$/m^{2}s^{-1}	$10^{10}D_H^{NMR}$/m^{2}s^{-1}
5	295	11	1.05	1.74	3.05
10	263	19	1.20	1.24	2.64
	295	6.6	1.05	2.82	8.12

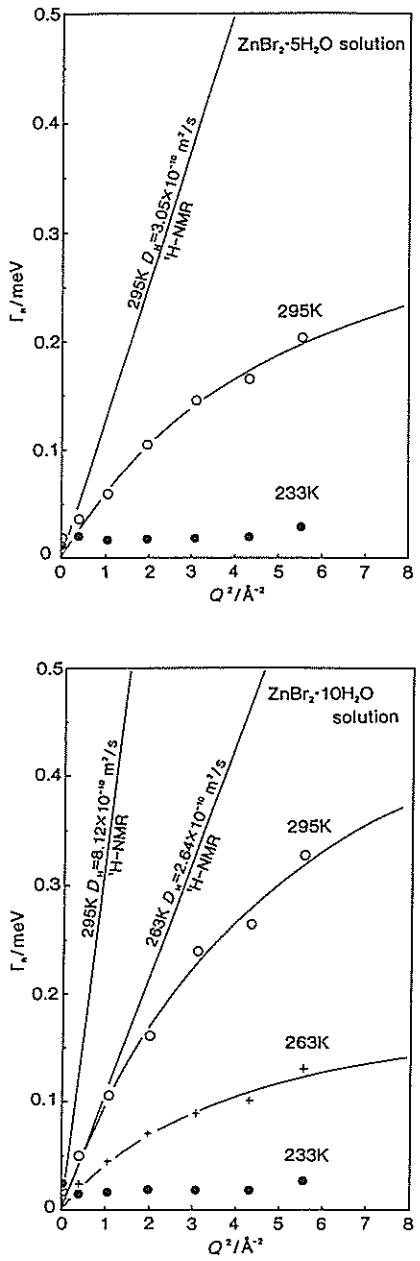

Fig. 2 The Q^2-dependence of HWHM on the quasi-elastic narrow component Γ_n for the solutions with R = 5 and 10. The straight lines are theoretical values based on the Fick's law using the D_H^{NMR} data in Table 1.

References

1) T. Takamuku, K. Yoshikai, T. Yamaguchi, and H. Wakita, Z. Naturforsch., 47a, (1992) in press.

2) T. Takamuku, T. Hirano, T. Yamaguchi, and H. Wakita, J. Phys. Chem., submitted.

3) M.-C. Bellissent-Funel, R. Kahn, A. J. Dianoux, M. P. Fontana, G. Maisano, P. Migliardo, and F. Wanderlingh, Mol. Phys., 52, 1479 (1984).

Structure of Na_2O-B_2O_3 Melts Measured by Pulsed Neutron Total Scattering

Y.KITA[1], M. MISAWA[2], N.UMESAKI[3], T.KIRIHAHA[4], T.FUKUNAGA[5] and T.IIDA[1]

1) Department of Materials Science and Processing, Faculty of Eng., Osaka Univ., Suita, Osaka 565
2) National Laboratory for High Energy Physics, 1-1 Oho, Tsukuba, Ibaraki 305
3) Material Physics Department, Government Industrial Research Institute, Ikeda, Osaka 563
4) Graduate School, Osaka University, (Now, Nippon Steel Co., Ltd., Shimada, Hikari, Yamaguchi 743)
5) Department of Crystalline Materials Science, Faculty of Eng., Nagoya University, Nagoya 464

Precise knowledge of the structure and properties of B_2O_3-based melts and glasses is required increasingly from the fundamental and practical viewpoints. Although some investigations have been performed on the structure of Na_2O-B_2O_3 glasses[1], a diffraction study on the structure of Na_2O-B_2O_3 melts has not yet been reported as far as the authors know. In the present study, pulsed neutron total scattering measurements have been carried out on Na_2O-B_2O_3 melts, and the structural change of B_2O_3 melt with the addition of Na_2O was investigated from the experimental results, by comparing with the results on B_2O_3 melt, obtained previously at the same experimental conditions[2].

Pulsed neutron scattering experiments were carried out on 10mol% Na_2O- and 30mol% Na_2O-B_2O_3 melts at 1073K by using the HIT spectrometer. The samples were prepared by melting and dehydrating mixtures of Na_2CO_3 and H_3BO_3 enriched with ^{11}B. In the scattering experiment, the sample was held in a Pt cell at 1073K under reduced pressure of about 0.1 torr. The time-of-flight intensity spectra were obtained for the sample contained in the cell, and for the blank cell. The coherent scattering intensities were determined after corrections for the cell, background, absorption and multiple and incoherent scatterings. S(Q) curves were obtained from the coherent intensities normalized to the intensity from the vanadium rod. The radial distribution functions RDF(r) were obtained by Fourier transform of Q(S(Q)-1).

The peak positions and overall shapes of Q(S(Q)-1) curves remained almost unchanged, with the addition of Na_2O to B_2O_3. The RDF(r) curves for B_2O_3, 10mol%Na_2O-B_2O_3 and 30mol%Na_2O-B_2O_3 melts were compared in Fig.1. The first peak position and the area under the first peak of RDF(r) are given in Table 1. As described in the previous paper on the structure of B_2O_3 melt[2], the first peak of RDF(r) is attributed to the B-O bond. With increase of Na_2O content, the first peak position of RDF, representing atomic spacing of B-O, shifted gradually from 0.137 nm for B_2O_3 to 0.139 nm for 30mol% Na_2O as shown in Table 1, and the first peak broadened asymmetrically, spreading to larger r side as shown in Fig.1. The coordination number of O atoms around a reference B atom $n_{B-O(expt)}$, and

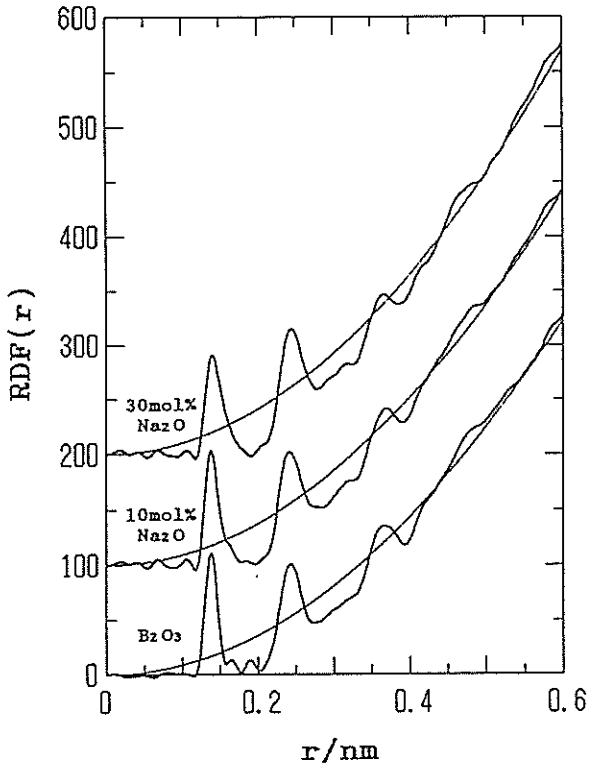

Fig.1 Radial distribution functions RDF(r) for Na_2O-B_2O_3 melts at 1073K

Table 1. First peak position r_1, area under the first peak of RDF(r) A_1, and the experimental and calculated coordination number n_{B-O} and n_{O-B}.

Melt/mol%	r_1/nm	A_1	$n_{B-O(expt)}$	$n_{B-O(calc)}$	$n_{O-B(expt)}$	$n_{O-B(calc)}$
B_2O_3	0.137	2.43	3.0	3.0	2.0	2.0
$10Na_2O$-$90B_2O_3$	0.138	2.58	3.2	3.1	2.0	2.0
$30Na_2O$-$70B_2O_3$	0.139	2.59	3.5	3.4	2.0	2.0

that of B atoms around a reference O atom $n_{O-B(expt)}$, determined from the area A_1 under the first peak of experimental RDF(r), are listed in Table 1. With the addition of Na_2O to B_2O_3, the coordination number $n_{B-O(expt)}$ increased from 3.0 to 3.5, showing variation of the configuration of O atoms around a reference B atom.

As regards the structure of alkali borate glasses, R_2O-B_2O_3, it has been confirmed from Raman[3,4] and NMR[5,6] spectroscopic study that the structure unit BO_3 triangle is converted to tetrahedron BO_4 by the addition of R_2O up to 33% into B_2O_3 as follows: On addition of one molecule of Na_2O to the B_2O_3 glass, two BO_3 units are converted into two BO_4 units. Assuming that the structure units in Na_2O-B_2O_3 melts are converted in the same way as in Na_2O-B_2O_3 glasses, we can express the fraction of three-coordinated and four-coordinated B atoms, N_3 and N_4 respectively, as follows:

$$N_3 = \frac{1 - 2x}{1 - x}, \qquad N_4 = \frac{x}{1 - x} \qquad (1)$$

where x is the mole fraction of Na_2O. Accordingly, the coordination number of O atoms around a reference B atom is:

$$n_{B-O} = 3N_3 + 4N_4 = 3 + \frac{x}{1 - x} \qquad (2)$$

The coordination number of B atoms around a reference O atom is:

$$n_{O-B} = \frac{C_B}{C_O} n_{B-O} = 2 \qquad (3)$$

The values of the coordination numbers $n_{B-O(calc)}$ and $n_{O-B(calc)}$ calculated from eqs.(2) and (3) are compared in Table 2 with $n_{B-O(expt)}$ and $n_{O-B(expt)}$ determined from the experimental RDF(r). The values of n_{B-O} and n_{O-B} calculated from eq. (2) and (3) agreed well with experimental values, respectively.

Thus, the experimental values of n_{B-O} and n_{O-B} could be explained successfully by the assumption that two BO_3 triangle structure units are converted into two BO_4 tetrahedron units by the addition of one Na_2O molecule into Na_2O-B_2O_3 melt. These results suggest that the structural change in Na_2O-B_2O_3 melts with the addition of Na_2O up to 30 mol% is similar to that in Na_2O-B_2O_3 glasses. It should be noted that the coordination number of B atoms around a reference O atom n_{O-B} remains a constant value, i.e. two, in other words, B-O bonds in Na_2O-B_2O_3 melts are not broken with the addition of Na_2O up to 30 mol%. This means that the network structure of Na_2O-B_2O_3 is stable, being not broken but only modified partially by the coordination of oxygen atoms provided from Na_2O around a boron atom. Seemingly, this is not compatible with the behavior of physical properties such as the viscosity[7,8], which decreases rapidly with the addition of a small amount of Na_2O to B_2O_3 melt. Further investigation will be needed for a clear understanding of the detailed structure of Na_2O-B_2O_3 melts.

References

1) For example, G.Herms et al : J.Non-Cryst. Solids, 88(1986), 381
2) M.Misawa : J.Non-Cryst.Solids, 122(1990), 33
3) W.L.Konijnendijk and J.M.Stevels: J.Non-Cryst. Solids, 18(1975), 307.
4) W.L.Konijnendijk and J.M.Stevels: Borate Glasses (Mater.Sci.Res. Vol.12), ed. L.D.Pye, V.D.Frèchette and N.J.Kreidl, Plenum, New York, (1978), 259.
5) P.J.Bray and J.G.O'Keefe: Phys.Chem.Glasses, 4(1963), 37.
6) G.E.Jellison,Jr and P.J.Bray: J.Non-Cryst. Solids, 29(1978), 187.
7) L.Shartsis, W.Capps and S.Spinner: J.Am. Ceram.Soc., 36(1953), 319.
8) G.H.Kaiura and J.M.Toguri: Phys.Chem.Glasses, 17(1976), 62.

Structure Study of Glasses in the Bi-containing Superconductor System

N. UMESAKI, M. TATSUMISAGO*, T. FUKUNAGA**, M MISAWA*** and T. MINAMI*

Government Industrial Research Institute, Osaka, 1-8-31, Midorigaoka, Ikeda, Osaka 563, Japan
* Department of Applied Chemistry, University of Osaka Prefecture, 4-cho, Ume-machi, Nakamozu, Sakai, Osaka 591, Japan
** Department of Applied Physics, Nagoya University, Furo-cho, Chibusa-ku, Nagoya 464, Japan
*** National Laboratory for High Energy Physic, 1-1, Ohno-machi, Tsukuba, Ibaraki 305, Japan

It is well known that a number of compositions in the Bi-Ca-Sr-Cu-O system become high-T_c superconducting oxides. Moreover, the vitrification has been reported for several compositions in this system successively by Komatsu et al.[1] and the present authors[2]. The glass formation of these superconducting oxides has possibilities of fiber-drawing and casting into various shapes such as rods and plates, which are essential for the application of these superconducting materials. The Bi-Ca-Sr-Cu-O glass-forming system is also a new one without glass-formers. This system is very interesting from the viewpoint of basic glass science. However, few studies have been conducted on the Bi_2O_3-based, and the glass structures are not understood yet. The main purpose of the present study is to obtain the basic knowledge for the structure of the rapidly quenched Bi-Ca-Sr-Cu-O glasses using pulsed neutron diffraction method.

The glass samples of different compositions in the system $Bi_xCaSrCu_2O_w$ (x:1, 2.7, 4, 8 and 16) were obtained by the use of the glass preparation apparatus combining a thermal-image furnace and a twin roller. The quenching rate was about 10^5K/s. Neutron scattering from the $Bi_xCaSrCu_2O_w$ glasses at room temperature was measured on the HIT spectrometer at the National Laboratory for High Energy Physics.

Figure 1 shows the structure factors S(Q) for the the $Bi_xCaSrCu_2O_w$ glasses of x=1, 2.7, 4, 8 and 16. This figure indicates the typical amorphous patters of these S(Q)'s except for the case x=1 in which the glass contains a small amount of crystalline part. The radial distribution functions were obtained as the Fourier transform of the S(Q)'s as shown in Fig. 2. The peak around 2Å can successfully be deconvoluted into two peaks of 1.96Å due to the nearest-neighbor Cu-O pairs and 2.17Å due to the nearest-neighbor Bi-O pairs. The third peak at 2.5Å is mainly due to alkali-earth-oxygen pairs but another contribution like oxygen-oxygen pairs also exist. The neutron results indicate that the rapidly quenched glasses in the system Bi-Ca-Sr-Cu-O are mainly constructed with Bi-O network.

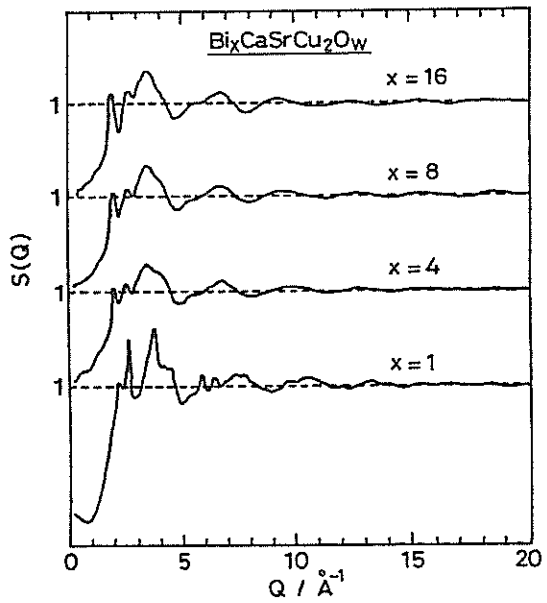

Fig. 1 Structure factors S(Q) for the rapidly quenched $Bi_xCaSrCu_2O_w$ glasses of x=1, 2.7, 4, 8 and 16.

References

1) T. Komatsu, R. Sato, K. Imai, K. Matusita and T. Yamashita, Jpn. Appl. Phys., 27, L550 (1988)
2) T. Minami, Y. Akamatsu, M. Tatsumisago, N. Tohge and Y. Kowada, Jpn. Appl. Phys., 27, L777 (1988)

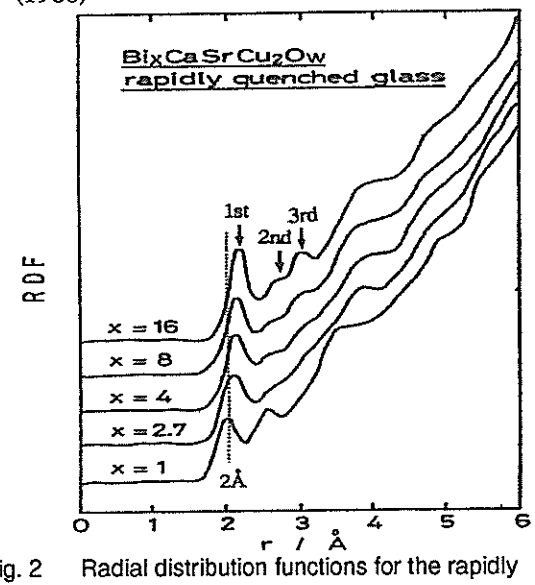

Fig. 2 Radial distribution functions for the rapidly quenched $Bi_xCaSrCu_2O_w$ glasses of x=1, 2.7, 4, 8 and 16.

NEUTRON DIFFRACTION STUDY ON THE STRUCTURE OF Na-Si-O-N OXYNITRIDE GLASSES

Jisun JIN, Toshinibu YOKO, Fumiaki MIYAJI, Sumio SAKKA
Toshiharu FUKUNAGA* and Masakatsu MISAWA**

Institute for Chemical Reserch, Kyoto University, Uji, Kyoto-Fu 611, Japan
*: Faculty of Engineering, Nagoya University, Nagoya, Japan
**: National Laboratory for High-Energy Physics(KEK), Tsukuba, Japan

The incorporation of nitrogen into silicate and phosphate glasses is known to change their physical and chemical properties to a considerable extent[1,2]. Such changes in properties are explained based on the Mulfinger model[3] that a nitrogen atom is bonded to three Si atoms to form dense glass network. This model has been proved by several measurements, such as density[4], elastic moduli[5] and IR[6], XPS[7] and ^{29}Si MAS NMR[8] spectroscopies.

On the other hand, recent studies on the nitrogen coordination state in oxynitride glasses on the basis of ^{15}N MAS NMR[9] and molecular dynamics calculation(MD)[10], however, indicated that the nitrogen atoms with one or two non-bridging bonds as well as three bridging bonds may coexist in oxynitride glasses(these three types of nitrogen atoms are hereafter called one-, two- and three-fold nitrogen atoms, respectively).

Since the cross-section of elements for neutron scattering does not decrease with decreasing atomic number differing from the case for X-ray diffraction, the neutron diffraction[11-14] appears to be useful for investigating the structure of glasses composed of light elements.

In the present study, neutron diffraction analysis of Na_2O-SiO_2 glass and Na_2O-SiO_2-Si_3N_4 glass has been carried out by use of a pulsed neutron source to determine the precise values of Si-N and Si-O bond lengths and the coordination state of nitrogen atoms in Na_2O-SiO_2-Si_3N_4 glass.

Glasses of the composition $20Na_2O\cdot(80-3x)SiO_2\cdot xSi_3N_4$ (x=0 and 4) have been prepared by melting the mixtures of oxide glass prepared beforehand and β-Si_3N_4 at 1500℃ for 2 hours in BN crucible under flowing nitrogen atmosphere.

The neutron diffraction measurements based on the time-of-flight method were carried out by use of the High Intensity Total scattering spectrometer (HIT) with a pulsed neutron source at the National Laboratory for High-Energy Physics (KEK, Tsukuba, Japan). The powder sample was loaded in a vanadium metal cylinder with wall thickness of 0.025mm, inner diameter of 8mm and length of 40mm, and set in a vacuum chamber to avoid moisture uptake and eliminate the background due to air scattering during the measurements.

The analyzed nitrogen content of x=4 glass was 4.4at% with an error of about 10%.

The structure factor S(Q) of x=0 and x=4 glasses was experimentally obtained over the range of scattering vector Q($=4\pi\sin\theta/\lambda$, θ: scattering angle, λ: neutron wavelength) from 1 to 300nm^{-1}. Fig. 1 shows the RDF for glasses of x=0 and x=4, which were obtained from the S(Q) with Q_{max} of 300nm^{-1}. The first peak in the RDF curves of x=4 glass appears to be shifted to longer bond lengths compared to that of x=0 glass. The first peak in the RDF curve of x=4 glass is deconvoluted as shown in Fig. 2. The first peak at r=0.1627nm in the RDF curve of x=0 glass is ascribed to the Si-O bond in the oxide glass, since no atomic pairs other than Si-O are actually present in this region. This value of the Si-O bond length agrees fairly well with the one(r=0.1631nm) previously reported for $33Na_2O\cdot67SiO_2$ glass[13].

The coordination numbers of Si and N atoms and the bond lengths of Si-O and Si-N pairs, which were calculated from the peak areas, are summarized in Table 1. It is seen from this table that the number of oxygens around a Si atom in the nitrogen-free glass is 3.91 which is close to 4.0 as expected, while in the nitrogen-containing glass the coordination numbers of silicon and nitrogen atoms are 3.82($=N_{Si\text{-}O} + N_{Si\text{-}N}$) and 2.42($=N_{N\text{-}Si}$), respectively. The sum of $N_{Si\text{-}O}$ and $N_{Si\text{-}N}$ can be assumed as four within the experimental error. On the other hand, the value of $N_{N\text{-}Si}$=2.42 is much smaller than three, which is beyond the experimental error. The cause will be discussed later. It is interesting to note that the bond length of Si-O pair remains unchanged upon incorporation of nitrogen.

Table 1 shows that the incorporation of nitrogen causes a decrease of the oxygen coordination

number around the Si atom from 3.91 to 3.43 and the nitrogen coordination number around the Si atom is 0.4 in the x=4 glass. Taking into account the experimental error of about 5%[13] in determining N_{Si-O} and N_{Si-N}, these indicate that every two and half Si atoms are bonded to one N atom, i.e., the Si-N bonds exist in the present oxynitride glass agreeing with the results obtained for other oxynitride glasses by IR[6] and XPS[7] measurements.

The coordination state of nitrogen in oxynitride

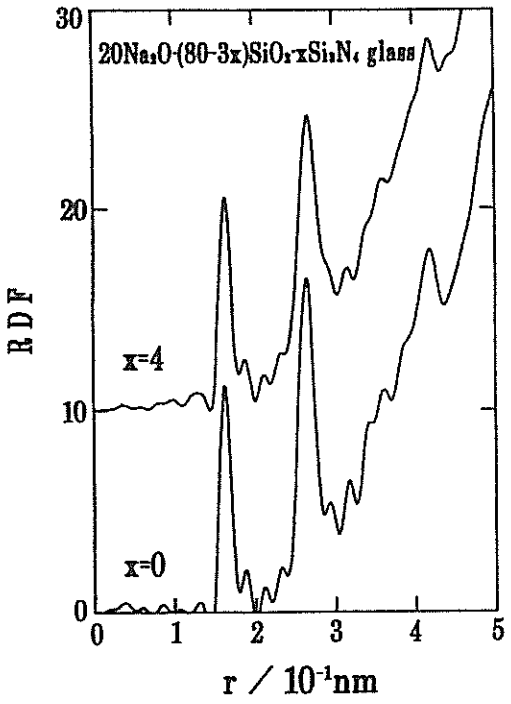

Fig. 1 Total RDF of oxide glass(x=0) and oxynitride glass(x=4). Fourier transformation of S(Q) to RDF is truncated at Q_{max}=300nm^{-1}.

glass has not been fully made clear yet, although it has been believed that a nitrogen atom is three-fold coordinated. The present neutron diffraction analysis revealed, however, that the average coordination number of nitrogen in the oxynitride glass studied is 2.42. This fact indicates that not all nitrogen atoms are three-fold coordinated, but there

Table 1. Atomic distance(d) and coordination number(N) for Si-O and Si-N pairs in glasses.

	Si-O			Si-N		
Sample	d/nm	N_{Si-O}	N_{O-Si}	d/nm	N_{Si-N}	N_{N-Si}
x=0	0.1627	3.91	1.74			
x=4	0.1626	3.43	1.71	0.1709	0.39	2.42

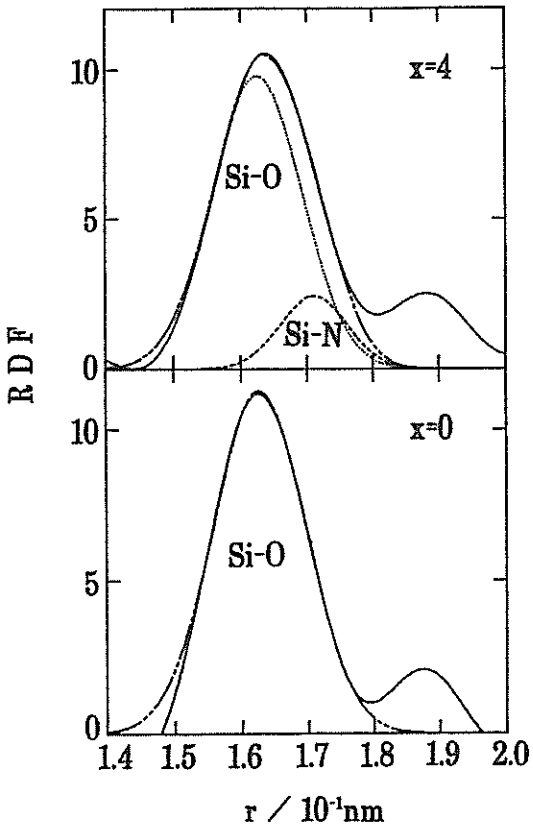

Fig. 2 Radial distribution functions of oxide glass(x=0) and oxynitride glass(x=4). Dotted and dashed curves indicate that Gaussian approximations for Si-O and Si-N pair distribution functions, respectively.

may possibly be some one- or two-fold nitrogen atoms besides three-fold ones.

On the assumption that only 2- and 3-fold coordinated nitrogen atoms exist in the present oxynitride glass, a simple calculation indicates that 58% of nitrogen atoms are bonded to two Si atoms and only 42% of nitrogen atoms are bonded to three Si atoms. This result coincides with the result by Unuma *et al.*[10], who obtained the value of about 2 as the average coordination number of nitrogen in the Na-Si-O-N oxynitride glasses by means of molecular dynamics calculation. ^{15}N MAS-NMR study of the Y-Al-Si-O-N oxynitride glasses[9] showed that 80% of nitrogen atoms are bonded to three Si atoms and 20% of nitrogen atoms bonded to two Si atoms. In the early XPS study by Brow and Pantano[7], it was pointed out that low-energy components of the N1s photoelectron spectra in the Na-Si-O-N and Na-Ca-Si-O-N oxynitride glasses

may arise from the presence of non-bridging nitrogen groups in analogy with non-bridging oxygens in oxide glasses. Hanada *et al.*[16] stated on the basis of O1s and N1s XPS spectra that the two-fold nitrogens coexist with the three-fold nitrogens in the Ca-Si-O-N oxynitride glasses containing 8at% nitrogen. Clables *et al.*[17] also reported from the N1s XPS data that nitrogens in two different chemical states, which may be taken as the two- and three-fold nitrogen atoms, are present in the Na-Ca-Si-O-N oxynitride glasses. It is interesting to note that crystalline $LaSi_3N_5$ also contains both two- and three-fold bridging nitrogens[18].

Referring to the mechanisms of the formation of one- and two-fold nitrogens in oxynitride glasses proposed by Hanada *et al.*[16] and Unuma *et al.*[10], we also propose the following two reaction models for the formation of two-fold nitrogens on addition of Si_3N_4 to Na_2O-SiO_2 glass. In the first model, Si_3N_4 reacts with Na_2O to form two-fold bridging nitrogens and non-bridging oxygens in the glass, analogously to the formation of non-bridging oxygen in sodium silicate glass.

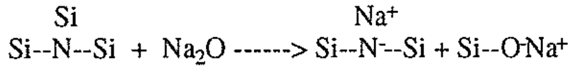

$$Si\text{--}\overset{Si}{N}\text{--}Si + Na_2O \text{------>} Si\text{--}\overset{Na^+}{N^-}\text{--}Si + Si\text{--}O^-Na^+$$

(1)

The second model involves a decrease in non-bridging oxygen as a result of the formation of two-fold coordinated nitrogens and bridging oxygens[10]

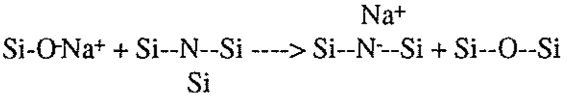

$$Si\text{-}O^-Na^+ + Si\text{--}\underset{Si}{N}\text{--}Si \text{---->} Si\text{--}\overset{Na^+}{N^-}\text{--}Si + Si\text{--}O\text{--}Si$$

(2)

Among the above two models proposed, eq.(2) is considered to be a more feasible model. This model can explain the improvements of physical and chemical properties commonly observed for oxynitride glasses, such as high Young's moduli and high chemical durability, because this model involves the conversion of the Si-O^- non-bridging bonds into Si-O-Si bridging bonds. Hater *et al.*[8] reported on the basis of ^{29}Si MAS-NMR study that the addition of Si_3N_4 to the Na_2O-SiO_2 glasses leads to an increase in Q^4 structural unit in the resultant oxynitride glasses, supporting the model based on eq.(2).

On the contrary, eq(1) involves breaking down of $\equiv Si_3N$ bridging bonds, followed by the simultaneous formation of SiO^- non-bridging bonds. Therefore, this model cannot explain the improvements of physical properties and chemical durability.

References

1) S. Sakka, Ann. Rev. Mater. Sci., 16(1986)29-46
2) J. Jin, S. Sakka, H. Kozuka and T. Yoko, *Nippon Seramikkusu Kyokai Gakujutsu Ronbunshi*, 100(1992)841-846
3) H. -O. Mulfinger, J. Am. Ceram. Soc., 49(1966)462-467
4) S. Sakka, K. Kamiya and T. Yoko, *J. Non-Cryst. Solids*, 56(1983)147-152
5) D. R. Messier and A. Broz, J. Am. Ceram. Soc., 65(1982)C123
6) C. Schrimpf and G. H. Frischat, *J. Non-Cryst. Solids*, 56(1983)153-160
7) R. K. Brow and C. G. Pantano, *J. Am. Ceram. Soc.*, 67(1984)C72-74
8) W. Hater, W. M-Warmuth and G. H. Frischat, *Glastech. Ber.*, 62(1989)328-334
9) D. Kruppa, R. Dupree and M. H. Lewis, *Mater. Lett.*, 11(5-6-7)(1991)195-198
10) H. Unuma, K. Kawamura, N. Sawaguchi, H. Maekawa and T. Yokokawa, Proceeding of the International Conference on Science and Technology of New Glasses(*ICNG*), *ed.* S. Sakka and N. Soga, (1991)341-346
11) K. Suzuki, *J. Non-Cryst. Solids*, 95&96(1987)15-30
12) K. Suzuki, *Nippon Kessyo-Gakkaishi.*, 22(1980)29-38 (in Japanese).
13) M. Misawa, D. L. Price and K. Suzuki, *J. Non-Cryst. Solids*, 37(1980)85-97
14) M. Misawa, T. Fukunaga, K. Niihara, T. Hirai and K.Suzuki, *ibid.*, 34(1979)313-321
15) N. Watanabe, T. Fukunaga, T. Shinohe, K. Yamada and T. Mizoguchi, *KENS Report* 2(1981)539-548
16) T. Hanada, N. Ueda and N. Soga, *Nippon Seramikkusu Kyokai Gakujutsu Ronbunshi(J. Ceram. Soc. Jap.)*, 96(1988)284-291(in Japanese).
17) J. G. Clables, R. E. Fern and G. H. Frischat, *J. Vac. Sci. Technol.*, A4(3), May/Jun(1986)1580-1584
18) Z. Inoue, M. Mitomo and N. Ii, *J. Mater. Sci.*, 15(1980)2915-2920

Neutron Diffraction Study on the Structure of Glassy Metal Halides

K. KINUGAWA, K. KADONO, H. TANAKA, S. OKAZAKI*, T. FUKUNAGA** and M. MISAWA***

Government Industrial Research Insitute Osaka, Midorigaoka, Ikeda, Osaka 563
*Department of Electronic Chemistry, Tokyo Institute of Technology, Nagatsuta, Midori-ku, Yokohama 227
**Department of Crystalline Materials Science, Nagoya Univ. Nagoya 464
***National Laboratory for High Energy Physics, 1-1 Oho, Tsukuba, Ibaraki 305

Alkali halides are most typical ionic compounds and have been therefore believed to be poor glass-former. However, it has recently been found that some mixtures mainly composed of alkali halides, LiX-KX-CsX-BaX_2 (X=Cl, Br and I), can be quenched into the glassy state.[1] In the present study, we have investigated the structure of such alkali halide-based glasses (0.55^7LiCl-$0.32KCl$-$0.08CsCl$-$0.05BaCl_2$, 0.55^7LiBr-$0.32KBr$-$0.08CsBr$-$0.05BaBr_2$ and 0.50^7LiI-$0.09KI$-$0.36CsI$-$0.05BaI_2$) by using the HIT instrument.

In this study, ^7LiX was prepared from the neutralization reaction of ^7LiOH with HX in aqueous solutions, followed by vaporization of water and drying under vacuum at 400 °C. Batch mixtures of 3 g with appropriate composition were melted in silica crucibles at about 570 °C. The melts were then poured on a brass plate cooled below 0 °C and were pressed together to prepare the glasses. The glasses were then shattered into powder and flakes (about 2-3 mm diameter). Each glass sample was contained in a silica capillary and corked with a silicone bung. All these experimental procedures were carried out in a dry box filled with N_2 gas.

Figure 1 shows the obtained radial distribution functions G (r) for the three glasses. Each negative peak is assigned to the ^7Li(b_c=-0.222x10^{-12} cm)-X correlation which has the shortest interionic distance among all the ionic pairs. The Li-X distances in the glasses are listed in Table 1 together with those of the LiX crystals (rocksalt structure). The Li-Cl distance is nearly equal to that in molten LiCl (2.3 Å).[3] The Li-X distances for all the glasses are short compared with those in the corresponding crystals. This shortening is so significant (about 0.2 Å) as to possibly decrease the coordination number of the Cl^- ions (from six to four).

Table 1. Interionic distances in the glasses and crystals.

Pair	$r_{Li\text{-}X}$/ Å (glass)	$r_{Li\text{-}X}$/ Å (crystal) [2]	ratio
Li-Cl	2.35	2.565	0.916
Li-Br	2.53	2.751	0.920
Li-I	2.83	3.000	0.943
Li-Cl(MD)	2.27	2.52	0.901

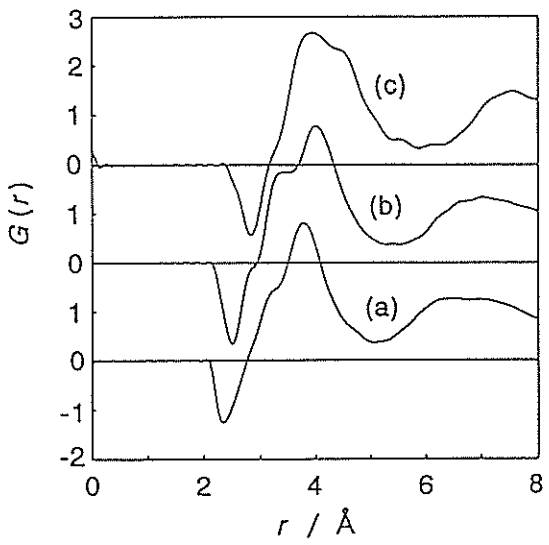

Fig. 1 Radial distribution functions G (r) for the glasses. (a) LiCl-KCl-CsCl-$BaCl_2$ glass; (b) LiBr-KBr-CsBr-$BaBr_2$ glass; (c) LiI-KI-CsI-BaI_2 glass.

The coordination number could not significantly be determined because of the G (r)-tail overlap between the first Li-X peak and the second peak and also because of the Fourier ripple. On the other hand, our molecular dynamics simulations[4] using the Tosi-Fumi potential indicate the fourfold coordination of the Cl^- ions around the Li^+ ions. The Li-Cl distances in the MD simulations are also listed in Table 1. Since the ratio of peak-distance (r (glass)/r (crystal)) found in the present experiment agrees well with that of MD simulation, we can conclude that the three measured glasses have tetrahedrally coordinated structure around the Li^+ ions.

References

1) K. Kadono, K. Mitani, K. Kinugawa and H. Tanaka, J. Non-Cryst. Solids 122, 214 (1990)
2) R.W.G. Wyckoff, *Crystal Structures*, 2nd ed. Vol. 1 (John Wiley, New York, 1963).
3) M.A. Howe and R.L. McGreevy, Phil. Mag. B 58, 485 (1988)
4) K. Kinugawa, K. Kadono and H. Tanaka, to be submitted

Network Structures of Silicate and Fluoride glasses

Y. Akasaka , I. Yasui and M. Misawa(KEK)

Institute of Industrial Science, Univ. of Tokyo Roppongi 7-22-1, Minato-ku, Tokyo 106, Japan

1. Introduction

Our previous paper on X-ray diffraction analysis concluded that alkali metasilicate glasses consisted mainly of $(SiO_3)_\infty$ straight chains, and the larger the size of the alkali ions, the smaller the bending angle of the chains, except in the case of $Li_2O{\cdot}SiO_2$ glass[1]. Although we had already reported the structure of this glass with X-ray diffraction[2], we could not well determine the position of Li ions due to its very small scattering factor.

Fluoride glasses would probably be hopeful optical materials. Though glasses based on AlF_3 need a rapid quench, it is reported that their glass-forming region spreads and fabrication becomes relatively easy when BaF_2, CaF_2, or YF_3 are added[3-5]. In the case of $AlF_3{\cdot}YF_3{\cdot}CaF_2$ (AYC) glass, which vitrifies more easily than $AlF_3{\cdot}BaF_2{\cdot}CaF_2$ (ABC) glass, Y^{3+} is a heavy metal and often hides information from lighter atoms Al^{3+} and F^- in X-ray diffraction measurement.

In this study the structure of $Li_2O{\cdot}SiO_2$ has been determined more precisely, and AYC glass has also been examined by the X-ray and neutron diffraction measurements in comparison with ABC glass data previously reported[6]. In neutron diffraction all constituent atoms have comparable scattering lengths and information about lighter atoms is obtained. Molecular Dynamics simulation (MD) was used for modeling glass structures.

2. Experimental

$Li_2O{\cdot}SiO_2$ glass was prepared by quenching the melt. Fluoride glass of $40AlF_3{\cdot}20YF_3{\cdot}40CaF_2$ was prepared by melting mixtures of pure CaF_2, YF_3, and AlF_3 under N_2 atmosphere and quenching rapidly by pressing between brass plates. X-ray diffraction was measured with a Mo-Kα radiation monochromatized with balanced filters and graphite monochrometer in a diffracted beam using Rigaku Denki RU-200 diffractomater. Neutron diffraction measurements were carried out by time of flight (TOF) with pulsed neutron using HIT. The structure models were calculated by MD simulations using Born-Mayer type pair potentials. As for $Li_2O{\cdot}SiO_2$ glass effective ionic charges were adopted (Si:+2.6 and O:-1.533) in order to take cobalency of Si-O bond into account. The RDFs for the structure models were calculated using a pair function method.

3. Results and Discussion

3.1 $Li_2O{\cdot}SiO_2$ glass

Fig. 1 shows the observed RDFs and calculated RDFs from the structure model obtained by MD simulation. In the observed ones, the first peak near 1.6Å is attributed to the nearest neighboring Si-O atomic pairs. While the second large peak around 2.0~3.0Å consists of the nearest Li-O and O-O pairs in X-ray RDF, clearly separated in neutron RDF . The peaks near 1.95Å and 2.65Å are attributed to Li-O and O-O atomic pairs, respectively. Observed and calculated RDFs show good agreement. This structure model consisted mainly of $(SiO_3)_\infty$ chains and bending angle of this chain was 20.2° in average which was somewhat degree smaller than that of crystal. The distances of Si-bridging oxygen were 1.63Å and those of Si-non-bridging oxygen were 1.60Å in average. This suggests that the SiO_4 tetrahedra were stretched in the direction of chain.

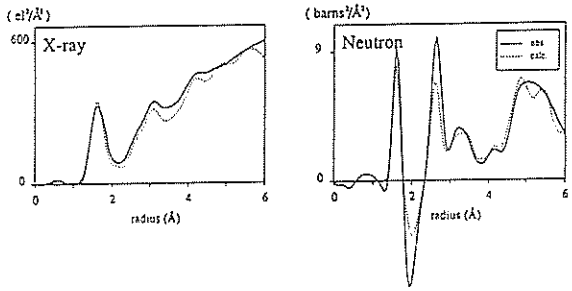

Figure 1 Observed and calculated RDFs of Li_2O-SiO_2glass.

The positions of Li ions with respect to the chains can be expressed schematically as shown in Fig. 2. The Li ion is surrounded by non-bridging and bridging oxygen atoms of the same tetrahedra and another oxygen of the same chain. This three coordination suggests that the Li ions will be a key factor to determine the bending angles of SiO_4 tetrahedra chains.

3.2 AYC glass

A comparison of observed RDFs between $40AlF_3 \cdot 20YF_3 \cdot 40CaF_2$ (AYC) glass and $40AlF_3 \cdot 20BaF_2 \cdot 40CaF_2$ (ABC) glass is shown in Fig. 3. The first peak near 1.85Å is attributed to the nearest neighboring Al-F atomic pairs, and the second peak around 2.5~3.0Å consists of the nearest pairs of Y-F (or Ba-F), Ca-F, and F-F. They show good agreement, except the second peak in X-ray RDF due to the difference of Ba^{2+} and Y^{3+} ion radius. This indicates that the structures of these two glasses are similar.

In MD simulation of AYC glass, a model fairly appropriate to the data of diffraction measurements was obtained. In this model, averaged F-Al-F bond angle in AlF_6 octahedra was 90.47° almost equal to the ideal angle 90°. But the standard deviation was 13.23°, bigger than that in ABC glass, and octahedra in AYC glass were distorted to a greater extent than those in ABC glass. Fig. 4 shows the linkage structure between AlF_X chains and YF_X polyhedra. YF_X polyhedra link the AlF_X chains and isolated AlF_6 octahedra. This will be one of the explanations for the higher tendency of AYC glass to vitrify.

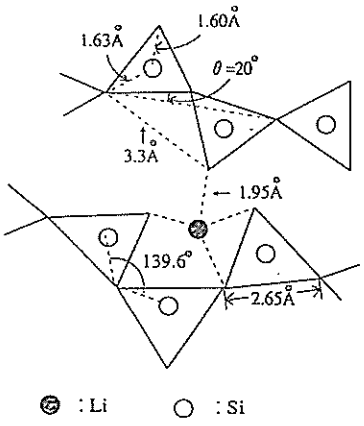

Figure 2 Schematic representation of typical coordination of a Li ion.

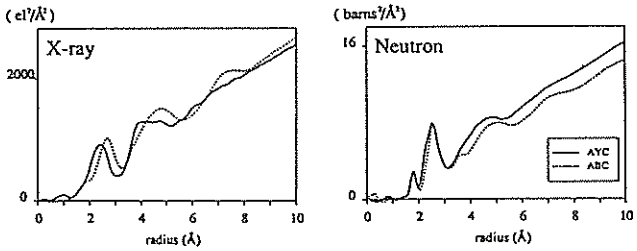

Figure 3 Observed RDFs of AYC and ABC glasses.

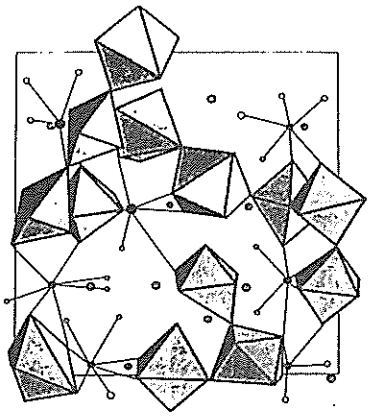

Figure 4 Linkage structure of AlF_6 octahedra and YF_X polyhedra.

4. Conclusion

It is proved that Li ion as well as Na, K, Cs ions determines the bending angles and Li metasilicate glass also has a structure governed by a rule that the larger is the size of the alkali ions, the smaller becomes the bending angle of the chains. In the structure of AYC glass, AlF_X polyhedra are joined to form chains as in the structure of ABC glass, while isolated AlF_X polyhedra, not found in ABC glass, exist and chain-forming polyhedra are distorted by the presence of Y^{3+}. YF_X polyhedra combine AlF_X polyhedra (chain like and isolated), which will cause higher tendency of AYC glass to vitrify.

5. References

1) I. Yasui et. al., Phys. Chem. Glasses 24 (1983) 65.
2) H. Hasegawa et. al., J. Ceram. Soc. Japan, 88 (1980) 271.
3) T. Kanamori et. al., J. Appl. Phys. 20 (1981) 59.
4) I. Yasui et. al., 32 & 33 (1988) 178.
5) H. Hefang et. al., Sci. Forum 5 (1981) 145.
6) T. Nanba et. al., Mater. Sci. Forum 32 & 33 (1988) 385.

Motion of solvent molecules in concentrated electrolyte solutions

H.HAYASHI, T.KAMIYAMA, Y.NAKAMURA and Y.IZUMI*

Department of Chemistry, Faculty of Science, Hokkaido Univ., Sapporo 060
* Macromolecular Research Laboratory, Faculty of Engineering, Yamagata Univ., Yonezawa 992.

From electrical conductance measurements[1] it has been suggested that concentrated solutions of $LiNO_3$ in 1,3-diaminopropane (DAP) is solvated at both molecular ends to Li^+ ions to form very viscous network liquids. In the present study, the molecular motion of the solvent molecules have been studied from the quasielastic neutron scattering using the LAM 40 spectrometer.

The sample solutions used in the present measurements were 25 and 40 mol% $LiNO_3$ in 1,3-DAP ($NH_2CH_2CH_2CH_2NH_2$), which have been found to form relatively stable glasses. Each sample solution was sealed in a double cylindrical container of aluminum, in which the sample thickenss was 0.1 mm. Corrections for multiple scatttering were not made in this work. Spectra were measured at seven different Q values ranging from 0.62 to 2.57 A^{-1}.

Measurements for the pure solvent were made only at room temperature. For the 25 and 40 mol% $LiNO_3$ solutions, measurements were carried out from 50 K to room temperature. The samples were first quenched in a cryostat with a quenting rate of 3 K/min and then measurements were made in glassy and supercooled liquid states on heating gradually from 50 K to a little bellow the cristallization temperature of each sample. Measuements were also made on the liquid samples below room temperature.

After suitable corrections for background, counter efficiency and the incident neutron spectrum, we have obtained the differental scattering cross section from the obsercved TOF spectra. From the cross section, we have determined the incoherent dynamical structure factor, $S_{inc}(Q,\omega)$. Fig. 1 shows the apparent width (FWHM) of the observed $S_{inc}(Q,\omega)$ at room temperature as a function of Q^2. The diffusion coefficent for the pure solvent dtermined from the slope of the plots is $D=1.4\times10^{-5}$ cm^2/sec. Values for the 25 and 40 % solutions were not determined due to the limit of the energy resolution of the spectrometer.

In figs. 2 and 3 we plot the temperature dependence of the elastic scattering peak, $S_{inc}(Q,\omega=0)$, for the two solutions. The quantity was nomalized to its value at 50 K for the respective Q values. At temperatures below the galss transiton temperature, T_g, the logarithmic elastic intensities show a linear temperatrue dependence, which may be described in terms of Debye model for harmonic solids. In this case the decrease of the elastic intensities with increasing temperature can be expressed in terms of the Debye-Waller factor, $f_Q(T)$,

$$S_{inc}(Q,\omega=0)(T) \propto f_Q(T) = \exp\left(1/3\langle r^2\rangle Q^2\right)$$

with

$$\langle r^2\rangle \propto T,$$

where $\langle r^2\rangle$ is the mean square displacement of protons in the solvent molecules. It is seen in figs. 2 and 3 that the elastic intensity decreases more rapidly above T_g, suggesting a significant deviation from the low temperature behavior of the Debye-Waller factor. In figs. 4 and 5 the logarithms of the Debye-Waller factor are plotted against Q^2 for several temperatures. Values of $\langle r^2\rangle$ determined from the slope of the plots are shown in fig. 6 as a function of T. A linear increase of $\langle r^2\rangle$ with T is found below T_g. The

values of $<r^2>$ start to increase rapidly around the respective glass transition temperatures, which are indicated by arrows in the figure. The absolute values of $<r^2>$ for the two solutions are similar and about 0.15 A^2 around T_g. The overall behavior of $<r^2>$ is also similar to that reported for o-terphenyl (a van der Waals glass)[2] and glycelol (a hydrogen bonded glass)[3]. It is interesting to note that the absolute values of $<r^2>$ at T_g are in the order of o-terphenyl> $LiNO_3$-1,3-DAP>glycerol. This indicates that the hindering of the motion of the protons at temperature around T_g in hydrogen-bonded glasses is larger than that in van der Waals glasses and that the present ion-solvated glasses are situated between these two types of glasses. Present neutron scattering data suggest that the motion of the solvent molecules begins to change from a lattice-like to liquid-like one at a temperature a little below the galss transition temperature. Above T_g and below room temperature, however, the motion of solvent molecules may not be described in terms of translational diffusion, since a broadening of quasielastic spectra was not found in the present experiment for this temperature region, as shown in fig. 1. This motion may be described as a rattling motion of the atoms in he solvent molecules within cages defined by neighboring atoms, which is intermediate betwee a harmonic lattice vibration and a translational diffuisive motion.

References

1) M.Morita and Y.Nakamura, J. Sol. Chem. 21, 305 (1992)
2) E.Bartsch, F.Fujara, M.Kiebel, H.Sillescu and W.Petry, Ber. Bunsenges. Phys. Chem. 93, 1252 (1989)
3) F.Fujara, W.Petry, R.M.Diehl, W.Schnauss and H.Sillescu, Europhys. Lett. 14, 563 (1991)

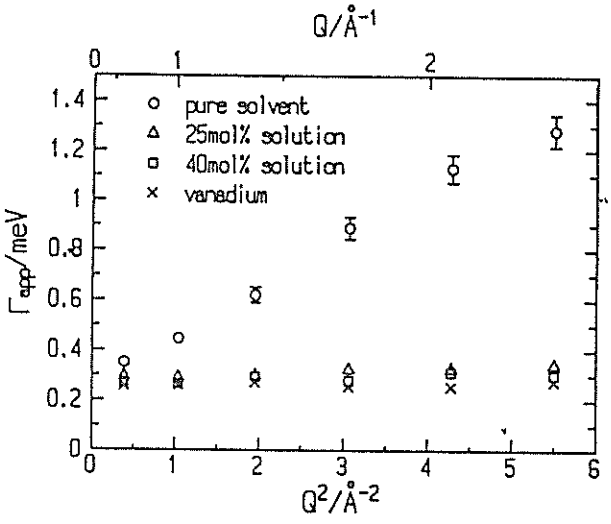

Fig. 1 Q^2 dependence of the apparent FWHM, Γ_{app}, at room temperature.

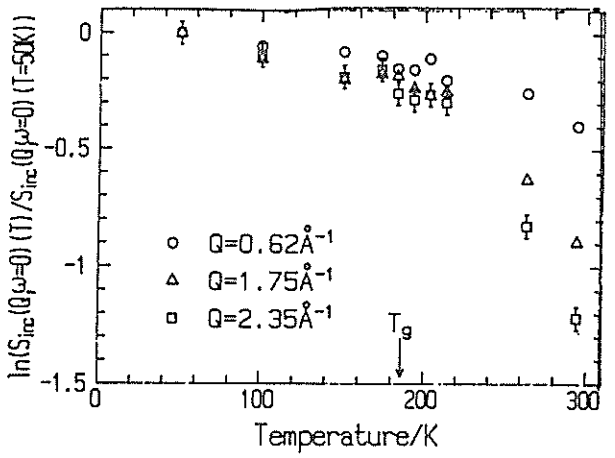

Fig. 2 Temperature dependence of the spectral peak intensity for the 25 mol% solution. The quantities are normalized to their values at 50 K.

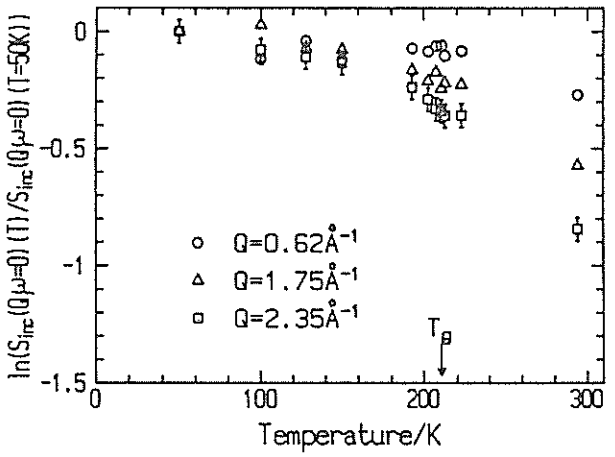

Fig. 3 Temperature dependence of the spectral peak intensity for the 40 mol% solution. The quantities are normalized to their values at 50 K.

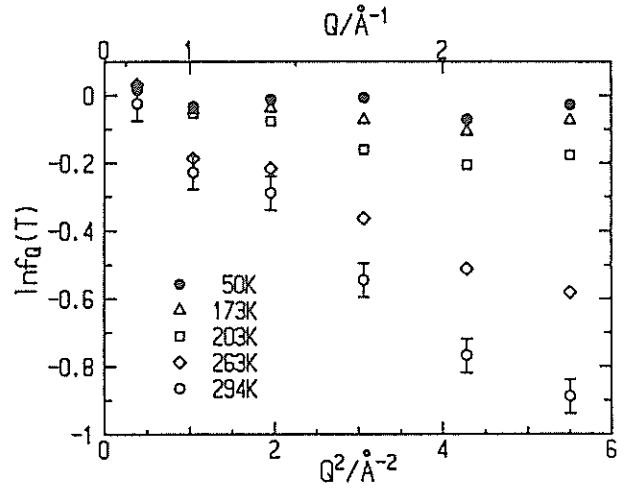

Fig. 4 Q^2 dependence of the Debye-Waller factor, $f_Q(T)$, for the 25 mol% solution at several temperatures.

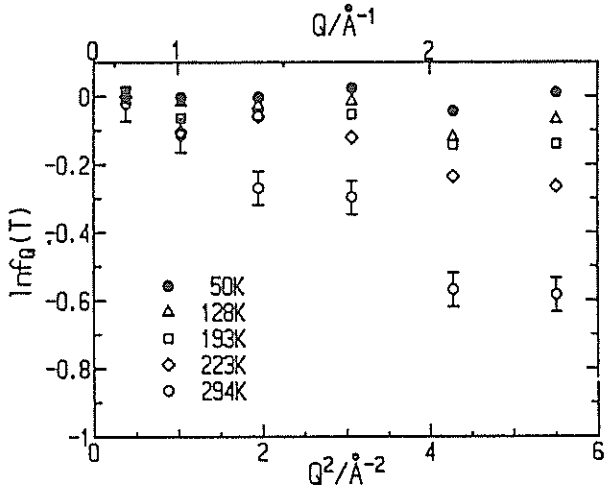

Fig. 5 Q^2 dependence of the Debye-Waller factor, $f_Q(T)$, for the 40 mol% solution at several temperatures.

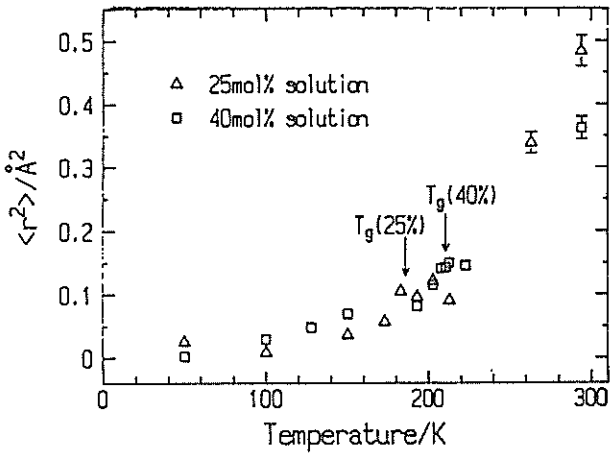

Fg. 6 Temperature dependence of mean square displacement, $\langle r^2 \rangle$, for the 25 and 40 Mol% solutions.

Dynamics of a NO_3^- Ion in Molten $RbNO_3$ and $LiNO_3$

T. Kamiyama*, K. Shibata and K. Suzuki

Institute for Materials Research, Tohoku Univ. 2-1-1 Katahira, Sendai 980
*Present Address: Department of Chemistry, Faculty of Science, Hokkaido Univ. Sapporo 060

1. Introduction

A molecule of a nitrate ion has a plane triangular shape. It is of interest that how to make intra-molecule diffusive motions of the ion are in molten metal nitrates. And some metal nitrate mixtures have the tendency of easy vitrification in spite of simple chemical components[1]. So there is another interest that what is the behavior of such motion when approaching to the glass transition.

The purpose of this study is to establish a way to analyse the coherent quasielastic neutron scattering for evaluating the motion of a polyatomic ion in melts. A simple alkali metal nitrate, $RbNO_3$ is chosen in this work. For the first step we try to analyse intra-nitrate ionic motion in molten $RbNO_3$ and discuss its microscopic geometrical mechanism. And one more system, $LiNO_3$, were measured for contrast. Some structural studies on molten $LiNO_3$ have been done by neutron scattering to obtain intra-ionic and inter-ionic structure[2].

2. Experimental

Commercial $RbNO_3$ powder (Soekawa Chemicals, Tokyo; 99%) was used in this study. Isotopically enriched $^7LiNO_3$ was prepared from ^7LiOH (98.2 atomic% ^7Li enriched) and commercial aqueous HNO_3. They were handled in vacuum or dry Ar gas atmosphere. After drying in vacuum at 100 to 150°C for one day, the powders were sealed into aluminum metal double cylindrical containers for neutron scattering under dry Ar gas atmosphere. The container is of 14mm in outer diameter, 8mm in inner diameter and 80mm in height. During inelastic neutron scattering experiment the container was held in an aluminum vacuum furnace. Measurements were carried out in a temperature range of 340 to 460°C for $RbNO_3$ or 270 to 400°C for $LiNO_3$.

Neutron scattering experiment was performed on the medium resolution time-of-flight (TOF) spectrometer LAM-40 at KENS[3]. On the inverted geometry spectrometer, pyrolytic graphite (PG-002 reflection) is used as neutron analyser mirrors. Under this operation, the energy resolution is about 200μeV at elastic scattering position and the momentum transfer is scanned over the range from 0.2 to 2.6Å^{-1}. The LAM-40 has another analyser mirrors using Ge 311 reflection. When the Ge mirrors are used, the energy resolution is about 900μeV at elastic scattering position and the momentum transfer is scanned over the wide range from 0.4 to 5.1Å^{-1}. Multiple scattering correction[4] was made to the observed scattering data to obtain the dynamical structure factors $S(Q,\omega)$ at the temperatures mentioned above.

3. Results and Discussion

Figure 1 shows the dynamical structure factors $S(Q,\omega)$ measured by PG mirrors. These $S(Q,\omega)$ were

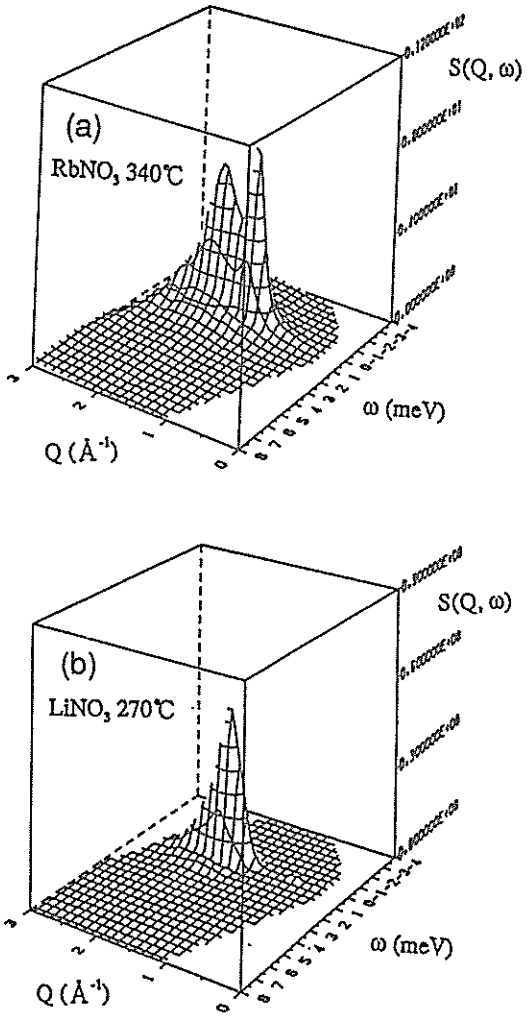

Fig. 1. Dynamical structure factor $S(Q,\omega)$ of (a) molten $RbNO_3$ measured at 340°C and (b) molten $LiNO_3$ measured at 270°C by using PG mirrors.

measured at 21 scattering angles between 13 and 120°.

We separated intra-ionic correlation and inter-ionic correlation on a quasielastic neutron scattering spectrum in the S(Q,ω). Diffusive motions in metal nitrate melts are classified according to relaxation time scales. We consider that the intra-nitrate ionic motion is a rotational motion and the translational motion of a nitrate ion is diffusion of center of gravity of each ion. The latter has inter-ionic correlation. Usually the intra-ionic motion (characteristic relaxation time = 10^{-13} sec) is more rapid than the inter-ionic motion (characteristic relaxation time = 10^{-12} sec). Therefore the intra-ionic motion is thermally averaged out in the time scale of inter-ionic motion. It is generally assumed that there is no correlation between translation and rotation of each ion. Furthermore it is supposed that nitrate ions rotate independently from one another. Based on the assumptions described above the dynamical structure factor S(Q,ω) is written as follows[5]:

$$S(Q,\omega)=S^{tr}_{ion\text{-}ion}(Q,\omega)+S^{intra}_{NO_3}(Q,\omega) \quad , \qquad (1)$$

where $S^{tr}_{ion\text{-}ion}(Q,\omega)$ is the coherent dynamical structure factor contributed from the inter-ionic correlations of three different kinds of pairs, i.e. cation-cation, cation-anion and anion-anion, and $S^{intra}_{NO3\text{-}}(Q,\omega)$ is the dynamical structure factor for intra-nitrate ionic motions.

Based on he theoretical consideration described above, Eq. (1) is empirically fitted to a model of double Lorentz functions;

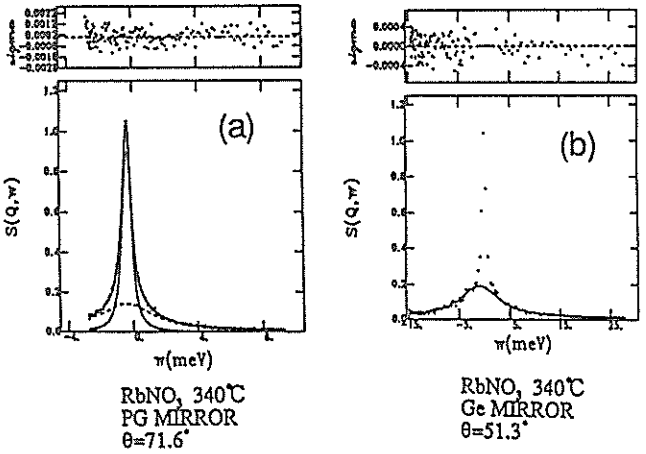

Fig. 2. Quasielastic neutron scattering spectra of molten $RbNO_3$ at 340°C. (a) Spectrum measured by PG mirrors at Q=1.74Å^{-1}; solid line represents the fitted result consisting of narrow (dotted line) and broad (broken line) quasielastic components. (b) Spectrum measured by Ge mirrors at Q=2.53Å^{-1}; solid line represents the result fitted to broad quasielastic component.

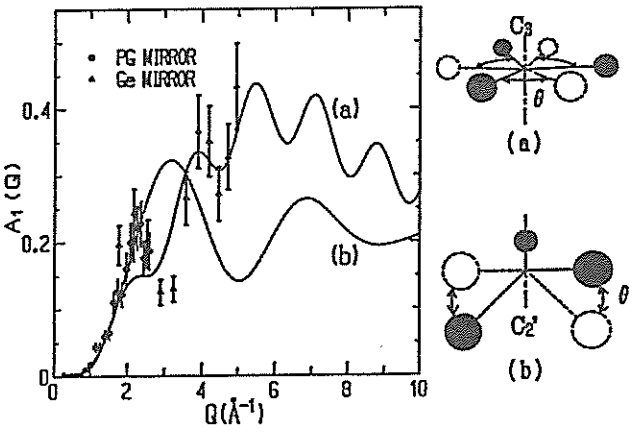

Fig. 3. Momentum dependence of energy-integrated intensity for broad component of molten $RbNO_3$ at 340°C. Solid line (a) represents $A_1(Q)$ calculated from the rotational two sites jump motion centered around C_3 axis with θ=20°. Broken line (b) represents $A_1(Q)$ calculated from the librational two sites jump motion centered around C_2' axis with θ=45°.

$$S(Q,\omega)=\frac{S(Q)}{\pi}\left\{(1-A)\frac{D_1Q^2}{\omega^2+(D_1Q^2)^2}+A\frac{D_2Q^2}{\omega^2+(D_2Q^2)^2}\right\}, \qquad (2)$$

where A, D_1, and D_2 are the parameters decided by a least-squared fitting. The first term (D_1 term) in Eq. (2) corresponds to narrow component in the spectrum describing the inter-ionic correlation. The broad component for intra-nitrate ionic correlation is represented by the second term (D_2 term) in Eq. (2).

In Fig. 1 a modest undulation is observed in the Q dependence around quasielastic region. This suggests that momentum dependence of the fast intra-ionic motion is existing.

Figure 2(a) shows that the model function Eq. (2) gives an excellent agreement with the experimental spectrum obtained by PG mirrors. Two Lorentzian components are shown in Fig. 2(a). The broad one corresponds to the intra-nitrate ionic motion and the narrow one the inter-ionic motion. An example of fitting the model function to the spectrum obtained by Ge mirrors is shown in Fig. 2(b), where we have fitted one Lorentzian to the broad component of spectrum. This Lorentzian refers to the intra-nitrate ionic motion.

The momentum dependence of energy-integrated intensity for broad component in spectrum is shown in Figure 3. The intensity has characteristic momentum dependence in oscillation. This feature comes from time correlations of atomic sites varied by the intra-nitrate ionic motion.

In order to explain the intra-nitrate ionic motion, we use rotational jump diffusion models[6], assuming that

nitrate ion is a rigid one and its shape is a regular triangle. The center of gravity of a nitrate ion is on the nitrogen atom. Therefore we consider only the scattering from oxygen atoms when calculating the rotational motion of nitrate ion. Let us consider rotational jump between two equivalent sites, m and n, of oxygen atoms around the nitrogen atom. The neutron intermediate scattering function I(Q,t) can be evaluated as follows:

$$I(Q,t)=\langle \exp(iQr(t))\cdot\exp(-iQr(0))\rangle$$
$$=\sum_{m=1}^{2}\sum_{n=1}^{2} P(m,t;n,0)\cdot P(n,0)\cdot\sum_{j=1}^{3}\sum_{k=1}^{3}\exp\left(iQ(r_{jm}-r_{kn})\right), \quad (3)$$

where P(m,t;n,0) is the probability that the nitrate ion is found at site m at time t under the condition that it stayed at site n at t=0. P(n,0) denotes the probability that a nitrate ion is found at site n at t=0. Now considering the equivalent two site model, P(n,0) is equal to 1/2. Mark j or k shows each oxygen atom in the nitrate ion. The r_{jm} and r_{kn} denote the oxygen positions on the site m or n respectively. The probability P(m,t;n,0) can be get easily by solving rate equations. Finally we obtain following equation:

$$I(Q,t)=A_0(Q)+A_1(Q)\cdot\exp(-2t/\tau) \quad . \quad (4)$$

Calculating the time Fourier transformation of time dependent term in I(Q,t), the scattering law for rotational motion of a nitrate ion can be written,

$$S_{NO_3^-}^{intra}(Q,\omega)=A_1(Q)\cdot\frac{1}{\pi}\frac{2\tau}{4+\omega^2\tau^2} \quad , \quad (5)$$

where $A_1(Q)$ is the term that shows the correlation between site n and site m. $A_1(Q)$ can be calculated by assuming the nitrate jump sites centered around nitrogen atom.

Calculating $A_1(Q)$ models are drawn by a solid line and a dashed line for comparison with the integrated intensity of intra-nitrate component in Fig. 3. The model (a) (the solid line) was calculated from the rotational two sites jump motion at a suitable angle with both sites centered around C_3 axis on the nitrate ion. The model (b) (the dashed line) means the librational two sites jump motion centered around C_2' axis. The Q dependence of energy-integrated intensity seems to be close to model (a). We have attempted to calculate another models having different angles between sites or various equiangular sites. However, the model (a) gives a most reasonable result, which implies that a nitrate ion in $RbNO_3$ melt is subjected to the rotational vibration centered around C_3 axis on he ion. MDsimulation indicates that Rb^+ ion is located on the plane of nitrate ion[7]. Such a location of Rb^+ ions hinders the librational motion around C_2' axis and allows the rotational motion around C_3 axis.

A contrast between the intra-ionic motion in $LiNO_3$ melt and in $RbNO_3$ melt is shown in Figure 4. In either

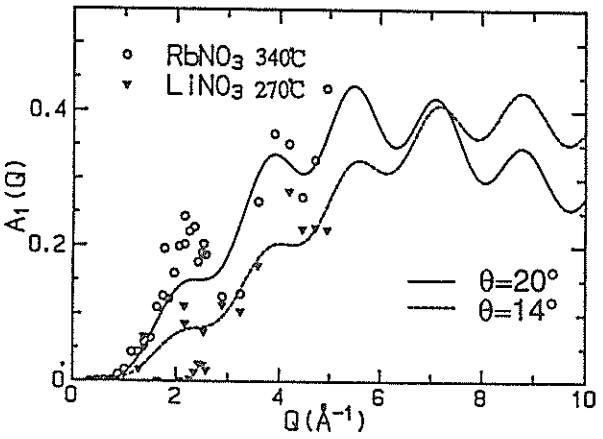

Fig. 4. Momentum dependence of energy-integrated intensity for broad component of molten $RbNO_3$ at 340°C and $LiNO_3$ at 270°C. Solid line represents the calculated $A_1(Q)$ from the rotational two sites jump motion centered C_3 axis with θ=20°. Broken line represents the calculated $A_1(Q)$ from the same motion with θ=14°.

case the oscillating feature dose not change, namely, the nitrate ion moves within the framework of moving around C_3 axis on the ion. However the nitrate motion in $LiNO_3$ is the librational motion which amplitude is smaller than in $RbNO_3$ melt. This fact shows that the motion of nitrate ions in $LiNO_3$ is restricted strongly by surrounding cations.

References

1) F. Mezei, W. Knaak and B. Farago, Phys. Rev. Lett. 58 (1987) 571.
2) K. Suzuki and Y. Fukushima, Z. Naturef. A 32(1977)1438.; Y. Kameda, S. Kotani and K. Ichikawa, Mol. Phys. 75(1992)1.
3) K. Inoue, Y. Ishikawa, N. Watanabe, K. Kaji, Y. Kiyanagi, H. Iwasa and M. Kohgi, Nucl. Instr. and Meth. A238 (1985) 401.
4) K. Inoue, Bull. Facul. Eng. Hokkaido Univ. 124 (1985) 49.
5) K. Shibata, T. Kamiyama, K. Suzuki and I. Inoue, J. Non-Cryst. Solids 117/118 (1990) 120.
6) M. Bée, Quasielastic Neutron Scattering (Adam Hilger, Bristol and Philadelphia, 1988) ch. 6.
7) T. Yamaguchi, I. Okada, H. Ohtaki, M. Mikami and K. Kawamura, Mol. Phys. 58 (1986) 349.

A quasielastic neutron scattering study of titanium alkoxide solution in the sol-gel process

T. Kamiyama, K. Shibata, N. Yoshida, T. Kamiyama* and K. Suzuki

Institute for Materials Research, Tohoku Univ. Sendai 980
*Department of Chemistry, Faculty of Science, Hokkaido Univ. Sapporo 060

Titanium oxide glass is known to be a useful material for the application in the form of a fiber or a coating-film, whose preparation is well suited to the sol-gel method. We study the change in dynamic properties of titanium tetra-iso-propoxide (Ti(O-iPr)4) attended by the hydrolysis and condensation reaction with viscosity and quasielastic neutron scattering measurements.

Ti(O-iPr)4 was mixed with distilled C_2H_5OH and H_2O-26.7 % HCl solution at the molar ratio of Ti(O-iPr)4 : C_2H_5OH : H_2O = 1 : 2 : 2. The solution was aged for gelation at room temperature. It was set in a polyethylene container whose lid has one percent of the surface area exposing to the air. The viscosity for Ti(O-iPr)4 solution was measured as a function of reaction time by a cone and plate viscometer at 20 °C with various shear rates as shown in figure 1. The solution is a Newtonian liquid at least in the viscosity region less than 3000 cP.

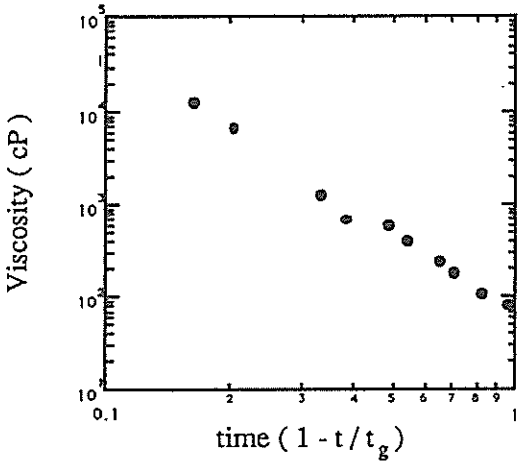

Fig. 1 Viscosity of Ti(O-iPr)4 solution as a function of relative time t/t_g. t_g is the gelation time.

Viscosity of the solution increases with reaction time t approximately following the relation $(t_g - t)^{-k}$, as measured in the silicon alkoxide solutions.[1), 2)]

Quasielastic neutron scattering measurement for the Ti(O-iPr)4 solutions were made by the time-of-flight spectrometers LAM-40 installed in KENS. After making correction for background, counter efficiency and the incident beam spectrum, the scattered intensity was determined as a function of energy transfer.

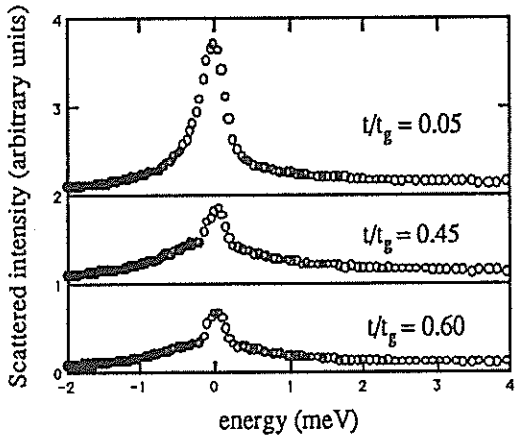

Fig. 2 Quasielastic neutron-scattering spectra at Q = 1.76 $Å^{-1}$ for the Ti(O-iPr)4 solution as a function of reaction time t.

Figure 2 shows that the scattered intensities are composed of two quasielastic scattering components, one is a relatively narrow component with about 0.5 meV FWHM and another is a broad one with about 1.6 meV FWHM. Because the observed scattered intensity is mainly dominated by incoherent scattering of hydrogen atoms, two kinds of hydrogen atoms must exist. One kind corresponds to the hydrogen atoms which has smaller diffusion constants and the other corresponds to those of larger diffusion constants. As the reaction proceeds, the narrow component of the scattered intensity decreases compared to the broad one. That is, hydrogen atoms which constitute a titanium propoxide or hydroxide molecule are removed from titanium oxide polymers, as the polymers evolve attended by the hydrolysis and condensation reaction.

References

1) H. Kozuka, H. Kuroki and S. Sakka, J. Non-Cryst. Solids 95 & 96, 1181 (1987)
2) R. Winter, D.W. Hua, X. Song, W. Mantulin and J. Jonas, J. Phys. Chem. 94, 2706 (1990)

Atomic Structure of Al-(Cr, Mn)-Si Ternary Amorphous Alloy

T. Fukunaga and U. Mizutani

Department of Crystalline Materials Science, Nagoya University, Furo-cho, Chikusa-ku, Nagoya 464

Aluminum-based metallic glasses have been reported to be formed in the Al-Si-TM and Al-Ge-TM (TM=Mn,Fe,Co or Ni) alloy systems by the rapid quenching technique[1]. Some of them exhibit a good bending ductility. The ductile nature was attributed to the existence of two amorphous phases, as suggested by a splitting of the first X-ray and electron halos as well as by a modulated contrast in transmission electron micrographs[1]. However, the atomic structure of these ternary metallic glasses has not yet been well elucidated. The atomic structure observed experimentally in a ternary amorphous system consists of the weighted sum of six partial atomic correlations. Hence, it is practically impossible to deduce the respective partial atomic correlations with reasonable accuracy.

In this report we demonstrate how it is possible to ingenuously extract the partial atomic correlations in quaternary Al-(Cr, Mn)-Si metallic glasses by taking full advantage of the neutron diffraction technique. Especially, attention is focused on the role of Mn and Cr atoms in these materials.

$Al_{55}(Cr_{1-X}Mn_X)_{15}Si_{30}$ (X=0, 0.49, 1) metallic glasses were prepared by rapid quenching from the molten state in an Ar gas atmosphere. The neutron diffraction measurements were carried out using the HIT spectrometer.

The total structure factor S(Q) for the ternary Al-TM-Si (TM=$(Cr_{1-X}Mn_X)$) metallic glasses is expressed as the weighted sum of the six partial structure factors associated with Al-Al, Al-Si, Si-Si, Al-TM, TM-TM and Si-TM pair correlations. Here, the coherent neutron scattering lengths of Cr and Mn atoms are 0.3635×10^{-12} cm and -0.373×10^{-12} cm, respectively. Provided that Cr atoms are randomly substituted for Mn atoms in these $Al_{55}(Cr_{0.51}Mn_{0.49})_{15}Si_{30}$ metallic glasses, a neutron zero scattering alloy (<b>=0) can be formed at the composition $Cr_{0.51}Mn_{0.49}$ and then one would observe only the atomic structure of the quasibinary $Al_{55}Si_{30}$ metallic glass.

The total S(Q) for the $Al_{55}(Cr_{1-X}Mn_X)_{15}Si_{30}$ (X=0, 0.49, 1) metallic glasses is calculated as follows;

$Al_{55}Cr_{15}Si_{30}$

$$S(Q)=0.2647S_{AlAl}(Q)+0.3474S_{AlSi}(Q)+0.1140S_{SiSi}(Q)+0.1522S_{AlCr}(Q)+0.0219S_{CrCr}(Q)+0.0999S_{SiCr}(Q) \quad \text{---------- (1)}$$

$Al_{55}Mn_{15}Si_{30}$

$$S(Q)=0.5397S_{AlAl}(Q)+0.7083S_{AlSi}(Q)+0.2324S_{SiSi}(Q)-0.3184S_{AlMn}(Q)+0.0470S_{MnMn}(Q)-0.2089S_{SiMn}(Q) \quad \text{---------- (2)}$$

$Al_{55}(Cr_{0.51}Mn_{0.49})_{15}Si_{30}$: TM=$(Cr_{0.51}Mn_{0.49})$

$$S(Q)=0.3646S_{AlAl}(Q)+0.4784S_{AlSi}(Q)+0.1570S_{SiSi}(Q)+0.0\,S_{AlTM}(Q)+0.0\,S_{TMTM}(Q)+0.0\,S_{SiTM}(Q) \quad \text{------- (3)}$$

The structure factor S(Q) for the $Al_{55}(Cr_{1-X}Mn_X)_{15}Si_{30}$ (X=0, 0.49, 1) metallic glasses is shown in Fig. 1. Each S(Q) has characteristic features which depend on the weighting factors of partial correlations mentioned above. In addition, it is clear that S(Q) for the $Al_{55}(Cr_{0.51}Mn_{0.49})_{15}Si_{30}$ metallic glass , which is expected to show S(Q) for the quasibinary Al-Si metallic glass, possesses a split first peak.

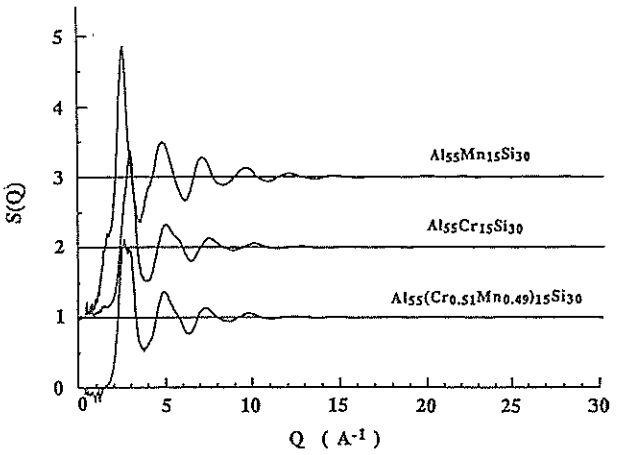

Fig. 1 Structure factors of the $Al_{55}(Cr_{1-X}Mn_X)_{15}Si_{30}$ (X=0, 0.49, 1) metallic glasses.

The Fourier transformation of S(Q) into real space yields the radial distribution function RDF(r), which also possess a characteristic distribution. A negative peak observed at r≈2.42 Å should be attributed to either the Mn-Al or Mn-Si correlation because of the negative neutron scattering length of Mn.

The contribution of the Al-TM and Si-TM (TM=Cr or Mn) pair correlations can be intentionally reduced to zero by choosing appropriate coefficients in the linear combination of eqs (1) and (2). The linear

combination with vanishing coefficients for $S_{AlTM}(Q)$ and $S_{SiTM}(Q)$ is expressed as;

$$S_1(Q)-1= (1/3.093)\{(S(Q)-1):[Al_{55}Mn_{15}Si_{30}] + 2.09\,(S(Q)-1):[Al_{55}Cr_{15}Si_{30}]\}$$
$$= (1/3.093)\{1.094\,(S_{AlAl}(Q)-1)+ 1.435\,(S_{AlSi}(Q)-1)+ 0.471\,(S_{SiSi}(Q)-1) +0.000(S_{AlTM}(Q)-1)+0.093(S_{TMTM}(Q)-1) +0.000\,(S_{SiTM}(Q)-1)\}. \quad (4)$$

It happens that the coefficient of $S_{TMTM}(Q)$ also becomes very small and, hence, can be ignored. Accordingly, $S_1(Q)$ can be thought of as representing the structure factor of the Al-Si binary metallic glass. The measured S(Q) of the quasibinary $Al_{55}(Cr_{0.51}Mn_{0.49})_{15}Si_{30}$ metallic glass and the synthesized $S_1(Q)$ are shown in Fig. 2. The two spectra are surprisingly in good agreement with each other, within the experimental error. The pair distribution functions, g(r), obtained from these two S(Q)'s are also essentially identical to each otheras shown in Fig. 3. The good agreement in both the structure factor and the pair distribution function leads to the conclusion that Cr and Mn atoms are randomly distributed without any discrimination.

Utilizing the conclusion about the random substitution of Cr for Mn atoms, that is, $S_{MnMn}(Q)=S_{CrCr}(Q)$, $S_{AlMn}(Q)=S_{AlCr}(Q)$ and $S_{SiMn}(Q)=S_{SiCr}(Q)$ we can extract the S(Q) associated with the Al-TM and Si-TM (TM=Cr or Mn) pair correlations by taking the following linear combinations;

$$S_2(Q)-1=(1/0.3879)\{(S(Q)-1):[Al_{55}(Cr_{0.51}Mn_{0.49})_{15}Si_{30}] -0.6755(S(Q)-1):[Al_{55}Mn_{15}Si_{30}]\}$$
$$=(1/0.3879)\{0.2151(S_{AlMn}(Q)-1)-0.0317(S_{MnMn}(Q)-1)+0.1411(S_{SiMn}(Q)-1)\} \quad (5)$$

$$S_3(Q)-1=(1/0.274)\{(S(Q)-1):[Al_{55}Cr_{15}Si_{30}]- 0.7261(S(Q)-1):[Al_{55}(Cr_{0.51}Mn_{0.49})_{15}Si_{30}]\}$$
$$=(1/0.274)\{0.1522(S_{AlCr}(Q)-1)+0.0219(S_{CrCr}(Q)-1)+0.0999(S_{SiCr}(Q)-1)\}. \quad (6)$$

The resulting pair distribution function, g(r), for the Al-TM and Si-TM (TM=Cr or Mn) pair correlations is shown in Fig. 4. The first peak at r=2.54 Å is much sharper than that of the quasibinary Al-Si metallic glass shown in Fig. 3. The small full width at half maximum height, FWHM, of the first peak in g(r) implies the presence of strong chemical affinities for the Al-TM and Si-TM pairs. From the point of view of thermodynamics, the enthalpy of mixing is strongly related to the chemical affinity. The enthalpies of mixing for the Al-Mn, Si-Mn, Al-Cr and Si-Cr pairs calculated by Niessen and Miedema[4] are -19, -28, -10

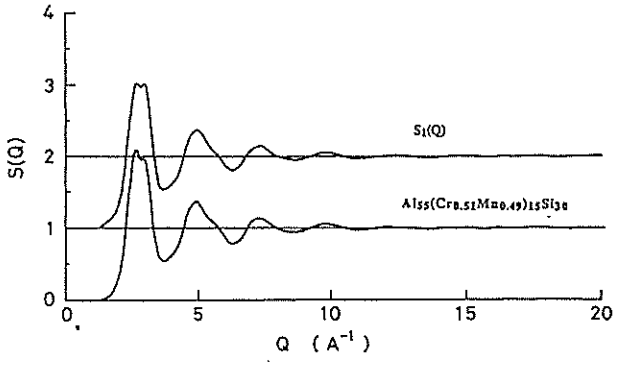

Fig. 2 Strcuture factor of the $Al_{55}(Cr_{0.51}Mn_{0.49})_{15}Si_{30}$ metallic glass and the synthesized $S_1(Q)$, which presents S(Q) of the quasibinary Al-Si metallic glass.

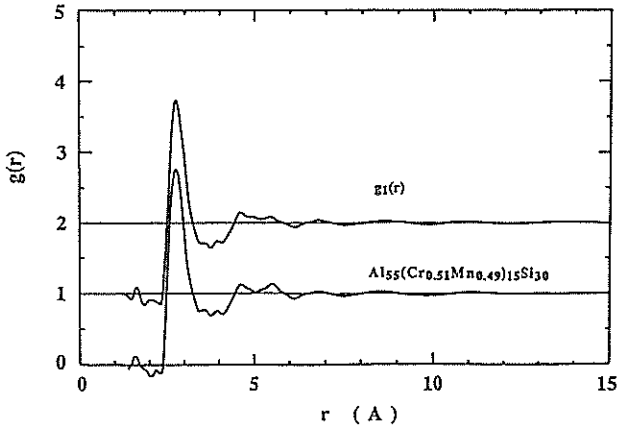

Fig. 3 Pair distribution function of the $Al_{55}(Cr_{0.51}Mn_{0.49})_{15}Si_{30}$ metallic glass and the synthesized $g_1(r)$.

and -20 (kJ/mol), respectively. A large negative value of the enthalpy of mixing is consistent with the existence of a strong attractive interaction for the Al-TM and Si-TM (TM=Mn or Cr) pairs. In contrast, the Al-Si interaction would be weakly attractive, or even perhaps repulsive, since no intermetallic compound exists in the Al-Si phase diagram. Therefore, the structural and thermodynamic arguments developed above suggest that Mn and Cr atoms act as "glues" to allow bondingbetween the light elements Al and Si and, hence, play an essential role in the glass formation of the Al-TM-Si ternary system.

The S(Q) of the TM-TM (TM=Cr or Mn) pair correlation can be also separated by taking an appropriate linear combination of eqs. (5) and (6), in spite of increasing statistical errors. The g(r) thus derived is shown in Fig. 5, in which the first peakofthe TM-TM distribution can be seen to be spread

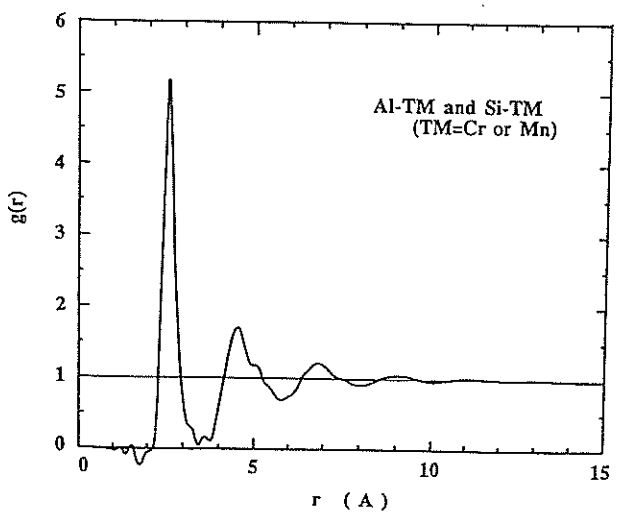

Fig. 4 Pair distribution function of the Al-TM and Si-Tm (TM=Cr or Mn) pair correlations.

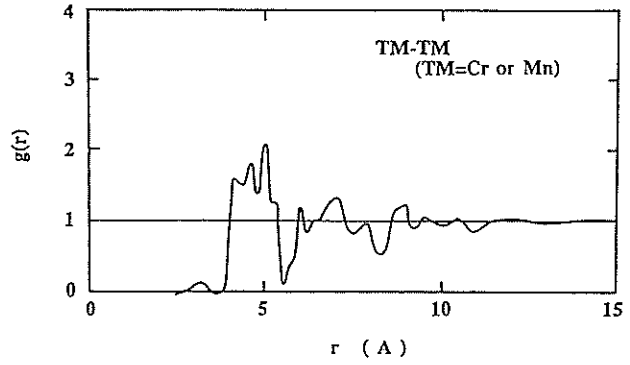

Fig. 5 Pair distribution function of the TM-TM (TM=Cr or Mn) pair correlation.

overthe range of 4 to 5.4 Å. The result indicates that TM atoms are homogeneously distributed over a wide range and are located apart from each other in these Al-TM-Si metallic glasses.

The S(Q) function for a quasibinary Al-Si metallic glass was obtained by taking full advantage of the neutron diffraction technique for the series of $Al_{55}(Cr_{1-X}Mn_X)_{15}Si_{30}$ (X=0, 0.49, 1) metallic glasses. It is clearly demonstrated that Cr and Mn atoms are randomly distributed without direct contact with each other. The sharp distribution of Al-TM and Si-TM correlations in the first neighbor shell was taken as evidence that a strong attractive interaction exists between Al-TM and Si-TM pairs and that Cr and Mn atoms play an essential role in the formation of an amorphous phase.

References

1) A. Inoue, M. Yamamoto, H.M. Kimura, T. Masumoto, J. Mater. Sci. Lett. 6, 194 (1987) 194.
2) V.F. Sears, AECL-8490 (1984)
3) A.K. Niessen and A.R. Miedema, Calphad 7, 51 (1983)

Amorphization of the Immiscible Cu-V System by MA under the N_2 gas atmosphere

T. Fukunaga, N. Kuroda, C. H. Lee, M. Misawa* and U. Mizutani

Department of Crystalline Materials Science, Nagoya University, Furo-cho, Chikusa-ku, Nagoya 464
*National Laboratory for High Energy Physics, 1-1 Oho, Tsukuba-shi, Ibaraki 305

Mechanical alloying(MA) has been recognized as a novel technique in synthesizing new unstable crystalline and amorphous materials[1]. MA has been usually carried out under an inert gas atmosphere in order to protect sample powders from oxidation during milling. Recently, however, MA under a reactive gas atmosphere has been reported to produce an amorphous phase through the solid-gas reaction[2]. In this study, we focus on the structural changes during the amorphization process induced by nitrogen atoms.

Pure elemental powders of vanadium (99.5%, average size 50μm) and copper (99.9%, average size 150μm) were mixed to give starting compositions of $V_{70}Cu_{30}$. MA for $V_{70}Cu_{30}$ powders in a planetary ball mill (Fritsch Pulverisette 5) under the N_2 gas atmosphere of 2 atmospheric pressure. During milling, N_2 gas was supplied to resume 2 atmospheric pressure at every twenty hours. The total content of nitrogen atoms absorbed in the powders was determined, using the nitrogen-oxygen analyzer (Horiba EMGA-650). A structural study was carried out by using the combination of X-ray with Mo-Kα radiation and neutron diffractions.

Cu and V atoms are mutually immiscible even in the liquid state and its system is characterized by a positive heat of mixing ΔHmix=5 kJ/mol. The MA of $V_{70}Cu_{30}$ powders in the Ar gas atmosphere has been reported to produce the bcc solid solution[3].

The S(Q) observed by X-ray diffraction clearly shows that the amorphization proceeds with increasing the milling time. The content of the nitrogen atoms absorbed after 0, 40, 120 and 200 hours of milling was determined as 0, 3.4, 9.2 and 11.7 at%N, respectively. After 200 hours of milling, the S(Q) shows a characteristic feature of an amorphous state, though some small Bragg peaks remain due to small amount residual unreacted crystals.

The S(Q) observed by neutron diffraction is shown in Fig. 1. The spectrum after 200 hours of milling possesses a mixture of both amorphous and crystal states. Since the coherent scattering length of the V atom in the neutron diffraction is negligibly small, small crystal peaks should be due to the Cu crystal. More detailed inspection of S(Q) allows us to identify the growth of a new peak at Q≈ 4.25 $Å^{-1}$ after 40 and 120 hours of milling, which disappears after 200 hours of milling. This peak is attributable to the bcc-Cu crystal formed by dissolving Cu atoms into the bcc-V lattice[3]. Therefore, we consider that the bcc solid solution is formed at the early stage of milling but is becomes amorphized due to the gradual incorporation of nitrogen atoms in the subsequent stage of milling. The Cu atoms first dissolve into the V lattice and apparently prevent V atoms from the formation of nitrides. Indeed, we confirmed that the MA of pure V powders in the N_2 gas atmosphere results in only VN crystalline compound.

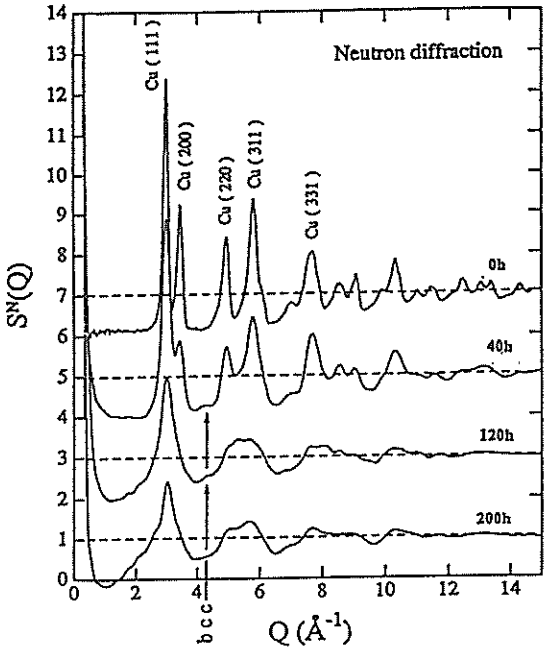

Fig. 1 Neutron structure factors S(Q) of $(V_{70}Cu_{30})_{1-X}N_X$ powders after 0, 40, 120 and 200 hours of MA.

References

1) C.C. Koch, O.B. Calvin, C.G. Mckamey and J.O. Scarbrough, Appl. Phys. Lett., 43, 1017 (1983)
2) Y. Ogino, S. Murayama and Y. Yamazaki, J. Less-Comm. Met., 168, 221 (1991).
3) T. Fukunaga, M. Mori, M. Misawa and U. Mizutani, Material Science Forum (Trans Tech Pub.) 88-90, 663 (1992).

Crystal to Amorphous Transition of Immiscible Cu-Ta Powders Subjected to Mechanical Alloying

T. Fukunaga, C. H. Lee and U. Mizutani

Department of Crystalline Materials Science, Nagoya University, Furo-cho, Chikusa-ku, Nagoya 464

The amorphization in the solid state reaction has been considered to be driven by two possible processes[1]: one is an energetically down-hill process driven by chemical reation at the interface between the two adjacent layers and the other an energetically up-hill process driven by accumulating strains and defects. Only the latter process is believed to be responsible for the amorphization of an intermetallic compound and a mixture of two different pure metals with a positive heat of mixing, since no chemical driving force is expected in both cases. Whether or not the solid state amorphization proceeds through the latter process has been tested by applying the ball milling technique to the Cu-Ta system, the atomic pair of which is characterized by a positive heat of mixing[2-4].

In this report we present structural evidences for the amorphization due to ball milling for a mixture of pure Cu and Ta powders.

The ball milling was carried out at room temperature for a mixture of pure Cu(99.9%, 150 μm in size) and Ta(99.9%, 50 μm in size) powders with an atomic ratio 3:7. A planetary ball mill (Fritsch Pulverisette 5) was used with its intensity 5. The vial and balls are made of the Cu-Be (1.8-2.0%Be) alloy.

Figure 1 shows the structure factor S(Q) deduced from neutron diffraction spectra as a function of milling time for the Cu-Ta powders. We see that the Cu line selectively disappear first and the profile become typical of an amorphous phase after 120h. The radial distribution function RDF(r) is shown in Fig. 2. The RDF(r) spectrum for 120 h sample is smooth and continuous and is characterized by the lack of a long range order. Therefore, it can be concluded from the observed change in both S(Q) and RDF(r) that the Cu-Ta powders are indeed amorphized by ball milling.

The corresponding DSC spectra were measured up to 630°C with a heating speed of 20°C/min. A sharp exothermic peak attributed to the crystallization of an amorphous phase was observed at about 560 °C. he second run was made for each sample after the fist DSC run and the area enclosed by two runs is calculated. We consider it to represent a total enthalpy accumulated during ball milling. The total enthalpy tends to saturate at the value of 12 kJ/mol. It happens that the value is close to the calculated energy of 11 kJ/mol[5] necessary to raise the enthalpy of a 3:7 mixture of pure Cu and Ta to that of a liquid or equivalently an amorphous state. Hence, it is also thermodynamically possible to assume the formation of an amorphous phase in this system.

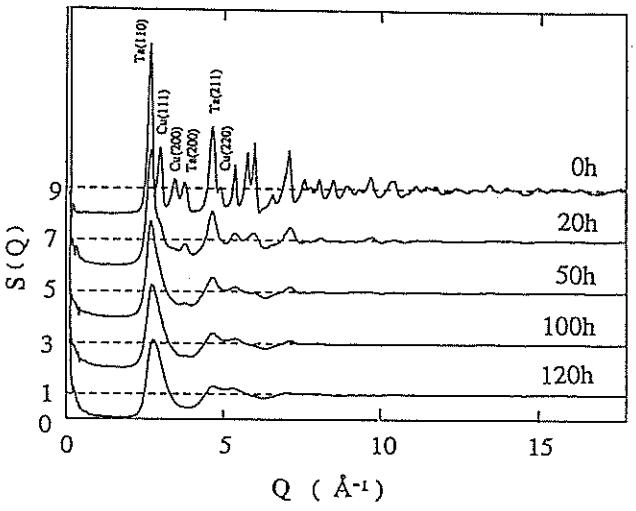

Fig. 1 Structure factor S(Q) deduced from neutron diffraction spectra for a 3:7 mixture of Cu-Ta powders ball-milled for different time intervals.

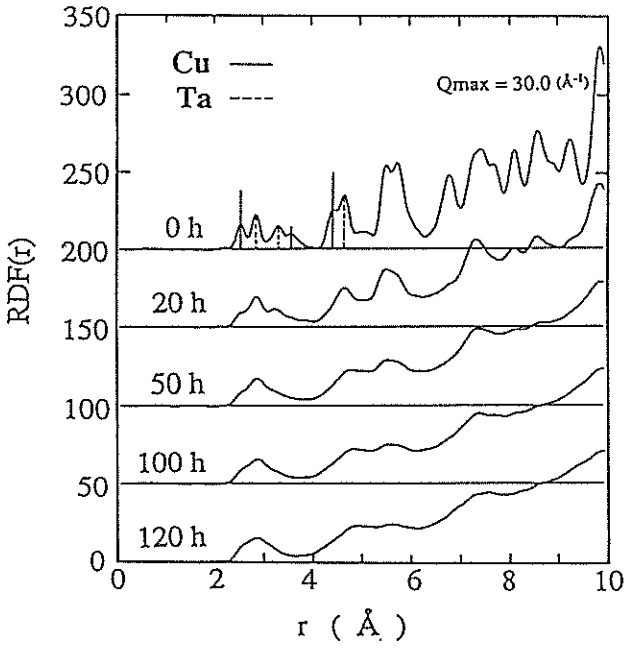

Fig. 2 The radial distribution function RDF(r) for a 3:7 mixture of Cu-Ta powders ball-milled for different time intervals.

It is of greate interest to evaluated a change in the atomic environments around Cu and Ta atoms due to ball milling by analyzing the first nearest neighbor peak of the total pair distribution function g(r) for the sample before ball milling or starting powders and that after 120h-milling. As metioned above, the latter sample may well be regarded as being in an amorphous single phase for the present analysis. The gaussian fitting to the three partial pair distribution functions was made under the conditions that the first peak consists of only Cu-Cu and Ta-Ta pairs in the starting powders and of Cu-Cu, Ta-Ta and Cu-Ta pairs in the 120h-sample.The results are shown in Fig.3 and relevant numerical data are listed in Table 1.

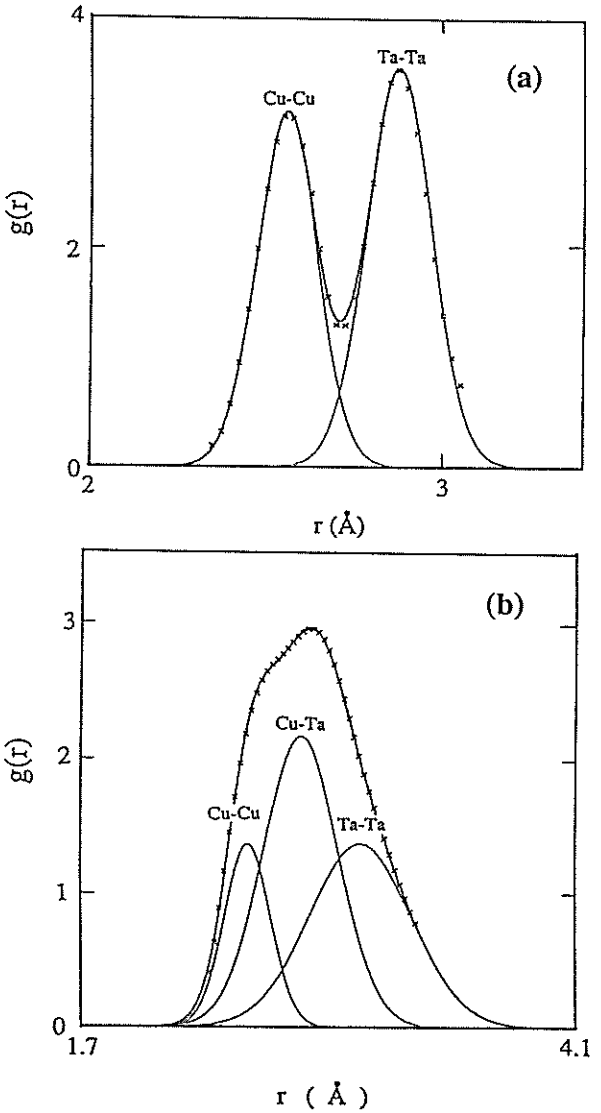

Fig. 3 The first peak of the total pair distribution function g(r) for 3:7 mixture of Cu-Ta powders (a) before milling aand (b) after milling for 120 h. It is clear that the respective peaks can be decomposed into Cu-Cu and Ta-Ta correlations in (a) and into Cu-Cu, Ta-Ta and Cu-Ta correlations in (b)

Table 1. Coordination number (C.N.) and interatomic spacing (d) for relevant atomic pairs in a mixture of pure Cu and Ta and in an amorphous Cu30Ta70 alloy obtained by ball milling for 120 h.

	Atomic pairs	C.N.	d (Å)
MA 0h	Cu-Cu	11.7	2.56
	Ta-Ta	7.6	2.88
MA 120h	Cu-Cu	4.6	2.51
	Cu-Ta	8.3	2.77
	Ta-Cu	3.5	2.77
	Cu-Cu	8.3	3.06

It is seen from Table 1 that the Ta-Ta distance substantially expands as a result of amorphization in contrast to only a weak shrinkage in the Cu-Cu distance. We tend to believe from this observation that the preferential penetration of smaller Cu atoms into the bcc Ta lattice is most likely the process towards amorphization. This conclusion is also supported by the spectra in Fig.3 where the Ta-Ta and Cu-Ta distribution are much wider than that of the Cu-Cu one. As listed in Table 1, the coordination number of the Cu-Cu and Ta-Ta pairs in the starting sample naturally agrees well with that of 12 and 8 characteristic of fcc and bcc structures, respectively. After baii milling, however, the coordination number around Cu and Ta atoms becomes 12.9 and 11.8, respectively, which indicates a dense random packing arrangement of Cu and Ta atoms.

We conclude that an amorphous phase is indeed formed by ball milling for a 3:7 mixture of pure Cu and Ta, the evidence for which has been deduced from the thermodynamic and structural analysis based on the DSC and neutron diffraction spectra.

References

1) W.L. Johnson, Prog. Mat. Sci. **30**, 81 (1986)
2) T. Fukunaga, T. Nakamura, K. Suzuki and U. Mizutani, J. Non-Cryst. Solids **117/118**, 700 (1990)
3) K. Sakurai, Y. Yamada, C.H.. Lee, T. Fukunaga and U. Mizutani, Mat. Sci. Eng. **A132**, 1414 (1991)
4) C.H. Lee, T. Fukunaga and U. Mizutani, Mat. Sci. Eng. **A132** 1334 (1991)
5) A.R. Miedema and A.K. Niessen Suppl. to Trans. JIM **29**, 209 (1988)

Chemical Short Range Structure for $(Ti_{76}Ni_{24})_X(Ti_{70}Cu_{30})_{1-X}$ Neutron Zero Scattering Amorphous Alloy

T. Fukunaga, K. Okasaka and U. Mizutani

Department of Crystalline Materials Science, Nagoya University, Furo-cho, Chikusa-ku, Nagoya 464

Physical and chemical properties of amorphous alloys depend sensitively on the short range atomic environment. The chemical short range order of Ti-Cu and Ti-Ni binary amorphous alloys has been reported to be quite different from each other[1-5], even though Ni, being located next to Cu in the periodic table, has an atomic size which is almost the same as that of Cu. In the amorphous state Cu atoms are in hard contact with each other but Ni atoms are not [3,4]. Different environment of Cu and Ni atoms in the respective binary amorphous alloys is believed to be caused by the stronger chemical affinity of Ni atoms to Ti atoms than that of Cu atoms to Ti atoms.

In this report we studied a change of the short range atomic arrangement as a function of the concentration of constituent elements in $(Ti_{76}Ni_{24})_X(Ti_{70}Cu_{30})_{1-X}$ ternary amorphous alloys by using the neutron diffraction technique. Here, only the concentration-concentration correlation function can be extracted in the amorphous alloy system, because the composition is chosen such that the average neutron scattering amplitude is set to be zero.

The Ti-Cu-Ni ternary amorphous alloys were prepared by the mechanical alloying(MA) technique [6,7]. MA could amorphize the $(Ti_{76}Ni_{24})_X(Ti_{70}Cu_{30})_{1-X}$ neutron zero scattering alloys over all compositions ($0 \leq X \leq 1$), even though liquid quenching method could not.

Pure elemental powders of nickel (99.9%, average size 100μm), titanium (99.9%, average size 50μm) and copper (99.9%, average size 50μm) were mixed so as to give an average composition of $(Ti_{76}Ni_{24})_X(Ti_{70}Cu_{30})_{1-X}$ (X=0, 0.1, 0.25, 0.5, 0.75, 0.9, 1). Strictly speaking, $Ti_{76}Ni_{24}$ and $Ti_{70}Cu_{30}$ represent the composition ratio of Ti:Ni=75.74:24.26 and Ti:Cu=70.05:29.95, respectively, so that the averaged neutron scattering amplitudes become zero. MA was carried out in a conventional ball-milling apparatus with the rotating speed of 110 rpm under the Ar gas atmosphere. The structural measurements were carried out by neutron diffraction.

The $(Ti_{76}Ni_{24})_X(Ti_{70}Cu_{30})_{1-X}$ alloys can be rewritten as the pseudo-binary form $[Ni_{24X}Cu_{30(1-X)}]Ti_{70+6X}=TM_{30-6X}Ti_{70+6X}$ (TM=Ni and Cu). The structure factor S(Q) for a binary system is obtained according to the Bhatia-Thornton definition[8]. The Bhatia-Thornton partial structure factors $S_{NN}(Q)$, $S_{CC}(Q)$ and $S_{NC}(Q)$ stand for the number density-number density correlation, the concentration-concentration correlation and the cross term, respectively. Since the $(Ti_{76}Ni_{24})_X(Ti_{70}Cu_{30})_{1-X}$ (X=0, 0.1, 0.25, 0.5, 0.75, 0.9, 1) amorphous alloys satisfy the condition $\langle b \rangle = 0$ as a result of a negative value of $b_{Ti}(=-0.33\times10^{-12}$ cm), the observed total S(Q) represents directly the quantity $S_{CC}(Q)/C_{TM}C_{Ti}$, where $C_{TM}=C_{Ni}+C_{Cu}$.

The Bhatia-Thornton type structure factor S(Q) for the $(Ti_{76}Ni_{24})_X(Ti_{70}Cu_{30})_{1-X}$ (X=0, 0.1, 0.25, 0.5, 0.75, 0.9, 1) amorphous alloys is shown in Fig. 1. The results reflect well the concentration-concentration structure factor $S_{CC}(Q)$. For the $Ti_{70}Cu_{30}$ amorphous alloy the first broad peak is observed at Q≈2 $Å^{-1}$ with a subsidiary maximum on the low Q side. The subsidiary maximum disappears when X exceeds 0.5.

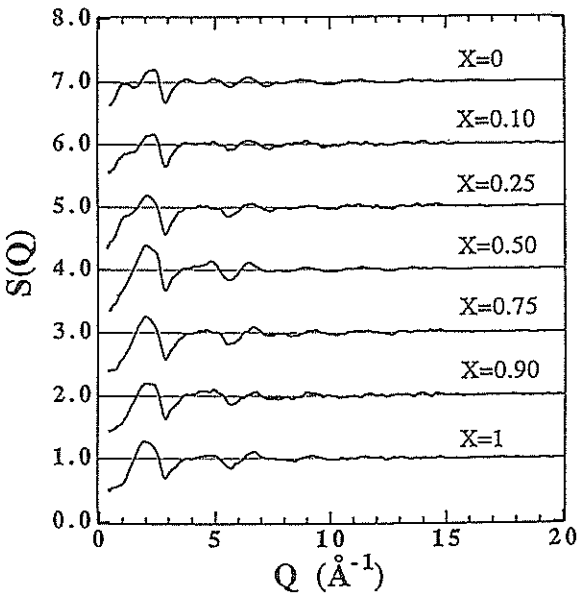

Fig. 1 Structure factors for the $(Ti_{76}Ni_{24})_X(Ti_{70}Cu_{30})_{1-X}$ (X=0, 0.1, 0.25, 0.5, 0.75, 0.9, 1) amorphous alloys

The radial concentration function $RCF(r)=rG_{CC}(r)$ obtained from the Fourier transformation of the $S_{CC}(Q)$ for the $(Ti_{76}Ni_{24})_X(Ti_{70}Cu_{30})_{1-X}$ amorphous alloys is shown in Fig. 2. RCF(r) for the $Ti_{70}Cu_{30}$ amorphous alloy has a positive peak at r≈2.4 Å and a negative peak at r≈2.7 Å. The positive and negative peaks can be identified as the Cu-Cu and Cu-Ti correlations respectively, since Cu and Ti atoms have

a positive and negative cross-section for neutrons, respectively. The Ti-Ti correlation may be located at about 3.0 Å, because the radius of a Ti atom is 1.47 Å. The positive peak at r≈2.4 Å in RCF(r) for the $Ti_{70}Cu_{30}$ amorphous alloy rapidly reduces its intensity with increasing Ni content. The RCF(r) for the $Ti_{76}Ni_{24}$ amorphous alloy has only a negative peak at the nearest neighbor distance.

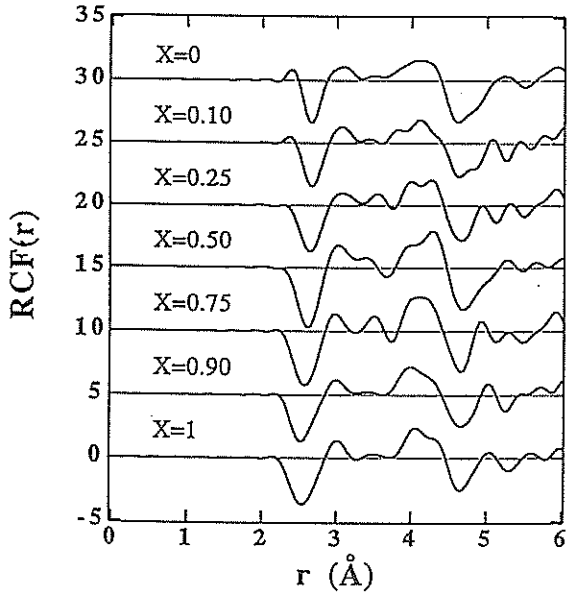

Fig. 2 Radial concentration functions for the $(Ti_{76}Ni_{24})_X(Ti_{70}Cu_{30})_{1-X}$ (X=0, 0.1, 0.25, 0.5, 0.75, 0.9, 1) amorphous alloys

Figure 3 shows a comparison of $G_{CC}(r)=4\pi r\rho_{CC}(r)$ for the $Ti_{76}Ni_{24}$ amorphous alloys prepared by MA and by the liquid quenching (LQ), together with Ti-Ti, Ni-Ti and Ni-Ni atomic distribution of the Ti_2Ni crystalline compound. It can be seen that the negative peak at r≈2.54 Å coincides well with the Ni-Ti atom pair in the Ti_2Ni crystalline compound, the interatomic spacing being much smaller than that calculated from the diameter of Ni and Ti atoms ($(\sigma_{Ni}+\sigma_{Ti})/2$=2.71 Å). This strongly suggests that, in the amorphous alloy, there exists a chemical affinity between Ni and Ti atoms similar to that of the Ti_2Ni crystalline compound. On the contrary, the atomic structure of the $Ti_{70}Cu_{30}$ amorphous alloy was found to be much different from that of the Ti_2Cu crystalline compound as shown in Fig. 4. The positive peak at r≈2.4 Å is clearly visible in $G_{CC}(r)$ of the $Ti_{70}Cu_{30}$ amorphous alloy, which has been reported to correspond to the Cu-Cu correlation[3]. However, in the Ti_2Cu crystalline compound the distance of the Cu-Cu pair is the farthest among the three kinds of pairs. The present results implies that the chemical affinity between Ti and Cu should be weaker than that of the Ti_2Cu crystalline compound and that Cu and Ti atoms in the amorphous state most likely distribute randomly, as opposed to the preferential distribution of Ti and Ni atoms in the $Ti_{76}Ni_{24}$ amorphous alloy.

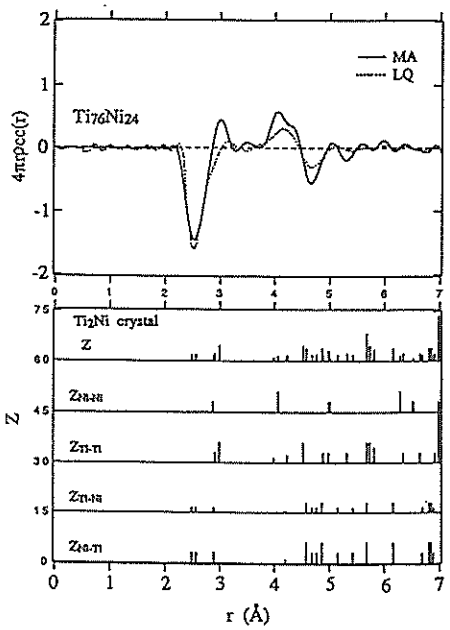

Fig. 3 Reduced concentration correlation function $G_{CC}(r)=4\pi r\rho_{CC}(r)$ for the $Ti_{76}Ni_{24}$ neutron zero scattering amorphous alloys prepared by MA and LQ, and Ti-Ti, Ni-Ti and Ni-Ni correlations in Ti_2Ni crystalline compound.

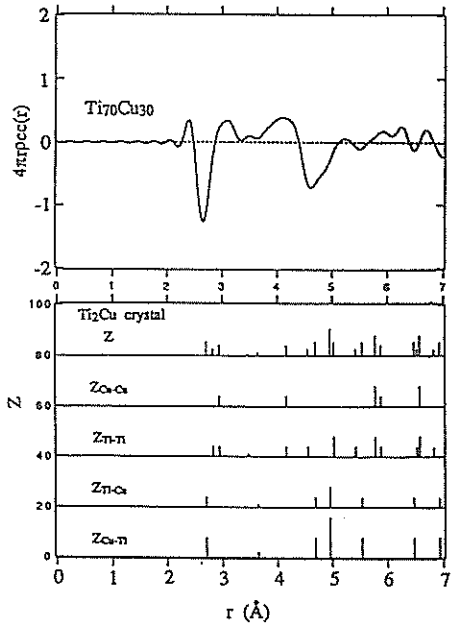

Fig. 4 Reduced concentration correlation function $G_{CC}(r)=4\pi r\rho_{CC}(r)$ for the $Ti_{70}Cu_{30}$ neutron zero scattering amorphous alloys prepared by MA and LQ, and Ti-Ti, Ni-Ti and Ni-Ni correlations in Ti_2Ni crystalline compound.

To gain further insight into the chemical short range structure around a Cu or Ni atom, we calculated the Warren chemical short range order parameter α[9] for the pseudo-binary $[Ni_{24X}Cu_{30(1-X)}]Ti_{70+6X}=TM_{30-6X}Ti_{70+6X}$ amorphous alloys. The order parameter α is shown in Fig. 5 as a function of Ni content. The value of α for the $Ti_{70}Cu_{30}$ amorphous alloy is negative but near to zero. The $Ti_{76}Ni_{24}$ amorphous alloys prepared by MA and LQ have essentially the same value of α. The value is more negative than that of the $Ti_{70}Cu_{30}$. The results indicate that the degree of the preference for unlike-atom neighbors for the $Ti_{76}Ni_{24}$ amorphous alloy is definitely stronger than that for the $Ti_{70}Cu_{30}$ amorphous alloy. The composition dependence of α provides further interesting information on the chemical short range order. Here, the order parameter α for a hypothetical structure averaged over the $Ti_{70}Cu_{30}$ and $Ti_{76}Ni_{24}$ amorphous alloys would be given as a dotted line shown in Fig. 5. It can be seen that the experimental value of α derived from the $G_{CC}(r)$ is more negative than the dotted line throughout the composition range $0 \leq X \leq 1$, indicating that the bonding between unlike-atom neighbors is much stronger than the averaged structure. The experimental value of α rapidly increases in a negative direction and deviates far below the dotted line when a small amount of Ni is substituted for Cu atoms. As is clear from Fig. 5, Cu atoms apparently behave as if they were Ni atoms in the $(Ni_{24X}Cu_{30(1-X)})Ti_{70+6X}$ amorphous alloys when 50% of the Cu atoms are replaced by Ni atoms. Therefore, it can be concluded that the chemical short range order of the $(Ti_{76}Ni_{24})_X(Ti_{70}Cu_{30})_{1-X}$ amorphous alloy when X exceeds 0.5, becomes essentially the same as that of the $Ti_{76}Ni_{24}$ binary amorphous alloy.

The preference of unlike-atom neighbors for the $Ti_{70}Cu_{30}$ amorphous alloy is much weaker than that for the $Ti_{76}Ni_{34}$ amorphous alloy. The chemical short range structure of the $Ti_{70}Cu_{30}$ amorphous alloy is described as the nearly random distribution of Cu and Ti atoms. The Warren chemical short range order parameter α sharply increases in a negative direction with increasing Ni concentration. This can be interpreted as a rapid increase in the degree of preferential bonding between (Cu, Ni) and Ti unlike-atom neighbors. It is also shown that the atomic arrangement around a Cu atom completely changes into the one characteristic of the $Ti_{76}Ni_{24}$ amorphous alloy when X exceeds approximately 0.5.

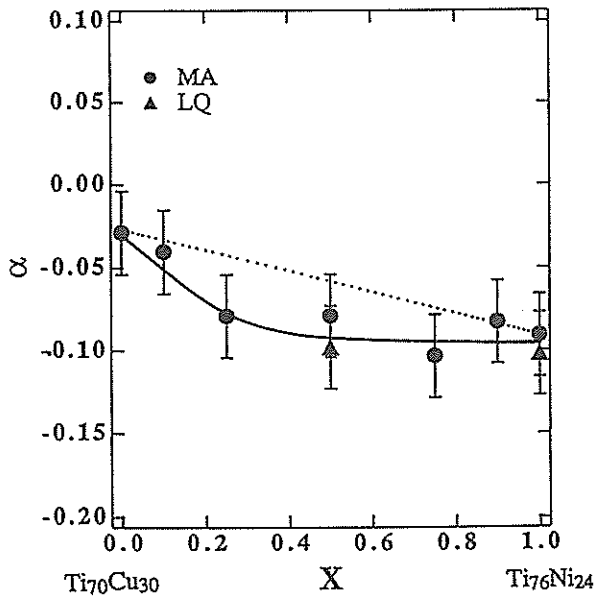

Fig. 5 Warren chemical short range order parameter as a function of X for the pseudo-binary $(Ni_{24X}Cu_{30(1-X)})Ti_{70+6X}=TM_{30-6X}Ti_{70+6X}$ (TM= Ni and Cu) (X=0, 0.1, 0.25, 0.5, 0.75, 0.9, 1) amorphous alloys

References

1) C.N.J. Wagner, J. Non-Cryst. Solids 42, 3 (1980)
2) M. Sakata, N. Cowlam and H.A. Davies, Proc. 4th Int. Conf. on Rapidly Quenched Metals (Sendai, 1981) p.327.
3) T. Fukunaga, K. Kai, M. Naka, N. Watanabe and K. Suzuki, Proc. 4th Int. Conf. on Rapidly Quenched Metals (Sendai, 1981) p.347.
4) T. Fukunaga, N. Watanabe and K. Suzuki, J. Non-Cryst. Solids 61&62, 343 (1984)
5) T. Fukunaga, N. Hayashi, K. Kai, N. Watanabe and K. Suzuki, Physica 120B, 352 (1983)
6) A.E. Ermakov, V.A. Barinov and E.E. Yurchikov , Fiz. Metal Metalloved. 52, 1184 (1981)
7) C.C. Koch, O.B. Cavin, C.G. MaKamey and J.O. Scarbrough, Appl. Phys. Lett. 43, 1017 (1983)
8) A.B. Bhatia and D.E. Thornton, Phys. Rev. B2, 3004 (1970)
9) B.E. Warren, B.L. Aberbach and B.W. Roberts, J. Appl. Phys., 22, 1493 (1951)

Formation of Metastable Phases subjected to MA in V-M(M=Fe, Cu) Systems

T. Fukunaga, M. Mori, M. Misawa* and U. Mizutani

Department of Crystalline Materials Science, Nagoya University, Furo-cho, Chikusa-ku, Nagoya 464
*National Laboratory for High Energy Physics, 1-1 Oho, Tsukuba-shi, Ibaraki 305

Mechanical alloying technique has been recognized as one of the novel methods in synthesizing non-equilibrium alloys. Koch et al.[1] reported, for the first time, that amorphous alloys can be produced when a mixture of elemental metal powders are ball-milled in an inert gas atmosphere. Moreover, Schwarz et al.[2] has noted that even an initially homogeneous intermetallic compound can be transformed to an amorphous phase by ball milling. The former is often referred to as mechanical alloying(MA) and the latter as mechanical grinding(MG).

In this report we present the formation of metastable crystalline phases by the MA and MG in the $V_{70}Cu_{30}$ and $V_{50}Fe_{50}$ systems; the former is characterized by a positive heat of mixing and the latter a negative heat of mixing. The MA and MG processes for the V-M (M=Cu or Fe) system were studied by and neutron diffraction measurements. The transformation processes studied by neutron diffraction unable us to single out only the M-M correlations, because of a negligibly small coherent scattering length of the vanadium atom relative to that of the copper or iron atom.

Pure elemental powders of copper (99.5%, average size 150μm), iron (99%, average size 50μm) and vanadium (99.5%, average size 50μm) were mixed to give starting compositions of $V_{70}Cu_{30}$ and $V_{50}Fe_{50}$. The σ-VFe crystalline compound was produced by arc-melting of pure iron(99.5%) and vanadium(99.5%) and was crushed into small pieces. These powder samples were ball milled under the Ar gas atmosphere, using the vial and balls made of Cu-Be (1.8-2%Be) for the $V_{70}Cu_{30}$ and of stainless steel (SUS304) for the $V_{50}Fe_{50}$ and σ-VFe. Ball milling was carried out in a planetary-type mill (Fritsch P-5) with the intensity 7 or the rotating speed of 570 rpm for the $V_{70}Cu_{30}$ powders and in a vibrating-type mill (NEV-MA-8, Nissin-Giken) with the intensity 3 for the $V_{50}Fe_{50}$ powders and σ-VFe powders. The structural changes were studied by neutron diffraction using HIT spectrometer.

Following the Faber-Ziman definition[3], the total structure factor S(Q) observed by neutron diffraction for the V-M (M=Cu or Fe) binary systems is expressed as the weighted sum of the three partial structure factors $S_{VV}(Q)$, $S_{VM}(Q)$ and $S_{MM}(Q)$ associated with V-V, V-M and M-M pair correlations. Here, the coherent scattering length of a vanadium atom in neutron scattering is very small (b_V=-0.0382x10^{-12} cm) compared with that of a copper or iron atom. (b_{Cu}=0.7718x10^{-12}, b_{Fe}= 0.954x10^{-12} cm). The total S(Q)'s for the $V_{70}Cu_{30}$, $V_{50}Fe_{50}$ and σ-VFe alloy powders are calculated as follows;

$V_{70}Cu_{30}$

$$S(Q)=0.017S_{VV}(Q)-0.295S_{VCu}(Q)+1.278S_{CuCu}(Q) \quad \text{-------- (1)}$$

$V_{50}Fe_{50}$ and σ-VFe

$$S(Q)=0.0017S_{VV}(Q)-0.087S_{VFe}(Q)+1.085S_{FeFe}(Q) \quad \text{------- (2)}$$

The weighting factor of the V-V correlation turned out to be negligible relative to those of Cu-Cu and Fe-Fe correlations. The V-M correlation makes a negative contribution of about 23% to the total S(Q) for the $V_{70}Cu_{30}$ and 8% for the $V_{50}Fe_{50}$ and σ-VFe. Therefore, any positive peaks, if they appear, should be attributed to the partial structure factor $S_{MM}(Q)$ due to the M-M correlation.

I. V-Cu system

It has been reported that the $V_{50}Cu_{50}$ powders[4] can be partially amorphized by MA and simultaneously the metastable BCC copper crystal is formed by dissolving copper atoms into the BCC vanadium lattice, even though the V-Cu system is characterized by a positive heat of mixing. Furthermore, MA of the $V_{70}Cu_{30}$ powders was carried out if the metastable BCC copper crystal is still formed. It was found that the BCC solid solution has been formed and that the copper concentration far exceeds its solubility limit (about 2at%Cu at room temperature) in the V-Cu phase diagram.

The X-ray diffraction patterns of the $V_{70}Cu_{30}$ powders after MA indicate that Bragg peaks associated with the BCC crystal remain visible though the FCC diffraction peaks of copper crystal disappear after 30 h of MA. The peak positions in the BCC diffraction pattern were slightly shifted to high angles with increasing MA time. The lattice

constant calculated from the (110) Bragg peak of the BCC crystal decreases and levels off with increasing MA time. The decrease of the lattice constant is attributed to the dissolution of smaller copper atoms into the BCC vanadium lattice. Therefore, we believe that the copper atoms occupy randomly the BCC lattice site in the course of MA, and, hence, the partial structure factor of the Cu-Cu correlation changes from the FCC pattern into the BCC one.

Figure 1 shows S(Q)'s of the $V_{70}Cu_{30}$ powders after 0, 30, 60 and 120 h of MA. Vertical lines drawn in the figure refer to Bragg peaks of the BCC copper crystal calculated under the assumption that the atomic diameter is the same as that of the FCC copper crystal. Since the measured total S(Q) is essentially equivalent to the partial $S_{CuCu}(Q)$, as mentioned above, the $S_{CuCu}(Q)$ observed before MA should reflect an FCC pattern of the copper crystal. With increasing MA time, however, the Bragg peaks of the FCC copper decrease and, instead, Bragg peaks corresponding to the BCC crystal newly grow. The results clearly demonstrate that the FCC structure of the copper crystal transforms into the BCC structure by dissolving copper atoms into the vanadium BCC lattice during the course of mechanical alloying.

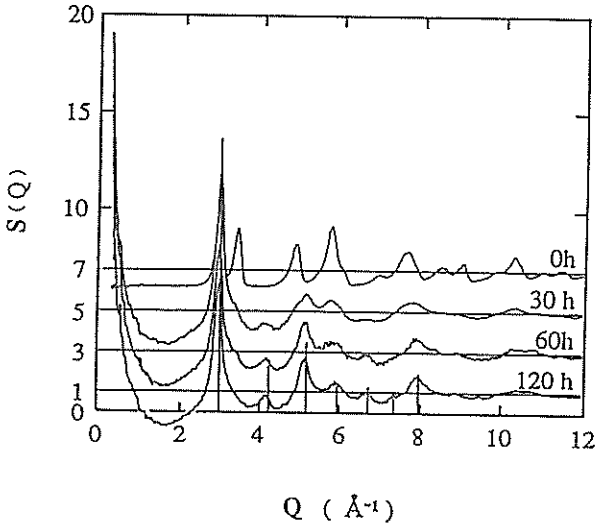

Fig. 1 Total structure factors S(Q) of the $V_{70}Cu_{30}$ samples after 0, 30, 60, and 120 hours of MA, together with vertical lines corresponding to Bragg peaks of the BCC-copper crystal.

II. V-Fe system

Figure 2 shows a series of X-ray diffraction spectra for the $V_{50}Fe_{50}$ powders as a function of MA time. Bragg peaks of (110), (200), (211) and (220) planes characteristic of the V and Fe BCC structures are observed in the starting powders but, with increasing milling time, they are gradually replaced by new peaks, which are located in between the Bragg peaks of pure vanadium and iron. Finally, a single phase solid solution with BCC structure apparently remains in the powders after 120 h of MA. A change in the lattice constant also indicates that the mixing proceeds down to an atomic level and an α-phase solid solution was formed in spite of the fact that the σ-phase exists as a stable phase at room temperature.

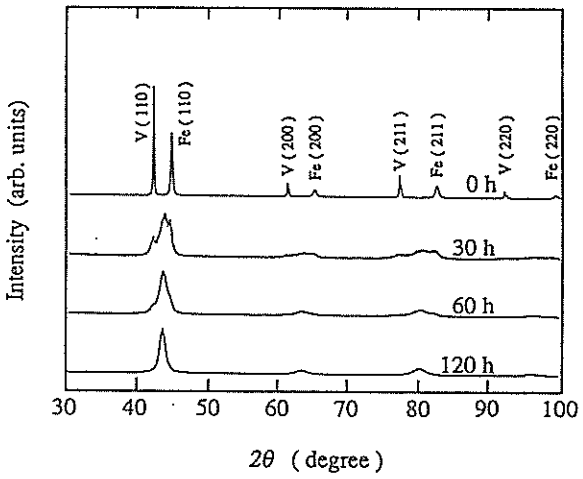

Fig. 2 X-ray diffraction patterns of $V_{50}Fe_{50}$ samples after 0, 30, 60 and 120 hours of MA.

Figure 3 shows the radial distribution functions RDF(r)'s for the $V_{50}Fe_{50}$ powders after 0, 30, 60 and 120 h of MA deduced from neutron diffraction data. It is seen that the RDF(r) reflects well the Fe-Fe correlation described in equation 2. The radial distribution of iron atoms can be well fitted to the BCC structure, which does not change substantially with increasing milling time. The peaks of the Fe-Fe correlation, however, slightly shifted into large distances. The present results are interpreted by the formation of the α-phase solid solution, when subjected to MA, in which the average Fe-Fe distance is expanded upon substituting larger vanadium atoms for smaller iron atoms in the BCC lattice.

The MG of the σ-VFe powders give rise to a dramatic structural change, as shown in figure 4, where the S(Q) deduced from neutron diffraction data is shown. After 120 h of MG, the Fe-Fe distribution of the σ-phase VFe tetragonal structure with 30 atoms in a unit cell[5] is found to change into that of the BCC structure, though the (101) diffraction peak of the σ-phase still slightly remains.

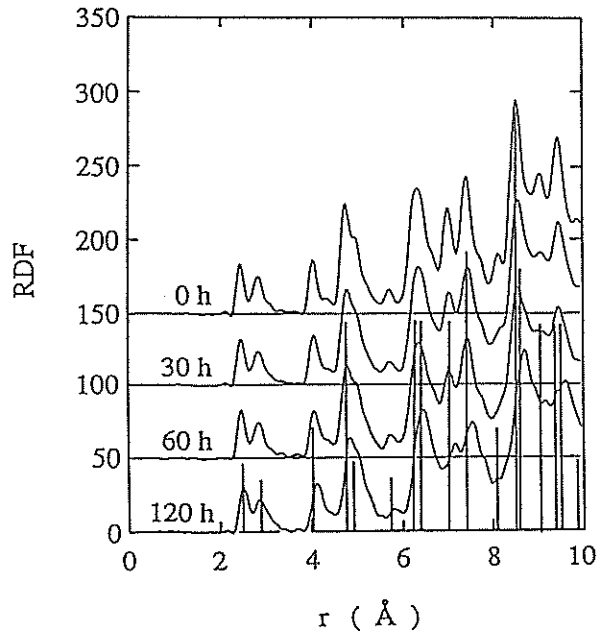

Fig. 3 Total radial distribution functions for the $V_{50}Fe_{50}$ samples after 0, 30, 60 and 120 hours of MA, together with the calculated atomic distribution of the BCC iron crystal

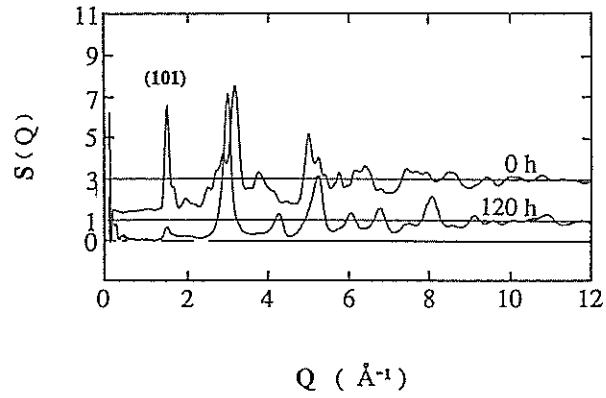

Fig. 4 Total structure factors S(Q) of the $V_{50}Fe_{50}$ samples after 0 and 120 hours of MG

Therefore, we found that the MG caused the σ-phase VFe compound transform into the α-phase $V_{50}Fe_{50}$ of the BCC structure which is known as a high temperature phase above 1200°C.

Observation of the MA process for the $V_{30}Cu_{70}$ powders by neutron diffraction allowed us to extract the evidence that the FCC distribution of copper atoms changes into the BCC. From this result we conclude that the BCC copper is formed by dissolving copper atoms into the vanadium BCC lattice and that the metastable BCC solid solution region produced by MA is indeed substantially widen relative to that in the phase diagram.

The metastable high temperature phase was formed both by MA for the $V_{50}Fe_{50}$ powders and by MG for the σ-phase VFe powders. In particular, the neutron diffraction studies, using vanadium atoms with negligibly small coherent scattering length as a partner element, provided the unique opportunity in observing directly the transformation of the tetragonal structure of iron atoms into the BCC structure.

References

1) C.C. Koch, O.B. Calvin, C.G. Mckamey and J.O. Scarbrough: J. Appl. Phys. Lett., 43, 1017 (1983)
2) R.B. Schwarz, R.R. Petrich and C.K. Saw: J. Non-Cryst. Solids, 76, 281 (1985)
3) T.E. Faber and J.M.Ziman: phil. Mag., 11, 153 (1965)
4) T. Fukunaga, M. Mori, K. Inou and U. Mizutani: Mat. Sci. Eng. A, 134, 863 (1991)
5) J.S. Kasper and R.M. Watarastrat: Acta. Cryst., 9, 289 (1956)

Amorphization of the $(Cr_{0.7}Fe_{0.3})$-N System by Mechanical Alloying

T. Fukunaga, E. Ishikawa, T. Koyano, M. Misawa* and U. Mizutani

Department of Crystalline Materials Science, Nagoya University, Furo-cho, Chikusa-ku, Nagoya 464
*National Laboratory for High Energy Physics, 1-1 Oho, Tsukuba-shi, Ibaraki 305

Mechanical alloying(MA) has been recognized as a novel technique in synthesizing new unstable crystalline and amorphous materials[1]. MA has been usually carried out under an inert gas atmosphere in order to protect sample powders from oxidation, since a fresh cleavage surface created during milling is of vital importance in the solid state reaction. Recently, however, MA under a reactive gas atmosphere has been reported to produce an amorphous phase through the solid-gas reaction[2]. In this study, we focus on the structural changes during the amorphization process induced by nitrogen atoms.

Pure elemental powders of chromium (99.9%, average size 75μm) and iron (99%, average size 75μm) were mixed to give starting compositions of $Cr_{70}Fe_{30}$ powders was carried out in a vibrating ball mill(Nissin Gikken, Super MISUNI) under the N_2 gas atmosphere of 2 atmospheric pressure. During milling, N_2 gas was supplied to resume 2 atmospheric pressure at every twenty hours. Amorphization was confirmed by the DSC measurement and X-ray diffraction with Cu-Kα radiation. The total content of nitrogen atoms absorbed in the powders was determined, using the nitrogen-oxygen analyzer (Horiba EMGA-650). A detailed structural study was carried out by using the combination of X-ray with Mo-Kα radiation and neutron diffractions. The X-ray diffraction measurement revealed that the metal atoms change their respective positions during the amorphization process. But the presence of nitrogen atoms is hardly visible in the spectrum because of its negligibly small scattering factor. Instead, neutron diffraction allows us to observe atomic rearrangements around a nitrogen atom since the coherent scattering length of a nitrogen atom is almost the same as or even larger than those of the metal atoms.

The Cr-Fe system has a small negative heat of mixing and is characterized by the complete solid solution over an entire composition range. The MA of this powders under Ar gas atmosphere has been reported to only yield the bcc solid solution. In contrast, the $Cr_{70}Fe_{30}$ powders were amorphized by MA in the N_2 gas atmosphere[3].

Figure 1 shows the neutron structure factor S(Q) for $(Cr_{70}Fe_{30})_{1-X}N_X$ powders subjected to the MA process for different time intervals. It is seen that Bragg peaks of the bcc Cr and Fe crystals become broadened with increasing the milling time. A halo pattern dominates after 320 hours of MA. The concentration of nitrogen atoms absorbed during MA increases with increasing the milling time and approaches about 15at%N after 320 hours of milling. This result indicates that the nitrogen atom apparently contributes to destroy the bcc structure and to form an amorphous structure.

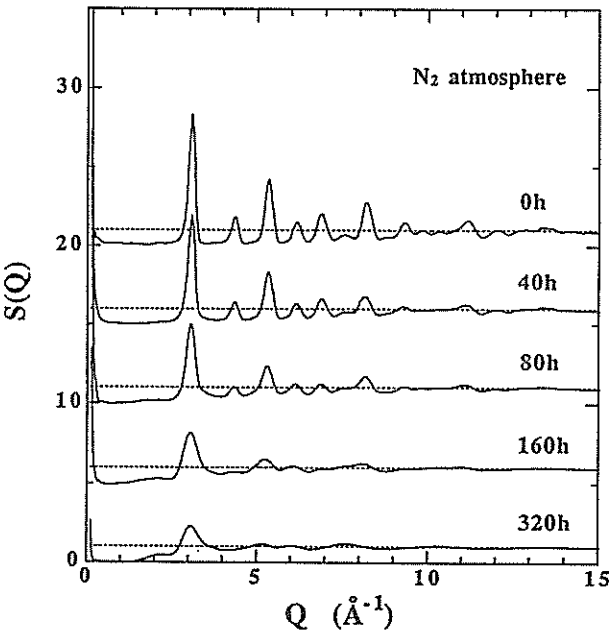

Fig. 1 Neutron structure factors S(Q) of $(Cr_{70}Fe_{30})_{1-X}N_X$ powders after 0, 40, 80, 160 and 320 hours of MA.

The X-ray diffraction spectra also clearly reveal the amorphization of the $Cr_{70}Fe_{30}$ powders by MA under the N_2 gas atmosphere. The radial distribution function RDF(r) derived from the Fourier transformation of the X-ray S(Q) is shown in Fig. 2. As marked by an arrow, the 2nd nearest neighbor atoms in the bcc crystal preferentially reduces the number during the amorphization process. It is also seen that the 1st nearest neighbor distance between metal atoms expands with increasing the milling time. We found further that the nearest coordination number around a metal atom within about 3.3 Å decreases from 14 to 11.9 atoms. We are, therefore, led to conclude that the

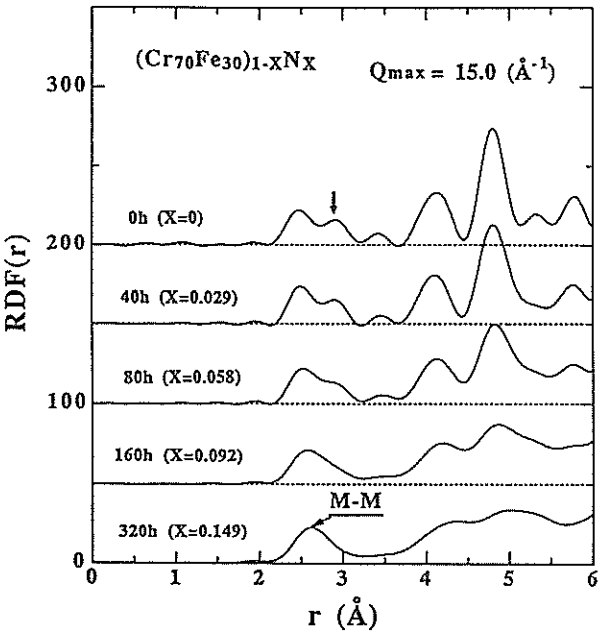

Fig. 2 X-ray radial distribution functions RDF(r) of $(Cr_{70}Fe_{30})_{1-X}N_X$ powders after 0, 40, 80, 160 and 320 hours of MA.

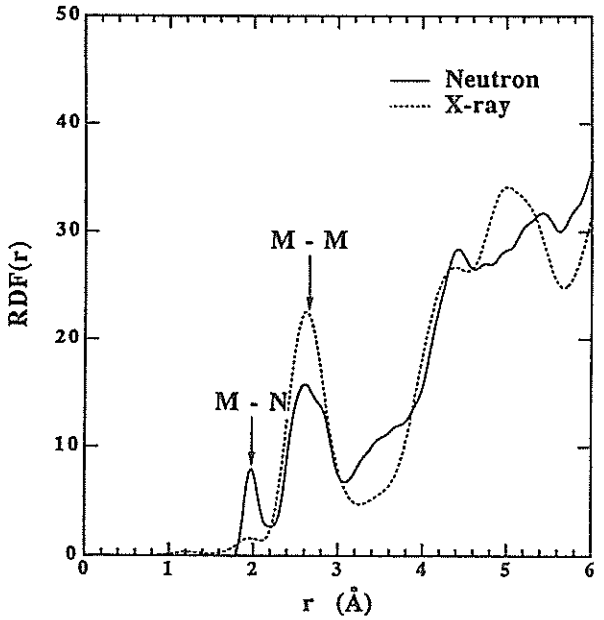

Fig. 3 Radial distribution functions RDF(r) of $(Cr_{70}Fe_{30})_{0.85}N_{0.15}$ powders observed by X-ray and neutron diffractions.

octahedral unit in a bcc structure is preferentially destroyed and is transformed into the tetrahedral unit during the amorphization process. An increase in the metal-metal distance of the 1st nearest neighbor with increasing milling time can be interpreted by assuming that nitrogen atoms are accomodated in the center of a polyhedron formed by metal atoms.

Neutron diffraction experiments can provide further detailed information about the local structure surrounding the nitrogen atom. Figure 3 compares RDF(r) of $(Cr_{70}Fe_{30})_{0.85}N_{0.15}$ powders deduced from both X-ray and neutron diffractions.

The peak at about 2 Å observed only in the neutron diffraction spectra can be safely ascribed to the metal-nitrogen atom (M-N) correlation. The coordination number of metal atoms around a nitrogen atom is calculated to be 4, if a nitrogen atom is located in the center of the polyhedron formed by Cr and Fe atoms. However, provided that a nitrogen atom is situated in the center of the polyhedron formed by only Cr atoms, due to the stronger chemical affinity of a nitrogen atom with a Cr atom than with a Fe atom, the coordination number around a nitrogen atom turns out to be 6. This result may imply that the nitrogen atom is located at a center not only of the tetrahedron but also of the octahedron formed by metal atoms to stabilized the amorphous phase.

References

1) C.C. Koch, O.B. Calvin, C.G. Mckamey and J.O. Scarbrough, Appl. Phys. Lett., 43, 1017 (1983)
2) Y. Ogino, S. Murayama and Y. Yamazaki, J. Less-Comm. Met., 168, 221 (1991).
3) T. Fukunaga, M. Mori, M. Misawa and U. Mizutani, Material Science Forum (Trans Tech Pub.) 88-90, 663 (1992).
4) T. Fukunaga, Y. Homma, M. Misawa and K. Suzuki, J. Non-Cryst. Solids, 117/118, 721 (1990).
5) C.H. Lee, M. Mori, T. Fukunaga, K. Sakurai and U. Mizutani, Material Science Forum (Trans Tech Pub.) 88-90, 399 (1992).

Atomic Structure During MA Process for $Ti_{51}Al_{49}$ Powders

T. Fukunaga, K. Okasaka, M. Misawa* and U. Mizutani

Department of Crystalline Materials Science, Nagoya University, Furo-cho, Chikusa-ku, Nagoya 464
*National Laboratory for High Energy Physics, 1-1 Oho, Tsukuba-shi, Ibaraki 305

Mechanical alloying (MA) technique has been used for the production of oxide-dispersion strengthened super alloys. Recently, MA technique has been proved to be applicable to the preparation of an amorphous alloy from a mixture of pure elemental crystal powders. MA may be continued to a stage where the starting elemental powders are mixed to dimensions of an atomic spacing or the formation of an amorphous phase. During the process the crystal structure loses a long-range periodicity. In this report, we present the structural change subjected to MA for the Ti-Al system powders that have a large negative heat of mixing(ΔHmix=-30kJ/mol).

Pure elemental powders of aluminum(99.9%, average size 50μm) and titanium(99.9%, average size 50μm) were mixed so as to give an average composition of $Ti_{51}Al_{49}$. Since the composition is chosen as so-called a neutron zero scattering alloy, only the concentration-concentration correlation function can be extracted by an advantage of neutron diffraction. MA was carried out in a conventional ball-milling apparatus, where the rotating speed is 110 rpm, under the Ar gas atmosphere.

Figure 1 shows the X-ray diffraction patterns before and after MA for 400 and 800 hours. Braggpeaks of the fcc-Al crystal disappeared and those of hcp crystal remain but broaden and slightly shift to the higher angle side after 400 hours of milling. This hcp crystal means Ti_3Al-type crystal containing excess Al element. After 800 hours of MA a halo pattern characteristic of an amorphous phase can be observed. The results clearly indicate that the amorphization proceeds after formation of the Ti_3Al-type (=$(Ti,Al)_3Al$) crystal.

Figure 2 shows the radial concentration correlation function RCF(r) observed by neutron diffraction for the $(Ti,Al)_3Al$ crystal and the $Ti_{51}Al_{49}$ amorphous alloy. The negative peak at 2.8 Å in both RCF(r) reflects the formation of the unlike atom correlation between Al and Ti atoms in the nearest neighbor distance and its position coincides well with that of the first Al-Ti atom pair in the Ti_3Al crystal. This result strongly suggests that the atomic arrangement in the nearest neighbor of the $Ti_{51}Al_{49}$ amorphous alloy is much similar to that of the Ti_3Al crystal due to a strong chemical affinity between Al and Ti atoms. The difference of the atomic arrangement between the $Ti_{51}Al_{49}$ amorphous alloy and the Ti_3Al crystal exists in the region over the second nearest neighbor as shown in Fig. 2.

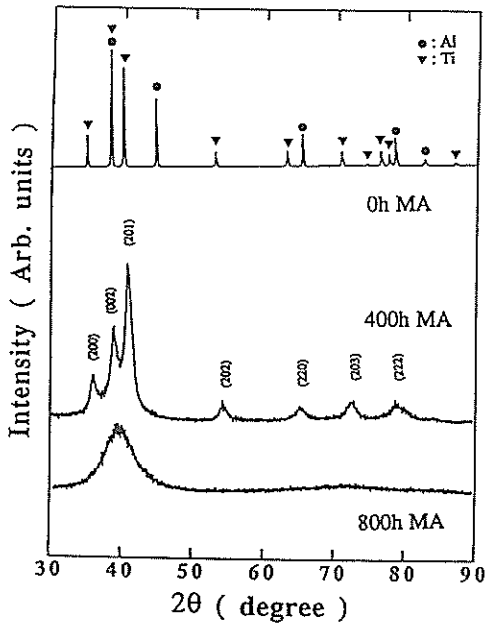

Fig. 1 X-ray diffraction patterns of $Ti_{51}Al_{49}$ powders after 0, 400 and 800 hours of MA.

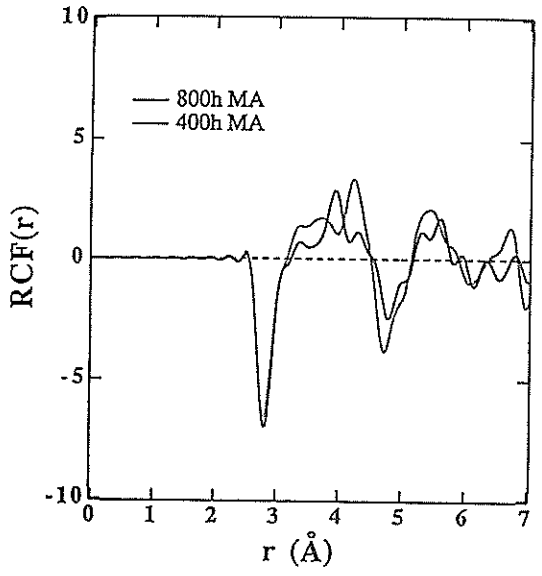

Fig. 2 The radial concentration correlation function RCF(r) of the $(Ti,Al)_3Al$ crystal and the $Ti_{51}Al_{49}$ amorphous alloy.

Structural Observation During MA Process for the Immiscible Mg-Ti System

T. Fukunaga, K. Okasaka, M. Misawa* and U. Mizutani

Department of Crystalline Materials Science, Nagoya University, Furo-cho, Chikusa-ku, Nagoya 464
*National Laboratory for High Energy Physics, 1-1 Oho, Tsukuba-shi, Ibaraki 305

The mechanical alloying(MA) has been considered to be driven by two possible processes: one is an energetically down-hill process driven by chemical reaction between the atoms of different species and the other an energetically up-hill process driven by accumulating strain and defects. The amorphization subjected to MA in the Cu-Ta system with a positive heat of mixing (ΔH_{mix}=2kJ/mol), which is characterized by up-hill process, has been reported from the viewpoint of the thermodynamics, atomic structure and electronic states[1,2,3]. In this report, we present the structural change subjected to MA in the Mg-Ti system with a larger positive heat of mixing(ΔH_{mix}=16kJ/mol) than that of the Cu-Ta system.

Pure elemental powders of magnesium(99.9%, average size 750μm) and titanium(99.9%, average size 50μm) were mixed so as to give an average composition of $Ti_{62}Mg_{38}$. Since the composition is chosen as so-called a neutron zero scattering alloy, only the concentration-concentration correlation function can be extracted by an advantage of neutron diffraction when the mixing goes on into an atomic level. MA was carried out in a conventional ball-milling apparatus, where the rotating speed is 110 rpm, under the Ar gas atmosphere.

Figure 1 shows the Bhatia-Thornton type structure factor S(Q) observed by neutron diffraction for $Ti_{62}Mg_{38}$ powders after 0, 800 hours of MA. No clear Bragg peak is observed in S(Q) of the MA800h sample. However, the X-ray diffraction patterns show the formation of a HCP-type solid solution and the amorphization could not be detected. A small angle scattering definitely became observed after 800 hours of MA, indicating concentration fluctuations, as shown in Fig.1.

Figure 2 shows the Bhatia-Thornton type radial distribution function G(r) of $Ti_{62}Mg_{38}$ powders after 0, 800 hours of MA. A positive peak is seen at the nearest neighbor in G(r) of the MA800h sample. This result and the small angle scattering in S(Q) teach us that there is little formation of the unlike atom correlation between Ti and Mg atoms during milling and so the preference for like atom neighbors yields the concentration fluctuation in the $Ti_{62}Mg_{38}$ powders after 800 hours of MA

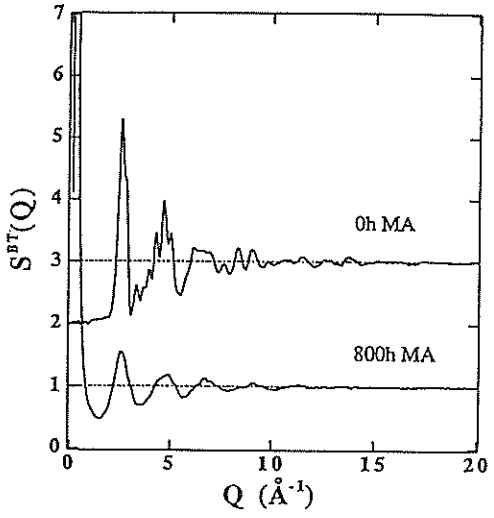

Fig. 1 Bhatia-Thornton type structure factor S(Q) observed by neutron diffraction for $Ti_{62}Mg_{38}$ powders after 0, 800 hours of MA

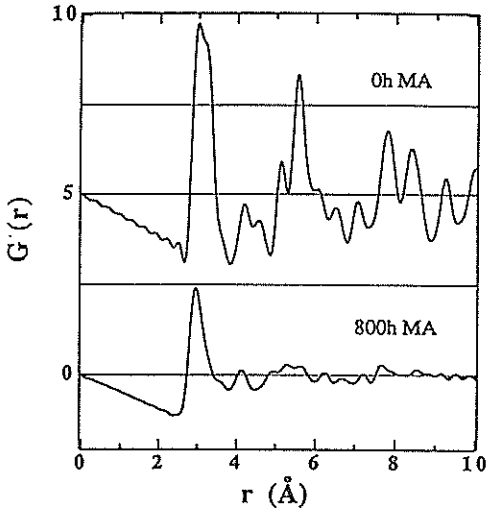

Fig. 2 Bhatia-Thornton type radial distribution function G(r) of $Ti_{62}Mg_{38}$ powders after 0, 800 hours of MA

References

1) T. Fukunaga, T. Nakamura, K. Suzuki and U. Mizutani, J. Non-Cryst. Solids 117/118, 700 (1990)
2) C.H. Lee, M. Mori, T. Fukunaga, K. Sakurai and U. Mizutani, Mater. Sci. Forum 88-90, 399 (1992)
3) U. Mizutani,C.H. Lee, T. Fukunaga, M. Takaki and K. Tanaka, Mater. Sci. Forum 88-90, 407 (1992)

Small-Angle Thermal Neutron Scattering from a Crown Ether 18-Crown-6 Molecule in Heavy Water

KAZUHIKO ICHIKAWA, TETSURO YAMANAKA, AND NOBUO NIIMURA*

Department of Chemistry, Hokkaido Univ., Sapporo 060
*Laboratory of Nuclear Science, Tohoku Univ., Sendai 980

An important consideration in understanding the recognition of metal ions by macrocyclic hosts is concerned in the change of the conformations between the free host and the metal-ion complex. The scattering function I(Q) measured in the Q range 10^{-2}-10^{-1}Å^{-1} by using the small-angle neutron scattering installed at thermal neutron sources (SANST) was different from that in the Q range 10^{-4}-10^{-3}Å^{-1} by the conventional installed at cold neutron sources (SANSC). This paper will give preliminary results and analyses of the scattering data for a typical macrocyclic host of crown ether 18-crown-6 (18C6) in solution.

Experimental

Materials: 18C6 was recrystallized from hexanes dried in a vacuum desiccator.
Diffracation measurements: a SANST experiment was performed on 18C6+D_2O solutions by using the time-of-flight spectrometer named as WIT, installed onto a thermal neutron beam line.

Results and Analyses

Guinier plots were derived from the scattering functions I(Q) for 18C6 in heavy water with the different concentrations. The abrupt decrease of I(Q) at very low Q may originate from the intermolecular interaction because of the high concentration at 444 mg 18C6/ml. The radius of gyration Rg for a 18C6 molecule is calculated by using a least-squares fitting of Guinier plots in the Q range 0.1-0.3 Å^{-1} at the different concentrations of 18C6; Rg is equal to 3.9±0.3 Å. If a 18C6 molecule in a queous solution is assumed to be of ellipsoid with semiaxes a, b, and c, Rg is given by $Rg^2=(a^2+b^2+c^2)/5$. With the help of CPK molecular model and the crystal structure of 18C6, a, b, and c are roughly evaluated to be 4.5, 4.5 and 6.0 Å, respectively and Rg becomes equal to 4 Å.

Comparisons of the crystal structure of the uncomplexed host 18C6 with that of its Na^+ complex indicate that the complexing act must be accompanied by host reorganization and desolvation in aqueous solutions. Thus, we can expect the effect of the host reorganization on Rg.

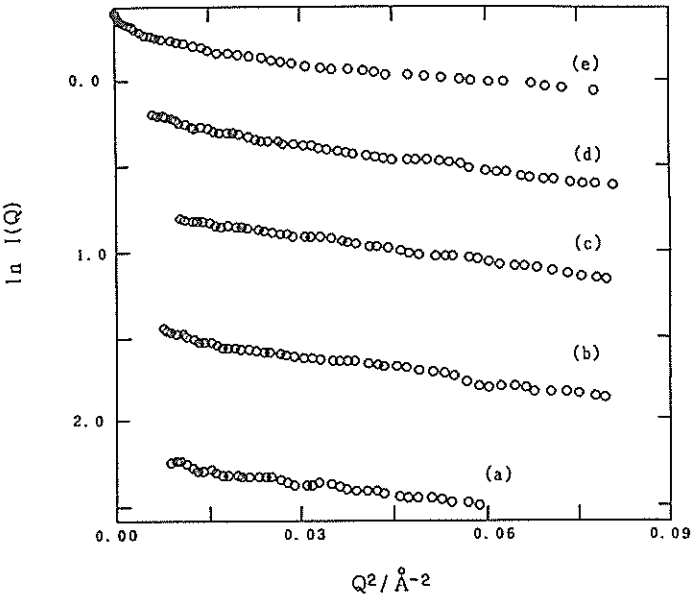

Fig. 1 Guinier plot of a host 18C6 molecule in the heavy water for the different concentrations (a) 27.8 mg 18C6/ml, (b) 55.5 mg/ml, (c) 111 mg/ml, (d) 222 mg/ml and (e) 444 mg/ml.

Structure of liquid CCl_4 near the liquid-gas critical point

H. Akatsuka, M. Misawa*, T. Fukunaga and U. Mizutani

Department of crystalline Materials Science, Nagoya Univ., Furo-cho, Chikusa-ku, Nagoya, 464
*National Laboratory for High Energy Physics, 1-1 Oho, Tsukuba-shi, Ibaraki 305

Previously we measured the structure factors Sm(Q) of liquid carbon tetrachloride CCl_4 in the temperature range from -20 to 160°C[1]. The aim of the present experiment is to obtain the $S_m(Q)$ of liquid CCl_4 at the higher temperature close to the critical point by using the HIT and SAN instruments. The measurements were carried out at 20, 195, 215, 235, 255 and 275°C for the liquid and at 275°C for the gas along the liquid-vapor coexisting curve. Figure 1 shows the coexisting curve on the P-V diagram and experimental points. The critical temperature and pressure are T_c=283.1°C and P_c=45atm.

The sample was kept in the quartz glass cell (5.7mm in inner diameter and 2.0mm in wall thickness) instead of the Ti-Zr null alloy cell used in the previous experiment, because the alloy was chemically attacked by the liquid CCl_4 above 200°C. Figure 2 shows the diffraction pattern from the sample in the cell and that from the empty cell at 20°C. We confirmed that the scattering intensity from the cell could be subtracted with sufficient accuracy, since the $S_m(Q)$ of the liquid at 20°C obtained in this work is in good agreement with the previous one[1] within experiment error. The experimental $S_m(Q)$'s are shown in Fig.3.

Since the HIT instrument can not observe the $S_m(Q)$ in the lower Q region, the lower Q part of the $S_m(Q)$ was measured by using the SAN instrument.

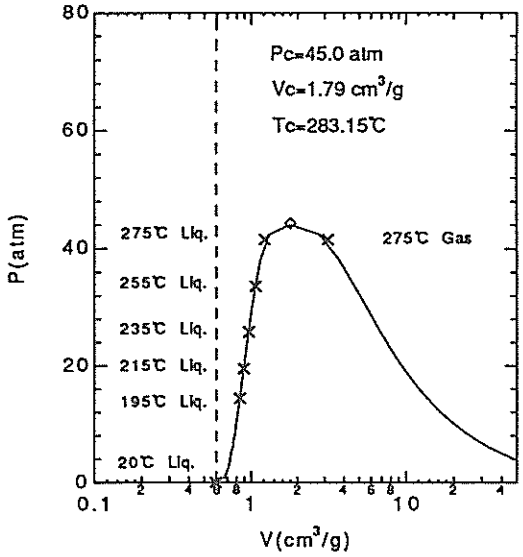

Fig. 1 The liquid-vapor coexisting curve and the experiment points.

Both patterns were joined at the Q region near 0.6A^{-1}. The details of the SAN experiment and data analysis are given in a separate report [2].

Some characteristic features of temperature dependence of the $S_m(Q)$ are observed: (1) the first peak becomes broader and shifts toward the lower Q region as temperature is raised; (2) a small peak located about 2.2A^{-1} and a valley following, which are related to the orientational correlations, also become broad ; and (3) the small angle scattering is getting greater and greater over 200°C. The characteristics (1) and (2) are already observed at lower temperature[1].

The radial distribution functions obtained by Fourier transform of the experimental $S_m(Q)$'s truncated at 20A^{-1} are compared in Fig.4. The intramolecular structure does not depend largely on temperature, while the intermolecular structure depends on temperature and the number of neighboring molecules is decreasing as temperature increases.

In a previous report[1] it was found that the orientational correlation between CCl_4 molecules exists in the liquid even at 160°C. It may be interesting to examine whether or not the orientational correlation

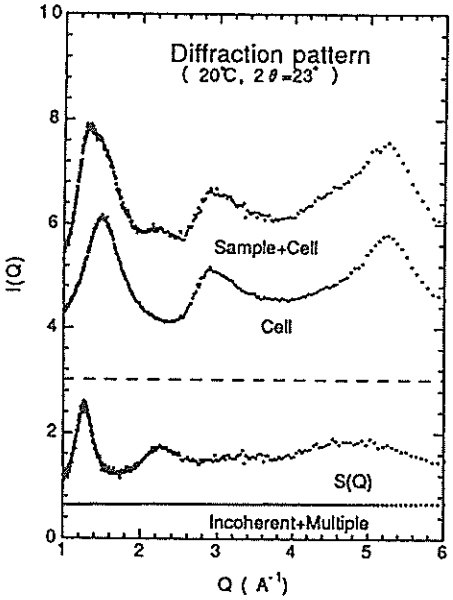

Fig. 2 A comparison of the experimental S(Q) with the experimental diffraction patterns from the sample plus cell and from the empty cell. The latter two curves are shifted in vertical scale by 3.0. Estimated incoherent and multiple scattering are also shown.

still exists in the liquid neat the critical point. The $S_m(Q)$ can be written as

$$S_m(Q)=S_m^u(Q)+\Delta S_m(Q),$$

where $S_m^u(Q)$ is a structure factor for the liquid of completely uncorrelated molecules and $\Delta S_m(Q)$ is a correction for the orientational correlation. $S_m^u(Q)$ is given by

$$S_m^u(Q)=F_1(Q)+F_u(Q)(S_c(Q)-1),$$

where $F_1(Q)$ and $F_u(Q)$ are intramolecular and intermolecular form factors, respectively. $F_1(Q)$ is experimentally determined from the experimental $S_m(Q)$ in a high Q region. $S_c(Q)$ is a molecular center structure factor. Figure 5 compares $S_m(Q)$'s of the liquid measured at 20 and 275°C and that of the gas at 275°C with $F_1(Q)$ and $F_u(Q)$. About the liquid at 20°C, the measured $S_m(Q)$ and $F_1(Q)$ do not coincide with each other in the range of Q from 2 to 3.2A^{-1}, where $F_u(Q)$ is very small. Therefore, the orientational correlation exists in the liquid at 20°C as reported previously[1]. About the liquid at 275°C, we still find discrepancy between $S_m(Q)$ and $F_1(Q)$ in the same Q region, suggesting an existence of the orientational correlation in the liquid even at 275°C. On the other hand $S_m(Q)$ of the gas at 275°C is similar to $F_1(Q)$ in the Q region where $F_u(Q)$ is very small. Therefore, we can conclude that the orientational correlation still exists in liquid CCl_4 near the critical point while it does not in the gaseous state near the critical point.

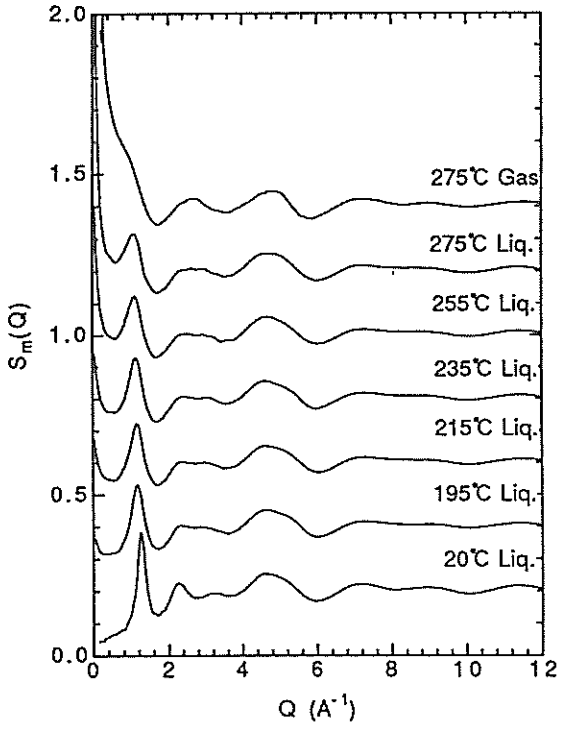

Fig. 3 Experimental structure factors $S_m(Q)$ of the liquid at 20, 195, 215, 235, 255, 275°C and that of the gas at 275°C.

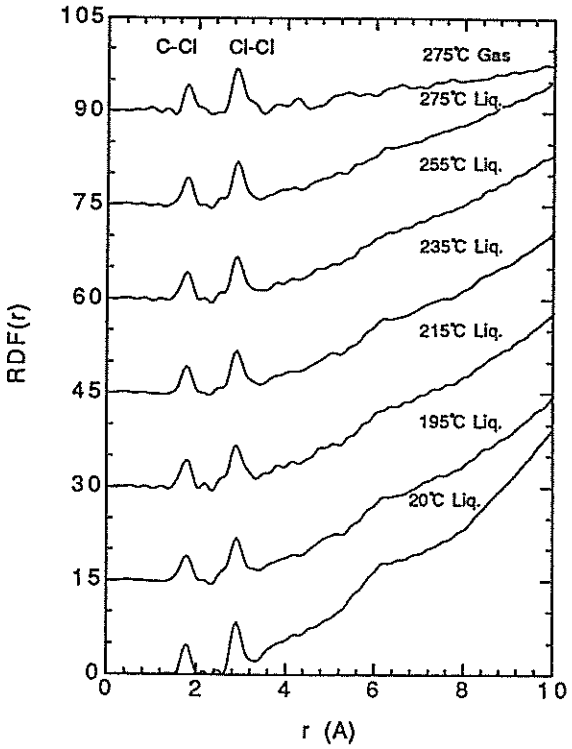

Fig. 4 Experimental radial distribution functions of the liquid at 20, 195, 215, 235, 255, 275°C and that of the gas at 275°C.

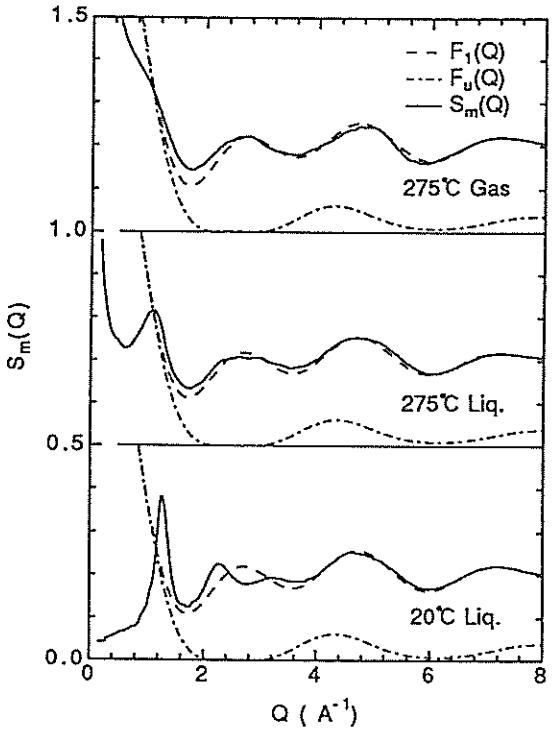

Fig. 5 Experimental structure factor $S_m(Q)$, intramolecular form factor $F_1(Q)$, and intermolecular form factor for uncorreleted molecules $F_u(Q)$.

References

1) M.Misawa,J.Chem.Phys.91 (1989) 5648

2) H. Akatsuka et al. KENS REPORT-IX

Small angle scattering measurement on liquid CCl_4 near the critical point

H. Akatsuka, M. Misawa*, T. Furusaka*, Y.Yoshimura**, T. Fukunaga and U. Mizutani

Department of crystalline Materials Science, Nagoya Univ., Furo-cho, Chikusa-ku, Nagoya, 464
*National Laboratory for High Energy Physics, 1-1 Oho, Tsukuba-shi, Ibaraki 305
**Department of Science and Technology, Nihon Univ., Surugadai, Chiyoda-ku, Tokyo, 101

During the measurement of S(Q) by use of the HIT instrument[1], small angle scattering was observed from the liquid CCl_4 above 200°C. We intended to make more accurate measurements on the small angle scattering by using the SAN instrument. The measurements were carried out for CCl_4 both in the liquid and gaseous states along the liquid vapor coexisting curve close to the critical point. The critical temperature (T_c) and pressure (P_c) of CCl_4 are T_c=283.1°C and P_c=45atm. Experimental structure factors S(Q) for the liquid at 195, 215, 235, 255 and 275°C and for the gas at 275°C are shown in Fig.1. Small angle scattering was observed even at 195°C which is far below the critical point, and increased with increasing temperature.

According to the Ornstein-Zernike approximation theory, S(Q) due to density fluctuations near the critical point is given by a Lorentzan,

$$S(Q)=S(0)/(1+\xi^2Q^2),$$

where ξ is a correlation length which characterizes the density fluctuations. Near the critical point, the small angle scattering is much stronger than the scattering intensity due to the atomic scale structure. On the contrary in the present case, small angle scattering is not so large that we can not neglect the scattering intensity from the atomic scale structure. It is, however, hard to estimate the latter contribution accurately. Therefore we simply extrapolated the value of S(Q) measured by HIT at the higher Q region, and subtracted the extrapolated value from the value of S(Q) measured by SAN.

Ornstein-Zernike plots, i.e. 1/S(Q) vs Q^2, are shown Figure 2. The value of ξ calculated from the plots increases with increasing temperature; 7.7 A at 215°C and 16.8 A at 275°C for the liquid and 17.5 A at 275°C for the gaseous state. The value of ξ may have some ambiguity because of the reason described above, but we believe the order of the value is meaningful. Since the effective diameter of CCl_4 molecules is about 5A, the present values of ξ correspond to the several molecules.

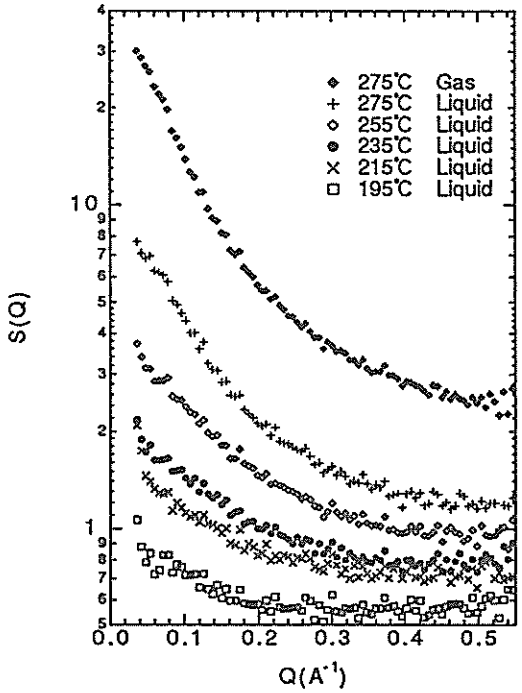

Fig. 1 Logarithmic plots of the experimental structure factor S(Q).

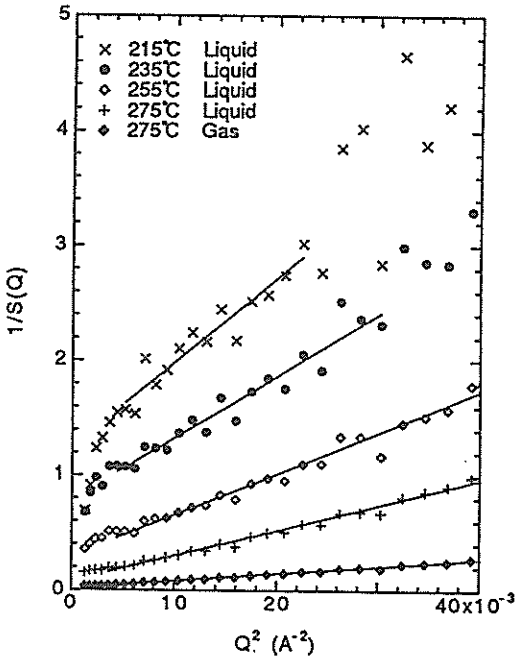

Fig. 2 Ornstein-Zernike plots, 1/S(Q) vs Q^2.

Reference
1) H. Akatsuka et al. KENS REPORT-IX

Structure of liquid SbX_3 (X=Cl, Br and I)

M. MISAWA and T. FUKUNAGA*

National Laboratory for High Energy Physics, 1-1 Oho, Tsukuba-shi, Ibaraki 305
*Department of Crystalline Materials Science, Nagoya University, Nagoya 464

Structure factors S(Q) of liquid antimony trihalides SbX_3 (X=Cl, Br and I) have been measured by using HIT instrument. Since the $SbCl_3$ molecule has a trigonal pyramidal shape in the gaseous state and a large electric dipole moment (3.93 Debye), the local structure of liquid SbX_3 is expected to be largely affected by both the anisotropic molecular shape and strong dipole-dipole interactions between the molecules.

The structure factors S(Q) of liquids SbX_3 (X=Cl, Br and I) measured near their melting points are shown in Fig.1.

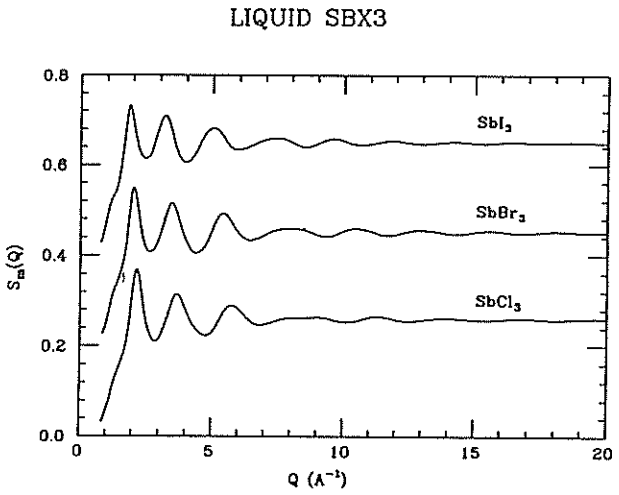

Fig. 1 Structure factors S(Q) of liquid antimony trihalides: liquid $SbCl_3$ at 80°C, liquid $SbBr_3$ at 110°C and liquid SbI_3 at 180°C.

Figure 2 shows the radial distribution functions RDF(r) of the liquids obtained by Fourier transform of the experimental S(Q)'s. The first peak is clearly separated from other atomic distributions in each of the RDF(r) curves. This experimental fact as well as the characteristic behavior of S(Q)'s in the high Q region concluded that the liquids consist of trigonal pyramidal molecules. Analysis of the present S(Q) combined with the X-ray S(Q)[1] by using the same method[2] as used for simple molecular liquids suggests that there are at least two different orientational correlations in the $SbCl_3$ liquids: one is a parallel orientation in which the pyramidal axis (C_3 axis) of one molecule is nearly parallel to that of the neighboring molecule; and another is an anti-parallel orientation in which the axis is nearly anti-parallel to the neighboring one. Strong dipole-dipole interaction expected for SbX_3 molecules as well as the pyramidal shape of the molecules may play an important role in these characteristic orientations of SbX_3 molecules in the liquid state.

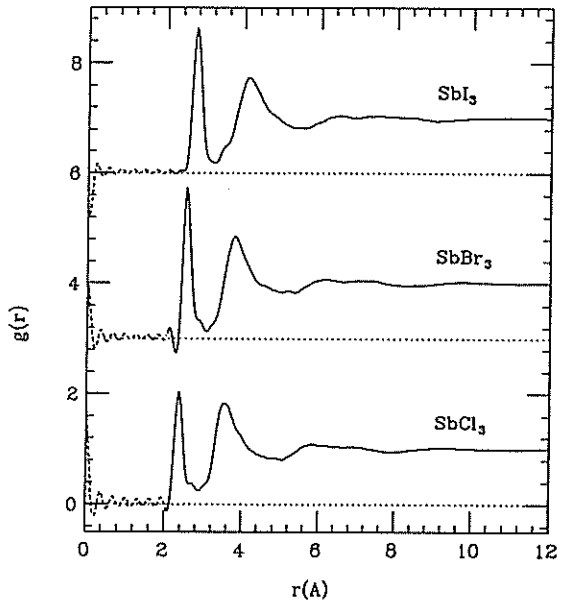

Fig. 2 Radial distribution functions RDF(r) of liquids antimony trihalide SbX3 (X=Cl, Br and I).

References

1) R.Triolo and A.H.Narten, J. Chem. Phys. 69, 3159 (1978)
2) M. Misawa, J. Chem. Phys. 90, 6563 (1989)

Structural analysis of liquid tellurium by short chain model

M. MISAWA

National Laboratory for High Energy Physics, 1-1 Oho, Tsukuba-shi, Ibaraki 305

Structure factors S(Q) of liquid tellurium (Te) were measured at 490, 670 and 800°C by using the HIT instrument. The local structure of liquid Te as a function of temperature has received considerable attention because of its characteristic behavior regarding electronic and thermodynamic properties. A structural evolution from a twofold atomic configuration to a threefold one with increasing temperature was proposed as being a structure model of liquid Te so far. Another possible structural model may be a short-chain model, since the Te atoms form infinite helical chains in the crystalline state. The latter model has not been examined in detail, however. The aim of this study is to examine experimentally the short-chain model.

Figure 1 shows the experimental structure factors S(Q) of liquid Te. Figure 2 shows a pair distribution function g(r) of liquid Te at 490°C.

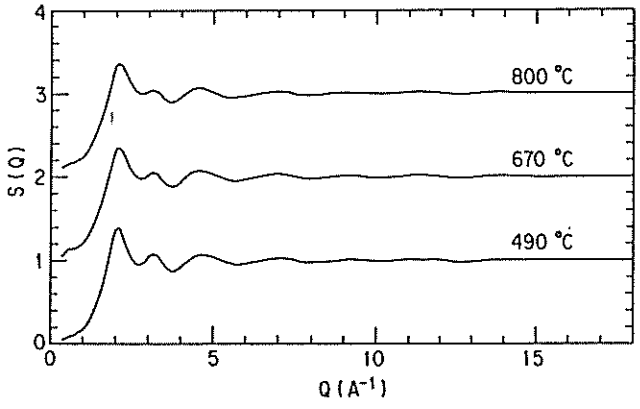

Fig. 1 Structure factors S(Q) of liquid tellurium at 490, 670 and 800°C.

The S(Q) and g(r) are analyzed in a following way: Te_n long chains are decomposed into Te_2 dimers; then the dimers are distributed at random; finally they are repolymerized into short chains and redistributed so as to reproduce the experimental S(Q) and g(r). The average length of the short chains and the interchain configuration are fitting parameters. The g(r) calculated by the above-mentioned method is shown by a dotted curve in Fig.2 in comparison with the experimental one (solid curve).

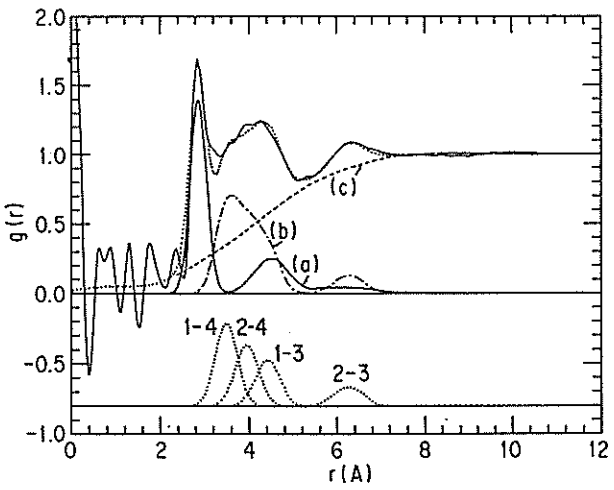

Fig. 2 Comparison of the experimental pair distribution function g(r) (solid curve) with the fitted one (dotted curve) for liquid tellurium at 490°C. Curve (a) is an intrachain distribution, (b) the interchain distribution between correlated chains, and (c) the interchain distribution between uncorrelated chains.

The calculated g(r) is composed of three different distribution functions (a), (b) and (c) as shown in Fig.2; the curve (a) is an intrachain atomic distribution; the curve (b) is an interchain atomic distribution for chains correlated in orientation; and the curve (c) is that for uncorrelated chains. The mean chain length <L> evaluated from the intrachain distribution (curve (a)) obtained at each temperature is rather short: about 14, 8, and 6 (Te atoms/chain) at 490, 670 and 800°C, respectively. The temperature dependence of <L> suggests that the enthalpy of scission of a Te-Te bond in the liquid state is about 14.5kcal/g-atom (0.63eV). The details will be reported in a separate paper[1].

References

1) M. Misawa, J. Phys.:Condensed Matter (at press)

Pattern Formations in Polymer-Surfactant Systems

T.KAWAKATSU,[1,2] K.KAWASAKI,[1,2] M.FURUSAKA,[3]
H.OKABAYASHI[4] and T.KANAYA[5,6]

[1] *Department of Physics, Kyushu University 33, Fukuoka 812*
[2] *IFF Theorie III, Forschungszentrum Jülich, 5170 Jülich, Germany*
[3] *BSF, National Laboratory for High Energy Physics, Tsukuba 305*
[4] *Department of Applied Chemistry, Nagoya Institute of Technology, Nagoya 466*
[5] *The Institute for Chemical Research, Kyoto University, Uji 611*
[6] *Max-Planck Institut für Polymerforschung, W-6500 Mainz, Germany*

Dynamics of phase separation processes is one of the widely investigated problems using the neutron scattering technique. Use of the polymer systems as a target enabled us to study the dynamics of pattern formation processes associated with the phase separation throughout the whole time range from the early stage to the late stage, because the dynamics is considerably slowed down in such polymer systems.

Another important method to investigate the problem is the computer simulation technique. Considering the highly complex nature of the polymer systems, one can understand that theoretical approaches to the dynamics of polymer systems require extensive computer simulations using appropriately simplified models which retain some minimal features of the system. The validity of such computer simulations as well as the modelling can be checked by comparing the simulation results with experimental results like neutron scattering experiments.

In this article, we report the results of the computer simulations on the phase separation dynamics of polymer blends to which an amphiphile, *i.e.* a surfactant, is added. In the polymer case, the most familiar example of such amphiphiles is the block copolymer, which is composed of two distinct polymer chains connected at the ends. If an A-b-B block copolymer is dissolved into an immiscible A/B homopolymer mixture, the block copolymer chains are adsorbed onto interfaces between A-domains and B-domains and lower the interfacial tension considerably. In view of the fact that the driving force of the phase separation is the interfacial tension, the added blockcopolymer is expected to have an important effect on the phase separation dynamics. Now we consider an A/B/A-b-B three component mixture, which is quenched from above the critical temperature down into the coexistence region. The dynamics of the phase separation should be discussed for the early stage and the late stage separately. As we will see below, the amphiphilic effects in these two stages act in different manners.

Our computer simulations are based on the *Hybrid Model*, where the binary polymer mixture is described by a continuous scalar field, *i.e.* the local composition, while the blockcopolymer is described by discrete molecule. Since the details of this model have already been described elesewhere,[1] we only give some important results and also give a comparison between the simulation results and experimental results. Computer simulations have been done for a 2-dimensional system without the hydrodynamic interactions. Such a situation can be experimentally realized by a thin layer of a polymer melt mixture containing block copolymers placed between two parallel glass plates (Hele-Shaw cell). In Fig.1, we show a snapshot picture of the system obtained by the computer simulation. The shaded regions and the white regions show A-domains and B-domains, respectively. A block copolymer molecule is shown by a small square with a short line, which points the direction from

the center of the B-subchain to the center of the A-subchain. In this figure, one can see a bicontinuous domain structure similar to those found in real polymer systems.

First, we consider the early stage dynamics. It is well known for polymer systems that the scattering structure function grows exponentially in time in the very early stage, *i.e.*:

$$S(k,t) \sim \exp(\lambda t) \qquad (1)$$

where $S(k,t)$ is the spherically averaged scattering function (or circularly averaged scattering function in the present 2-d case) and λ is the growth rate. Such a behavior can be understood by the so-called Cahn's linear theory of fluctuations. A similar analysis for the Hybrid Model[2] tells us that the growth rate λ is increased by the dissolved block copolymer. This acceleration originates from the composition fluctuation in the initial homogeneous state induced by the block copolymer chains, which is due to the amphiphilic nature of the block copolymer. Such an acceleration effect is detectable only when the gyration radius of the block copolymer chain is the same order as the charcteristic wave length of the initial phase separation. When the block copolymer is not long enough, it acts as an impurity, and deccelerates phase separation.

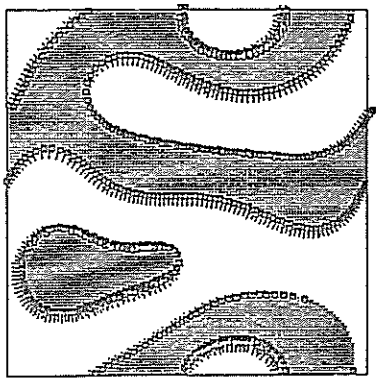

Fig.1 A bicontinuous domain structure obtained by the computer simulation using the Hybrid Model.

In Fig.2, we show the temporal evolutions of the peak height of $S(k,t)$ in the very early stage obtained from the computer simulation using the Hybrid Model. One can find the acceleration of the phase separation due to the added block copolymer as is predicted in the linear analysis. Such an acceleration has not been found in real experiments,[3] where the chain length of the block copolymer seems to be too short to detect the amphiphilic effects.

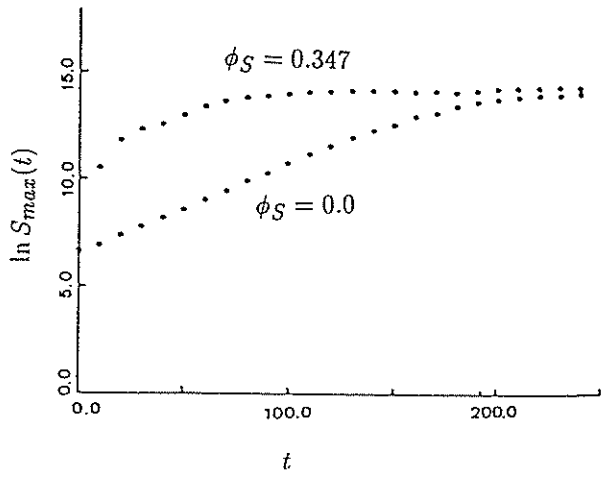

Fig.2 Temporal evolution of the peak height of $S(k,t)$ calculated with the Hybrid Model. ϕ_S shows the number density of the block copolymer.

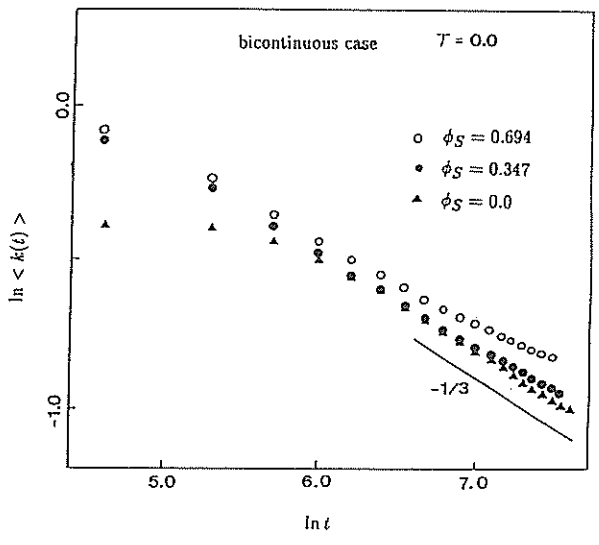

Fig.3 Temporal evolution of $< k(t) >$ for different values of the block copolymer density.

Next, we consider the late stage dynamics.[4] In Fig.3, we show the temporal evolution of the characteristic wave number $< k(t) >$, which is defined as the first moment of $S(k,t)$. When there is no added block copolymer, $< k(t) >$ decreases as $t^{-1/3}$, which is peculiar to the spinodal decomposition without hydrodynamic effects. As the amount of the added block copolymer is increased, a slowing down of the coarsening takes place and the growth exponent is considerably reduced in the very late stage. Such a slowing down is also observed in a real experiment.[3]

We also found that the dynamical scaling holds in the late stage even in the case with the added block copolymers, where the scattering function $S(k,t)$ shows the following scaling behavior:

$$S(k,t) =< k(t) >^{-d} \tilde{S}(k/ < k(t) >) \qquad (2)$$

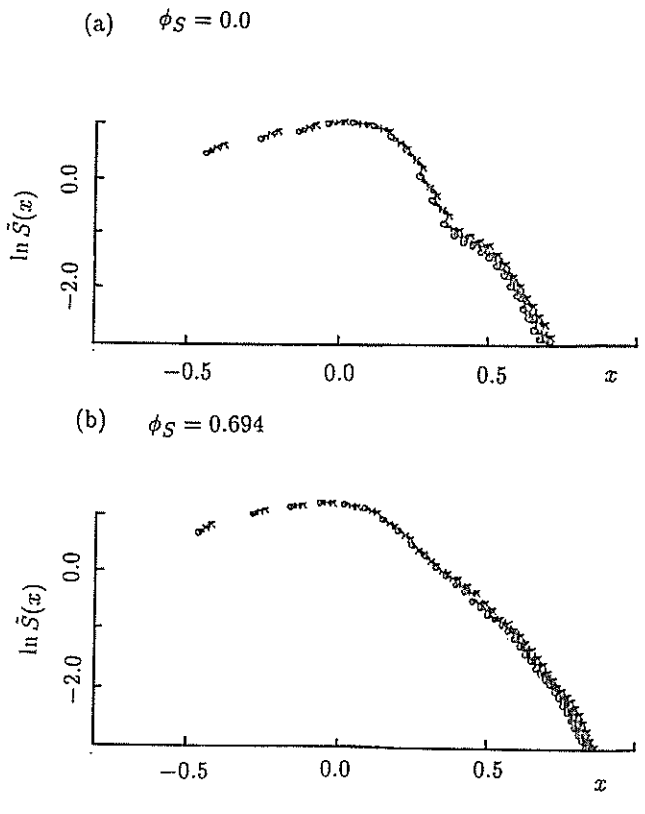

Fig.4 Scaled structure functions for (a) $\phi_S = 0.0$ and (b) $\phi_S = 0.694$ in double logarithmic polts.

where d is the dimensionality and $\tilde{S}$ is the so-called scaling function. In Fig.4, we give the scaling functions in the double logarithmic plots for (a) the case without block copolymer and for (b) the case with block copolymer added. In the case (a), one can see a second peak besides the main peak, which is regarded as a sign of the local periodic structures, like a local lamellar structures. On the other hand in (b), the main peak is broadened and the second peak becomes less pronounced. Such a broadning of the main peak can be understood as a consequence of the interfacial undulation due to the adsorbed block copolymers on the interfaces, which form an almost incompressible fluid layer.

In conclusion, we performed extensive computer simulations and investigated the early stage as well as the late stage dynamics of the phase separation of the systems containing amphi-philes. Pronounced effects of the amphiphilic nature have been found. Some predictions still have not been confirmed by real experiments and therefore further experimental studies on this problem are desired.

On the other hand, the present model need to be improved to be more realistic. For the Hele-Shaw cell, effects such as wetting of various components on glass plates have to be included. For 3-d systems, hydrodynamic effects are indispensable. These should be our next goal.

T.Kawakatsu was supported by the Yamada Science Foundation and IFF. He thanks Professor T.Hashimoto and Dr.K.Fuchizaki for discussions. K.K. and T.Kanaya were supported by the Alexander von Humboldt Foundation.

References

1) T.Kawakatsu and K.Kawasaki, *Physica* A **167**, 690 (1990).
2) T.Kawakatsu and K.Kawasaki, *J. Colloid Interface Sci.* **145**, 413 (1991), *ibid* 420.
3) T.Hashimoto, private communication.
4) T.Kawakatsu *et.al.*, unpublished.

Phase Structure Study of the Barium Ethyl(octyl)phosphate-Water System by Small Angle Neutron Scattering

H. OKABAYASHI, T. YOSHIDA, K. TAGA, H. HIRATA,
Y. YAMADA and M. FURUSAKA*

Department of Applied Chemistry, Nagoya Institute of Technology, Gokiso-cho, Showa-ku, Nagoya 466
** BSF, National Laboratory for High Energy Physics, 1-1 Oho, Tsukuba-shi, Ibaraki 305*

Recently, barium ethyl(octyl)phosphate (EOP), a new surfactant, has been synthesized.[1] EOP is a double chain anionic surfactant having a very short ethyl chain and a relatively long octyl chain. A structural ordering problem of the two chains in the EOP aggregates is particularly interesting.

In the present paper, we report the microstructure of aggregates in the EOP-water binary system studied by small angle neutron scattering (SANS).

A phase diagram of the binary EOP-water system is shown in Fig. 1. It consists of four regions (I, II, III and IV). In region I, a critical micelle concentration (CMC, 1.2wt%) was found, indicating the presence of a monomer ⇔ micelle equilibrium. Region II is a two-phase area in which regions I and III coexist. Region III is a homogeneous transparent solution, and the lamellar-like aggregates are preferentially stabilized in this region.[1),2)] However, in region III the monomers and micelles may also coexist in addition to the lamellar-like aggregates.

In region I, the EOP anions are in the monomer state below the CMC and a monomer ⇔ micelle equilibrium exists above this limit.

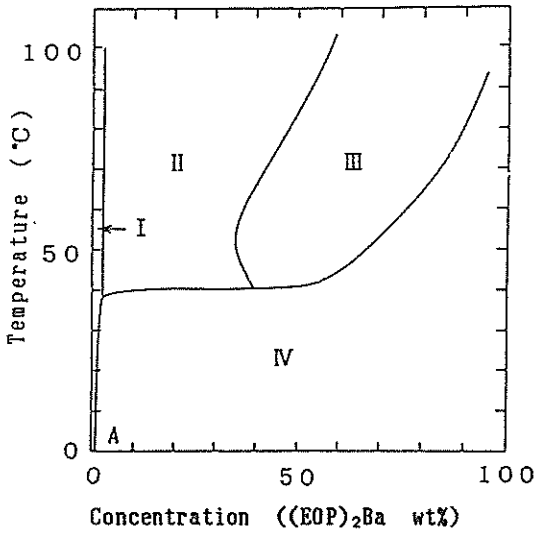

Fig. 1 Phase diagram of EOP-water system.

SANS spectra of the EOP1.2wt%-D_2O solution and the EOP2wt%-D_2O solution were measured in this region. For the EOP2wt% solution, the neutron scattering intensity (I(Q)) differs from that of the monomer solution (1.2wt%). A Guinier plot for the scattering of the 2wt% solution provided a straight line in the small Q region at around room temperature to 50°C. This observation indicates that the EOP micelles are mono-dispersed in region I. The I(Q) of the 2wt% EOP solution is shown in Fig. 2. Contributions from the monomers were subtracted using the scattering from the 1.2wt% solution.

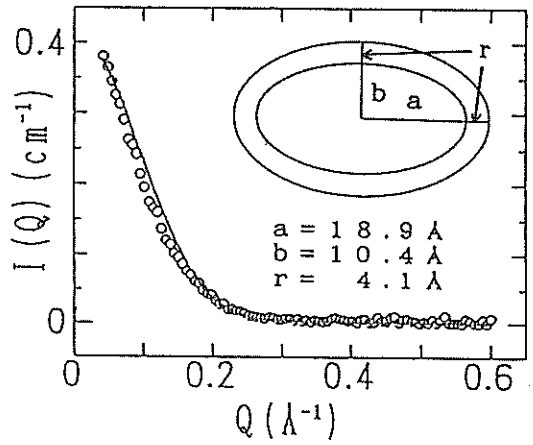

Fig.2 Observed (o) and fitted (solid line) SANS intensity profiles of EOP-D_2O (2wt%) at 323°K. Insert shows an EOP micellar model, which consists of a core of semimajor radius a, semiminor radius b, and a hydrophilic head layer (thickness:r). Geometric parameters of an EOP anion are as follows.

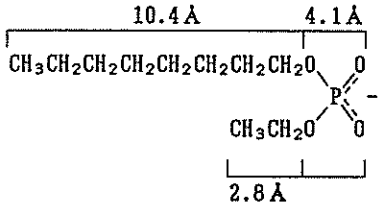

The I(Q) for the proposed micellar structure were calculated byequation (1) [3]

$$I(Q)=N_pP(Q)S(Q)\cdots(1)$$

where I(Q) is a neutron scattering intensity per unit volume, N_p the number of micelles per unit volume, P(Q) the form factor containing the effect of micellar size and shape, and S(Q) the interparticle structure factor. In the present study, S(Q) was assumed to be unity. To evaluate P(Q), an EOP micelle was assumed to be a prolate-ellipsoidal oil drop in a mono-dispersed state. Apparent molar volumes (V_a) of an EOP anion in water were measured by a Lipkin-Davison type pycnometer. V_a(EOP anion) = 347.14 Å^3, V_a(hydrocarbon part) = 310.52 Å^3 and V_a(polar part) = 36.62 Å^3 were used to calculate the P(Q). The calculated profile best-fitted with the observed intensity pattern is also shown in Fig. 2. It was estimated from the fit that an EOP micelle has an aggregation number of 50 and is prolate ellipsoid in shape. The micellar model is inserted in Fig. 2.

SANS spectrum in region III is shown in Fig. 3. The scattering intensities arising from monomers and micelles were subtracted. The best-fit profile using a randomly oriented paracrystal model [4] is also shown in the figure. The parameters obtained from the calculation are listed in Table I. The lamellar model and its structural parameters are shown in Fig. 4. The thickness of the hydrophilic layer implies that the layer contains the polar part of EOP molecules and a water-layer. The calculated value (13.7 Å) for the thickness of the hydrophobic layer is very close to the summation of the length of the octyl-chain and that of the ethyl-chain. It provides evidence that the hydrocarbon parts in the lamellar structure may be densely packed in a manner which alternatively combines ethyl and octyl groups.

In conclusion, the SANS intensity profiles of regions I and III were successfully explained by a prolate-ellipsoidal micelle having an aggregation number of 50, and the randomly oriented lamellar structure, respectively.

X-ray low-angle diffraction studies shows that the aggregate structure of EOP in region III strongly depends upon its concentration.[1] In order to elucidate the microstructure of aggregates in region III, concentration- and temperature-dependence of the SANS spectrum in this region are highly desirable.

wt%	d	L(O)	L(P)
65.0	26.6Å	13.7Å	12.9Å

Table. I Fitted values of the paracrystal parameters for the EOP65wt%-D_2O solution.
d :interlamellar distance
L(O):thickness of hydrophobic layer
L(P):thickness of hydrophilic layer

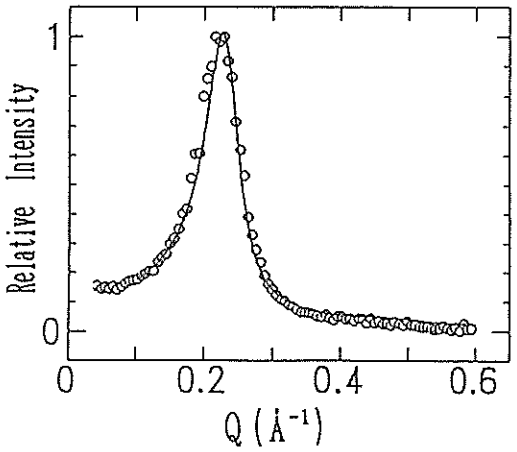

Fig.3 Observed (o) and fitted (solid line) SANS intensity profiles of EOP-D_2O (65wt%) at 323°K.

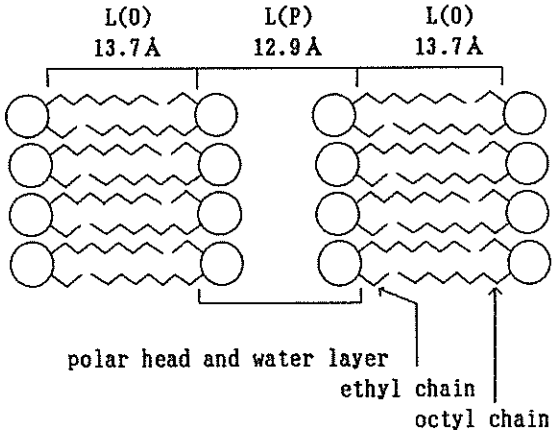

Fig.4 Lamellar model for aggregates and its structural parameters in region III.

References

1) T. Yoshida, K. Miyagai, S. Aoki, K. Taga and H. Okabayashi,
Colloid Polym. Sci., 269, 713 (1991).

2) T. Yoshida, K. Miyagai, K. Taga, H. Okabayashi and K. Matsushita,
Magn. Reson. in Chem., 28, 715 (1990).

3) T. -L. Lin, S. -H. Chen, N. E. Gabriel and M. F. Roberts,
J. Am. Chem. Soc., 108, 3499 (1986).

4) M. Kotlarchyk and S. M. Ritzau,

Structure Change of PVA Gel upon Heating

M. OHKURA, T. KANAYA , K. KAJI and M. FURUSAKA*

Institute for Chemical Research, Kyoto University, Uji, Kyoto 611
*National Laboratory for High Energy Physics, 1-1 Oho, Tsukuba-shi, Ibaraki 305

It is well known that solutions of poly(vinyl alcohol) (PVA) show a transition from sol to gel on cooling in various solvents. The PVA physical gels exhibit interesting mechanical properties and they are developed to important applications in industry. Recently, it was reported that PVA gels formed in mixtures of dimethyl sulfoxide (DMSO) and water show very interesting features, e. g., the gels obtained below 0°C are transparent, the elasticity is very high, and the gelation rate is very fast compared with the case of aqueous solutions[1]. However, the structure of the gels is not well understood from microscopic viewpoints. In this study, structural change of the PVA gel upon heating is investigated by small angle neutron scattering.

The gel sample was prepared as follows. PVA with degree of polymerization Pn=1640 was dissolved in a mixture of deuterated dimethyl sulfoxide (DMSO-d_6) and D_2O (60/40 vol/vol) in a sealed test tube at about 130°C in an autoclave to be homogenized. The PVA concentration is 5 g/dl. Before the measurements, the sample solution was heated in the test tube above 100°C for ca. 15 min, shaked well and transferred to quartz cells of 2 mm beam path, and then quenched to 23°C to allow to stand for 28 h. SANS measurements were made at 23, 40, 55, 70, 85 and 100°C. The sample was kept at the given temperature for more than 30 min. before the measurement. SANS measurements were carried out with the SAN spectrometer installed at the pulsed cold neutron source at KENS. A 2-D detector was located at the 3m-position, corresponding to the Q range of 0.01 to 0.2 $Å^{-1}$. The observed scattering intensity was corrected for the incident neutron spectrum, detector efficiency, sample transmission and background scattering.

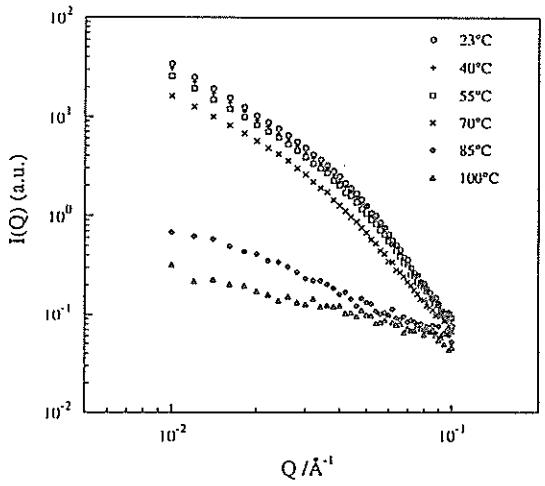

Fig.1. Small angle neutron scattering intensity I(Q) from the gel formed at 23°C as a function of temperature.

Incoherent scattering contribution from hydrogen atoms in the gel samples was evaluated by measuring the scattering intensity from methanol dissolved in the mixed solvent with the same hydrogen concentration as the gel samples.

Observed scattering intensity I(Q) is shown in Fig.1 as a function of temperature. The intensity I(Q) decreases gradually with increasing temperature up to 70°C and decreases drastically in the temperature range between 70°C and 85°C, and decreases slightly even above 85°C. Macroscopically the sample shows a transition from gel to sol at about 75°C. As reported in this volume[2], the Bragg peak intensity of PVA crystallites in the gel decreases with increasing the temperature and is no longer observed above 80°C. This suggests that the crystallites are dissolved

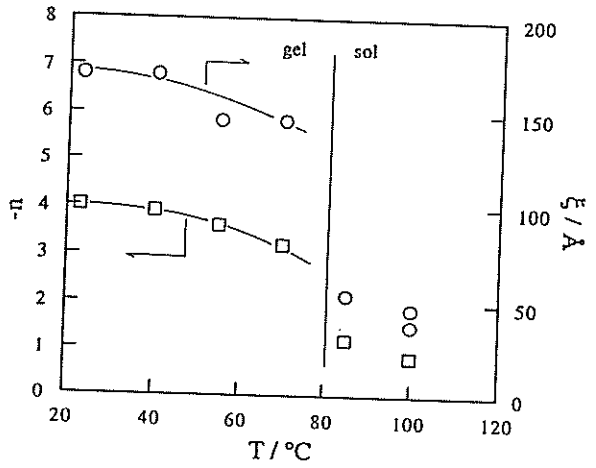

Fig.2. Temperature dependence of the correlation length x and the exponent (-n).

gradually with increasing temperature. Because the main contribution to I(Q) should be from crystallites, the decrease in intensity is due to the dissolution of them.

As reported before[3], I(Q) of the gel can be described by $I(0)/[Q^2\xi^2+1]$ in the Q ranges of 0.01 to 0.04Å^{-1} where ξ is a correlation length, and Q^n in the range of 0.05 to 0.1Å^{-1}. The correlation length and the exponent are shown in Fig.2. Both ξ and -n decrease gradually with increasing temperature and dropped around 80°C associated with the transition from gel to sol.

For the gel sample, the correlation length ξ is related to the distance between the the nearest neighboring crystallites and the exponent n to the surface fractal dimension Ds through Ds=n+6. The distance between the crystallites slightly decreases with increasing temperature and the surface fractal dimension changes from 2 to 3. It suggests that the smooth surface of the crystallites becomes rough with increasing temperature.

For the sol sample, the exponent n is no longer related to the surface fractal dimension Ds because Ds is lager than 3 (see Fig.2). The main contribution to I(Q) may be from the solutions but not from the crystallites. However, I(Q) at 85°C still shows stronger Q dependence and higher intensity than I(Q) at 100°C,. It indicats that the system contains some of large crystallites which are not dissolved even at 85°C.

Distance distribution functions P(r) for the gel and sol states were calculated by inverse Fourie transformation of I(Q) as shown in Fig.3. In the case of the gel, the two peaks or shoulders at about 70 and 220Å in P(r) have been assigned to the intra- and intercrystallite correlations, respectively. In order to separate the contributions from the intra- and inter-crystallites correlations, P(r) in the r-range smaller than 100Å was fitted with the theoretical function $P_{intra}(r)$. In the model calculation, it was assumed that shape of the crystallites are spheres and the radius distribution is Gaussian. In the case of 23°C, the average radius AR and the standard deviation σ were determined to be 77.1Å and 18.7Å, respectively. The radius distribution at 23°C is shown in Fig.4. For the fit at higher temperatures above 23°C, it was further assumed that the crystallites with radius less than lower limit radius LR(T) in the distribution at 23°C are all dissolved. In the case of 40°C, for example, the dissolved part of the crystallites is shown by shadow in Fig.4. LR(T) at 40, 55 and 70°C were calculated to give the best fit so as to P(r) in the r-range less than 100Å. The resulting LR(T) are 60, 70 and 79 Å for 40, 55, and 70°C, respectively (see Fig.4).

In Fig.3(a), the calculated $P_{intra}(r)$ and $P_{inter}(r)$ is shown in thin dotted lines and $P_{intra}(r)$ in thin dashed lines. It is noted that the peak position of $P_{inter}(r)$ are almost independent of temperature, suggesting that the characteristic distance between the nearest neighboring crystallites may not be changed upon heating. If the crystallites are randomly distributed in the system, the distance between the nearest neighboring crystallites should increase with temperature. Therefore, it is considered that in the gel there are clusters each of which consisits of crystallites larger than about 80Å (see Fig.4).

The distance distribution functions for the sol sample were also analyzed in the same way described above. The results are shown in

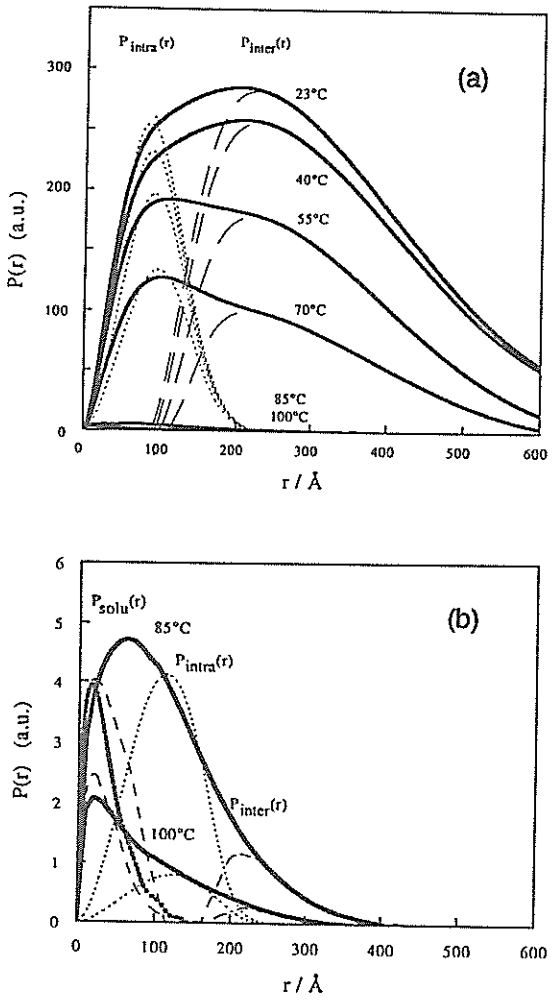

Fig.3. Distance distribution function P(r) as a function of temperature for the gel (a) and the sol (b) of PVA. Dotted and dashed lines are the distance distribution function due to the intra- and inter-correlations $P_{intra}(r)$ and $P_{inter}(r)$, respectively. For details, see text. Bold dashed line is P(r) of homogeneous PVA solution.

Fig.3(b). The lower limit radii LR(T) are 99 and 109Å for 85 and 100°C, respectively. The difference between P(r) and calculated $P_{intra}(r)$ shows two peaks at about 20 and 200Å. The peak at 200Å may correspond to the correlation $P_{inter}(r)$ between the nearest neighboring crystallites which still remain even above the macroscopic sol-gel transition temperature. $P_{inter}(r)$ for 100°C is negligibly small,

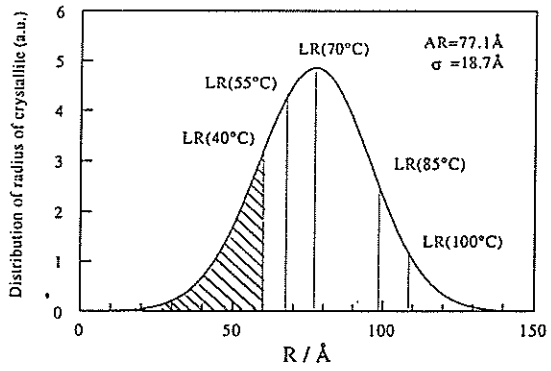

Fig.4. Distribution of the crystallite radius for the gel at 23°C. The lower limit radius LR(T) at each temperature is indicated in the figure.

suggesting that the crystallites are isolated in solution. The peak at about 20Å may come form solution part $P_{solu}(r)$ of the system because it is almost identical with P(r) of the solution, which is indicated by bold dotted line in Fig.3(b). The peak position of $P_{inter}(r)$ at 85°C and 100°C are almost identical with those evaluated for the gels. It is suggested that finite clusters of PVA chains, which may be formed at the early stage of the gelation, still remain even above macroscopic sol-gel transition temperature.

References

1) M. Ohkura, T. Kanaya, K. Kaji, Polymer in press.
2) T. Kanaya, M. Ohkura, K. Kaji, M. Misawa, in this volume.
3) T. Kanaya, M. Ohkura, K. Kaji, M. Furusaka, M. Misawa, H. Yamaoka, G.D. Wignall, Physica, B180&181, 549 (1992).

Structure of Crosslinking Points of Poly(vinyl alcohol) Gel

T. KANAYA, M. OHKURA, K. KAJI and M. MISAWA*

Institute for Chemical Research, Kyoto University, Uji, Kyoto 611
*National Laboratory for High Energy Physics, 1-1 Oho, Tsukuba-shi, Ibaraki 305

Structure of crosslinking points in physical gels is concerned to the whole physical quantities of the gels. Therefore, various methods have been applied to investigation of structure of the crosslinking points. Poly(vinyl alcohol) (PVA) is one of typical crystalline polymers so that the crosslinking points in the gel are believed to be crystalittes. However, it has never been confirmed directly so far. In this study, we have investigated the structure of crosslinking points in PVA gel by wide angle neutron scattering.

Deuterated atactic-poly(vinyl alcohol) (at-PVA-d_4) was employed for the scattering measurements. The number-average degree of polymerization is 2000 and the molecular weight distribution Mw/Mn is 2.01. The solvent used was a mixture of deuterated dimethyl sulfoxide (DMSO-d_6) and heavy water (D_2O) with the ratio of 60/40 by volume. The gel samples were prepared as follows. A given amount of at-PVA-d_6 was dissolved in the mixed solvent at about 130°C to be homogenized in a sealed glass tube. After the homogenization, the solution was transfered to a scattering sample cell and quickly quenched in a bath kept at 23°C and allowed to stand for 3 days and 20 days.

Wide angle neutron scattering measurements were carried out with the TOF type high intensity total scattering spectrometer HIT[1] installed at the pulsed thermal neutron source in KENS. The observed neutron scattering intensity were corrected for attenuation in both sample and cell, subtraction of cell intensity, normalization of the incident neutron spectrum and neutron emission delay time.

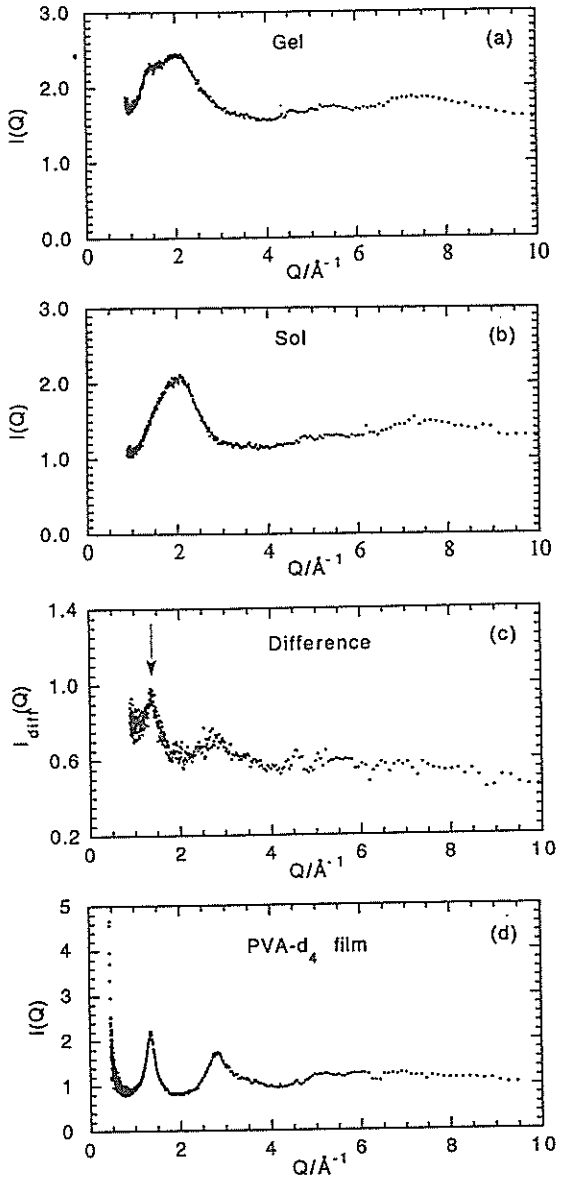

Fig. 1 Wide angle neutron scattering intensity I(Q). (a) at-PVA-d_4 gel, (b) solvent: mixture of DMSO-d6 and D2O (60/40 v/v), (c)difference: (a)-(b), (d) solid film of at-PVA-d4.

First of all, we conducted wide angle neutron scattering measurements on the at-PVA-d_4 gel with concentration of 10g/dl, which was obtained 30 days after quenching to 23°C from the homogeous solution. The observed scattering intensities I(Q)'s are shown for the gel and the solvent in Figs.1(a) and (b), respectively, in the Q range of 0.8 to 10 $Å^{-1}$. Both the scattering curves are very similar to each other especially in the Q range above 2.0$Å^{-1}$ while we can clearly recognize a weak shoulder at about Q=1.40 $Å^{-1}$ in the scattering curve of the gel, but it is absent in that of the solvent. We then subtracted the scattering intensity of the solvent from that of the gel taking into account the volume of solvent molecules replaced by PVA in the gel. The result of the subtraction is shown in Fig.1(c), where the strongest peak is observed at Q=1.39 $Å^{-1}$ which corresponds to the Bragg diffractions from (101) and (10$\bar{1}$) planes in PVA crystals. For comparison, scattering curve from a PVA-d_4 solid film measured by the HIT spectrometer is shown in Fig.1(d) . The difference scattering curve between the gel and solvent [Fig.1(c)] is basically identical with that of the solid film though the widths of the peaks of the gel are rather broader than those of the film. It is confirmed that in the PVA gel there do exist crystallites though it is not proved at this stage whether or not they are the cross-linking points in the PVA gel. It should be noted that the scattering curves at 23°C are almost identical for the gels obtained 30 days and 3 days after quenching to 23°C.

In order to confirm that the crystallites are the cross-linking points, wide angle neutron scattering measurements were conducted as a function of temperature, focusing the strongest Bragg peak at Q=1.39$Å^{-1}$. Temperature dependence of the scattering intensity I(Q) from the gel is shown in Fig.2 where the scattering intensity from the solvent at the corresponding temperature has been subtracted. The Bragg peak at Q=1.39$Å^{-1}$ is clearly observed at 23°C. The scattering intensity gradually decreases with increasing temperature and the Bragg peak

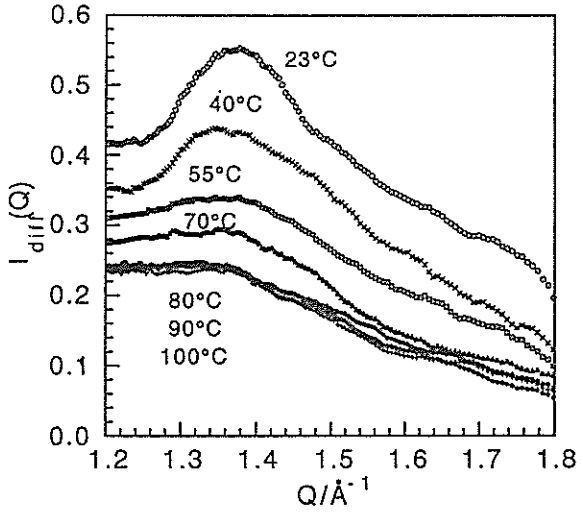

Fig.2. Wide angle neutron scattering intensity $I_{diff}(Q)$ of at-PVA-d_4 gels a function of temperature. The solvent contribution has been subtracted.

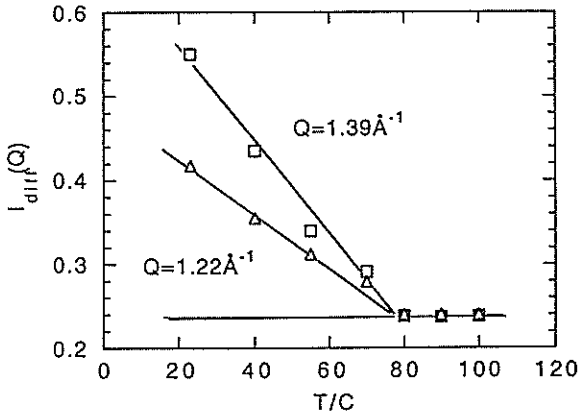

Fig.3. Temperature dependence of the scattering intensity at the Bragg position (Q=1.39$Å^{-1}$) and the off-Bragg position (Q=1.22$Å^{-1}$).

is no longer observed in the scattering curve above 80°C. The scattering intensities at Q=1.39$Å^{-1}$ were plotted against temperature in Fig.3. The intensity decreases approximately linearly with increasing temperature and becomes independent of temperature at about 75°C. This temperature agrees well with the melting temperature T_m of the PVA gel determined by macroscopic observation,[2] indicating that the cross-linking points in the gel are crystallites. The scattering intensity at

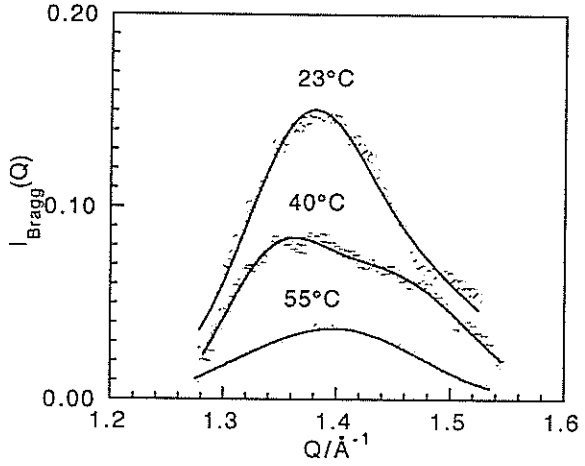

Fig.4. Bragg scattering intensity $I_{Bragg}(Q)$ from the crystallites at 23, 40 and 55°C. Solid lines are the best fits with sum of two Gaussians.

off-Bragg positions near the Bragg peak at Q=1.39Å^{-1} also decreases with increasing temperature. This decrease of the intensity is too large to explain by a temperature factor. The off-Bragg intensity at Q=1.22Å^{-1} is plotted as a function of temperature in Fig.3. The intensity decreases with increasing temperature and becomes independent of temperature at about 75°C. This temperature dependence is identical to that of the Bragg peak intensity at Q=1.39 Å^{-1}, This result suggest that amorphous-like structure of PVA exists near or around the crystallites and it is dissolved in the solvent in accordance with the melting of the crystallites. The intensity at the off-Bragg position near the Bragg peak may be assigned to the amorphous parts of PVA in the gels.

In the next step, we evaluated size of the crystallite from the width of the Bragg peak. In the gel states, some parts of a PVA chain between the cross-linking points must be dissolved while some other parts are in the crystallites or in the amorphous parts. It is natural that structure of the dissolved parts of PVA chains in the gel is identical to that in the sol. Therefore, assuming that the scattering curve at 80°C can be regarded as a scattering from the dissolved parts of PVA chains, we then subtracted the curve at 80°C from those at the lower temperatures. Next, we subtracted the contribution of the amorphous part, which was evaluated from the average intensity in the Q range of 1.20 to 1.24Å^{-1}. The resulting Bragg diffractions are shown in Fig.4 for 23°C, 40°C and 55°C. In order to evaluate the widths of the diffraction peaks, these diffraction peaks were fitted by a sum of two Gaussians representing the two Bragg reflections from the (101) and (10$\bar{1}$) planes. The solid lines in Fig.4 show the best fit with the experimental curves. The apparent widths of the Bragg peaks evaluated here include broadening effects due to the Q-resolution of the spectrometer HIT, which is $\Delta Q/Q=0.13$ at Q=1.4Å^{-1}. Using this value, we evaluated the real broadening due to the finite size of the crystallites, which give us the sizes of the crystallites perpendicular to (101) and (10$\bar{1}$) planes. The sizes are in the range of 46~71Å and almost independent of temperature though they are rather scattered due to the experimental errors. It should be noted that we neglected the effect of defects in the crystallites which also broaden the width of the diffraction peaks. Therefore, the fact that the apparent size is independent of temperature suggests that the size increases with temperature because the defects in the crystallites should increase with temperature. This picture agrees well with the results obtained by small angle scattering reported in this volume[3].

We can directly confirm that the cross-linking points of the PVA gels in the mixed solvent of DMSO-d_6 and D_2O are crystallites. This gives us a basis for interpretation of the small angle scattering data of the same system.[3]

References

1) M. Misawa, T.Fukunaga, T. Yamaguchi and N. Watanabe, ICANS IX, 1986.
2) M.Ohkura, T. Kanaya and K. Kaji, Polymer, in press.
3) M. Ohkura, T. kanaya , K. Kaji and M. Furusaka, in this vilume.

Dynamics of trans-1,4-polychloroprene near the Glass Transition

T. KAWAGUCHI, T. KANAYA and K. KAJI

Institute for Chemical Research, Kyoto University, Gokasho, Uji-shi, Kyoto 611

The glass transition is a universal phenomenon not only for amorphous polymers but also for other amorphous materials. Many investigations have been performed on the glass transition, though most of them have been so far engaged in phenomenological models for the macroscopic nature such as mechanical and thermal properties. Recently, a microscopic theory, the so-called mode coupling theory[1)2)], has been developed based on an equation for the density autocorrelation function containing a nonlinear memory function and gives some detailed pictures and predictions for the dynamical process involving in the glass transition.

The aim of this work is to study local motions of amorphous polymers near the glass transition using quasielastic neutron scattering technique and to elucidate the relation between local motions and the transition.

Quasielastic neutron scattering measurements were carried out with the two spectrometers LAM-40 and LAM-80ET installed at the pulsed spallation cold neutron source in the National Laboratory for High Energy Physics (KEK), Tsukuba. The sample used for this work was trans-1,4-polychloroprene (Tg~228K). The measurements were carried out in a temperature range between 129K and 300K.

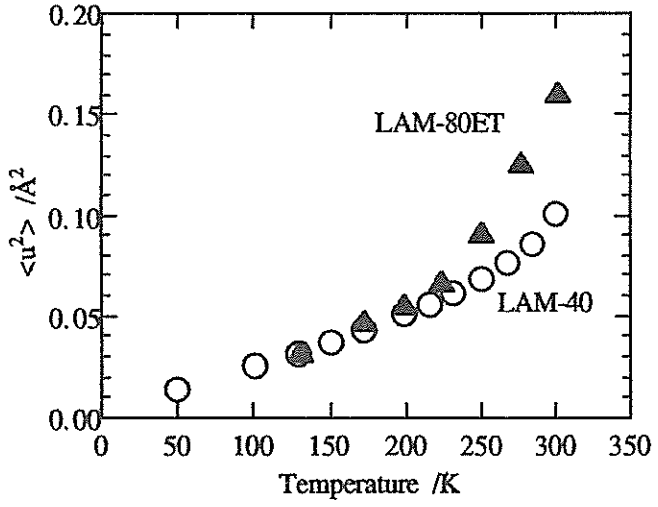

Fig. 1 The mean-square-displacement $\langle u^2 \rangle$ measured by LAM-40 (Open circle) and LAM-80ET(Solid triangle).

The elastic scattering intensity decreases with increasing temperature and begins to decrease steeply around Tg. The elastic scattering intensity $I_{el}(Q)$ shows , the Debye-Waller type Q-dependence; $I_{el}(Q) \sim \exp(-\langle u^2 \rangle Q^2)$, so that the mean square displacement $\langle u^2 \rangle$ was evaluated at each temperature (Fig.1). The $\langle u^2 \rangle$ from LAM-40 data increases linearly with temperature and begins to deviate from this linear relation ca. 30K below Tg . On the other hand, the $\langle u^2 \rangle$ from LAM-80ET data exceeds the $\langle u^2 \rangle$ of LAM-40 data above Tg. The linear relation of $\langle u^2 \rangle$ vs. T at low temperatures shows that the dominant motion is vibrational.

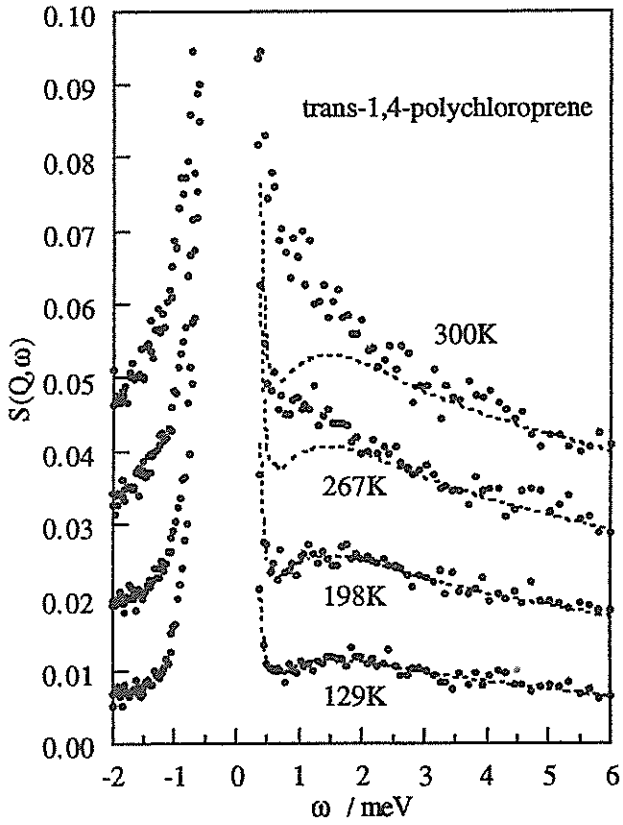

Fig. 2 Dynamic scattering laws S(Q,w)'s measured by LAM-40. The spectra were obtained by summing up 6 spectra at scattering angle 24, 40, 56, 88 and 104° and the average Q value is 1.54 Å^{-1}. The spectra are shifted by 0.01 for each. Dashed lines are the values expected from the Bose factor, which were calculated based on the spectrum at 129K.

Dynamic scattering laws S(Q,w)'s measured by LAM-40 are shown in Fig. 2 as a function of temperature. In the spectra low enough below Tg, a broad "low energy excitation" peak is observed, which is universal for most of all amorphous materials. The temperature dependance of the "low energy excitation" intensity can be normalized by Bose-factor.[3] On the other hand, the quasielastic scattering intensity below 3 meV begins to exceed the expected value from Bose-factor about 30K below Tg (see Fig. 2). This excess quasielastic scattering intensity corresponds to the decrease of $\langle u^2 \rangle$ from LAM-40. This motion may correspond to β-relaxation of mode coupling theory.

In the case of LAM-80ET measurement, we can observe the slower quasielastic component with the width of several ten μeV, which appears just above Tg as shown in Fig. 3. This appearance coincides with the deviation of the $\langle u^2 \rangle$ of LAM-80ET data from that of LAM-40 data (see Fig. 1).

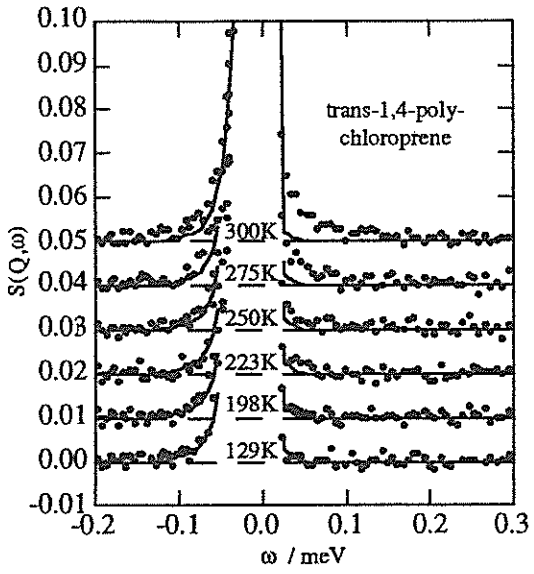

Fig. 3 Dynamic scattering laws S(Q,w)'s measured by LAM-80ET. The spectra were obtained by summing up 3 spectra at scattering angles 35, 80 and 135° and the average Q value is 1.21 $Å^{-1}$. Flat dashed lines are the contributions of the faster quasielastic component observed LAM-40. The solid lines are the resolution function of LAM-80ET.

The excess quasielastic scattering component observed by LAM-40 was fitted with a Lorentzian convoluted with the resolution function of LAM-40. The estimated HWHM is ca. 1 meV and almost independent of temperature in the examined temperature range.

We have found similar fast motion in PB melts and assigned it to the damped vibrational motion in the C–C-torsional potential. The activation energy for this damped vibrational motion is ca. 0.5 kcal/mol. On the other hand, we found that the energy barrier height of the asymmetric double well potential is in the range of 0.1 to 0.4 kcal/mol in the study of "low energy excitation". This height is very close to the activation energy observed in the melts. Therefore, we may consider the asymmetric double well potential to be a frozen state of the distorted potential in the melts.

The observed motions LAM-80ET (several tens μeV) may be related to local conformational transition.[4]

We might picture the process of the grass transition as follows. The atomic groups are gradually activated as temperature increases and begin to surmount the bottom barrier of asymmetric double well potential at critical temperature which may be observed by LAM-40. As temperature increase furthermore, the atomic groups are activated enough to surmount the C-C torsional potential barrier, leading to structural relaxation at Tg (Fig 4).

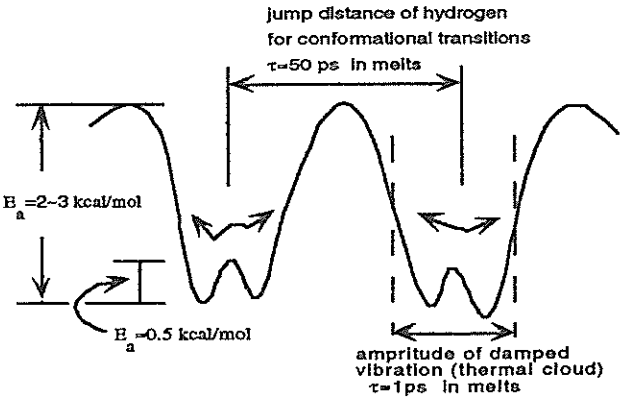

Fig. 4 Schematic potential representation for local conformational transitions along the reaction coordinate. The atomic groups begin to surmount the bottom barrier of asymmetric double well potential at critical temperature which exists below Tg. At higher temperature,the atomic groups begin conformational transition, leading to structural relaxation at Tg

References

1) W. Götze, Z.Phys. 56 (1984) 139;W. Götze, Phys. Scr. 34 (1986) 415.
2) E. Leutheusser, Phys. Rev. A29 (1984) 2764
3) K. Inoue, T. Kanaya, S. Ikeda, K. Kaji, K. Shibata, M. Misawa and Y. Kiyanagi, J. Chem. Phys. 95 (1991) 5332.
4) T. Kanaya, K. Kaji and K. Inoue, Macromolecules, 24 (1991) 1826

Thermoreversible Sol-Gel Transition of Atactic Polystyrene/Carbon Disulfide Revealed by Neutron Quasielastic Scattering

Y. Izumi and M. Kobayashi

Macromolecular Research Laboratory, Faculty of Engineering, Yamagata University, Yonezawa-shi, Yamagata-ken 992

The purpose of the present work is to study the molecular mechanism of the sol-gel transition of aPS/CS_2 system, using neutron quasielastic scattering, and to reveal yhe molecular origin of the local segmental motion appearing in this system.

The normal aPS (aPSH) (M_w=100,000, M_w/M_n<1.06) and the purified CS_2 were used. Neutron quasielastic scattering measurements were performed with the inverted geometry TOF spectrometer LAM-80ET[2] installed at the pulsed spallation cold neutron source in KEK. The neutron scattering measurements on aPS in CS_2 were carried out in a range of temperature from 170 to 300 K over a range of concentration from 0.01 to 0.20 g/cm^3.

The temperature dependence of the time-of-flight spectra showed the following features: The spectrum around room temperature is a typical one for a diffusive mode reflecting the sol phase. The diffusive mode rapidly decreases in the gel phase. Two types of spectra narrowing (central and background components) are observed. Both components are quasielastic components and described by the Lorentzian. Therefore, these are based on the random molecular motion.

After making corrections for background, counter efficiency, and the incident neutron spectrum, the observed TOF spectrum was converted to a differential scattering cross-section. The latter quantity can be directly related to the dynamic scattering law, from which we can estimate the full-width at half-maximum (FWHM). Apparent HWHM (Γ) is linear in q^2. [3] The temperature dependences of apparent diffusion coefficient (D_{app} Γ_{app}/q^2) are shown in Fig. 1, where they are plotted in the Arrhenius fashion. We can observe two straight lines. The slopes give the apparent activation energy of about 4 kcal/mol for sol and about 2 kcal/mol for gel. The molecular origin may be ascribed to the difrence of the apparent friction constant between monomer and solvent. Analysing the whole energy spectra of the scattered neutron, new aspects of the dynamic behavior of the sol-gel transition of the present system will be revealed.

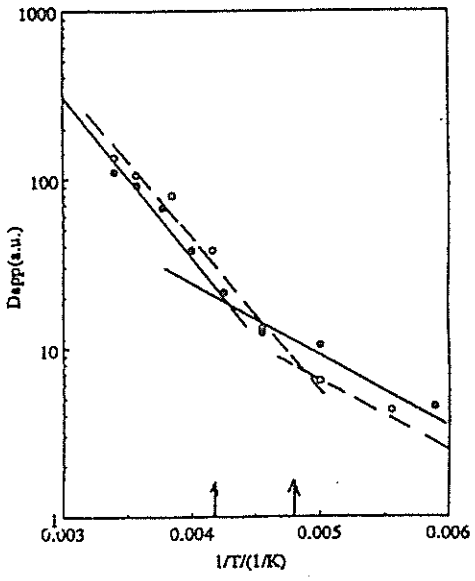

Fig. 1 Temperature dependence of the apparent diffusion coefficient Dapp at c= 0.043 g/cm^3 (the broken lines) and 0.10 g/cm^3 (the solid lines) The apparent activation energy is about 4 kcal/mol for sol and 2 kcal/mol for gel, respectively.

References

1) Y. Izumi et al., Physica B 180 & 181, 542(1992)
2) K. Inoue et al., Nucl. Instr. and Meth. A309, 294(1991)
3) A. Z. Ackcasu et al., Polymer 21, 866(1980)

Thermoreversible Sol-Gel Transition of Atactic Polystyrene/Carbon Disulfide Revealed by Neutron Small-Angle Scattering

Y. Izumi, M. Kobayashi and M. Furusaka*

Macromolecular Research Laboratory, Faculty of Engineering, Yamagata University, Yonezawa-shi, Yamagata-ken 992
*National Laboratory foir High Energy Physics, Tsukuba-shi, Ibaragi-ken 305

Since the discovery that certain chemically inactive polystyrene solutions can exhibit gelation, there has been a growing interest in the phenomena of physical gelation. Among many solvents, carbon disulfide (CS_2) was revealed to promote atactic polystyrene (aPS) gelation at highest temperature. Recent neutron scattering studies[1,2] have furnished strong evidence that the aPS chain in CS_2 behaves like a branched polymer with increasing cross-linking points, as the temperature is lowered. However, this result is based on the data analysis in the intermediate scattering vector q. Therefore, more direct determination of the conformation from the Guinier region has been desired.

In this study, the conformation of the deuterated aPS (aPSD, M_w=27,000, M_w/M_n<1.06) in CS_2 over a temperature range from 170 K to 300 K has been investigated by neutron small-angle scattering. The concentrations chosen here are 0.002 and 0.004 g/cm^3, far below the overlapping concentration c* of this system. The scattering intensity I(q,T) at low q was analyzed using the Guinier equation: $I(q,T) = I(0,T) \exp[- R_a(T)^2q^2/3]$, where I(0,T) is the square of the total particle scattering length and $R_a(T)$ is the apparent radius of gyration. The results were compared with the results of the Kratky plot.

In Fig. 1, the values of I(0,T) and $R_a(T)$ of aPSD in CS_2 at 0.002 g/cm^3 are plotted as a function of temperature. We can distinguish three domains: the chain branching, the formation of the branched polymer with a constant cross-linking density (droplet), and the interference between droplets. The temperature dependence of the Kratky plots in the same system also indicated the corresponding three behaviors.

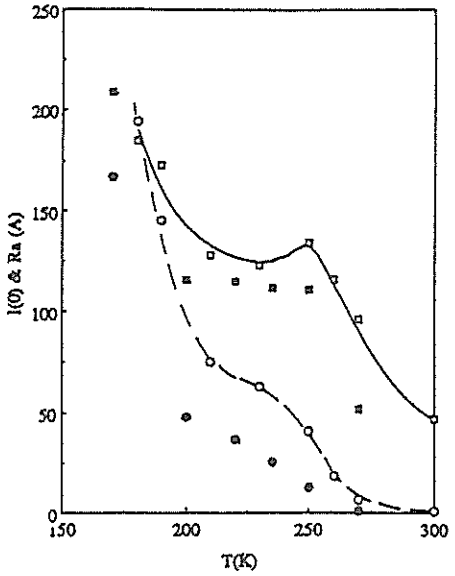

Fig. 1 Temperature dependence of the apparent I(0,T) and $R_a(T)$.
Ra(T): heating (■), cooling (□)
I(0,T): heating (●), cooling (○).

We note that the branching in the present system appeared at low temperature and even in the dilute solution. However, any effect of the branching did not appear near room temperature. The result suggests that the strength of the interaction, which promotes the branching, is the order of thermal energy and that the appearance of the branching at low temperature is the reason why CS_2 promotes aPS gelation at highest temperature.

References

1) Y. Izumi et al., Physica B 180 & 181, 539(1992)
2) Y. Izumi et al., Physica B 180 & 181, 545(1992)

Small-angle Neutron Scattering Studies of Proteoglycan from Shark Fin Cartilage in 100% and 0% D_2O/H_2O Solution

Y.SANO, N.NIIMURA*, I.TANAKA*

National Food Research Institute, Tsukuba City, Ibaraki 305, Japan
*Laboratory of Nuclear Science, Tohoku University, Sendai 982, Japan

INTRODUCTION

Chondroitin sulfate, one of natural acid mucopolysaccharides, composes the primary part of the cartilage, together with collagen-like protein, and is present as proteoglycan in connective tissues and in various biological membranes, giving the charge and the anisotropic structure of biological membranes, and controlling the transport of the drugs through the membrane. The maintenance of the integrity connective tissue is, in part, dependent on the macromolecular properties of its constituent proteoglycan.

In this study, the gross structural properties of mucopolysaccharides and their neutron scattering length density, the size and shape of the isolated proteoglycan complexes in native state were determined by the small-angle neutron scattering (SANS) method in aqueous solution of 100% and 0% D_2O/H_2O ratio, where a unit of the ratio is mol%.

MATERIALS AND METHOD

The native complexes of proteoglycans were isolated from shark fin cartilage by means of cold ethanol fractionation method. The molecule may be composed of three major components: a protein backbone in the center, chondroitin sulfate (mainly C-type) and other mucopolysaccharides (small quantity) in the core part. The molecular weight determined by the Zimm plot with laser light scattering method was 3.7×10^6.

SANS experiments were performed at the instrument SAN(5m position) of the KENS, Tsukuba in Japan. Sample thickness was selected in accordance with D_2O/H_2O ratio by taking transmission into account, and was 4mm quart cell for 100% and 2mm for 0% D_2O/H_2O, respectively. Sample concentration was 10.4, 1.04, 0.52, 0.26 mg/ml and pH of the solution is kept at 7.2 with using 10 mM phosphate buffer (ionic strength is 0.02).

RESULTS AND DISCUSSION

The scattering function I(Q) obtained are shown in Fig. 1. At this concentration of the proteoglycan complexes (10.4 mg/ml) the scatter of the data was relatively small and I(Q) monotonously increased at the smallest Q-range.

The Guinier plots derived from the above I(Q) are shown in Fig. 2 and showed a good straight lines in each cases. The radius of gyration, obtained are 17.5nm for 100% D_2O/H_2O and 18.2nm for 0% D_2O/H_2O, respectively. These Q-ranges observed in the present SANS experiment correspond to the second peak, if the molecular shape is approximated as a hard sphere model. Therefore, the radius of gyration observed may be small. The reasonable radius of gyration was obtained by using the more long camera length such as SANS-U (JRR-3M)instrument of the JAERI.

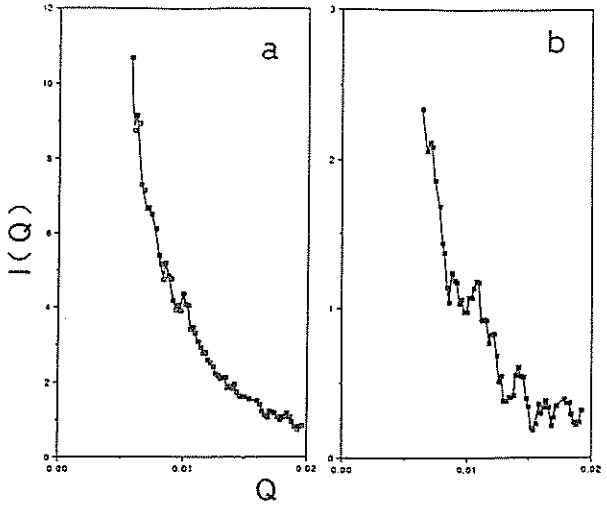

Fig. 1. Scattering functions of proteoglycan complexes (10.4mg/ml) in aqueous solution at 100%(a) and 0%(b) D_2O/H_2O ratio.

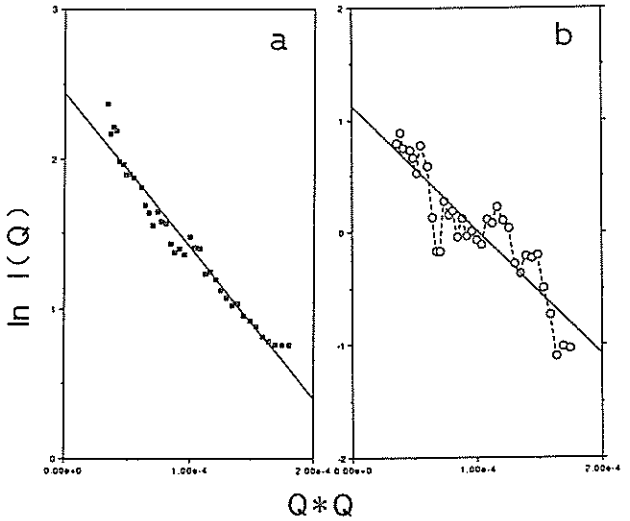

Fig. 2. Guinier plot of proteoglycan complexes (10.4mg/ml) in aqueous solution at 100%(a) and 0%(b) D_2O/H_2O ratio.

Solution Scattering Study of Bacterial Histone-like Protein HU and DNA Complex

I.TANAKA, N.NIIMURA, T.MIYAJI*1, I.TANAKA*1, M.KATAOKA*2, F.TOKUNAGA*2 and R.K.HEENAN*3

Laboratory of Nuclear Science, Tohoku University, Sendai 982, Japan
*1Faculty of Science, Hokkaido University, Sapporo 060, Japan
*2Faculty of Science, Osaka University, Osaka 565, Japan
*3Neutron Division, Rutherford Appleton Laboratory, Didcot, UK

The DNA double helix in eukaryotic cell would span thousand times of the cell nucleus if it were streched out. Histones play an important part in packing this very long DNA molecule in an orderly way into a nucleous of only a few micrometers in diameter. A major advance in our understanding of chromatin structure came with the discovery of the fundamental packing unit known as the nucleosome.

In prokaryotes, although the genome is much smaller, it has been made clear that there is a sort of DNA packaging. Following the gentle lysis of *Escherichia coli* cells, chromosomes can be isolated in a folded and supercoiled conformation. In addition, several DNA-binding proteins have been identified for which a histone-like role has been proposed. One of these proteins exibits clear histone-like properties. This small basic protein has been shown to induce the formation of bead-like structures along double-stranded DNA in a manner similar to the histones, which has been confirmed by the electron microscopy[1]. In *Escherichia coli* such a protein has been referred to by several authors as HU protein.

The crystal structure of HU-protein has been determined by one of the applicants[2], but the structure of HU protein-DNA complex is not yet known. This is mainly because the HU-DNA complex cannot be obtained independently, since the complex exists only under the equilibrium

$$HU + DNA \rightleftarrows HU\text{-}DNA, \qquad (1)$$

so that in an acqueous solutions three kinds of solutes (HU, DNA and HU-DNA complex) coexist. We have tried to determine the structure of HU-DNA complex in solutions by using small angle X-ray and neutron scattering method.

HU protein was extracted from the thermophilic bacterium *Bacillus stearothermophilus* and purified. 20 base-paired double stranded DNA bound to HU protein was synthesized so that at both ends are CG bases and inner 80% of base pairs are AT.

At first small angle neutron (SANS) and X-ray (SAXS) scattering of HU protein in solutions were carried out by using SAN (pulsed neutron scatterinf facility in Japan) and WIT at KENS and LOQ at ISIS (pulsed neutron scattering facility in U.K.) and X-rays at PF (synchrotron radiation at KEK in Japan.) .

The results obtained using each SANS instrument are more or less similar each other and one example is shown in Figure 1, which shows Guinier plot of HU protein in D_2O solution, the concentration of which is 8.1 mg/ml. The radius of gyration (R_g) is obtained as 17.9A. The concentration dependence of R_g is measured by using X-rays at PF and the result shows that there is no concentration dependences and SANS resultwas found to coincide with that of SAXS. R_g is calculated by using the atomic coordinates of HU dimer which have been determined by X-ray crystallography and is obtained as 18.4A. The value coinsides with one of SANS and SAXS very well, and this indicates that HU protein exists as a dimer in the solution.

The solution scattering of HU-DNA complex was carried out by using SANS-U in JAERI, and the preliminary result of R_g is obtained as 34.2A. The more complete experiment is scheduled.

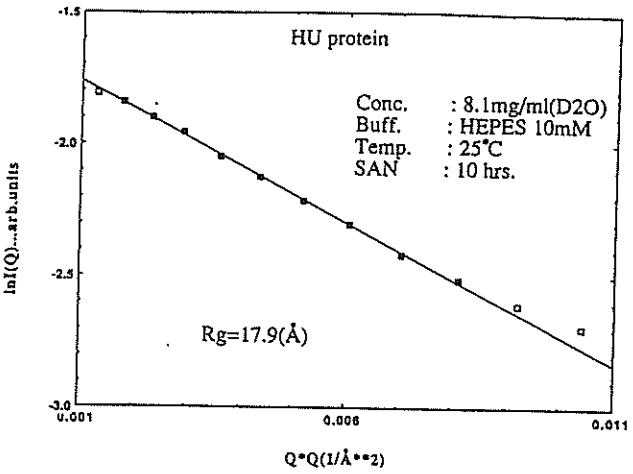

Figure 1. Guinier plot of HU protein.

References

1) J.D.Griffith: Proc. Natl. Acad. Sci. USA; 73 (1976) 563
2) I.Tanaka *et al* Nature **310** (1989) 376

Structure study of phosphatidylinositol diphosphate and bovine serum albumine complex

K. MIKAMI, N.NIIMURA and K. HAYASHI*1

Laboratory of Nuclear Science, Tohoku University, Sendai 982, Japan
*1Faculty of Education, Ibaraki University, Mito 310, Japan

A wide variety of extra cellular signals which activate cellular functions and proliferation throug hinteraction with membrane receptors have been shown to provoke the break-down of phosphatidylinositol diphosphate (PIP_2) in their target tissues. The primary products of the reaction are diacylglycerol (DG) and inositol triphosphate (IP_3). Because of this reason PIP_2 is considered to be important material even though it is a very minor component in membranes.

On the other hand, from the biochemical viewpoints PIP_2 itself has several distinctive features compared to other phodpholipids. PIP_2 is a highly hydrophilic phospholipid rich in nnervous tissues, and it is soluble in water and becomes insolubleby adding Ca^{2+}. In water-methanol and chloroform solvents PIP_2 is distributed to the upper water-methanol phase and by adding Ca^{2+} it transfers to the lower chloroform phase. PIP_2 forms a complex with proteins such as bovine serum albumine (BSA) which is soluble in the upper phase, and on adding Ca^{2+} precipitatesbetween the interfaces. These facts suggest that PIP_2 itself is not only the source of DG and IP_3, but also PIP_2 might play an important role inthe nerve excitation through the regulation by Ca^{2+} ions *via* PIP_2- protein complex.

A small angle neutron scattering study of PIP_2-BSA complex has been carried out to examine the structural role of the complex.

PIP2 was extracted from bovine brain and purified by conventional methods.[1)]

Small angle neutron scattering of PIP_2-BSA complex has been carried out by the use of WIT installed at KENS. Figure 1 shows the Guinier plot obtained by the scattering profiles of PIP_2-BSA complex. Here, the number of PIP_2 molecules per one BSA molecule is varied as a parameter. The square root of I(0) is extracted from Fig. 1 and is shown as a function of the number of PIP_2 in Fig. 2.

In our experiment concentration (number of the complex) is kept to be constant, square root of I(0) is written as

$$\sqrt{I(0)} \propto M_{BSA} + N_{PIP} * M_{PIP}$$

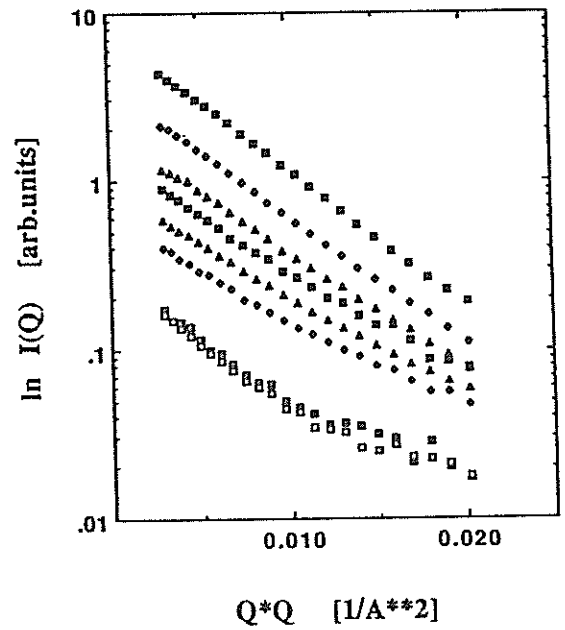

Fig. 1 Guinier plot of PIP_2-BSA complex. PIP_2/BSA is 400, 200, 100, 75, 50, 25, 4 and 0, respectively, from the top.

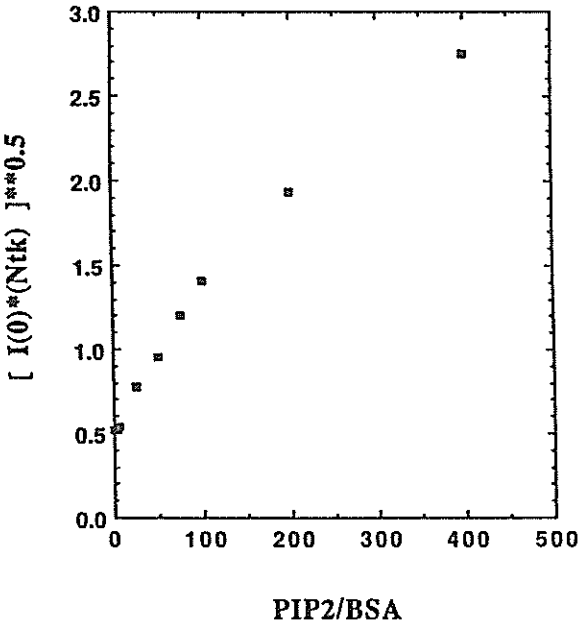

Fig. 2 Square root of I(0) *vs.* PIP_2/BSA

where M_{BSA} and M_{PIP} mean molecular weight of BSA and PIP_2, which are about 36kDa and 1kDa, respectively and N_{PIP} is the number of molecule which binds to one BSA molecule.

As shown in Fig. 1, Guinier plot of each solution is obtained as a straight line, and this suggests that the complex solution is monodispersive. Moreover, Fig. 2 indicates that the complex is stoichiometric.

Figure 3 shows Guinier plot of 50 PIP_2/BSA complex under the contrast variation technique. Here, 50 PIP_2/BSA means that 50 PIP_2 molecules and one BSA molecule are mixed to produce PIP_2-BSA complex. The scattering at D_2O 40% is the result of the matching point of BSA and PIP_2 head group and only PIP2 tail group can be seen, and the R_g of the system is 11.4A. This value is very small and this means that PIP_2 does not bind uniformly on the suface of BSA (R_g would be 35-40 A fo a uniform distribution of PIP_2 on BSA surface), but locally on one portion of the BSA. This is also demonstrated in the Stuhrman plot . Figure 4 shows the Stuhrmann plot of the 50 PIP_2/BSA complex . The plot is fitted with a hyperbola and the curvature of the hyperbola means the distance between the geometrical center and the scattering length densities center of gravity. As shown in Fig. 4 , the crvature is rather large, and this indicates that the binding of PIP_2 on BSA surface is asymmetric.

It is well known biochemically that PIP_2 forms a complex with BSA and this fact is confirmed by SANS experiment and the nature of the complex is indicated as follows:

(1) PIP_2 combines with BSA stoichiometrically such as $(PIP_2)_{25}$-BSA, $(PIP_2)_{50}$-BSA and so on.

(2) PIP2 binds outside of the BSA surface, and apparently on one region of the BSA surface.

In order to conclude whether these findings are related to the production of DG and IP3. further investigations are under way.

Reference

1) J.Folch, J. Biol. Chem. 177 (1949) 97

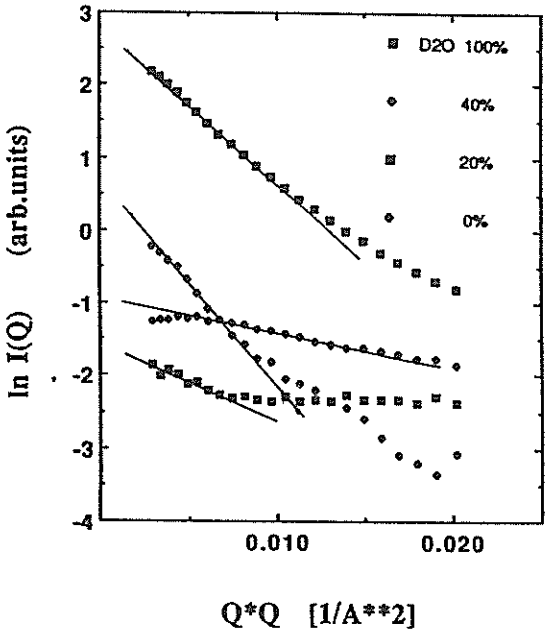

Fig. 3 Guinier plot of (PIP2)50-BSA complex under the contrast variation technique.

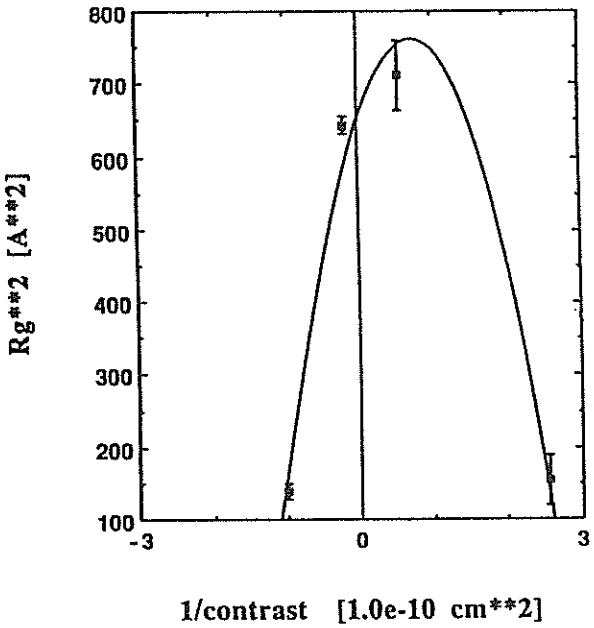

Fig. 4 Stuhrmann plot of $(PIP_2)_{50}$-BSA complex

Small-Angle Neutron Scattering Study of Ovotransferrin in Aqueous Solution

H. YAJIMA, A. KAWAMURA, R. ENDO, and N. NIIMURA*

Department of Applied Chemistry, Faculty of Science, Science University of Tokyo, Tokyo 162
* Laboratory of Nuclear Science, Tohoku University, Mikamine 1-2, Sendai 982

Transferrins (Tfs) comprise a group of homologous iron binding glycoproteins ubiquitously distributed among cells and physiological fluids of vertebrates[1]. They include serum transferrin (seroTf), ovotransferrin (ovoTf) from avian egg white, and lactoferrin (lactoTf) present in the milk of most mammals. Each Tf molecule consists of a glycosylated single polypeptide chain with a molecular weight approximately 80 kDa, which has two major homologous domains and a short connecting part[2]. Two globular lobes correspond to the N- and C-terminal halves of the molecule. Each domain has one site capable of binding various metal ions, such as iron, copper, and aluminium, with the different binding affinities[3]. The amino acid sequences of the two domains show considerably homology[4], and the residues in the metal-binding sites are the same[5]. The concomitant binding of a particular divalent anion, physiologically (bi)carbonate, is required for the formation of a stable metal-Tf complex[6]. Furthermore, recent X-ray crystallographic studies have revealed that structure of each domain with an ellipsoid structure consists of two subdomains and two peptides connecting these two subdomains[7,8]. These connecting peptides play a role of a hinge. With regard to the conformational change induced by metal binding, the model that metal ion is trapped at a wide open cleft formed by the two subdomains and then the cleft is closed through two hinges has been presented. From the small angle X-ray scattering studies of seroTf and ovoTf, it is fairly recognized that the radius of gyration of diferric transferrin is smaller than that of apotransferrin[9].

Although the amino acid sequences of the two domains in Tf and the ligand environments for the two binding sites are homologous, there are significant heterogeneity between the N and C-domains for metal binding properties and the stabilization of the metal-Tf complexes[10,11]. Sasaki et al.[12] have reported from the dynamic light scattering study of ovoTf that the contraction of ovoTf originates predominantly from a metal-binding to the C-site compared to the N-site.

In order to rationalize the heterogeneity between the N- and C-domains, we have scrutinized the change in the structural characteristics of ovoTf due to iron binding with small-angle neutron scattering.

OvoTf from chicken egg white was obtained from Sigma Chemical Co. Apo-ovoTf of 20 mg/mL in aqueous solution of different D_2O/H_2O ratio, i.e. 100%, 80%, 60%, 20%, and 0%, was prepared in 10mM Tris-HCl buffer containing 10mM $NaHCO_3$ at pH 8.0, and then Fe_2-ovoTf by adding excess amount of Fe(III) as a nitorilotriacetate complex. A unit of the D_2O/H_2O ratio is a volume fraction of D_2O (ϕ_D). Small-angle neutron scattering measurement was made using WIT[13] for apo- and Fe_2-ovoTf in aqueous solutions with various ϕ_D. Sample thickness was selected in

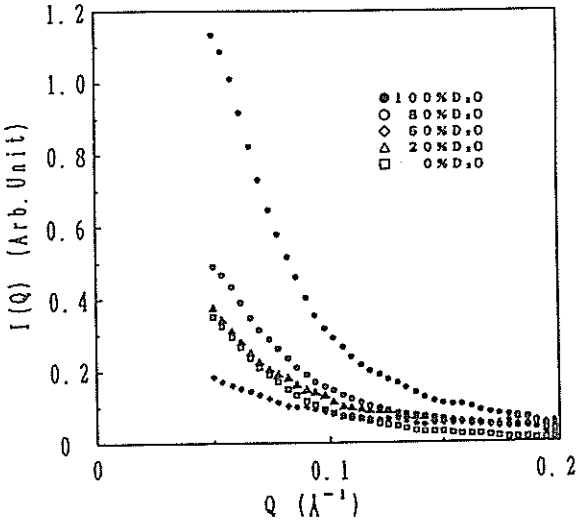

Fig. 1 Scattering functions of apo ovoTf in aqueous solution at different D_2O/H_2O ratio.

accordance with ϕ_D by taking transmission into account, and was 4mm for ϕ_D=100%, 80% and 60%, and 2mm for ϕ_D=20% and 0%.

The measured scattering functions I(Q) for apo-ovoTf of different ϕ_D are shown in Fig.1, where Q is the scattering vector, $Q = 4\pi\sin(\theta/2)/\lambda$, and the base line of the each function is shifted arbitrarily to see easily.

The Guinier plots derived from the above function I(Q) are shown in Fig.2. A radius of gyration Rg of apo-ovoTf at each ϕ_D was calculated using the least square fitting of Q range 0.05 - 0.074 A^{-1} at the different ϕ_D. Likewise, the Rg value of Fe_2-ovoTf at each ϕ_D was obtained in the same manner as with apoTf.

Contrast matching points for apo- and Fe_2-ovoTf were estimated to be 43.83% and 46.91 % in ϕ_D, respectively, using $I(0)^{1/2}$ vs ϕ_D as shown in Fig.3, where I(0) was an extrapolated intercept of the ordinate of Guinier plot. The mean scattering densities $\bar{\rho}$ of the solutes, i.e. apo- and Fe_2-ovoTf were determined as 2.49 and 2.71 x 10^{-14} cmA^{-3} from the relation $\bar{\rho} = \hat{\rho} - \rho_s$, where $\hat{\rho}$ is the mean excess scattering density and ρ_s the mean scattering density of solvent given by $\rho_s=(-0.00562+0.0697\phi_D)\times10^{-12}$ cmA^{-3}.

The relationship between Rg and $\bar{\rho}$ is given by

$$Rg^2 = Rgc^2 + \alpha(1/\bar{\rho}) - \beta(1/\bar{\rho})^2$$

where Rgc, α, and β are the radius of gyration of the particle at infinite contrast ($\bar{\rho}$=0), a radial second moment of the scattering density distribution and a displacement of the center of the scattering density distribution with respect to the center of the geometrical shape, respectively[14]. The plots of Rg^2 vs $1/\bar{\rho}$ (Stuhrmann plots) for apo- and Fe_2-ovoTf are shown in Fig.4. The obtained values of parameters are summarized in Table I.

The Rgc value was decreased by iron binding. This behavior is in agreement with the previous results of the small angle X-ray scattering[9], although the magnitudes of Rgc were appreciably smaller than the previous ones: Rg = 31.4 A for apo-ovoTf and 30.4 A for Fe_2-ovoTf, because of the lower limit of the observable Q-range in WIT.

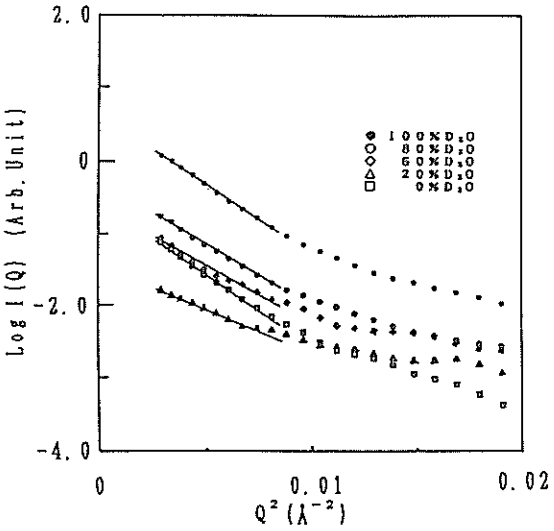

Fig. 2 Guinier Plot of ovoTf in aqueous solution at different D_2O/H_2O ratio.

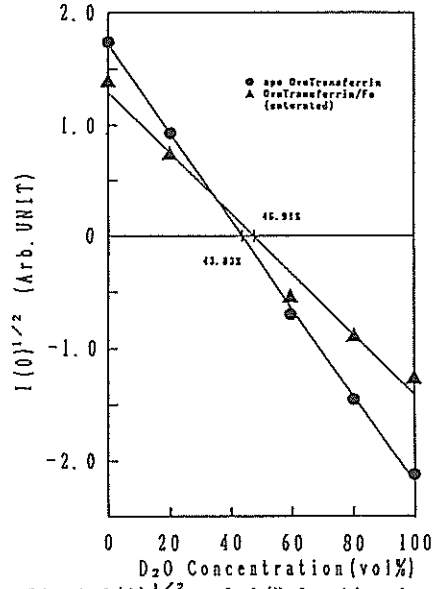

Fig. 3 $I(0)^{1/2}$ vs D_2O/H_2O ratio of ovoTf in aqueous solution.

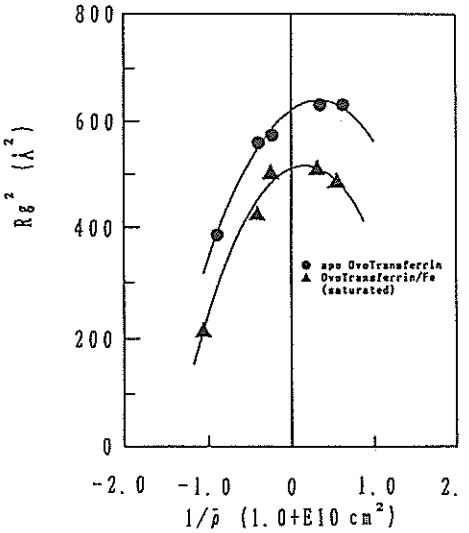

Fig. 4 Stuhrmann plot of ovoTf in aqueous solution.

Table. 1 Rgc, α and β of ovoTf

	Rgc (Å)	α (Å^{-1})	β (Å^{-2})
apo-ovoTf	25.0	111	171
Fe_2-ovoTf	22.6	68	205

In view of the fact that the parameter β has a significant value and the β value for Fe_2-ovoTf is larger than that for apo-ovoTf, it is inferred that the structure of the ovo-Tf molecule is intrinsically distorted in aqueous solution, irrespective of the presence of metal ions, and the distortion is elevated by iron binding. The structural distortion of apo-ovoTf would be attributed to the difference in chain flexibilities between the N- and C-domains. In correlation with this suggestion, the X-ray crystallographic studies of apo-lactoTf presented that the binding cleft in the N-lobe is wide open, whereas the cleft in the C-lobe is closed even in the absence of metal ion[8]. However, no clear-cut interpretation has yet established with regard to the structural distortion of iron bound ovoTf.

On the other hand, the α value is decreased by iron binding. This implies that the external distribution of proton in ovoTf is increased by iron binding, compared to the internal one.

To elucidate the structural heterogeneity between the N- and C-domains in the Tf molecule, more extensive experiments of the small angle neutron scattering, in particular for N- or C-domain fragment is required.

References

1) P. Aisen, "Iron in Biochemistry and Medicine, II", Eds. by A. Jacobs and M. Worwood, Academic Press, London & New York, pp.87-129 (1980).

2) B. F. Anderson, H. M. Baker, E. J. Dodson, G. E. Norris, S. V. Rumball, J. M. Wates. and E. N. Baker; Proc. Natl. Acad. Sci., 84 (1987) 1769.

3) T. Yamamura, S. Hagiwara, K. Nakazato, K. Satake; Biochem. Biophys. Res. Commun., 119 (1984) 298.

4) F. Yang, J. B. Lum, J. R. McGill, C. M. Moore, S. L. Naylor, P. H. van Bragt, W. D. Baldwin, and B. H. Bowman; Proc. Natl. Acad. Sci., 81 (1984) 2752.

5) J. Williams, T. C. Elleman, I. B. Kingston, A. G. Wilkina, K. A. Kuhn; Eur. J. Biochem., 122 (1982) 297.

6) R. E. Cowart, N. Kojima, G. W. Bate; J. Biol. Chem., 257 (1982) 7560.

7) B. F. Anderson, H. M. Baker, G. E. Norris, D. W. Rice, and E. N. Baker; J. Mol. Biol., 209 (1989) 711.

8) B. F. Anderson, H. M. Baker, G. E. Norris, S. V. Rumball, E. N. Baker; Nature, 344 (1989) 784.

9) T. Yamamura, K. Ichimura, K. Satake, Y. Tachi'iri, H. Kihara, and Y. Amemiya; Photon Factory Activity Reports, 4 (1986) 308.

10) P. Aisen, A. Leibman, and J. Zwier; J. Biol. Chem., 253 (1978) 1930.

11) K. Nakazato, T. Yamamura, and K. Satake; J. Biochem., 103 (1988) 823.

12) N. Sasaki, H. Honda, H. Yajima, H. Momomi, K. Ichimura, K. Satake, and R. Endo; Nippon Kagaku Kaishi, (1990) 185.

13) N. Niimura et al.; KENS REPORT VIII, (1989/90).

14) H. B. Stuhrmann and H. Fuess; Acta Cryst., A32(1976), 67.

Magnetic Excitations fron Ordered and Disordered Fe_3Pt Alloy

Y. Tanaka, K. Tajima, Y. Todate# and H. Ikeda$
Department of Physics, Keio University, Hiyoshi Yokohama 223
 # Department of Physics, Ochanomizu University, Otsuka, Bunkyo-ku Tokyo 112
$ National Laboratory for High Energy Physics, Tsukuba, Ibaraki 305

Fe_3Pt is a ferromagnetic alloy with f.c.c. structure and exhibits a typical Invar charactor. The Curie temperature of the ordered Fe_3Pt alloy (Cu_3Au type structure) is about 500 K which is almost 200 K higher than that of the disorderd alloy. Another magnetic properties as well as the Invar properties are not so much sensitive to atomic ordering. The study of the exchange mechanism in Fe_3Pt is quite interesting to understand both magnetic and Invar properties. The spin wave dispersion relation in ordered Fe_3Pt was measured using a triple axis spectrometer[1]. Experiments were performed up to about 80 meV, however, the dispersion relations along the [110] and [111] directions could not be obtained up to the zone boudary. The results were analyzed based on a Heisenberg model, but clear understanding about the exchange mechanism in the alloy was not obtained.

In order to elucidate the exchange interaction mechanism in Fe_3Pt, the experiment has been made to observe the defference of the spin wave dispersion relation between ordered and disordered Fe_3Pt alloy. The dispersion relation up to 40 meV has been observed along the [111] direction using MAX spectrometer. Typical examples of the TOF spectrum in both ordered and disordered sample at T=20K are shown in Fig.1. These two spectra were observed with the same detector No.8 and with same collimations. It is interesting to note that the appreciable difference of the spin wave energy as well as the line width between ordered and disordered states was not detected within the observed q range, although the difference of the Curie temperature of the two states is about 200K. The observed spin wave constant D is about 90 meVA for both atomic ordering states. The results indicate that the spin wave with the long wave length is insensitive to the atomic ordering, therefore, the exchange interaction of Fe in Fe_3Pt may be rather uniform in distance and is not affected sensitively by surrounding atoms. Further observation of the spin waves at large q region is required to understand the mechanism in more detail.

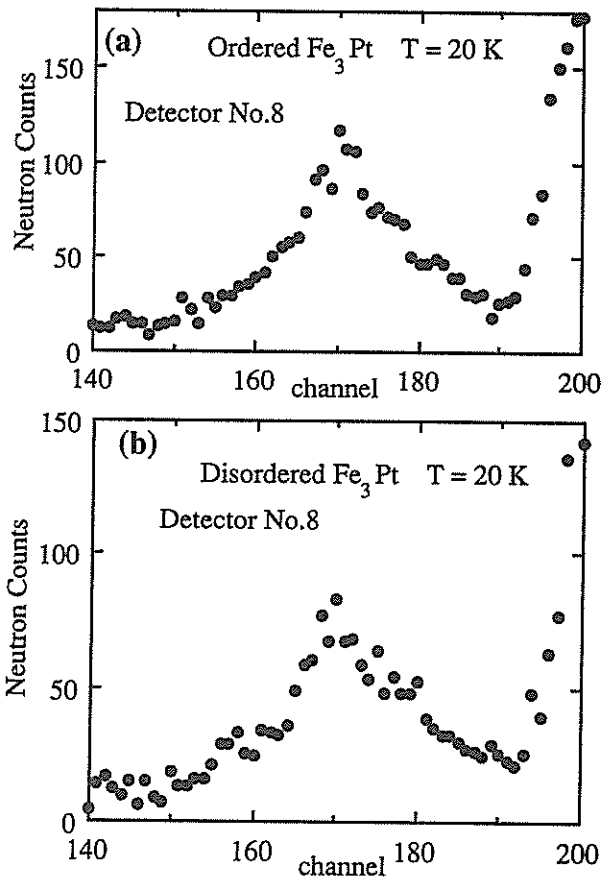

Fig.1. TOF spin wave spectra observed with a detector No.8 : (a) ordered , and (b) disordered alloy. The peak channel of the spectra corresponds to the excitation energy of 23 meV.

References

1)Y.Ishikawa, K.Tajima and N.Wakabayashi;
J. Phys. Soc. Jpn.48 1097 (1980)

Magnetization Process of Multilayer Films with Giant Magnetoresistance Effect

N.HOSOITO, K.MIBU, T.ONO, T.SHINJO and Y.ENDOH*

Institute for Chemical Research, Kyoto Univ. Uji, Kyoto-fu 611
*Department of Physics, Tohoku Univ. Sendai 980

Electric transport properties of some multilayer films in the external magnetic field have attracted much attention. Several kinds of multilayer films, such as Fe/Cr, Co/Cu, NiFe(Permalloy)/Cu/Co/Cu etc., show a "giant magnetoresistance effect". This means that electric resistance indicates a huge change as a function of external field. In a typical case, a relative change of electric resistance $\Delta R/R$ is more than 50%, which is about ten times larger than the anomalous magnetoresistance effect in ferromagnetic materials. The giant magnetoresistance effect was first reported in Fe/Cr multilayers[1]. The condition in which the giant magnetoresistance effect occurs is now well known. The enhancement of the resistance is observed when the magnetization vectors of adjacent ferromagnetic layers spaced by a non-magnetic layer take an antiparallel alignment during the magnetization process. The antiparallel alignment is realized by two different mechanisms. One is the RKKY-type magnetic interaction between adjacent ferromagnetic layers through the non-magnetic layer with appropriate thicknesses. The other is a difference in the coercive fields of two magnetic layers. Multilayer films of Fe/Cr and Co/Cu correspond to the first type, and multilayer films such as NiFe/Cu/Co/Cu correspond to the second one. The antiparallel alignment of the magnetization vectors in adjacent magnetic layers is confirmed by several experimental techniques with magnetic/non-magnetic/magnetic trilayer samples.

We have carried out polarized neutron diffraction experiments of Fe/Cr and NiFe/Cu/Co/Cu multilayers with using the TOP spectrometer. The direction and strength of the magnetization vector in each magnetic layer of the multilayer film were determined in the presence of various external fields. From these experiments, the magnetization process of each magnetic layer is elucidated. This enables us a quantitative comparison between the magnetic structure and the enhancement of the electric resistance.

Fe/Cr multilayer

As detailed reports were published elsewhere[2,3], we will discuss the main points of the results. The nominal layer structure of the Fe/Cr multilayer film used for the measurements is [Fe(27Å)/Cr(12Å)]×30. The measurements were carried out at room temperature. The external field is applied parallel to the film plane and the scattering vector is perpendicular to the film plane. The time-of-flight spectra below the external field of 5kOe show the half and first order diffraction peaks, which are assigned to the chemical period. The half order peak disappears above 5kOe. These facts indicate that the magnetization vectors of the adjacent Fe layers form antiferromagnetic structures in weaker fields, as is expected. The intensities of the half and first order peaks and the magnetization curve are well reproduced with a model that the magnetization process is a rotation of the Fe magnetization vectors with keeping the length of the vectors constant. If the magnetization vector of some Fe layer turns clockwise, the magnetization vectors of the adjacent Fe layers turn anticlockwise. Therefore the antiparallel structure is formed by a component of the Fe magnetization vector perpendicular to the applied field, which is named the transverse component. Polarization analysis of the half order peak in the field of 50Oe indicates that about 80% of neutrons are scattered with a spin-flip process. This fact also proves that the antiparallel structure is formed by the transverse component of the Fe magnetization vectors. Furthermore it is indicated that the resistance change $\Delta R(H)$ is proportional to the square of the transverse component of the Fe magnetization vector in the field of H except a very weak field region. In summary from the neutron diffraction measurements, the resistance enhancement is quantitatively related to the magnetic structure of the Fe/Cr multilayer film.

NiFe/Cu/Co/Cu multilayer

The giant magnetoresistance effect of this system was found by the authors' group[4]. The existence of the antiparallel alignment state is supposed from the M vs. H loop of the sample, which shows steps during the magnetization process. We used the sample of [NiFe(10Å)/Cu(36Å)/Co(10Å)/Cu(36Å)]×20 for measurements. In this sample, temperature dependence of resistance change $\Delta R(77K)/\Delta R(300K)$ is 1.91. On the other hand, temperature dependence of the saturation magnetization $M_s(77K)/M_s(300K)$ is 1.12. This means that the resistance change is much larger than the change in the magnetization. One may

think that temperature dependence of the surface magnetic moments is much larger than that of the bulk. However this conjecture was denied by Mössbauer spectroscopy[5]. We have two purposes for the neutron diffraction experiments of NiFe/Cu/Co/Cu multilayer films. The first is to elucidate the magnetization process of NiFe and Co layers separately and confirm the antiparallel alignment state. The second is to make clear the origin of the large temperature change in the magnetoresistance ΔR.

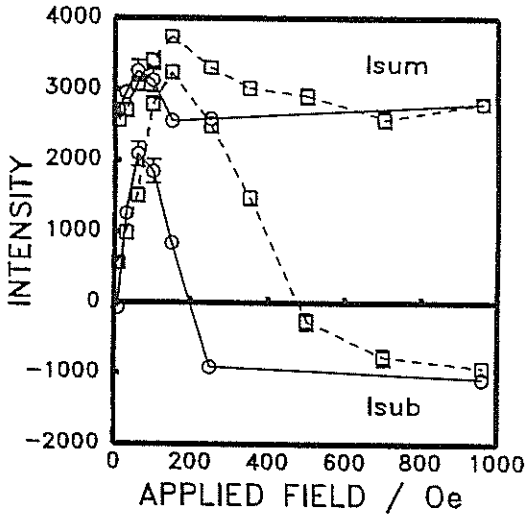

Fig. 1 Neutron diffraction intensities of 1st order Bragg peaks at 300K (O) and 77K (□). After applying -960Oe, the data are obtained with increasing the field.

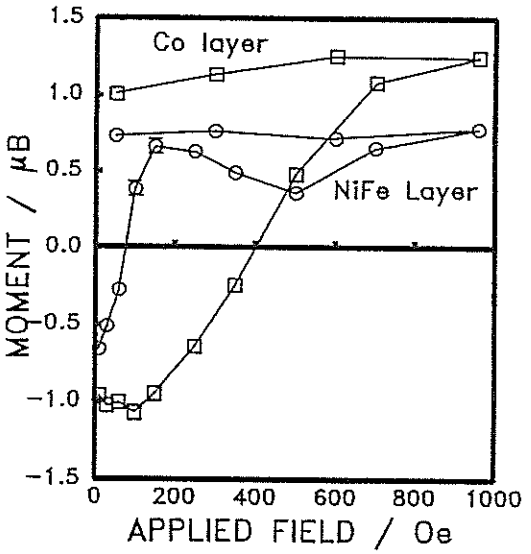

Fig. 2 Magnetization curves of the NiFe (O) and Co layers (□) at 77K determined from the neutron diffraction and magnetization measurements.

Neutron diffraction measurements were performed at 77K and 300K. The diffraction geometry is the same as that of the Fe/Cr case. Figure 1 shows the diffraction intensities of the first order Bragg peaks as a function of the applied field. In the figure, I_{sum} is defined as $I_+ + I_-$ and I_{sub} as $(I_+ - I_-)/P_B$, where I_+ (I_-) is the diffraction intensity with neutron moments parallel (antiparallel) to the applied field, and P_B polarization of initial neutrons. If the NiFe and Co layers are uniformly magnetized, I_{sum} is proportional to $(M_{NiFe}-M_{Co})^2$ + a nuclear scattering term, and I_{sub} $M^z_{NiFe}-M^z_{Co}$, where M_j is a magnetization vector of j layer and M^z_j is a parallel component of the magnetization vector of j layer to the external field. We define $(\Delta M)^2=\max((M_{NiFe}-M_{Co})^2)$ and $\Delta M^z=\max(|M^z_{NiFe}-M^z_{Co}|)$ with respect to the applied field. From the analysis of the intensities, it is found that $(\Delta M(77K))^2/(\Delta M(300K))^2$ is 1.84±0.32 and $\Delta M^z(77K)/\Delta M^z(300K)$ is 1.55±0.15. As $\Delta R(77K)/\Delta R(300K)$ is 1.91, it is known that $(M_{NiFe}-M_{Co})^2$, which can be regarded as a measure of antiparallel degree, is related to the magnetoresistance change. If we neglect x and y components of the magnetization vectors, the magnetization curves of NiFe and Co layers can be determined from the neutron diffraction and magnetization data. The results at 77K are shown in Fig. 2. It is clear that the antiparallel alignment is realized around the field of 150Oe during the magnetization process. The present neutron diffraction studies make clear the relationship between the giant magnetoresistance effect and the magnetic structure of NiFe/Cu/Co/Cu multilayer films.

References

1) M.N.Baibich et al., Phys.Rev.Lett. 61,272(1988)
2) N.Hosoito, S.Araki, K.Mibu and T.Shinjo, J.Phys. Soc.Jpn. 59,1925(1990)
3) N.Hosoito, K.Mibu, S.Araki, T.Shinjo, S.Itoh and Y.Endoh, J.Phys.Soc.Jpn. 61,300(1992)
4) T.Shinjo and H.Yamamoto, J.Phys.Soc.Jpn. 59,3061 (1990)
5) T.Shinjo, H.Yamamoto, T,Okuyama, S.Araki, K.Mibu, and N.Hosoito, Hyper.Int. 68,333(1991)

Observation of the time evolution of the 1st order magnetic phase transition in Dy-4%Yalloy

Y.Shinoda,K.Tajima,T.Suzuki*,H.Nojiri**

Department of Physics, Faculty of Science & Technology, Keio Univ.
*Department of Physics,Tsukuba Univ.
**Faculty of Science,Kobe Univ.

The 1st order temperature-induced magnetic phase transition of spiral to ferromagnetic structure in Dy-4%Y alloy was studied by means of X-ray diffraction.[1),2)] Below the transition temperature Tc of spiral to ferromagnetic structure, ferro and spiral phases coexist down to low temperature and the development of the ferromagnetic phase exhibits a time dependence which is proportional to log t. The observation of the magnetic transition was made through the hexagonal to orthorhombic crystal distortion accompanying the 1st order magnetic phase transition.

In order to observe the magnetic transition in Dy-4%Y directly,neutron diffraction experiment has been performed using MRP diffractometer installed at KENS.

The $(002)^{\pm}$ satellite peak and magnetic part of the (002) reflection has been studied to detect the phase transiton. Observation was made after decreasing temperature from the spiral phase.Comparing the satellite peak intensities normalized by monitor counts with that of initial state,the volume ratio of spiral phase could be obtained. Below Tc=55K, ferro and spiral phases coexist as has been observed in the previous work.[1),2)] The time evolution of the (002) reflections has been also observed and the results of the time evolution of the ferromagnetic phase at T=45K is illustrated in Fig.1.

These results were found to be consistent with the previous X-ray measurements [1)] and Synchrotron X-ray measurements.[2)]

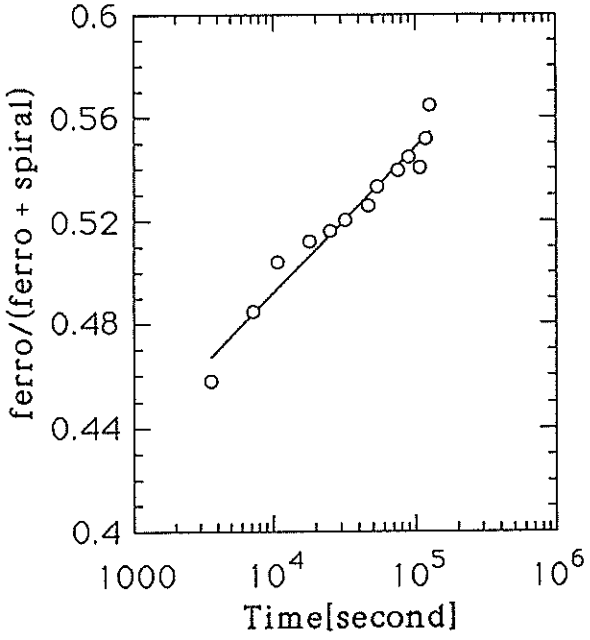

Fig.1 The time evolution of the spiral phase of Dy-4%Y alloy when the temperature was lowered from 70K to 45K.

References

1)K.Oguchi, K.Tajima and Y.Shinoda;
J. Phys. Soc. Jpn. **60** (1991) 2371
2)K.Tajima, J.Akimitsu, M.Akimitsu, L.Rebelsky, G.Grübel and G.Shirane ;
J. Magn. Magn. Mat. **104-107** (1992) 177

Neutron Diffraction in Pulsed High Magnetic Field

M.Mino, K.Ubukata, T.Bokui, H.Nojiri* , M.Arai# and M.Motokawa

Department of Physics, Faculty of Science, Kobe University, Rokkoudai, Nada, Kobe 657
*Institute for Solid State Physics, University of Tokyo, Tokyo 106
#National Laboratory for High Energy Physics, Tsukuba, Ibaraki 305

Some magnetic materials which show magnetic phase transitions in high magnetic fields have been studied. As is well known, in order to determine magnetic structures, neutron diffraction measurements are very useful. Usually, a superconducting magnet system which generates DC field is employed to observe the field induced structures in the neutron diffraction experiments. However, the complicated configuration of apparatuses limits the field strength up to about 10T. On the other hand, the great part of magnetic phase transitions are induced in a very high field. Our system is capable of producing fields up to 20T every 2 sec. Investigation of $PrCo_2Si_2$ in pulsed high magnetic fields have been reported[1]. In these experiments a solenoid type magnet, which provides a horizontal field almost parallel to the neutron beam, have been employed. Recently we have developed another split type magnet. As shown in Fig.1, the magnetic field direction is vertical and perpendicular to the neutron beam. This new type magnet has some advantages. For example a scattering angle becomes large, so that a minute resolution is achieved. We bring these magnets into use in order to study high field magnetic structures of Mn_2SiO_4. Mn_2SiO_4 is an antiferromagnet with an orthorhombic structure. In specific heat measurement and Neutron diffraction experiments in zero field, two transitions are observed. The upper transition (47K) corresponds to the change from a paramagnetic state to collinear antiferromagnetic ordering of the Mn moments along a-axis, another transition (12K) corresponds to the change from the collinear to a canted spin structure[2]. Recently, high field magnetization measurements at 4.2K have predicted a magnetic transition at 13.5T [3]. We have carried out neutron diffraction measurements in a pulsed magnetic field at liquid He temperature. The magnetic fields is applied parallel to the a-axis. Fig.2 shows the field dependence of the normalized integrated intensity of magnetic (001) Bragg peaks. At 9.4T, the integrated intensity is slightly smaller than that at zero field. But at 14T, increase of Bragg peak intensity is observed. This change indicates that a transition of magnetic structures occurs. On the other hand, the intensity of (011) Bragg peak grows monotonously as the field increase up to the transition field. Behaviors of (011) and other Bragg peak above the transition field is now being examined.

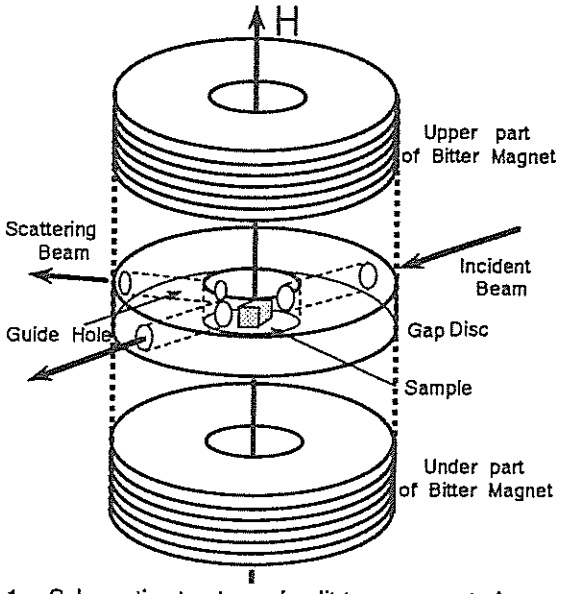

Fig. 1. Schematic structure of split type magnet. A center gap disk is sandwiched between water cooling Bitter magnets. Neutron beams pass the guide holes.

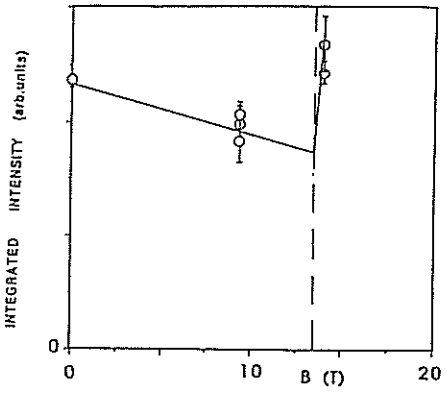

Fig. 2 Field dependence of integrated intensity of (001) Bragg peak.

References

[1]H.Nojiri *et al.*, J.Phys.Soc.Jpn. 60(1991)2380.
[2]R.A.Robi *et al.*, Am.Mineral 67(1982)470.
W.Loffermoser and H.Fuess,
Phys.status.Solid. 109(1988)587.
[3]H.Kato: private communication.

Reentrant Spin Glass State in $Ni_{77}Mn_{23}$

T. SATO, T. ANDO and M. FURUSAKA*

Department of Instrumentation Engineering, Faculty of Science and Technology, Keio Univ., Yokohama 223
*National Laboratory for High Energy Physics, 1-1 Oho, Tsukuba-shi, Ibaraki 305

Our previous neutron depolarization analysis brought out a peculiar behavior in the reentrant spin glass $Ni_{77}Mn_{23}$; enhancement of local induction B was observed at temperatures below the spin glass temperature T_g (≈65 K)[1,2]. Frustrated spins in spin glass state should cause decrease in B with decreasing temperature which was verified for typical reentrant AuFe[3]. To clarify the origin of such behavior in $Ni_{77}Mn_{23}$, we would like to obtain information about intra-domain spin configuration. However, the spatial resolution of the depolarization technique (> 1000 Å) is not sufficient to investigate such spin correlation. In contrast to it, typical resolution of SANS technique is around 10 ~ 1000 Å. Hennion et al. found the intense diffuse scattering centered at q = 0 in zero field and q ≠ 0 in magnetic field in reentrant NiMn[4,5]. Therefore, we measured SANS in $Ni_{77}Mn_{23}$ sample which was used in our previous neutron depolarization measurements.

SANS measurements of polycrystalline $Ni_{77}Mn_{23}$ were performed in a field of 0 ≤ H ≤ 4 kOe at temperatures above 15 K using SAN spectrometer at KENS. Magnetic contributions were separated using scattering intensity obtained at R.T. as nonmagnetic contribution.

Figure 1 shows the wave number dependent scattering intensity I(q) of $Ni_{77}Mn_{23}$ at various temperatures in zero field. The scattering intensity rapidly decreases with temperature for q < 0.03 $Å^{-1}$, whereas weak temperature dependance was observed for q > 0.03 $Å^{-1}$.

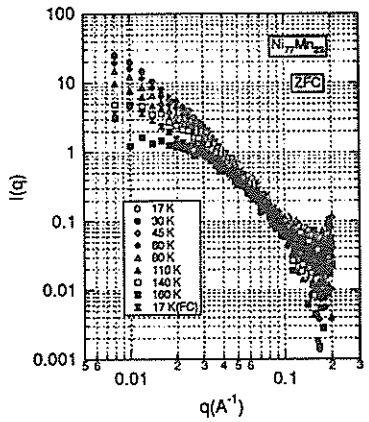

Fig. 1 Wave number dependent neutron scattering intensity of $Ni_{77}Mn_{23}$ at various temperatures in zero field.

The scattering curves in low q region (q < 0.03$Å^{-1}$) can be fitted with Lorenzian at temperatures below the Curie temperature T_C (≈160 K)

$$I(q) = A / [q^2 + \kappa^2] , \quad (1)$$

where A and κ are the scattering amplitude and the inverse correlation length, respectively. In Fig.2 inverse of intensity are shown against square of q in the q range of 0.008 ≤ q ≤ 0.03 $Å^{-1}$. Temperature dependence of A and κ is shown in Fig.3.

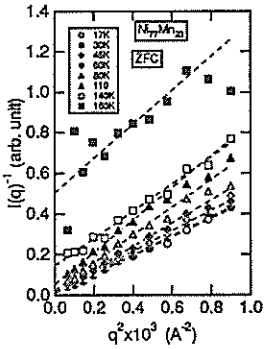

Fig. 2 Lorentzian plot of the scattering intensity in $Ni_{77}Mn_{23}$ in the q range of 0.008 ≤ q ≤ 0.03 $Å^{-1}$

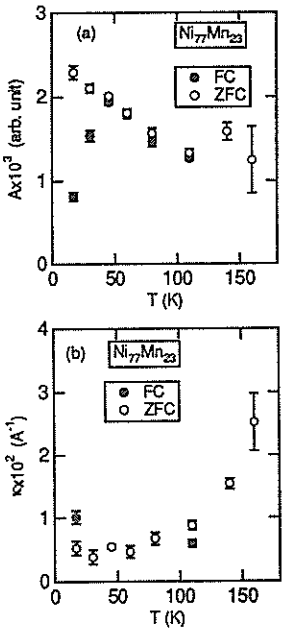

Fig. 3 Temperature dependence of scattering amplitude A and inverse correlation length κ.

The amplitude A obtained from the fit under ZFC condition monotonically increases with decreasing temperature except around T_C. The inverse correlation length κ decreases with decreasing temperature down to 60 K and becomes almost constant (0.005 $Å^{-1}$ at 60 K) at temperatures lower than 60 K . We should note that the spin correlation grows with decreasing temperature without critical behavior around T_g. Sample cooled under H_c = 1 kOe shows a small hump centered at q = 0.03 $Å^{-1}$ at 17 K as shown in Fig.1. The FC scattering curves can also be fitted with Lorentzian in the q range of $0.008 \leq q \leq 0.024$ $Å^{-1}$. The decrease in A shown at temperatures below 50 K reflects the domain orientation under field cooling condition[1,2]. On the other hand, we must mention that κ^2 obtained under field cooling condition has negative value in temperature region between 30 and 80 K (these values of κ are not shown in Fig.3(b)). These extraordinary behavior of κ suggests that the Lorenzian with peak centered at q = 0 is inadequate to fit the FC data.

Figure 4(a) shows the spherically averaged scattering intensity in a field with $0 \leq H \leq 4$ kOe at 19 K. With increasing field, the intensity centered at q = 0 decreases and an intensity peak at a finite q becomes more pronounced. The x-component gives dominant contributions to the peaks as shown in Fig.4(b), where magnetic field is applied along the x-direction. This would indicate a modulated structure of transverse spin components induced in an applied field. The small hump in the FC scattering intensity at 17 K suggests that an induced spin modulation in field can be partly maintained even in H = 0 due to the stable unidirectional magnetic anisotropy induced under FC condition[6].

Finally, we discuss our previous results of neutron depolarization measurements of $Ni_{77}Mn_{23}$ on the basis of the information obtained from SANS studies. Since the polarization measurement is performed in magnetic field, the neutron depolarization analysis should include contributions from the induced spin modulation detected in SANS measurement. In neutron depolarization measurement, we obtained the wave length dependent polarization of spins in a weak field (H = 30 and 90 Oe) and deduced B from period of oscillatory polarization as a function of wavelength. Assuming that Larmor precession of neutron spins in sample is accelerated due to some spin structure modified in field, the growth of modulated spins would be identical to increase in the local induction. A candidate for such spin modulation would be helical or vortex type[7] one of transverse spin components. The peculiar behavior of local induction can be explained in terms of transverse spin correlation induced in field.

In conclusion, the transverse spin correlation in reentrant spin glass state of $Ni_{77}Mn_{23}$ is perturbated by application of field as characterized with intensity peak in SANS. The temperature dependent local induction estimated from the neutron depolarization measurement would reflect the spin configuration modified by applied field.

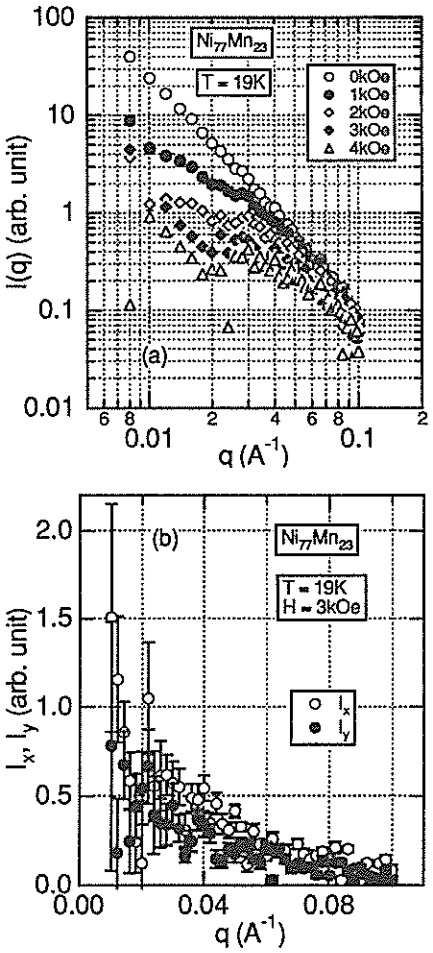

Fig. 4 Scattering intensity of $Ni_{77}Mn_{23}$ measured in a field at 19 K (a) the x- and y-component of intensity in H = 3 kOe.

References

1) T. Sato et al., KENS REPORT-VIII (1989/90), KEK Progress Report 90-2, 148
2) T. Sato et al., J. Magn. Magn. Mater. 104-107, 1625(1992)
3) S. Mitsuda et al., J. Phys. Soc. Jpn. 60,1721(1991)
4) M. Hennion et al., J. Magn. Magn. Mater. 54-57, 121(1986)
5) M. Hennion et al., Europhys. Lett. 2,393(1986)
6) T. Sato, Phys. Rev. B41,2550(1990)
7) H. Kawamura and M. Tanemura, J. Phys. Soc. Jpn. 55,1802(1986)

Domain Configuration in Reentrant Spin Glass $Ni_{77}Mn_{23}$

T. SATO, T. ANDO, T. WATANABE*, S. ITOH* and Y. ENDOH*

Department of Instrumentation Engineering, Faculty of Science and Technology, Keio Univ., Yokohama 223
*Department of Physics, Tohoku University, Aramaki, Aoba-ku, Sendai 980

Reentrant spin glass properties of $Ni_{1-x}Mn_x$ have been interpreted by the idea of the domain-anisotropy model[1]. The domain model was well supported by the transmission electron microscopy observation[2] and the neutron depolarization analysis[3-5], which gave the basis of the mean field picture for reentrant phase in $Ni_{1-x}Mn_x$. Recently, the induced anisotropy was investigated by the electron spin resonance (ESR)[6], the transverse ac susceptibility[7] and the rotational magnetic measurement[8], while insufficient information about the field dependent domain configuration has caused some inconsistency in the interpretation for nature of the anisotropy. Then, we tried to investigate the field dependent domain configuration in $Ni_{77}Mn_{23}$ using the neutron depolarization measurements in some fields larger than those used in the previous work.

Neutron depolarization measurements of a plate $Ni_{77}Mn_{23}$ sample of 1.04 mm thick were performed using TOP spectrometer at KENS. All the incident neutron spins were polarized along the z-direction. The polarization $P(\lambda)$ along the z-direction is measured as a function of the wavelength (3-9 Å) just after the neutron passes through the sample along the x-direction. Magnetic field was applied along the z-direction up to 1020 Oe. Further, the procedure of π-rotating the sample in the y-z plane is performed to apply an external field antiparallel to the anisotropy field H_A induced by cooling field. Hereafter, we will regard a field applied antiparallel to H_A as being applied in the - direction. The geometry of neutron depolarization measurement is described in Fig.1.

Figure 2 shows the field dependent neutron polarization after cooling down to 15 K in H = 1020 Oe. The polarization in a field along the - direction was measured after applying magnetic field up to +1020 Oe. The damped oscillation, expected for a ferromagnetic sample in the mono-domain state[9], is observed in fields between -90 and 90 Oe where larger depolarization is recognized in a field along the + direction. On the other hand, the wavelength dependent polarization in H = -315 Oe is fitted by following equation

$$P(\lambda) = \exp\{ -c_1[1 - \cos(c_2\lambda)\exp(- c_3\lambda^2)]\}, \qquad (1)$$

while the following simple form

$$P(\lambda) = e^{-\alpha\lambda^2} \qquad (2)$$

gives only insufficient agreement. These field dependent polarization data give some important information about domain configuration, i.e., the mono-domain configuration can no be retained in negative field with amplitude larger than 315 Oe

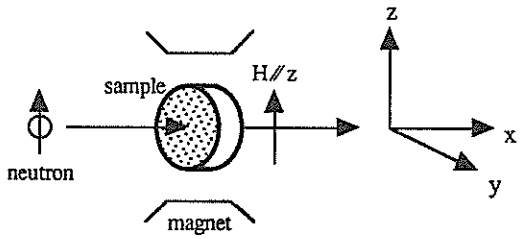

Fig. 1 Geometry of neutron depolarization measurement.

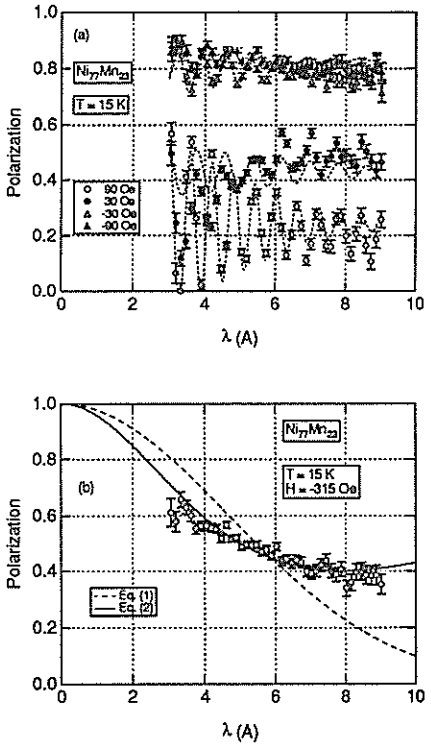

Fig. 2 Field dependent neutron polarization $P(\lambda)$ at 15 K of $Ni_{77}Mn_{23}$as a function of wavelength.

in which the magnetization reversal is attained as recognized in magnetization curve. In other words, the idea of rigid rotating magnetization with rotating field under the field cooling condition should be denied from viewpoint of the neutron depolarization analysis. Further, we note that no oscillation was observed even in H = -90 and -30 Oe after field was applied down to -1020 Oe.

The damped oscillation of polarization can be fitted with the following form

$$P(\lambda) = c_1 + c_2\exp(c_3\lambda^2)\cos(c_4\lambda + c_5). \quad (3)$$

Figure 3 shows the external field dependence of parameter c_4 which is practically proportional to the local magnetic induction B[9]. In fields larger than +90 Oe, c_4 is scarcely dependent on field, while the decrease in c_4 with increasing amplitude of field is observed in fields along the - direction. Considering that the induced anisotropy field is antiparallel to the external field along the - direction, the decrease in c_4 should be attributed with decrease in average length of spins and/or disordering of spins due to weak effective field which contains anisotropy field.

Sample cooled in zero field down to a temperature below spin glass temperature Tg (≈65 K) shows the small polarization with no oscillation in field lower than 320 Oe. Typical ZFC polarization data shown in Fig.4 can be fitted by Eq.(1), which suggests the nonrandom domain orientation due to application of comparatively high field. Mirebeau et al. found that the magnetization in a domain is essentially identical to the spontaneous magnetization even under ZFC condition on the basis of the neutron polarization measurements of $Ni_{77}Mn_{23}$ in very low field[3]. Therefore, our ZFC field dependent polarization should reflect the behavior of domain motion. The field dependence of parameter c_1 at temperatures below T_g given in Fig. 5 has the following feature:

1) The increase in c_1 starts at lower field with increasing temperature.

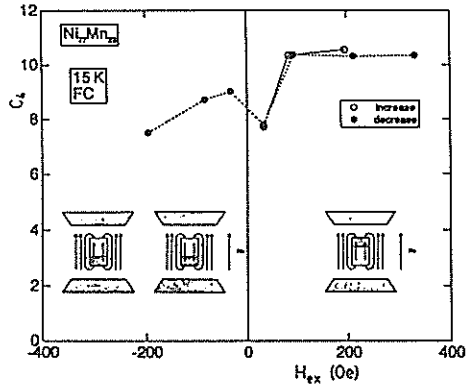

Fig. 3 The parameter c4 of $Ni_{77}Mn_{23}$ in a field.

2) Irreversible behavior with cycle of field is large at 33K which is considerably below Tg.

These feature is consistent with the idea of a slowing down of the domain mobility below Tg and the temperature dependance of the hysteresis loss in $Ni_{81}Mn_{21}$[10].

In conclusion, we claim that the neutron depolarization analysis gives detailed information about the domain configuration in $Ni_{77}Mn_{23}$ in magnetic field for the first time.

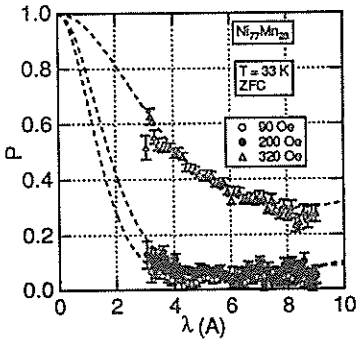

Fig. 4 Neutron polarization of $Ni_{77}Mn_{23}$ at 33K under ZFC condition.

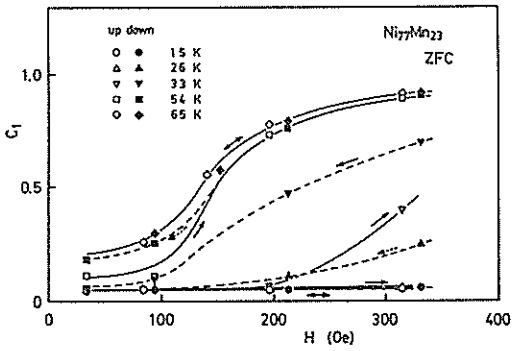

Fig. 5 Field dependent c_1 at various temperatures of $Ni_{77}Mn_{23}$.

References

1) J. S. Kouvel, W. Abdul-Razzaq and Kh. Ziq, Phys. Rev. B35,1768(1987)
2) S. Senoussi, S. Hadjoudj and R. Fourmeaux, Phys. Rev. Lett. 61,1013(1988)
3) I. Mirebeau et al., Phys. Rev. B44,5120(1991)
4) T. Sato et al., KENS REPORT-VIII (1989/90), KEK Progress Report 90-2, 148
5) T. Sato et al., J. Magn. Magn. Mater. 104-107, 1625(1992)
6) B. Aktas, Y. Oner and E. A. Harris, Phys. Rev. B39,528(1989)
7) T. Sato, Phys. Rev. B41,2550(1990)
8) Kh. A. Ziq and J. S. Kouvel, Phys. Rev. B41, 4579(1990)
9) S. Mitsuda et al., J. Phys. Soc. Jpn. 60,1721(1991)
10) S. Senoussi, J. Phys. (Paris) 45,315(1984)

New Reentrant Spin Glass Transition in $Cr_{0.81}Mn_{0.19}Ge$

T. SATO, T. ANDO and M. FURUSAKA*

Department of Instrumentation Engineering, Faculty of Science and Technology, Keio Univ., Yokohama 223
*National Laboratory for High Energy Physics, 1-1 Oho, Tsukuba-shi, Ibaraki 305

The B-20 type compound CrGe shows nearly ferromagnetic behavior[1], and the substitution of Mn for Cr causes diversity of magnetic properties[2-5]. The $Cr_{1-x}Mn_xGe$ shows ferromagnetism for $x \leq 0.15$, and higher Mn concentration ($x \geq 0.24$) leads to spin glass. While a transition from ferromagnetic to spin glass phase at low temperature would be expected for $0.15 < x < 0.24$, we have not obtained definite evidence for the reentrant transition from the magnetic data. Recent neutron depolarization measurements of $Cr_{0.81}Mn_{0.19}Ge$ using TOP spectrometer suggest no ferromagnetic domain in low field ($H \leq 100$ Oe)[6]. To investigate nature of the magnetic transition, we measured small angle neutron scattering (SANS) of $Cr_{0.81}Mn_{0.19}Ge$.

SANS studies of polycrystalline $Cr_{0.81}Mn_{0.19}Ge$ were performed in a field of $0 \leq H \leq 2$ kOe at temperatures from 5K to 20K using SAN spectrometer at KENS. Magnetic contribution was separated using scattering intensity obtained at 50 K as nonmagnetic term.

Figure 1 shows the scattering intensity under zero field cooling condition in zero field. Peaks were observed at finite q at all temperatures below 14 K. They were fitted by Lorentzian:

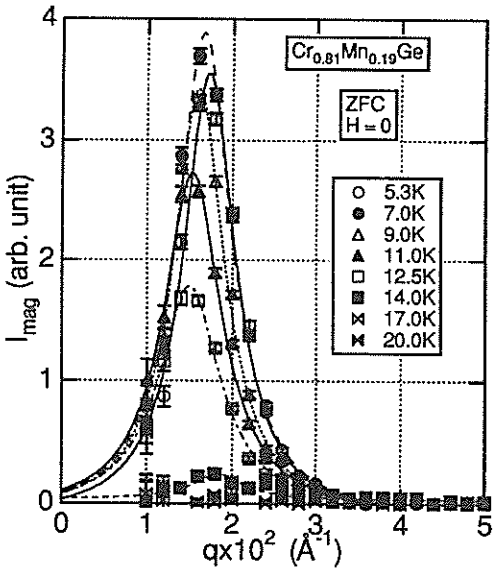

Fig. 1 Temperature dependent SANS intensity of $Cr_{0.81}Mn_{0.19}Ge$ under ZFC condition. Data are fitted by Lorentzian.

$$I(q) = A / [(q - q_0)^2 + \Delta q^2], \quad (1)$$

where q_0 and Δq are the peak position and the full width at half minimum, respectively. Temperature dependent integrated intensity I_{tot}, q_0 and Δq were obtained from the fit as shown in Fig.2.

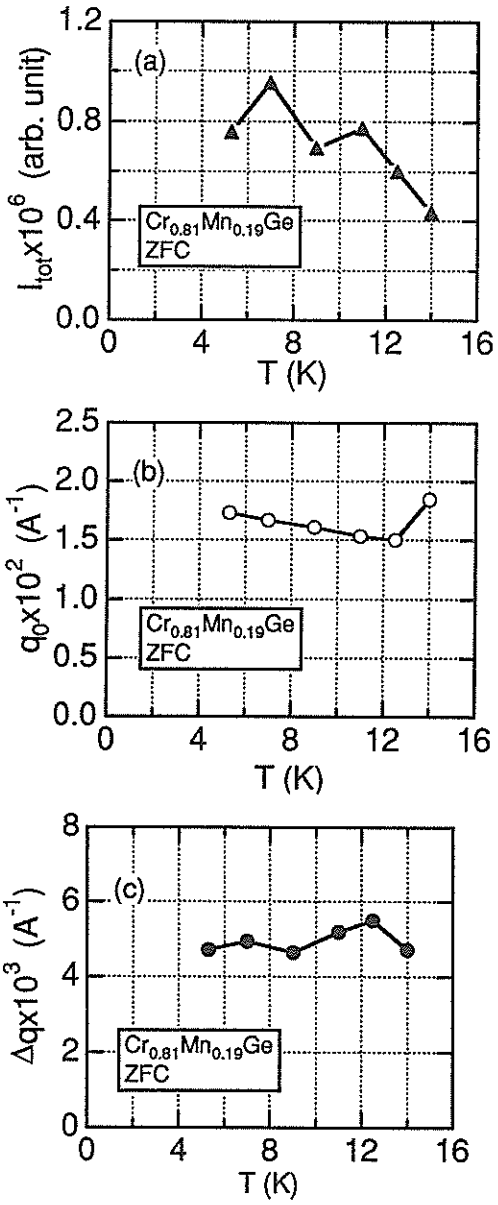

Fig. 2 Temperature dependence of parameters obtained from the Lorentzian fitting.

The intensity peak centered at a finite q suggests a possible spin configuration other than ferromagnetic ordering in reentrant spin glass like $Cr_{0.81}Mn_{0.19}Ge$. Magnetic behavior of our sample resembles to that of the itinerant electron type helical magnet MnSi[7], i.e., no spontaneous magnetization, spin flip like behavior in magnetization curve and insufficiently saturated magnetization in high fields at low temperatures. Therefore, the SANS data suggest the helical spin structure in $Cr_{0.81}Mn_{0.19}Ge$ at all temperatures below 14 K which is regarded as the order-disorder transition temperature. From temperature dependence of the peak position q_0, period of helical spin structure is obtained. It increases with increasing temperature from 360 Å at 5.1K to 420 Å at 12.5K.

There are intensity maxima at 11 and 7K, while q_0 and Δq do not show any singular behavior at both temperatures. The former temperature corresponds to a temperature at which a cusp is observed in the temperature dependent magnetic susceptibility. At temperatures below the latter temperature, an irreversible behavior in magnetic susceptibility is pronounced. This correspondence suggests that another magnetic ordering coexists in addition to the helical magnetism. Although we can not mention about detailed picture of the coexisting spin ordering, the origin should be ascribed to spin glass like interaction.

Figure 3 shows x- and y-components of neutron scattering intensity at 5.1 K in a field below 2 kOe, where the magnetic field was applied along the x-direction. The intensity in 100 Oe is essentially identical to that in 0 Oe. Applied fields of 200 and 400 Oe result in complex changes in q dependence of the both components. The x-component has two peaks centered at finite values of q where q_0 of the low q peak is essentially identical to that in H = 0. The y-component at a finite q rapidly decreases with applying field, and intensive scattering at very small q appears. Higher field above 1000 Oe suppresses the x-component. The field dependent scattering of $Cr_{0.81}Mn_{0.19}Ge$ is interpreted as follows:

1) Below 100 Oe, spins of helical structure are restricted in planes perpendicular to the crystal axis, therefore, the scattering is isotropic in polycrystalline sample.

2) Applied field of 200 Oe changes the direction of the q-vector to the magnetic field, results in the rapid increase in x-component.

3) Under 400 Oe, the helical spin structure changes to the conical type structure. The magnetization component induced along x-direction causes scattering in the y-component at very small q.

4) The higher q peak of the x-component around q = 0.025 $Å^{-1}$ in H = 200 and 400 Oe suggests appearance of higher harmonics originated from the interaction of two helical structure with different q vector[7].

5) Application of high field above 1000 Oe results in transition to the ferromagnetic spin ordering via the conical type spin structure.

These interpretation is consistent with the magnetic measurements. In conclusion, $Cr_{0.81}Mn_{0.19}Ge$ is the itinerant electron type helical magnet, and the spin glass like interaction gives additive magnetic contribution to the spin configuration at low temperatures.

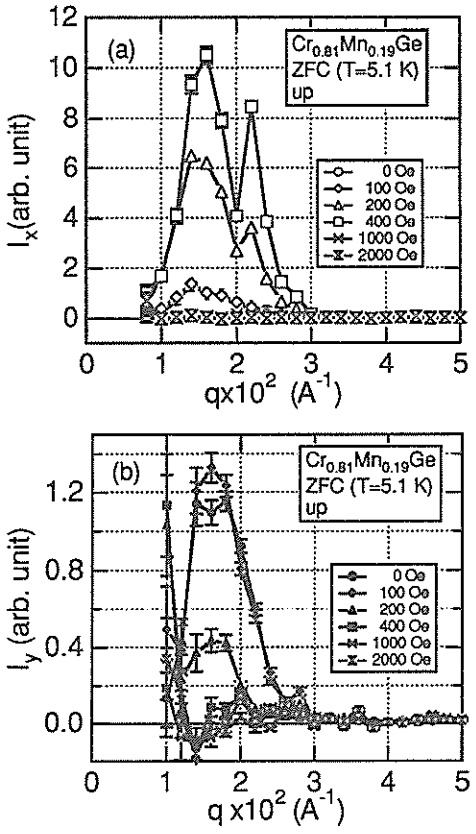

Fig. 3 X- and y-components of SANS intensity of $Cr_{0.81}Mn_{0.19}Ge$ in magnetic field at 5.1 K.

References

1) T. Sato and M. Sakata, J. Phys. Soc. Jpn. 52,1807 (1983)
2) T. Sato et al., J. Magn. Magn. Mater. 70,411(1987)
3) T. Sato et al., J. Phys. Soc. Jpn. 57,639(1988)
4) T. Sato et al., J. Phys. F: Met. Phys. 18,1593(1988)
5) T. Nemoto et al., J. Magn. Magn. Mater. 78,43 (1989)
6) T. Sato et al., unpublished
7) Y. Ishikawa et al., Solid State Commun. 19,525 (1976)

Magnetic Phase Transition of Oxygen Monolayer

Y.Murakami, I.Makundi, T.Shibata, H.Suematsu, M.Arai*, H.Ikeda* and N.Watanabe*

Department of Physics, Faculty of Science, Tokyo Univ. Bunkyo-ku, Tokyo 113
*National Laboratory for High Energy Physics, 1-1 Oho, Tsukuba-shi, Ibaraki 305

Oxygen (O_2) molecules physisorbed on graphite form an ideal two-dimensional (2D) lattice. The interaction between O_2 molecules is a Heisenberg-like antiferromagnetic one which is ascribed to the direct exchange interaction. So, we can regard the O_2 monolayer system as a good model of the 2D Heisenberg antiferromagnet with a small anisotropy.

In a simplified phase diagram of this system there are two principal phases depending on coverage C; C=1 is defined so as to form the triangular $\sqrt{3}x\sqrt{3}$ superlattice referred to the graphite lattice. The dense phase, ζ-phase (C > 1.8), has the in-plane triangular lattice incommensurate with graphite substrate, in which the molecular axis of O_2 is normal to graphite surface, while the dilute phase, δ-phase (C < 1.3), has the centered rectangular lattice with the molecular axis parallel to the surface[1-3]. By neutron diffraction experiments Nielsen et al. revealed the structural phase transition of ζ- to ε-phase , and reported that ε-phase which has a deformed triangular lattice is a antiferromagnetic long-range-ordered phase, although the observed intensity of the magnetic Bragg diffraction was of the order of the statistical deviation[1].

This neutron diffraction measurements were carried out at MRP port in KENS using the time of flight technique. ^{3}He detectors were placed at low angles (2θ = 15°, 35° and 45°) for observation of the magnetic diffraction peak and at high angles (2θ = 60°, 80° and 120°) for the nuclear diffraction peak; three detectors were set up at each angle. The sample was set in such a way that the scattering vector is parallel to the graphite surface. The O_2 monolayer crystal was prepared on Grafoil (a exfoliated graphite) sheets of about 35 g, which has a specific surface area of 24 m^2/g. O_2 gas was introduced at T=54 K and the sample was cooled gradually as annealing at the melting temperature.

We could clearly observe the magnetic Bragg peak at Q=1.17 Å in ε-phase. Figure 1 shows the magnetic Bragg peaks of C=1.90 at some temperatures. We obtained these spectra by subtracting the spectrum at T=17 K from the original ones. The magnetic peak decreases with increasing temperature and completely disappears at T= 12 K. This is a direct evidence of the magnetic long-range-order in ε-phase. The line-shape is not symmetrical and has a tail at high Q. This is ascribed by a mosic feature of the substrate. The higher order of the magnetic peak is not clearly observed, which may be attributed to the finiteness of the spin correlation.

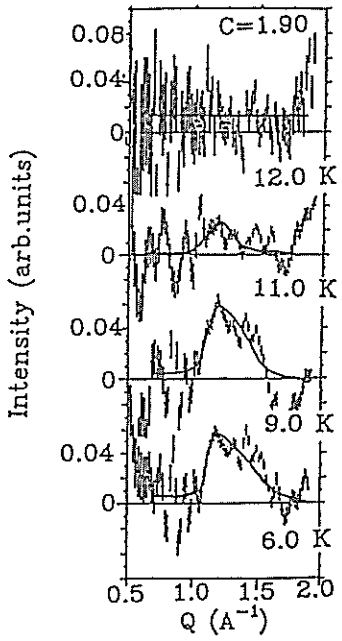

Fig. 1 The magnetic diffraction spectra of C=1.90 at some temperature.

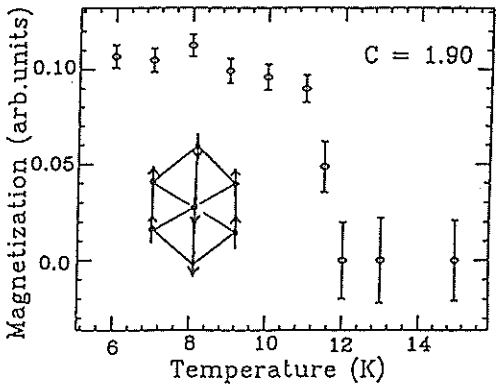

Fig. 2 The temperature dependence of the square root of the integral intensity, i.e., the sublattice magnetization. The inset shows the spin structure in ε-phase.

Figure 2 shows the temperature dependence of the square root of the integral intensity of magnetic peak, that is, the sublattice magnetization. The transition temperature is determined to be T_N=11.7 K, which is consistent with the previous works[1-3]. However, the intensity decreases abruptly above T=11 K; this temperature dependence is not consistent with the result of the previous neutron experiment, in which they showed a continuous change of the magnetization with temperature[1].

In Fig. 3 we show the nuclear peaks for some temperature at C=1.90. Below T_N we observe two peaks at Q= 2.21 Å and 2.34 Å, and above T_N a single peak at Q=2.25 Å. This splitting comes from a magnetically-induced lattice deformation. The Q value of the high Q peak below T_N is just twice as large as that of the magnetic peak. The two splitting peaks are in the ratio of the integral intensity 2:1. These facts is consistent with the spin structure proposed by the previous neutron experiment[1] shown in the inset of Fig.2.

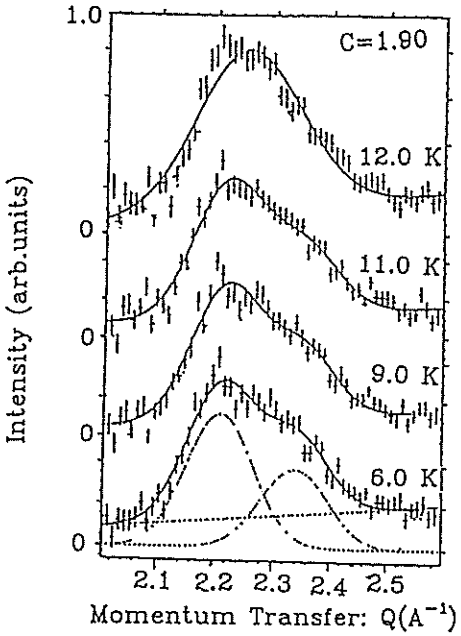

Fig. 3 The spectra of the nuclear peaks of C=1.90 at some temperature.

Figure 4 shows the coverage dependence of the nuclear peaks at T= 8.0 K. The peaks at C=1.00 and 1.70 correspond to those of δ-phase and of ε-phase first layer, respectively. When we increase coverage, O_2 molecules make the second layer of ε-phase. The nuclear peak of the second layer appears at Q=2.30 Å, but this peak is not split below T_N. The structure of the second layer is a little dense one compared with that of the first layer in ζ-phase. Meanwhile, the magnetic peak of the second layer is not observed clearly. These facts indicate that the second layer is not ordered, which is consistent with the susceptibility measurements[2].

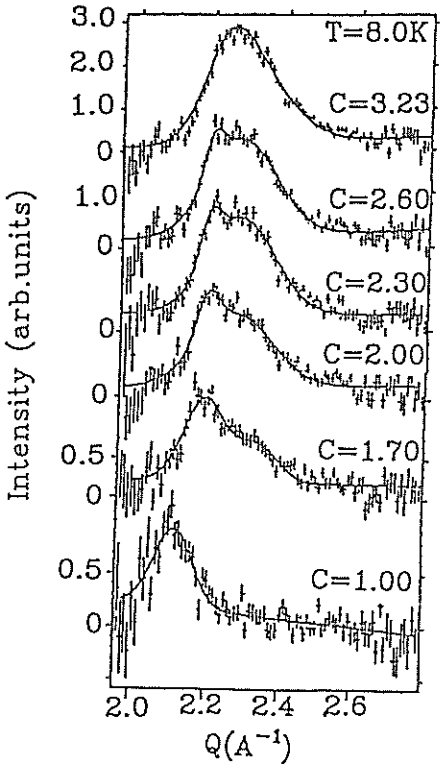

Fig. 4 The spectra of the nuclear peak for some coverage at T=8.0 K.

In conclusion, we have observed the magnetic Bragg peak in ε-phase which is a direct evidence of the magnetic long-range-order. The coverage dependence of the nuclear peak shows that the second layer in ε-phase is not distorted alike the first layer and the magnetic peak is not observed, which implies the second layer is not ordered.

References

1) M.Nielsen and J. P. McTague, Phys. Rev. B 19, 3096 (1979).
2) H. Suematsu and Y. Murakami, J. Magn. Magn. Mater. 90&91, 749 (1990).
Y. Murakami and H. Suematsu, Surf. Sci. 242, 211 (1991).
3) S. G. J. Mochrie, M. Sutton, J. Akimitsu, R. J. Birgeneau, P. M. Horn, P. Dimon and D. E. Moncton, Surf. Sci. 138, 599 (1984).

Neutron Depolarization Study on Iron Fine Particles

S.ITOH, I.MIREBEAU*, C.BELLOUARD*, M.HENNION*, T.WATANABE**, H.YASUDA** and Y.ENDOH**

National Laboratory for High Energy Physics, Tsukuba 305
*Laboratoire Leon Brillouin, CEN Saclay, 91191 GIF-SUR-YVETTE CEDEX, France
**Department of Physics, Tohoku University, Sendai 980

A neutron depolarization measurement on an iron small particle system[1] was performed on the TOP spectrometer. In this system small iron particles are dispersed in an alumina matrix by the sputtering of iron and alumina onto an aluminium matrix. In the present measurement we used a S12 sample[1]. The iron particles are about 30 Å in diameter. This system shows a superparamagnetic behavior at room temperature. Small angle neutron scattering and neutron depolarization measurements were performed using a monochromatic beam[2]. With decreasing temperature, the small angle scattering intensity increased and the neutron beam was depolarized. These results have been interpreted as a strong correlation between the magnetic moments of the particles at low temperatures.

In a monochromatic beam only one point in the wavelength-dependence of the polarization of the transmitted beam, $P(\lambda)$, was measured; and the result has been discussed assuming an exponential dependence $P(\lambda)=\exp(-\alpha\lambda^2)$[2]. The present experiment clarifies the wavelength-dependence using a polychromatic beam.

The $P(\lambda)$ of the sample S12 was measured in a weak external field (7Oe) of the guide magnet after cooling the sample without an external field. Figure 1 (a) shows the typical result. The neutron depolarization was very little at the lowest temperature in the measurement (5K) and at the temperatures higher than 60K. On the other hand, depolarization was observed at intermediate temperatures and peaked at 20K. Each data fitted well to the following wavelength-dependence;

$$P(\lambda) = C_1 + (1 - C_1) \cos C_2 \lambda .$$

The solid lines in Fig.1 (a) are the fitted curves. The temperature dependence of the coefficient C_2 was obtained by fitting the data to the above dependence and the result is shown in Fig.1 (b). C1 was fixed to 0.95 in the fitting because the constant value of $C_1=0.95$ was obtained by fitting the data at the temperatures between 10 and 40K.

In the system of small particles dispersed in a nonmagnetic medium the coefficient C_2 in $P(\lambda)$ is proportional to the mean magnetization over the sample if the time of flight of the neutron through the particle, τ_F, is less than the period of the Larmor precession of the neutron spin around the magnetization within the particle, τ_L[3]. This condition is realized for the present system because the typical values are $\tau_F=10^{-11}$sec and $\tau_L=10^{-7}$sec for an iron particle of 10^2Å in diameter and 10Å of the neutron wavelength. Therefore C_2 should be proportional to the sample magnetization. In fact C_2 has the same behavior as the magnetization and AC susceptibility. The peak in the temperature dependence of C_2 corresponds to the cusp in the susceptibility around 20 - 25K[1]. The cusp is interpreted as the blocking temperature in the superparamagnetic Néel model[4].

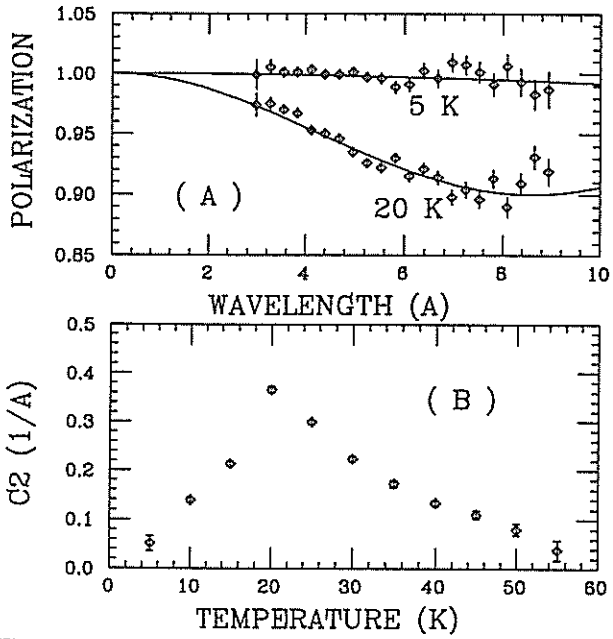

Fig. 1 The wavelength and the temperature dependence of the polarization of the transmitted beam. $P(\lambda)$ is well fitted to $C_1+(1-C_1)\cos C_2\lambda$ as shown in (A) and the temperature dependence of C_2 is indicated in (B).

References

1) J. L .Dormann et al., J. Phys. C: Solid State Phys. 21, 2015 (1988)
2) I.Mirebeau et al., J. Magn. Magn. Mat. 104-107, 1560 (1992)
3) S. Itoh et al., J. Magn. Magn. Mat. 111, 56 (1992)
4) L. Néel, Ann. Geophys. 5, 99 (1949)

Spin Waves in $BaNi_{1/2}W_{1/2}O_3$

Y Todate and A Yazaki†

Department of Physics, Faculty of Science, Ochanomizu University, Bunkyo-ku, Tokyo 112
†Department of Physics, Faculty of Science, Keio University, Hiyoshi Yokohama 223

$BaNi_{1/2}W_{1/2}O_3$ is an oxide which has so-called ordered perovskite structure. In this structure, Ni^{2+} and W^{6+} alternately align in the B positions of cubic perovskite ABO_3 structure and therefore the edge of the unit cell is doubled[1]. Magnetically this oxide shows antiferromagnetism below 50K. Since Ni ions are separated by two O^{2-} and one W^{6+}, there exist extremely long range (8.06Å) superexchange interactions between them. It has been reported that the antiferromagnetic (AF) structure is of type-II with the spin direction perpendicular to [111]-direction, which is similar to NiO, and that the magnetic moment is $1.9\mu_B$ at 4.2K[2]. The crystal structure is cubic at all temperatures. Note that there are two types of interaction path, i.e. 180°(J_2) and 90°(J_1) interaction interposed by W^{6+} ,which is considered to be diamagnetic. It has been speculated that these two interaction have nearly the same strength[1], contrasted to the case of NiO. It seems, however, that this speculation is not always evident. It has also shown that the effect of covalency on the superexchange interaction should be treated more correctly[3]. It is therefore interesting to determine the accurate magnitude and the sign of these two types of interaction by measuring spin-wave dispersion relations.

Neutron inelastic scattering measurements were carried out with MAX spectrometer using a single crystal sample grown by the floating-zone method. Inelastic peaks have been observed at 18K and their energies are plotted in Fig. 1.

The spin-wave dispersion relation for the type-II AF structure has been calculated from the Hamiltonian,

$$H = \sum_{m,m',j,j'} J_{m,m',j,j'} S_{m,j} S_{m',j'} + \sum_{m,j} \left[D_1 \left(S^x_{m,j} \right)^2 + D_2 \left(S^y_{m,j} \right)^2 \right],$$

where D_1 and D_2 are easy-plane and inplane type anisotropy constant respectively. D_1 would be much larger than D_2. The dispersion relation is

$$\left(\hbar\omega_{\left(\frac{1}{2}\right)} \right)^2 = \left(A_q - B_q + D_{\left(\frac{1}{2}\right)} \right) \left(A_q + B_q + D_{\left(\frac{1}{2}\right)} \right),$$

where A_q and B_q are Fourier transforms of the exchange interactions. J_1, J_2 and D_1 have been determined by fitting this expression to the experimental data:

J_1=+1.4 (K), J_2=-8.4(K) and D_1=2.6 (K).

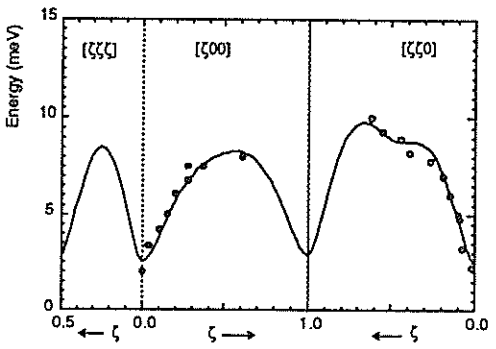

Fig. 1 Plot of the measured peak position and the calculated dispersion relation along [100], [110] and [111] direction.

Splitting of the energy due to D_1 and D_2 has not been detected. The values of two exchange parameters are significantly different. Although the data is not sufficient at this moment, smallness of J_1 seems to be consistent with the lack of contamination from different domains in the type-II AF structure[4]. As a result the role of W^{6+} on this super exchange interaction should be correctly taken into consideration.

We wish to thank Prof. A.Itoh of Ochanomizu Univ. for help of the single crystal preparation.

References

1) S.Nomura and T.Nakagawa, J. Phys. Soc. Japan, **21** (1966) 1679.
2) D.E.Cox, G.Shirane and B.C.Frazer, J. Apple. Phys. **38** (1967) 1459.
3) J.Zaanen and G.A.Sawatzky, Can. J. Phys. **65** (1987) 1262.
4) M.T.Hutchings and E.J.Samuelsen, Solid State Commun. **9** (1971) 1011.

Spin Waves in a Metallic Antiferromagnet Mn_3Pt

S. Tomiyoshi[1], Y. Todate[2], T. Kaneko[3], H. Yasui[3], K. Tajima[4] and H. Ikeda[5]

[1]Department of Materials Science and Engineering, Faculty of Engineering, Ehime University, Matuyama 790
[2]Department of Physics, Faculty of Science, Ochanomizu University, 2-1-1 Otuka, Bunkyo-ku, Tokyo 112
[3]The Institute for Materials Research, Tohoku University, Sendai 980
[4]Department of Physics, Faculty of Science and Technology, Keio University, Hiyoshi, Yokohama 233
[5]National Laboratory for High Energy Physics, 1-1 Oho, Tukuba-shi, Ibaraki 305

Mn_3Pt(cubic Cu_3Au type crystal structure) is a metallic antiferromagnet having relatively large magnetic moment. It shows very interesting first order magnetic phase transition. According to Krén et al.[1] the magnetic structure of the low temperature phase has a triangular spin structure with the spins lying in (111) plane and it transforms at about 356K to a layered structure in which the crystallographically equivalent Mn site is divided into two magnetic sites; the one with $0\mu_B$/Mn and the other with $3.4\mu_B$/Mn. The change of the spin structure from the triangular one to the layered one does not accompany any change of the crystal symmetry except a large increase in volume.

In order to elucidate the anomalous magnetic phase transition of this compound we investigated spin wave excitations by neutron inelastic scattering using MAX spectrometer[2,3].

The single crystals of Mn_3Pt used in the present experiment were grown by the Bridgman technique using a RF furnace in He gas of 5 atm. pressures. The size of the crystal is 10ϕX30L and the mosaic width is about 0.6 deg.

Spin waves has been measured along the [100] direction on (001) reciprocal plane scanning through reciprocal points (010),(110),(210) at several temperatures in both of the low and high temperature phases. This scanning is the best one for measuring higher energies in the present experimental configurations. Dispersion relations of spin waves have been obtained from the peak positions of TOF neutron scattering data. Figure 1 shows dispersion relations measured in the low temperature phase at 383K. Below 20meV the dispersion cone was not resolved into doublet peaks due to a steep slope dispersion and a broadening of spin waves, however, above that a singlet peak was found to split into a doublet, and the line width was not broad compared with that in an itinerant antiferromagnet like Mn_3Si[4]. The spin wave have a q-linear dispersion relation in low-q region except an energy gap at q=0. The q-linear coefficient is determined to be 155meVÅ in small q region at 383K and 166meVÅ at room temperature. In reference 2 the c-value at room temperature is reported to be 136meVÅ which is a little small compared with the present value. We believe that the present value is more reliable. The spin-wave energies at the zone boundary is 55meV in triangular phase at room temperature and keeps almost same value at 383K, showing small temperature dependence.

In the high temperature phase the Brillouin zone reduces to half of that in the low temperature phase along [100] direction. The inelastic peaks have been observed mainly in (3/2,1,0) zone in this phase. Figure 2 shows the acoustic branch of the spin wave at 431K which is just above the transition temperature. The stiffness constant is c=127meVÅ and the energy at the zone boundary is estimated to be about 30meV or so. At 459K the stiffness constant is c=120meVÅ and the energy at the zone boundary is about 30meV. The spin-wave dispersion relation in both of the low and high temperature phases is not much temperature dependent as suggested in reference 2. This is one of the most important result in the present experiments. In addition to the acoustic spin-wave branch we observed several inelastic peaks probably corresponding to the optical branch, but intensities of these peaks are not enough to identify the optical branches. It seems that large reduction of the spin wave energy is mainly due to the reduction of the exchange energy, but the change of the zone boundary could have large effect on the dispersion relation of the acoustic mode. These points must be confirmed by theoretical studies and also by experiments measuring along another directions with much better counting statistics.

In the high temperature phase we observed pronounced enhancement of the back ground level around zero energy transfer in neutron inelastic scattering data. As easily seen by comparing figures 3(a)and 3(b) which are measured by counter 6 with almost the same scanning condition along [100] direction, the back ground scattering in the high temperature phase has a broad peak around energy zero. This paramagnetic-like scattering appears in the high temperature phase. In spite of the ordered phase the presence of such a scattering is very interesting. The layered spin structure proposed by Krén et al.[1] contains a Mn atom which has a magnetic moment of $0\mu_B$. If the disappearance of the magnetic moment is due to the spin fluctuation, then which contributes to the paramagnetic-like scattering. However, the layered spin structure is questioned recently from the isotropic nature of spin wave dispersion relations determined by Yasui et al.[5] by using steady reactor in lower energy region (energy transfer less than 23mV), so in order to discuss the magnetic

excitations and phase transition of Mn_3Pt, correct spin structure is essential.

References

1) E.Krén, G.Kádár, L.Pál, J.Sólyom, P.Szabó and T.Tarnóczi, Phys. Rev. 171(1968) 574.
2) S.Tomiyoshi, H.Yasui, T.Kaneko, Y.Yamaguchi, H.Ikeda, Y.Todate and K.Tajima, J.Mag.Mag.Mater. 90 & 91(1990) 203.
3) S.Tomiyoshi, T.Kaneko, U.Steigenberger, A.J.Chapell, M.Hagen and Y.Todate, Physica B 180 &181(1992)227.
4) S. Tomiyoshi, Y.Yamaguchi, M.Ohashi, R.Cowly, G. Shirane, Phys. Rev. B 36(1987)2181.
5) H.Yasui, Y.Yamaguchi, S.Funahashi, M.Yamada, M.Ohashi and T.Kaneko, Physica B180&181 (1992)235.

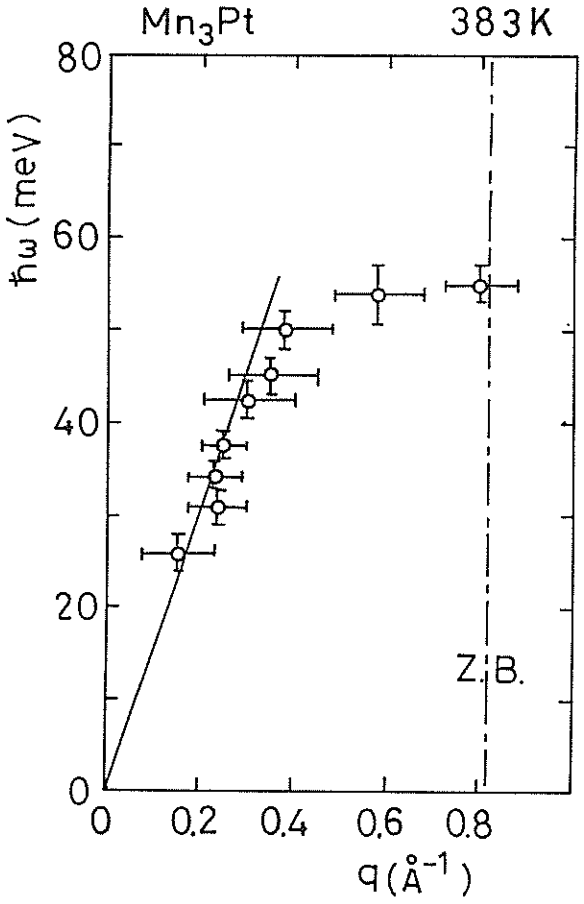

Fig. 1 Spin wave dispersion relation of Mn_3Pt in low temperature phase at 383K along [100] direction. The straight line in the figure represent the stiffness constant c=155meVÅ.

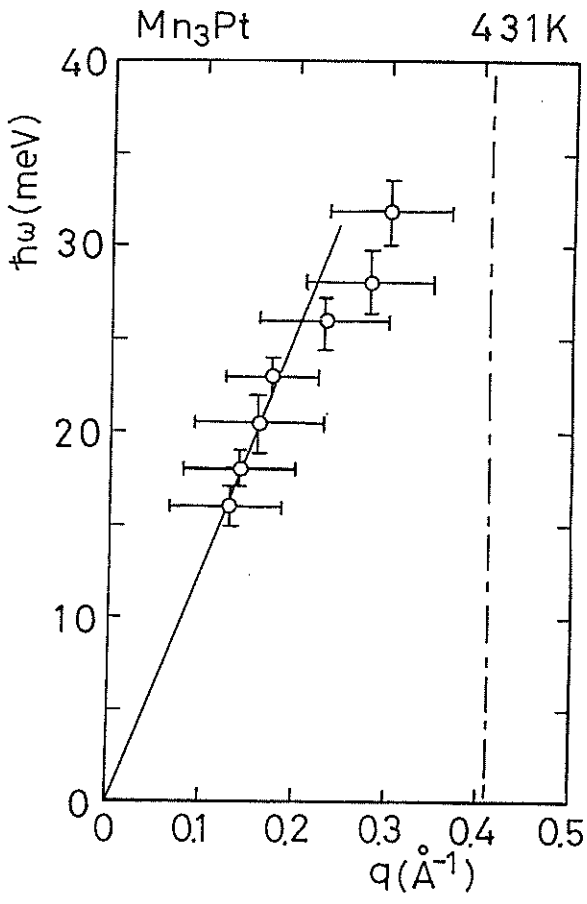

Fig. 2 Spin wave dispersion relation of Mn_3Pt in high temperature phase at 431K along [100] direction. The straight line in the figure represents the stiffness constant c=127meVÅ.

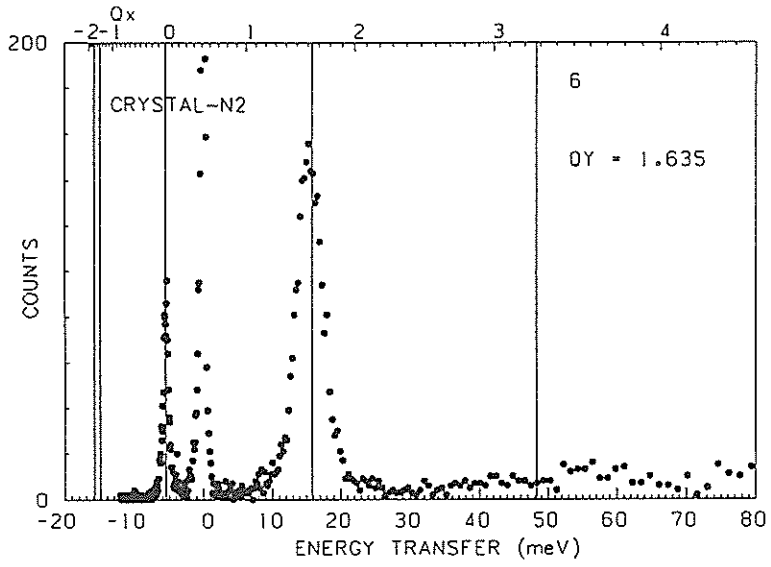

Fig. 3 (a)Neutron inelastic data by counter 6 at 383K.

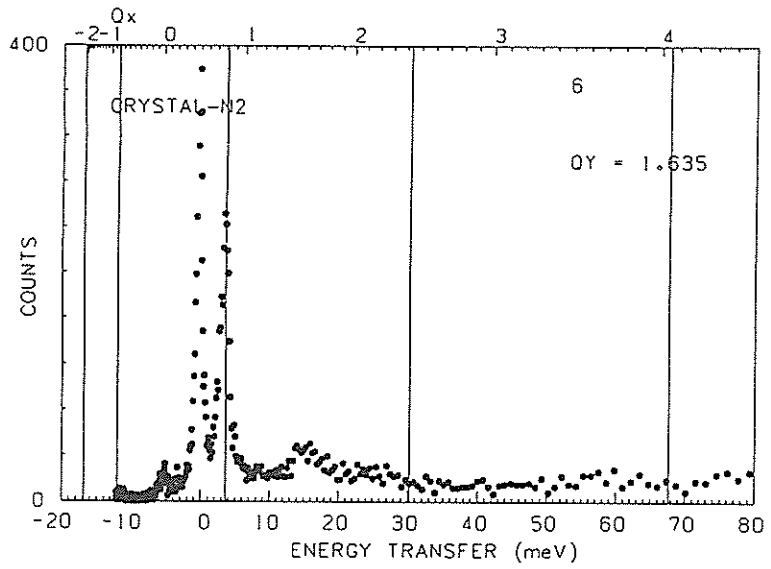

Fig. 3 (b)Neutron inelastic data by counter 6 at 431K.

Polarized Neutron Diffraction Studies on the Triangular Helix of Mn_3Sn

S. Tomiyoshi[1], T. Yano[1], M. Takeda[2], Y. Endoh[2]

[1]Department of Materials Science and Engineering, Faculty of Engineering, Ehime University, Matuyama 790
[2]Department of Physics, Faculty of Science, Tohoku University, Sendai 980

Intermetallic compound Mn_3Sn (hex.DO_{19} type crystal structure) shows complicated magnetic behavior. Kouvel and Kasper[1] revealed that Mn_3Sn have a triangular spin structure and is accompanied with a weak ferromagnetic remanence above 270K, below the temperature corresponding to the decrease of the remanence, magnetic satellite peaks appear in the neutron diffraction pattern. By using polarized neutron diffraction the spin structure at room temperature has been determined to be a so called inverse triangular spin structure in the c-plane[2]. This triangular spin structure was shown to be stabilized due to the Dzyaloshinski-Moriya (D-M) interaction. Since the inverse spin triangle has the spin symmetry incompatible with the crystal symmetry, it deforms, resulting in a weak ferromagnetic remanence in the c-plane. Recently, Ohmori et al.[3] showed that single crystal samples of Mn_3Sn annealed at 850°C had a transition from a triangular structure to a triangular helix structure at 250K in agreement with the early powder neutron diffraction results given by Kouvel and Kasper[1]. The triangular helix of Mn_3Sn has a propagation vector of q=1/12c along the c-direction and the q-vector is almost independent of temperature.

As the origin of the triangular helix, two mechanisms, i.e. the D-M interaction and the balance of the exchange parameters, are considered. The helix arising from the former origin has an unique q-vector direction, and that from the latter one has degenerate states with +q and -q vectors, so by observing satellite peaks by polarized neutrons with the neutron polarization parallel and antiparallel to the scattering vector we can very easily distinguish the mechanisms. In the present work we investigated the helix of Mn_3Sn by using polarized neutron diffractometer TOP. The single crystal we used in the present experiment was $Mn_{3.2}Sn$ which has the transition from the triangular spin structure to the triangular helix at 250K.

The most important point in the present experiment is to attain single q-state. Because $Mn_{3.2}Sn$ has weak ferromagnetic component in the c-plane above 250K, the domain structure in the triangular phase can be controlled to a single domain by applying the magnetic field in the c-plane, and cooling through the transition point the single domain structure in the triangular phase could be transformed to a single q-state in the helix.

The single crystal was mounted with its a-axis vertical to the scattering plane. The sample was cooled from room temperature through the transition point in the magnetic field of 9.4kOe along the a*-axis and then was rotated about 90 deg. to observe the magnetic satellite (0, 0, 1/12c). The polarization of the incident neutrons is changed parallel and antiparallel to the scattering vector by using spin flipper .

Figures 1 and 2 show Bragg peaks corresponding to magnetic satellites of (0, 0, 1/12c) at 26 channel position as a function of wavelength measured at 35K and 270K, respectively. The peak at 35K disappears at 270K, so it corresponds to the magnetic satellite peaks. As is shown in figure 1 appreciable intensity change between flipper off and on has not been observed. This result shows that the domains with +q and -q have the same population in the triangular helix corresponding to the degeneracy of the helical state with +q and -q vectors. So the triangular helix of Mn_3Sn is an usual proper screw originating from a balance of the several exchange interactions. However we must also consider the field cooling effect. If it is not completely perfect it would produce no effect on the flipping ratio. Such a situation may occurs because the direction of the ferromagnetic remanence is perpendicular to the propagation vector of the helix, which may lead to equal q-vector population. But some unbalance in the experimental condition will produce unequal population of the q-domain. So from the present results it is reasonable to consider that the triangular helix of Mn_3Sn is the usual proper screw.

References

1) J.S. Kouvel and J.S. Kasper, Proc. Conf. on Magnetism, Nottingham 1964 (London, Inst. Physics) p.169.
2) S. Tomiyoshi and Y. Yamaguchi, J. Phys. Soc. Japan 51(1982)2478.
3) H. Ohmori, S. Tomiyoshi, H. Yamauchi and H . Yamamoto, J. Mag. Mag. Materials 70 (1987) 249.

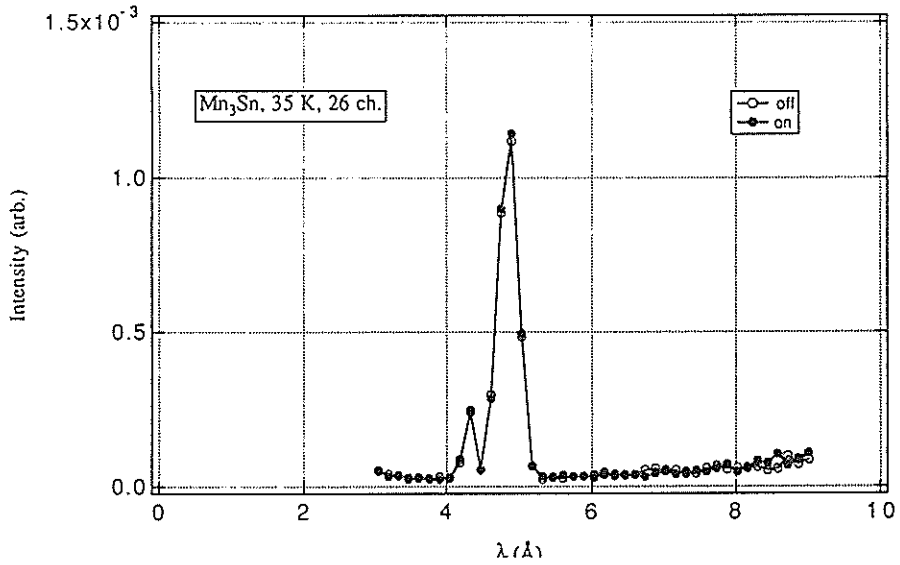

Fig. 1 Neutron diffraction pattern of (0, 0, 1/12c) satellite at 26 channel position at 35K

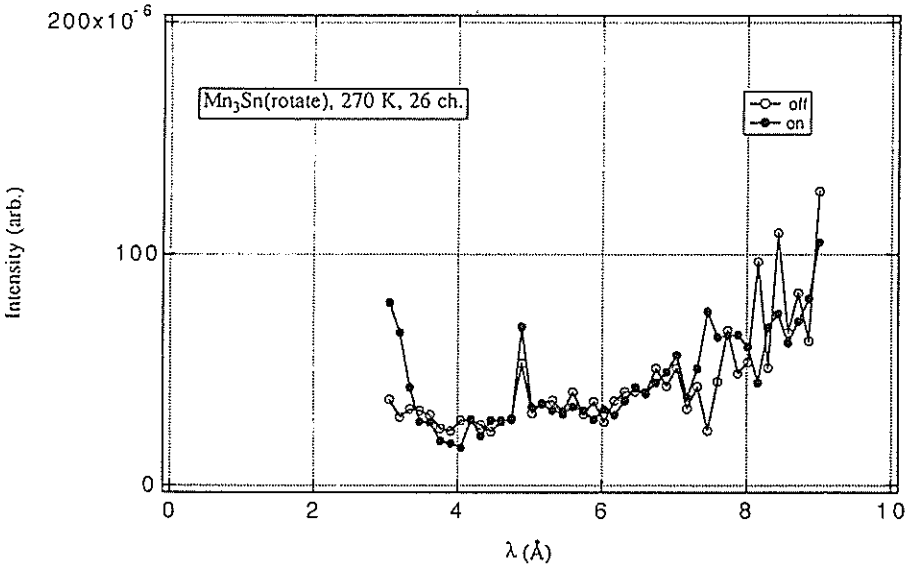

Fig. 2 Neutron diffraction pattern of (0, 0, 1/12c)satellite at 26 channel position at 270K

Neutron Scattering Study of CeTSn (T=Ni, Pd, Pt)

M. Kohgi, K. Ohoyama, T. Osakabe, M. Kasaya, T. Takabatake# and H. Fujii#

Department of Physics, Tohoku University, Sendai 980, Japan
#Faculty of Integrated Arts and Science, Hiroshima University, Hiroshima 730, Japan

1. Introduction

The ε-TiNiSi type inter-metallic compound CeNiSn attracts attention because of its anomalous magnetic and transport properties [1, 2]. The compound shows no magnetic ordering down to 0.4 K. Its electrical resistivity shows a Kondo-like anomaly above about 100 K though strongly anisotropic. The magnetic susceptibility, which is also anisotropic, shows clear deviation from that expected for a trivalent Ce compound though its temperature dependence is rather strong. These experimental results indicate that this system is located just on the boundary of the VF regime and the Kondo regime. More interestingly, the compound shows additional anomalies below about 10 K which are characterized by the gap formation at the Fermi energy. The energy gap was estimated to be about 6 K. No clear explanation for the origin of the gap formation has been given yet.

Compared to CeNiSn, the isomorphous compounds CePdSn and CePtSn are rather normal. Both are metallic, and show quite similar magnetic properties (antiferromagnetic below about 7 K [3]) although the crystal field in CePtSn has been suggested to be much stronger than that in CePdSn [4]. The Kondo anomaly in these materials is rather weak [5].

We performed neutron scattering experiments on CeNiSn as well as on its reference materials CePdSn and CePtSn [3, 6] to investigate the difference of the 4f electron states in these materials from the microscopic point of view.

2. Experimental details

Polycrystalline samples of CeNiSn, CePdSn and CePtSn of about 60 g to 100 g were used in the experiments. They were made by arc melt. The X-ray powder diffraction analysis showed that there is no appreciable other phases than the target material in the samples.

The inelastic neutron scattering experiments were performed on the chopper spectrometer INC and the crystal analyzer spectrometers LAM-D and LAM-40 at KENS.

In the experiments at the INC spectrometer, the incident neutron energy was chosen at 60 meV. The resolution (FWHM) was 3.3 meV at elastic position (E=0). The raw data were corrected for monitor normalization, background subtraction, absorption correction and detector efficiency, and put to the absolute scale by using the data obtained for a vanadium standard sample. The phonon contribution in the raw data was estimated from the high scattering angle(~120°) data and subtracted from the low angle data[3].

The high resolution neutron scattering experiments at the LAM-D and LAM-40 spectrometers were performed only on CeNiSn. Both spectrometers employ several large-solid-angle energy-focusing type analyzers composed of pyrolytic graphite, each with its own beryllium filter and detector and with final energy of 4.6 meV. LAM-D views an ambient temperature water moderator, whereas LAM-40 views a solid-methane moderator. Thus, the former has a high sensitivity at the energy transfer of the thermal energy region, whereas the latter at the lower energy region, but with same resolution of 0.35 meV (FWHM) at E=0.

3. Results and discussions

First, we show the result of the INC experiment on the compounds. Fig. 1(a), (b) and (c) show the inelastic magnetic response of CeNiSn, CePdSn and CePtSn, respectively, at about 20 K taken in the low angle bank of detectors ($2\theta = 5°$ to $12°$). The estimated phonon contribution is subtracted from the raw data. The insets in the figures show the raw data and the estimated phonon contribution for each compound. The rather high level of the phonon contribution in the CeNiSn data comes from the large neutron scattering cross section of Ni nucleus.

Well-defined crystal field excitations were observed for CePdSn and CePtSn. The solid curves in the Figs. 1(b) and 1(c) show the best fits to the data using a sum of two Lorentzians as the spectral function. The obtained excitation energies for CePdSn are 17.4 and 25.8 meV with the linewidths (HWHM) of 2.2 and 2.7 meV, whereas those for CePtSn are 23.6 and 36.6 meV with the line widths of 2.0 and 3.6 meV. The observed overall crystal field splitting in CePtSn is about 40 % larger than that of CePdSn.

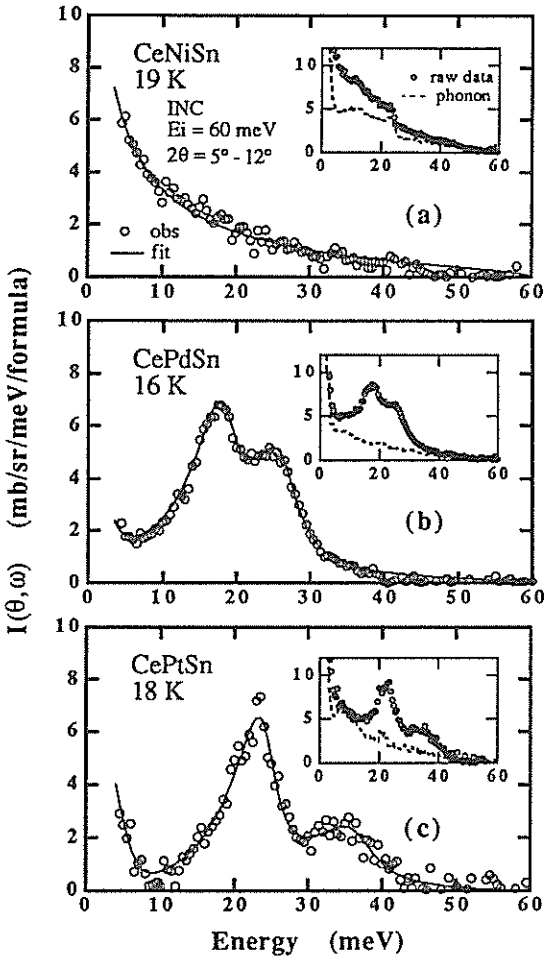

Fig. 1 Magnetic responses of (a) CeNiSn, (b) CePdSn and (c) CePtSn at about 20 K observed with the INC spectrometer. The solid curves indicate the results of the least squares fitting to the data using Lorentzian(s) as the spectral function. Insets show the raw data and the estimated phonon contribution for each compound.

The spectrum of CeNiSn is rather structure-less above about 5 meV. The solid curve in Fig.1(a) shows the best fit to the data using a single Lorentzian centered at E=0 as the spectral function. The fit gives the width of 2.2 meV.

Fig.2 shows the spectra of CeNiSn at 3 and 15 K obtained with the LAM-D spectrometer at the scattering angle of 35°. The raw data were corrected for the wavelength variation of the incident spectrum, detector efficiency and absorption effect. No correction was done for phonon contribution because of the limited Q range which is covered by the LAM-D spectrometer. The result shows that the spectrum below about 10 meV is not a monotonous function of energy but has a peak at about 4 meV which is strongly temperature dependent and cannot be seen in the INC data at 19 K because of the resolution limitation of the spectrometer. The overall features of

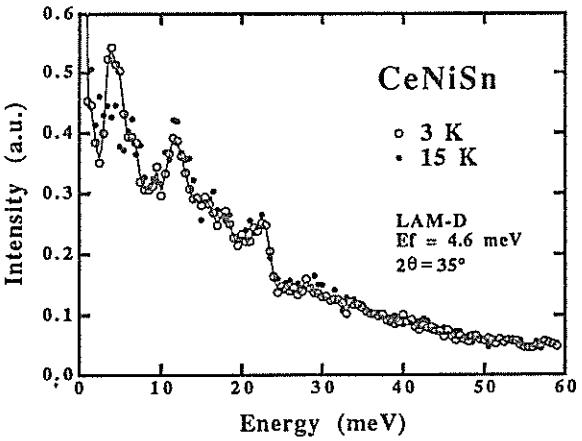

Fig. 2 Spectra of CeNiSn observed with the LAM-D spectrometer.

the spectrum above about 10 meV is not so different from the raw data of the INC experiment (see the inset in Fig. 1(a)). The apparent difference between the two spectra is due to the difference of the scattering triangles, of phonon contribution and of the resolution.

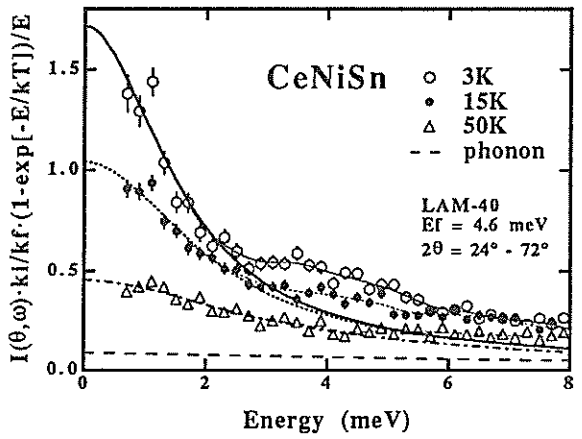

Fig. 3 Spectra of CeNiSn observed with the LAM-40 spectrometer. The thick solid, dotted and chained lines indicate the results of the Lorentzian fit to the data between 0.7 and 2.5 meV at 3, 15 and 50 K, respectively. Broken line represents the estimated phonon contribution.

Fig. 3 shows the response functions of CeNiSn at 3, 15 and 50 K at small energy transfer obtained with the LAM-40 spectrometer. After the same correction as the case of LAM-D data, the raw data, each of which is the sum of the counts at 24°, 40°, 56° and 72° detectors, were corrected for the k_f/k_i term and the temperature factor $\hbar\omega/[1-\exp(-\hbar\omega\beta)]$ in the cross section to get the response function (= $\mathrm{Im}[\chi(Q,\omega)/\omega]$ + phonon background). In this correction, we neglected the resolution effect because it is small enough for the present purpose. The data at the energy transfers less

transfers less than 0.7 meV are omitted in the figure because of the strong contamination of the incoherent elastic scattering. The broken line in the figure indicates the phonon contribution estimated from the measurement on LaNiSn with the same experimental condition as the measurement on CeNiSn. The phonon contribution is clearly small in this energy region.

The overall height of the observed magnetic response function decreases with increasing temperature. This is qualitatively consistent with the behavior of the reported temperature dependence of the bulk susceptibility. Each spectrum below about 2.5 meV increases monotonically with decreasing energy transfer though a small hump is seen around 1.1 meV. The solid, dotted and chained lines in the figure show the best fit Lorentzian function centered at E=0 to the data between 0.7 and 2.5 meV at 3, 15 and 50 K, respectively. The agreement is rather good in the energy region. The obtained widths of the Lorentzians are 1.6, 2.1 and 3.0 meV, respectively. Note that the width of 2.1 meV at 15 K is comparable to the result of the Lorentzian fit to the INC data at 19 K which gives the width of 2.2 meV.

However, the spectra show more complicated features at higher energy transfer. At 3 K, the spectrum starts to deviate from the Lorentzian above about 2.5 meV and show a broad peak around 4 meV. At 15 K, the spectrum also shows broad peaks around 4.5 to 7 meV, as also seen in the LAM-D data(Fig. 2). However, the intensity around 4 meV is considerably smaller than that at 3 K, whereas the intensity around 7 meV is the same as that at 3 K. At 50 K, no peak is seen around 4 meV. Instead, the spectrum starts to deviate from the Lorentzian around that energy.

The experimental results demonstrate that the 4f electron state in CeNiSn is quite different from those of CePdSn and CePtSn. In the latter compounds, two well-defined crystal field excitations were observed, and this indicates that the 4f electron is well localized. The reason of the rather large difference of the crystal field splitting between them is not well known.

No well-defined crystal field excitations were observed for CeNiSn. Instead, it shows a Lorentzian-like broad response centered at E=0 with a broad peak at about 4 meV. The temperature dependence of the peaks is quite anomalous. Similar anomalous spectra for CeNiSn were also reported by other groups[2, 7] but the agreement with our results is not satisfactory. The magnetic response might be understood as that of over-dumped crystal field excitations, but, it is difficult to explain the temperature dependence of the peak around 4 meV by a simple model. It is clear, anyhow, that the hybridization effect in CeNiSn is much stronger than in CePdSn or CePtSn and that its 4f eleçtron state is more like valence fluctuating. We suggest that the anomalous temperature dependence of the peak around 4 - 7 meV indicates the development of a short range magnetic correlation at the low temperatures.

References

[1] T. Takabatake, F. Teshima, H. Fujii, N. Nishiguri, T. Suzuki, T. Fujita, Y. Yamaguchi, J. Sakurai and D. Jaccard, Phys. Rev. B41(1991)9607; T. Takabatake and H. Fujii: Jpn. J. Appl. Phys., to be published, and references herein.

[2] F.G. Aliev, V.V. Moshchalkov, M.K. Zalyalyutdinov, G.I. Pak, R.V. Scolozdra, P.A. Alekseev, N.N. Lazukov and I.P. Sadikov, Physica B163(1990)358.

[3] M. Kohgi, K. Ohoyama, T. Osakabe and M. Kasaya, J. Magn. Magn. Mater., 108(1992)187.

[4] T. Takabatake, H. Iwasaki, G. Nakamoto, H. Fujii, H. Nakkote, F.R. de Boer and V. Sechovsky, Physica B, to be published.

[5] M. Kasaya , T. Tani, H. Suzuki, K. Ohoyama and M. Kohgi, J. Phys. Soc. Jpn., 60(1991)2542.

[6] M. Kohgi, K. Ohoyama, Y. Osakabe, T. Takabatake and H. Fujii, Physica B, to be published.

[7] G. Appli, E. Bucher and T.E. Mason: *Physical Phenomena at High Magnetic Fields*, (Adison-Wesley, 1992)p.175.

Crystal Field State of a Low Carrier System CeP under High Pressure

M. Kohgi, T. Osakabe, T. Suzuki, Y. Haga, N. Mori#, H. Takahashi#, and S. Ikeda†,

Department of Physics, Tohoku University, Sendai 980, Japan
#Institute for Solid State Physics, University of Tokyo, Roppongi, Tokyo 106, Japan
†National Laboratory for High Energy Physics, Tsukuba 305, Japan

1. Introduction

Ce-monopnictide CeX (X=P, As, Sb, Bi) is a low carrier system which exhibits unusual magnetic and transport properties with Kondo anomalies. Thus, it has been a target of many experimental and theoretical works[1]. So far the studies of this system were mainly concentrated on the heavier Ce-monopnictides CeSb and CeBi because these compounds exhibit highly unusual properties such as a very small crystal field splitting or a complex magnetic phase diagram, and it has been realized that the unusual properties are due to the strong effect of the mixing of Ce 4f electron with the valence p electrons on the pnictogen atoms (p-f mixing effect). Recently, the lighter compounds CeP and CeAs have also attracted attention since it has been revealed that the carrier numbers in CeP and CeAs are very small, the order of 10^{-3} carriers per a formula[2,3], which is a factor ten smaller than that of CeAs or CeBi, and that these compounds also exhibit unusual magnetic phase diagrams. Both compounds show the type I antiferromagnetic ordering below about 10 K at ambient pressure. However, with applying a pressure above about 0.3 GPa(CeP) or 1.1 GPa(CeAs), a new magnetic phase with a ferromagnetic component is seen just above the antiferromagnetic phase in each compound[4]; the obtained P-T phase diagram is quite similar for both compounds, but CeP shows the anomaly at lower pressure. These facts indicate that the 4f electronic state in these compounds is quite similar and very sensitive to the atomic distance. Considering the fact that the crystal field splitting in these two compounds is also anomalously small[5], the pressure effect of the p-f mixing is thought to be an origin of the anomalous magnetic phase diagram. Thus, it is quite interesting to study the pressure dependence of the crystal field state in the compounds by neutron scattering.

In this report, we present a recent result of the neutron scattering study on CeP under high pressure using the chopper spectrometer INC.

2. Experimental details

The neutron scattering experiments were performed on the chopper spectrometer INC at the pulsed neutron source KENS in the National Laboratory for High Energy Physics. The pressed CeP polycrystalline sample of about 10 g was sealed in a thin aluminum cell(the sample space is 1 cm diameter and 5 cm long) with the non-hydrogenous pressure media(Fluorinert, Sumitomo 3M Co., Ltd.). The cell was inserted in a clamp-type high pressure sample container made by Aluminum. Then, the sample was pressurized up to 0.8 GPa. The outer diameter of the sample container is 8 cm. However, two cuts with the depth of 2 cm are made on the wall along the neutron incident beam(1 cm by 5 cm) and the scattered neutron paths with the scattering angle less than 12° to decrease the scattering from the Aluminum wall. All the surfaces of the high pressure container except those in the neutron paths were covered by cadmium sheets of 0.5 mm thick. The container was mounted within a closed cycle refrigerator cryostat on the INC spectrometer. The neutron scattering measurements were done at 20, 40, 60 and 80 K. The incident neutron energy was chosen at 40 meV. The resolution of the spectrometer for this energy is about 2.2 meV(FWHM) at $\hbar\omega = 0$.

The measurement on LaP was also done at 20 and 80 K with the same condition but only at ambient pressure to estimate the phonon background originated from the sample its self as well as from the wall of the high pressure sample container. The amount of the LaP sample was chosen so that its total nuclear scattering cross section becomes equivalent to that of the CeP sample.

3. Results and Discussion

Fig. 1 (a), (b), (c) and (d) show the pressure dependence of the magnetic response from CeP at 20, 40, 60 and 80 K, respectively, which were obtained from the CeP data by subtracting the LaP data as the phonon background. For the phonon background at 40 and 60 K, the LaP data at 20 and 80 K, respectively, were used. This may be allowed since the temperature dependence of the LaP data is rather small. The pressure dependence of the phonon background was also assumed to be negligible. Clearly, the peaks around 13 meV correspond to the Γ_7 - Γ_8 crystal field excitations in CeP. The solid and broken curves in the

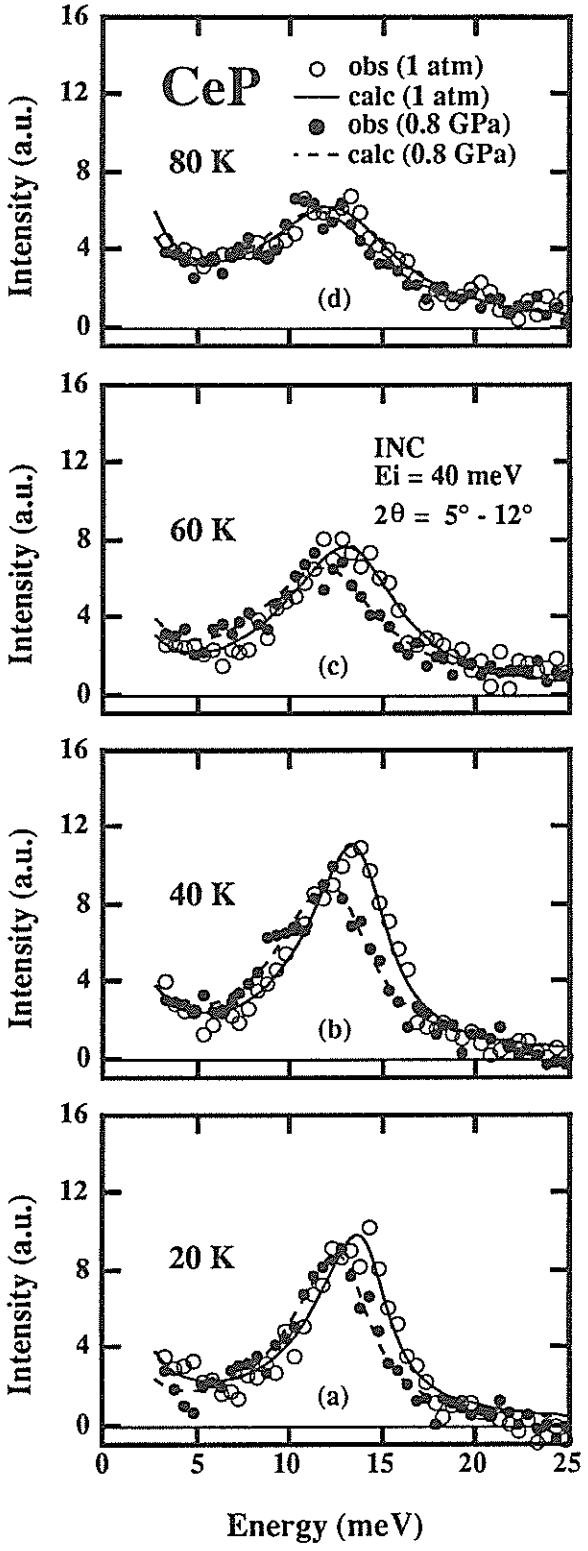

Fig. 1 Magnetic responses from CeP at (a) 20 K, (b) 40 K, (c) 60 K and (d) 80 K. Open and close circles show the observed spectra at ambient pressure and 0.8 GPa, respectively. Solid and broken lines represent the results of least squares fit to the data at ambient pressure and 0.8 GPa, respectively.

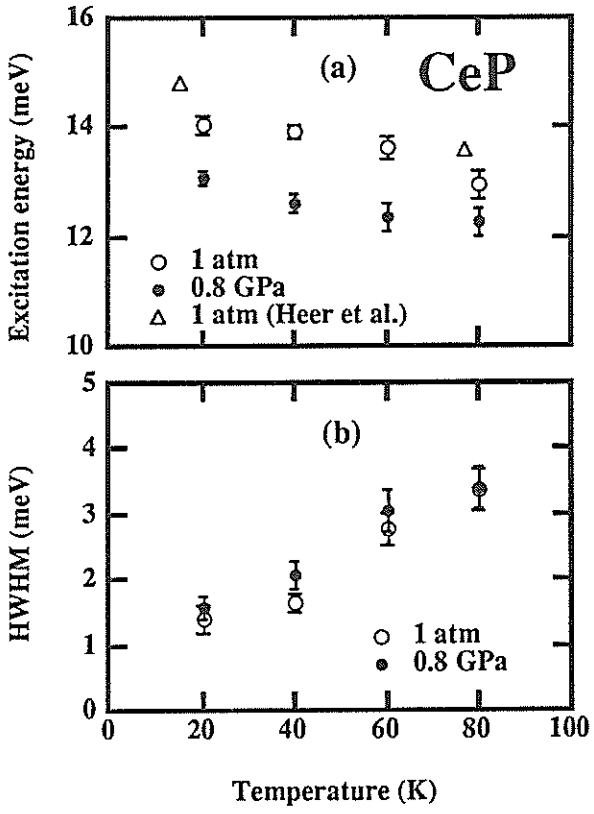

Fig. 2 Results of (a) crystal field excitation energies and (b) linewidths(HWHM) vs. temperature. Open and closed circles show the results at ambient pressure and 0.8 GPa, respectively. Open triangles show the reported crystal field splitting values at ambient pressure by Heer et al.[7].

Fig. 1 shows the results of a least squares fit procedure to the data at ambient pressure and at 0.8 GPa, respectively, where the spectral shape function was assume to be a sum of two Lorentzians, one for the quasi-elastic scattering and the other for the crystal field excitation. The peak positions of the crystal field excitations decrease by applying the pressure. However, no big change of the spectral shape is seen.

The peak positions of the crystal field excitations and their linewidths obtained from the Lorentzian fitting are summarized in Fig. 2 (a) and (b), respectively. The peak position at ambient pressure decreases linearly with temperature up to 60 K, and shows a bit faster decrease at 80 K. The values at 20 and 80 K are about 5 % smaller than those reported by Heer et al. at 15 and 77 K, respectively[7]. At 0.8 GPa, the peak position also decreases linearly with temperature up to 60 K but with about 10 % lower value than that at ambient pressure, whereas the value at 80 K is almost same as that at 60 K, thus the

pressure dependence of the peak position becomes small(about 5 %) than that at lower temperature. The linewidth at ambient temperature increases first slowly from 20 K to 40 K, but becomes to be almost proportional to the temperature above 40 K. At 0.8 GPa, the linewidth behaves nearly same as that at ambient pressure but with about 10 to 20 % larger value than that at ambient pressure up to 60 K and again the pressure dependence becomes small(almost same linewidth) at 80 K.

The above features of the pressure dependence of the crystal field excitation seem to be correlated with the observed anomalies in the electrical resistivity[4]. At ambient pressure, the resistivity shows a sharp peak at the Néel temperature(about 10 K). After passing through a minimum at about 20 K, the resistivity shows a broad peak at around 70 K, above which it shows a Kondo-like decrease with increasing temperature. At the pressure of about 0.8 GPa, the broad peak shifts to about 10 % lower temperature. The observed decrease of the crystal field splitting at 0.8 GPa is also about 10 % at low temperatures as described above. This coincidence suggests that the broad peak of the resistivity is strongly related with the crystal field splitting. Another interesting feature is that, at 80 K which is the temperature just above the broad peak of the resistivity, the pressure dependence of the crystal field excitation is small compared with those at the lower temperatures. This indicates that the electronic state of CeP at the temperature region below the broad peak position of the resistivity is more sensitive to the pressure than that at higher temperature.

More detailed study including the experiment at higher pressure is under way.

References

[1] see for example: T. Kasuya, Y.S. Kwon, T. Suzuki, K. Nakanishi, F. Ishiyama and K. Takegahara, J. Magn. Magn. Mater. 90&91 (1990)389 and references herein.

[2] Y.S. Kwon, Y. Haga, O. Nakamura, T. Suzuki and T. Kasuya, Physica B171(1990)324.

[3] Y.S. Kwon, Y. Haga, S. Ozeki, T. Suzuki and T. Kasuya, Physica B169(1991)497.

[4] N. Mori,Y. Okayama, H. Takahashi, Y. Haga and T. Suzuki, to appear in "Physical Properties of Actinide and Rare Earth compounds"(Jpn. J. Appl. Phys. Series).

[5] R. J. Birgeneau, E. Bucher and J.P. Maita, Phys. Rev. B8(1973)5345.

[6] Y. Okayama, Y. Ohara, S. Mitsuda, H. Takahashi, H. Yoshizawa, T. Osakabe, M. Kohgi, Y. haga, T. Suzuki and N. Mori, in this issue.

[7] H. Heer, A. Furrer, W. Hagt and O. Vogt, J. Phys. C12(1979)5207.

Spin Dynamics of YbX (X=N, P, As)

K. Ohoyama, M. Kohgi, T. Otomo*, T. Osakabe A. Oyamada and T. Suzuki
Department of Physics, Tohoku University, Aramaki Aoba Sendai 980, Japan
*Institute for Materials Research, Tohoku University, Katahira Aoba Sendai 980, Japan

1. Introduction

YbX (X= N, P and As), which crystallizes in the NaCl structure, is a semimetallic compound with low carrier density (a few percent per formula). At low temperatures around 0.5 K, YbX undergoes antiferromagnetic long range ordering [1]. However, the saturation moment and entropy at the Néel temperature are considerably smaller than the expected values of the crystal field ground state doublet. It also shows an anomalously enhanced specific heat around 5 K. These are considered to be the characteristic features of the Kondo effect. We have studied the low carrier Kondo effect in this system by means of neutron inelastic and quasi-elastic scattering. Some results of the inelastic scattering work were reported elsewhere [2] [3], and the neutron quasi-elastic scattering (QES) experiments on these compounds are presented here.

2. Experimental

We performed neutron quasi-elastic scattering experiments on powder samples of YbX (X=N, P and As) on both the crystal analyzer type spectrometer, LAM-D, at the spallation neutron source KENS in KEK, and the triple axis spectrometer, TOPAN, at the JRR-3M in Japan Atomic Energy Research Institute (JAERI). LAM-D uses a fixed final neutron energy of about 4.5 meV. This condition facilitates the high resolution experiments in lower energy transfer. The samples were the same as those used in the inelastic scattering work.

3. Results and Discussions

Figure 1 shows QES spectra of YbN at a scattering angle of 35° using LAM-D at 14 K (upper portions) and room temperature(lower portions). Figures 1(a) and (b) show the same observed spectra and results of different methods of analysis, as described below. The observed spectra (open circles) were corrected for the background, absorption and wavelength dependence of incident neutron flux. The results of the least squares fit of the QES spectra to calculated line shapes are also shown in Fig.1 (chain lines). The QES spectra are fitted to either a Gaussian (Fig.1(a)) or a Lorentzian (Fig.1(b)) line shape convoluted with the instrumental resolution. The dotted lines correspond to the incoherent elastic scattering parts of the spectra and indicate the energy resolution as well. The dependence of the intensity on the temperature cannot be discussed here since the experimental conditions for the spectra at 14 K and room temperature are not identical. As seen in the figures, the QES spectra at lower temperatures below 50 K are explained well by the Gaussian line shape, whereas, at higher temperatures, the Lorentzian line shape gives somewhat better agreement than the Gaussian one. The QES spectra of YbP and YbAs show exactly the same features.

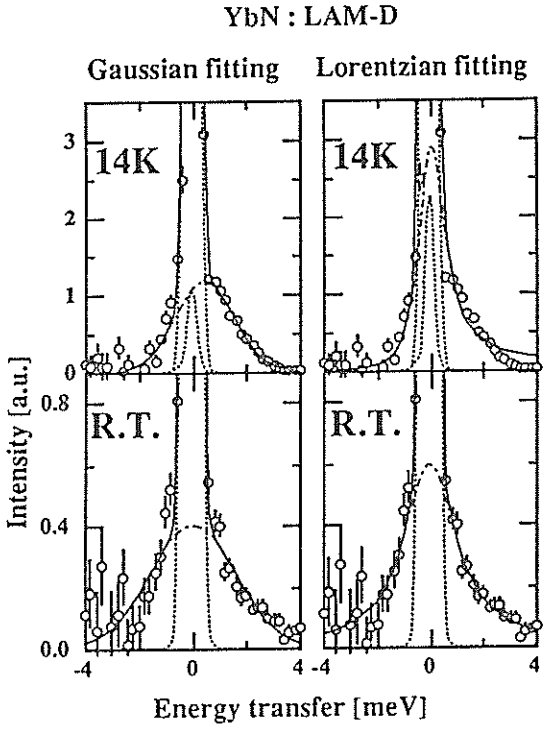

Fig.1 QES spectra of YbN at 2θ=35° using LAM-D with E_f=4.5 meV at 14 K and room temperature. The solid lines indicate the Gaussian (a) and Lorentzian (b) spectra convoluted with the instrumental resolution. The chain lines and dotted lines show the quasi-elastic and incoherent elastic parts of the spectra, respectively.

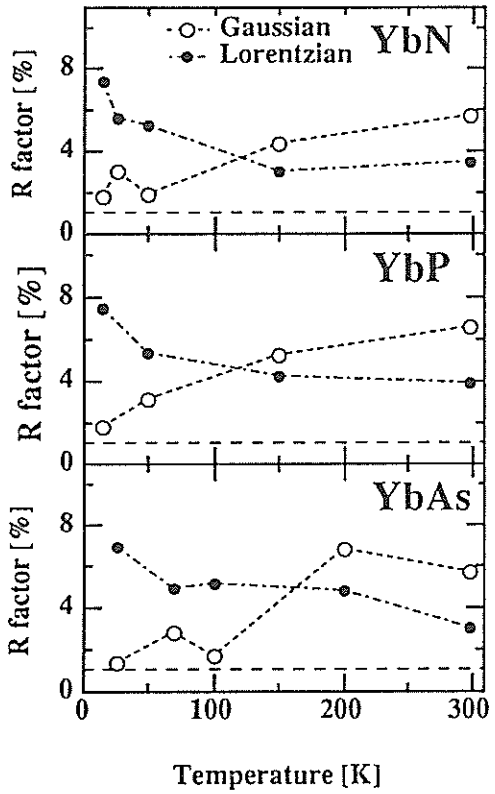

Fig.2 R-factors for the Gaussian (open circles) and Lorentzian (closed circles) fits as a function of the temperature. The lower dashed lines indicate the statistical minimum values of the R-factors.

The important feature of the crossover from the Gaussian line shape to the Lorentzian one with the increase of temperature is seen in the plot of the temperature dependence of the reliability parameter, called the R-factor of fitting, which is defined as follows,

$$R \equiv \sqrt{\sum_i \left(I_i^{obs} - I_i^{cal} \right)^2} \Big/ \sum_i I_i^{obs} \qquad (1)$$

, where $I_i^{obs(cal)}$ indicates the intensity at the i-th channel for an observed (calculated) spectrum. Figure 2 shows the temperature dependence of the R-factors obtained by the Gaussian (open circles) and Lorentzian (closed circles) fitting for the three compounds. The lower dashed lines indicate statistical minimum values of the R-factors. It is quite remarkable that the behavior of the crossover is common for these compounds. Furthermore, the transition point of about 150 K is also the same for the compounds.

In Fig.3, the linewidths of the QES spectra (HWHM) of YbN (circles), YbP (squares) and YbAs (triangles) determined from the fitting are plotted against temperature. Open and closed symbols indicate the results of the Gaussian and Lorentzian fittings, respectively. The data below 10K were taken with the triple axis spectrometer TOPAN with incident neutron energy of 14 meV. The results observed with TOPAN are consistent with those observed with LAM-D at higher temperatures. The results of the Lorentzian fitting below 50 K and those of the Gaussian fitting above 200 K are not shown in Fig.3, because the QES spectra cannot be explained well by these line shapes. The observed linewidths of the QES spectra of these three compounds are almost the same, and increase with temperatures up to 50 K. They are almost constant or even decrease slightly above 150 K.

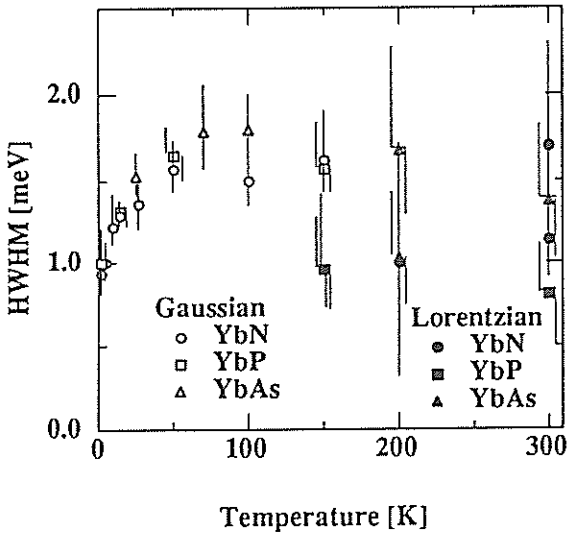

Fig.3 Temperature dependence of the quasi-elastic linewidth (HWHM) of YbN (circles), YbP (squares) and YbAs (triangles). The open and closed symbols represent the Gaussian and Lorentzian linewidths, respectively.

We have also measured the momentum transfer (Q) dependence of QES spectra of YbN at 10 K and room temperature and of YbP at 1.5 K and room temperature using TOPAN for $1.1\ \text{Å}^{-1} \le Q \le 1.7\ \text{Å}^{-1}$. Figure 4 shows the Q dependence of the linewidth (a), HWHM, and integrated intensity (b) of YbN at 10 K. The dotted line in Fig.4(b) indicates the Q dependence of the square of the magnetic form factor f(Q) of free Yb^{3+} ion [4]. It is concluded that the linewidth and integrated intensity are nearly independent of Q. We

also observed the Q-independent feature of QES spectra of YbP at 1.5 K. No appreciable Q dependence of the QES spectra of either compound was observed at room temperature. Therefore, the spatial magnetic correlations in these compounds might not be strong enough to be detectable in powder samples.

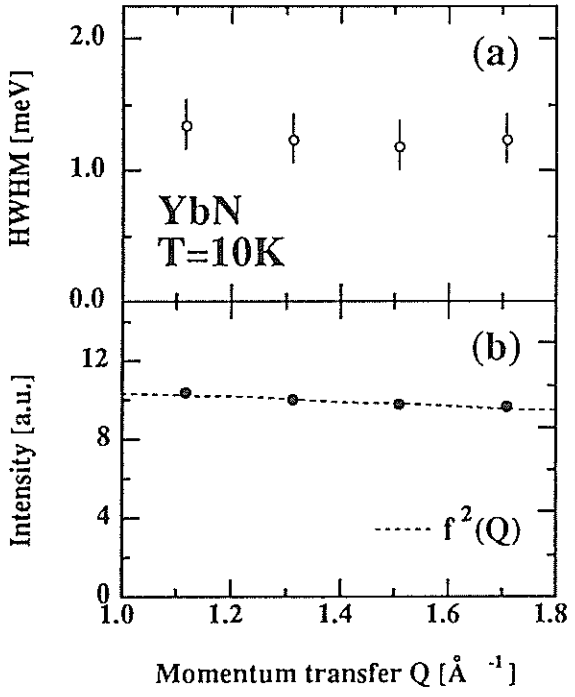

Fig.4 Q dependence of the linewidth (a) and integrated intensity (b) of the QES spectra of YbN at 10 K using TOPAN with E_i=14 meV. The dotted line indicates the square of the magnetic form factor of free Yb^{3+} ion [4].

Now, we discuss the magnetic fluctuations for the ground state Γ_6 in Yb monopnictides. The c-f mixing effects for the ground states are concluded to be common in Yb monopnictides, since the QES spectra are essentially the same for these three compounds. The spin fluctuations at low temperatures are governed by the RKKY type interatomic exchange interactions since the observed QES spectra of the YbX compounds are explained well by the Gaussian function rather than the Lorentzian one below about 50 K. The characteristic energy of the exchange interactions in these compounds is estimated to be about 20 K from the linewidth at about 50 K. The big difference between the actual Néel temperatures (~0.5 K) and the exchange energy (~20 K) arises in the strong suppression of the magnetic ordering by the Kondo effect. It is also concluded that the characteristic energy T_K in the YbX compounds is about the same value due to the complete suppression of the magnetic ordering. This value is about four times larger than the value previously estimated from the anomalous peak of the specific heat based on the impurity Kondo model [5].

The gradual change of the spectral line shape from the Gaussian-like function to the Lorentzian-like one with increasing temperature indicates that the single-site relaxation process is not appreciable at low temperatures, but becomes important at higher temperatures. The Lorentzian linewidth of 10 K at room temperature is relatively small compared with those of the typical dense Kondo materials such as CeB_6, $CeAl_2$ or $CeCu_2Si_2$ [6]. However, if the fact that the carrier density is very low is taken into account, it should be noted that the c-f mixing effect in the YbX system is rather strong.

4. Conclusion

In conclusion, the experimental results have revealed that YbX is characterized as a system in which the magnetic ordering is strongly suppressed due to the competition between the interatomic exchange interaction and the single-site Kondo effect and in which the c-f mixing effect is rather strong in spite of the low carrier number.

A more detailed study of the QES spectra using single crystal samples is now in progress.

References

[1] H. R. Ott, H. Rudigier and F. Hulliger, Solid State Commun. 55(1985)113.
[2] M. Kohgi, K. Ohoyama, A. Oyamada, T. Suzuki and M. Arai, Physica B 163 (1990) 625.
[3] K. Ohoyama, M. Kohgi, T. Nakane, M. Arai, A. D. Taylor, A. Oyamada and T. Suzuki, Physica B 180&181 (1992) 250.
[4] A. J. Freeman and J. P. Desclaux, J. Magn. Magn. Mat. 12(1979)11.
[5] S. Takagi, A. Oyamada and T. Kasuya, J. Phys. Soc. Japan 57(1988)1456.
[6] S. Horn and F. Steglich, Physica B 107 (1981) 103.

NEUTRON SCATTERING STUDIES OF $Ce(Zn_{1-x}Cu_x)_2$

T. Osakabe, M. Kohgi, K. Ohoyama and T. Kitai*

Department of Physics, Tohoku University, Sendai 980, Japan
*Department of Electronics, Kyushu Institute of Technology,Kitakyushu 804, Japan

1. Introduction

$CeZn_2$, which has the same crystal structure as $CeCu_2$ (Imma space group), orders antiferromagnetically below 7.5 K with a metamagnetic magnetization process along the easy b-axis. It shows a Kondo behavior in the electrical resistivity[1]. The substitution of 25% of Zn atoms by Cu atoms suppresses the ordering temperature considerably (T_N<1.5 K) [2] and yields more similar magnetic properties as those of $CeCu_2$ which shows typical properties of Kondo lattice. This indicates that there is a possibility that there exists a competition between the Kondo effect and the RKKY interaction in the mixed compound $Ce(Zn_{1-x}Cu_x)_2$. Of course there is another possibility that the phenomena are caused by a competition between the different kind exchange interactions or between different magnetic anisotropy since both side compounds show different types of magnetic ordering at low temperatures[3,4]. In order to clarify this point we have performed neutron scattering experiments as well as susceptibility measurements. In this paper, we report the results of the neutron scattering and magnetic susceptibility measurements.

2. Experimental details

Polycrystalline samples were prepared by melting together the required amount of Ce(3N), Zn(5N) and Cu(4N) in tantalum crucibles in 3 hours at 1150 °C, cooling at the rate of 1 °C/min. and holding for 24~48 hours at 450 °C. Single crystal samples were picked from the products. The susceptibilities were measured on the single crystal samples with x = 0.1, 0.15, 0.2 and 0.25 along a, b and c axis using a SQUID magnetometer in the temperature range from 1.9 K to 270 K under applied field of 5 kOe. For x = 0.2, we observed the susceptibility between 0.5 K and 5 K using Faraday method in a ^{3}He cryostat. The Néel temperatures were determined from the cusps of the susceptibilities.

The neutron scattering experiments were carried out on the chopper spectrometer INC and the crystal analyzer spectrometers LAM-D at the spallation neutron source KENS in KEK. Polycrystalline samples of $Ce(Zn_{1-x}Cu_x)_2$ with x = 0, 0.05, 0.1, 0.15, 0.2 and 0.25 were used in the experiments.

3. Results

Fig. 1 shows the results of the susceptibility measurements of the compounds with x = 0.1, 0.15, 0.2 and 0.25. The anisotropy of the magnetic susceptibilities of the compounds is large due to the low symmetry of the crystal structure. The easy axis changes systematically from b-axis to a-axis with increasing x.

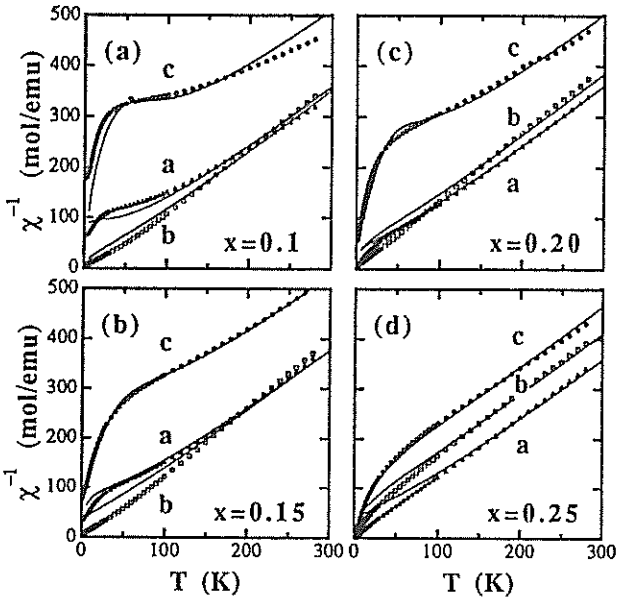

Fig.1 Temperature dependence of the reciprocal susceptibilities of the compounds $Ce(Zn_{1-x}Cu_x)_2$ with (a) x = 0.1, (b) x = 0.15, (c) x = 0.20 and (d) x = 0.25. The solid lines indicate the results of least squares fit to the data using the CEF model.

The solid lines in fig.1 are the results of least squares fit to the data with the theoretical magnetic susceptibility, $\chi^{-1} = \chi_{CEF}^{-1} + \lambda$. Here, λ is the molecular field parameter and χ_{CEF} is the

susceptibility derived from the crystal electric field (CEF) Hamiltonian :

$$H_{CEF} = B_2^0 O_2^0 + B_2^2 O_2^2 + B_4^0 O_4^0 + B_4^2 O_4^2 + B_4^4 O_4^4 \qquad (1)$$

where B_l^m and O_l^m are the CEF parameters and Stevens' operators.

Fig. 2 show the inelastic magnetic response of the compounds with x= 0, 0.05, 0.1, 0.15, 0.2 and 0.25 at about 20 K observed with the INC spectrometer in the low angle bank of detectors (2θ = 5° to 12°). The phonon contribution is subtracted from the raw data.

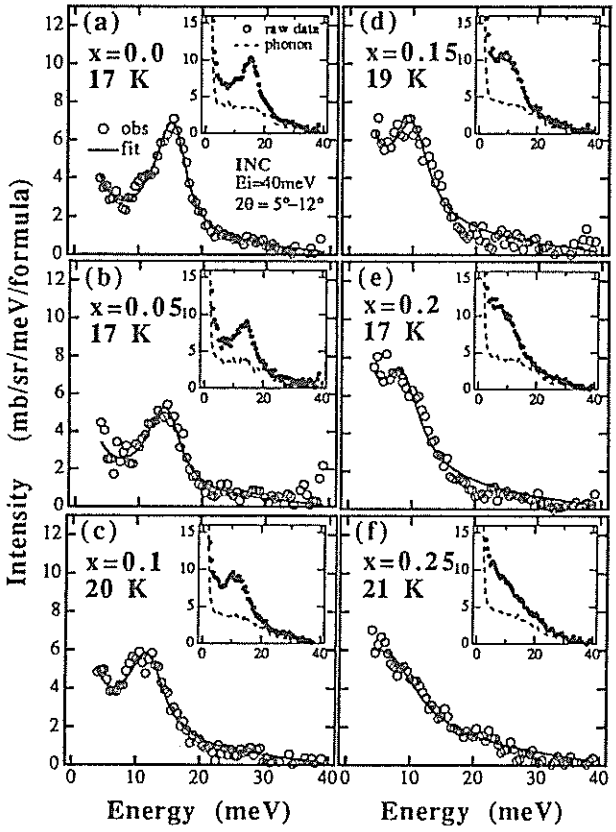

Fig. 2 Inelastic magnetic responses of $Ce(Zn_{1-x}Cu_x)_2$ with (a) x = 0, (b) x = 0.05, (c) x = 0.1, (d) x = 0.15, (e) x = 0.20 and (f) x = 0.25. at about 20K observed with the INC spectrometer. The solid lines indicate the result of the least squares fitting to the data using Lorentzian as the spectral function. Insets show the raw data and the estimated phonon contribution for each compound.

The solid lines in the fig. 2 show the best fits to the data using a Lorentzians as the spectral function. The insets in the figures show the raw data and phonon contribution estimated by scaling the high angle data (2θ = 112° to 130°) using a scalng factor which was obtained from the measurement on a non-magnetic reference material LaPdSn.

Well-defined CEF excitation from the ground state to the first excited state was observed for $CeZn_2$ at 16meV. With increasing x, the excitation energy decrease lineally, while its linewidth increases with upward curvature. Table 1 lists the CEF excitation energies from the ground state to the first excited state obtained from the fit together with those obtained by the susceptibility measurements.

Table 1 Concentration dependence of the CEF excitation energy from the ground state to the first excited state. E_{01}(neu.) is determined by the neutron inelastic scattering experiments. E_{01}(sus.) is obtained from the fit to the susceptibilities.

X	0.0	0.1	0.15	0.2	0.25
E_{01} (neu.)	16.1 ±0.4	12.5 ±0.5	10.7 ±0.7	9.1 ±0.8	7.0 ±1
E_{01} (sus.)	12.5†	10.3	4.9	5.6	3.4

† From ref. [2] (unit:meV)

Fig. 3 shows the quasi-elastic spectra of the compounds with x = 0, 0.1, 0.15 and 0.25 at scattering angle of 35° at 30 K, 23 K, 24 K and 24 K, respectively. The raw data were processed for background subtraction, incident flux normalization and absorption correction.

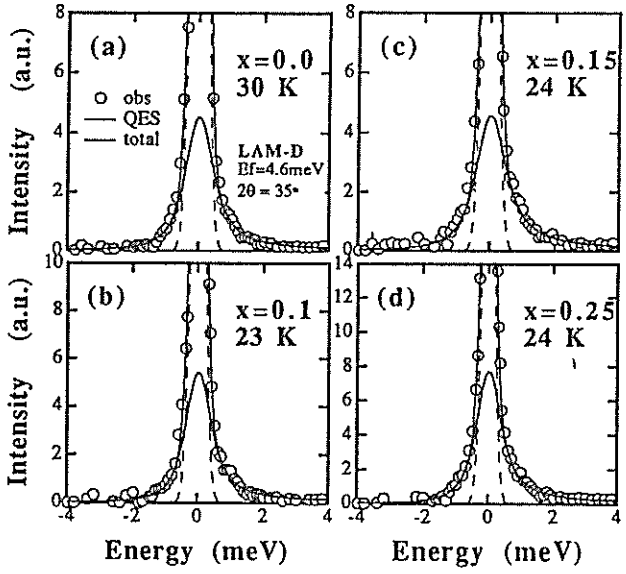

Fig. 3 Spectra of $Ce(Zn_{1-x}Cu_x)_2$ with (a) x = 0, (b) x = 0.1, (c) x = 0.15 and (d) x = 0.25 observed with the LAM-D spectrometer. The lines indicate the result of the least squares fitting to the data between -4meV to 4meV using Lorentzian as the spectral function.

The lines in fig. 3 show the best fits to the data with a Lorentzian as the spectral function of the quasi-elastic scattering, where the thick solid lines and the broken lines correspond to the quasi-elastic and incoherent elastic scattering, respectively. We also tried to fit with a Gaussian, but the agreement with the data was not satisfactory.

Fig.4 summarizes the results of the neutron scattering experiments. The closed and open circles are the linewidths of the CEF scattering and quasi-elastic scattering, respectively. The Néel temperatures determined from the susceptibility measurements are also plotted by open squares. For x=0.2, no magnetic ordering was found down to 0.5 K.

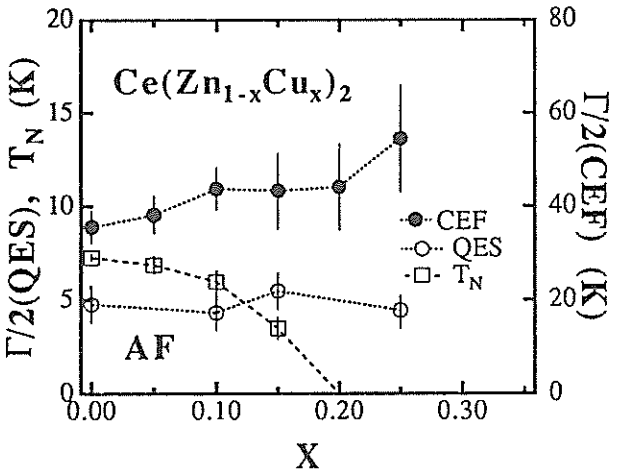

Fig. 4 Concentration dependence of the line widths of the CEF scattering and the quasi-elastic scattering, and the Néel temperature.

4. Discussion

As seen in table 1, the CEF excitation energies obtained from the susceptibilities by using the least squares fit procedure are qualitatively in agreement with those determined by the neutron inelastic scattering experiments. This indicates that 4f electrons in this system are well localized and the susceptibility is explained rather well by the crystal field model .

The result of the quasi-elastic scattering experiment shows that the spectra of $Ce(Zn_{1-x}Cu_x)_2$ are reproduced well by a Lorentzian spectral function at around 20 K. However the linewidth of the spectra remains constant with increasing x (HWHM ≈ 0.4 meV) . This means that, though the spin fluctuations of the the ground state in this system are mainly caused by the single site spin relaxation process at about 20 K, the energy spread of the spin fluctuations does not change with increasing x. It indicates that the Kondo temperature of this system is almost constant with increasing x in spite of the sudden decrease of the Néel temperature. The Kondo temperature is estimated to be less than 5 K from the linewidths of the quasi-elastic scattering.

From the result of the present experiments, we suggest that the suppression of the ordering temperature in $Ce(Zn_{1-x}Cu_x)_2$ is mainly caused by the competition between different kind exchange interactions or between different magnetic anisotropy due to the substitution of Zn atom by Cu atom rather than the competition between the Kondo effect and the RKKY interaction as expected earlier, since there is no sign of the increasing of the Kondo temperature with increasing x. Thus, the broadening of the linewidth of the CEF scattering is thought to be a result of disorder effect caused by the random substitution of Zn atom by Cu atom. However, it is still possible that the Kondo effect exists at a certain amount in this system. Since the total exchange energy becomes small around x = 0.2, the competition between the Kondo effect and the RKKY interaction will be significant in the compound $Ce(Zn_{1-x}Cu_x)_2$ with x around 0.2.

Acknowledgements

We would like to thank T. Kamiyama and K. Shibata for assistance with the experiments at the LAM-D spectrometer and N. Sato for helping the susceptibility measurements with the ^{3}He cryostat.

References

[1] M. Yamashita, M. Kurisu, H. Kadomatsu, I. Oguro and H. Fujiwara, J. Phys. Soc. Jpn., 56(1987)32.

[2] J. Voiron, P. Morin, D. Gignoux and R. Aleonard, J. Physique, 12(1988)C8-419.

[3] D. Debray, M. Sougi and P. Meriel, J. Chem. Phys., 56(1972)4325.

[4] R. Trump, S. Thierfeldt, M. Loewenhaupt and T. Chattopadhyay, J. Appl. Phys. 69(1991)4699.

Neutron diffraction studies of Fe/Cr superlattice by TOP

M. Takeda, H. Yasuda, T. Watanabe, Y. Endoh, A. Kamijo*, J. Mizuki+

Department of Physics, Faculty of Science, Tohoku University, Sendai, 980
*Fundamental Research Labs, NEC Corp., 4-1-1 Miyazaki, Miyamae-ku, Kawasaki, 216
+Fundamental Research Labs, NEC Corp., 34 Miyukigaoka, Tukuba, 305

Fe/Cr artificial multilayers are known to be the first multilayer system that shows a giant magnetoresistance (GMR) effect[1]. Experimentally it has been concluded that antiferromagnetic coupling of magnetic moments in adjacent Fe layers is essential to the GMR effect[2] and that the magnitude of the GMR effect oscillates as a function of the thickness of the Cr layer[3]. On the other hand, the origin of the antiferromagnetic coupling and of the GMR effect were still unknown. Recently several theoretical models were proposed which claimed that interfacial roughness between the Fe layers and Cr layers played an important role[4]. Neutron reflection and diffraction studies are a powerful tool in investigating such interfacial roughness. We have performed neutron diffraction measurements on Fe/Cr artificial multilayers in order to clarify the relation between the GMR effect and the interfacial roughness.

A sample was prepared by MBE at NEC Corp., consisting of an Al_2O_3(1102) substrate upon which is grown first a Nb(100) chemical buffer of 2000Å thickness and then an Cr(100) seed layer of 750Å thickness. A [Fe(100) -30Å /Cr(100) -10Å] bilayer is grown 80 times on the seed layer. The shape of the sample is rectangular, the crystal face being the (100) plane of bcc-Fe and bcc-Cr atoms. The dimensions were 30×40 mm^2. A neutron diffraction study has done at TOP spectrometer at KENS. Two bands of incident neutrons, 3-9Å and 11-18Å, were used for the experiment. The scattering vector of neutrons was perpendicular to the (100) plane.

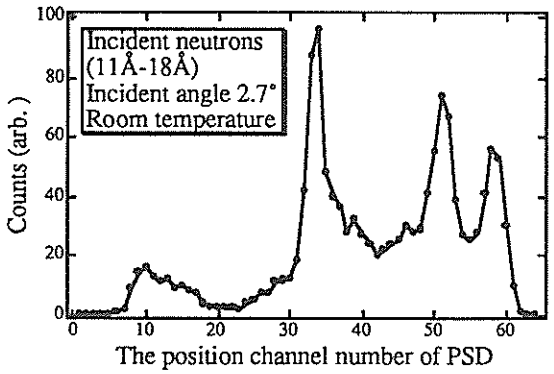

Fig. 1. Counts of total neutrons at each position channels of PSD. Band of incident neutrons is 11-18Å with the incident angle of 2.7°

Figure 1 shows the counts of neutrons at each position channel of the PSD when incident neutrons from 11Å-18Å band were directed to the sample at an incident angle of 2.7°. The peak at channels 32 and 33 in the spectrum are due to the direct beam, which did not pass through the sample and transmitted neutrons which underwent small refraction. The reflected beam observing the specular condition (the incident angle is equal to the reflection angle) was detected at channel 51. The geometrical condition of the experiment is displayed in Fig. 2.

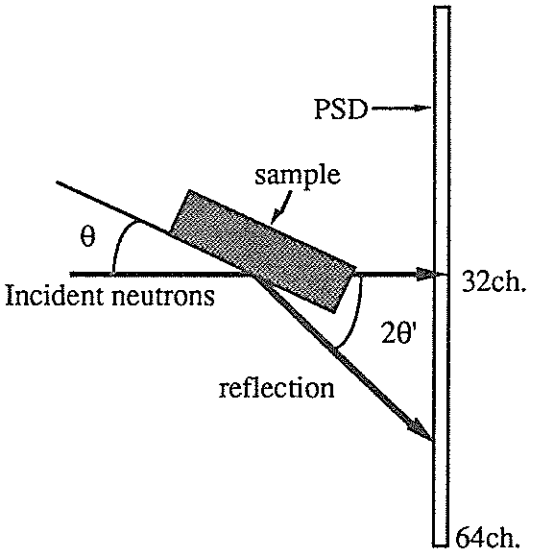

Fig. 2 Geometrical configuration of the PSD.

It is noted that clear reflection under off-specular conditions was visible at channel 57. At this position the reflection angle is equal to 3.6°. When the band of incident neutrons was shifted from 11Å-18Å to 3Å-9Å, two Bragg peaks were observed under the same conditions as in Fig. 1. One is the diffraction peak from the superlattice of [Fe(30Å)/Cr(10Å)] bilayer itself, and another corresponds to the antiferromagnetic diffraction peak of the Fe layers with twice the lattice spacing of the bilayer. In this case only reflection under specular condition was observed, however, the divergence of the reflected beam seemed to be large. It is convenient to make a contour map of intensities of reflected neutrons in

which the horizontal axis is the number of position channel of the PSD (reflection angle) and the vertical axis is the number of time channel (wavelength of neutrons) (Fig. 3).

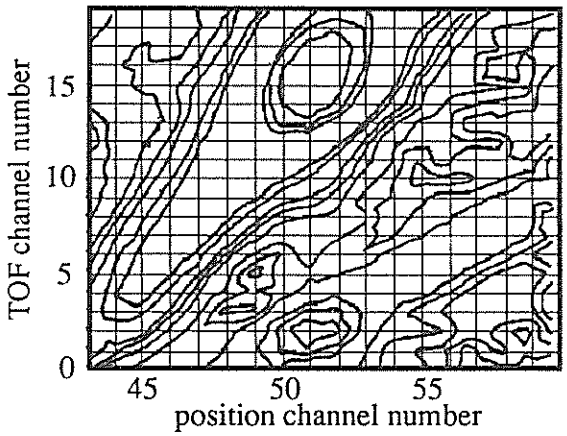

Fig. 3 Contour map of intensities. The horizontal axis corresponds to reflection angle and the vertical one to wavelength of neutrons. Two Bragg peaks are observed at points (51,2) and (51,16).

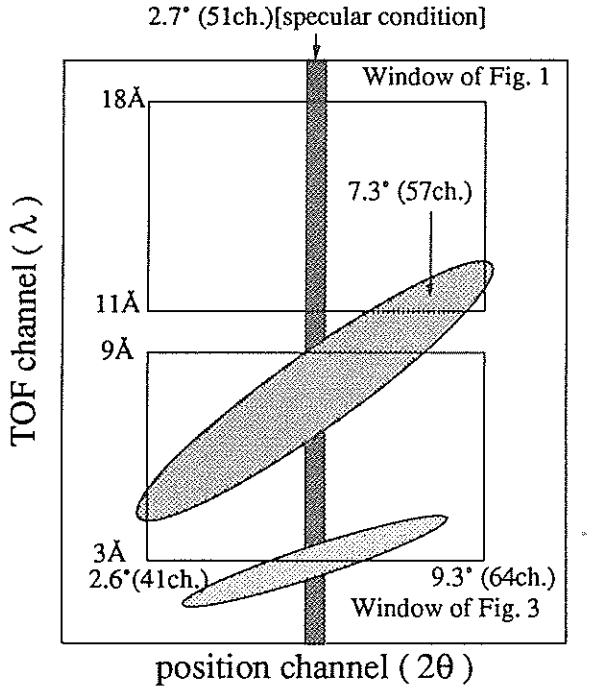

Fig. 4 Schematic representation of the wavelength-reflection angle window in Fig. 1 and Fig. 3.

Since the incident angle was fixed at 2.7°, specular reflection was observed at channel 51. The peak at (51,16) is due to magnetic Bragg scattering and that at (51,2) corresponds to the superlattice of the bilayer. The map shows that the peaks, especially the magnetic Bragg one, are widely spread. The difference of the reflection angle-wavelength window between Fig. 1 and Fig. 3 are schematically displayed in Fig. 4.

It is obvious that the extra reflection at channel 57 in Fig. 1 is the foot of magnetic diffuse scattering around the magnetic Bragg peak. Such large magnetic diffuse scattering suggests that there exists an in-plane magnetic disorder at the interface between the Fe layers and the Cr layers. This is the first observation of in-plane magnetic disorder in Fe/Cr superlattice structures. In order to get more information on the magnetic disorder at the interface and on the relation between the magnetic disorder and the GMR effect, we are currently measuring the magnetic field dependence of the magnetic diffuse scattering. The results will be reported in the near future.

References

1) M. N. Baibich, J. M. Broto, A. Fert, F. Nguyen Van Dau, F. Petroff, P. Etienne, G. Creuzet, A. Friedrich and J. Chazelas: Phys. Rev. Lett. **61** (1988) 2472.
2) N. Hosoito, K. Mibu, S. Araki, T. Shinjo, S. Itoh, Y. Endoh: J. Phy. Soc. Jpn. **61** (1992) 300.
3) S. S. P. Parkin, N. More and K. P. Roche: Phys. Rev. Lett. **64** (1990) 2304.
4) J. Inoue and S. Maekawa: Prog. Theor. Phys. Suppl. **106** (1991) 187.

Molecular Spectroscopy in Methanol Monolayer Adsorbed on the Surface of Graphite

A. INABA, T. KARIMATA and K. SHIBATA*

Department of Chemistry, Faculty of Science, Osaka University, Toyonaka 560
* Institute for Materials Research, Tohoku University, Sendai 980

Methanol forms a crystalline monolayer at low temperatures on the surface of graphite. Since graphite is hydrophobic, the system has been expected to have hydrogen bonds within the monolayer as the bulk solid does. An X-ray study reported that the monolayer has zigzag chains of alternating weak and strong hydrogen bonds.[1] It is now interesting to know the molecular vibrations for such system by molecular spectroscopy. While the heat capacity measurement at low temperatures enabled us to estimate an averaged frequency for the librational modes as well as that for the two-dimensional lattice modes,[2] the incoherent inelastic neutron scattering would give us the direct information.

The spectrometer LAM-D was used to obtain the spectrum in the energy range up to 30 meV at 15 K. Since the graphite specimen (Grafoil MAT) which we used has a preferred orientation, we first tried to observe the modes parallel to the surface (Q//). An aluminium container of cylindrical shape was used. It has a needle valve which is workable at low temperatures. The cell contained 16 g of graphite which had been degassed at 400°C. The amount of methanol adsorbed was only 90 mg, corresponding to the coverage well below the monolayer.

The result is shown in Fig. 1. The contribution from the adsorbed film amounted to the same magnitude as that from the background including graphite. Overall, the spectrum clearly indicates that the system is in a crystalline phase. Among several discernible peaks, two modes peaked at 7 meV and 12 meV can be assigned as a lattice mode and a librational mode, respectively. The latter seems to be consistent with the result obtained from the heat capacity measurement (13meV). There also seems to be a shoulder around 15 meV which can be ascribed to another librational mode.

Unfortunately, however, any evidence of the existence of short hydrogen bonds could not be obtained. We should know the complete structure including the position of the hydrogen atoms by neutron diffraction. Nevertheless, the present demonstrative result would encourage us to investigate the molecular vibrations of such diluted system successfully with LAM-D spectrometer.

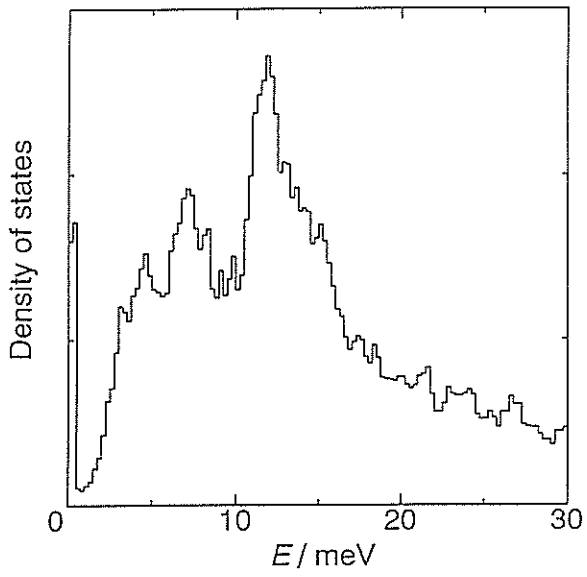

Fig. 1. Density of states of the monolayer methanol adsorbed on the surface of graphite obtained at 15 K.

References

1) K. Morishige, K. Kawamura and A. Kose: J. Chem. Phys. 93 (1990) 5267.
2) A. Inaba and K. Karimata: unpublished work.

Quasielastic Neutron Scattering in Methyl Chloride Monolayer Adsorbed on the Surface of Graphite

A. INABA, K. SHIBATA* and T. KANAYA**

Department of Chemistry, Faculty of Science, Osaka University, Toyonaka 560
* Institute for Materials Research, Tohoku University, Sendai 980
** The Institute for Chemical Research, Kyoto University, Uji 611

Methyl chloride forms two types of the monolayer on the surface of graphite, depending upon the coverage.[1,2] While the low-density phase (ca. 5 molecule/nm_2) melts at 120 K, the high-density phase (ca. 7 molecule/nm_2) melts at 146 K and has a phase transition at 128 K in its two-dimensional solid phase. Since the bulk solid has no phase transition, it is interesting to know the dynamics of both the methyl groups and the whole molecule, particularly in the high-density solid phase.

The purpose of the present experiment was to see the dynamics of the adsorbed molecules in the high-density phase by neutron scattering. We used two spectrometers LAM-40 and LAM-80ET. The spectra obtained at 110 K for LAM-40 and LAM-80ET showed that the system has at least two quasielastic components as illustrated in Figs. 1 and 2, respectively. The former indicates that the correlation time would be around 4×10^{-12} s which is presumably due to the rotational motion of the methyl group of the molecule. The latter indicates that the correlation time would be around 8×10^{-11} s which can be ascribed to the overall rotation of the molecule. It is necessary to investigate those contributions carefully and more in detail by looking at the Q dependence as well as the temperature dependence. In this stage, however, we can safely conclude that the molecular motions should be much more vigorous on the surface of graphite compared with those for the bulk solid.

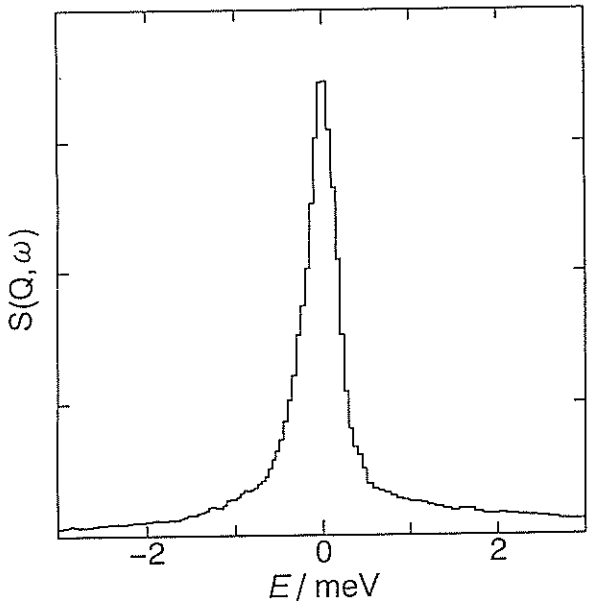

Fig. 1. A quasielastic component observed at 110 K for the high-density monolayer of methyl chloride on graphite (LAM-40).

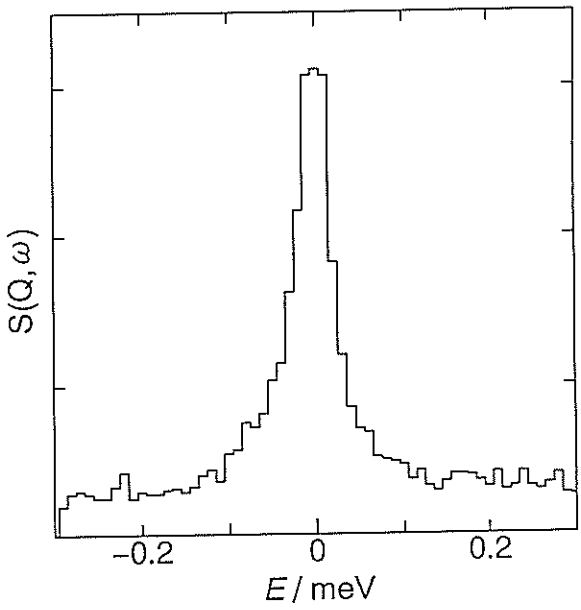

Fig. 2. A quasielastic component observed at 110 K for the high-density monolayer of methyl chloride on graphite (LAM-80ET).

References

1) A. Inaba and H. Chihara: J. Phys. Soc. Jpn. 60 (1991) 17.
2) K. Morishige, Y. Tajima, S. Kittaka, S. M. Clarke and R. K. Thomas: Mol. Phys. 72 (1991) 395.

Rotational Tunneling Spectroscopy at Sub-Kelvin Temperatures for Methane Monolayers Adsorbed on the Surface of Graphite

A. INABA, T. SHIRAKAMI, K. SHIBATA* and S. IKEDA**

Department of Chemistry, Faculty of Science, Osaka University, Toyonaka 560
* Institute for Materials Research, Tohoku University, Sendai 980
** National Laboratory for High Energy Physics, Tsukuba 305

Monolayer methane on graphite is in many ways a model system for the study of physisorption. Methane adopts a commensurate structure at coverages well below a monolayer and the molecules are orientationally ordered at low temperatures. The rotational tunneling of CH_4 in the commensurate phase is the only spectrum of an adsorbed molecule that has been treated quantitatively to obtain the rotational potential.[1)]

There are three spin species A, T and E for a CH_4 molecule. The conversion between them is forbidden: A calorimetric investigation[2)] demonstrated that for pure CH4 on graphite the spin system never reach equilibrium at low temperatures. When some small amount of oxygen is added as a magnetic impurity, the system comes to equilibrium. The rate of the spin conversion depends upon the temperature and the concentration of O_2.

The purpose of the present experiment is to see the catalytic effect of oxygen in accelerating the conversion. To do that we look at the detailed balance in the tunneling spectrum obtained at sufficiently low temperature.

We first designed a helium-3 cryostat of an adsorption type. It was installed at the spectrometer LAM-80ET. The bottom temperature we obtained was 0.3 K and it lasted for one day.

Fig. 1 shows the spectrum obtained at 0.32 K for the pure CH_4 monolayer, whereas Fig. 2 shows that obtained at 0.32 K for the CH_4 monolayer doped with 1 % of O_2. The results demonstrated a remarkable effect of O_2 as a catalyst. The system reached complete equilibrium. It is now important to follow the equilibration process (time evolution) to clarify the mechanism of the spin conversion. It is also interesting to know the concentration dependence of O_2. Further experiments ought to be done.

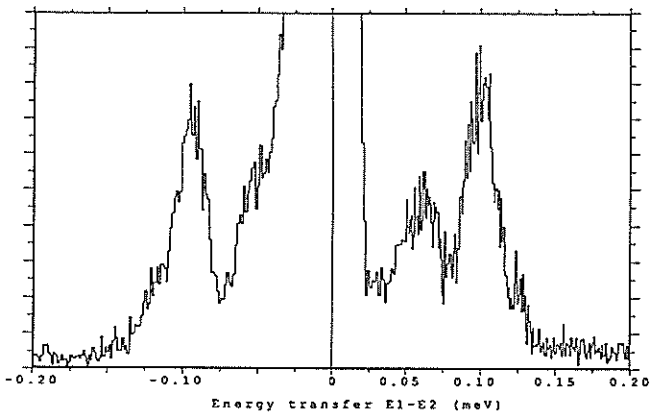

Fig. 1. Rotational tunneling spectrum obtained at 0.32 K for the pure CH_4 monolayer.

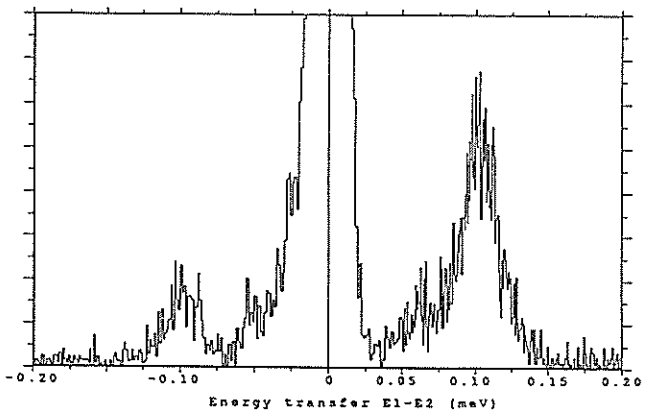

Fig. 2. Rotational tunneling spectrum obtained at 0.32 K for the CH_4 monolayer doped with 1 % of O_2.

References

1) M.V. Smalley, A. Huller, R.K. Thomas and J.W. White: Mol. Phys. 44 (1981) 533.
2) A. Inaba and T. Shirakami: unpublished work.

Crystal Analyzer Type Spectrometer LAM-D at KENS Spallation Thermal Neutron Source

K. Inoue, T. Kanaya*, K. Kiyanagi, K. Shibata**, K. Kaji* S. Ikeda***, H. Iwasa, and Y. Izumi****

Department of Nuclear Engineering, Faculty of Engineering, Hokkaido University, Sapporo 060
*Institute for Chemical Research, Kyoto University, Uji, Kyoto-fu 611
**Institute for Material Research, Tohoku University, Sendai, Miyagi-ken 980
***National Laboratory for High Energy Physics, 1-1 Oho, Tsukuba-shi, Ibaraki 305
****Macromolecular Research Laboratory, Faculty of Engineering, Yamagata University, Yonezawa-shi, Yamagata-ken 992

In the previous paper, we reported two crystal analyzer type quasielastic neutron scattering spectrometers LAM-40 and LAM-80 which were installed at the KENS spallation cold source[1]. The pyrolytic graphite (PG) analyzer mirrors were used in these spectrometers. Applying mica crystals as the analyzer mirror, we have recently made a great progress on LAM-80 in the energy resolution. This new machine, LAM-80ET, has been reported elsewhere[2]. The energy transfer ranges covered by these spectrometers are not so narrow compared with other machines which have the same order of the energy resolution. However, it is often essential to measure in a wide energy range up to several hundred meV for some physical phenomena. Therefore, we designed and constructed an inelastic scattering spectrometer, LAM-D, to cover the energy range up to 300 meV with the energy resolution of $\Delta\varepsilon/E_1$ less than 6 % in the energy range above 10 meV. The basic principle of LAM-D is the same as LAM-40 and LAM-80, while some special considerations have been made on the design of LAM-D for the high energy transfer measurements.

Fig. 1 shows the configuration of the LAM-D spectrometer. The LAM-D is installed at the H-9 thermal neutron beam hole at KENS. The flight path from the moderator to the sample is evacuated and the length (l_1) is 7.25 m. Each analyzer mirror is made from 56 PG crystal pieces of 12 mm x 12 mm x 2 mm in size with a mosaic spread of 1.2°. The distance between the sample and the crystal analyzer mirror is 27 cm. The distance between the mirror and the detector is also 27 cm. The flight path of the scattered neutron is thus fixed to be 54 cm.

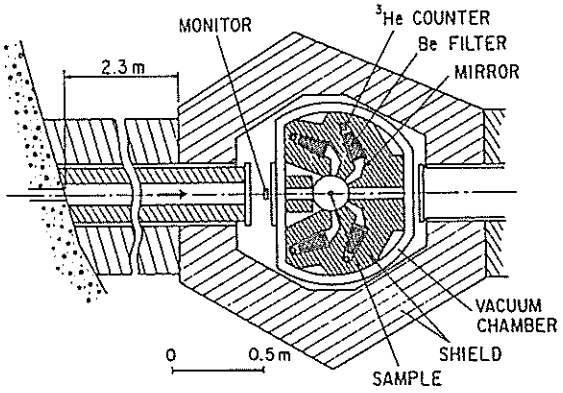

Fig. 1 The inelastic spectrometer LAM-D.

As seen in Fig. 1, two analyzer mirrors are symmetrically mounted at the scattering angle 35° and the other two at 85°. The 20 cm beryllium (Be) filters, which are cooled by liquid nitrogen, diminish the higher order reflections from the analyzer crystals. The length of the Be filter was determined by Monte Carlo simulation for transmission of neutrons with total atomic-cross section of both σ_t=0.5 and 7.5 barns, which corresponds to those below and above the Be cutoff wavelength. The results of the simulation is given in Fig. 2. In the case of 20 cm, the ratio of transmission $P_t(\sigma_t=7.5)/P_t(\sigma_t=0.5)$ is about 10^{-5}, which seems enough to remove the higher order reflection from the PG mirror.

The set of the mirrors and Be-filters is housed in an evacuated container surrounded by neutron shield made of borated resin and

cadminium sheets. Moreover, each analyzer mirror has its own inner shield.

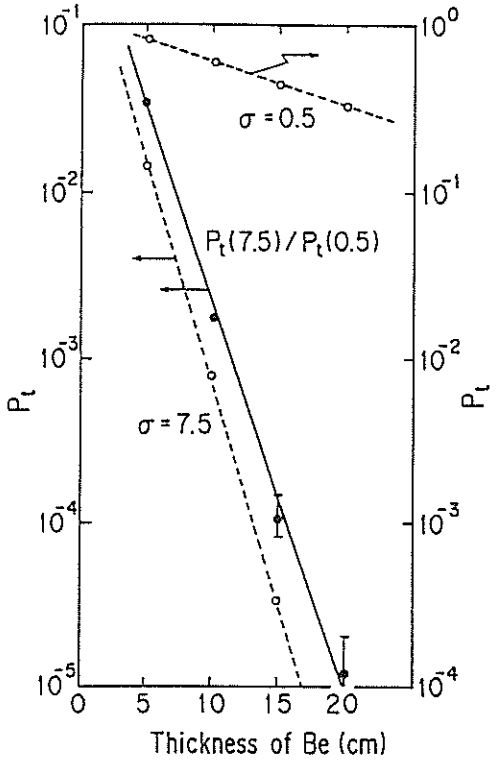

Fig. 2 Results of the Monte Carlo simulation for neutron transmission through Be-filter. Calculation was performed for neutrons below and above the Be cutoff wavelength. The corresponding atomic cross sections are 7.5 and 0.5 barns, respectively.

TOF spectra of vanadium measured with LAM-D are shown in Fig. 3 for the scattering angles of 35° and 85°, respectively. Each spectrum was obtained by summing up two spectra measured at the symmetrical position with the same scattering angle. The thickness of the vanadium sample is 2 mm and the measuring time is 8 hours. The counts of the elastic peaks are 241/μs and 269/μs for the scattering angle 35° and 85°, respectively. which enable us to estimate the intensity performance of the LAM-D. Expanding the spectra by a factor 12 in the elastic region, inelastic scattering from phonons in vanadium is cleary observed. Background levels for the expanded spectra are indicated by dashed lines in Fig. 3. Full-width at half-maximum (FWHM) of the elastic peak evaluated from vanadium spectrum is 0.40meV, which agrees with the theoretical value.

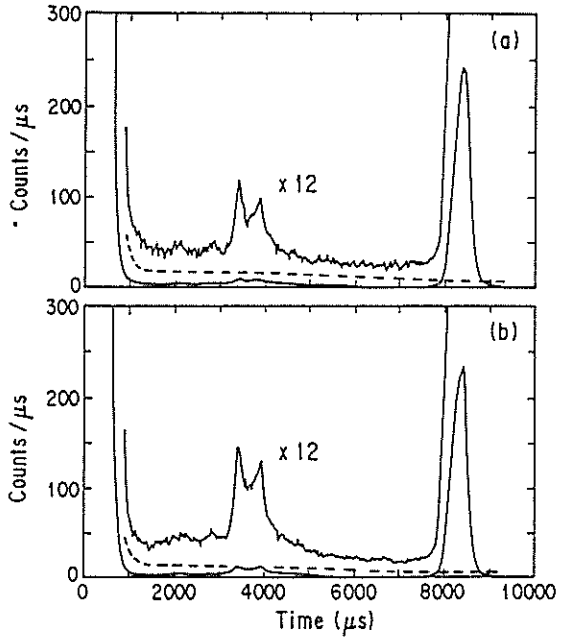

Fig. 3 TOF spectrum of vanadium measured by LAM-D.

LAM-D has been applied to studies of molecular motions in condensed matters [3,4]. LAM-D in combination with the pulsed thermal neutron source has demonstrated satisfactory perfomance for the measurements of inelastic scattering in the energy range up to 300 meV. The basic principle of LAM-D is the same as that of the quasielastic spectrometers LAM-40 and LAM-80 so that the data reduction methods developed for LAM-40 and LAM-80 can be applied to data of LAM-D with small modifications. Combinations of these spectrometers allows us to cover the energy range from 1μeV to 300 meV.

References

1) K. Inoue et al., Nucl. Instr. and Meth. A238, 401(1985)
2) K. Inoue et al., Nucl. Instr. and Meth. A309, 294(1991)
3) T. Kanaya, K.Kaji and K.Inoue, Physica B 180 & 181, 814(1992)
4) H. Ikeda and K. Ohoyama, Phys. Rev. B 45, 7484(1992)

Performance of New CAT (CAT-II)

I. TAMURA, A. AGUI*, Y. NAKAI**, S. IKEDA***

Department of physics, Faculty of science, Chiba Univ. Inage-ku Chiba-shi.263
*Department of physics, Faculty of science, Ochanomizu Univ. Bunkyo-ku, Tokyo.112
**Institute of Materials Science, Univ. of Tsukuba Tsukuba-shi,Ibaraki 305
***National Laboratory for High Energy Physics, 1-1 Oho, Tsukuba-shi, Ibaraki 305

The CAT spectrometer is a time-of-flight type crystal analyzer spectrometer with an inverted geometry at KENS, and has been used for the measurements of incoherent neutron scattering at a large energy transfer ($\varepsilon > 100$ meV). A layout of the CAT is shown in Fig.1, in which a white neutron beam is scattered upon a sample, and then scattered neutrons at a fixed energy E_f are selected by the analyzer crystal with Bragg angle θa.

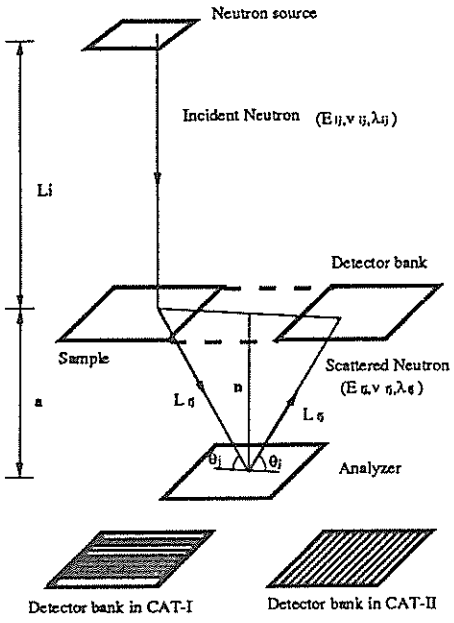

Fig. 1 Layout of CAT.

In order to adopt a time focusing principle, the planar sample and the planar detector are set on the same plane which is parallel to the planar analyzer crystal, as shown in Fig.1. A beryllium filter cooled down to 30K is installed between the analyzer and the detector with a post cross-collimator made of cadmium. It eliminates neutrons due to the higher order-reflection of the analyzer crystal. By adopting the time-focusing principle and the beryllium filter, the high energy resolution of $\Delta\varepsilon/\varepsilon = 2\%$ at $\varepsilon > 100$ meV and the low background were realized in the CAT. However, it has been recently desired to measure the local vibration spectra of hydrogen in metals, hydrogen-bonded ferroelectric compounds and biological materials in a low energy-range of $\varepsilon < 10$ meV. Based on this demand, the CAT spectrometer was improved to achieve the higher energy-resolution around $\varepsilon = 0$ and the lower background. This paper reports the details of the improvements in the CAT spectrometer.

In a detector bank of the old CAT (CAT-I), eight ^{3}He neutron counters (1/2"-diameter, 12"-active length and 20 atm) had been installed horizontally (see Fig.1). In this case, the energy resolution is given by[1)]

$$\left(\frac{\Delta\varepsilon}{\varepsilon}\right)^2 = m\,[\,V_f^4\cot\theta_a^2\,(\Delta 2\theta)^2+\left(\frac{V_i^2}{L_i}\right)^2(\Delta L_i)^2 +8\left(\frac{m\,d}{h}\right)^2\left(\frac{V_i^3}{L_i}\right)^2(\Delta a)^2 +\left(\frac{V_i^3}{L_i}\right)^2(\Delta t_p^2+\Delta t_m^2+\Delta t_c^2)] \qquad (1)$$

where m is the neutron mass, V_f the scattered neutron velocity, V_i incident neutron velocity, L_i incident flight-path length and d the d-spacing of the analyzer crystal. $\Delta 2\theta$ corresponds to the ambiguity of θa. Since the detectors are set horizontally, $\Delta 2\theta$ is fairly large. Δa is a distance between the analyzer plane and the sample plane (same to the detector plane). Δt_m and Δt_c are the neutron pulse-width and the channel-width of the time-analyzer, respectively. Here no mosaic spread of the analyzer crystal is assumed. In a case of CAT-I, all terms in Eq.(1) are calculated and drawn as solid lines in Fig.2. Obviously, the contribution of ΔL_i is almost constant and very small in a wide energy range; that of $\Delta 2\theta$ is large only at $\varepsilon <$ 200 meV; that of Δa is dominant only at $\varepsilon > 200$ meV. From these results, it is easily concluded that the smaller $\Delta 2\theta$ is indispensable for realizing the higher energy-resolution around ε=0. Therefore, twelve detectors (1/2"-diameter, 6"-length and 10 atm) in the new CAT (CAT-II) were set vertically (see Fig.1). In this case, the energy-resolution can be described with $(\Delta 2\theta)_j$ for a detector (j) which is much smaller than

$\Delta 2\theta$. Since V_{fj} or θ_{aj} for the detector (j) can be determined by a time of the elastic peak, the neutron scattering spectrum $I(\varepsilon)$ can be determined by each detector (j). By summing up the obtained $I(\varepsilon)$'s, the neutron scattering spectrum with the higher energy-resolution around ε=0 can be obtained without decreasing the intensity. Dashed lines in Fig.2 show the contribution of $(\Delta 2\theta)_j$ and the total resolution in the case of CAT-II.

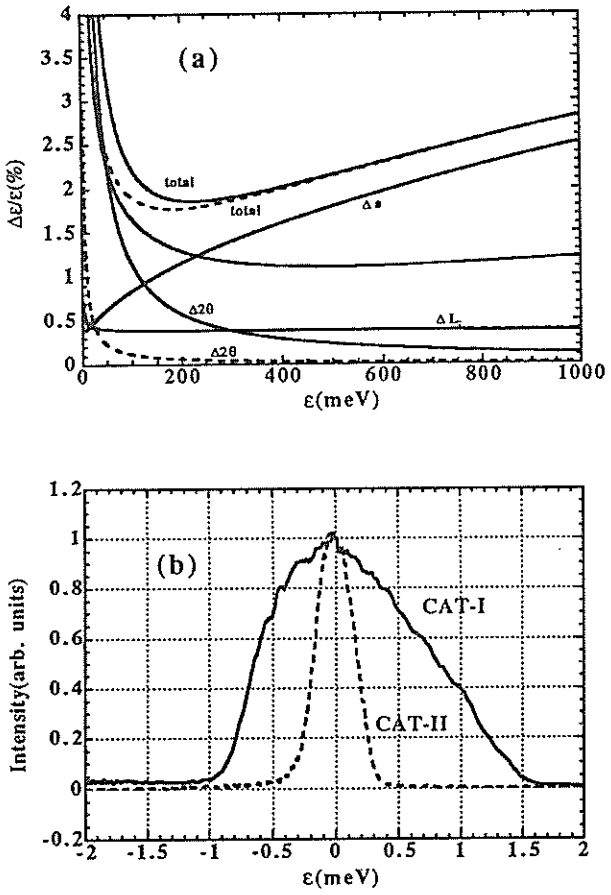

Fig. 2 (a) Total and partial energy-resolutions and (b) observed elastic peaks.

In order to test the performance of CAT-II, local vibrational spectrum in T_iH_2 was observed. The observed elastic peaks in cases of CAT-I and -II are also shown in Fig. 2. A solid line shows the elastic peak observed by CAT-II and a dashed line shows that of CAT-I. It indicates that the energy-resolution around ε=0 was improved from $\Delta\varepsilon$=1.4 meV to $\Delta\varepsilon$=0.35 meV.

In an inverted geometry spectrometer such as the CAT spectrometer, the energy of the detected neutrons is fixed (a fixed energy of the CAT spectrometer is about 4 meV). Therefore, if the neutron detecting efficiency of the installed detectors is high at about 4 meV but low at the other energy region, the low background can be realized. Generally, the detecting efficiency of ^{3}He-detector, D(E), is given by

$$D(E) = 1 - \exp\left(-N_a\, p_0 \frac{1.12\times10^{-3}}{\sqrt{E}}\, x\right) \qquad (3)$$

where p_0 is a pressure of ^{3}He, σ_a absorption cross section of ^{3}He and x the thickness of detector. Figure 3 shows the energy-dependence of D(E) in cases of p_0=6, 10 and 20 atm (x=1/2") and p_0=10 atm (x=1/4"). From these results, the ^{3}He-pressure in detectors for CAT-II was selected to be 10 atm. in spite of 20 atm. It was expected that the low background could be obtained by this change. Figure 4 shows the actual neutron scattering spectra of T_iH_2 observed with CAT-I and CAT-II, respectively. It is clear that the lower background has been realized in CAT-II.

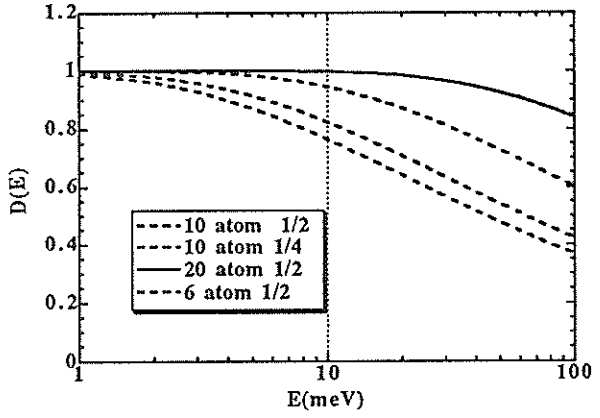

Fig. 3 Efficiency of ^{3}He-detector.

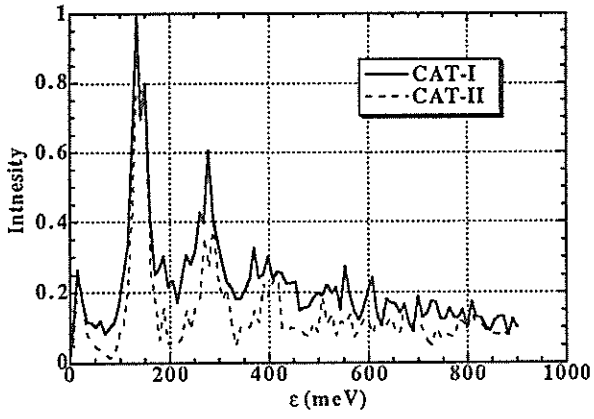

Fig. 4 neutron scattering spectra of TiH2 observed with CAT-I and CAT-II.

References

1) S. Ikeda and N. Watanabe, Nucl. Instr. Meth. **221** (1984) 571

Future Program

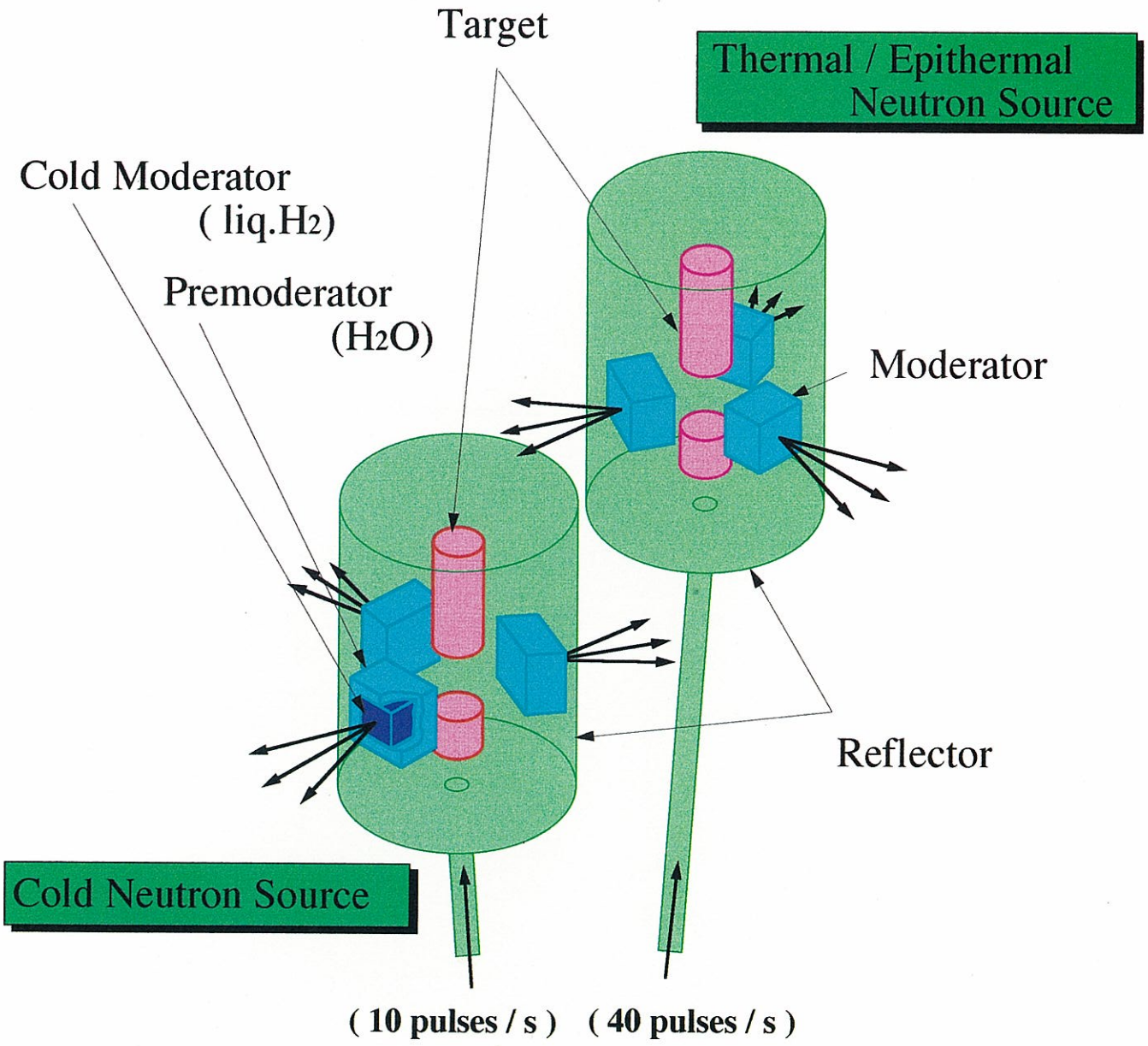

Target Station Proposed in Future Plan JHP.

Preliminary Neutronic Studies on a Pulsed Spallation Neutron Source Using 3 GeV Protons

Y. KIYANAGI, N. WATANABE* and M. ARAI*

Department of Nuclear Engineering, Faculty of Engineering, Hokkaido Univ., Sapporo 060
*National Laboratory for High Energy Physics, 1-1 Oho, Tsukuba-shi, Ibaraki 305

When we consider an intense pulsed spallation neutron source, a high intensity proton accelerator such as compressor ring, synchrotron or FFAG is indispensable combined with a high-current proton linac of a full energy or an appropriate injection energy. From an accelerator point of view, a higher energy but with a modest current is more feasible due to the existence of space charge limit. Merits and demerits for using higher energy protons (E_p>0.8 GeV, which is typical in the existing large-scale facilities) are being discussed extensively at various laboratories (e.g. for ESS, a next generation European spallation neutron source). We had a similar problem in the choice of the proton energy in Japanese Hadron Project (JHP) where KENS-II, a next-generation pulsed spallation neutron source in Japan, is involved. The neutron society stressed to adopt a lower energy, say 1 GeV, while the nuclear physics society claimed a higher energy, at least 2 GeV (hopefully 3 GeV). We performed some neutronic calculations[1][2] to understand the proton-energy dependence of neutron intensity using a hadron transport code NMTC/JAERI[3] and some low-energy neutron transport codes. Our results was very much unfavorable for higher proton energies. Based on this result we chose 1 GeV as a proton energy in the first-phase JHP.

Recently we have found our earlier calculation which was reported at ICANS-X[2] to be some misleading. NMTC/JAERI gave smaller neutron yields at higher proton energies (above 1 GeV). After that, the code was revised and confirmed to give consistent results with those using an HETC code in some benchmark calculations[4] and with some measured results[5]. We performed re-calculations using the revised NMTC/JAERI on the target-moderator-reflector system same as in the previous calculations, since the results is so important for the strategy of a new source. The present paper reports briefly the new calculated results, mainly focused on the slow-neutron intensity with 3 GeV protons comparing with 0.8 GeV case.

Figure 1 shows the calculated results of the intensities of O5R neutrons as a function of proton energy for various target materials with a size of 32 cm long and 10 cm in diameter. O5R neutrons mean those below 15 MeV directly obtained from a hadron transport calculation, which dose not include neutron transport below 15 MeV. However, O5R neutron will be a simple but good measure of the neutronic performance of a target (full calculations are given later). In the present results the intensities are increasing more linearly with proton energy. It turns out that tungsten is one of the best candidates for the target material among the non-fissile materials studied. The lower intensities in the lead target are due to its lower number density; i.e. the diameter of 10 cm is too small for lead.

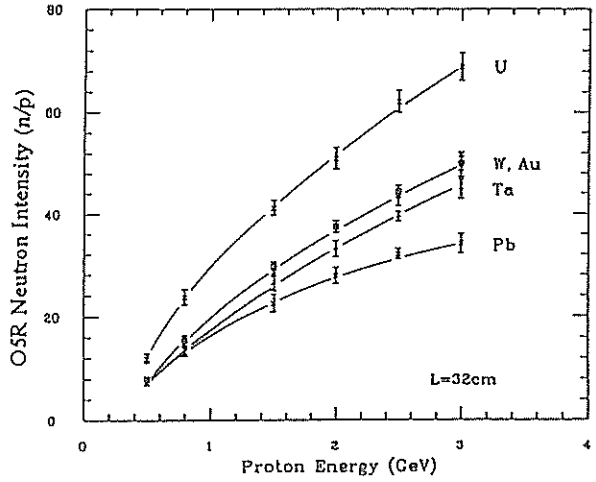

Fig.1 O5R neutron intensities for various target materials as a function of proton energy.

Axial distributions of O5R neutrons in the uranium (depleted U) target are shown in Fig.2 for various proton energies. In the present results, by increasing proton energy the peak position shifts towards the downstream and the peak intensities increase, contrasting with the previous results where the shifts of the peak position were not small and the peak intensities were almost saturated at higher energies (say above 2 GeV).

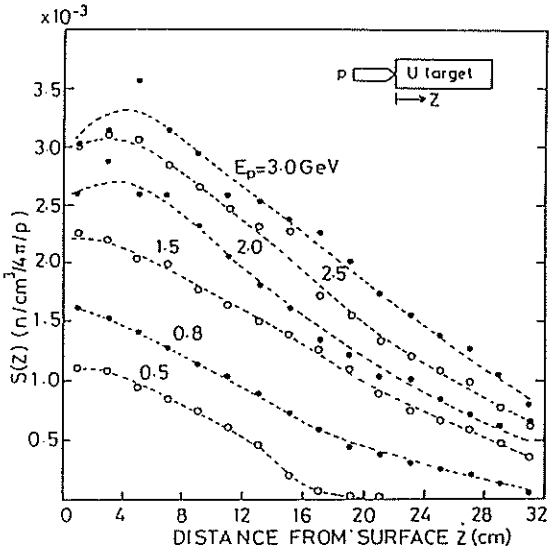

Fig.2 Axial distributions of O5R neutrons in a uranium target at various proton energies.

When we utilize higher energy protons the escape of energetic hadrons from the target, especially at the downstream, might be a problem from neutronic point of view. Figure 3 shows the radial distributions of the O5R neutron intensities for 3 GeV protons. The result shows that neutrons are mainly produced within the proton beam size (2.35cm in radius), almost independent of the axial position in the target, suggesting that the present target radius is sufficient for a proton-beam profile of this size. However, when a higher current of 3 GeV proton-beam is utilized, the larger leak of energetic hadrons from the target will result in reduction of the neutron production, since the beam size is approaching a target size in order to keep the heat density at an acceptable level.

Next, we calculated the intensities of escape fast neutrons from the cylindrical

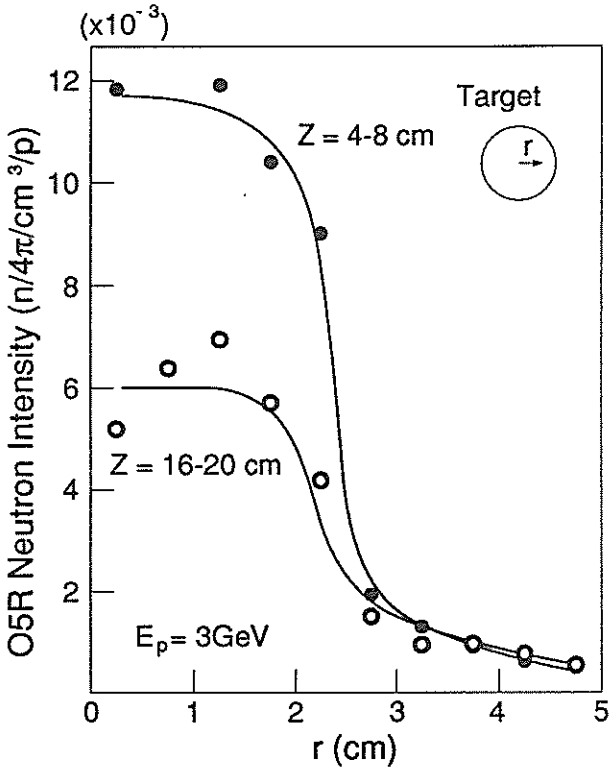

Fig.3 Radial distributions of O5R neutrons in a uranium target at proton energy of 3 GeV at two axial positions.

surfaces of the various targets, since the slow-neutron intensities from the moderators are directly related to those neutrons. Figure 4

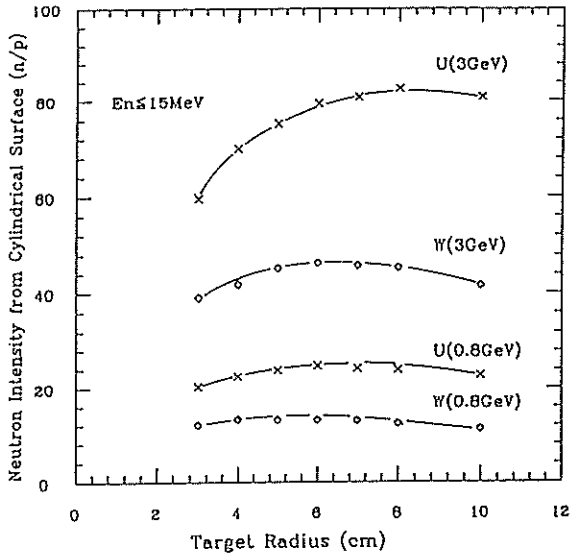

Fig.4 Escape fast neutron intensities from cylindrical surfaces of the targets as a function of target radius.

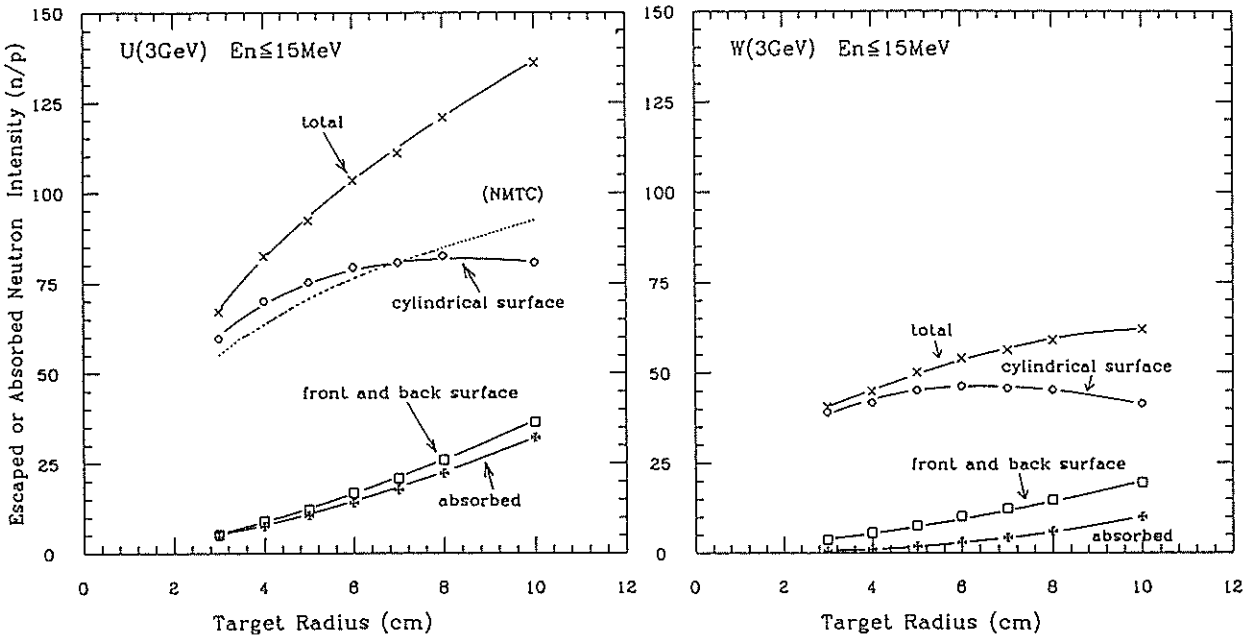

Fig.5 Contribution of each process (escape and absorption) as a function of target radius. The curve indicated by "NMTC" is intensity of O5R neutrons.

shows the escape fast neutron intensities as a function of target radius. In this calculation the secondary neutron production below 15 MeV during neutron transport in the target was included. Although the total number of neutrons produced in the target increases with target radius, the intensity of escape neutrons from cylindrical surface does not increase monotonically due to the escape from the end surfaces and the absorption in the target. Figure 5 shows contributions of each process (escape and absorption) for uranium and tungsten targets. The absorption in the uranium target is considerable compared to the tungsten case, since cross sections of (n,f) and (n,xn) are significant.

We calculated slow neutron intensities (E_n< 0.9 eV) from the moderators in the model target-moderator-reflector system shown in reference (3). In this model two reference light water moderators were put on the target, although in a real system it will be typical to put four moderators with different neutronic characteristics (2 above, another 2 below the target). This model will be sufficient to examine the slow neutron intensities from the moderators. The slow-neutron intensities as a function of target radius are shown in Fig. 6 for proton energies , 0.8 and 3 GeV. The neutron intensity increases with target radius and forms a peak. This is partly due to the fact shown in Fig.4. However, the peak appears at a smaller radius than in Fig.4. This is due to the fact that the coupling between target and moderator becomes loose with

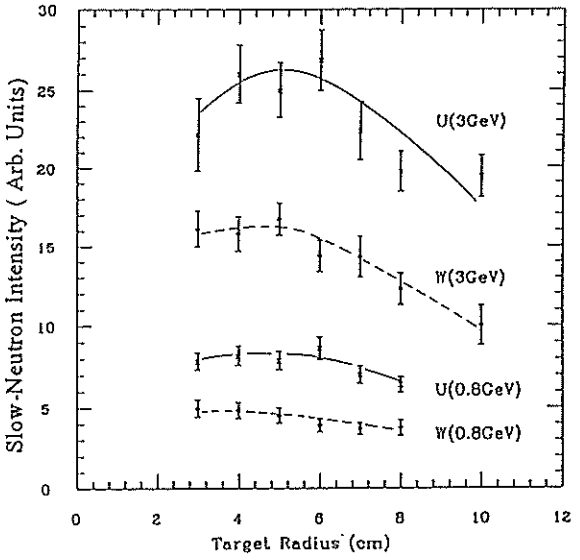

Fig.6 Sum of slow-neutron intensities from two reference moderators as a function of target radius.

increasing target radius. The optimal target radius is 4-5 cm. We chose a radius of 5 cm in the following calculations.

In Fig.7 the sum of the slow-neutron intensities from the two moderators set at the optimal positions are plotted as a function of proton energy. The intensity increases almost linearly with proton energy. The proton energy dependence of the slow-neutron intensity $I^S(E_p)$ at higher energy region (say $E_p \geq 0.8$ GeV) is expressed to a good approximation as

$$I^S(E_p)=AE^x.$$

Vassil'kov[5] showed that the total neutron yield from a target $Y(E_p)$ can be expressed as

$$Y(E_p)=C+BE_p^y,$$

where A, B and C are constants. The values of y determined by the measurement for a lead target (20 cm in diam.) was y=0.75~0.85. The present value of x for slow-neutron intensity turns out to be close to this value. The ratio of slow neutron intensity for uranium target to that for tungsten one is about 1.7 at 0.8 GeV, while it seems to be decreasing a bit at higher proton energies.

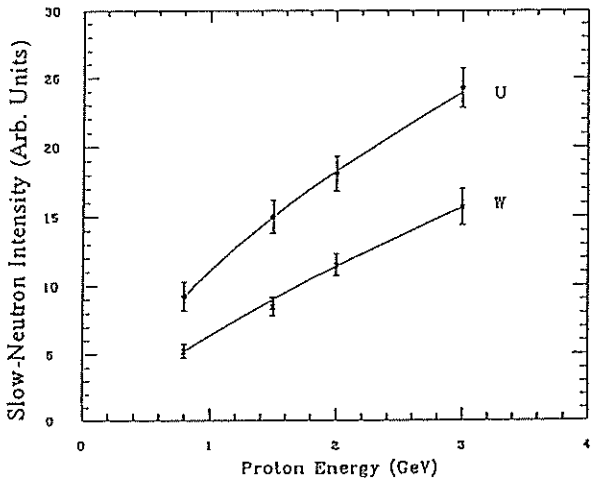

Fig.7 Sum of slow-neutron intensities from reference moderators optimally placed as a function of proton energy.

In summarizing the results, the slow-neutron intensities can be increased by about factor 3 when the proton energy is increased from 0.8 to 3 GeV. This number should be compared to the increase of the proton beam power, 3.75 times. The slow-neutron production efficiency per beam power with 3 GeV protons is about 80 % of the 0.8 GeV case. This value is very acceptable. If it is difficult to construct a higher current pulsed accelerator, the use of 3 GeV protons but with a reduced current will be a good choice. The lower efficiency with 3 GeV protons can be compensated by taking full advantage of the wider axial distribution of the fast neutrons. Studies for such possibilities are under progress.

References

(1) M. Arai et al., KENS REPORT-VI(1985/86), KEK Progress Report 86-2, 263

(2) Y. Kiyanagi, M. Arai and N. Watanabe, "Advanced Neutron Source 1988", Institute of Physics Conference Series Number 97, Institute of Physics, Bristl and New York, pp.753 (1988).

(3) Y. Nakahara and T. Tsutsui, JAERI-M 82-198 (1982).

(4) H. Takada, private communications.

(5) R. G. Vassil'kov and V. I. Yurevich, Proc. Int. Collaboration on Advanced Neutron Sources (Tsukuba, October 22-26, 1990) pp.340.

Some Possibilities for Increasing Slow-Neutron Beam Intensity from Flux-Trap Moderators

Y. KIYANAGI and N. WATANABE*

Department of Nuclear Engineering, Faculty of Engineering, Hokkaido Univ., Sapporo 060
*National Laboratory for High Energy Physics, 1-1 Oho, Tsukuba-shi, Ibaraki 305

Flux-trap moderators were proposed by the Los Alamos group[1] and discussed extensively[2][3][4]. However, we found that this configuration has various possibilities for increasing the slow-neutron beam intensity in comparison with a wing one. We examined such possibilities by computer simulation.

The calculations were performed for a proton energy of 1 GeV since this proton energy is proposed for KENS-II, the next generation pulsed-spallation neutron source in Japan. For simplicity a cylindrical beam profile of a radius 2.35 cm was assumed (a reasonable size as in existing facilities). The calculational model of the target-moderator-reflector system is shown in Fig.1. The target is split into two parts; the first target on which protons are injected and the second target after the void space. The length of the first target was kept at 7.5 cm, optimal length, and the target radius at 5 cm[3]. For simplicity, the targets are assumed to be made of pure tungsten metal, being not diluted by coolant and cladding materials as in LANCE, Los Alamos National Laboratory. The total target length is fixed at 34.5 cm which is sufficient for 1 GeV protons. As a reference system, four decoupled light-water moderators (10 x 10 x 5 cm^3) are placed around the void space between the two target halves with a distance between moderator and target center-line, d, 7 cm. A beryllium reflector, at least 30 cm thick, is used as shown in the figure. The beam holes in the reflector are lined with B_4C decouplers. The decoupling energy was adjusted to 20 eV. The moderators are also covered by the same decouplers except for the viewed surfaces. The height and the opening angle of the beam holes in the reflector are 10 cm and ±25 degrees, respectively. For the low-energy neutron transport calculation a Monte Carlo code, MORSE-DD[5][6], was used combined with a high-energy hadron transport code, NMTC/JAERI[7]. An S_N neutron transport code, TWOTRAN-II[8], was used for the calculation of the spatial distributions of low-energy neutrons. For both calculations the cross section library, ENDF-B/IV[9], was used.

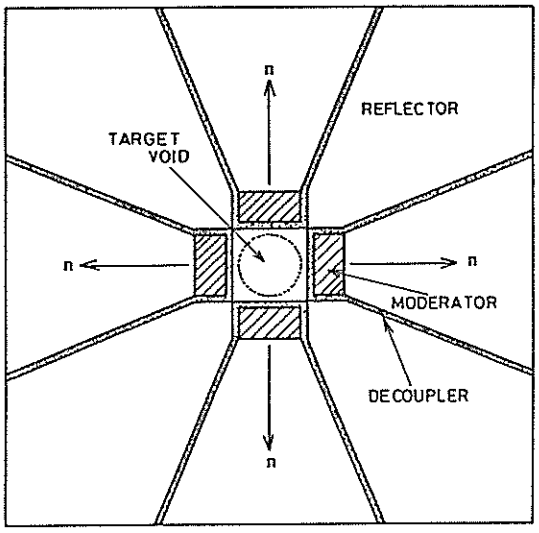

Fig.1 Calculational model of the flux-trap type target-moderator-reflector system.

What will happen if we increase the height, h, of the moderator with a larger separation, *l*, of target halves? Figure 2 shows the calculated results. The beam intensities are normalized to that for the reference case (l = 14 cm, d = 7 cm, 10 x 10 x 5 cm^3 moderators at the center of the void height). Although the beam intensity decreases with a larger separation of the target halves, it increases almost linearly with moderator height (up to 2.3 at h = 26 cm with l = 30 cm). One can take full advantage of a higher beam intensity obtained with such an extended moderator in some classes of experiments in which the beam collimation is

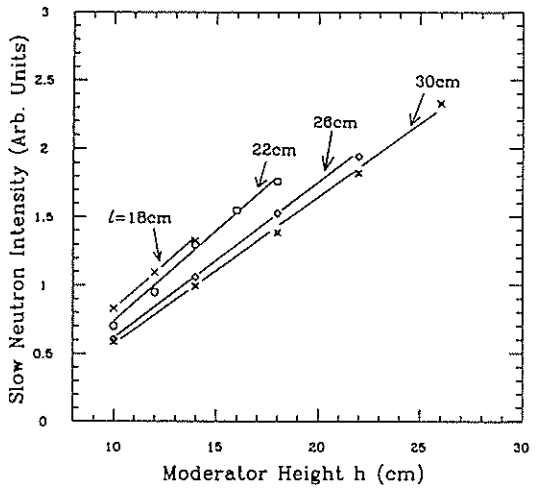

Fig.2 Slow-neutron intensities from extended moderators.

not so important. In order to understand the above results we calculated the spatial distribution of neutron intensities on the viewed surface along the proton beam direction. Since a three-dimensional Monte Carlo calculation is much time consuming to obtain required statistics, we performed a two dimensional calculation using TWOTRAN-II for a two dimensional model as shown in Fig. 3, where

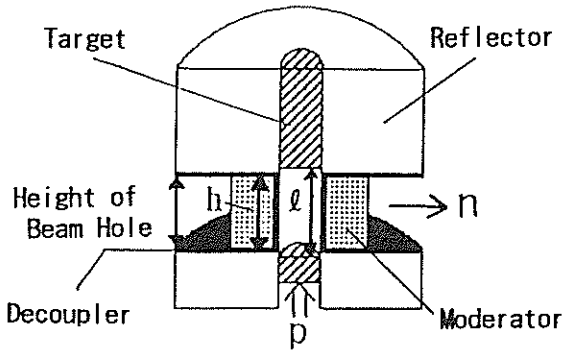

Fig. 3 Calculational model for the two-dimensional calculation.

the moderator is an annulus with a thickness of 5 cm at d = 7 cm and l =h + 4 cm. Figure 4 shows the results of the distributions of slow-neutron beam intensities along the proton beam direction, Z. The distributions are rather flat and symmetric than those for a wing geometry moderator where the asymmetry (peaking towards the target) is more enhanced. This is

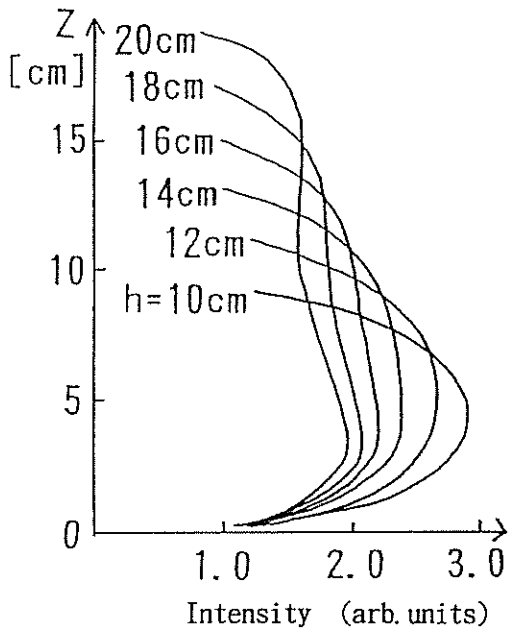

Fig.4 Vertical spatial distributions of slow-neutron intensities on extended moderators .

the reason why the intensities increase linearly with moderator height h. For reference, the calculated results of the spatial distributions on a moderator of h = 10 cm during the slowing-down process are shown in Fig. 5. The distribution in the fast neutron region (E_n=0.821-1.35MeV) strongly reflects the distribution of the first collision density of neutrons in the moderator. With decreasing energies the distribution becomes more flat.

Even in the case that neutrons from such extended moderators cannot be utilized due to a required angular collimation of the neutron beams, those moderators with a limited viewed surface of 10x10 cm^2 will give a higher slow-neutron intensity than the reference moderator of 10x10x5 cm^3, by overlapping the moderator with the target as shown in the inset of Fig. 6, keeping the separation of the target halves at 14 cm. We examined such moderators and obtained the results as shown in Fig. 6. A moderator with a larger height gives higher intensity by about 10 %. When the width of the moderator, w, is also increased to 12 cm, a gain about 1.3 comes out in total for the case of 10x10 cm^2 viewed surface and about 1.5 for a larger viewed surface of 10 cm high and 12 cm

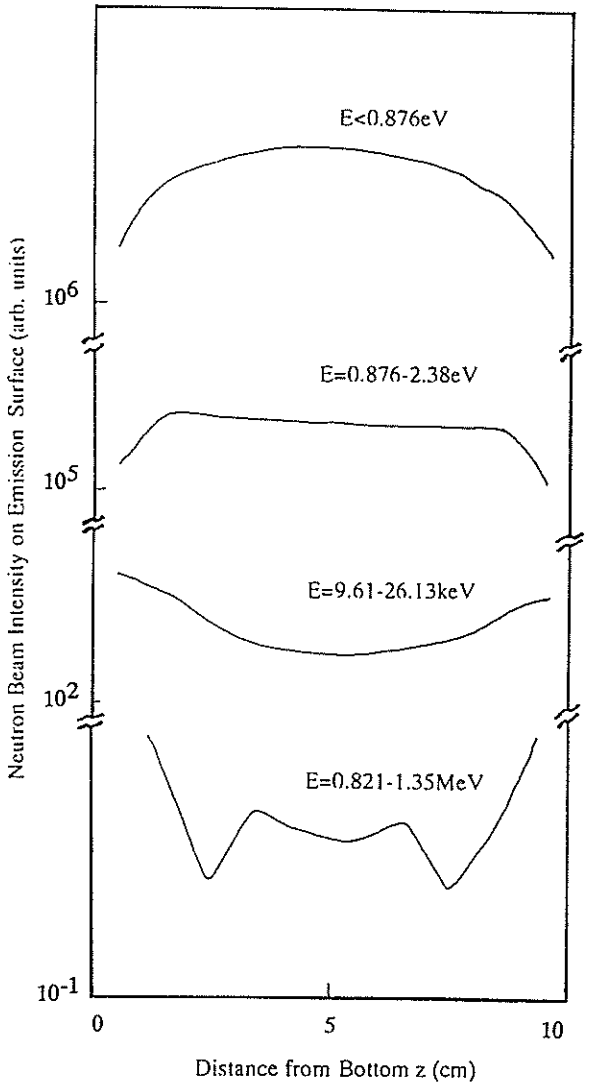

Fig.5 Spatial distributions of neutrons during slowing-down process.

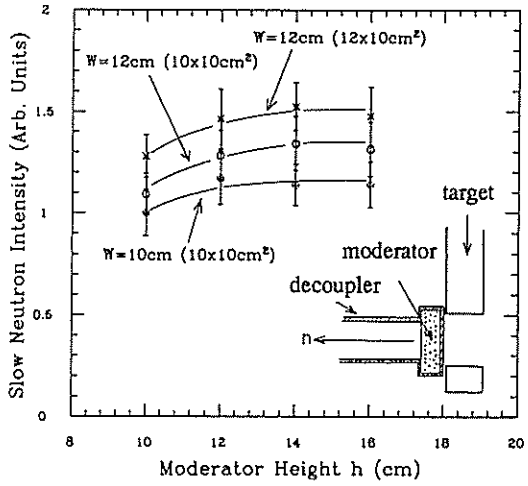

Fig.6 Slow-neutron intensities from overlap moderators. W is moderator width. Areas of viewed surfaces are indicated in parentheses.

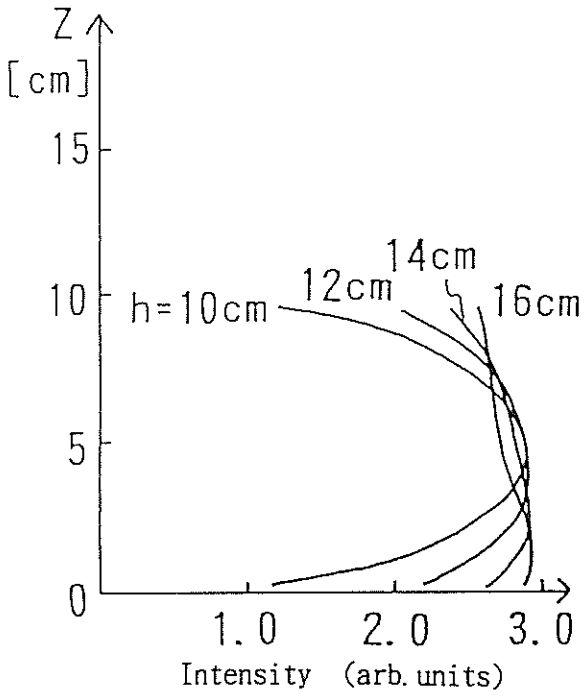

Fig.7 Vertical spatial distributions of slow-neutron intensity on the viewed surfaces of the overlap moderators.

wide. Vertical spatial distributions are also calculated. The results are shown in Fig. 7. The increase in the intensity is to be mainly due to the more flat distributions with the unchanged peak height.

For a direct comparison of the flux-trap moderator to the wing one, we calculated the relative intensity for each reference moderator. The relative values was about 0.94; almost comparable. However, by adopting extended moderators we have a relative intensity of about 2.3x0.94 and by overlap moderator about 1.5x0.94 to the wing.

The combination of a slab moderator with a burst suppression chopper and/or a curved guide tube is sometimes discussed for a higher intensity. Our calculation showed the relative intensity of a reference slab moderator to the reference flux-trap one is about 1.5. An overlap

moderator in a flux-trap geometry will be much better than the slab: the intensity is comparable to the slab, but with much less fast and high-energy neutron backgrounds.

We reported[10] that a coupled liquid hydrogen moderator with a hydrogenous premoderator at ambient temperature in a wing geometry can provide a much higher cold-neutron beam intensity; about 6 times higher than a typical decoupled one. Such moderators at a flux-trap geometry are expected to have similar advantage to the ambient temperature moderator in this geometry. This possibility is to be studied experimentally.

REFERENCES

(1) G. J. Russell, H. Robinson, G. L. Legate, R. Woods, E. R. Whitaler, A. Bridge and K. J. Hughes: Proc. 9th meeting of International Collaboration on Advanced Neutron Sources, ICANS-IX (Villigen, Sept. 22-26,1986) pp.177.

(2) G. J. Russell: Proc. ICANS-XI (Tsukuba, Oct. 22-26 1990) pp.335.

(3) Y. Kiyanagi and N. Watanabe: Proc. ICANS-XI (Tsukuba, Oct. 22-26 1990) pp.408.

(4) N. Watanabe and Y. Kiyanagi: Physica B. 180 & 181, 893 (1992).

(5) E. A.Straker et. al.: ORNL-4585(1970).

(6) M. Nakagawa and T. Mori: JAERI-M 84-126(1984).

(7) Y. Nakahara and T. Tsutsui: JAERI-M 82-198(1982).

(8) K. D. Lathlop and F. W. Brinkley: LA-4848-MS(1973).

(9) ENDF/B Summary Documentation, BNL-NCS-17541(ENDF-201), 2nd Edition, compiled by D. Garber, avairable from the National Nuclear Data Center, BNL, Upton, N.Y.(1975).

(10) Y. Kiyanagi, N. Watanabe and H. Iwasa: Nucl. Instrum. Meth., A312, 561 (1992).

List of Proposals Accepted

(1991 - 1992)

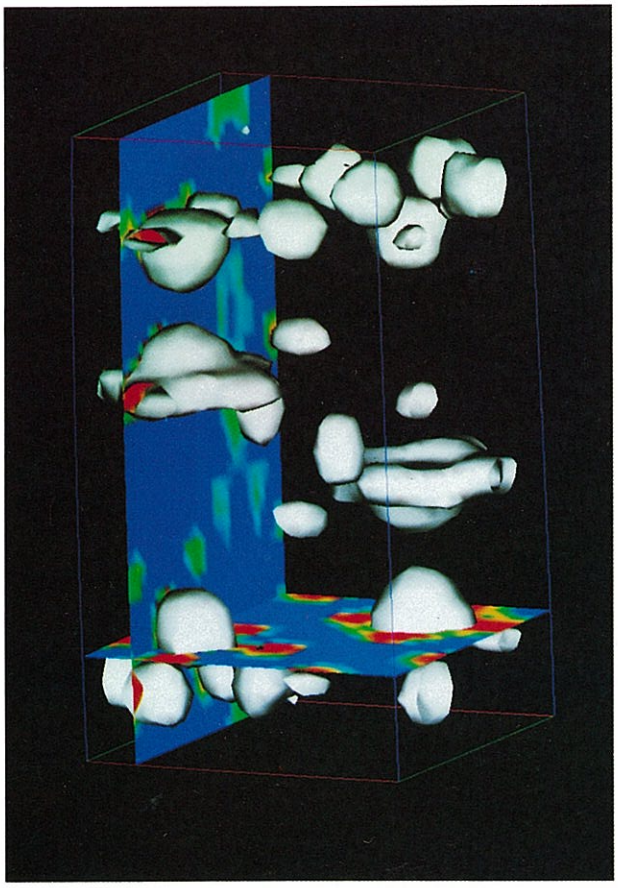

Isosurface of 3-D Fourier map obtained by neutron diffraction ($CD_3ND_3BF_4$).

Proposals accepted (April 1991 -March 1992).

1991-A2-1 LAM-80 Izumi Y Yamagata Univ.
Application of LAM-80 Spectrometer to Experiments Under Extreme Conditions

1991-B1-1 HRP Asano H Univ. of Tsukuba
High-resolution Powder Diffraction on Materials

1991-B1-2 TOP Endoh Y Tohoku Univ.
Search for Magnetic Disturbance with TOP Spectrometer

1991-B1-3 LAM Izumi Y Yamagata Univ.
Quasielastic Neutron Scattering Studies of Fluctuational and Low-energy Excitational Motions in Condensed Matters

1991-B1-4 WIT Niimura N Tohoku Univ.
Quasi-micro Structural Study by using the Thermal Neutron Small Angle Scattering Instrument (WIT)

1991-B1-5 MRP Nojiri H Kobe Univ.
Structural Studies of Magnetic Materials with and without High Magnetic Fields at MRP

1991-B1-6 HIT Fukunaga T Nagoya Univ.
Structure Study of Liquids and Amorphous Solids

1991-B1-7 INC Kohgi M Tohoku Univ.
Study of High Energy Excitations in Condensed Matter by Chopper Spectrometer

1991-B1-8 MAX Todate Y Ochanomizu Univ.
Study of Elementary Excitations Using Multi-crystal Analyzer Spectrometer

1991-B1-9 PEN Masuda Y KEK
Polarized Neutron Experiment by Using Polarized Proton Filter

1991-B1-10 WINK Furusaka M KEK
Materials Science by Small/Medium-Angle Diffractometer (WINK)

1991-B1-11 SAN Furusaka M KEK
Materials Science by Pulsed Neutron Small-Angle Scattering Instrument (SAN)

1991-B1-12 RAC Ikeda S KEK
eV Neutron Scattering Study on Condensed Matter

1991-B1-13 FOX Oshima K Univ. of Tsukuba
Microscopic Structural Study of Spin-glass Noble Metal Alloys

1991-B2-1 SAN Satoh T Keio Univ.
Magnetization Process in Reentrant Spin Glass $Cr_{0.81}Mn_{0.19}Ge$

1991-B2-2 HIT Umesaki N Osaka Univ.
A Structural Study of New Functional Glasses with High Resolution

1991-B2-3 LAM Oshima K Univ. of Tsukuba
Dynamics of Proton Diffusion in $Sr(Zr,Y)O_3$

1991-B2-4 HRP Takita H Univ. of Tsukuba
Superconductivity Breaking Effects of Pr and Crystal Structure of YBCO-Related Materials

1991-B2-5 MRP Suematsu H Univ. of Tokyo
Magnetic Phase Transition of Oxygen Monolayer

1991-B2-6 HRP Yuzuri M Yokohama Nat. Univ.
Neutron Diffraction of Magnetic Properties in $Cr_7Se_xTe_{8-x}$ Systems

1991-B2-7 WIT Yajima H Science Univ. of Tokyo
Conformational Changes of Ovotransferrin Induced by the Metal Binding

1991-B2-8 LAM Itoh Y Univ. of Tokyo
Studies of Dynamics of Enzyme Hexakinase

1991-B2-9 LAM Takeda S Osaka Univ.
Coupled Tunneling of Methyl Groups of Hexamethylbenzene Molecule in the Matrix of Hexabromobenzene

1991-B2-10 LAM Takeda S Osaka Univ.
Tunneling of Methyl Group in $Sc(CH_3COO)_3$ Crystal

1991-B2-11 LAM Inaba A Osaka Univ.
Rotational Tunneling Spectroscopy at Sub-Kelvin Temperature for methane Monolayers Adsorbed on the Surface of Graphite

1991-B2-12 LAM Inaba A Osaka Univ.
Density of States of Phonon in the Monolayers of Methyl Fluodide and Methane Adsorbed on the Surface of Graphite

1991-B2-13 LAM Inaba A Osaka Univ.
Quasielastic Neutron Scattering in Methyl Chloride Monolayers Adsorbed on the Surface of Graphite near the Phase Transition Points

1991-B2-14 HRP Suga H Osaka Univ.
Structures and Phase Transition of Organo-ionic Crystals Including Methylammonium

1991-B2-15 HIT Kakinuma F Niigata Coll. of Pharmacy
The Structure of Liquid Te-I Mixtures

1991-B2-16 TOP Shinjo T Kyoto Univ.
Magnetic Structure of Magnetic/Magnetic-Metal Artificial Superstructure Films

1991-B2-17 MAX Takano M Kyoto Univ.
Inelastic Neutron Scattering of $CsCuCl_3$ Having an Incommensurate Spin Structure

1991-B2-18 LAM Oguni M Tokyo Inst. Tech.
Orientational Tunneling of Pyridinium ion in $[C_5H_5NH]^+I^-$ Crystal

1991-B2-19 LAM Hamanaka T Osaka Univ.
The pH Dependence of the Dynamic State of Bacterorhodopsin

1991-B2-20 LAM Kobayashi M Osaka Univ.
Low-frequency Excitation in Lipids Crystals and their Properties

1991-B2-21 HIT Uemura O Yamagata Univ.
Neutron Diffraction of Chalcogenide Glass Ge-S-X(X=Br, I) System

1991-B2-22 LAM Kataoka M Tohoku Univ.
Canges of Protein Dynamics upon Folding Studied by Neutron Inelastic Scattering

1991-B2-23 MRP Shiosaki T Kyoto Univ.
Neutron Diffraction Profile Analysis on Fractional Coordinates of Dxygen Atoms in Oxide Ferroelectric Materials

1991-B2-24 LAM Sakuma T Ibaraki Univ.
Low-energy Excitation in Superionic Conductors

1991-B2-25 LAM Sakuma T Ibaraki Univ.
Inelastic Neutron Scattering Study of Superionic Conductors Chalcogenidehalides of Copper

1991-B2-27 FOX Ishigame N Tohoku Univ.
Structure Analysis of Protonic Conductors

1991-B2-28 HRP Akiba E NCLI
Structure Refinement of Metal Hydrides and Oxide Superconductors

1991-B2-29 HIT Yoko T Kyoto Univ.
High Resolution Neutron Diffraction Study on the Structure of New Functional Glasses

1991-B2-30 HIT Sumiyama K Tohoku Univ.
Neutron Total Scattering Study of the Short Range Structures on Amorphous Ce Alloy Produced by Vapor Quenching

1991-B2-31 LAM Suzuki K Tohoku Univ.
Dynamic Structure Studies of Alkali Nitrate Melts by Means of Quasielastic Neutron Scattering

1991-B2-32 HIT Suzuki K Tohoku Univ.
Total Neutron Scattering Study of Structure Relaxation Process on Amorphous $Mg_{80}Ni_{15}Y_5$

1991-B2-33 LAM Sumiyama K Tohoku Univ.
Annealing Effect of Structural Relaxation on Amorphous $Ni_{40}Pd_{40}P_{20}$

1991-B2-34 HRP Tomiyoshi S Tohoku Univ.
Crystal Structure Studies on the Proton Doped $YBa_2Cu_3O_7$

1991-B2-35 TOP Tomiyoshi S Tohoku Univ.
Polarized Neutron Diffraction Studies on the Triangular Helix of Mn_3Sn

1991-B2-36 LAM/CAT Inaba A Osaka Univ.
Molecular Spectroscopy in Methanol Monolayer Adsorbed on the Surface of Graphite

1991-B2-37 LAM Nakamura Y Hokkaido Univ.
Motion of Solvent Molecules in Concentrated Electrolyte Solutions

1991-B2-38 SAN Izumi Y Yamagata Univ.
Sol-Gel Transitions and Multicritical Phenomena of the Atactic Polystyrene-Diluents at Low Temperature

1991-B2-39 LAM Kaji K Kyoto Univ.
Local Motion of PVA Gels

1991-B2-40 SAN Okano K Univ. of Tokyo
Small-angle Neutron Scattering from Poly(Vinyl methyl ether) in Alcohol/Water Solution

1991-B2-41 TOP Kanaya T Kyoto Univ.
Adsorption of Polymers on Solid-Liquid Interface

1991-B2-42 SAN Kanaya T Kyoto Univ.
Structure of Chemically Crosslinked PVA Gels

1991-B2-43 HIT Kanaya T Kyoto Univ.
Structure of Crystallite in Poly(vinyl alcohol) Gels

1991-B2-44 SAN Kaji K Kyoto Univ.
Structure of Polymer-Microemulsions

1991-B2-45 LAM Yamaguchi T Fukuoka Univ.
Dynamics of Electrolyte Solutions in the Undercooled and Glassy States

1991-B2-47 SAN Niimura N Tohoku Univ.
Structure and Kinetics of HU Protein-DNA Complex

1991-B2-49 HRP Uchinokura K Univ. of Tokyo
Structure and Superconductivity in 1-2-3 High-Tc Superconductors -Contribution of CuO Linear Chain-

1991-B2-50 SAN Okabayashi H Nagoya Inst. Tech.
Aggligation Structure of Water Solution of Surfactant (Ba-EOP) which has Asymmetric Atomic Structure

1991-B2-51 HRP Kanno R Kobe Univ.
Transition to High Ionic Conductive State and Its Structural Change

1991-B2-52 HIT Mizutani U Nagoya Univ.
Atomic Structure of Mg-Ni-La Ternary Amorphous Alloys and its Aging Effect

1991-B2-53 SAN Noda I Nagoya Univ.
Conformation of Polymer Molecules under the Shear Flow

1991-B2-54 INC Fukunaga T Nagoya Univ.
Inelastic Scattering of Immiscible Cu-X (X=V,Ta) Amorphous Alloys Prepared by Mechanical Alloying

1991-B2-55 SAN Misawa M KEK
Critical Fluctuations and Inter-atomic Interactions in Molecular Solutions near Upper/Lower Critical Points

1991-B2-56 WINK/SAN Misawa M KEK
Concentration Fluctuation of Immiscible Cu-X (X=Ta, V) and Miscible Ni-X (X=Ta, V) Amorphous Alloys Prepared by Mechanical Alloying

1991-B2-57 SAN Yajima H Science Univ. of Tokyo
Effect of Mucopolysaccharides on the Formation Process and Structure of Collagen Fibril

1991-B2-58 INC/LAM/HRP Suzuki T Tohoku Univ.
Study of Rare-earth Pnictides - Kondo Materials with Low Carrier Number -

1991-B2-59 LAM/HRP Kohgi M Tohoku Univ.
Study of Spin Fluctuations in Systems with Competition between the Kondo Effect and RKKY Interactions

1991-B2-60 LAM Kamiyama T Tohoku Univ.
Inelastic Neutron Scattering Study of Sol-Gel Process on Silica-Glass

1991-B2-61 FOX Asano H Univ. of Tsukuba
Space Group of $La_2CuO_{4+\delta}$ and $La_2NiO_{4+\delta}$ Crystals

1991-B2-62 HRP Tsunekawa S Tohoku Univ.
Structural Analyses of Rare-Earth Orthoniobates and Orthotantalates

1991-B2-63 PEN Morimoto K KEK
T-violation Experiment on Neutron Induced Reaction

1991-B2-64 HRP Komatsubara T Tohoku Univ.
Crystal and Magnetic Structures in Heavy Fermion System U_2PtSi_3

1991-B2-65 INC/LAM/HRP Kasaya M Tohoku Univ.
Crystal Field Splitting in Dense Kondo Materials

1991-B2-66 HRP Noda Y Chiba Univ.
Crystal Structure of $K_3H(SO_4)_2$ and $K_2Ba(NO_2)_4$

1991-B2-67 INC Yamada K Tohoku Univ.
High Energy Spin Fluctuationms in 2D Antiferromagnets

1991-B2-68 INC Endoh Y Tohoku Univ.
Spin Fluctuationms in Copper Oxide Superconductors

1991-B2-71 SAN/LAM Suzuki K Tohoku Univ.
Formation Processes of Ceramics by Thermal Decomposition of Organic-Metal Compounds

1991-B2-72 HRP Mohri N Univ. of Tokyo
R&D of High Pressure Technique for Crystal Structure Analysis and Its Application to High-Tc Oxide Superconductors

1991-B2-73 (C2) Yoshiki H KEK
Generation and Storage of UCN

1991-B2-74 LAM Hiraoki T Hokkaido Univ.
Side Chain Dynamics of Polyamino-acid

1991-B2-75 LAM Arai M KEK
Phonon-Fracton Dispersion Relation on g-SiO_2

1991-B2-78 HRP Akimitsu J Aoyama Gakuin Univ.
Crystal Structure Determination on Low-dimensional Magnetic Systems

1991-B2-79 HRP Otaka O Osaka Univ.
Structural Analysis of High Pressure Phase of HfO_2 by Neutron Diffraction

1991-B2-80 (HITAC) Kawakatsu T Kyushu Univ.
Pattern Formations in Polymer-Surfactant Systems

1991-Urg-1 LAM Yugami H Tohoku Univ.
Study of Fractal Structures in Porous Glasses using Inelastic Neutron Scattering

1991-Urg-2 SAN Hatta I Nagoya Univ.
Measurement of Water Molecule Distribution in Acidic Phospholipid/Polylysine System by Neutron Diffraction

1991-Urg-3 LAM Kajitani T Tohoku Univ.
Dynamics of Protons in an Organic Superconductor

Proposals accepted (April 1992 -March 1993).

1992-A2-1 LAM-80 Izumi Y Yamagata Univ.
Application of LAM-80 Spectrometer to Experiments Under Extreme Conditions

1992-A2-2 UCN Yoshiki H KEK
Development of EDM Measuring Apparatus

1992-B1-1 FOX Oshima K Univ. of Tsukuba
Microscopic Structural Study of Spin-glass Noble Metal Alloys

1992-B1-2 MAX Todate Y Ochanomizu Univ.
Study of Elementary Excitations Using Multi-crystal Analyzer Spectrometer

1992-B1-3 LAM Izumi Y Yamagata Univ.
Quasielastic Neutron Scattering Studies on Fluctuational and Low-energy Excitational Motions in Condensed Matters

1992-B1-4 HIT Fukunaga T Nagoya Univ.
Structure Study of Liquids and Amorphous Solids

1992-B1-5 HRP Asano H Univ. of Tsukuba
Structural Study by High-resolution Powder Diffraction

1992-B1-6 SAN Furusaka M KEK
Materials Science by Pulsed Neutron Small-Angle Scattering Instrument (SAN)

1992-B1-7 WINK Furusaka M KEK
Materials Science by Small/Medium-Angle Diffractometer (WINK)

1992-B1-8 PEN Masuda Y KEK
Polarized Neutron Experiment by Using Polarized Proton Filter

1992-B1-9 RAC Ikeda S KEK
eV Neutron Scattering Study on Condensed Matter

1992-B1-10 INC Kohgi M Tohoku Univ.
Study of High Energy Excitations in Condensed Matter by Chopper Spectrometer

1992-B1-11 WIT Niimura N Tohoku Univ.
Quasi-micro Structural Study by using the Thermal Neutron Small Angle Scattering Instrument (WIT)

1992-B1-12 TOP Endoh Y Tohoku Univ.
Search for Magnetic Disturbance with TOP Spectrometer

1992-B1-13 MRP Motokawa M Kobe Univ.
Structural Studies of Magnetic Materials with and without High Magnetic Fields at MRP

1992-B2-1 HRP Kanno R Kobe Univ.
Crystal Structure and Metal Insulator Transition of the Lead Pyrochlore

1992-B2-2 HIT Uemura O Yamagata Univ.
Neutron Diffraction of Aqueous Amino Acid Solutions

1992-B2-3 HIT Kakinuma F Niigata Coll. of Pharmacy
The Structure of Liquid Sn-Se Alloys

1992-B2-4 HIT Umesaki N Goverment Industrial Research Institute, Osaka
Structural Investigation of Frozen α-AgI in Superionic AgI-based Glasses

1992-B2-5 HIT Umesaki N Goverment Industrial Research Institute, Osaka
Network-structual Analysis of Oxide Melts and Glasses with Low Melting Points

1992-B2-6 LAM Suzuki K Tohoku Univ.
Dynamic Structure of Molten Alkali and Alkaline Earth Nitrate Mixture in High Viscosity Region

1992-B2-7 LAM Misawa M KEK
Neutron Quasielastic and Inelastic Scattering Measurements on Liquid Carbon Tetrachloride near the Critical Point

1992-B2-8 LAM Misawa M KEK
FRequency Distribution Change of o-, m-, p-Dichlorobenzene on Melting

1992-B2-9 SAN Misawa M KEK
Small Angle Neutron Scattering on Liquid Carbon Tetrachloride near the Critical Point

1992-B2-10 LAM Hamanaka T Osaka Univ.
The pH Dependence of the Dynamic State of Bacteriorhodopsin

1992-B2-11 HIT Yoko T Kyoto Univ.
Neutron Diffraction Study on the Structure of Na-Si-O-N Glasses

1992-B2-12 TOP Shinjo T Kyoto Univ.
Magnetization Process of Artificial Superstructure Films with Giant Magnetoresistance Effect

1992-B2-13 LAM Kobayashi M Osaka Univ.
Low-frequency Excitation in Lipids Crystals and their Properties

1992-B2-14 HRP Yuzuri M Yokohama Nat. Univ.
Neutron Diffraction of Magnetic Properties in $Cr_7Se_xTe_{8-x}$ Systems

1992-B2-15 MRP Ito T Shimane Univ.
Magnetic Structure of PrPdIn Single-Crystal Compound

1992-B2-16 HIT Mizutani U Nagoya Univ.
Chemical Fluctuation Induced by Alloying the Thirdelement into Neutron Zero Scattering Alloys

1992-B2-17 WINK Fukunaga T Nagoya Univ.
Concentration Fluctuation of Immiscible Cu-X (X=Ta, V) and Miscible Ni-X (X=Ta, V) Amorphous Alloys Prepared by Mechanical Alloying

1992-B2-18 INC Fukunaga T Nagoya Univ.
Inelastic Scattering of Miscible Ni-Ta and Immiscible Cu-Ta Amorphous Alloys Prepared by Mechanical Alloying

1992-B2-19 WIT Sano H Nat'l Food Res. Inst.
Internal Structure of Tabaco Mosaic Virus-RNA

1992-B2-20 SAN Sano H Nat'l Food Res. Inst.
Interior Structure of Mucoprotein Complexes

1992-B2-21 LAM Kaji K Kyoto Univ.
Quasielastic Neutron Scattering Study of Polymer Liquid Crystals-Hydroxypropylcellurose Derivatives-

1992-B2-22 SAN Izumi Y Yamagata Univ.
Sol-Gel Transitions and Multicritical Phenomena of the Atactic Polystyrene-Diluent Systems at Low Temperature

1992-B2-23 HRP Tsunekawa S Tohoku Univ.
Structure Analyses of Rare-earth Ortho-niobates and -tantalates

1992-B2-24 LAM Sakuma T Ibaraki Univ.
Low-energy Excitation in Superionic Conductors

1992-B2-25 HIT/WINK Kanaya T Kyoto Univ.
Structure and Gelation Mechanism of Syndiotactic Polystyrene

1992-B2-26 LAM Inaba A Osaka Univ.
Molecular Motions in Buthyl Alcohol Monolayers Adsorbed on the Surface of Graphite

1992-B2-27 LAM Inaba A Osaka Univ.
Dynamical Study of Neopentane Monolayer Adsorbed on the Surface of Graphite

1992-B2-28 LAM Inaba A Osaka Univ.
Dynamical Study of Methyl Chloride Monolayers Adsorbed on the Surface of Graphite

1992-B2-29 LAM Inaba A Osaka Univ.
Rotational Tunneling Spectroscopy at Sub-Kelvin Temperature for methane Monolayers Adsorbed on the Surface of Graphite

1992-B2-30 HIT Yasui I Univ. of Tokyo
Structural Analysis of Glasses Containing Heavy Metals Ion

1992-B2-31 FOX Tazuke Y Hokkaido Univ.
Magnetic Moments in a Ferromagnetic Alloy

1992-B2-32 SAN/WINK Kaji K Kyoto Univ.
Structure Formation of Polyethylene terephthalate During the Induction Period of Crystallization

1992-B2-33 LAM Tazuke Y Hokkaido Univ.
Excitation Spectrum of an Ising Spin Glass

1992-B2-34 SAN Tazuke Y Hokkaido Univ.
Spin Correlation of an Ising Spin Glass

1992-B2-35 SAN Kita Y Osaka Univ.
Surface Structure of Non-metallic Inclusions in Molten Metals by Small Angle Neutron Scatterimng

1992-B2-36 TOP Sato T Keio Univ.
Intraparticle Structure of Pd Fine Particles

1992-B2-37 HRP Akiba E NCLI
Structure Refinement of Metal Hydrides

1992-B2-38 HRP Suga H Osaka Univ.
Structures and Phase Transitions of Organo-ionic Crystals Including Methylammonium

1992-B2-39 MRP Shiosaki T Kyoto Univ.
Neutron Diffraction Profile Analysis on Fractional Coordinates of Dxygen Atoms in Oxide Ferroelectric Materials

1992-B2-40 SAN/WINK Kondo S Nagasaki Univ.
Study on Magnetic Behavior of Cu-Co-X (X=Cr, Fe) Alloys by Small Angle Scattering

1992-B2-41 (HITAC) Kawakatsu T Kyushu Univ.
Pettern Formations in Polymer-Surfactant Systems

1992-B2-42 HRP Takita H Univ. of Tsukuba
Pair Breaking and Structure Modulation in Pr-Substituted Superconductor with YBCO-Structure

1992-B2-43 MRP Suematsu H Univ. of Tokyo
Magnetic Phase Transition of Oxygen Monolayer

1992-B2-44 LAM Kataoka M Tohoku Univ.
Canges of Protein Dynamics upon Folding Studied by Neutron Inelastic Scattering

1992-B2-45 HRP Hashimoto M Kobe Univ.
Ferroelectric Phase Transition in Trichloroacetoamide

1992-B2-46 CAT/RAT Mizoguchi K Ochanomizu Univ.
Study on Local Mode of RbH_2PO_4 and RbD_2PO_4

1992-B2-47 WINK Yamaguchi T Fukuoka Univ.
Small-angle Neutron Scattering from Solution of Bile Salt

1992-B2-48 LAM Yamaguchi T Fukuoka Univ.
Dynamics of Electrolyte Solutions in the Undercooled and Glassy States

1992-B2-49 FOX Fujishita H Kanazawa Univ.
Crystal Structure of Intermediate Phase of $PbZrO_3$

1992-B2-50 INC Kadowaki H Univ. of Tokyo
Local Singlet-Triplet Excitation in Magnetic Materials

1992-B2-51 HIT Adachi G Osaka Univ.
Structural Analyses of Hydrogenated Amorphous $LaNi_{5.0}$ Films Using Neutron Scattering

1992-B2-52 CAT Adachi G Osaka Univ.
Studies on Local Environment around Hydrogen Atoms in Amorphous $LaNi_{5.0}$ Films

1992-B2-54 SAN Okano K Shinshu Univ.
SANS from Semidilute Aqeous Solution of Poly(N-isopropylacrylamide)

1992-B2-55 WINK/WIT Yabuki S Gunma Univ.
The Interactions of the Hydrophilic Complex Lipids, Gangliosides, with the Glycoproteins

1992-B2-56 FOX Asano H Univ. of Tsukuba
The Crystal Structure of Oxide Superconductors

1992-B2-57 HRP Mohri N Univ. of Tokyo
R&D of High Pressure Technique for Crystal Structure Analysis and Its Application to High-Tc Oxide Superconductors

1992-B2-58 LAM Nakamura Y Hokkaido Univ.
Dynamical Structure of Glass-forming Aqeous Electrolyte Solutions

1992-B2-59 HIT Nakamura Y Hokkaido Univ.
Structure of the $LiNO_3$-1,3Diaminopropane System in the Liquid and Glassy States

1992-B2-60 LAM Nakamura Y Hokkaido Univ.
Motion of Solvent Molecules in Concentrated Electrolyte Solutions

1992-B2-61 SAN Noda I Nagoya Univ.
Molecular Conformation of Polymers Under the Steady Shear Flow

1992-B2-62 LAM Takeda S Osaka Univ.
Tunneling of Methyl Group in $Sc(CH_3COO)_3$ Crystal

1992-B2-63 LAM Takeda S Osaka Univ.
Tunneling of Hydrogen Chloride Molecules in the Hydroquinone Clathrate Compounds

1992-B2-64 LAM Kohgi M Tohoku Univ.
Study of Low Energy Magnetic Excitations in RTSn (R=Ce, Yb; T=Ni, Pd)

1992-B2-65 LAM/HRP Kohgi M Tohoku Univ.
Study of the Low Carrier Concentration Heavy Fermion System Yb_4As_3

1992-B2-66 INC/LAM/MRP Suzuki T Tohoku Univ.
Neutron Scattering Study of the Low Carrier Concentration Kondo System CeX (X=P,As) Under High Magnetic Field and High Pressure

1992-B2-67 PEN Asahi K Tokyo Inst. Tech.
He-3 Polarization Experiment for T-violation Test

1992-B2-68 LAM Kamiyama T Tohoku Univ.
Quasielastic Neutron Scattering Study of Sol-Gel Process on Silica Glass

1992-B2-69 WINK/LAM Sai A Tohoku Univ.
Neutron Scattering Study of Amorphous and Quasicrystal $Al_{75}Cu_{15}V_{10}$

1992-B2-70 LAM/HRP Kohgi M Tohoku Univ.
Magnetic Excitation in UX_2 (X=Ga, Ge)

1992-B2-71 WINK Okabayashi H Nagoya Inst. Tech.
Phase Structure Study of the Barium Ethyl(octyl)Phosphate-Water System

1992-B2-72 HRP Akimitsu J Aoyama Gakuin Univ.
Structural Refinment of Low-dimensional Magnet

1992-B2-73 INC/LAM Kasaya M Tohoku Univ.
Determination of Crystalline-field Splitting of $Ce_3Au_3Sb_4$ and $Ce_3Pt_3Sb_4$ by Means of Neutron Scattering

1992-B2-74 LAM/HIT Suzuki K Tohoku Univ.
Neutron Scattering Study of Local Structural Change on Soda Silicate Glass SiO_2+xNa_2O

1992-B2-75 LAM Ikeda S KEK
Hydrogen Bond under High Pressure

1992-B2-76 LAM Arai M KEK
Low Energy Phonon Measurements of High-Tc Superconductor $YBa_2Cu_3O_7$

1992-B2-77 HRP Arai M KEK
Medium Angle Diffraction on High-Tc Superconductor $YBa_2Cu_3O_7$

1992-B2-78 HIT Endoh H Kyoto Univ.
Structure of Strongly Supercooled Tellurium Nano-droplets

1992-B2-79 HIT Ichikawa K Hokkaido Univ.
Intramolecular Structure of Homopolyatomic Species in Liquid State; Coordination Structure of Biological Important Molecules around Metal Ions

1992-B2-80 SAN Ikeda H KEK
Small Angle Neutron Scattering from Percolated Magnets with Fractal Geometry

1992-B2-81 MRP/HRP Ikeda H KEK
Magnetic Structure of One-dimensional Systems with Competing Interactions

1992-B2-82 INC Ikeda H KEK
Quantum Effects on One-dimensional Antiferromagnet with S=1/2 Including Magnetic Impurity

1992-B2-83 WINK Seto H Hiroshima Univ.
Structural Phase Transition in Microemulsion

1992-B2-84 MAX Takano M Kyoto Univ.
Inelastic Neutron Scattering of $CsCuCl_3$ Having an Incommensurate Spin Structure

1992-B2-85 LAM Inaba A Osaka Univ.
Rotational Tunneling of the Methyl Groups of Tribromo-trimethyl-benzene Diluted in Hexa bromobenzene Crystal

1992-B2-86 LAM Kearley G J ILL
True Free Rotation of NH_3 Groups in $Ni(NH_3)_2Ni(CN)_42[C_6D_6]$

1992-B2-87 LAM Fillaux F LASIR, CNRS
Quantum Tortional Dynamics of Methyl in p-Tert-buthylcalix[4]arene(1:1)toluene

1992-B2-88 HRP Tsutsumi K Kanazawa Univ.
Study of the Crystal Structure in the Low-temperature Phase of α-$TiCl_3$

1992-Urg-1 RAC Matsuo T Osaka Univ.
Study of Short Hydrogen Bond Systems by Neutron Compton Scattering

1992-Urg-2 LAM Kohgi M Tohoku Univ.
Magnetic Excitation in Hevy Fermion System YbBiPt

1992-Urg-3 LAM Kajitani T Tohoku Univ.
Dynamics of Protons in an Organic Superconductor

1992-Urg-4 LAM Achiwa N Kyusyu Univ.
Incoherent Inelastic Neutron Scattering Study on 1-Br-Adamantane

1992-Urg-5 SAN Imae T Nagoya Univ.
Investigation of Molecular Assemblies by Small-angle Neutron Scattering

1992-Urg-6 SAN Murani A P ILL
Paramagnetic Response in $CePd_{3-x}Ni_x$

Appendices

Publications

1. General

KEK Neutron Source and Neutron Scattering Research Facility
Ishikawa Y and Watanabe N.
Presented at 2nd Meeting Int. Collaboration on advanced Neutron Sources, (Rutherford Lab., July 10-15, 1978), and KEK Report KEK-78-19

Neutron Scattering Experiments at Pulsed Spallation Neutron Source (KENS)
Ishikawa Y, Endoh Y, Watanabe N and Inoue K.
Proc. Symp. Neutron Scattering (Argonne, Aug. 12-14, 1981)57

Present Status of the KENS Facility
Ishikawa Y.
Proc. 4 th Meeting Int. Collaboration on Advanced Neutron Sources (KEK, Tsukuba, Oct. 20-24, 1980), KENS Report -II (1981)89

Present Status and Future Program of KENS
Watanabe N, Sasaki H, Ishikawa Y, Endoh Y and Inoue K.
Proc 5th Meeting Int. Collaboration on Advanced Neutron Sources (Jülich, June 22-26, 1981)21

Status and Neutron Scattering Experiments at KENS
Watanabe N, Sasaki H, Ishikawa Y, Endoh Y and Inoue K.
Proc. 6th Meeting Int. Collaboration Advanced Neutron Sources (Argonne, June 28-July 2), ANL-82-80 (1982)15

Present Status of Booster Synchrotron Utilization Facility at KEK
Sasaki H.
Proc. 7th Meeting Int. Collaboration on Advanced Neutron Sources (Chalk River, Sept. 13-16, 1983), AECL-8488 (1984)15

Studies of Condensed Matter with Pulsed Neutron Source (KENS)
Ishikawa Y.
Physica 120B(1983)3

Neutron Scattering and Muon Spin Rotation
Ishikawa Y.
Proc. Yamada Conf. VII, Muon Spin Rotation (Shimoda, 1984), Hyperfine Interactions 17-19(1984)17

Neutron Scattering Spectrometers at KENS Cold Spallation Neutron Source
Ishikawa Y, Endoh Y and Inoue K.
Proc. International Conf. on Neutron Scattering in '90s, (Jülich, 14-18 Jan. 1985), IAEA-VIENNA, IAEA-CN46/027 (1985)285

Pulsed Polarized Neutron Studies
Endoh Y and Ishikawa Y.
Physica B 136(1985)64

Present Status and Future Project of KENS Facility
Ishikawa Y and the KENS Group
Proc. 8th Meeting Int. Collaboration on Advanced Neutron Sources (Rutherford Appleton Lab., July 8-12, 1985), RAL-85-110 (1985)17

Physics of Spallation Neutrons
Endoh Y.
Phys. Chem. Research 80(1986)38

Status Report on the KENS Facility
Watanabe N, Endoh Y, Inoue K and Misawa M.
Proc. 9th Meeting Int. Collaboration on Advanced Neutron Sources (SIN, Villigen, Switzerland, Sept. 22-26, 1986)65

KENS Program —Present and Future—
Watanabe N, Misawa M and Sasaki H.
Proc. Int. Workshop on Hadron Facility Technology (Santa Fe, Feb. 2-5, 1987)169

Progress at the Pulsed-Spallation Neutron Facility KENS
Watanabe N.
Advanced Neutron Sources 1988 (Proc. ICANS X) (Los Alamos, Oct. 3-7, 1988)P.53

Pulsed-Spallation-Neutron Facility KENS and Neutron Scattering Instruments for Polymer Science
Watanabe N.
Int. Conf. on Polymer Research by Neutron Scattering. The Taniguchi Conference (Kyoto, Nov. 7-9, 1989) (1989)39

The Research of Condensed Matter Physics Research by Usinf Inense Proton Accelerator
Endoh Y.
Proc. of the 2nd International Syymposium on Advanced Nuclear Energy Research -Evolution by Accelerators - (Mito, Jan. 24-26, 1990)141

Status of KENS-I' and KENS-II
Watanabe N.
Proc. 11th Meeting of the Int. Collaboration on Advanced Neutron Sources (KEK, Tsukuba, Oct. 22-26, 1990)61

KENS Neutron Scattering Facility (Correspondents' Reports)
Furusaka M.
Neutron News 3(1992)8

2. Accelerator and Beam Line

Injection System of H2S(-) Beam in KEK Booster Synchrotron
Kawakubo T, Sasaki H, Sakai I and Suetake M.
Proc.3rd.Symp.on Accelerator Science and Technology (Osaka Univ. Aug. 27-29, 1980)31

500 MeV Proton Beam Line for KEK Booster Synchrotron Utilization Facility
Sakai I, Someya H, Adachi T, Irie Y and Sasaki H.
Proc.3rd.Symp.on Accelerator Science and Technology (Osaka Univ. Aug. 27-29, 1980)33

The Booster Synchrotron Utilization Facility at KEK
Sasaki H.
Proc. 4th Meeting Int. Collaboration on Advanced Neutron Sources (KEK, Tsukuba, Oct. 20-24, 1980), KENS Report-II (1981)77

BSF Beam Control System
Irie Y.
Proc. 4th Meeting Int. Collaboration on Advanced Neutron Sources (KEK, Tsukuba, Oct. 20-24, 1980), KENS Report-II (1981)406

Proton Synchrotron for Intense Neutron and Meson Beam
Adachi T, Inagaki S, Irie Y, Kaneko N, Kawakubo T, Kumada N, Sakai I, Someya Y, Baba H, Matsumoto S, Miki M and Yano Y.
Proc.4th Symp.on Accelerator Science and Technology (RIKEN, Nov. 24-26, 1982)281

Evaluation of the Field Homogeneity of the Magnet by Phase Space Mapping
Kumada K.
Proc. 4th Symp. on Accelerator Science and Technology (RIKEN, Nov. 24-26, 1982)87

Present Status of Booster Synchrotron Utilization Facility at KEK
Sasaki H.
Proc. 4th Symp. on Accelerator Science and Technology (RIKEN, Nov. 24-26, 1982)21

80MeV Injector Linac for BSF Future Project
Inagaki S, Baba H, Miki M and Sasaki H.
Proc. 7th Meeting on Linear Accelerators (KEK, Aug. 24-26, 1982)110

Bi-resonant Circuit for Excitation of Synchrotron Magnet
Someya H, Adachi T, Kumada M, Baba H, Matsumoto S, Sasaki H and Sakai I.
Proc.4th Symp.on Accelerator Science and Technology (RIKEN, Nov. 24-26, 1982)317

Optimization on the End-Shaping of Quadrupole Magnet
Kumada M, Sasaki H, Someya H and Sakai I.
Nucl. Instrum. Methods 211(1983)283

Accelerator Project GEMINI for Intense Pulsed Neutron and Meson Source at KEK
Sasaki H and GEMINI Study Group
ICANS-VII(Chalk River, Sept. 13-16, 1983), AECL-8488 (1984) and Proc. 5th Symp. on Accelerator Science and Tech. (KEK, Sept. 26-28, 1984)394

The First Experiment of Test H- Charge Exchange Injection in the KEK Booster
Kawakubo T, Sakai I, Suetake and Sasaki H.
Proc. 5th Symp.on Accelerator Science & Technology (KEK, Sept. 26-28, 1984)274

Magnetic Field Measurement of High Gradient $SmCo_5$ Permanent Quadrupole Magnets
Kumada M, Kaneko N, Inagaki S, Baba H and Sasaki H.
Proc.5th Symp.on Accelerator Science & Technology (KEK, Sept. 26-28, 1984)203

The First Acceleration Test of H- Charge Exchange Injection in the KEK Booster
Kawakubo T, Sakai I, Suetake M and Sasaki H.
KEK Report 84-6(1984)274

Application of GTO Thyristor to a Dual Resonant Frequency Circuit for Excitation of Synchrotron Magnet
Someya H, Adachi T, Irie Y, Yano Y and Sasaki H.
Proc.5th Symp.on Accelerator Science & Technology (KEK, Sept. 26-28, 1984)221

Beam Chopper for GEMINI
Yano Y, Kawakubo T, Kumada M and Sasaki H.
Proc. 5th Symp. on Accelerator Science and Technology (KEK, Sept. 26-28, 1984)166

Application of Rare Earth Permanent Magnet to a High Energy Accelerator
Kumada M, Kaneko N and Sasaki H.
Proc. Symp on Rare Earths (Tokyo, March 3, 1985)38

Application of a GTO Thyristor to a Dual Resonant Frequency Circuit for the Magnet of a Rapid-Cycling Synchrotron
Someya H, Adachi T, Baba H, Irie Y, Matsumoto S, Sasaki H and Yano Y.
Proc. The 1985 Particle Accelerator Conf. (Vancouver, May 13-16, 1985) IEEE NS-32 (1985)3775

250T/m Rare Earth Permanent Quadrupole Magnet
Kumada M, Kaneko N, Baba H, Inagaki S and Sasaki H.
Proc. 9th Int. Conf. on Magnet Technology (Zurich Sept. 9-13, 1985)142

Construction and Calculation of High Gradient Rare Earth Permanent Magnet
Kumada M, Inagaki S, Kaneko N, Baba H and Sasaki H.
Proc. 11th Meeting on Linear Accelerators (KEK Sept. 1-3, 1986)42

Performance of Prototype Rapid Cycling Magnet and Power Supply for KEK GEMINI Project
Sasaki H, Someya H, Adachi I, Sakai I and Nakanishi M.
Proc Int. Workshop on Hadron Facility Technology (Santa Fe, Feb. 2-5, 1987)408

Drive Stage for Cathode Follower RF System
Irie Y.
Proc. Int. Workshop on Hadron Facility Technology (Santa Fe, Feb. 2-5, 1987)349

Present Status of a Model RF System with Cathode Follower for a High Intensity Synchrotron
Irie Y, Kaneko N, Baba H and Miki M.
KEK Report 87-28 (Feb. 1988) (1988)

Magnet Exciting System with Dual Resonant Frequency Circuit
Adachi T, Someya H and Sasaki H.
European Particle Accelerator Conf. (Rome, June 7-11, 1988)

Particle Tracking in the BSF Beam Line
Adachi T.
Proc. 11th Meeting of the Int. Collaboration on Advanced Neutron Sources (KEK, Tsukuba, Oct. 22-26, 1990)270

Progress during the Decade of the BSF Beam-Line
Irie Y, Adachi T, Yano Y, Fujimori H, Kaneko N, Kobayashi Y and Tahara T.
KEK Report 91-6, July 1991

Non-Destructive Profile Monitor in a Beam Transport Line
Adachi T and Kawakubo T.
Proc. Int. Workshop on Advanced Beam Instrumentation (Apr. 22-24, 1991, KEK)160

3. Neutron Source

Target-Moderator Mock-up Experiment for KENS
Watanabe N, Misawa M and Yamaguchi S.
Presented at 2nd Meeting Int. Collaboration on advanced Neutron Sources (Rutherford Lab., July 10-15, 1978)

Shielding Design for KENS
Watanabe N, Katoh K and Thomas R.H.
KEK Report, KEK-78-7 (1978)29

Experimental Studies of the Induced Radioactivities in a Uranium Target
Katoh K, Ban S, Hirayama H, Ikeda S, Irie K, Kondoh K, Miyajima M, Sato S, Watanabe N and Yamaguchi S.
Proc. 4th Meeting Int. Collaboration on Advanced Neutron Sources (KEK, Tsukuba, Oct. 20-24, 1980), KENS Report-II (1980)381

KENS Target Station
Watanabe N, Ikeda S and Ishikawa Y.
Proc.Proc. 4th Meeting Int. Collaboration on Advanced Neutron Sources (KEK, Tsukuba, Oct. 20-24, 1980), KENS Report-II (1981)181

KENS Cold Neutron Source
Ikeda S, Ishikawa Y and Inoue K.
Proc. 4th Meeting Int. Collaboration on Advanced Neutron Sources (KEK, Tsukuba, Oct. 20-24, 1980), KENS Report-II (1981)200

Some Neutronic Aspects of Solid Methane Moderator System
Inoue K, Kiyanagi Y, Iwasa H, Jinguji K, Watanabe N, Ikeda S and Ishikawa Y.
Proc. 5th Meeting Int. Collaboration on Advanced Neutron Sources (Jülich, June 22-26, 1981), Jul-Conf-45 (1981)519

Radioactivity and Radiolysis of the Solid Methane Used as a Cold Neutron Moderator in the KENS Target Assembly
Kondoh K and Hozumi K.
Proc. 4th Meeting Int. Collaboration on Advanced Neutron Sources (KEK, Tsukuba, Oct. 20-24, 1980), KENS Report-II (1981)381

Characteristics of KENS Cold Neutron Guide Tube
Mizuki J, Endoh Y, Ishikawa Y and Ikeda S.
Proc. 4th Meeting Int. Collaboration on Advanced Neutron Sources (KEK, Tsukuba, Oct. 20-24, 1980), KENS Report-II (1981)521

KENS Radiation Shield
Ban S and Hirayama H.
Proc. 4th Meeting Int. Collaboration on Advanced Neutron Sources (KEK, Tsukuba, Oct. 20-24, 1980), KENS Report-II (1981)355

KENS Radiation Activity: Structural Materials
Hirayama H and Ban S.
Proc. 4th Meeting Int. Collaboration on Advanced Neutron Sources (KEK, Tsukuba, Oct. 20-24, 1980), KENS Report-II (1981)376

Grooved Cold Moderator Tests
Inoue K, Kiyanagi Y, Iwasa H, Watanabe N, Ikeda S, Carpenter J.M and Ishikawa Y.
Proc. 6th Meeting Int. Collaboration on Advanced Neutron Sources (Argonne, June 28 -July 2, 1982), ANL-82-80 (1982)391

Grooved Cold Moderator at KENS
Ishikawa Y, Ikeda S, Watanabe N, Kondoh K, Inoue K, Kiyanagi Y, Iwasa H and Tsuchihashi K.
Proc. 7th Meeting Int. Collaboration on Advanced Neutron Sources (Chalk River, Sept. 13-16, 1983), AECL-8488230

On the 20K Methane Moderator and its Application to the Intense Pulsed Cold Neutron Source
Inoue K.
Nucl. Instrum. Methods 216(1983)537

Monte Carlo Program fot the Cold Neutron Beam Guide
Yoshiki H.
KEK Report 84-21 (Feb. 1985) (1985)

Mock-up Experiments for KENS-I' Cold Moderator
Ishikawa Y, Furusaka M, Itoh S, Ikeda S, Watanabe N, Inoue K and Iwasa H.
Proc. 8th Meeting Int. Collaboration on Advanced Neutron Sources (Rutherfofd Appleton Lab., July 8-12, 1985) RAL-85-110(1985)329

A Consideration of Cold Neutron Source for KENS-II
Watanabe N.
ICANS -X (Los Alamos, Oct. 3-7, 1988), Inst. of Phys. Conf. Series No. 97, Institute of Physics, Bristol and New York,P.763

Some Neutronic Calculations for KENS-II
Kiyanagi Y, Arai M, and Watanabe N.
ICANS -X (Los Alamos, Oct. 3-7, 1988), Inst. of Phys. Conf. Series No. 97, Institute of Physics, Bristol and New York,P.753

Preliminary Optimization Experiments of Coupled Liquid Hydrogen Moderator for KENS-II
Watanabe N, Kiyanagi Y, Inoue K, Furusaka M, Ikeda S, Arai M, and Iwasa H.
ICANS-X (Los Alamos, Oct. 3-7, 1988), Inst. of Phys. Conf. Series No. 97, Institute of Physics, Bristol and New York,P.787

Intense Neutron Source for Material Research
Watanabe N.
Proc. of the 2nd International Syymposium on Advanced Nuclear Energy Research -Evolution by Accelerators - (Mito, Jan. 24-26, 1990)

Reflector Optimization for Coupled Liquid Hydrogen Moderator
Kiyanagi Y, Watanabe N, Furusaka M and Iwasa H.
Proc. 11th Meeting Int. Collaboration on Advanced Neutron Sources (KEK, Oct. 22-26 1990)401

Some Neutronic Studies on Flux-trap Type Moderator
Kiyanagi Y and Watanabe N.
Proc. 11th Meeting Int. Collaboration on Advanced Neutron Sources (KEK, Oct. 22-26 1990)408

A Design Concept for KENS-II Cold Neutron Souce
Watanabe N, Furusaka M and Kiyanagi Y.
Proc. Int. Workshop on Cold Neutron Source (Los Alamos, March 5-8, 1990)491

A Design Concept of Target-Moderator-Reflector Assemblies for KENS-II
Watanabe N.
Proc. 11th Meeting Int. Collaboration on Advanced Neutron Sources (KEK, Oct. 22-26 1990)471

Optimization Studies on Coupled Liquid Hydrogen Moderator
Kiyanagi Y, Watanabe N, Furusaka M, Iwasa H and Fujikawa I.
Proc. 11th Meeting Int. Collaboration on Advanced Neutron Sources (KEK, Oct. 22-26 1990)388

Towards a High-Efficiency Pulsed Spallation Neutron Source
Watanabe N and Kiyanagi Y.
Physica B

Experimental Studies on Neutronic Performance of Coupled Liquid-Hydrogen Moderator for Pulsed Spallation Neutron Souces
Kiyanagi Y, Watanabe N and Iwasa H.
Nucl. Inst. Methods A312(1992)561

Development of a Chopper Spectrometer at KENS
Arai M, Kohgi M, Endoh Y and Watanabe N.
Proc. of the 2nd International Syymposium on Advanced Nuclear Energy Research -Evolution by Accelerators - (Mito, Jan. 24-26, 1990)631

4. Instrumentations

The High Intensity Total Scattering Spectrometer (HIT)
Watanabe N, Fukunaga T, Shinohe T, Yamada K and Mizoguchi T.
Proc. 4th Meeting Int. Collaboration on Advanced Neutron Sources (KEK, Tsukuba, Oct. 20-24, 1980), KENS Report-II (1981)539

Small Angle Scattering Spectrometer (KENS-SAN)
Ishikawa Y, Furusaka M, Arai M, Niimura N, Ikeda S and Hasegawa K.
Proc. 4th Meeting Int. Collaboration on Advanced Neutron Sources (KEK, Tsukuba, Oct. 20-24, 1980), KENS Report-II (1981)563

Time of Flight Spectrometer with Optical Polarizer
Endoh Y, Mizuki J and Ono H.
Proc. 4th Meeting Int. Collaboration on Advanced Neutron Sources (KEK, Tsukuba, Oct. 20-24, 1980), KENS Report-II (1981)609

The Ultra Cold Neutron Production at KENS
Yoshiki H.
Proc. 4th Meeting Int. Collaboration on Advanced Neutron Sources (KEK, Tsukuba, Oct. 20-24, 1980), KENS Report-II (1981)715

Neutron Polarization by Polarized Proton Filter
Ishimoto S.
Proc. 4th Meeting Int. Collaboration on Advanced Neutron Sources (KEK, Tsukuba, Oct. 20-24, 1980), KENS Report-II (1981)630

KENS Data Acquisition System
Niimura N, Kohgi M, Arai M, Tomiyoshi S, Tajima K, Isobe M, Furusaka M and Fujino Y.
Proc. 4th Meeting Int. Collaboration on Advanced Neutron Sources (KEK, Tsukuba, Oct. 20-24, 1980), KENS Report-II (1981)663

Application of Position Sensitive Detectors to Structure Analysis Using Pulsed Neutron Source
Niimura N, Ishikawa Y, Arai M and Furusaka M.
Proc. Symp. Neutron Scattering (Argonne, Aug. 12-13, 1981)8

Multi Analyzer Crystals Spectrometer at KENS
Tajima K, Kanai K, Ishikawa Y, Tomiyoshi S and Windsor C.G.
Proc. 4th Meeting Int. Collaboration on Advanced Neutron Sources (KEK, Tsukuba, Oct. 20-24, 1980), KENS Report-II (1981)600

Large Analyzer Mirror Low Energy Spectrometer LAM(KEK) and LANDAM(HU), and Electron Linac Cold Source
Inoue K, Kiyanagi Y, Kohgi M, Ishikawa Y, Watanabe N, Iwasa H, Sakamoto Y and Jinguji K.
Proc. 4th Meeting Int. Collaboration on Advanced Neutron Sources (KEK, Tsukuba, Oct. 20-24, 1980), KENS Report-II (1981)592

Polarized Epithermal Neutron Spectrometer at KENS
Kohgi M.
Proc. 6th Meeting Int. Collaboration on Advanced Neutron Sources (Argonne, June 28-July 2, 1982), ANL-82-80 (1982)171

Test of a Resonance Detector Spectrometer for Electron-Volt Spectroscopy
Carpenter J.M, Watanabe N, Ikeda S, Masuda Y and Satoh S.
Proc. 6th Meeting Int. Collaboration on Advanced Neutron Sources (Argonne, June 28-July 2, 1982), ANL-82-80 (1982)265

A Multi Analyzer Crystal Spectrometer (MAX) for Pulsed Neutron Source
Tajima K, Ishikawa Y, Kanai K, Windsor C.G and Tomiyoshi S.
Nucl. Instrum. Methods 201(1982)491

Crystal Analyzer TOF Spectrometer (CAT) for High Energy Incoherent Neutron Scattering
Watanabe N, Ikeda S and Kai K.
Proc. 6th Meeting Int. Collaboration on Advanced Neutron Sources (Argonne, June 28-July 2, 1982), ANL-82-80 (1982)279

Position Sensitive Neutron Detectors using Li-6 Glass Scintillators
Niimura N, Yamada K, Kubota T, Matsumoto A and Hoshino S.
Physica 120B(1983)104

Polarized Neutron Scattering using Pulsed Spallation Neutron Source at KEK
Endoh Y, Sasaki H, Ono H, Mitsuda S and Ikeda S.
Physica 120B(1983)45

Time Focussing and Resolution in Resonance Detector Neutron Spectrometer
Carpenter J.M and Watanabe N.
Nucl. Instrum. Methods 213(1983)311

Position Sensitive Neutron Detectors using Li-6 Glass Scintillators and Fibre Optic Encoding
Niimura , Yamada K, Kubota T, Matsumoto A and Hoshino S.
Nucl. Instrum. Methods 211(1983)203

Crystal Analyzer TOF Spectrometer (CAT)
Ikeda S. Watanabe N and Kai K.
Physica B 120(1983)131

A Resonance Detector Spectrometer at KENS
Carpenter J.M, Watanabe N, Ikeda S, Masuda Y and Satoh S.
Physica B 120(1983)126

Neutron Quasi-Elastic Scattering Studies of Molecular liquids and Polymers by Pulsed Cold Neutron Source
Inoue K, Kiyanagi Y, Kohgi M and Kaji K.
Physica B 120(1983)422

Multi-Analyzer Crystal Spectrometer (MAX) for Pulsed Neutron Source and Its Application to Various Problem
Tajima K, Ishikawa Y, Kanai K, Tomiyoshi S and Todate Y.
Physica B 120(1983)136

Resonance Detector Instruments
Watanabe N.
Proc. Workshop on High-Energy Excitation in Condensed Matter (Los Alamos, Feb. 13-15, 1984)56

Simple Thermo-Level Meter for He I and He II by a Dynamic Method
Yoshiki H.
Cryogenics (1984)704

High Resolution TOF Crystal Analyzer Spectrometer for Large Energy Transfer Incoherent Neutron Scattering
Ikeda S and Watanabe N.
Nucl. Instrum. Methods 221(1984)571

Detector Resolution of a Resonance Detector Neutron Spectrometer
Rauh H and Watanabe N.
Nucl. Instrum. Methods 222(1984)507

Experimental Study of the Time-Focussing Effect in Resonance Detector Neutron Spectrometer
Rauh H, Ikeda S and Watanabe N.
Nucl. Instrum. Methods 224(1984)469

Resonance Detector Methods in Spectrometers
Watanabe N.
Neutron Scattering in the 'Nineties, IAEA Vienna (1985)279

TOF Spectrometer with Optical Polarizer for Cold Neutrons
Endoh Y, Ikeda S, Mitsuda S and Fujimoto H.
Nucl. Instrum. Methods A240(1985)115

TOF Type Small Angle Scattering Spectrometer SAN at KENS Pulsed Cold Neutron Source
Ishikawa Y, Furusaka M, Niimura N, Arai M and Hasegawa K.
Proc. 8th Meeting Int. Collaboration on Advanced Neutron Sources (Rutherford Appleton Lab., July 8-12, 1985), RAL-85-110 (1985)454

Pulsed Polarized Neutron Studies at KENS
Endoh Y and Ishikawa Y.
Proc. Int Conf. on Neutron Scattering (Santa Fe, Aug. 19-23, 1985)

Cold Neutron Scattering Spectrometers at the Spallation Neutron Facility, KENS
Ishikawa Y, Endoh Y and Inoue K.
Neutron Scattering in the 'Nineties, IAEA Vienna (1985)285

Crystal Analyzer Type Quasielastic Spectrometers using the Pulsed Cold Neutron Source
Inoue K, Ishikawa Y, Watanabe N, Kaji K, Kiyanagi Y, Iwasa H and Kohgi M.
Nucl. Instrum. Methods A238(1985)401

Development of Polarized Epithermal Neutron Spectrometer PEN at KENS
Ishida M, Ishikawa Y, Ishimoto S, Kohgi M, Masaike A, Masuda Y, Morimoto K and Nakajima T.
Proc. 8th Meeting Int. Collaboration on Advanced Neutron Sources (Rutherford Appleton Lab., July 8-12, 1985), RAL-85-110 (1985)612

Slow Neutron Polarization by Longitudinally Polarized Proton Filter
Ishimoto S, Isagawa S, Masaike A, Masuda Y, Morimoto K, Nakajima T, Ishida M, Ishikawa Y, Kohgi M and Newsam J.M.
Jpn. J. Appl. Phys. 25(1986)L246

TOF Type Small Angle Scattering Spectrometer SAN at KENS Pulsed Cold Neutron Source
Ishikawa Y, Furusaka M, Niimura N, Arai M, Hasegawa K.
J. Appl. Cryst. 19(1986)229

Liquid and Amorphous Total Scattering Instrument at KENS —HIT—
Misawa M, Fukunaga T, Yamaguchi T and Watanabe N.
Proc. 9th Meeting Int. Collaboration on Advanced Neutron Sources (SIN. Villigen, Switzerland, Sept. 22-26, 1986)539

A Multi-Angle Rotor Spectrometer at the Pulsed Neutron Source ISIS
Taylor A.D, Ward R.G, Williams W.G, Endoh Y and Watanabe N.
Proc. 9th Meeting Int. Collaboration on Advanced Neutron Sources (SIN, Villigen, Switzerland, Sept. 22-26, 1986)535

Dynamically Polarized Proton Filter for a Low Energy Neutron Polarizer
Masuda Y, Hiramatsu S, Isagawa S, Ishida M, Ishikawa Y, Ishimoto S, Kohgi M, Masaike A, Morimoto K and Nakajima T.
Proc. 6th Int. Symp. on Polarization Phenomena in Nucl. Phys., (Osaka, 26-30 Aug. 1985) Supplement to Phys. Soc. Jpn. 55(1986)Suppl.1070

Evaluation of Data from 1D-PSD Used in TOF Methods
Niimura N.
J. Phys. Colloq. (France) 47(1986)C5-129

High Resolution Neutron Powder Diffractometer with a Solid Methane Moderator at Pulsed Spallation Neutron Source
Watanabe N, Asano H, Iwasa H, Satoh S, Murata H, Karahashi K, Tomiyoshi S, Izumi F and Inoue K.
Jpn. J. Appl. Phys. 26(1987)1164

Epithermal and Thermal Neutron Beam Monitor using ^{6}Li Glass Scintillator
Hirai M, Niimura N and Ishida A.
Nucl. Instrum. Methods A259(1987)497

Production of Highly Polarized White Epithermal Neutron Beams by Dynamically Polarized Proton Filter
Ishida M, Hiramatsu S, Isagawa S, Ishikawa Y, Ishimoto S, Kanno K, Kohgi M, Masaike A, Morimoto K, Nakajima T and Newsam J.M.
Nucl. Instrum. Methods (1988)

Dynamically Polarized Proton Filter as a Neutron Spin Polarizer by the Use of a ^{3}He-^{4}He Heat Exchanger
Masuda Y, Ishimoto S, Masaike A, Ishida M, Ishikawa Y and Kohgi M.
Nucl. Instrum. Methods A264(1988)169

New KENS Data Acquisition System
Arai M, Furusaka M and Satoh S.
Advanced Neutron Sources 1988 (Proc. ICANS X) (Los Alamos, Oct. 3-7, 1988)P.529

Application of eV Neutron Scattering and eV Neutron Absorption Techniques
Ikeda S.
ICANS -X (Los Alamos, Oct. 3-7, 1988), Inst. of Phys. Conf. Series No. 97, Institute of Physics, Bristol and New York,P.341

Development of a Chopper Spectrometer at KENS
Arai M, Kohgi M, Itoh M, Iwasa H, Watanabe N, Ikeda S, and Endoh Y.
ICANS -X (Los Alamos, Oct. 3-7, 1988), Inst. of Phys. Conf. Series No. 97, Institute of Physics, Bristol and New York,P.297

Thermal Neutron Small-Angle Scattering Spectrometer (WIT) Using a 2D Converging slit and Annular Glass Scintillator Detectors at KENS
Niimura N, Hirai M, Ishida A, Aizawa K, Yamada K and Ueno M.
Physica B 156&157(1989)611

Several Experiences of Using Li-Glass Scintillators
Niimura N, Hirai H, Aizawa K, Yamada K and Okamura F.
Proc. 11th Meeting Int. Collaboration on Advanced Neutron Sources (KEK, Oct. 22-26 1990)967

Resolution Function and Recent Developments of the Multi Analyzer Crystal Spectrometer MAX
Todate Y, Tajima K, Ikeda H and Tomiyoshi S.
Jpn. J. Appl. Phys. 29(1990)1220

Recent Progress on MAX
Todate Y, Ikeda H, Tajima K and Tomiyoshi S.
Proc. 11th Meeting Int. Collaboration on Advanced Neutron Sources (KEK, Oct. 22-26 1990) (1990)739

Thermal Neutron Small-Angle Scattering Spectrometer (WIT)
Niimura N, Aizawa K, Hirai M, Sangawa U and Yamada K
Proc. 11th Meeting Int. Collaboration on Advanced Neutron Sources (KEK, Oct. 22-26 1990)1091

Why Total Performance
Watanabe N.
Proc. 11th Meeting Int. Collaboration on Advanced Neutron Sources (KEK, Oct. 22-26 1990) (1990)637

Total Performance of Small-Angle Machines at Pulsed source
Furusaka M, Watanabe N, Suzuya K, Fujikawa I and Satoh S.
Proc. 11th Meeting Int. Collaboration on Advanced Neutron Sources (KEK, Oct. 22-26 1990)677

Total Performance of LAM-80ET
Inoue K, Kanaya T, Kiyanagi Y, Shibata K, Kaji K, Iwasa H and Izumi Y.
Proc. 11th Meeting Int. Collaboration on Advanced Neutron Sources (KEK, Tsukuba, Oct. 22-26, 1990)684

Applications on Pulsed Cold Neutron Small Angle Scattering Instruments
Furusaka M.
Proc. of the 2nd International Syymposium on Advanced Nuclear Energy Research -Evolution by Accelerators - (Mito, Jan. 24-26, 1990)632

A Semicircle One-Dimensional Position Sensitive Detectors for the Neutron Time-of-Flight Single Crystal Diffractometer
Niimura N, Kawada I, Isove M, Okamura F and Yamada K.
J. Appl. Cryst. (1990)

Crystal Analyzer Type Spectrometer LAM-D at KENS Spallation Thermal Neutron Source
Inoue K, Kanaya T, Kiyanagi Y, Shibata K, Kaji K, Ikeda S, Iwasa H and Izumi Y.
Proc. 11th Meeting of the Int. Collaboration on Advanced Neutron Sources (KEK, Tsukuba, Oct. 22-26, 1990)1082

First Results from the UK-Japanese Spectrometer MARI
Taylor A. D, Arai M, Bennington S. M, Bowden Z. A, Osborn R, Andersen K, Stirling W. G, Nakane T, Yamada K and Welz D.
Proc. 11th Meeting Int. Collaboration on Advanced Neutron Sources (KEK, Oct. 22-26 1990) (1990)705

Crosscorrelation Method Using a Pulsed White Polarized Neutron Beam
Kohgi M, Fujimoto H, Ohoyama K, Yamada K and Motoya M.
Proc. 11th Meeting Int. Collaboration on Advanced Neutron Sources (KEK, Oct. 22-26 1990) (1990)733

Recent Progress in TOP Spectrometer
Itoh S, Watanabe T and Endoh Y.
Proc. 11th Meeting Int. Collaboration on Advanced Neutron Sources (KEK, Oct. 22-26 1990) (1990)792

Performance of Chopper Spectrometers
Arai M, Taylor A. D, Bennington S. M, Bowden Z. A, Osborn R, Kohgi M, Ohoyama K and Nakane T.
Proc. 11th Meeting Int. Collaboration on Advanced Neutron Sources (KEK, Oct. 22-26 1990) (1990)644

MARI-A New Spectrometer for Liquid and Amorphous Materials
Arai M, Taylor A. D, Bennington S.M and Bowden Z. A.
Recent Developments in the Physics of Fluids, Int. Symp. Oxford UK 1991 Section 5F321

Small Angle Thermal Neutron Scattering Spectrometer (WIT)
Niimura N, Aizawa K, Hirai M and Sangawa U.
Proc. Int. Conf. Neutron Scattering (Oxford, 27-30 Aug. 1991), P3-B-155, Physica B

A TOF Neutron Diffraction System for High Pressure and Low Temperature
Kamigaki K, Ishikawa Y, Suzuki T and Tomiyoshi S.
High Pressure Research 8(1991)501

A High-Resolution Neutron Spectrometer Using Mica Analyzers and the Pulsed Cold Neutron Source
Inoue K, Kanaya T, Kiyanagi Y, Ikeda S, Shibata K, Iwasa H, Kamiyama T, Watanabe N and Izumi Y.
Nucl. Instrum. Methods A309(1991)294

Neutron Diffraction Studies of High-Tc Superconductors at KENS
Asano H.
Proc. of the 2nd International Syymposium on Advanced Nuclear Energy Research -Evolution by Accelerators - (Mito, Jan. 24-26, 1990)633

5. Crystal Structures

Refinement of the Structure of Ta_2D by High-Resolution Powder Neutron Diffraction
Murata H, Asano H, Izumi F, Tomiyoshi S, Iwasa H, Satoh S and Watanabe N.
Trans. Jpn. Inst. Met. 26(1985)795

Neutron Diffraction Study on the Low-Temperature Monoclinic form of $CeCu_6$
Asano H, Umino M, Onuki Y, Komatsubara T, Izumi F and Watanabe N.
J. Phys. Soc. Jpn. 55(1986)454

Time-of-Flight Neutron Diffraction Study of Li_3N at High Temperature
Kawada I, Isobe M, Okamura F, Watanabe H, Ohsumi K, Horiuchi H, Sata T and Ishii T.
Mineral. J 13(1986)28

Time-of-Flight Neutron Diffraction Study on the Deformed Heusler Alloy
Kamiyama T, Tomiyoshi S, Shinohara T, Asano H, Yamamoto H, Watanabe N.
Proc. Int. Symp. on Physics of Magnetic Materials (Sendai, Apr. 1987), World Scientific, Singapore (1987)579

Neutron Diffraction Study on the Low-Temperature Monoclinic Form of $PrCu_6$
Asano H, Umino M, Onuki Y, Komatsubara T, Izumi F and Watanabe N.
J. Phys. Soc. Jpn. 56(1987)2245

Neutron and X-ray Diffraction Studies of $RBa_2Cu_3O_{7-x}$
Asano H, Takita K, Ishigaki T, Izumi F, Takayama -Muromachi E, Uchida Y and Watanabe N.
Physica B 148(1987)302

Rietveld Refinement of the Structure of $Ba_2YCu_3O_{7-x}$ with Neutron Powder Diffraction Data
Izumi F, Asano H, Ishigaki T, Takayama -Muromachi E, Uchida Y, Watanabe N and Nishikawa T.
Jpn. J. Appl. Phys. 26(1987)L649

Rietveld Analysis of Powder Patterns Obtained by TOF Neutron Diffraction using Cold Neutron Source
Izumi F, Asano H, Murata H and Watanabe N.
J. Appl. Cryst. 20(1987)411

Crystal Structure of the Tetragonal Form of $Ba_2YCu_3O_{7-x}$
Izumi F, Asano H, Ishigaki T, Takayama -Muromachi E, Uchida Y and Watanabe N.
Jpn. J. Appl. Phys. 26(1987)L1214

Crystal Structure of the Tetragonal Form of Ba_2YCu3O_{7-x}
Izumi F, Asano H, Ishigaki T, Takayama -Muromachi E, Uchida Y and Watanabe N.
Jpn. J. Appl. Phys. 26(1987)L1214

Crystal Structure of $Ba_2ErCu_3O_{7-x}$ Determined by Neutron Powder Diffraction
Ishigaki T, Asano H, Takita K, Katoh H, Akinaga H, Izumi F and Watanabe N.
Jpn. J. Appl. Phys. 26(1987)1681

Cation Distribution in $(M', M)_3Se_4$:II.$(V,Ti)_3Se_4$ and $(Cr,V)_3Se_4$
Hayashi A, Ueda Y, Kosuge K, Murata H, Asano H, Watanabe N and Izumi F.
J. Solid State Chem. 71(1987)237

Cation Distribution in $(M', M)_3Se_4$:I. $(Cr,Ti)_3Se_4$
Hayashi A, Ueda Y, Kosuge K, Murata H, Asano H, Watanabe N and Izumi F.
J. Solid State Chem. 67(1987)346

Crystal Structure of the Superconductor $Ba_{1.8}Nd_{1.2}Cu_3O_{7-y}$
Izumi F, Takekawa S, Matsui Y, Iyi N, Asano H, Ishigaki T and Watanabe N.
Jpn. J. Appl. Phys. 26(1987)1616

Crystal Structure of Orthorhombic Form of $Ba_2YCu_3O_{7-x}$ at 42K
Izumi F, Asano H, Ishigaki T. Takayama-Muromachi E, Uchida Y and Watanabe N.
Jpn. J. Appl. Phys. 26(1987)L1193

Crystal Structure of $Ba_2HoCu_3O_{7-x}$ Determined by Neutron Powder Diffraction

Asano H, Takita K, Ishigaki T, Akinaga H, Katoh H, Masuda K, Izumi F and Watanabe N.
Jpn. J. Appl. Phys. 26(1987)1341

Neutron Powder Diffraction from Polymorphs of $BaPb_{0.75}Bi_{0.25}O_3$

Asano H, Oda M. Endoh Y, Hidaka Y, Izumi F, Ishigaki T, Karahashi K, Murakami T and Watanabe N.
Jpn. J. Appl. Phys. 27(1988)1638

Neutron Diffraction Study of the Metastable g Titanium Deuteride

Numakura H, Koiwa M, Asano H and Izumi F.
Acta metall. 36(1988)2267

Time-of-Flight Powder Neutron Diffraction Study of $LaNi_5D_3$

Hayakawa H, Nomura K, Ishido Y, Akiba E, Shin S, Asano H, Izumi F and Watanabe N.
J. Less-Common. Met. (1988)

Structural Study of $La_{1+x}Ba_{2-x}Cu_3O_y$

Izumi M and Uchinokura K.
Proc. Int. Conf. High Temp. Superconductors Materials and Mechanisms of Superconductivity (Interlaken, Feb. 29-Mar. 4, 1988), Physica B

Neutron Diffraction Study of Nonstoichiometry in $Ba_{1.5}La_{1.5}Cu_3O_y$

Izumi F, Takayama-Muromachi E, Kobayashi M, Uchida Y, Asano H, Ishigaki T and Watanabe N.
Jpn. J. Appl. Phys. 27(1988)L824

Crystal Structure of Oxide Superconductors

Asano H.
Proc. Int. Conf. Electronic Materials (Tokyo, 1988)15

Determination of Space Group and Refinement of Structure Parameters for $La_2CuO_{4-\delta}$

Yamada K, Kudo E, Endoh Y, Tsuda K, Tanaka M, Kokusho K, Asano H, Izumi F, Oda M, Hidaka Y, Suzuki M and Murakami T.
Jpn. J. Appl. Phys. 27(1988)1132

Formation of the Metastable g Hydride in Titanium

Numakura H, Koiwa M, Asano H and Izumi F.
Trans. JIM suppl. 29(1988)439

Rietveld Structure Refinement of Superconducting $YBaSrCu_3O_{7-\delta}$ Using X-Ray and Neutron Powder Diffraction Data

Akiba E, Hayakawa H, Mizuno M, Izumi F and Asano H.
Proc. Int. Symp. Superconductivity (Tsukuba, 1989)95

Oxygen Deficiency in the Electron-Doped Superconductor $Nd_{2-x}Ce_xCuO_{4-y}$

Takayama-Muromachi E, Izumi F, Uchida Y, Kato K and Asano H.
Physica C159(1989)634

Structural Properties of the Superconductor $LaBa_2Cu_{3-y}O_{7-z}$ in the Solid Solution System $La_{1+x}Ba_{2-x}Cu_{3-y}O_{7-z}$

Izumi M, Yabe T, Wada T, Maeda A, Uchinokura K, Tanaka S and Asano H.
Phys. Rev. B40(1989)6771

Unusually Simple Crystal Structure of an Nd-Ce-Sr-Cu-O Superconductor

Sawa h, Suzuki S, Watanabe M, Akimitsu J, Matsubara H, Watabe H, Uchida S, Kokusho K, Asano H, Izumi F and Takayama-Muromachi E.
Nature 337(1989)347

Structure Refinement of $La_{1.9}Ca_{1.1}Cu_2O_6$ with neutron Powder Diffraction Data

Izumi F, Takayama-Muromachi E, Nakai Y and Asano H.
Physica C 157(1989)89

EXAFS and Neutron Diffraction Studies of Local and Average Structures for $YB_2C_{2.8}Z_{0.2}O_{7-\delta}$

Maeda H, Koizumi A, Bamba N, Takayama-Muromachi E, Izumi F, Asano H, Shimizu K, Moriwaki H, Maruyama H, Kuroda Y, Yamazaki H.
Physica C157(1989)483

Neutron and Electron Diffraction Study of the Electron-Doped Superconductor $Nd_{1.845}Ce_{0.155}CuO_{4-y}$

Izumi F, Matsui Y, Takagi H, Uchida S, Tokura Y and Asano H.
Physica C158(1989)433

New Family of Layered Copper Compounds with Ordered Cations: Prospective High-Temperature Superconductors
Tokura Y, Takagi H, Watanabe H, Matsubara H, Uchida S, Hiraga K, Oku T, Mochiku T and Asano H.
Phys. Rev. B 40(1989)2568

Metal Ordering and Oxygen Displacement in (Nd, Sr, Ce)$_2$CuO$_{4-y}$
Izumi F, Takayama-Muromachi E, Fujimori A, Kamiyama T, Asano H, Akimitsu J and Sawa H.
Physica C 158(1989)440

Oxygen Deficiency and Atomic Displacement in Superconducting $(Ba_{1-x}Nd_x)_2$ $(Nd_{1-y}Ce_y)_2Cu_3O_{8+x}$
Izumi F, Kito H, Sawa H, Akimitsu J and Asano H.
Physica C 160(1989)235

Nonstoichiometry and Mixed Pr Valency in $(Pr_{1-x}Sr_x)(Pr_{1-y}Ce_y)CuO_{4-z}$
Kito H, Sawa H, Akimitsu J, Izumi F, Ishigaki T and Asano H.
Jpn. J. Appl. Phys. 29(1990)L1803

Rietveld Analysis of the Modulated Structure in the Superconducting Oxide $Bi_2(Sr, Ca)_3Cu_2O_{8+x}$
Yamamoto A, Onoda M, Takayama-Muromachi E, Izumi F, Ishigaki T and Asano H.
Phys. Rev. B 42(1990)4228

Neutron-Diffraction Study of $Tl_2Ba_2CuO_{6+\delta}$ with Various T_c's from 0 to 73 K
Shimakawa Y, Kobo Y, Manako T, Igarashi H, Izumi F and Asano H.
Phys. Rev. B 42(1990)10165

Structural Analysis of Orthorhombic ZrO_2 by High Resolution Neutron Powder Diffraction
Ohotaka O, Yamanaka T, Kume S, Hara N, Asano H and Izumi F.
Proc. Jpn. Academy 66(1990)193

Sr-Induced Oxygen Defects in $La_{2-x}Sr_xCuO_{4-\delta}$: A Neutron Powder Diffraction Study
Kamiyama T, Izumi F, Asano H, Takagi H, Uchida S, Tokura Y, Takayama-Muromachi E, Matsuda M, Yamada K, Endoh Yand Hidaka Y.
Physica C 172(1990)120

Neutron and X-Ray Diffraction Study of a Valence Fluctuating Compound $YbInCu_4$
Kojima K, Nakai Y, Suzuki T, Asano H, Izumi F, Fujita T and Hihara T.
J. Phys. Soc. Jpn. 59(1990)792

Neutron Diffraction Study of the Cu Ferromagnet $La_4Ba_2Cu_2O_{10}$
Ogawa N, Mizuno F, Masuda H, Hirabayashi I, Tanaka S, Mochiku T, Asano H and Izumi F.
Physica B 165&166(1990)1687

Crystal Structure of the Ferromagnetic Copper Oxide $La_{4-x}Ba_{2+x}Cu_2O_{10}$
Mochiku T, Asano H, Mizuno F, Masuda H, Hirabayashi I, Tanaka S and Izumi F.
Proc. 3rd Int. Symp. Superconductivity (Sendai, 1990)347

Crystal Structure Analysis of the Dense Kondo System $CeSi_x$
Kohgi M, Ito M, Satoh T, Asano H, Ishigaki T and Izumi F.
J. Main. & Magn. Mater. 90&91(1990)433

Anomalous Paramagnetic Property of $NdNbO_4$ Single Crystals
Yamauchi H, Tsunekawa S, Tomiyoshi S, Fukuda T, Kamiyama T and Asano H.
J. Phys. Soc. Jpn. 59(1990)2602

High-Resolution Neutron Powder Diffraction of Superconducting $La_2CuO_{4+\delta}$
Kamiyama T, Asano H, Shibutani K, Ogawa R, Endoh Y, Izumi F, David W.I.F, Ibberson R and Yamaguchi Y.
Proc. 3rd Int. Symp. Superconductivity (Sendai, 1990)343

Effect of Annealing under High Oxygen Pressure on the Structure and Superconductivity of $(Ba_{0.85}Nd_{0.15})_2NdCu_3O_{6+z}$
Mochiku T, Asano H, Akinaga H, Ohshima T, Takika K, Izumi F, Takeda Y, Takano M and Mizoguchi K.
Physica C 167(1990)560

Effect of Deformation on Pd_2MnSn Heusler Alloy Studied with Transmission Electron Microscopy, Profile Analysis of Neutron Powder Diffraction Pattern, and Magnetization Measurement
Kamiyama T, Shinohata T, Tomiyoshi S, Minonishi Y, Asano H and Watanabe N.
J. Appl. Phys. 68(1990)4741

Synthesis and Structure Refinement of $SrT_xV_{6-x}O_{11}$ (T=Ti, Cr and Fe)

Kanke Y, Izumi F, Takayama-Muromachi E, Kato K, Kamiyama T and Asano H.
J. Solid State Chem. 92(1991)261

Structural Changes Accompanying Oxygen Incorporation in $(Pb_{0.65}Cu_{0.35})Sr_2(Y_{0.7}Ca_{0.3})Cu_2O_{7+\delta}$

Maeda T, Sakuyama K, Izumi F, Yamauchi H, Asano H and Tanaka S.
Physica C 175(1991)393

Structural Study of Oxide Superconductors by Neutron Diffraction

Asano H.
Solid State Ionics 49(1991)17

Temperature Dependence of the Structure of $Tl_2Ba_2CuO_{6+\delta}$: A Neutron Powder Diffraction Study

Kamiyama T, Izumi F, Asano H, Shimakawa Y, Kubo Y, Manako T and Igarashi H.
Physica C 185-189(1991)881

Hole-Doping Effects on the Magnetic Properties of the $La_4Ba_2Cu_2O_{10}$ Ferromagnet

Mizuno F, Masuda H, Hirabayashi I, Tanaka S, Mochiku T, Asano H and Izumi F.
Proc. 2nd ISSP Int. Symp. (Tokyo, 1991)389

Superconductivity in Pb-Based "1222" Copper Oxides

Sakai N, Maeda T, Izumi F, Asano H and Yamauchi H.
Proc. 4th Int. Symp. Superconductivity (Tokyo, 1991)217

Three-Dimensional Antiferromagnetic Order and Anisotropic Magnetic Properties in Bi_2CuO_4

Yamada K, Takada K, Hosoya S, Watanabe Y, Endoh Y, Tomonaga N, Suzuki T, Ishigaki T, Kamiyama T, Asano H and Izumi F.
J. Phys. Soc. Jpn. 60(1991)2406

Relationship between Crystal Structure and Long-Time Response to DC Electric Field in Niobium-Doped $BaTiO_3$ Ceramics

Ikeda M, Yoshida M, Satoh A, Nishikawa K, Izumi F and Asano H.
Jpn. J. Appl. Phys. 30(1991)2295

Neutron Diffraction Study of the Ferromagnetic Copper Oxide $La_{1.8}Ba_{1.2}CuO_5$

Mochiku T, Asano H, Izumi F, Mizuno F, Masuda H, Hirabayashi I and Tanaka S.
J. Phys. Soc. Jpn. 60(1991)1959

Oxygen Contents, Crystal Structures and Physical Properties of $Tl_2Ba_2CuO_{6+z}$

Kubo Y, Shimakawa Y, Manako T, Igarashi H, Izumi F and Asano H.
Supercond. Sci. Technol. 4(1991)S82

Low-Temperature Specific Heat and Ferromagnetism in $La_4Ba_2Cu_2O_{10}$ and Related Compounds

Mizuno F, Masuda H, Hirabayashi I, Tanaka S, Hasegawa M, Mizutani U, Mochiku T, Asano H and Izumi F.
Supercond. Sci. Technol. 4(1991)S301

Crystal Structure and Superconducting Properties of Layered Copper Oxides Containing "123" Block and Single-MO_2-Unit Fluorite Block : $(Ho_{2/3}Ce_{1/3})_2(La_{1/3}Ba_{1/3})_2Cu_3O_{8+z}$

Ichinose A, Wada T, Yaegashi Y, Nara A, Izumi F, Yamauchi H, Asano H and Tanaka S.
Physica C 185-189(1991)609

Oxygen Nonstoichiometry and Metal Substitution in $TlSr_2CaCu_2O_{7-x}$

Izumi F, Kondo T, Shimakawa Y, Manako T, Kubo Y, Ishigaki H and Asano H.
Physica C 185-189(1991)615

Neutron Diffraction Study of Superconducting $La_{1.82}Ca_{1.18}Cu_2O_6$

Kinoshita K, Izumi F, Yamada T and Asano H.
Physica C 185-189(1991)537

Oxygen and Cation Nonstoichiometry in Tl-Based Superconductors

Shimakawa Y, Kubo Y, Manako T, Igarashi H, Izumi F and Asano H.
Solis State Ionics 49(1991)53

Neutron Powder Diffraction Study of the Pb-Based Copper Oxide Containing Thick Fluorite Blocks: $(Pb,Cu)Sr_2(Ho,Ce)_3Cu_2O_{11+z}$

Wada T, Ichinose A, Izumi F, Nara A, Yamauchi H, Asano H and Tanaka S.
Physica C 179(1991)455

The Crystal Structure of the Superconducting Copper Oxide Carbonate $(Ba_{1-x}Sr_x)_2Cu_{1+y}O_{2+2y+z}(CO_3)_{1-y}$
Izumi F, Kinoshita K, Matsui Y, Yanagisawa K, Ishigaki T, Kamiyama T, Yamada T and Asano H.
Physica C 196(1992)227

Structural Properties of the Nonsuperconductor $(Ho,Ce)_2(Sr,Ba,La)_2\ Cu_3O_{8+z}$
Ichinose A, Wada T, Yaegashi Y, Izumi F, Yamauchi H, Asano H and Tanaka S.
Physica C 191(1992)205

Neutron Diffraction Studies of Oxide Superconductors
Asano H and Kamiyama T.
JJAP Series 7 Mechanisms of Superconductivity (1992)55

Crystal Structures of the Two Dimensional Antiferromagnets RFe_2O_4 (R=Y, Er) and Their Magnetic Properties under Pressure
Matsumoto T, Mori N, Iida J, Tanaka M, Siratori K, Izumi F and Asano H.
Physics B 180&181(1992)603

Structure Refinements of Superconducting and Nonsuperconducting $La_{1.82}Ca_{1.18}Cu_2O_{6\pm\delta}$
Kinoshita K, Izumi F, Yamada T and Asano H.
Phys. Rev. B 45(1992)5558

Cation Distribution in $ZnFe_2O_4$ Fine Particles Studied by Neutron Powder Diffraction
Kamiyama T, Haneda K, Sato T, Ikeda S and Asano H.
Solid State Comm. 81(1992)563

Rietveld Analysis of the Composite Crystal in Superconducting $Bi_{2+x}Sr_{2-x}CuO_{6+y}$
Yamamoto A, Takayama-Muromachi E, Izumi F, Ishigaki T and Asano H.
Physica C 201(1992)137

Structural properties of $(Pb,Cu)\ (Sr,Nd)_2(Ho,Ce)_2Cu_2O_{9-\delta}$
Maeda T, Sakai N, Izumi F, Wada T, Yamauchi H, Asano H and Tanaka S.
Physica C 193(1992)73

Structural Changes and Redistribution of Holes by Sr-Doping in $YBa_2Cu_4O_8$
Ishigaki T, Izumi F, Wada T, Suzuki N, Yaegashi Y, Asano H, Yamauchi H and Takada S.
Physica C 191(1992)441

6. Structure of Liquids and Glasses

High Resolution Short-range Structure of Ni-Ti and Cu-Ti Alloy Glasses by Pulsed Neutron Total Scattering
Fukunaga T, Kai K, Naka M, Watanabe N and Suzuki K.
Proc. 4th Int. Conf. Rapidly Quenched Metals (Sendai, Aug. 24-28, 1981)347

Atomic and Electronic Structure of Amorphous CuTi Alloys
Mizoguchi T, Gubler U, Oelhafen P, Guntherodt H.J, Akutsu N and Watanabe N.
Proc. 4th Conf. on Rapidly Quenched Metals (Sendai, 1981)1307

Structure Modification of Pd-Zr Alloy Glasses due to Hydrogen Absorption
Kai K, Fukunaga T, Nomoto T, Watanabe N and Suzuki K.
Proc. 4th Int. Conf. Rapidly Quenched Metals (Sendai, 1981)1609

Structure and Physical Properties of Amorphous (Fe, Co, Ni, Pd)-Zr Alloys
Mizouguchi T, Yamada S, Suemasa T, Nishioka J, Akutsu N, Watanabe N and Takayama S.
Proc. 4th Conf. on Rapidly Quenched Metals (Sendai, 1981)89

Structure Characterization of Amorphous Alloys by T-O-F Pulsed Neutron Scattering using Accelerator Neutron Source
Suzuki K.
Proc. 4th Conf. on Rapidly Quenched Metals (Sendai, 1981)89

Neutron Diffraction Study of Amorphous Binary Alloys
Mizoguchi T, Nishioka J, Yamada S, Suemasa T, Yoda S, Akutsu A, Narumi H, Kudoh T, Aimitsu M, Watanabe N, Nishi M and Motoya K.
J. Phys. Colloq. (France) 43(1982)C9-659

Layer Correlation in a-As $(Se_xS_{1-x})_3$ System
Mori T, Yasuoka H, Saegusa H, Okawa K, Kato M, Arai T, Fukunaga T and Watanabe N.
Jpn. J. Appl. Phys. 22(1983)1784

Chemical Short-Range Structure of Ni_xTi_{1-x} (x=0.26-0.40) Alloy Glasses
Fukunaga T, Hayashi N, Kai K, Watanabe N and Suzuki K.
Physica B 120(1983)352

Local Structures of Amorphous As-Chalcogenide Systems by Means of High-Q Neutron Scattering and Infrared Reflection
Arai T, Onari S, Katoh M, Mori T, Saegusa H, Yasuoka H, Hatori M, Ohkawa K, Fukunaga T and Watanabe N
Physica 117B&118B(1983)965

Structure and Properties of Amorphous Metal Hydrides
Suzuki K.
J. Less-Common. Met. 89(1983)183

Hydrogen Atom Environment in a Hydrogenated ZrNi Glass
Suzuki K, Hayashi N, Tomizuka Y, Fukunaga T, Kai K and Watanabe N.
J. Non-cryst. Solids 61 & 62(1984)637

Experimental Determination of Partial Structures in $Ni_{40}Ti_{60}$ Glass
Fukunaga T, Watanabe N and Suzuki K.
J. Non-Cryst. Solids 61 & 62(1984)343

Indirect and Direct Correlations between Unlike Ions in Incompletely Hydrated Solution
Ichikawa K, Kameda Y, Matsumoto T and Misawa M.
J. Phys. C. Solid State 17(1984)L725

The Structure of Same Univalent Metal Nitrate Melts Studied by Means of Pulsed Neutron Diffraction
Yamaguchi T, Tamura Y, Okada I, Ohtaki H, Misawa M and Watanabe N.
Z. Naturforsch. 40a(1985)490

What Difference Exists in the Structure of SiO_2 and GeO_2 between Melt-quenched Bulk Glass and Sputter-Deposited Amorphous Film
Suzuki K, Misawa M and Kobayashi Y.
J. Phys. Colloq. (France) 46(1985)C8-617

Local Atomic and Magnetic Structures of Amorphous $Fe_{1-x}B_x$ Alloys Studied by Neutron Scattering
Xianyu Ze, Ishikawa Y, Fukunaga T and Watanabe N.
J. Phys. F : Met. Phys. 15(1985)1799

Compositional Variations in the Short-range Structure of $Ni_{1-x}B_x$ (x=0.18-0.40) Alloy Glasses
Suzuki K, Fukunaga T, Itoh F and Watanabe N.
Proc. 5th Int. Conf. Rapidly Quenched Metals, Elsevier Science Publishers B.V. (1985)479

Structural Study of an Amorphous $Ni_{36}Zr_{64}$ Alloy
Mizoguchi T, Yoda S, Akutsu N, Yamada S, Nishioka J, Suemasa T and Watanabe N.
Proc. 5th Int. Conf. Rapidly Quenched Metals, Elsevier Science, Publisher B.V. (1985)483

Partial Structure Functions of NiZi Alloy Glass Determined by an Isotope-Substitution Neutron Diffraction Methods
Fukunaga T, Hayashi N, Watanabe N and Suzuki K.
Proc. 5th Int. Conf. Rapidly Quenched Metals, Elsevier Science Publishers B.V. (1985)475

Structural Analysis of Sodium Silicate Glassed Containing TiO_2 by Pulsed Neutron Scattering Measurement
Hidaka H, Iwamoto N, Umesaki N, Fukunaga T and Suzuki K.
J. Mat. Sci. 20(1985)2497

Structure and Local Anisotropy of Amorphous Tb-Fe Alloys
Hatta S, Mizoguchi T and Watanabe N.
Proc. 5th Int. Conf. Rapidly Quenched Metals, Elsevier Science Publishers B.V. (1985)589

Short Range Structural Analysis of Lead Silicate Glasses by Pulsed Neutron Total Scattering
Yamada K, Matsumoto A, Niimura N, Fukunaga T, Hayashi N and Watanabe N.
J. Phys. Soc. Jpn. 55(1986)831

X-ray and Neutron Diffraction and Molecular Dynamics Simulation on Molten Lithium and Rubidium Nitrate
Yamaguchi T, Okada I, Ohtaki H, Mikami N and Kawamura K.
Mol. Phys. 58(1986)349

A Neutron Diffraction Study of Liquid D_2O in the Temperature Range of 25°-200°C
Yamaguchi T, Tamura Y, Ohtaki H and Misawa M.
Abstract of Int. Okazaki Conf. (1986)

Neutron Diffraction of As-Quenched Ge_{20} Te_{80} Glass near the Glass-Undercooled Liquid Transition
Ichikawa K, Kameda Y, Xu Q and Misawa M.
J. Non-cryst. Solids 95/96 (Part I) (1987)185

X-Ray and Neutron Diffraction Analysis of Barium Silicate Glass
Hasegawa H and Yasui I.
J. Non-cryst. Solids 95 & 96(1987)201

Atomic Scale Structure of Hydrogenated Amorphous Alloys by Pulsed Neutron Scattering
Suzuki K.
Key Engineering Materials B-15(1987)697

Characterization of Atomi-Scale Structures of Amorphous Gerawies and Metals Depending on Different Preparation Methods
Suzuki K.
Diffusion and Defeet Data 53(1987)233

Chemical Fluctuation of Ti-Zr Isomorphous Alloy obtained by Rapid Quenching
Fukunaga T, Shibuya S, Suzuki K and Misawa M.
J. Material Sci. Lett. 6(1987)1435

Intermolecular Structure around Lithium Monovalent Cation in the Molten $LiAlCl_4$
Kameda Y and Ichikawa K.
J. Chem. Soc., Faraday Trans. 2(1987)2925

Atomic-Scale Structure of CVD Amorphous Si_3N_4-BN Composite
Fukunaga T, Goto T, Misawa M, Hirai T and Suzuki K.
J. Non-Cryst. Solids 95&96(1987)1119

A Structure Analysis of (Ti, Zr)-X Ternary Alloy Glasses by Neutron Scattering
Fukunaga T, Shibuya S, Misawa M and Suzuki K.
J. Non-cryst. Solids 95 & 96(1987)263

Diffraction Studies of AlF_3-BaF_2-CaF_2Glasses
Nanba T, Inoue H, Arai Y, Hasegawa H, Misawa M and Yasui I.
Material Science Forum 32-33(1988)385

Partial Structure of Ni-Ni Correlation in Ni-42at%V Amorphous Alloy by Neutron Diffraction
Fukunaga T, Urai S, Watanabe N and Suzuki K.
J. Phys. F: Metal Phys. 18(1988)99

Temperature Dependence of Structure of Liquid Carbon Tetrachloride Measured by Pulsed Neutron Total Scattering
Misawa M.
J. Chem. Phys. 91(1989)5648

The Intra-Molecular Structure of a Water Molecule in Hydrated and Incompletely Hydrated LiCl solutions
Ichikawa K and Kameda Y.
J. Phys.: Condense. Matter 1(1989)257

Molecular Orientational Correlation in Liquid Halogens
Misawa M.
J. Chem. Phys. 91(1989)2575

Experimental Estimation of Orientational Correlation in Liquid Bromine
Misawa M.
J. Chem. Phys. 91(1989)6563

Structure of Vitreous and Molten B_2O_3 Measured by Pulsed Neutron Total Scattering
Misawa M.
J. Non-Cryst. Solids 122(1990)33

Structure of Liquid Benzene and Naphthalene Studied by Pulsed Neutron Total Scattering
Misawa M and Fukunaga T.
J. Chem. Phys. 92(1990)3495

Structure of Borate Glasses Containing Heavy Metal Ions
Yasui I, Hasegawa H, Saito Y and Akasaka Y.
J. Non-Cryst. Solids 123(1990)71

Structure Factor of X_4 Tetrahedral molecular Liquid : Competition between Intramolecular and Intermolecular Atomic Spacing
Misawa M.
J. Chem. Phys. 93(1990)6774

Effective Diameter of Molecules and Liquid-Gas Critical Point
Misawa M.
J. Chem. Phys. 93(1990)8401

Molecular Dynamics Studies on Molten Alkali Hydroxides. I. Static Properties of Molten LiOH
Okazaki S, Ohtori N and Okada I.
J. Chem. Phys. 92(1990)7505

The Ni-Ni Partial Structure in Ni-V Alloy System Observed by Neutron Scattering during Mechanical Alloying Amorphization Process
Fukunaga T, Homma Y, Misawa M and Suzuki K.
J. Non-Cryst. Solids. 117/118(1990)721

Amorphization of Immiscible Cu-Ta System by Mechanical Alloying and its Structure Observation
Fukunaga T, Nakamura K, Suzuki K and Mizutani U.
J. Non-Cryst. Solids 117/118(1990)700

Diffraction and X-ray Absorption Studies of Electrolyte Solutions
Yamaguchi T.
Pure & Appl. Chem. 59(1990)2251

Pulsed Neutron Diffraction Study on a Molten NaOD Structure using a Nickel Metal Cell
Ohtori N, Okazaki S, Odawara O, Okada I, Misawa M and Fukunaga T.
J. Phys.: Condense. Matter 2(1990)5825

Structural Study on Molten MOD (M=^{7}Ki, Na and K) by Pulsed Neutron Diffraction
Ohtori N, Okazaki S, Odawara O, Okada I, Misawa M and Fukunaga T.
J. Phys.: Condense. Matter 2(1990)8439

Molecular Dynamics Studies on Molten Alkali Hydroxides. II. Rotational and Translational Motions of Ions in Molten LiOH
Okazaki S, Ohtori N and Okada I.
J. Chem. Phys. 93(1990)5954

Orientational Correlation in Liquid Phosphorous Tribramide Studied by Pulsed Neutron Total Scattering
Misawa M, Fukunaga T and Suzuki K.
J. Chem. Phys. 92(1990)5486

Structural Characterization of Ni-V Amorphous Alloys Prepared by Mechanical Alloying
Fukunaga T, Homma Y, Misawa M and Suzuki K.
Mat. Sci. Eng. A134(1991)987

Molecular Dynamics Studies on Molten Alkali Hydroxides. III. One-Particle Dynamics of Ions in Molten LiOH
Okazaki S and Okada I.
Mol. Simul. 6(1991)265

Local Structure of Polyethylene Melt Studied by Pulsed Neutron Total Scattering
Misawa M, Kanaya T and Fukunaga T.
J. Chem. Phys. 94(1991)8413

Pulsed Neutron Diffraction Studies on Lanthanide (III) Hydrogen in Aqueous Perchlorate Solutions
Yamaguchi T, Tanaka S, Wakita H, Misawa M, Okada I, Soper A. K. and Howells S. W.
Z. Naturforsch. 46a(1991)84

Intra-and Intermolecular Correlations in Liquid Selenium-Halogen Systems
Murayama K, Kawakita Y, Yao M, Endoh H and Misawa M.
J. Phys. Soc. Japan 60(1991)3032

Neutron-Diffraction Investigation of the Intramolecular Structure of a Water Molecule in the Liquid Phase at High Temperatures
Ichikawa K, Kameda Y, Yamaguchi T, Wakita H and Misawa M.
Molec. Phys. 73(1991)79

Amorphization in Immiscible Cu-V System by Mechanical Alloying and its Structure Observation by Neutron Diffraction
Fukunaga T, Mori M, Inou K and Mizutani U.
Mat. Sci. Eng. A 134(1991)863

Structural Observation of Metastable Phases Prepared by MA in V-M (M=Fe, Cu) Systems
Fukunaga T, Mori M, Misawa M and Mizutani U.
Material Science Forum (Trans Tech. Pub.) 88-90(1992)663

The Intramolecular Structure of Oxonium Ion in Concentrated Aqueous Deuterochloric Acid Solutions
Kameda Y and Uemura O.
Bull. Chem. Soc. Jpn. 65(1992)2021

The Structure around the Nitrite Ion in Concentrated Aqueous Solutions
Kameda Y, Arakawa H, Hangai K and Uemura O.
Bull. Chem. Soc. Jpn. 65(1992)2154

Structural Study of Liquid Sb-Se Alloys
Kakinuma F, Fukunaga T, Misawa M and Suzuki K.
J. Non-Cryst. Solids 150(1992)53

Structure and Dynamics of Undercooled and Glassy Aqueous Ionic Solution by NMR, X-ray and Neutron Diffraction
Yamaguchi T, Yamagami M, Takamura T, Hirano T and Wakita H.
AIP Conf. Proc. 256(1992)89

Structural Analysis of Sol-Gel Derived SiO_2 Gels by Neutron Diffraction
Wada M, Kamiya K, Nasu H, Matsuoka J, Yoko T, Fukunaga T and Misawa M.
J. Non-Cryst. Solids 149(1992)203

Atomic Structure of $Al_{55}(Cr_{1-X}Mn_X)_{15}Si_{30}$ Metallic Glasses
Fukunaga T, Suzuki K and Mizutani U.
J. Non-Cryst. Solids 150(1992)15

Inter-Molecular Structure around Lithium Monovalent Cations and Nitrogen Atoms in Molten $LiNO_3$
Kameda Y, Kotani S and Ichikawa K.
J. Molec. Phys. 75(1992)1

Structural Evidence for the Amorphization of Mechanically Alloyed Cu-Ta Powders Studied by Neutron Diffraction
Lee C.H, Mori M, Fukunaga T, Sakurai K and Mizutani U.
Material Science Forum (Trans Tech. Pub.) 88-90(1992)399

Chemical Short-Range Order Structure of Ni-Ti Neutron Zero Scattering Amorphous Powders Synthesized by MA
Fukunaga T, Misawa M, Suzuki K and Mizutani U.
Material Science Forum (Trans Tech. Pub.) 88-90(1992)325

Diffraction Study of the Sol-Gel-Derived SiO_2 Gels
Kamiya K, Wada M, Matsuoka J, Nasu H, Fukunaga T and Misawa M.
Bol. Soc. Esp. Ceram. Vid. 31-C(1992)33

Crystal-to-Amorphous Transition of NiV and NiZr Intermetallic Compound by Mechanical Milling
Homma Y, Fukunaga T, Misawa M and Suzuki K.
Material Science Form (Trans Tech Pub.) 88-90(1992)339

Short Range Structure of $(C_{40}Ti_{60})_X(Ni_{40}Ti_{60})_{1-X}(0\leq x<1)$ Ternary Metallic Glasses Studied by Neutron Diffraction
Fukunaga T, Suzuki K and Mizutani U.
J. Non-Crys. Solids. 150(1992)10

Structural Analysis of AlF_3-CaF_2-YF_3 Glass by Diffraction Methods
Akasaka Y, Nanba T, Inoue H, Osuka T and Yasui I.
J. Non-Cryst. Solids. 140(1992)249

Orientational Correlation in Molecular Liquids Estimated from Experimental S(Q)'s
Misawa M.
J. Non-Cryst. Solids 150(1992)58

Network Structure of AlF_3-BaF_2-CaF_2 Glass
Nanba T, Osaka A, Takada J, Miura Y, Inoue H, Akasaka Y, Hagihara H and Yasui I.
J. Non-Cryst. Solids. 140(1992)269

Nitrogen-Induced Amorphization due to Mechanical Alloying
Fukunaga T, Ishikawa E, Kuroda N, Lee C. H and Mizutani U.
Proc. 4th Japan-Russia Sympo. on Mechnochemistry (Nagoya 23-26 March 1992)69

7. Magnetic Structures and Excitations

Application of Neutron Diffraction to the Study of Interface Magnetization on Thin Film with Artificial Superlattices
Endoh Y, Hosoito N and Shinjo T.
J. Magn. & Magn. Mater. 35(1982)93

Magnetism of Fe Interface Studied by Neutron Diffraction
Endoh Y, Ono H, Hosoito N and Shinjo T.
J. Magn. & Mang. Mater. 31-34(1982)881

Studies on the Magnetism at the Surface and Interface Using Polarized Neutrons
Endoh Y.
J. Phys. Colloq. (France) 43(1982)C7-159

Magnetic Properties of $Cr_{1/3}$ NbS_2
Miyadai M, Kikuchi K, Kondoh H, Sakka S, Arai M and Ishikawa Y.
J. Phys. Soc. Jpn. 52(1983)1394

Interface Magnetism of Fe-Sb Multilayer Films with Artificial Superstructure from ^{57}Fe and ^{121}Sb Mössbauer Spectroscopy, Neutron Diffraction and NMR Experiments
Shinjo T, Hosoito N, Kawaguchi K, Tabata T, Endoh Y, Ajiro Y and Friedt J.M.
J. Phys. Soc. Jpn. 52(1983)3154

Spin Glass Properties and Magnetic Correlation in $FeTiO_3$-Fe_2O_3 System
Ishikawa Y , Arai M, Kohgi M and Takei H.
J. Magn. & Magn. Mater. 31-34(1983)1381

Magnetism of Iron Interface in Contact with Vanadium
Shinjo T, Hosoito N, Kawaguchi K, Takada T and Endoh Y.
J. Phys. Colloq. (France) 45(1984)C5-361

Re-Entrant Spin-Glass Behavior of the Randomly Mixed Insulating Ferromagnet and Antiferromagnet, Rb_2 $Mn_{(1-x)}Cr_x$ Cl_4
Katsumata K, Tanimoto M, Mitsuda S and Endoh Y.
J. Phys. Soc. Jpn. 53(1984)3315

Magnetic Phase Diagram of MnSi near Critical Temperature Studied by Neutron Small Angle Scattering
Ishikawa Y and Arai M.
J. Phys. Soc. Jpn. 53(1984)2726

Time of Flight Spectrometer with Optical Polarizer for Cold pulsed Neutrons
Endoh Y, Mitsuda S, Ikeda S and Fujimoto H.
Nucl. Instrum. Methods A240(1985)115

Magnetic Properties of Artificial Metallic Superlattices
Shinjo T, Hosoito N, Kawaguchi K, Nakayama N, Takada T and Endoh Y.
J. Magn. & Magn. Mater. 54-57(1985)737

Helicity of the Helical Spin Density Wave in MnSi - II polarized Neutron Diffraction
Ishida M, Endoh Y, Mitsuda S, Ishikawa Y, Tanaka M and Takayashi H.
J. Phys. Soc. Jpn. 54(1985)2975

A New Oxide Spin Glass System of (1-x) $FeTiO_3$-xFe_{23} III. Neutron Scattering Studies of Magnetization Processes in a Cluster type Spin Glass 90 $FeTiO_3$$Fe_2O_3$
Arai M and Ishikawa Y.
J. Phys. Soc. Jpn. 54(1985)795

Neutron Depolarization Studies on Magnetization Process Using Pulsed Polarizing Neutrons
Mitsuda S and Endoh Y.
J. Phys. Soc. Jpn. 45(1985)1570

Stability and Winding of the Long Period Helical Spin Structure in $Fe_{1-x}Co_xSi$
Ishimoto K, Yamaguchi Y, Mitsuda S, Ishida M and Endoh Y.
J. Main. & Magn. Mater. 54-57(1985)1003

A New Oxide Spin Glass System of (1-x) $FeTiO_3$-xFe_2O_3 I. Magnetic PropertiesA New Oxide Spin Glass System of (1-x) $FeTiO_3$-xFe_2O_3 II. Neutron Scattering Studies of a Clu
Ishikawa Y, Saito N, Arai M, Watanabe Y and Takei H.
J. Phys. Soc. Jpn. 54(1985)312

Evidence for the Correlation of the Magnetic Inhomogeneous Structure with the Fluctuation of Chemical Composition in Fe-Ni Invar Alli
Komura S, Takeda T and Endoh Y.
J. Magn. & Magn. Mater. 50(1985)1570

Crystal Chirality and Helicity of the Helical Spin Density Wave in MnSi, II Polarized Neutron Diffraction
Ishida M, Endoh Y, Mitsuda S, Ishikawa Y and Tanaka M.
J. Phys. Soc. Jpn. 54(1985)2975

Magnetic Properties of Fe-V Multi Layered Films with Artificial Superstructures
Hosoito N, Kawaguchi K, Shinjo T, Takada T and Endoh Y.
J. Phys. Soc. Jpn. 53(1985)2659

A New Oxide Spin Glass System of (1-x) $FeTiO_3$-xFe_2O_3 IV. Neutron Scattering Studies on a Re-entrant Spin Glass of 79 $FeTiO_3$21FeO_3 Single Crysta
Arai M , Ishikawa Y and Takei H.
J. Phys. Soc. Jpn. 54(1985)2279

A New Oxide Spin Glass System of (1-x) $FeTiO_3$-xFe_2O_3 II. Neutron Scattering Studies of a Cluster type Spin Glass 90$FeTiO_3$10Fe_2O_3A New Oxide Spin Glass System of (1-x)
Arai M, Ishikawa Y, Saito N and Takei H.
J. Phys. Soc. Jpn. 54(1985)781

Neutron Scattering Study on Artificial Metallic Superlattices
Endoh Y.
Applied Magnetism Seminar. (1986)37-43

Spin Dynamics in a Quasi 2-Dimensional Antiferromagnet $MnTiO_3$
Todate Y, Ishikawa Y, Tajima K, Tomiyoshi S and Takei F.
J. Phys. Soc. Jpn. 55(1986)4464

Magnetic and Transport Properties of Ce_2Sb and Ce_2Bi
Isobe A, Ochiai A, Onodera S, Yamada K, Kohgi M, Endoh Y, Suzuki T and Kasuya T.
J. Magn. & Magn. Mater. 70(1987)391

Small-Angle Scattering of Polarized Neutrons from an $Fe_{65}20^{60}Ni_{35}$ Inver Alloy
Takeda T, Komura S, Miyazaki T, Endoh Y and Itoh S.
J. Magn. & Magn. Mater. 70(1987)431

Monolayer of Ferromagnetic MnSb
Shinjo T, Nakayama N, Moritani I and Endoh Y.
J. Phys. Soc. Jpn. 55(1987)2512

Small-Angle Neutron Scattering from Dynamically Polarized Hydrogenous Materials
Kohgi M, Ishida M, Ishikawa Y, Ishimoto S, Kanno K, Masaike A, Masuda Y and Morimoto K.
J. Phys. Soc. Jpn. 56(1987)2681

Study of ferrofluids by Neutron Depolarization
Itoh S, Endoh Y and Pynn R.
J. Main. & Magn. Mater. 73(1988)L1

Magnetic Excitations in Low-Dimensional Antiferromagnets Measured with the MAX Spectrometer
Tajima K, Todate Y and Ikeda H.
Physica B 156&157(1989)301

Magnetic Excitations in the Two-Dimensional Random Antiferromagnets $Rb_2Co_cNi_{1-c}F_4$
Todate Y, Ikeda H, Sano E, Shibata F, Tajima K and Endoh Y.
J. Phys.: Condens. Matter 1(1989)5895

Neutron Diffraction Studies on Magnetic Properties of Fe/Dy artificial Superstructural Films
Hosoito N, Yoden K, Mibu K, Shinjo T and Endoh Y.
J. Phys. Soc Japan 58(1989)1775

Neutron Depolarization Studies on Reentrant Spin Glass
Mitsuda S, Yoshizawa H and Endoh Y.
submitted to ISSP TECHNICAL REPORT (Phys. Rev. B) (1989)

Long-Period Magnetic Structures along the Axial Direction in the Layered Antiferromagnetic Compound
Ikeda H and Tamura T.
Physica B 156&157(1989)318

Magnetic Phase Transition in $CsVF_4$
Ikeda H, Hidaka M and Wanklyn B. M.
Physica B 160(1990)287

Neutron Diffraction Study in Pulsed High Magnetic Field
Motokawa M, Nojiri H, Uchi M, Watamura S, Kawai H and Endoh Y.
Proc. 11th Meeting Int. Collaboration on Advanced Neutron Sources (KEK, Oct. 22-26 1990) (1990)979

Neutron Scattering at Ultra-Low Temperatures
Kakurai K.
Proc. 11th Meeting Int. Collaboration on Advanced Neutron Sources (KEK, Oct. 22-26 1990)1010

Ordering Kinetics in a Two-Dimensional Percolation Magnet
Ikeda H, Endoh Y and Itoh S.
Physical Review Letters 64(1990)1266

Polarized Neutron Studies of Ferrofluids
Itoh S, Endoh Y and Charles S. W.
submitted to J. Main. & Magn. Mater. (1990)

Small Angle Neutron Scattering Studies on $Fe_{0.715}Al_{0.285}$ Reentrant Spin Glass
Suzuki J, Endoh Y, Arai M, Furusaka M and Yoshizawa H.
J. Phys. Soc. Jpn. 59(1990)718

Neutron Depolarization in Reentrant Spin Glasses $Ni_{1-x}Mn_x$
Mirebeau I, Itoh S, Mitsuda S, Watanabe T, Endoh Y, Hennion M and Calmettes R.
J. Appl. Phys. 67(1990)5232

Measurements of Two-Dimensional Antimagnetic Spin Wave by Using Chopper Spectrometer Installeed in Pulsed Neutron Source
Yamada K, Arai M, Taylor A. D, Hosoya S, Sano A, Nakajima K, Ohoyama K, Kohgi M, Nakane T, Perring T and Endoh Y.
Proc. 11th Meeting Int. Collaboration on Advanced Neutron Sources (KEK, Tsukuba, Oct. 22-26, 1990)1078

Evidence for Antiferromagnetic Coupling between Fe Layers through Cr from Neutron Diffraction
Hosoito N, Araki S and Mibu K.
J. Phys. Soc. Jpn. 59(1990)1925

Crystal Field Excitations in $CeSi_x$

Kohgi M, Satoh T, Ohoyama K, Arai M and Osborn R.
Physica B 163(1990)137

Anomalous Region in the Magnetic Phase Diagram of (Fe, Co) Si

Ishimoto K, Yamauchi H, Yamaguchi Y, Suzuki J, Arai M, Furusaka M and Endoh Y.
J. Magn. & Mang. Mater. 90&91(1990)163

Neutron Depolarization Studies on Reentrant Spin Glass AuFe Alloy

Mitsuda S, Yoshizawa H, Watanabe T, Itoh S, Endoh Y and Mirebeau I.
submitted to ISSP TECHNICAL REPORT (J. Phys. Soc. Japan) (1990)

Magnetic Excitations in Mn_3Pt at high energies by the TOF Method

Tomiyoshi S, Yasui H, Kaneko T, Yamaguchi Y, Ikeda H, Todate Y and Tajima K.
J. Main. & Magn. Mater. 90&91(1990)203

Neutron Depolarization in a Reentrant Spin-Glass System: Amorphous Fe-Mn

Mirebeau I, Itoh S, Mitsuda S, Watanabe T, Endoh Y, Hennion M and Papoular R.
Phys. Rev. B 41(1990)11405

Crystal Field Excitations in Yb Monopnictides

Kohgi M, Ohoyama K, Oyamada A, Suzuki T and Arai M.
Physica B 163(1990)625

Neutron Scattering in Yb Monopunictides

Ohoyama K, Kohgi M, Nakane T, Arai M, Taylor A.D and Oyamada A.
Proc. Int. Conf. Neutron Scattering (Oxford, 27-30 Aug. 1991), P1-A-81, Physica B

Neutron Depolarization Studies on Mesoscopic Magnetism

Endoh Y, Itoh S, Watanabe T and Mitusda S.
Proc. Int. Conf. Neutron Scattering (Oxford, 27-30 Aug. 1991), S3-C-1, Physica B

Magnetic Excitation in Highly Diluted Magnets

Ikeda H and Ohoyama K.
Proc. Int. Conf. Neutron Scattering (Oxford, 27-30 Aug. 1991), P1-A-72, Physica B

Magnetic Excitations in Isolated Clusters of a Diluted Heisenberg Magnet Rb $Mn_{0.15}Mg_{0.85}F_3$

Takahashi M, Ikeda S and Ikeda H.
J. Phys. Soc. Jpn. 60(1991)387

Neutron Scattering Studies of CeTSn (T=Ni, Pb)

Kohgi M, Ohoyama K, Osakabe T and Kasaya M.
J. Main. & Magn. Mater. (1991)

Two Dimensional Antiferromagnetism and Spin Dynamics in "2-1-4" Oxides

Yamada K, Arai M, Birgeneau R.J, Endoh Y, Hosoya S, Kakurai K, Kastner M.A, Matsuda M, Nakajima K, Shirane G, Taylor A.D, and Thurston T.R.
Proc. Int. Conf. Neutron Scattering (Oxford, 27-30 Aug. 1991), S4-C-2, Physica B

Neutron Diffraction Study of $PrCo_2Si_2$ in Pulsed High Magnetic Field

Nojiri H, Uchi M, Watamura S, Motokawa M, Kawai H, Endoh Y and Shigeoka T.
J. Phys. Soc. Jpn. 60(1991)2380

Magnetic Excitations in Mn_3Pt

Tomiyoshi S, Kaneko T, Steigenberger U, Chappell A.J, Hagen M and Todate Y.
Proc. Int. Conf. Neutron Scattering (Oxford, 27-30 Aug. 1991), P1-A-66, Physica B

Dynamical process of Disordering in a Percolation magnet under Random Fields

Itoh S, Ikeda H, Suzuki T and Endoh Y.
J. Phys. Soc. Jpn. 60(1991)3238

Kinetics of Ordering in the Percolation Magnet

Ikeda H.
Presented at Int. Symp. Slow Dynamics in Conclensed Matter (Fukuoka, Nov. 4-8, 1991)

Competition between the Kondoh Effect and RKKY Interactions in $CeSi_x$
Kohgi M, Satoh T, Ohoyama K and Arai M.
Physica B 169(1991)501

Anomalous Crystal Field Splitting in YbN
Ohoyama K, Kohgi M, Osakabe T, Arai M, Taylor A.D, Oyamada A and Suzuki T.
Physica B (1991)

Crystal Field Excitations in $Ce(Zn_{1-x}Cu_x)_2$
Kohgi M, Osakabe T, Ohoyama K and Kitai T.
J. Main. & Magn. Mater. (1991)

Complete Two-Dimensional Antiferromagnetic Spin-Wave Disperison Relation of La_2NiO_4 Determined by Chopper Spectrometer Installed at the Pulse Nuetron Source
Yamada K, Arai M, Endoh Y, Hosoya S, Nakajima K, Perring T and Taylor T.D.
J. Phys. Soc. Jpn. 60(1991)1197

High Energy Spin-Waves in the Chain Antiferromagnet $KFeS_2$
Welz D, Arai M, Nishi M, Kohgi M and Endoh Y.
Proc. Int. Conf. Neutron Scattering (Oxford, 27-30 Aug. 1991), S1-C-3, Physica B

Dynamics of Percolation Magnets with Fractal Geometry
Ikeda H, Itoh S and Takahashi M.
Proc. Int. Conf. Neutron Scattering (Oxford, 27-30 Aug. 1991), S2-A-4, Physica B

Neutron Scattering Study of CeNiSn
Kohgi M, Ohoyama K, Osakabe T, Kasata M, Takabatake T and Fujii H.
Physica B (1992)

Pressure Dependence of the Crystal Field State of a Low Carrier System CeP
Kohgi M, Osakabe T, Mori N, Takahashi H, Okayama Y, Yoshizawa H, Ohora Y, Ikeda S, Suzuki T and Haga Y
Physica B (1992)

Neutron Scattering Studies of Ce $(Zn_{1-x}Cu_x)_2$
Osakabe T, Kohgi M, Ohoyama K and Kitai T.
Physica B (1992)

Crystal Field levels in YbBiPt
Robinson R. A, Kohgi M, Osakabe T, Canfield P. C, Kamiyama T, Nakane T, Fisk Z and Thompson J. D.
Physica B (1992)

Spin Dynamics of YbX (X=N, P, As)
Ohoyama K, Kohgi M, Otomo T, Osakabe T, Oyamada A and Suzuki T.
Physica B (1992)

Neutron Diffraction on Metamagnetic $PrCo_2Si_2$ in Pulsed High Magnetic Fields
Motokawa M, hojiri H and Endoh Y.
Physica B 177(1992)279

Neutron Diffraction Experiment in Pulsed High Magnetic Fields
Nojiri H, Motokawa M, Nishida N and Endoh Y.
Physica B 180&181(1992)31

Polarized Neutron Diffraction Studies of Fe/Cr Multilayered Films with Giant Magnetoresistance Effect
Hosoito N, mibu K, Araki S, Shinjo T, Itoh S and Endoh Y.
J. Phys. Soc. Jpn. 61(1992)300

Coexistence of Ising Cluster Excitations and Intra-Culuster Exciations in Diluted Ising Magnets
Ikeda H and Ohoyama K.
Phys. Rev. Lett. (1992)

Spin Reorientation in Fe/Nd Multilayered Films from Neutron Diffraction Experiments
Hosoito N, mibu K, Shinjo T and Endoh Y.
J. Phys. Soc. Jpn. 61(1992)2477

Reentrant Spin Glass Properties of $Ni_{77}Mn_{23}$Studied by Neutron Depolarization Analysis
Sato T, Ando T, Watanabe T, Ito S and Endoh Y.
J. Magn. Magn. Mater. 104-107(1992)1625

Small Angle Scattering on Reentrant Spin Glass $Fe_{1-x}Al_x$
Suzuki J, Endoh Y and Arai M.
J. Main. & Magn. Mater. 104(1992)1657

8. Dynamics in Solids and Liquids

The Local Environment around Hydrogen Atoms in Hydrogenated $NiTi_2$ Alloy Glass
Kai K, Ikeda S, Fukunaga T, Watanabe N and Suzuki K.
Physica 120B(1983)342

High-Q Neutron Scattering with the Resonance Detector Neutron Spectrometer RAT at the Pulsed Spallation Neutron Source KENS
Rauh H and Watanabe N.
Presented at Symp. Neutron Scattering (Berlin, Aug. 6-8, 1984)

Determination of the Momentum Distribution of Scattering Particles from High Q Scattering Spectra of a Resonance Detector Neutron Spectrome
Rauh H and Watanabe N.
Nucl. Instrum. Methods 228(1984)147

Neutron Compton Spectroscopy of Pyrolitic Graphite
Rauh H and Watanabe N.
Phys. Lett. 100A(1984)244

Low Energy Excitations in Ag_3SI
Shibata K and Hoshino S.
J. Phys. Soc. Jpn. 54(1985)3671

Neutron Scattering from Superfluid ^4He at Very Large Momentum Transfer
Ikeda S and Watanabe N.
Phys. Lett. A 121(1987)34

Phonons in $(La_{1-x}Sr_x)_2CuO_4$ and $BaPb_{1-x}BixO_3$
Masaki A, Satoh H, Uchida S, Katsuzawa K, Tanaka S and Inoue K.
Jpn. J. Appl. Phys. 26(1987)L405

Local Modes and Hydrogen Potential in Metal Hydrides
Ikeda S and Watanabe N.
J. Phys. Soc. Jpn. 56(1987)565

Low Energy Excitation Measurement on Epoxy Resin: The Possibility of Fracton and Phonon-Assisted Migration
Arai M and Jorgensen J. E.
Phys. Lett. A 133(1988)70

Copper and Oxygen Vibrations in La_2CuO_4 and $YBa_2Cu_3O_7$
Ikeda S, Misawa M, Tomiyoshi S, Suzuki T and Omori M.
Phys. Lett. A 134(1989)191

Low-Energy Excitation in b-Cu_2Se
Sakuma T and Shibata K.
J. Phys. Soc. Jpn. 58(1989)3061

Hydrogen Wave Functions in the Metal Hydrides ZrHz and $NbH_{0.3}$
Ikeda S, Furusaka M, Fukunaga T and Taylor A.D.
J. Phys. Condens. Matter 2(1990)4675

Dynamic Structure of Molten $0.80RbNO_3$-$0.20Sr(NO_3)_2$ Mixture by Neutron Quasielastic Scattering
Shibata K, Kamiyama T, Suzuki K and Inoue K.
J. Non-Cryst. Solids 117/118(1990)120

Low-Energy Excitation in Copper Ion Conductors
Sakuma T, Shibata K and Hoshino S.
Solid State Ionics 40/41(1990)337

Rotatinal Tunneling and LAM-80ET
Ikeda S, Watanabe N, Inoue K, Kiyanagi Y, Inaba A, Takeda S, Kanaya T, Shibata K, Kamiyama T, Izumi Y, Ozaki Y and Carlile C.
Proc. Int. Conf. Neutron Scattering (Oxford, 27-30 Aug. 1991), P3-B-113, Physica B

High Resolution Neutron Spectrometer LAM-80ET and Rotational Tunneling in 4-Methylpyridine N-Oxide
Ikeda S, Watanabe N, Inoue K, Kiyanagi Y, Izumi Y, Ozaki Y and Carlile C.J.
J. Phys. Soc. Jpn. 60(1991)3340

High Resolution S(Q,w) Measurement on g-SiO_2
Arai M, Hannon A.C, Wright A.C, Sinclair R.N, Misawa M, Price D.L and Taylor A.D.
Proc. Int. Conf. Neutron Scattering (Oxford, 27-30 Aug. 1991), S4-B-1, Physica B

Isotope Effects in Hydrogen-Bonded Crystal KH_2PO_4
Sugimoto H and Ikeda S.
Phys. Rev. Lett. 67(1991)1306

Phonon Density of States of Super-and Non-Superconducting States in $La_{1.85}Sr_{0.15}Cu_{1-x}Zn_xO_4$ (x=0, 0.02)
Arai M, Yamada K, Hidaka Y, Taylor A.D and Endoh Y.
Physica C 181(1991)45

Phonon Density of States of $La_{1.85}Sr_{0.15}Cu_{1-x}Zn_xO_4$ (x=0, 0.02)
Arai M, Yamada K, Taylor A.D, Endoh Y and Hidaka Y.
Proc. Int. Conf. Neutron Scattering (Oxford, 27-30 Aug. 1991), P3-A-38, Physica B

Incoherent Inelastic Neutron Scattering from Hydrogen-Bonded Compound KH_2PO_4
Shibata K and Ikeda S.
J. Phys. Soc. Jpn 61(1992)411

Local Dynamics of cis-1.4-Polybutadiene near the glass Transition Temperature Tg
Kanaya T, Kawaguchi T and Kaji K.
Physica B 182(1992)403

Dynamical Properties of Solutions of $LiNO_3$ in (1, 3)-Diaminopropane in the Liquid and Glassy States
Hayashi H, Kamiyama T, Nakamura Y and Izumi Y.
J. Non-Cryst. Solids 150(1992)297

The Polycarbosilane-to-Si_xC_{1-x} conversion Studied by Inelastic Neutron scattering and Infrared Absorption
Suzuya K, Shibata K, Okamura K and Suzuki K.
J. Non-Cryst. Solids 150(1992)255

A Coherent Quasielastic Neutron Scattering Study of NO_3^- Ion Motion in Molten $RbNO_3$
Kamiyama T, Shibata K and Suzuki K.
J. Non-Cryst. Solids 150(1992)292

Neutron Scattering from Hydrogen Bonded Compounds KH_2PO_4, PbH_2PO_4 and $PbHPO_4$
Shibata K and Ikeda S.
J. Phys. Soc. Jpn. (1992)

Low-Energy Excitation in CuI
Sakuma T, Shibata K and Hoshino S.
Solid State Ionics 53-56(1992)1278

9. Materials Science

Influence of Microstructure on the Flux Pining in Nb-Ti Multifilamentary Superconducting Wires
Gotoda H, Osamura K, Furusaka M, Arai M and Suzuki J.
Phil. Mag. B 60(1989)819

10. Polymers

Compensation Point in Semi-Dilute Polymer Solutions as Observed by SANS
Okano K, Kurita K, Nakajima S, Wada E, Furusaka M and Ishikawa Y.
Physica 120B(1983)413

Folding-Unfolding of alpha-Lactalbumin
Izumi Y, Miyake Y, Kuwajima K, Sugai S, Inoue K, Iizumi M and Katano S.
Physica 120B(1983)444

Molecular Spectroscopy of Polymers by Neutron Inelastic Scattering
Kaji K, Kanaya T and Inoue K.
Proc. 1st SPSJ Int. Polymer Conf. (Kyoto, Aug. 20-24, 1984)288

Local Motion of Polymers in the Rubbery State Studied by Neutron Quasielastic Scattering
Kanaya T, Kaji K, Kitamaru R and Inoue K
Proc. 1st SPSJ Int. Polymer Conf. (Kyoto, Aug. 20-24, 1984)237

Neutron Inelastic Scattering Spectra of Native and Regenerated Celluloses
Kaji K, Kanaya T, Inoue K, Kitamaru R and Sakurada I.
Cellulose Chem. Tehnol. 19(1985)321

Coexistence Curve of Semidilute Polymer Solutions
Okano K, Ichimura T, Kurita K, and Wada E.
Polymer 28(1987)693

Monoclinic to Orthorhombic Transformation in Polyethylene
Takahashi Y, Ishida T and Furusaka M.
J. Polym Sci. Poly. Phys. (1988)

Quasielastic Neutron Scattering from Amorphous Polymers above Glass Transition Temperature
Inoue K, Kanaya T, Kaji K, Kiyanagi Y and Shibata K.
J. Phys. Soc. Japan 57(1988)2862

Low-Energy Excitations in Polyethylene: Comparison between Amorphous and Crystalline Phases
Kanaya T, Kaji K, Ikeda S and Inoue K.
Chem, Phys. Lett. 150(1988)334

Low Energy Excitations in Amorphous Polymers
Kanaya T, Kaji K and Inoue K.
Int. Conf. Polymer Research by Neutron Scattering (The Taniguchi Conference, Kyoto, 1989)119

Vibrational Modes of trans-1, 4-Polychloroprene by Neutron Incoherent Inelastic Scattering
Kanaya T, Ohkura M and Kaji K.
Bull. Inst. Chem. Res. Kyoto Univ. 60(1989)68

Sol-Gel Transition of Atactic Polystyrene Solutions
Izumi Y.
Int. Conf. on Polymer Research by Neutron Scattering. The Taniguchi Conference (Kyoto, Nov. 7-9, 1989)155

Structure and Dynamics of Polyelectrolyte Solutions
Kaji K, Kanaya T, Urakawa H, Kitamaru R, Higgins J. S. and Gabrys B.
Int. Conf. on Polymer Research by Neutron Scattering. The Taniguchi Conference (Kyoto, Nov. 7-9, 1989) (1989)27

Thermoreversible Gelation of the System of Atactic Polystyrene-Carbon Disulfide. VIII
Izumi Y, Katano S, Funahashi S, Furusaka M and Arai M.
Repts. Prog. Polym. Phys. Jpn. 33(1990)15

Low-Energy Excitations in Amorphous Polymers
Inoue K, Kanaya T, Ikeda S, Kaji K, Shibata K, Misawa M and Kiyanagi Y.
J. Chem. Phys. 95(1991)5332

Structural Study on the Sol-Gel Transition of Atactic Polystyrene in Carbon Disulphide
Izumi Y, Katano S, Funahashi S, Furusaka M and Arai M.
Proc. Int. Conf. Neutron Scattering (Oxford, 27-30 Aug. 1991), P1-B-112, Physica B

Local Motions of cis-1.4-Polybutadiene in the Melts. A Quasiclastic Neutron-Scattering Study
Kanaya T, Kaji K and Inoue K.
Macromolecules 24(1991)1826

Dynamics of Polyethylene Studied by High Resolution Nuetron Spectrometer LAM-80ET
Kanaya T, Kaji K, Inoue K, Ikeda S, Shibata K, Izumi Y, Kamiyama T and Furusaka M.
J. Phys. Soc. Jpn, 61(1992)1984

Quasielastic Neutron Scattering on the Sol-Gel-Glass Transition of Atactic Polystyrene in Carbon Disulphide
Izumi Y, Kanaya T, Shibata K and Inoue K.
Physica B 180&181(1992)542

Dynamics of Polymers in the Bulk State by Neutron Scattering
Kanaya T, Kaji K, Kawaguchi T and Inoue K.
Bull. Inst. Chem. Res. Kyoto Univ. 70(1992)236

Conformation of Atactic Polystyrene in Carbon Disulphide Observed at a Low Temperature
Izumi Y, Katano S, Funahashi S, Furusaka M and Arai M.
Physica B 180&181(1992)539

Small Angle Neutron Scattering from Poly (vinyl alcohol) Gels
Kanaya T, Ohkura M, Kaji K, Furusaka M, Misawa M, Yamaoka H and Wignall G. D.
Physica B 180&181(1992)549

Low Energy Excitations in Amorphous Polystyrene
Kanaya T, Kaji Kand Inoue K.
Physica B 180&181(1992)814

Tanaka I, Niimura N, Miyaji I, Kataoka M and Heenan R. K.
Int. Symp. on Molecular Structure and Life, Yokohama, Dec. 1991

11. Biology

Small Angle Neutron Scattering Studies of the Structure of Nucleosome Cores at Low Ionic Strength
Mita K, Zama M, Ichimura S, Niimura N, Kaji K, Hirai M and Ishikawa Y.
Physica 120B(1983)436

Studies of Constrained Dynamics of the Phase Transition in the Artificial Bilayer Membrane of Dialkyl Ammonium Amphiphile by Quasielastic Neutron Scatter
Ito Y, Shigekawa N, Harada M, Inoue K, Boni P.
J. Phys. Soc. Jpn. 52(1987)2060

Interparticle Interactions and Structural Change of Nucleosome Core Particles in Low-Salt Solution
Hirai M, Niimura N, Zama M, Mita K, Ishimura S, Tokunaga F and Ishikawa Y.
Biochemistry 27(1988)7924

Small Angle Thermal Neutron Scattering of Hen Egg-White Lysozyme in Aqueous Solution
Nimura N and Sungawa U.
Proc. Int. Conf. Neutron Scattering (Oxford, 27-30 Aug. 1991), P3-B-130, Physica B

Structure Study of Phosphatidylinositol Diphosphate and Bovine Scrum Albumin Complex
Niimura N, Mikami K and Hayashi K.
Proc. Int. Conf. Neutron Scattering (Oxford, 27-30 Aug. 1991), P3-B-129, Physica B

12. Non-Equilibrium Systems

Spinodal Decomposition in Fe-Cr Alloys Studied by Small Angle Neutron Scattering
Furusaka M, Ishikawa Y, Yamaguchi Y and Fujino Y.
Physica 120B(1983)383

Early Stage of Phase Separation Processes in FeCr and AlZn Alloys
Furusaka M, Ishikawa Y and Mera M.
Phys. Rev. Lett. 54(1985)2611

Studies on Early and Late Stages of Formation of d'Phase in Al-Li Alloys by Neutron Small Angle Scattering
Fujikawa S, Furusaka M, Sakauchi M and Hirano K.
J. Phys. C3(1987)365

The Very Early Stage of Phase Separation Process in Al-Li Alloys Studies by Small-Angle Neutron Scattering
Furusaka M, Fujikawa S, Sakauchi M and Hirano K.
Proc. Int. Symp. on Dynamics of Ordering Process in Condensed Matter (Kyoto, Aug. 27-30, 1987)281

Computer Simulations of Domain Growth under Shear Flow
Ohta T, Nozaki H and Doi M.
Phys. Lett. A 145(1990)304

Phase Separation of Al-Li Alloys Studied by Small Angle Neutron Scattering
Fujikawa S, Furusaka M.
Proc. Int. Conf. on Recent Advances in Science and Engineering of Light Metals (1991, Sendai)965

13. Nuclear Physics

Present and Future of Spin Physics at KEK
Masaike A.
Proc. 7th Int. Symp on High Energy Spin Physics (Serpukhov, USSR, Sept. 1986)

Parity Non-Conserving Effect in the Neutron Radiative Capture Reaction
Masuda Y, Adachi T, Ishimoto S, Kikutani E, Koiso H, Morimoto K and Masaike A.
Hyperfine Interactions 34(1987)143

Feasibility Study of a Strong Ultra Cold Neutron Source
Yoshiki H and Ishimoto S.
Z. Phys. B-Condensed Matter 67(1987)161

Helicity Dependence of Neutron Radiative Capture Reactions
Masuda Y, Adachi T, Ishimoto S, Masaike A and Morimoto K.
Proc. Test of Time Reversal Invariance in Neutron Physics (Chapel Hill, Apr. 17-19, 1987), World Scientific191

Neutron Scattering by Inhomogenous Distribution of Proton Polarization Produced by the Dynamic Nuclear Polarization
Masuda Y.
Hyperfine Interactions 35(1987)1071

Measurement of Longitudinal Asymmetry in Neutron Radiative Capture Reactions
Masuda Y, Adachi T, Ishimoto S, Kikutani E, Kohgi M, Koiso H, Masaike A and Morimoto K
Proc. PANIC '87 (Kyoto, Apr. 20-24, 1987), Nucl. Phys. A478(1988)737C

From Ultracold Antineutrons to Neutron Spin Echo- the Bootstrap offers Significant gains in Sensitivity
Golub R, Yoshiki H and Gaehler R.
Nucl. Inst. and Methods in Phys. Research A284(1989)16

Enhancement of Parity-Violating Effect in Neutron-Nucleus Interaction
Masuda Y.
Proc. 17th INS Int. Symp. on Nuclear Physics at Intermediate Energy (Nov. 15-17, 1988 Tokyo, World Scientific)424

Longitudinal Asymmetry in Neutron Radiative Capture Reaction of ^{139}La
Masuda Y, Adachi T, Masaike A and Morimoto K.
Nuclear Physics A504(1989)269

Parity Violation in Neutron Capture Reaction
Masuda Y.
A.I.P. Conf. Proc. the 8th Int. Symp. on High Energy Spin Physics (Univ. of Minnesota, Minneapolis, Sep. 12-17, 1988)482

P- and T-violation in Slow- Neutron Scattering
Masuda Y.
Proc. The XXIII Yamada Conf. on Nuclear Weak Process and nuclear Structure (June 12-15, 1989, Osaka, World Scientific)151

Ultra-Cold-Anti-Neutron (UCN): (I), The Approach to the Semi-Classical Limit
Golub R and Yoshiki H.
Nucl. Physics A501(1989)869

Lanthanum Nuclear Polarization for T-violation Experiment
Masuda Y, Adachi T, Ishimoto S, Masaike A, Morimoto K and Shimizu H.M.
Proc. 11th Meeting Int. Collaboration on Advanced Neutron Sources (KEK, Oct. 22-26 1990)1002

T Violation in Neutron-Nucleus Interaction
Masuda Y.
Proc. Int. Workshop on Polarized Ion Sources and Polarized Gas Jets KEK Report 90-15 (Feb. 12-17, 1990, KEK)249

P-Violation and T-Violation Experiments on Neutron-Nucleus Interaction at KEK
Masuda Y.
Proc. the VI Int. School on Neutron Physics (Alushta, USSR, Oct. 8-18, 1990)

Scintillation Detector System in Neutron-Nucleus Experiments
Shimizu H. M, Adachi T and Masuda Y.
Proc. 11th Meeting Int. Collaboration on Advanced Neutron Sources (KEK, Oct. 22-26 1990)937

Present Status of P Violation and Future T Violation Experiments on Neutron-Nucleus Interaction at KEK
Masuda Y, Adachi t, Ishimoto S, Masaike A, Morimoto K and Shimizu H.M.
Proc. The 18th INS Int. Symp. on Physics with High-Intensity Hadron Accelerators (Tokyo, Mar. 14-16, 1990)

Parity-Non-Conservation in Neutron Radiative Capyure Reaction
Adachi T, Masaike A, Masuda Y, Morimoto K and Shimizu H.M.
Proc. 4th Conf. the Intersections between Particle and Nuclear Physic, (Tucson, Arizona, May 24-29, 1991)

A Resonance Spectrometer without Doppler Broadening
Masuda Y, Adachi T and Shimizu H.M.
Proc. Int. Conf. Neutron Scattering (Oxford, 27-30 Aug. 1991), P3-B-167, Physica B

T-Violation Neutron Experiment and Polarized ^{3}He
Masuda Y, Asahi K, Kura J, Mori Y, Sato H and Shimizu H.M.
Hyperfine Interactions149

Longitudinal Asymmetry and γ-ray Angular Distribution in Neutron Radiative Capture Reactions
Shimizu H.M, Adachi T, Ishimoto S, Masaike A, Masuda Y and Morimoto K.
Nucl. Phys. A. (1992)

Neutron Polarization for P- and T-Violation Experiments
Masuda Y, Adachi T, Asahi K, Doi M, Iimura M, Ishimoto S, Masaike A, Matsuda Y, Moritomo K, Mori Y, Sakai K, Sato H, Simizu H.M and Jian J
Riken Int. Symp. "Unstable Nuclei and Particles as Probes in Physics and Chemistry", (Wako, Saitama, Aug. 31-Sept. 2, 1992)

Parity Nonconservation in Neutron Radiative Capture Reactions
Shimizu H. M.
Memories of the Faculty of Science, Kyoto Univ. Series A of Physics, Astrophysics, Geophysics and Chemistry XXXVIII(1992)203

Polarized ^{3}He System for T- and P-Violation Neutron Experiments
Sato H, Masuda Y, Sakai K, Doi M, Asahi K, Jian Z.Z, Mori Y, Delheij P.P.J, Matsuda Y, Iinuma M, Shimizu H.M and Masaike A
Riken Int. Symp. "Unstable Nuclei and Particles as Probes in Physics and Chemistry", (Wako, Saitama, Aug. 31-Sept. 2, 1992)

Neutron Spin Rotation and P-Violation
Sakai K, Masuda Y, Sato H, Doi M, Asahi K, Jian Z.Z, Matsuda Y, Shimizu H.M, Iinuma M and Masaike A.
Riken Int. Symp. "Unstable Nuclei and Particles as Probes in Physics and Chemistry", (Wako, Saitama, Aug. 31-Sept. 2, 1992)

Neutron Spin as a Probe Concerning P- and T-Violation
Masuda Y, Adachi T, Asahi K, Doi M, Ishimoto S, Masaike A, Matsuda Y, Morimoto K, Mori Y, Sakai K, Sato H, Shimizu H.M and Jian Z.
Proc. III Int. Symp. "Weak and Electromagnetic Interactions in Nuclei", (JINR, Dubna, Russia, 16-22 June, 1992)

Phase Separation kinetics of Binary Systems: Effects of hydrodynamic Interaction and Surfactants
Kawasaki K, koga T and Kawakatsu K.
Proc. of the MRS Fall Meeting 1991

14. Theories (Condensed Matter)

Hybrid Models for the Dynamics of an Immiscible Binary Mixture with Surfactant Molecules
Kawakatsu T and Kawasaki K.
Physica A 167(1990)690

Computer Simulation of Domain Growth under Shear Flow
Ohota T and Nozaki H.
Phys. Lett. A 145(1990)304

Ostwald Ripening in Open Systems
Nakahara A, Kawakatsu T and Kawasaki K.
J. Chem. Phys. 95(1991)4407

Dynamics of Ordering Processes in Immiscible Binary Mixtures with a Surfactant. II. Analytical Treatments
Kawakatsu T and Kawasaki K.
J. Colloid and Interface Science 145(1991)420

Computer Experiments of Systems Containing Surfactants
Kawakatsu T and Kawasaki K.
Molecular Dynamics Simulations; Proc. Taniguchi Int. Symp. (1991)

Dynamics of Ordering Processes in Immiscible Binary Mixtures with a Surfactant. I. Computer Experiments
Kawakatsu T and Kawasaki K.
J. Colloid and Interface Science 145(1991)413

A Monte Carlo Study of Phase Separation Processes in Immiscible Binary Mixtures with a Surfactant
Kawakatsu T and Kawasaki K.
J. Colloid and Interface Science 148(1992)23

Molecular Dynamics Simulations of Phase Separation Processes of Binary Soft Sphere Fluid Mixtures Containing Amphiphilic Block Copolymers
Kawakatsu T and Kawasaki K.
J. Chem. Phys.

Equilibrium Shape of Two-component Unilamellar Membranes and Vesicles
Andelman D, Kawakatsu T and Kawasaki K.
Europhys. Lett.

Phase Transitions in Binary Systems in the Presence of Amphiphilic Molecules
Kawakatsu T and Kawasaki K.
"From Phase Separations to Chaos" (World Scientific)

15. Theories (Nuclear Physics)

On the Value of V_{ud} from the Kobayashi-Maskawa Matrix
Gudkov V. P.
KEK Preprint 90-171 (1990)

About the Resonance Approximation in Nuclear Induced Reactions
Gudkov V.P.
Z. Phys. A-Hadronsand Nuclei 340(1991)1

Parity Violation in Neutron Induced Reactions
Gudkov V. P.
KEK Report 91-2

On CP-Violation in Nuclear Reactions
Gudkov V. P.
Phys. Rep. 212(1992)77

Recoil Effects and CP-Violation in Neutron Scattering
Gudkov V. P.
Phys. Rev. C 46(1992)357

Sign Correlations and the Mechanism for Parity Violation
Gudkov V. P.
Phys. Rev. C (1992)

The In-medium Behavior of the QCD θ-Term and the Value of CP Violation in Nuclei
Gudkov V. P.
Phys. Rev. C (1992)

The Weinberg Gluonic Operatof and The CP-Odd Nucleon Coupling Constant
Gudkov V. P.
J. Phys. A (1992)

16. Publications in Japanese

Pulsed Neutron Source and KENS Project
Watanabe N.
J. Cryst. Soc. Jpn. 21(1979)151

Chemistry of High-Tc Superconductivity
Izumi F.
J. Jpn. Marine Soc. 704(198)36

Pulsed Spallation Neutron Source and Neutron Scattering at KEK
Watanabe N, Sasaki H and Ishikawa Y.
J. At. Energy Soc. Jpn. 23(1981)389

Neutron Position Sensitive Detector using ^{6}Li-glass Scintillator
Niimura N.
J. Cryst. Soc. Jpn. (1982)396

Sealing with Gasket and Flanges of Superfluid Helium II
Ishimaru H and Yoshiki H.
Cryogenic Eng. 17(1982)222

Neutron Scattering Studies on Biological materials (I), (II), (III), (IV)
Niimura N and Kaji H.
Chemistry and Biology 21(1983)250,328,405,466

Neutron Scattering Instruments at National Laboratory for High Energy Physics
Watanabe N.
J. Cryst. Soc. Jpn. 26(1984)294

Neutron Scattering Instruments at National Laboratory for High Energy Physics
Watanabe N.
J. Cryst. Soc. Jpn. 26(1984)294

Construction of High Gradient Permanent Quadrupole Magnets for 400MHz Linac
Kumada M, Baba H, Inagaki S, Kaneko N and Sasaki H.
Proc. 9th Meeting on Linear Accelerator (Kyoto, July 20-22, 1984)42

Neutrons in Biology
Niimura N.
Gekkan Physics 5(1984)96

Neutron Scattering Facility at National Laboratory for High Energy Physics
Watanabe N and Ishikawa Y.
Butsuri 39(1984)826

Operation of a Superfluid Ultra-cold Neutron Converter
Yoshiki H.
KEK Report 84-2 (1984)

Chemical Short-range Structure of Amorphous Metals
Fukunaga T and Suzuki K.
Gekkan Physics 5(1984)209

High Intensity Proton Synchrotron GEMINI and Intense Pulsed Neutron Source KENS-II
Sasaki H and Watanabe N.
Spallation Neutron Engineering, Atomic Energy Society Japan (1984)173

Generation and Utilization of Ultra-Cold Neutrons, Application in Condensed Matter Research and Elementary Particle Physics
Utsuro M and Yoshiki H.
Gekkan Physics 5(1984)135

Structural Studies of Materials by Neutron Diffraction
Horiuchi H and Kawada I.
Ceramics 19(1984)658

Recent Trend of Neutron Scattering Research
Ishikawa Y.
Gekkan Physics 5(1984)68

Pulsed Neutron Source and its Utilization in Condensed Matter Research
Watanabe N.
Gekkan Physics 5(1984)127

Spin Glasses in Dense Random System
Ishikawa Y.
Solid State Phys. 20(1985)229

Accelerator Based Cold Neutron Source and Cryogenic System
Inoue K, Yanai M and Ishikawa Y.
Cryogenic Eng. 20(1985)63

Direct Observation of Bose Condensation in ^{4}He-II by Neutron Scattering with Very Large Momentum Transfer
Watanabe N and Ikeda S.
Butsuri 40(1985)283

Neutron Sources Using Proton Accelerators and Their Utilization
Watanabe N.
Nuclear Engineering 32,3(1986)20

Short-Range tructure of Amorphous Metals and Oxide Glasses
Suzuki K.
New Glass Technology 5(1986)8

Determination of Water Structure and Inelastic Scattering Effect by Time-of-Flight Neutron Diffraction
Kameda Y and Ishikawa K.
J. Chem Soc. Jpn. 11(1986)1509

Partial Structure of Amorphous Metal
Fukunaga T.
J. Jpn. Inst. Met. 26(1987)481

Neutron Scattering (Topics:New Progress in High Tc Superconductor III)
Endoh Y.
Parity 2(1987)48

Rietveld Analysis of the High-T_c Superconductor $Ba_2YCu_3O_{7-x}$
Izumi F and Asano H.
Oyo-Butsuri 56(1987)1053

Research in Magnetism by Polarized Neutrons
Endoh Y.
Solid State Phys. 22(1987)117

High Tc Superconductor $YBa_2Cu_3O_{7-\delta}$ Observed by Pulsed Neutrons
Asano H, Izumi F and Watanabe N.
Butusuri 42(1987)901

Crystal Structire of the High-Tc Oxide Superconductor
Asano H and Izumi F.
J. Jpn. Inst. Met. 26(1987)950

Crystal Chemistry of Compounds with the Oxygen-Deficient Triperovskite Structure
Izumi F and Asano H.
Kagaku to Kogyo 40(1987)1000

Crystal Structure of High Tc Superconductor
Izumi F and Asano H.
Chemistry Today Nov.(1987)16

Gelation of Polymer Chains — Solid-Gel Transition —
Izumi Y and Miyake Y.
Butsuri 42(1987)327

Crystal Structure of High Tc Superconductors and Related Compounds
Izumi F and Nakai I.
J. Cryst. Soc. Jpn. 29(1987)365

Generation of Shortly Bunched Proton Beam for Pulsed Muon Facility in Japanese Hadron Project
Sasaki H.
JHP-13 (Dec. 1988), Institute of Nuclear Study, Univ. of Tokyo (1988)

Crystal Structure of High Tc Superconductor
Asano H.
Huntai oyobi Hunmatsuyakin 35(1988)301

Oxygen Distribution in High Tc Superconductors Observed by Neutrons
Watanabe N.
Parity 3(1988)42

Neutron Scattering for Industrial Application
Watanabe N.
Mirai-Sangyo Gijutsu IV, Kagaku-gijutsu Koho Zaidan (1988)1092

Recent Status of Neutron Scattering Facility at National Laboratory for High Energy Physics
Watanabe N.
J. Cryst. Soc. Jpn. 30(1988)223

Particle Physics by Ultra Low Energy Neutrons
Masaike A and Masuda Y.
Butsuri 44(1989)649

Amorphization by Milling and its Atomic Structure
Fukunaga T.
J. Adv. Sci. 1(1989)46

New Data Acquisition System at KENS Pulsed Neutron Source
Arai M and Furusaka M.
BUTSURI 44(1989)664

Is Epoxy Resin Fractal? -Measurement of Fractal Dimension by Pulsed Neutron Scattering-
Arai M.
Butsuri 44(1989)106

Structure and Dynamic Properties of Liquid Water in Micropores
Yamaguchi T.
Denki Kagaku 57(1989)632

Polarizer for Epithermal Neutrons : Development in New Field of Nuclear Physics, Particle Physics, Condensed Matter Physics and Bio-Phys
Masuda Y.
Butsuri 44(1989)755

Refinement of Crystal Structures by the Rietveld Method
Izumi F.
Oyo-Butsuri 59(1990)1

Influences of Composition and Pressure on the Structures of Superconductors
Izumi F.
J. Jpn. Inst. Met. 29(1990)684

Amorphization in Immiscible Cu-V System by Mechanical Alloying and its Atomic Structure
Mori M, Inou K, Fukunaga T and Mizutani U.
J. S. P. M. 37(1990)648

Atomic Structure of Ni-V Amorphous Alloy Prepared by Mechanical Alloying
Fukunaga T, Homma Y and Suzuki K.
J. S. P. M. 37(1990)644

Compulsory Mixing Down to an Atomic level Immiscible Systems by Ball Milling
Fukunaga T.
J. Adv. Sci. 2(1990)241

Structural Changes in V-M(Fe, Cu) Systems Induced by Mechanical Alloying
Mori M, Fukunaga T, Mizutani U and Misawa M.
J.S.P.M. 38(1991)71

Amorphization of Immiscible Cu-Ta Powders Subjected to Mechanical Alloying
Lee C.H, Sakurai K, Fukunaga T and Mizutani U.
J.S.P.M. 38(1991)83

A Grobal View for Japanese Neutrons
Endoh Y.
Butsuri 46(1991)1013

P AND T Violations
Masuda Y.
Butsuri 46(1991)1047

Dynamics in Noncrystalline States of Polymers
Kanaya T.
Butsuri 46(1991)1035

Formation of Unequilibrium Phase and Structural Changes in V-M (M=Cu, Fe) System Subjected to Mechanical Alloying
Fukunaga T, Mori H and Mizutani U.
Rep. Toyota Phys. Chemi. Res. Inst. 44(1991)104

Crystallochemical Approach to High-Tc Superconductors
Izumi F.
Chemistry Today, May (1991)12

Atomic Structure for Amorphous Materials
Fukunaga T and Misawa M.
Butsuri 46(1991)1042

Structural Observations during Amorphoization Process of the $(Cr_{0.7}Fe_{0.3})$-N System by MA
Fukunaga T, Ishikawa E and Mizutani U.
J. S. P. M. 38(1991)102

Invitation to the Neutron Scattering Research
Yamada Y and Watanabe N.
Butsuri 46(1991)998

Crystal and Magnetic Structures of High-Tc Copper Oxide Superconductor (Structure Fluctuations and Superconductivity)
Yamada Y.
J. Cryst. Soc. Jpn. 33(1991)55

Hydrophilicity of the Hydrophobic Regions in Biomembranes
Yabuki S.
Butsuri 46(1991)1037

Instruments at a Pulse Source KENS
Furusaka M.
Butsuri 46(1991)1010

Chemical Structure of Ni-Ti Neutron Zero Scattering Amorphous Powders Prepared by MA
Fukunaga T, Misawa M, Suzuki K and Mizutani U.
J. S. P. M. 38(1991)67

Crystal Structure of High-Tc Superconductors
Asano H.
Butsuri 46(1991)1023

Future prospect-Pulsed Neutron Source
Watanabe N.
Butsuri 46(1991)1016

Neutron Magne01. GENtic Scattering Studies from Strongly Correlated Electron Systems
Endoh Y.
Butsuri 46(1991)1019

Neutron Scattering Experiments in High Magnetic Field
Motokawa M.
Butsuri 46(1991)1028

Neutron Scattering from Fractal Objects
Ikeda H.
Butsuri 46(1991)1021

Chemical Short Range Structure of Amorphous Alloy Prepared by MA
Fukunaga T.
Rep. Toyota Phys. Chem. Res. Inst. 45(1992)1

Variegated Fields of Research Observed by Neutrons
Watanabe N.
Techno News Tsukuba (1992)11

Neutron Scattering with an Intense Spallation Neutron Source
Watanabe N.
Japan Scientific Monthly 45(1992)1001

TOF Neutron Powder Diffraction
Asano H and Kamiyama T.
J. Cryst. Soc. Jpn. 34(1992)2-22

Structural Change into Amorphous Phase Subjected to Mechanical Alloying
Fukunaga T.
Engineering Materials 40(1992)38

Thermal Property and Chemical Short Range Structure for $(Fe_6Ni_{24})_x(Ti_{70}Cu_{30})_{1-x}$ Amorphous Alloy Synthesized by MA
Fukunaga T, Okasaka K and Mizutani U.
J.S.P.M. 40(1993)96

Amorphization of Immiscible Cu-V Sysytem by MA under the N_2 Gas Atomsphere
Kuroda N, Fukunaga T and Mizutani U.
J.S.P.M. 40(1993)92

17. KEK Internal

Time Analyzer System
Satoh S, Ikeda S and Masuda Y.
KEK Internal 82-2 (Apr. 1982)

Time Analyzer System III
Satoh S.
KEK Internal 85-8 (Dec. 1985)

TOP Data Acquesition System Using the Personal Computer PC 9801
Mitusda S, Endoh Y and Itoh S.
KEK Internal 85-13

Safty Analysis of Depleted Uranium Target System for Pulsed Spallation Neutron Source
Kumada T, Sasaki H, Masuda Y, Misawa M, Watanabe N, Katoh K, Kondoh K and Miyajima M.
KEK Internal 88-11 (Oct. 1988)

ICP (Instrument Control Program) for KENS
Arai M, Johnson M.W. and Furusaka M.
KEK Internal 89-6

Chopper Phasing in KENS to Booster Synchrotron
Arai M, Arakida Y, Kohgi M and Hosoda M.
KEK Internal 89-9

CAMAC Crate Controller for Macintosh Computer
Satoh S.
KEK Internal 90-25

ECP (Evviroment Control Program) for KENS
Arai M, Watanabe T, Itoh S, Suzuki J and Ohoyama K.
KEK Internal 89-16

Guideline for Designing Accelerator Interlocks and Related Softy Equipments in KEK
Ishii K, Irie Y, Kobayashi K, Kobayashi H, Kondoh K, Sakai S, Takasaki M, Takeda S, Miyajima M, Ban S and Hirayama I
KEK Internal 90-1 (Apr. 1990)

Development of 8-Input Amplifier (K-AMP2) and Multi-Channel Time-Analyzer Modules (TA15 and TA16) for Nuetron Scattering Experimen
Satoh S and Furusaka M.
KEK Internal 92-4

18. Proceedings of Workshops

Proc. of the Meeting on BSF Future Prospects
Ed. Adachi T.
KEK Internal 82-6 (Aug. 1982)

Proc. of the Meeting on BSF Future Prospects-II
Ed. Adachi T and Masuda Y.
KEK Internal 83-7 (Dec. 1983)

Proc. of the Meeting on BSF Future Prospects-III
Ed. Watanabe N and Nagamine K.
KEK Internal 84-2 (Dec. 1984)

The First KEK Symposium on Ultra Cold Neutrons (UCN) (KEK, Tsukuba, March 10, 1988)
Ed Yoshiki H.
KEK Report 88-3

The Workshop on Neutron Scattering Research with Intense Spallation Neutron Source "Today and Tomorrow", (Tsukuba, October 6-7, 198
Ed. Watanabe N, Arai M et. al.
KEK Internal 88-9

Proc. of the Workshop on Spin Glass Systems (KEK, Tuskuba, February 21, 1989)
Ed. Arai M.
KEK Internal 88-22

The Workshop of the High Resolution Neutron Powder Diffraction Method, (KEK, Tuskuba, March 6, 1989)
Ed. Watanabe N and Asano H.
KEK Internal 89-3

JHP/KENS-II Workshop (KEK, Tuskuba, March 29, 1989)
Ed. Ikeda S and Misawa M.
KEK Internal 89-13

The 2nd KEK Symposium on Ultra Cold Neutrons (UCN) (KEK, Tsukuba, March 11, 1989)
Ed Yoshiki H.
KEK Report 89-13

Proc. of the Second Workshop of Japan-UK Collaboration on Neutron Scattering Research (KEK, Tsukuba, November 1, 1989)
Ed. Watanabe N, Arai M and Ikeda S.
KEK Report 89-19

Proc. of the Workshop on Polymer Science Studied by Neutron Scattering (KEK, Tuskuba, Mar. 15, 1989)
Ed. Kaji K., Kurita K, Izumi Y and Furusaka M.
KEK Internal 90-3

Proc. of the Workshop on Materials Science Studied by Neutron Scattering (KEK, Tuskuba, Apr. 14-15, 1989)
Ed. Furusaka M.
KEK Internal 90-4

Proc. of the Workshop on Structure Study of Biology by X-Ray and Neutron Scattering (KEK, Tsukuba, Mar. 6-7, 1989)
Ed. Niimura N and Furusaka M.
KEK Internal 90-5

Proc. of the Workshop on Small Angle Neutron Scattering (KEK, Tuskuba, Feb. 23, 1989)
Ed. Furusaka M.
KEK Internal 90-6

TUNNEL 901 (KEK, Tuskuba, March 8, 1990)
Ed. Ikeda S.
KEK Internal 90-7

TUNNEL 902, Japan-UK collaboration on Neutron Scattering Research (KEK, Tuskuba, April 24, 1990)
Ed. Ikeda S.
KEK Internal 90-17

Proc. of The Workshop on Statistical Physics on Magnetic Materials and Neutron Scattering (KEK, Tuskuba, February 23, 19
Ed. Yoshizawa H, Arai M and Endoh Y.
KEK Internal 90-18

Proc. of the Workshop on Polymer Science Studied by Neutron Scattering (KEK, Tsukuba, Mar. 20, 1990)
Ed. Kanaya T and Furusaka M.
KEK Internal 90-26

Current Status and Future Prospects of Powder Diffraction
Ed. Kamiyama T, Asano H and Furusaka M.
Proc. of the Japan-UK Joint Meeting on Neutron Powder Diffraction (KEK, Tuskuba, April 23, 1990), KEK Internal 90-30

Proc. of the Workshop on Neutrons in Biology at KENS (1990) (KEK, Tsukuba, Sept. 29, 1990)
Ed. Niimura N and Furusaka M.
KEK Proceedings 91-11

KDP 902 (KEK, Sept. 18, 1990)
Ed. Ikeda S.
KEK Proceedings 91-3

Proc. of the Workshop on Pulsed Neutron Scattering from Magnetic Materials (KEK, Tsukuba, Mar. 28, 1991)
Ed. Ikeda H.
KEK Proceedings 91-4

Proc. of the Workshop on Scattering Experiments under Extreme Conditions (KEK, Tsukuba, Oct. 12-13, 199
Ed. Sakai N, Ikeda H and Ando M.
KEK Proceedings 91-9

Current Status and Future Prospects of Diffraction JAPAN-USA Joint Meeting -Proc. of the Japan-USA Joint Meeting on Diffraction- (KEK, Tuskuba, Mar. 5, 19
Ed. Kamiyama T, Asano H and Furusaka M.
KEK Proceedings 92-1

Proc. of the Workshop on Formation of Supermolecular structures in Composite Fluid: Phase Rule and Dynamics (KEK, Tsukuba, Jul. 2-3, 19
Ed. Tanaka F, Ohota T and Ikeda H.
KEK Proceedings 92-10

Current Status and future Prospect of Space and Time Reversal Symmetry Violation on Low Energy Neutron Reactions (KEK, Tsukuba, June 10, 19
Ed. Masuda Y.
KEK Proceedings 92-18

KDP 903 (KEK, Jan. 21-22, 1992)
Ed. Ikeda S.
KEK Proceedings 92-3

19. KENS Report

KENS Report-I
Ed. Ishikawa Y.
KEK Internal 80-1 (Feb. 1980)

KENS Report-II, KEK (Mar. 1981)
Ed. Ishikawa Y, Watanabe N, Endoh Y, NIimura N and Newsam S. M.
Proc. of the 4th Meeting of Int. Collaboration on Advanced Neutron Sources (ICANS-IV) (KEK, Tsukuba, Oct. 20-24, 1980)

KENS Report-III
Ed. Ishikawa Y, NIimura N and Ikeda S.
KEK Internal 82-5 (July 1982)

KENS Report-IV
Ed. Ishikawa Y, Niimura N and Ikeda S.
KEK Internal 83-4 (Sept. 1983)

KENS Report-V (1984)
Ed. Ishikawa Y, Niimura N and Misawa M.
KEK Internal 84-2

KENS Report-VI (1985/86)
Ed. Watanabe N, Arai M, Endoh Y and Kohgi M.
KEK Internal 86-2

KENS Report-VII (1987/88)
Ed. Watanabe N, Arai M, Asano H and Endoh Y.
KEK Internal 88-2 M

KENS Report-VIII (1989/90)
Ed. Ikeda H, Furusaka M and Watanabe N.
KEK Internal 90-2 M

20. Proc. of Int. Conf.

Proc. of the 11th Meeting of Int. Collaboration on Advanced Neutron Sources (ICANS-XI)
Ed. Misawa M, Furusaka M, Ikeda H and Watanabe N.
(KEK Tuskuba, Oct. 22-26, 1990), Vol. 1 & 2

21. Other Publications

GEMINI Design Report
Ed. Kumada M and Ishigaki S.
KEK

Members of Committees

*Chairman
**Project Manager

Committee for Booster Synchrotron Utilization Facility

ENDOH, Yasuo	(Tohoku Univ.)
IMAZATO, Jun	(KEK)
IKEDA, Hironobu	(KEK)
KAMIMURA, Hiroshi*	(Science Univ. of Tokyo)
KIHARA, Motohiro	(KEK)
MASAIKE, Akira	(Kyoto Univ.)
KONDOH, Kenjiro	(KEK)
NAGAMINE, Kanetada	(Univ. of Tokyo)
TUJII, Hirohiko	(Univ. of Tsukuba)
WATANABE, Noboru	(KEK)
YAMANE, Isao	(KEK)

Neutron Scattering Program Advisory Committee

ENDOH, Yasuo*	(Tohoku Univ.)
FUJII, Yasuhiko	(Univ. of Tokyo)
IKEDA, Hironobu	(KEK)
MITSUI, Toshio	(Meiji Univ.)
NODA, Ichiro	(Nagoya Univ.)
SUZUKI, Kenji	(Tohoku Univ.)
WATANABE, Noboru	(KEK)
TAKAYAMA, Hajime	(Univ. of Tsukuba)

Japan-UK Steering and Program Advisory Committee

ENDOH, Yasuo*	(Tohoku Univ.)
FUJII, Yasyhiko	(Univ. of Tokyo)
IKEDA, Hironobu**	(KEK)
IWASAKI, Hiroshi	(KEK)
MITSUI, Toshio	(Meiji Univ.)
NODA, Ichiro	(Nagoya Univ.)
SUZUKI, Kenji	(Tohoku Univ.)
WATANABE, Noboru	(KEK)
TAKAYAMA, Hajime	(Univ. of Tsukuba)
TAKAHASHI, Kasuke	(KEK)